FINAL REPORT

Development of an Integrated Field Test/Modeling Protocol for Efficient In Situ Bioremediation Design and Performance Uncertainty Assessment

SERDP Project ER-2311

APRIL 2019

Linda M. Abriola
Tufts University

Natalie L. Cápiro
Tufts University (now Auburn University)

John A. Christ
US Air Force Academy (now S&B Christ Consulting)

Liyang Chu
Nobis Engineering

Eric L. Miller
Tufts University

Kurt D. Pennell
Tufts University (now Brown University)

SERDP
DOD · EPA · DOE

Page Intentionally Left Blank

Page Intentionally Left Blank

REPORT DOCUMENTATION PAGE

1. REPORT DATE (DD-MM-YYYY)	2. REPORT TYPE	3. DATES COVERED (From - To)
04/01/2019	SERDP Final Report	7/3/2013 - 7/3/2018

4. TITLE AND SUBTITLE	5a. CONTRACT NUMBER
Development of an Integrated Field Test/Modeling Protocol for Efficient In Situ Bioremediation Design and Performance Uncertainty Assessment	13-C-0011

5b. GRANT NUMBER

5c. PROGRAM ELEMENT NUMBER

6. AUTHOR(S)	5d. PROJECT NUMBER
Linda M. Abriola	ER-2311

5e. TASK NUMBER

5f. WORK UNIT NUMBER

7. PERFORMING ORGANIZATION NAME(S) AND ADDRESS(ES)	8. PERFORMING ORGANIZATION REPORT NUMBER
Tufts University	ER-2311

9. SPONSORING/MONITORING AGENCY NAME(S) AND ADDRESS(ES)	10. SPONSOR/MONITOR'S ACRONYM(S)
Strategic Environmental Research and Development Program 4800 Mark Center Drive, Suite 17D03 Alexandria, VA 22350-3605	SERDP

11. SPONSOR/MONITOR'S REPORT NUMBER(S)
ER-2311

12. DISTRIBUTION/AVAILABILITY STATEMENT

DISTRIBUTION A. Approved for public release: distribution unlimited.

13. SUPPLEMENTARY NOTES

14. ABSTRACT

The overarching goal of this research project was to develop and demonstrate a remediation design and performance assessment protocol that can efficiently assess the suitability of a remediation technology and predict remedial performance (e.g., mass removal/destruction) and the uncertainty associated with such predictions. This protocol couples careful characterization of the contaminant source with down-hole treatability testing and mathematical modeling.

15. SUBJECT TERMS

Integrated Field Test/Modeling Protocol, Efficient In Situ Bioremediation Design, Performance Uncertainty Assessment

16. SECURITY CLASSIFICATION OF:			17. LIMITATION OF ABSTRACT	18. NUMBER OF PAGES	19a. NAME OF RESPONSIBLE PERSON
a. REPORT	b. ABSTRACT	c. THIS PAGE			Linda M. Abriola
UNCLASS	UNCLASS	UNCLASS	UNCLASS	301	19b. TELEPHONE NUMBER (Include area code) 617-627-8685

Page Intentionally Left Blank

Table of Contents

List of Figures

List of Tables

List of Acronyms

ASTM	American Society for Testing And Materials
BD	Back Diffusion
BDI	Bio-Dechlor Inoculum
bgs	Below Ground Surface
BTC	Breakthrough Curve
Cis-DCE/DCE	Dichloroethene Isomers
CMT	Continuous Multi-Channel Tubing
CRF	Conditional Random Field
CV	Coefficient of Variation
DAD	Diode Array Detector
Dhc	*Dehalococcoides Mccartyi*
DHT	Down-Hole Treatability
DNA	Deoxyribonucleic Acid
DNAPL	Dense Non-Aqueous Phase Liquid
DOC	Dissolved Organic Carbon
DRF	Discriminative Random Field
DSP	Dispersivity
ECD	Electron Capture Detector
ESL	Tufts University Environmental Sustainability Laboratory
FAC	Flux Averaged Concentration
FID	Flame Ionization Detector
FOSM	First-Order Second-Moment
Geo	*Geobacter* Species
*Geo*sz	*Geobacter Lovelyii* Strain Sz
GC	Gas Chromatograph
GSLIB	Geostatistical Software Library
GTP	Ganglia-to-Pool
HDPE	High Density Polyethylene
HPLC	High Performance Liquid Chromatograph
IC	Ion Chromatograph
ICP-OES	Inductively Coupled Plasma-Optical Emission Spectrum
ITRC	Interstate Technology & Regulatory Council
MC	Monte Carlo
MCM	Markov Chain Model
MCMC	Markov Chain Monte Carlo
MH	Metropolis-Hastings
MLS	Multilevel Sampling
MODFLOW	Modular Three-Dimensional Finite-Difference Flow Model
MRD	Microbial Reductive Dechlorination
MRF	Markov Random Field
MRMT	Multi Rate Mass Transfer
MT3DMS	Modular Three Dimensional Transport Simulator
M-VALOR	Michigan Vertical and Lateral Organic Redistribution
MW	Molecular Weight
NRC	National Research Council
NRMSE	Normalized Root Mean Square Error
ODE	Ordinary Differential Equation

ORP	Oxidation Reduction Potential
PCE	Tetrachloroethylene
PF	Pool Fraction
PTFE	Polytetrafluoroethylene
PV	Pore Volume
QPCR	Quantitative Polymerase Chain Reaction
RDase	Reductive Dehalogenase
RMSE	Root Mean Square Error
RNA	Ribonucleic Acid
RRNA	Ribosomal Ribonucleic Acid
SABRE	Source Area Bioremediation
TCE	Trichloroethylene
TOC	Total Organic Carbon
TP/MC	Transition-Probability-based Markov Chain
USEPA	United States Environmental Protection Agency
UTCHEM	University of Texas Chemical Compositional Simulator
VC	Vinyl Chloride
VFA	Volatile Fatty Acid
VOA	Volatile Organic Analysis
VOC	Volatile Organic Compound
1-D	One Dimensional
2-D	Two Dimensional
3-D	Three Dimensional

Acknowledgements

Abstract

a. Objectives: Despite significant advances in our understanding of chlorinated solvent source zones and the maturation of several *in situ* remediation technologies (e.g., bioremediation), our ability to provide *a priori* predictions of the performance of remediation technologies in the field remains severely limited. This is attributed, in large part, to our inability to accurately quantify source zone mass and its spatial distribution, as well as to accurately estimate effective *in situ* mass transfer and transformation rates. The overarching goal of this research project was to develop and demonstrate a remediation design and performance assessment protocol that can efficiently assess the suitability of a remediation technology and predict remedial performance (e.g., mass removal/destruction) and the uncertainty associated with such predictions. This protocol couples careful characterization of the contaminant source with down-hole treatability testing and mathematical modeling,

b. Technical Approach: This project focused on a representative TCE-contaminated site (Commerce Street Superfund Site, Williston, VT) that supported the development, refinement and testing of the protocols and software tools. The project was implemented in three phases; Phase I involved the development of protocols and software tools for efficient estimation of key source characteristics (mass distribution metrics) governing remediation technology selection, design, and performance. In Phase II, work focused on laboratory scale batch and aquifer cell testing to (a) support source zone characterization, (b) provide kinetic data for testing and refinement of upscaled mathematical models, and (c) guide the design and implementation of field-scale reactivity tests. A down-hole treatability (DHT) test was then conducted in Phase III to estimate (confirm) the *in situ* rate parameters needed for subsequent site-specific protocol application. Upscaled models and uncertainty analysis tools were incorporated into the widely-used solute transport modeling platform, MT3DMS, to facilitate adoption by practitioners and site managers.

c. Results

Phase I: A novel statistical approach was developed and implemented for the reconstruction of source zone mass distributions and quantification of source zone metrics and associated uncertainty in heterogeneous subsurface formations. The approach employs trained discriminative random field (DRF) models, in conjunction with Monte-Carlo sampling methods, to generate contaminant mass realizations, conditioned on measured borehole data. Post-processing of these realizations yields estimates of source zone metrics (e.g., pool fraction, total mass) and associated uncertainty. These metrics and approximations of uncertainty can be used to predict source zone longevity, mass recovery behavior, and remedial performance and to inform further sampling for characterization and remediation. DRF model performance was evaluated through comparisons of predicted metrics with those obtained from 'true' mass distributions, generated with validated flow and transport models. Comparisons demonstrate that the trained DRF model can reconstruct realistic saturation and concentration fields for a range of NAPL spill scenarios, significantly outperforming traditional kriging approaches.

Phase II: A matrix of laboratory microcosm experiments, assembled from site soil and groundwater samples, was undertaken to estimate batch TCE dechlorination rates in unaugmented and SiREM KB-1®-amended systems. Results demonstrated the need for bioaugmentation at the Commerce St. site. An aquifer cell system was constructed with field site soil, pre-loaded with TCE, bioaugmented with KB-1®, and operated to mimic the field-scale downhole treatability test. Effluent and side port measurements of volatile fatty acid, chlorinated ethene and ethene, and biomass concentrations were used, in conjunction with an enhanced version of the transport simulator MT3DMS with batch-measured rates, to explore effective bio-reaction rates (e.g.,

maximum substrate utilization rate, μ_{max}) under representative heterogeneous subsurface conditions. Batch-measured rates provided a good prediction of aquifer cell behavior (average relative error of 19%) when heterogeneity was explicitly modeled and TCE and *cis*-DCE inhibition of VC transformation was neglected. However, ethene production was significantly under predicted when a uniform permeability was assumed, demonstrating the influence of local heterogeneity on dechlorination prediction accuracy. Ethene concentrations varied spatially within the domain, primarily associated with low permeability layers. To investigate the effect of the residence time on dechlorination, the flow rate was reduced by 50%. Under these conditions, the proportion of ethene (molar basis) increased from 26% to 54%. In this phase of the project, correlations for effective mass transfer coefficients were also developed to describe back-diffusion/desorption under a range of heterogeneous formation conditions.

Phase III: Employing aquifer cell-calibrated rate parameters adjusted for temperature effects, transport modeling of the field DHT test resulted in an over-prediction of ethene production by a factor of 2. Model sensitivity analyses suggest this discrepancy, observed despite the comparable sizes of the aquifer cell and pilot test treatment zone, was associated with unmodeled heterogeneity. Similar to the cell experiment, when the flow rate in the test zone was reduced by 50%, the observed proportion of ethene increased from 17% to 78% at the end of the treatment zone.

Adjoint sensitivity analysis was employed, in conjunction with a first-order second-moment (FOSM) uncertainty analysis method, to optimize borehole sampling for prediction of down-gradient flux-averaged concentration evolution at a contaminated site. The approach was implemented in MT3DMS, and initial source zone conditions were generated by averaging realizations of the DRF model. Results reveal that optimal sampling locations vary with the prediction time window. Comparison of predictions associated with the optimized versus a uniform sampling approach reveals that the FOSM model yields better estimates of down-gradient flux averaged concentration, associated with a significant reduction in variance.

Project results were integrated into a source zone remediation feasibility framework to guide practitioners on the use of the developed modeling methodologies. This framework provides an efficient method to perform site characterization and obtain screening-level forecasts of site behavior, with and without implementation of treatment remedies. Application of the framework to a realistic synthetic field scenario demonstrated its feasibility and potential benefits during conceptual site model refinement and remedial site management.

d. Benefits: This research provides site managers, regulatory officials and the scientific community with protocols and software tools to (a) efficiently characterize source zone mass metrics and associated uncertainty, (b) estimate relevant mass transfer and reaction rates for use in upscaled models, and (c) predict remedial performance (or evolution of down gradient plume) and associated uncertainty. The methodologies and tools, although developed for microbial reductive dechlorination, are designed with sufficient flexibility to allow for implementation with other remediation technologies or combinations of remedies. In addition, we anticipate that other types of remedial performance data, such as isotopic analysis and proteomics, could be incorporated into the developed models to allow for refined predictions of remedial performance and optimization of remediation-specific site characterization in near real-time.

Extended Abstract SERDP Project ER-2311: Development of an Integrated Field Test/Modeling Protocol for Efficient In Situ Bioremediation Design and Performance Uncertainty Assessment

Linda M. Abriola, Tufts University (PI)

Natalie L. Cápiro; John A. Christ; Liyang Chu; Eric L. Miller; Kurt D. Pennell (co-PIs)

Introduction

Widespread use of chlorinated solvents, such as tetrachloroethene (PCE) and trichloroethene (TCE), in dry cleaning and degreasing operations has resulted in groundwater contamination at thousands of industrial facilities and government installations throughout the United States and abroad (ITRC, 2011; NRC, 2005). In most cases, chlorinated solvent spill sites are conceptualized as consisting of two main regions, a highly contaminated source zone that often contains free product, commonly referred to as a dense non-aqueous phase liquid (DNAPL), and a down-gradient groundwater plume that contains both dissolved- and sorbed-phase contamination (ITRC 2003). The long-term persistence of DNAPLs (as entrapped ganglia or pools) in the source zone and the high local contaminant concentrations associated with their presence also creates a strong driving force for contaminant diffusion into lower permeability layers, where dissolved and sorbed mass is subsequently sequestered. Substantial laboratory and field research has demonstrated the importance of this sequestered mass to the persistence of down gradient contaminant plumes (e.g., DiFilippo and Brusseau, 2008; NRC, 2005; Parker et al., 2008; Suchomel and Pennell, 2006) and the long term performance (mass removal or transformation rates) of most remedial technologies, in particular those that require the delivery of chemical additives or amendments (e.g., Christ et al., 2010; Kaye et al., 2008; Stroo et al., 2003).

Although substantial progress has been made in the development of both noninvasive and invasive source zone characterization technologies in the past two decades (e.g., ITRC, 2003; Kavanaugh et al., 2003; Kram et al., 2002; NRC, 2005), these technologies can typically provide quantitative information on contaminant mass distributions only in the vicinity of the sampling location, which may not be representative of the entire source zone. To address the limitations associated with sparse sampling, it is now common practice to employ statistical interpolation approaches (e.g., kriging) to estimate contaminant concentration at unsampled locations using available borehole data. However, a primary drawback to such approaches is their limitation in interpolating highly sparse and discontinuous patches of DNAPL in heterogeneous domains (e.g., Maji et al. 2006).

The challenges posed by detailed (fine-scale) delineation of source zone mass have also led to the development and application of averaged characterization metrics, such as DNAPL mass spatial moments, pool fraction, trajectory-averaged saturation statistics, and 'source strength', that can represent the salient features of the mass distribution (e.g., Stroo et al. 2003; ITRC 2004; Jawitz et al., 2005; Christ et al., 2006; Saenton & Illangasekare, 2007; Chen and Jawitz 2009). Here, the hypothesis is that such metrics can be employed in upscaled mathematical models to predict source longevity and down-gradient flux evolution under natural or remedial conditions. Comparisons to laboratory data (Fure et al., 2006; Zhang et al., 2008; Christ et al., 2010; DiFilippo & Brusseau, 2011) and field data history matching exercises ((DiFilippo and Brusseau 2008; Falta et al. 2005b)) suggest that such approaches may hold promise, particularly for use in screening remedial alternatives.

Unfortunately, most laboratory treatability studies do not adequately mimic the mass transfer processes, such as rate-limited dissolution, diffusion and desorption, that control elution of sequestered mass and remedial system performance in a natural heterogeneous formation. Thus, such studies tend to overestimate potential treatment effectiveness. For example, a comparison of 138 chlorinated solvent bioremediation field and laboratory studies revealed that median laboratory rate constants were consistently higher (up to one order-of-magnitude) than observed field rate constants (Suarez and Rifai 1999). The assumptions underlying the selection of a down-hole treatability (DHT) methodology for this research are that: (a) even advanced assessment tools, such as molecular probes, fail to provide reaction rate information necessary to predict remediation extent in complex subsurface environments; and (b) the tool or method should provide information that is relevant at the field scale and can be readily incorporated into model(s) for simulation of remediation performance and uncertainty assessment.

The above discussion highlights the urgent need for better field treatability test methods to predict potential remedial system performance and for the development of improved, cost-effective, field characterization methods and associated modeling tools that encompass all source zone mass and facilitate the identification of the most critical source zone properties that will govern mass persistence and the performance of remedial options.

Objectives

The overarching goal of this research project is to develop and demonstrate a remediation design and performance assessment protocol that can efficiently assess the suitability of a remediation technology and predict remedial performance (e.g., mass removal/destruction) and the uncertainty associated with such predictions. This protocol couples careful characterization of the contaminant source with down-hole treatability testing and mathematical modeling. The research directly responds to the following specific objectives in the SERDP Statement of Need:

- Development of field measurements or methodologies that provide predictive capability of performance to reduce the uncertainty associated with long-term performance so that decisions can be made early in the remedial process to avoid years of suboptimal performance.
- Development of field measurements or methodologies that provide data to optimize treatment if current operations are not expected to meet performance objectives.
- Development of assessment procedures and methodologies that aid in the decision to discontinue operation of a technology and implement an alternative technology.

The fundamental hypothesis of this work is that it is impossible to provide reliable predictions of remedial performance, and its associated uncertainty, without consideration of the complex coupling between contaminant transformation/reaction rates, contaminant mass distribution (spatial configuration and phase partitioning), and the processes influencing the accessibility of this mass (e.g., heterogeneous flow paths, diffusion). Although the project utilizes microbial reductive dechlorination as a representative in situ remediation technology, the developed protocol and associated modeling tools are applicable to other remediation technologies, such as monitored natural attenuation and chemical oxidation.

Technology Approach

The research approach involves coupling of site characterization, remediation performance assessment (reaction rates), upscaled model development, and numerical simulations of remedial

performance and uncertainty. The study focused on a representative TCE-contaminated site (i.e. Commerce Street Superfund Site, Williston, VT) to facilitate the development, refinement and testing of protocols and software tools within the context of an actual field site.

To achieve its goal, the project was structured around three phases that addressed: (i) source and plume characterization, (ii) upscaled mass transfer and transformation rates, and (iii) field-scale reactivity and predictions of remedial performance. The project work plan is illustrated in Figure 1.

Figure E-1. Project work plan.

Phase I focused on the development and demonstration of methods/modeling tools to characterize the source zone for subsequent remedial design, implementation, and assessment. Here, the specific objective was to develop a protocol and software tools that employ measured field data to produce a representation of the subsurface source zone that captures the spatial distribution and uncertainty associated with key features (i.e., permeability, microbial activity/mass, and sequestered contamination [sorbed, immobile aqueous, and NAPL]) that control remedial performance.

Phase II focused on batch and bench-scale laboratory testing, and upscaled mathematical model development to support the design and implementation of a field remediation strategy. Here, the performance of microbial reductive dechlorination was evaluated in aquifer cells that were representative of field conditions, and the resulting data were employed to develop and evaluate upscaled models to describe effective mass transfer and reaction rates.

Phase III focused on the estimation and application of effective rate parameters in field-scale remediation. In this phase, a downhole treatability test was conducted at the Commerce Street Superfund Site to estimate effective *in situ* transformation/reaction rates and to support the design and assessment of site remediation strategies. Here a mathematical model, refined and validated in Phase II, was employed to estimate effective field transformation rates. Estimated rates were

then compared to batch- and aquifer cell-measured rates to shed light on the processes controlling remediation at the field scale. In addition, a traditional three-dimensional flow and transport simulator was adapted and employed, in conjunction with the source zone characterization and uncertainty results from Phase I, to propose an optimal sampling strategy coupling sensitivity analysis and uncertainty quantification.

Results and Discussion

Phase I

A novel statistical approach was developed and implemented for the reconstruction of non-aqueous phase liquid (NAPL) source zone realizations and the quantification of source zone metrics and associated uncertainty. This approach employed discriminative random field (DRF) models, originally introduced for computer vision applications, to model the spatial distributions and relationships among source zone properties (i.e. permeability, NAPL saturation and aqueous concentration distributions) consistent with commonly collected field data. Application of DRF models required a limited number of full-scale simulations to train the model parameters. Monte-Carlo sampling methods based on these trained models then provided an efficient method to generate contaminant mass realizations conditioned on measured borehole, bypassing the need to run computationally intensive, PDE-based simulations of physical flow and transport. Post-processing of these realizations yielded approximations of uncertainty to inform further sampling for characterization and remediation (Phase III). The reconstructed contaminant mass realizations provided sufficient information for calculating averaged characterization metrics, such as total contaminant mass and pool fraction (PF), used to predict source zone longevity, mass recovery behavior and remedial performance. The model performance was evaluated through comparisons of these predicted source zone metrics with those obtained from the 'true' mass distributions generated with validated flow and transport models. These comparisons clearly demonstrated that the trained DRF model can reconstruct realistic saturation and concentration fields conditioned to borehole data for a range of NAPL spill scenarios (see example in Figure E-2). The model was also shown to significantly outperform traditional kriging approaches in reconstructing NAPL mass distributions.
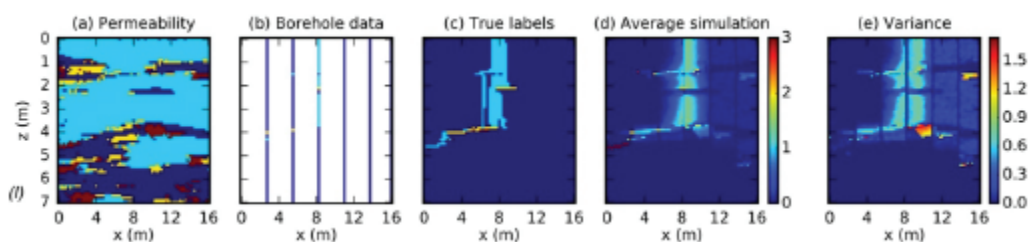
Figure E-2. Example output of BRAINS model for estimation of DNAPL saturation distribution profile in a heterogeneous formation. Depicted output (d) is the average of 2000 realizations.

Selected Conclusions from Phase I:

- **A discriminative random field (DRF) model (BRAINS) was developed and implemented for contaminant source zone characterization and uncertainty quantification.** The DRF model is completely characterized by a small collection of parameters (w and v vectors). These parameters are determined through a 'training' process, employing a set of source zone spill data specific to the selected DNAPL contaminant and geologic environment. Once the DRF parameters are determined, the model can be used to generate realizations of the DNAPL

saturation and aqueous phase concentration using off-the-shelf Metropolis sampling methods. This methodology is far superior to Monte Carlo approaches, which require extensive flow and transport simulations to generate a similar set of realizations and cannot easily account for measured data. .

- **Ensemble averages over realizations of the DRF model represent the expected values for concentration and saturation fields, while the variances provide a quantifiable measure of the uncertainty associated with permeability and contaminant source zone.** These uncertainty measurements were used in Phase III to identify optimal locations for further borehole sampling.

- Model performance was assessed by comparing estimated and 'true' metrics for contaminant mass distributions in a structured heterogeneous unconsolidated depositional aquifer environment. **The trained DRF model produced realistic saturation and concentration fields, conditioned to borehole data for a range of NAPL spill scenarios (release rates, spill ages, pool fractions). Comparison with a traditional kriging approach clearly demonstrated the superiority of BRAINS in reconstructing DNAPL saturation distributions and associated DNAPL architecture metrics.**

Phase II

Microcosms were provided with lactate and trichloroethene (TCE) to derive dechlorination rates in a batch system and one set was amended with SiREM KB-1®. Microcosm and batch reactor experiments demonstrated the need for bioaugmentation and biostimulation at the site to transform TCE to ethene. The native microbial population was capable of transforming TCE to *cis*-DCE using the dissolved organic carbon in site groundwater but completed the transformation more quickly when supplied with lactate as an electron donor. The absence of continued dechlorination in most reactors indicated a low population of *Dhc* harboring the RDase genes necessary to produce VC and ethene and a non-uniform distribution of organisms at the site. Bioaugmentation of reactors with KB-1® or BDI was successful, facilitating the transformation of TCE to ethene in an average of 37 days. A robust numerical model incorporating adsorption of contaminants to soil and partitioning into the bottle headspace was created to simulate microbial reductive dechlorination in the batch reactors and microcosms. The numerical model and Matlab fitting routine were able to match the chlorinated ethene and ethene concentrations observed in the KB-1® bioaugmented microcosms, providing culture-specific yield coefficients and substrate utilization rates that were used in later modeling work.

Concurrently, an aquifer cell system was constructed with soil from the Commerce Street field site, loaded with TCE, and configured to mimic the field-scale downhole treatability test. The aquifer cell was provided with lactate and then bioaugmented with KB-1®. Effluent and side port measurements of volatile fatty acid concentrations, chlorinated ethene and ethene concentrations, and biomass abundance were used in conjunction with an enhanced version of the modular three-dimensional multispecies transport simulator MT3DMS to explore effective bio-reaction rates (e.g., maximum substrate utilization rates (μ_{max}). This enhanced version of MT3DMS is capable of simulating anaerobic reductive dechlorination of multiple contaminants in heterogeneous environments, incorporating consumption of the carbon source by a competitor culture. Microbial reductive dechlorination is modeled with a modified Monod kinetic expression that accounts for limitations due to election donor availability and daughter product inhibition. Model simulations employing batch-measured rates provided a good prediction of aquifer cell behavior (average

relative error of 19%) only when heterogeneity was explicitly modeled and TCE and cis-DCE inhibition of VC transformation was neglected (see Figure E-3). This result was attributed to spatial variations in microbial population and substrate availability created by the presence of physical heterogeneity. Comparison of simulation results for models employing both heterogeneous and uniform domain properties, incorporating the same domain size and transformation rate parameters, revealed that ethene production was underpredicted by the uniform property model. This result contrasts with literature reports of field-scale reductions in observed effective transformation rates. Coupling of laboratory observations with modeling results suggests that transformation to ethene varied spatially within the domain, primarily associated with low permeability layers (zones with longer residence times). This variation demonstrates the influence of local heterogeneity on dechlorination prediction accuracy. To investigate the effect of the residence time on dechlorination, the flow rate was reduced by 50%, increasing the proportion of ethene in the aquifer cell (molar basis) from 26% to 54%.

Also in this project phase, upscaled modeling was undertaken to develop solutions and correlations to quantify effective mass transfer coefficients that describe back-diffusion/desorption and bioenhanced NAPL dissolution under a range of heterogeneous formation conditions.
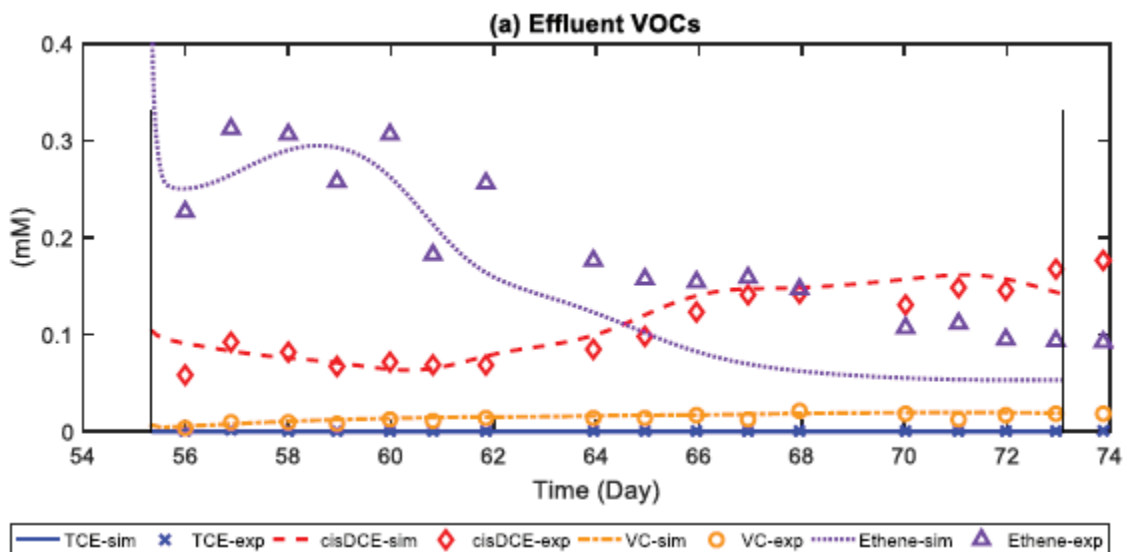
Figure E-3. Comparison between simulated and experiment effluent concentrations for chlorinated ethenes and ethene components. Competitive inhibition was neglected in this simulation.

Selected Conclusions from Phase II

- **An industry-standard groundwater transport simulator, MT3DMS, was adapted to incorporate multi-order Monod kinetics coupled with a microbial growth model to account for biotransformation of multiple components by multiple microbial populations**.

- **Bioenhanced desorption and back diffusion of chlorinated solvents play an important role in mass release in heterogeneous formations.** For the examined experimental conditions, the magnitude of this enhancement was observed to vary spatially and temporally (from 6-55%), with the largest enhancement measured at interfaces with fine-textured, highly sorptive media. These results demonstrate that bioenhanced desorption/back diffusion can significantly reduce plume persistence and remedial cleanup timeframes.

- **Temporal and spatial population shifts in the predominant strain of *Dhc* are observed with changes in electron acceptor abundance.** These observations demonstrate the importance of maintaining a robust dechlorinating community harboring multiple RDase genes. When the necessary genes are present, the microbial population is able to adapt to changes in electron acceptor availability associated with varying up gradient concentrations or the back diffusion of chlorinated ethenes from low permeability and highly sorptive materials.

- ***Dhc* cells are capable of penetrating low permeability porous media, including clays.**

- **Observed aquifer cell microbial transformation rates *were* consistent with microcosm (batch)-fitted values, when permeability variations were incorporated** in the model. **Thus, models must incorporate heterogeneity to make accurate predictions of dechlorination**

- **Competitive inhibition was found to be of little significance in heterogeneous-packed formations,** attributed to microenvironments in the aquifer cell and differences in soil/water ratios between microcosm and aquifer cell experiments.

- **Accurate representation of sorption processes (i.e., extent, rate limitations, and nonlinearity) in transport models is crucial to the accurate prediction of plume longevity,** particularly for the prediction of post-DNAPL dissolution longevity; **(de)sorption processes were observed to dominate the rate of mass release (back diffusion) to transmissive zones, following DNAPL dissolution.**

- **An upscaled model was developed and parameterized to describe effective mass transfer (desorption) rates in three dimensional heterogeneous systems.** This Multi-Rate Mass Transfer (MRMT) model, with two constant-in-time first-order rates, was shown to successfully reproduce breakthrough curves.

- **A screening level model was developed and implemented to estimate bioenhancement of DNAPL dissolution.** Nomographs were presented to facilitate graphical estimation of bioenhancement factor expressions for zero-order, first-order, and full Monod transformation kinetics as a function of the Péclet and Damköhler Numbers.

Phase III

A down-hole treatability (DHT) test was conducted at the Commerce St site and test observations were used, in conjunction with the enhanced MT3DMS model, to estimate effective *in situ* biotransformation rate parameters. Simulations of the field pilot test, using aquifer cell-calibrated rate parameters that had been adjusted for temperature effects, resulted in an over-prediction of ethene production by a factor of 2. Model sensitivity analyses suggested that this discrepancy, observed between laboratory and field transformation rates despite the comparable sizes of the aquifer cell and pilot test treatment zone, was associated with unmodeled heterogeniety in flow and biomass distributions. Similar to the behavior observed in the cell experiment, when the flow rate in the test zone was reduced by 50%, the observed proportion of ethene increased from 17% to 78% at the end of the treatment zone. These data demonstrate that controlling residence time is essential to completely detoxify TCE to ethene.

Also in this project phase, adjoint sensitivity analysis was employed, in conjunction with a first-order second-moment (FOSM) uncertainty analysis method, to develop a systematic approach to optimize borehole sampling for prediction of down-gradient flux-averaged concentration (FAC) evolution at a contaminated site. In this approach, an initial conditioned spatial distribution of

contaminant mass is first generated by averaging realizations of the DRF model developed in Phase I. The adjoint state method is then used to quantify the importance of local system properties on down-gradient FAC. The FOSM method, which uses linear approximations to directly propagate parameter and data uncertainties into system states via sensitivity matrices, is employed to estimate the uncertainty of FAC predictions. Both permeability and source zone mass compartments are treated as random variables to account for aquifer heterogeneity, flow irregularity, source zone morphology, and their interlinkages. Then in the decision process, data worth analysis is used to develop an optimal borehole sampling strategy by selecting additional measurements that yield the largest reduction in FAC uncertainty. The entire approach was implemented in the widely-used transport modeling platform MT3DMS to facilitate future adoption by practitioners and site managers. The utility of this approach was demonstrated using numerically generated, two-dimensional, heterogeneous DNAPL source zones. Results reveal that the model-guided sampling strategy recommends additional sampling locations that vary with the prediction time window; optimal borehole measurements are chosen further down-gradient for early time predictions, while up-gradient measurements have larger impact at later times. Locations with low permeability values and high DNAPL saturations are generally good potential candidates for additional measurements. Comparison of predictions associated with the optimized versus a uniform sampling approach reveals that the FOSM model yields better estimates of down-gradient flux averaged concentration, associated with a significant reduction in variance. This innovative sampling strategy, coupling sensitivity analysis and uncertainty quantification, shows promise for enhancement of our ability to guide characterization of source zones under realistic field conditions.

Finally, in this phase, project results were integrated into a source zone remediation feasibility framework to guide practitioners on the use of the developed modeling methodologies (see description in next section). This framework provides an efficient method to perform site characterization and obtain screening-level forecasts of site behavior, with and without implementation of treatment remedies. Application of the framework to a realistic synthetic field scenario in Section VII.A. of the report demonstrated its feasibility and potential benefits during conceptual site model refinement and remedial site management.

Selected Conclusions from Phase III

- **A FOSM uncertainty analysis modeling framework was developed and implemented to estimate variance in predicted flux averaged concentration along a transect down gradient of a DNAPL source zone.** The method honors borehole observations and enables consideration of the coupling among aquifer heterogeneity, flow irregularity, and source zone mass distribution (morphology). The FOSM model was coupled with data worth assessments and implemented in the modeling framework to guide acquisition of additional site data.

- **Application of the FOSM method to numerically generated, field-scale, source zone scenarios revealed that hydraulic conductivity variations and DNAPL saturation distributions tend to dominate FAC predictions.**

- **Down Hole Test results were consistent with trends observed in the aquifer cell experiment.** Bioaugmentation with KB-1® successfully provided a large, viable *Dhc* population capable of transforming *cis*-DCE to ethene over the duration of the pilot test. Lactate pulses were rapidly fermented and provided a growth substrate to increase the *Dhc* population. Growth stalled when the residence time was insufficient to increase the degree of

cis-DCE dechlorination. A reduction in pumping rate, increased the extent of transformation of *cis*-DCE to ethene and allowed the *Dhc* population to continue to increase in abundance.

Implications for Future Research and Benefits

This research provides site managers, regulatory officials, and the scientific community with protocols and software tools to (a) efficiently characterize site conditions, (b) obtain relevant reaction rates and develop upscaled models, and (c) predict remedial performance and associated uncertainty. The developed models and their associated implementation protocols are equally applicable to any remedial technology whose application is hindered by interphase mass transfer limitations, i.e., by heterogeneity in formation properties and contaminant mass distributions.

A straightforward framework (Figure E-4) was presented for implementation of the developed mathematical models for near-source site characterization and plume response prediction. This framework couples the 2D BRAINS model with an existing upscaled mass transfer model previously developed under SERDP sponsorship (Christ et al., 2010). The trained BRAINS model is used to generate a set of 2D representations of contaminant mass distributions along a plume centerline. These results enable the estimation of effective, or upscaled, parameters employed in the screening model, as well as the estimation of the uncertainty associated with screening model predictions.

Figure E-4 represents the work flow for site characterization and screening-level FAC assessment. Here, once a DNAPL source zone site has been selected, available data on the site geology/stratigraphy are collected and matched to a representative site subsurface permeability model. The permeability models are then linked to a library of machine learning characterization tools (i.e. BRAINS library).

After a site-matched characterization tool is obtained, BRAINS is employed, along with measured borehole data to estimate source zone metrics. This procedure requires only field-measured borehole data (permeability, saturation, sorption and aqueous concentration) as inputs, as well as some formation geostatistical characteristics. The first step in applying BRAINS to a real-word problem is to generate multiple realizations of the permeability field, conditioned on borehole measurements. Once the permeability realizations have been generated, the site-appropriate trained BRAINS model is applied to each permeability field to derive a set of equiprobable realizations of contaminant mass distribution along the plume centerline. Here all realizations are conditioned available site data (saturations and aqueous and sorbed mass concentrations).

A set of source zone characterization metrics, such as DNAPL mass spatial moments and pool fraction (PF), can then be calculated from the averages of the source zone (saturation and concentration) realizations. This procedure provides a simple and straightforward approach to predict the estimated range of characterization metrics across all equiprobable permeability realizations. Once the ranges for source zone metrics have been estimated, the Protocol employs an upscaled screening tool, presented by Christ et al., (2010), to predict mass recovery behavior. Screening tool output can then guide preliminary site remediation decisions and future in-source data collection. The case study presented in Section VII.A illustrates the used of this framework.

This research focused on the development and application of the BRAINS model for one representative heterogeneous unconsolidated formation type in 2D cross section. Thus, it should be viewed as a proof of principle for the application of this modeling approach and as the first step in generating a 3D characterization tool (i.e. library of models). It is anticipated that, while the

developed features and model structure are robust, the BRAINS model itself will need to be retrained for applications to different depositional environments. Future work should focus on the development of such a library of trained models and on the design and implementation of a field demonstration of the framework.
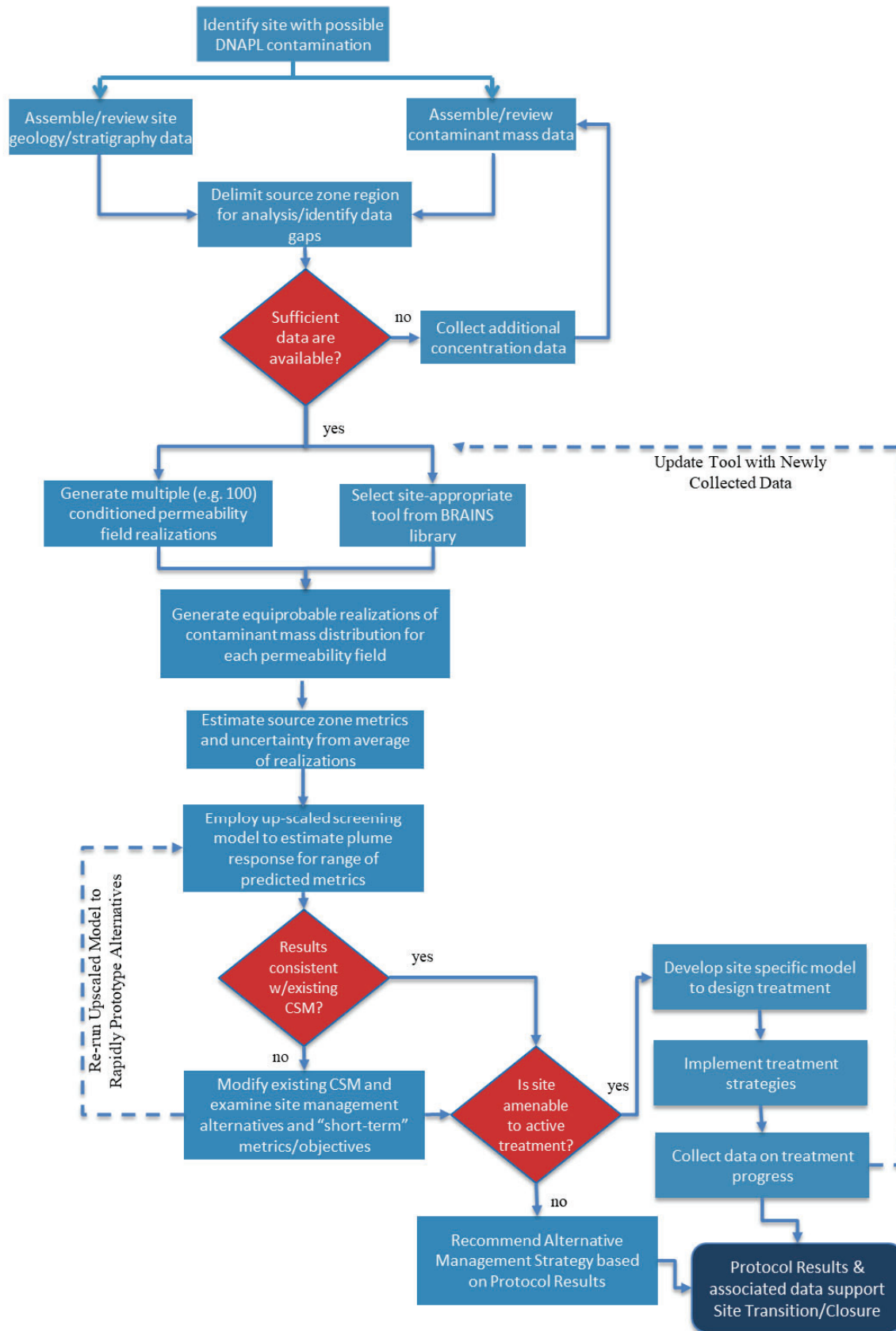
Figure E-4. Site Remediation Feasibility Protocol Flow Diagram

Literature Cited

Chen, X., and Jawitz, J. W. (2009). "Convergence of DNAPL Source Strength Functions with Site Age." *Environmental Science & Technology*, 43(24), 9374–9379.

Christ, J. A., Ramsburg, A. C., Pennell, K. D., and Abriola, L. M. (2006). "Estimating mass discharge from dense nonaqueous phase liquid source zones using upscaled mass transfer coefficients: An evaluation using multiphase numerical simulations." *Water Resources Research*, 42(11).

Christ, J. A., Ramsburg, A. C., Pennell, K. D., and Abriola, L. M. (2010). "Predicting DNAPL mass discharge from pool-dominated source zones." *Journal of contaminant hydrology*, 114(1–4), 18–34.

DiFilippo, E. L., and Brusseau, M. L. (2008). "Relationship between mass-flux reduction and source-zone mass removal: Analysis of field data." *Journal of Contaminant Hydrology*, 98(1–2), 22–35.

DiFilippo, E. L., and Brusseau, M. L. (2011). "Assessment of a simple function to evaluate the relationship between mass flux reduction and mass removal for organic-liquid contaminated source zones." *Journal of Contaminant Hydrology*, 123(3–4), 104–113.

Falta, R. W., Rao, P. S., and Basu, N. (2005). "Assessing the impacts of partial mass depletion in DNAPL source zones: I. Analytical modeling of source strength functions and plume response." *Journal of Contaminant Hydrology*, 78(4), 259–280.

Fure, A. D., Jawitz, J. . W., and Annable, M. D. (2006). "DNAPL source depletion: Linking architecture and flux response." *Journal of Contaminant Hydrology*, 85(3), 118–140.

ITRC. (2003). "Technology Overview: An Introduction to Characterizing Sites Contaminated with DNAPLS." The Interstate Technology & Regulatory Council, Washington, DC.

ITRC. (2004). "Strategies for Monitoring the Performance of DNAPL Source Zone Remedies." The Interstate Technology & Regulatory Council, Washington, DC.

ITRC. (2011). "Integrated DNAPL Site Strategy." The Interstate Technology & Regulatory Council, Washington, DC.

Jawitz, J. W., Fure, A. D., Demmy, G. G., Berglund, S., and Rao, P. S. C. (2005). "Groundwater contaminant flux reduction resulting from nonaqueous phase liquid mass reduction." *Water Resources Research*, 41(10).

Kavanaugh, M. C., Suresh, P., and Rao, C. (2003). *THE DNAPL REMEDIATION CHALLENGE: IS THERE A CASE FOR SOURCE DEPLETION?* U.S. ENVIRONMENTAL PROTECTION AGENCY, Office of Research & Development, WASHINGTON, DC.

Kaye, A. J., Cho, J., Basu, N. B., Chen, X., Annable, M. D., and Jawitz, J. W. (2008). "Laboratory investigation of flux reduction from dense non-aqueous phase liquid (DNAPL) partial source zone remediation by enhanced dissolution." *Journal of Contaminant Hydrology*, 102(1–2), 17–28.

Kram, M. L., Keller, A. A., Rossabi, J., and Everett, L. G. (2002). "DNAPL Characterization Methods and Approaches, Part 2: Cost Comparisons." *Groundwater Monitoring & Remediation*, 22(1), 46–61.

Maji, R., Sudicky, E. A., Panday, S., and Teutsch, G. (2006). "Transition Probability/Markov Chain Analyses of DNAPL Source Zones and Plumes." *Ground Water*, 44(6 Understanding), 853–863.

NRC. (2005). *Contaminants in the Subsurface: Source Zone Assessment and Remediation*. The National Academies Press, Washington, DC.

Parker, B. L., Chapman, S. W., and Guilbeault, M. A. (2008). "Plume persistence caused by back diffusion from thin clay layers in a sand aquifer following TCE source-zone hydraulic isolation." *Journal of Contaminant Hydrology*, Partial Source Zone Removal, 102(1), 86–104.

Saenton, S., and Illangasekare, T. H. (2007). "Upscaling of mass transfer rate coefficient for the numerical simulation of dense nonaqueous phase liquid dissolution in heterogeneous aquifers." *Water Resources Research*, 43(2).

Stroo, H. F., Unger, M., Ward, C. H., Kavanaugh, M. C., Vogel, C., Leeson, A., Marqusee, J., and Smith, B. P. (2003). "Remediating chlorinated solvent source zones." *Environmental Science & Technology*, 37(11), 224A-230A.

Suarez, M. P., and Rifai, H. S. (1999). "Biodegradation Rates for Fuel Hydrocarbons and Chlorinated Solvents in Groundwater." *Bioremediation Journal*, 3(4), 337–362.

Suchomel, E. J., and Pennell, K. D. (2006). "Reductions in Contaminant Mass Discharge Following Partial Mass Removal from DNAPL Source Zones." *Environmental Science & Technology*, American Chemical Society, 40(19), 6110–6116.

Zhang, C., Werth, C. J., and Webb, A. G. (2008). "Investigation of surfactant-enhanced mass removal and flux reduction in 3D correlated permeability fields using magnetic resonance imaging." *Journal of Contaminant Hydrology*, 100(3–4), 116–126.

Objectives

The overarching goal of this research project was to develop and demonstrate a remediation design and performance protocol that couples characterization of the contaminant source with down-hole treatability testing and mathematical modeling to efficiently assess the suitability of a remediation technology, either alone or in combination, and to estimate remedial performance (e.g., mass removal/destruction) and the uncertainty associated with such predictions.

This research directly responds to the following specific objectives in the SERDP Statement of Need):

- Development of field measurements or methodologies that provide predictive capability of performance to reduce the uncertainty associated with long-term performance so that decisions can be made early in the remedial process to avoid years of suboptimal performance.
- Development of field measurements or methodologies that provide data to optimize treatment if current operations are not expected to meet performance objectives.
- Development of assessment procedures and methodologies that aid in the decision to discontinue operation of a technology and implement an alternative technology.

The comprehensive research approach described herein, which couples geostatistical source zone characterization, field-measured rate coefficients, and numerical modeling, is viewed as essential to predict remedial performance and uncertainty at the field scale. The overarching hypothesis of this work is that it is impossible to provide reliable predictions of remedial performance, and its associated uncertainty, without consideration of the complex coupling between contaminant transformation/reaction rates, contaminant mass distribution (spatial configuration and phase partitioning), and the processes influencing the accessibility of this mass (e.g., heterogeneous flow paths, diffusion). Although the project utilized microbial reductive dechlorination as a representative in situ remediation technology, the developed protocol and associated modeling tools are applicable to other remediation technologies, such as monitored natural attenuation and chemical oxidation.

I. Background

Widespread use of chlorinated solvents, such as tetrachloroethene (PCE) and trichloroethene (TCE), in dry cleaning and degreasing operations has resulted in groundwater contamination at thousands of industrial facilities and government installations throughout the United States and abroad (ITRC, 2011; NRC, 2005). In most cases, chlorinated solvent spill sites are conceptualized as consisting of two main regions, a highly contaminated source zone that often contains free product, commonly referred to as a dense non-aqueous phase liquid (DNAPL), and a down-gradient groundwater plume that contains both dissolved- and sorbed-phase contamination (ITRC 2003). The long term persistence of DNAPLs (as entrapped ganglia or pools) in the source zone and the high local contaminant concentrations associated with their presence can lead to a strong driving force for diffusion and sequestration of (dissolved and sorbed) mass in lower permeability layers. Substantial laboratory and field research has demonstrated the importance of this sequestered mass to the persistence of down gradient contaminant plumes (e.g., DiFilippo and Brusseau, 2008; NRC, 2005; Parker et al., 2008; Suchomel and Pennell, 2006). In addition, it is now generally recognized that both the quantity and spatial distribution of immobile contaminant (source) mass will ultimately control the long term performance (mass removal or transformation rates) of most remedial technologies, in particular those that require the delivery of chemical additives or amendments (e.g., Christ et al., 2010; Kaye et al., 2008; Stroo et al., 2003).

Recognizing their importance for predictions of contaminant persistence and remediation effectiveness, substantial progress has been made in the development of both noninvasive and invasive source zone characterization technologies in the past two decades (e.g., ITRC, 2003; Kavanaugh et al., 2003; Kram et al., 2002; NRC, 2005). These technologies have been applied to both contaminant plume and DNAPL mass characterization. Noninvasive methods, such as soil gas surveys and surface geophysics (e.g., seismic refraction and reflection, electrical impedance and resistivity, and ground penetrating radar), tend to provide only qualitative lines of evidence to delineate the presence of contaminant mass. Because most geophysical methods are not currently able to detect and quantify DNAPL saturations (Kavanaugh et al., 2003; NRC, 2005), their application to source zone characterization has typically been limited to characterization of subsurface geology/groundwater flow or the extent of the contaminant plume. More invasive technologies, such as direct push sampling, core analysis, and partitioning inter-well tracer tests, can provide more quantitative information on DNAPL and/or sorbed mass. However, these types of measurements tend to be more costly and can provide data only in the vicinity of the sampling location, which may not be representative of the entire source zone.

To address the limitations associated with sparse sampling, it is now common practice to employ deterministic and stochastic plume interpolation approaches to estimate contaminant concentration at unsampled locations using the available borehole data. Kriging packages (Deutsch and Journel 1998) are among the stochastic methods that have been extensively used for contaminant plume characterization, to interpolate between point observations of mass concentrations at field sites (e.g., Gilbert & Simpson, 1985; Jones et al., 2005; Wu et al., 2005) in an attempt to estimate contaminant mass. Most kriging applications have focused on aqueous concentration measurements to delineate contaminant plumes (Reed et al. 2000; Wu et al. 2005; Basu et al. 2006; Rivett et al. 2006; Yu et al. 2006; Reed and Minsker 2004), failing to incorporate consideration of sequestered mass, specifically DNAPL, in their site conceptual model, potentially leading to gross underestimation of total mass and the associated remedial challenges. In particular, one of the main drawbacks of the application of kriging approaches in source zone characterization is their limitation in interpolating highly sparse and discontinuous patches of DNAPL in a heterogeneous domain (Maji et al. 2006).

Over the past decade, more sophisticated modeling methods have been considered for processing sparsely sampled data based on Markov chain models (Carle & Fogg, 1996, 1997). In the context of environmental remediation, these methods have been employed in a number of ways. In previous work (Elfeki, 2006a, 2006b), for example, Markov chain models were used to generate realizations of hydraulic conductivity into which contaminant was synthetically released, to explore how the addition of boreholes served to reduce uncertainty in plume shape and structure. The Markov approach was considered in Maji et al., (2006) as an alternative to kriging for interpolating sparse observations of DNAPL saturation and aqueous phase TCE concentration, but DNAPL volume and mean estimated modes of aqueous phase TCE tended to be underestimated. More recently, Harp and co-workers have considered the problem of estimating Markov transition models for conductivity in ways that match not just sparse borehole facies indicator data, but also observations of hydraulic head (Harp et al., 2008; Harp & Vesselinov, 2010). Statistical model parameters were then employed for the Monte-Carlo generation of a suite of conductivity realizations to quantify the probability of clay being present at a given position in the aquifer (Harp et al., 2008) or to develop probability maps for facies as a function of position (Harp & Vesselinov, 2010).

The challenges posed by detailed (fine-scale) delineation of source zone mass have also led to the development and application of averaged characterization metrics, such as DNAPL mass spatial moments, pool fraction, and trajectory-averaged saturation statistics, that can represent the salient features of the mass distribution (e.g., Jawitz et al., 2005; Christ et al., 2006; Saenton & Illangasekare, 2007). Here, the hypothesis is that such metrics can be employed in upscaled mathematical models to predict source longevity and down-gradient flux evolution under natural or remedial conditions. Comparisons to laboratory data (Fure et al., 2006; Zhang et al., 2008; Christ et al., 2010; DiFilippo & Brusseau, 2011) and field data history matching exercises ((DiFilippo and Brusseau 2008; Falta et al. 2005b)) suggest that such approaches may hold promise, particularly for use in screening remedial alternatives. To date, investigations pertaining to the identification of source zone metrics have focused primarily on the distribution of DNAPL, ignoring other sequestered mass sources such as sorbed and immobile aqueous mass.

Another metric of particular interest in remedial evaluation is 'source strength' (Chen and Jawitz 2009; Falta et al. 2005b; Goltz et al. 2007; ITRC 2004; Stroo et al. 2003). This metric provides a simple basis for comparing DNAPL contamination across sites of very different scales and geologic environments and its evolution in time or space has been used to assess the effectiveness of natural attenuation (Falta et al. 2005a) and alternative remediation technologies (Fure et al. 2006; Lemke et al. 2004a; Lemke and Abriola 2006). Source strength is represented as mass discharge $[MT^{-1}]$ or mass flux $[ML^{-2}t^{-1}]$ across a transect plane perpendicular to the direction of groundwater flow. Under remedial conditions, source strength is typically quantified through monitoring of concentrations within a transect perpendicular to the groundwater flow and down-gradient of the contaminant source zone. Although source strength estimation has typically been conducted using simple linear interpolation of measured concentrations, recent research has explored the use of geostatistics and conditional simulation to estimate mass flux and its uncertainty from multi-level sampler observations and hydraulic conductivity measurements in the transect (Cai et al. 2011, 2012; Li et al. 2007). Results of these investigations have highlighted the strong influence of velocity variation (physical heterogeneity) and sample density (location) on mass flux estimates (with estimates varying more than one order of magnitude).

Unfortunately, most laboratory treatability studies do not adequately mimic mass transfer processes, such as rate-limited dissolution, diffusion and desorption, that may control system performance at a heterogeneous field site. Thus, such studies tend to overestimate potential

treatment effectiveness. For example, a comparison of 138 chlorinated solvent bioremediation field and laboratory studies revealed that median laboratory rate constants were consistently higher (up to one order-of-magnitude) than observed field rate constants (Suarez and Rifai 1999). The premise underlying the down-hole treatability (DHT) methodology proposed herein is the recognition that: (a) even advanced assessment tools, such as molecular probes, fail to provide reaction rate information necessary to predict remediation extent in complex subsurface environments; and (b) the tool or method should provide information that is relevant at the field scale and can be readily incorporated into model(s) for simulation of remediation performance and uncertainty assessment.

The above discussion highlights the urgent need for better field treatability test methods to predict potential remedial system performance and for the development of improved, cost-effective, field characterization methods and associated modeling tools that encompass all source zone mass and facilitate the identification of the most critical source zone properties that will govern mass persistence and the performance of remedial options.

To achieve its goal, the project was structured around three phases that addressed: (i) source and plume characterization, (ii) upscaled mass transfer and transformation rates, and (iii) field-scale reactivity and predictions of remedial performance. The project work plan is illustrated in Figure B.1.1
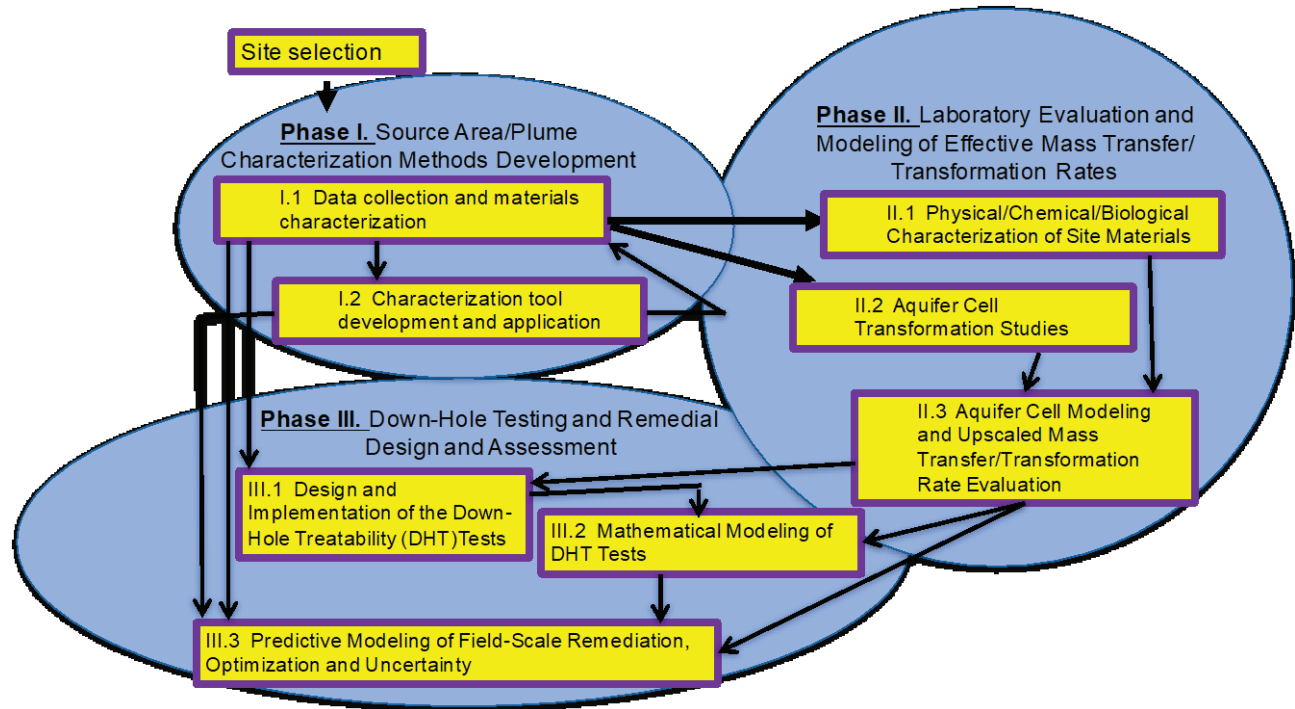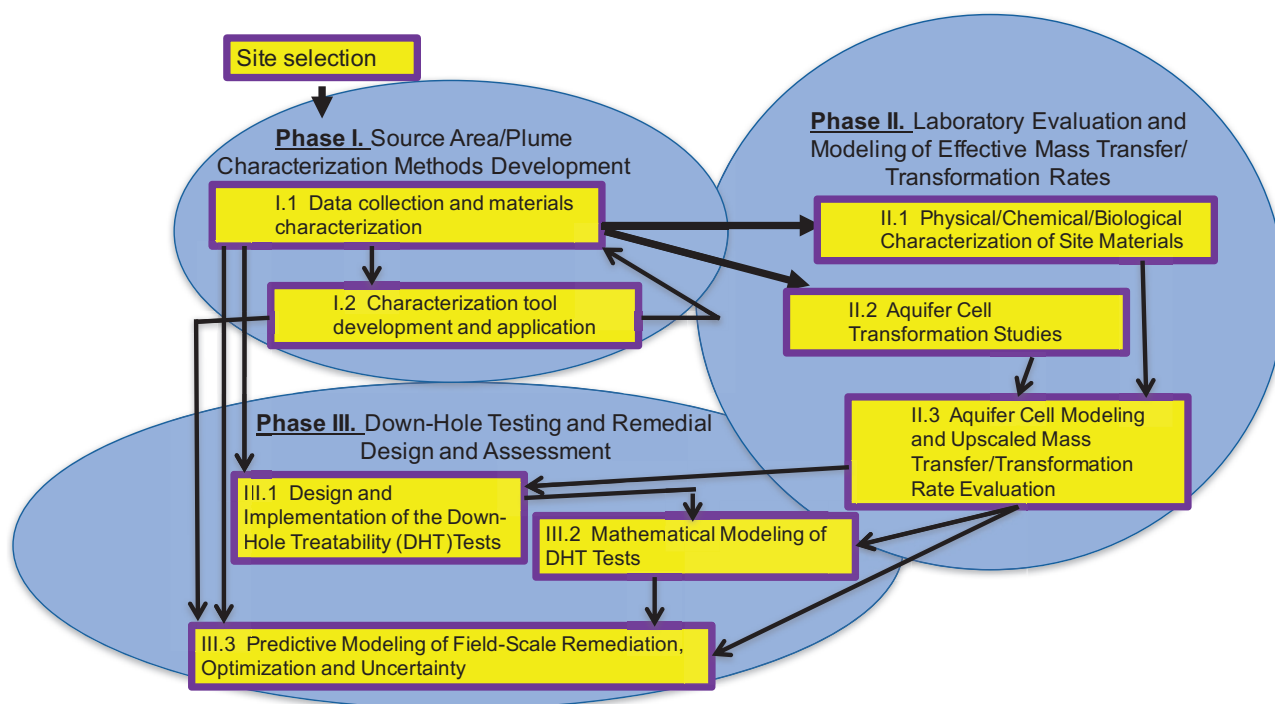

Figure B.1.1. Project work plan.

Phase I focused on the development and demonstration of methods/modeling tools to characterize the source zone for subsequent remedial design, implementation, and assessment. Here, the specific objective was to develop a protocol and software tools that employ measured field data to produce a representation of the subsurface source zone that captures the spatial distribution and uncertainty associated with key features (i.e., permeability, microbial activity/mass, and sequestered contamination [sorbed, immobile aqueous, and NAPL]) that control remedial performance.

Phase II focused on batch and bench-scale laboratory testing, and upscaled mathematical model development to support the design and implementation of a field remediation strategy. Here, the performance of microbial reductive dechlorination was evaluated in aquifer cells that were representative of field conditions, and the resulting data were employed to develop and evaluate upscaled models to describe effective mass transfer and reaction rates.

Phase III focused on the estimation and application of effective rate parameters in field-scale remediation. In this phase, a downhole treatability test was conducted at the selected field site (Commerce Street Superfund Site, Williston, VT) to estimate effective *in situ* transformation/reaction rates and to support the design and assessment of site remediation strategies. Here a mathematical model, refined and validated in Phase II, was employed to estimate effective field transformation rates. Estimated rates were then compared to batch- and aquifer cell-measured rates to shed light on the processes controlling remediation at the field scale.

Section II of this report describes the materials, methods, and general technical approaches associated with each of these project research phases, while Section III details research results. Section IV provides a summary of important conclusions and implications for future research. In Appendix A, we outline the procedure for application of the developed modeling tools in site characterization and remedial assessment.

II. Materials and Methods

II.1 Chemicals and Porous Media

II.1.1. Chemicals

Sodium bromide at a concentration of 10 to 16.5 mM (Fisher Scientific; Hampton, NH), sodium fluorescein at a concentration of 0.075 mM (Sigma Aldrich; St. Louis, MO), and/or erioglaucine A (Fluka Chemical; Seelze, Germany) at a concentration of 0.06 mM were used as non-reactive tracers. Sodium sulfide nonahydrate (Fisher Scientific; Hampton, NH) and L-cysteine (Sigma Aldrich; St. Louis, MO) were used as reductants to maintain anoxic conditions in laboratory experiments while KB-1® primer (SiREM; Guelph, ON) was used to maintain reducing conditions during the pilot test. Sodium DL-lactate solution, 60% w/w (Sigma Aldrich; St. Louis, MO [laboratory experiments] or ChemWorld; Taylor, MI [pilot test]) was used as an electron donor in all experiments. TCE (ACS reagent, >99.5%) with a density of 1.46 g/mL and an aqueous solubility of 1,100 mg/L was obtained from Sigma Aldrich; St. Louis, MO. Unless otherwise specified, aqueous solutions were prepared in deionized water produced by a Milli-Q® Integral Water Purification System (EMD Millipore; Burlington, MA).

Sodium hexametaphosphate (Alfa Aesar; Haverhill, MA) was used as a dispersing agent during hydrometer testing. Nitric acid (Fisher Scientific; Hampton, NH) was used as a preservative for metals samples. Methanol (Optima grade; Fisher Scientific; Hampton, NH) or isopropanol (Optima grade; Fisher Scientific; Hampton, NH) was used as a solvent to extract TCE and *cis*-dichloroethene (*cis*-DCE) from soil samples. Sodium chloride (Fisher Scientific; Hampton, NH) and calcium chloride (Fisher Scientific; Hampton, NH) were used as background electrolytes in aquifer cell experiments and sorption studies, respectively.

Groundwater for laboratory experiments was obtained from the Commerce Street Superfund Site in Williston, VT as described in Section II.3.2.2. Unless a specific well location is noted, the groundwater used was collected from numerous wells across the site and comingled to create a representative groundwater. Prior to use, the groundwater was sparged with nitrogen gas for at least four hours and amended with 1 mM L-cysteine and 0.2 mM sodium sulfide to remove oxygen from the stored groundwater and create an oxidation-reduction potential (ORP) of less than -150mV, similar to the site conditions.

II.1.2. Reduced Growth Medium and Inoculum

The bacterial growth medium used in microcosm and batch reactor experiments was prepared according to Löffler et al., (2005). During biotic experiments in the first aquifer cell, the background solution consisted of bacterial growth medium (Löffler et al. 2005) incorporating the modifications of Cápiro et al., (2015).

KB-1® (SiREM; Guelph, ON) inoculum was used in the pilot test, several batch experiments, and in the aquifer cell experiments. This inoculum is a methanogenic dechlorinating consortium of microbial species: *Acetobacterium sp., Geobacter sp. (Geo),* and multiple *Dhc* strains harboring the *vcrA, bvcA, and tceA* reductive dehalogenase (Rdase) genes. It was selected because of its relevance to the field, use in field-scale bioremediation applications, and demonstrated capability to dechlorinate PCE to ethene (Duhamel et al. 2002, 2004; Sleep et al. 2006). The culture used in the experiment was measured to have initial gene abundances of 2.4×10^7, 9.8×10^7, 2.9×10^6, and 6.0×10^5 gene copies per mL of the *Dhc* 16S rRNA, *vcrA*, *bvcA*, and *tceA* genes, respectively. The microbial species and strain breakdown is as follows (Roberts 2017):

- *Acetobacterium* (27 percent) is a genus of bacteria that produce acetate as a metabolic byproduct. Acetate is required by *Dehalococcoides* for producing cellular material, and *Dehalococcoides* consortia that contain *Acetobacterium* experience enhanced population growth (He et al. 2007).

- *Geobacter* (22 percent) is a genus of proteobacteria first discovered in 1987 (Lovley et al. 1987) that is capable of dechlorinating PCE and TCE but not *cis*-DCE or vinyl chloride (VC) (Duhamel and Edwards 2006).

- *Dehalococcoides* (22 percent) is a genus of bacteria that is capable of complete dechlorination of PCE to ethene. The strain of *Dehalococcoides* present in KB-1 was obtained from a site in Southern Ontario contaminated with TCE (Duhamel et al. 2002) and has been identified as belonging to the same subgroup (Pinellas) as the strain of *Dehalococcoides* present in BDI (Löffler et al. 2013).

- Synergistales (3 percent) is a phylum of bacteria that is thought to aid *Dehalococcoides* growth by producing acetate (Hug et al. 2012).

- *Treponema* (3 percent) is a genus of spiral-shaped bacteria that is thought to aid *Dehalococcoides* growth by producing hydrogen and acetate (Miura et al. 2015). Hydrogen is the only electron donor that *Dehalococcoides* is capable of using, and *Dehalococcoides* must use hydrogen generated by other microbes because it is not capable of producing it itself (Hug et al. 2012).

- Archaea (2 percent) are a domain of single-celled microorganisms. The Archaea present in KB-1 are methanogens that compete with the dechlorinating species (*Geobacter* and *Dehalococcoides*) for hydrogen and acetate (Hug et al. 2012).

- *Anaerolineaceae* (1 percent) are a family of methanogenic bacteria (Yamada et al. 2006) that also compete with the dechlorinating species for hydrogen and acetate (Hug et al. 2012).

Select batch reactor and microcosm experiments were bioaugmented with BDI-SZ, a non-methanogenic PCE-ethene dechlorinating microbial consortium. This inoculum contains several dechlorinating cultures including the PCE to *cis*-DCE dechlorinating species, *Dehalobacter* and *Geo*SZ, as well as three *Dhc* strains (FL2, GT, and BAV1) capable of completing the transformation of PCE to ethene. The BDI-SZ used was maintained in the Tufts University Environmental Sustainability Laboratory (ESL) with 0.33 mM PCE and 10 mM lactate at 35°C without shaking.

II.1.3. Porous Media

Porous media for laboratory experiments were obtained from the Commerce Street Superfund Site in Williston, VT as described in Section II.3.2.1. Site soil collected from the 10.7 to 11.3 m (35 to 37 foot) depth of boreholes CMT-4 and CMT-5, from the 10.4 to 10.7 m (34 to 35 foot) depth of CMT-4, and from the 10.4 to 10.7 m (34 to 35 foot) depth of DHT-2 were used in microcosm experiments. For the aquifer cell experiments, silty clay from the 12.2 to 12.8 m (40 to 42 foot) depth of borehole CMT-2 was used to create a confining layer in each experiment.

The first aquifer cell was comprised of an ASTM Standard 20/30 sand (US Silica Company; Ottawa, IL) background with four lenses (Figure M.4.1) consisting of Webster soil (Iowa State University Agricultural Experiment Station; Ames, IA), Appling soil (University of Georgia Agricultural Experiment Station; Eastville, GA), F-95 fraction of Ottawa Sand Standard sand

(Fisher Scientific; Hampton, NH), and loamy sand (69% sand, 22.5% silt, 3.5% clay) collected from the Commerce Street Superfund site (Williston, VT). The soil in the second aquifer cell, above the clay confining layer, was entirely comprised of material collected from the 6.4 to 10.7 m (21 to 35 foot) depth of borehole DHT-2. Natural materials used in the microcosms and first aquifer cell experiment (Webster, Appling, and Commerce Street) were ground with a mortar and pestle, then passed through a #30 mesh sieve to remove large particles.

Table M.1.1. Properties of porous media used in the first aquifer cell experiment

Material	Source	Organic Carbon Content (%)	Hydraulic Conductivity (m/day)	Reference
ASTM Standard 20/30 Sand	Ottawa, IL	0.01	200	Marcet et al., 2018; Shang, 2015
Webster Soil	Ames, IA	1.96	0.86	Marcet, 2014
Appling Soil	Eastville, GA	0.66	10.2	Marcet, 2014
F-95 Sand	Ottawa, IL	0.01	2.5	Marcet et al., 2018
Commerce Street Material	Williston, VT	0.09	0.03	Gaeth et al., 2016

II.2. Analytical Methods

II.2.1. Soil Analytical and Characterization Methods

Soil cores from the installation of the CMT wells and from the preliminary soil borings (Section II.3.2.1) were delivered to the ESL where they were opened and visually and manually inspected to determine the classification based on texture, plasticity, and color. Sample aliquots were collected at specific locations for physical characterization, chemical, and biological analyses. The soil was then segmented and segregated into Ziploc® bags representing 15 cm (6 inches) of borehole depth. Sample organic and inorganic carbon content were determined using a total organic carbon (TOC)-L analyzer (Shimadzu; Kyoto, Japan) using the subtraction method (total carbon minus inorganic carbon equals organic carbon) as described in Marcet, (2014). For select locations and depth, soil was oven dried and ground with a mortar and pestle, then sample grain size distribution was determined using sieve and hydrometer tests according to Das, (1997).

Soil hydraulic conductivity was measured by performing a static head test in a 15 cm by 2.5 cm inner diameter borosilicate glass chromatography column (ACE Glass Inc, Vineland, NJ). Oven-dried, ground soil was added to the column in approximately 2 cm intervals where it was then well mixed using a metal spatula and settled using a gentle vibration tool. The settled material was then tamped down before another 2 cm of material was added to the column. Once the column was packed completely full of material, it was flushed with carbon dioxide gas for at least 30 minutes, after which Milli-Q® water was driven through the column at a constant flow rate using a Rainin Dynamax RP-1 peristaltic pump (Mettler-Toledo; Columbus, OH). After the column was saturated with at least 5 PV of Milli-Q® water at 0.5 mL/min, the pump was removed and column was configured so flow was driven by a static head maintained at a constant height. The head height was measured with a ruler and the flow rate was measured by collecting and weighing the column effluent during a fixed period of time (1 to 10 minutes).

Soil TCE and *cis*-DCE concentrations were measured using an alcohol extraction procedure in which 5 to 10 mg of soil sample was placed in 10 mL of methanol (Optima grade; Fisher Scientific; Hampton, NH) or isopropanol (Optima grade; Fisher Scientific; Hampton, NH). After mixing and

allowing the soil and alcohol to equilibrate for 24 to 48 hours, the alcohol was analyzed for TCE or TCE and *cis*-DCE analysis. TCE and *cis*-DCE were measured in methanol extractions using an Agilent 7890B gas chromatograph (GC) with electron capture detector (Agilent Technologies; Santa Clara, CA). TCE in isopropanol extractions was measured using a 7890A GC with a flame ionization detector (FID) (Agilent; Santa Clara, CA). After analysis, the alcohol was removed and replaced and the extraction was repeated until chlorinated ethenes were no longer detected in the sample.

The extent and rate of mass transfer of TCE to site soil was performed through a series of adsorption and desorption batch reactor experiments. Three measurements were performed: 1) the rate to adsorption equilibrium; 2) the adsorption isotherm; and 3) the rate to desorption equilibrium. For each measurement performed, the aqueous phase was prepared by dissolving 0.38 to 7.6 mM (50 to 1000 mg/L) TCE in a 10 mM calcium chloride dehydrate solution in a sealed container and mixing for at least 24 hours. Sorption experiments were performed in 20 mL crimp top vials capped with a polytetrafluoroethylene (PTFE) lined rubber septum and aluminum crimp top. Approximately 5 g of dried, well mixed material was placed in each vial prior to completely filling the vial with the TCE-calcium chloride solution to eliminate headspace. Control reactors without soil were also prepared to account for loss of TCE through the septum. Vials were maintained on rotating shaker trays prior to sampling. High clay materials used in the sorption experiments were dried at 105°C overnight, then passed through an HM-375 soil grinder (Vicksburg, MI) and a #100 mesh sieve to create uniform material. The clay was then mixed with Milli-Q® water on a 1:1 mass basis and allowed to sit overnight prior to use in sorption experiments.

To measure the rate to adsorption equilibrium, vials containing a 3.8 mM TCE solution were destructively sampled daily for one week, then again after 10-, 15-, and 21-days or until the aqueous concentration differed from the previous sample's aqueous concentration by <2%, whichever came first. When the 3.8 mM TCE reactors had reached equilibrium, additional reactors containing 0.38, 0.76, 1.9, and 7.6 mM (50, 100, 250, and 1000 mg/L) TCE solutions were sampled to create an adsorption equilibrium isotherm. Vials containing TCE solution only (no soil) were also sampled to account for any losses through the septa caps. All samples were collected destructively. Vials were centrifuged at 1000 rpm for 30 minutes, then 3 (control reactors) or 5 (vials containing soil) 0.5 mL samples were drawn from the vial through the septum using a needle and syringe. Each sample was passed through a 0.2 µm filter and placed in a 2.0 mL glass autosampler vial containing 0.5 mL of isopropanol for measurement by GC-FID. The solid phase was then removed from the vial and the sorbed TCE concentration was measured using the isopropanol extraction procedure described above.

Additional reactors were prepared as described above but were not destructively sampled after reaching equilibrium and were used to measure the rate of TCE desorption. Following aqueous phase sampling, the remaining solution in the vials was removed and replaced with 10 mM calcium chloride dihydrate solution, added until there was no headspace. After shaking overnight, the aqueous phase was sampled, then removed and replaced with TCE-free calcium chloride solution. This process was repeated until TCE was no longer detected in the aqueous phase.

II.2.2. Aqueous Analytical Methods

Groundwater samples for chlorinated ethene and ethene analysis were prepared and analyzed according to previously described methods (Amos et al. 2007a, 2008, 2009). Chlorinated ethene and ethene concentrations were measured using an Agilent 7890B GC system with a DB-625 column and an FID (Agilent Technologies; Santa Clara, CA) (Amos et al. 2007a). Samples were

introduced to the GC by a Telemark HT3 headspace autosampler (Teledyne Technologies; Thousand Oaks, CA) using a constant heating program.

After preparing the sample for GC analysis, a 0.5 mL aliquot of the sample remaining in the volatile organic analysis (VOA) vial was collected and analyzed for volatile fatty acid (VFA) concentrations by high pressure liquid chromatography (HPLC) using an Aminex HPX-87H column (Bio-Rad Laboratories; Hercules, CA) as described by (He et al. 2003) and modified to use a 1200 Agilent HPLC System with diode array detector (DAD; Agilent Technologies; Santa Clara, CA). Additional aliquots of select samples were used for dissolved organic carbon (DOC) analysis with a TOC-L analyzer using the non-purgeable organic carbon method (Shimadzu; Kyoto, Japan) and anion (chloride, nitrate, nitrite, and sulfate) analysis using a Dionex ICS-2100 ion chromatograph (IC) (Dionex; Sunnyvale, CA). Dissolved metals were measured in 10 μm filtered, nitric acid preserved samples via EPA Method 200.7 using an Optima 7000 inductively coupled plasma-optical emission spectrum (ICP-OES) (Perkin Elmer; Waltham, MA).

Bromide concentrations in large volume samples (field samples and aquifer cell effluent samples) were measured using a bromide combination electrode (Cole Parmer; Vernon Hills, IL) connected to a Model 50 conductivity meter (Accumet Engineering; Hudson, MA); for small volume (aquifer cell port) samples, bromide concentrations were measured by IC using a Dionex ICS-2100 IC system with IonPac AS-18 Fast column (Thermo Scientific; Waltham, MA).

II.2.3. Biological Analytical Methods

Aqueous biomass samples from laboratory experiments (15 mL aquifer cell effluent samples, 1 mL aquifer side port samples, or 1 mL samples from batch reactors) were prepared by centrifugation as described by Cápiro et al. (2015). After removing the supernatant, pellets were stored at -20°C. Microbial genomic DNA was extracted from laboratory experiment aqueous samples using the QIAamp DNA Mini Kit (Qiagen; Hilden, Germany), from field-collected groundwater using the Mo-bio PowerWater Kit (Qiagen; Hilden, Germany), and from field-filtered (Sterivex) samples using the Mo-bio PowerSoil Kit (Qiagen; Hilden, Germany) with all extractions performed in accordance with the manufacturers' protocols. All extracted DNA was stored at -20°C until quantitative polymerase chain reaction (qPCR) analysis.

Dhc cell abundance was quantified by qPCR analysis targeting the *Dhc* 16S rRNA gene using a Step One Plus Real-Time PCR System (Applied Biosystems; Foster City, CA) under standard operating conditions and TaqMan-based chemistry (Ritalahti et al. 2006). *Geobacter lovelyi* Strain SZ (*Geo*SZ) 16S rRNA gene copies were measured using SYBR Green detection chemistry according to described protocols (Amos et al. 2007b; Duhamel and Edwards 2006) with the modifications introduced by Amos et al. (2009). All qPCR analyses were measured in triplicate. Primers and probes were obtained from IDT Technologies (Coralville, IA) or ThermoFisher and the TaqMan Universal PCR Master Mix from Applied Biosystems (Foster City, CA). For each analysis, a standard curve was generated using 10-fold serial dilutions of a stock solution containing a known concentration of plasmid DNA with a single copy of the target gene (Ritalahti et al. 2006).

II.3. Commerce Street Site: Data and Materials Collection

II.3.1. Overview of Commerce Street Superfund Site

The Commerce Street Superfund Site (hereafter referred to as "the site") is located at the Alling Industrial Park (AIP) in Williston, Vermont, approximately 4 miles east of Burlington, Vermont (Figure M.3.1). The test area for this research study (Figure M.3.2) constitutes a small portion of the entire Superfund site. The site is located within the Winooski River watershed at an elevation ranging from 330 to 350 feet above mean sea level (AMSL).

The site is zoned for mixed residential, business, and industrial uses. Commerce Street and the areas to the east are predominantly commercially zoned lots that are currently developed or in the process of being developed. Kirby Lane and South Brownell Road are zoned residential, with limited commercial development on South Brownell Road. The ground surface over the entire area exhibits little relief and slopes gently to the southwest. Surface water consists of a small unnamed stream and its three tributaries, which flow in a southerly direction to Muddy Brook. The unnamed stream is a habitat for two State-designated threatened species and is a State-designated area for protection and maintenance of aquatic life under the Clean Water Act. The Winooski River downstream of the Test Area is a known fishery.

The Site is currently being evaluated by the VTDEC (with funding by EPA) as part of the ongoing Remedial Design under the Comprehensive Environmental Response, Compensation, and Liability Act (CERCLA) of 1980, as amended by the Superfund Amendments and Reauthorization Act (SARA) of 1986; and the National Oil and Hazardous Substances Pollution Contingency Plan (NCP).

The primary sources of contamination are a former unlined lagoon and a former leaching field where plating rinse water and sludge wastes containing heavy metals and solvents were disposed of intermittently from 1960 to 1984. Previous studies identified three properties/lots as locations of former manufacturing and/or fabrication operations that could have contributed to groundwater contamination. Volatile Organic Compounds (VOCs) including tetrachloroethene (PCE), trichloroethene (TCE), dichloroethene (DCE), petroleum hydrocarbons, and metals including chromium, cadmium, and nickel were detected in soil and groundwater throughout the site. TCE was detected at the highest concentrations and is the most extensive contaminant. The three lots and potential sources are described below:

1. Lot 19-11 (Mitec property/96 Commerce Street): The property formerly leased by Mitec Systems Corp. (Mitec) currently includes one building. A wastewater disposal lagoon west of the building and a leach field south of the building are suspected sources of PCE and/or metals.

2. Lot 19-12 (Bove-Fagan property/87 Commerce Street): Two underground storage tanks were removed from this lot in 1994 revealing a previous release of BTEX compounds.

3. Lot 19-2 (Former EMCO property/63 Commerce Street): Manufacturing operations began in 1947 and both a disposal pit and outfall pipe to the unnamed stream have been identified.

The source for the plume lobe included in the test area has not been confirmed. Previous investigations showed that the water table is located from 3 to 11 feet below the ground surface. The primary (upper) aquifer consists of medium to fine sand and has a total thickness of approximately 40 feet. Pumping tests of the primary aquifer yielded hydraulic conductivity values ranging from 1 ft/day to 29 ft/day. Because of the extensive TCE contamination and high estimated

potential for delivery of bio-stimulation amendments (high permeability), the Commerce Street Superfund Site was chosen for this research project.
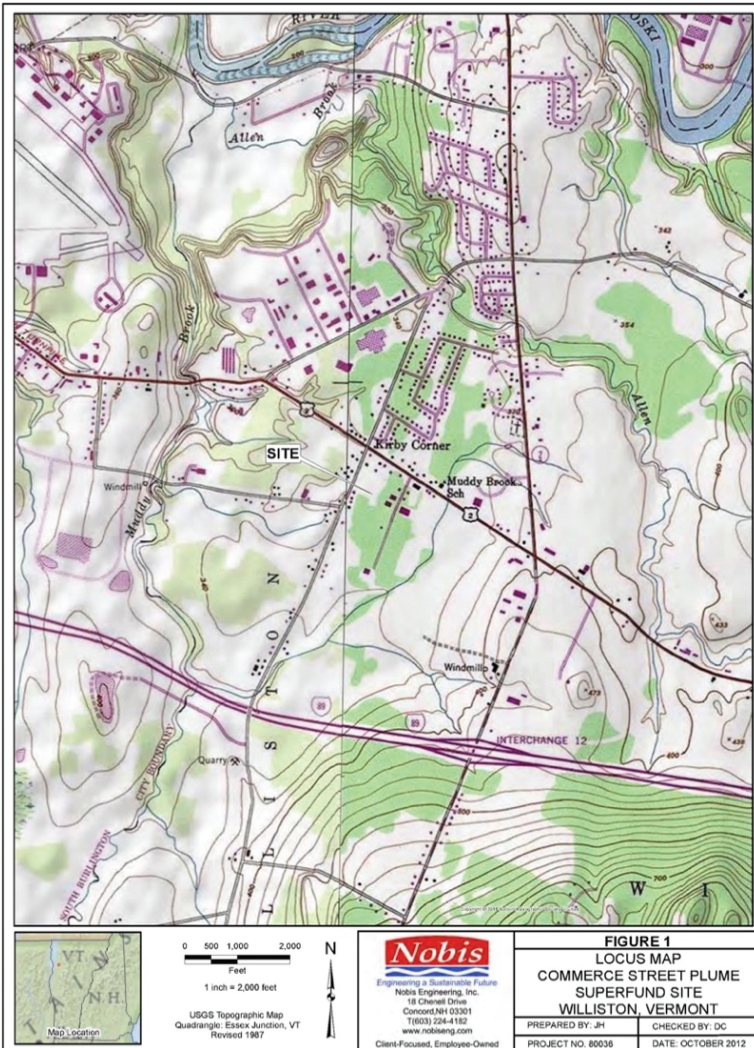
Figure M.3.1. Commerce street superfund site location map.

Measurements of groundwater contamination and hydraulic head were interpolated with the software ArcGIS using two different methods: the Inverse Distance Weighted method and the Empirical Bayesian Kriging method. The two methods yielded similar interpolations. Contours of hydraulic head developed using the Inverse Distance Weighted method are shown in Figure M.3.3.

The contaminated sand unit is approximately 40 feet deep. It is relatively homogeneous, but with a slightly fining trend downwards, and is bounded below by a consistent clay layer. Recorded (interpolated) groundwater levels indicate a small gradient from the northern part of the site towards both the southwest and the southeast. While the southeasterly flow follows the surface topology, the southwesterly flow component is thought to originate from intermittent sump pumping in residential buildings on the western part of the site, performed to mitigate basement flooding. The rate of pumping is unknown. There is a shallow brook on the eastern part of the site, with low flow.
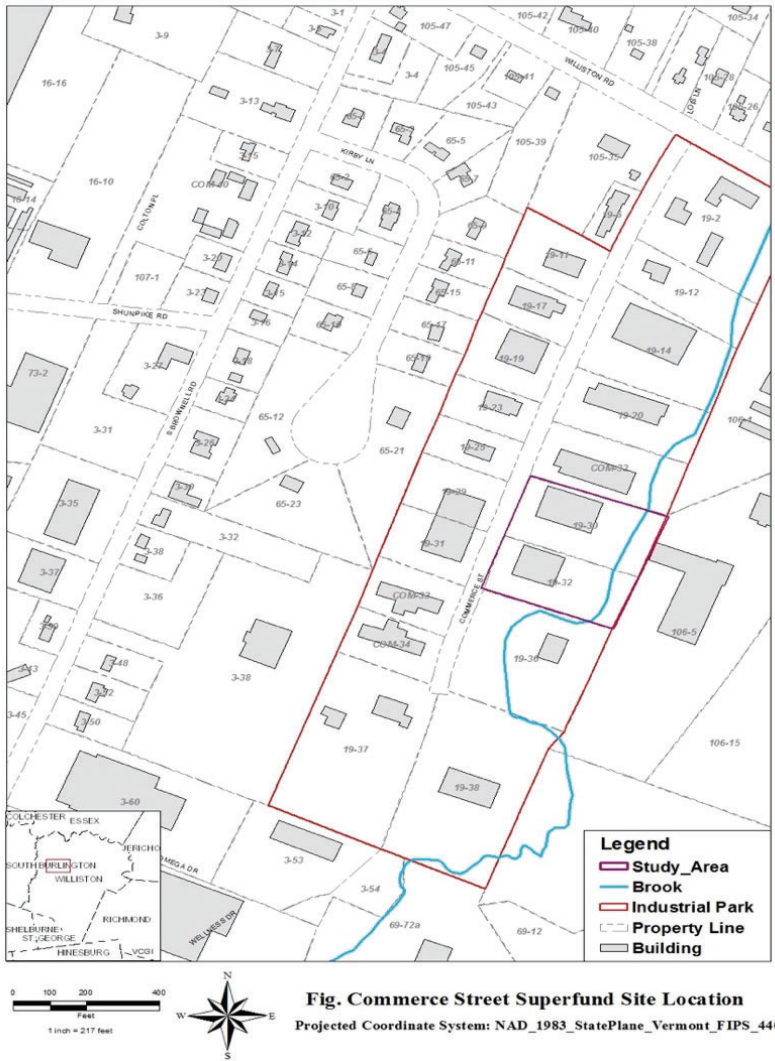
Figure M.3.2. Study area location within Commerce street superfund site.

Inspection of available site contaminant concentration data revealed the presence of a complex source zone, characterized by a number of high concentration areas, and multiple chlorinated solvent plumes (see Figure M.3.4). Contoured data suggested the existence of more than one source area at the site. A persistent high concentration area (source) close to Commerce Street was chosen as the focus of this project (see Figure M.3.2). Head observations in this area indicate that vertical groundwater flow is negligible and that the lateral flow direction in the proximity of this source area is towards the southeast. In addition, comparison of plume contours between the years 2000 and 2011 (see Figure M.3.4) revealed that plume spreading occurred towards the southeast in this period, consistent with the head data.

II.3.1.1. Previous Site Investigation Work

The following section is a description of previous site investigation work prepared by Nobis (Nobis Engineering Inc., 2018).

12
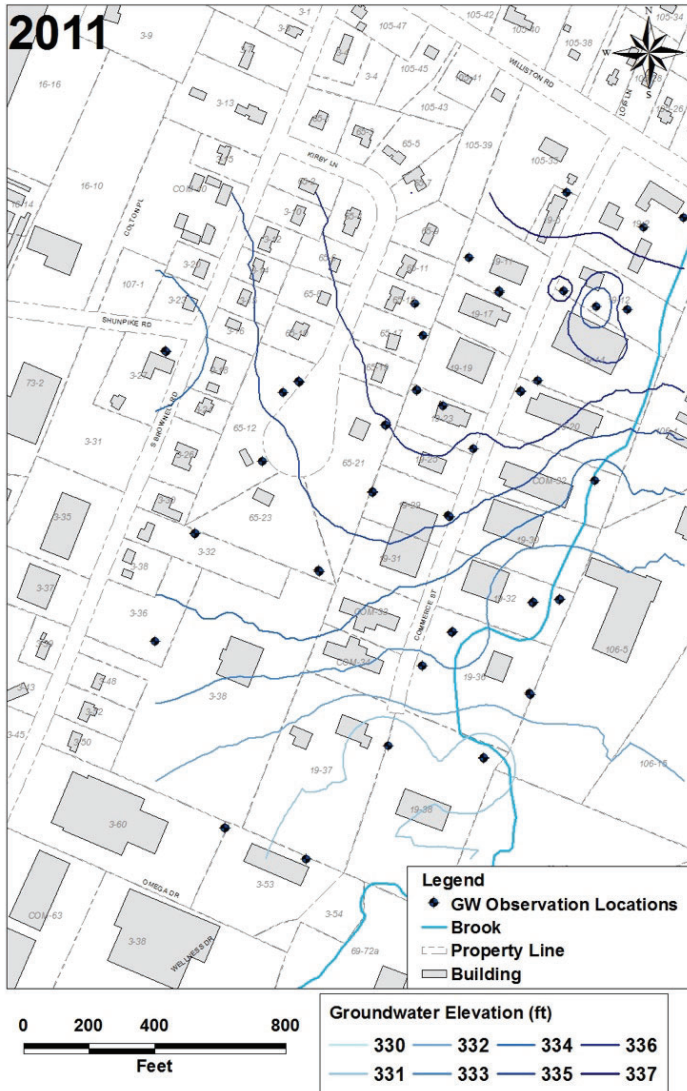
Figure M.3.3. Groundwater contour map.

Previous investigations at the site were performed by Nobis and other companies between 1986 and 2012. The available data encompass stratigraphic records from soil borings; a seismic survey to determine the extension of a clay layer underlying the contaminated sand/silt unit; 21 slug tests/pump tests to determine the hydraulic conductivity at different depths; and over 200 measurements of groundwater levels and geochemical parameters such as pH and dissolved organic carbon (since 2008). Chemical analyses of groundwater, soil, surface water and sediment samples had been performed with respect to VOCs (in total over 1000 samples) and other compounds such as dioxin, heavy metals and BTEX.

A comprehensive, chronological list of previous environmental investigations associated with the Site is presented below. Locations of existing monitoring wells installed prior to 2014 are shown in Figure M.3.5. For a complete discussion of previous environmental investigations, refer to the Remedial Investigation (RI) report (Nobis Engineering Inc. 2015). Previous investigations included:
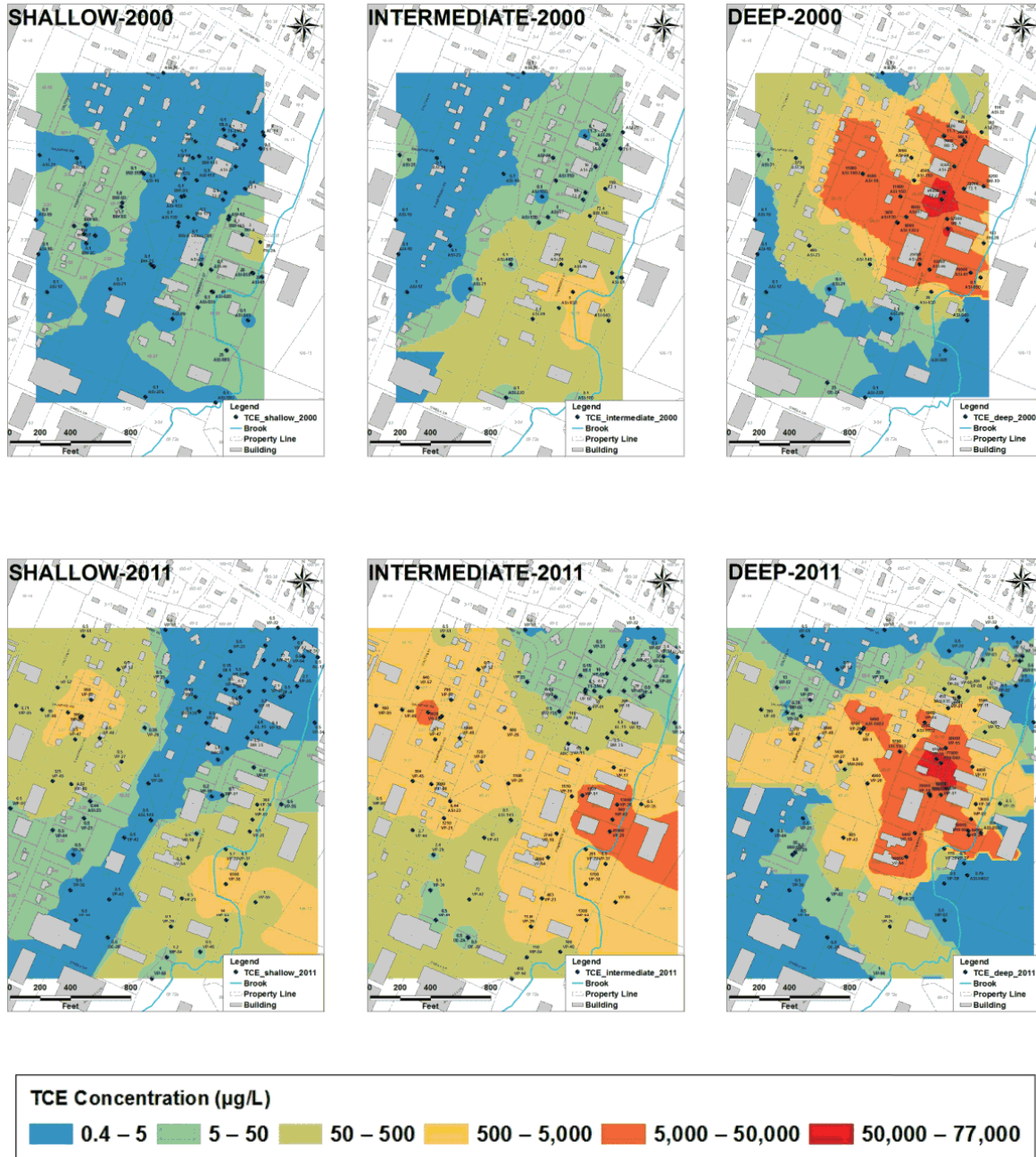
Figure M.3.4. TCE concentration contours.

- December 1984: Mitec (Lot 19-11) contracted an environmental consultant to install monitoring wells MI-1 through MI-9, which were located adjacent to the wastewater disposal lagoon and to the west of Lot 19-11. The wells were installed to a maximum depth of 17 feet below ground surface (feet bgs).

- March – May 1985: Mitec hired a contractor to remove 30 cubic yards of material from the wastewater lagoon.

14

- June – July 1985: Six private potable water supply wells on South Brownell Road were found to be contaminated with TCE and PCE above the State Health Advisory Levels. All residences were subsequently connected to the Williston public water supply system.

- 1985 – 1986: VTDEC installed and sampled monitoring wells AL-1 through AL-21. The results identified VOC and metal contaminated groundwater downgradient of the Lot 19-11 wastewater disposal lagoon. TCE was detected in shallow groundwater east of Commerce Street. Investigators assumed additional sources were present at the AIP.

- March 1987: A CERCLA Preliminary Assessment (PA) completed for Lot 19-11 by an EPA contractor recommended further investigation.

- February 1989: VTDEC completed a PA of AIP. The PA recommended further investigation, including suspected contamination on Lot 19-2.

- 1990: A site investigation (SI) was conducted for Lot 19-20 on behalf of the property owner. Groundwater monitoring wells BM-1D, BM-2S, BM-2D, BM-3S, and BM-3D were installed and sampled. Maximum concentrations of TCE and PCE in groundwater were reported as 2,110 micrograms per liter (µg/L) and 7.27 µg/L, respectively.

- 1993: A CERCLA Site Inspection of the AIP, with a primary focus on Lot 1-2, was conducted for the EPA. Limited sampling and analysis did not reveal the suspected source for the TCE contamination east of Commerce Street.

- July 1993: An SI was conducted for Lot 19-5 on behalf of the property owner. Monitoring wells PO-North and PO-South were installed and sampled. No VOC contamination was observed. Low concentrations of metals detected were assumed to be associated with the downgradient Lot 19-11.

- September 1994: An SI performed on Lot 19-23 included soil sampling and installation of monitoring wells ARC-1, ARC-2, and ARC-3. Metals contamination was detected in soil and groundwater; VOC contamination was not detected in groundwater from shallow monitoring wells.

- June 1994: An SI was performed on Lot 19-12 in response to a petroleum release. Shallow monitoring wells were installed and analysis revealed the presence of BTEX contamination in groundwater.

- July 1995: An SI was performed on Lot 19-30. Monitoring wells NO-1 through NO-4 were installed and sampled. TCE was detected at concentrations ranging up to 19,000 µg/L.

- January 1996: A summary report of the various investigations of properties in the AIP was prepared on behalf of the VTDEC. The report identified data gaps in previous work performed in the area.

- October 1996: An SI was performed on behalf of VTDEC to further investigate the AIP. Several monitoring wells were installed, and TCE-contaminated groundwater was identified under the leach field on Lot 19-11.

- July 1999: A limited groundwater investigation was completed for the VTDEC. TCE was the primary contaminant noted, with concentrations up to 91,000 µg/L in groundwater. The report stated that based on the observed concentrations, the presence of non-aqueous phase liquids (NAPL) was possible.

- January 2000: An SI was performed within the AIP and adjacent residential areas on behalf of Mitec. The SI confirmed the presence of PCE, TCE, and BTEX-contaminated groundwater, surface water, and sediments throughout the area, and identified Mitec's leased property (Lot 19-11) and Lot 19-23 as likely sources of groundwater contamination.

- April 2005: The Site was placed on EPA's National Priorities List (NPL).

- December 2008: Nobis conducted a well survey to locate historical wells and re-develop those deemed viable for groundwater sampling. Nobis also conducted a round of groundwater elevation measurements and sampling, and later produced a Data Summary Report and updated Conceptual Site Model (CSM). The report concluded that the majority of TCE resides in the deep overburden groundwater.

- May-November 2010: Nobis conducted a geophysical survey, pore-water sampling of the unnamed stream, groundwater vertical profiling, soil boring and dense non-aqueous phase liquid (DNAPL) testing, monitoring well installations, and a full round of groundwater monitoring well sampling. Nobis later produced a 2010 Data Summary Report and updated the CSM. Report findings include more detailed groundwater quality information with respect to plume delineation, including TCE west of the AIP, pore-water discharge, stratigraphy, and data gaps.

- August-September 2011: Nobis oversaw vertical profiling to collect groundwater samples and determine relative hydraulic conductivity. Samples were sent to an on-site mobile laboratory for VOC screening, and the results used to determine additional sample locations. A subset of samples was sent for confirmatory analyses of VOCs, dissolved and total metals, and 1,4-dioxane. Nobis also collected additional groundwater elevation measurements.

- June-August 2012: Nobis collected groundwater samples from 17 monitoring wells for analysis of VOCs, SVOCs and metals. In addition, soil samples collected from six soil borings were sent for analysis of VOCs, SVOCs and metals to fill data gaps from the 2011 sampling effort.

- June 2012-January 2013: EPA collected indoor air and soil vapor samples from five residential and two commercial buildings. EPA also collected surface water, sediment, and aquatic invertebrate samples within the unnamed stream to better define local conditions.

- January 2013: Nobis performed slug tests at five monitoring wells to characterize areas without previous hydraulic conductivity data.

- December 2013: a contractor for VTDEC installed soil borings and piezometers, collected groundwater samples, and performed a soil vapor and sensitive receptor survey in the area of South Brownell Road and Shunpike Road.

- April 2014: VTDEC collected indoor air and one sump water sample from a property at South Brownell Road. Elevated TCE and PCE were detected, and VTDE installed a remedy that included sump vapor capture and water discharge outside to the lawn. EPA performed follow-up sampling in December 2014, and PCE and TCE were not detected.

- July 2014: Nobis performed a sump investigation at nine properties. Nobis collected shallow soil samples and sump samples (water samples if present and soil samples from the sump if dry), and EPA representatives collected air samples from eight of the properties based on water quality results.

An 2015 EPA Record of Decision selected the following components for the final remedy planned for the Site: excavation of approximately 630 cubic yards of contaminated soil at 96 Commerce Street, in-situ groundwater treatment in the plume core, institutional controls to limit groundwater use and soil exposure and to require continuing access to and operation of existing vapor treatment systems, additional vapor mitigation measures if required, long-term groundwater monitoring, and five-year reviews.
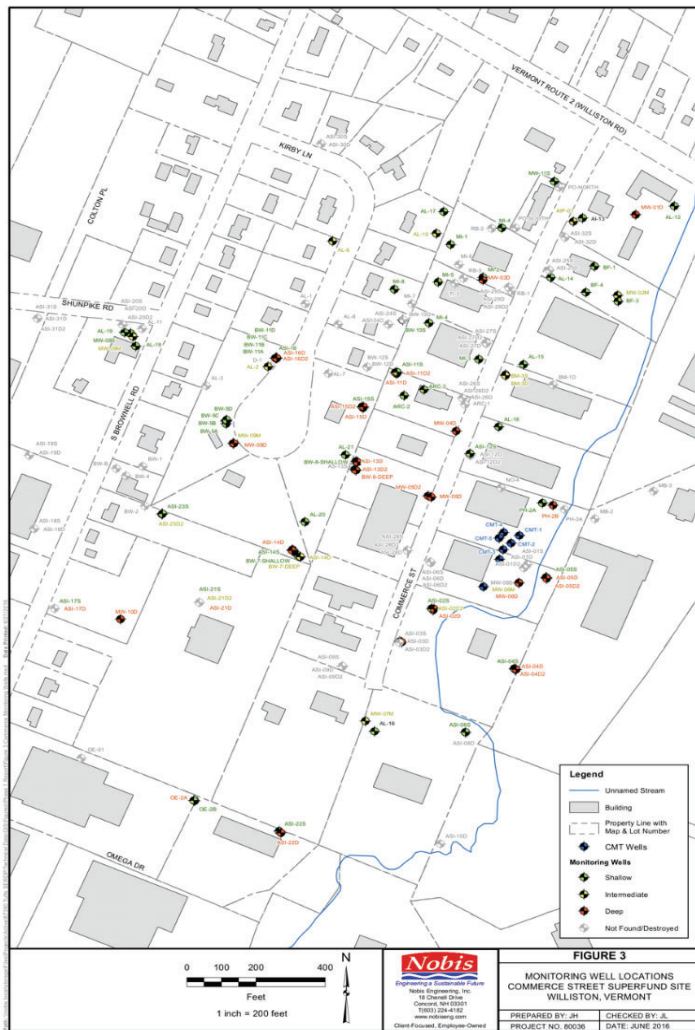
Figure M.3.5. Location of previously installed monitoring wells.

II.3.2. Project Site Data and Materials Collection

The selected area for performance of the Down-Hole Treatability Test (DHT) was a 5 m long transect east of a commercial office building at 237 Commerce Street. At this location, TCE has been naturally attenuated to *cis*-DCE with concentrations up to 0.30 mM. The DHT area is generally flat with a gradual slope to the west from 103 m to 102 m above mean sea level. Surface water drains to an unnamed tributary west of the site within the Winooski River watershed. Groundwater flows to the south and west with a low natural gradient of 0.0036 m/m.

II.3.2.1. Soil Boring and Well Installation

Soil was collected during three soil boring and well installation events. All borings were completed using a direct-push drill rig to the depth of the clay confining layer, 11.3 to 12.2 m (37 to 40 feet)

bgs), with soil samples collected in 1.2 m (4 foot) acetate sleeves. The first event was a preliminary site investigation consisting of two soil borings (SB-1 and SB-2) installed south of the pilot test area (Figure M.3.6). Soil cores were opened on site where engineers from Nobis Engineering (Lowell, MA) visually examined the cores and documented the subsurface lithology. Aliquots of soil were collected and submitted to a commercial laboratory for VOC analysis. Additional soil volumes were transported to the ESL for analysis of soil physical properties.

Subsequently, five continuous multichannel tubing (CMT) multilevel wells were installed in the proposed treatment area to provide additional VOC plume concentration data to guide the design and configuration of the pilot test. CMT well locations were selected based on groundwater elevation data, earlier groundwater sampling results, the TCE and *cis*-DCE concentration data from the preliminary soil borings, and the location of subsurface utilities (Figure M.3.6). The wells were installed in two transects perpendicular to the expected groundwater flow direction; two wells in the upgradient transect and an additional three wells in a transect downgradient. Each CMT multilevel well consisted of seven discrete channels screened at discrete intervals to allow groundwater samples to be collected from specified depths beneath the water table. Based on concentration and lithology data obtained from earlier borings, the well screens were installed at 4.7 to 4.9 m (15.5 to 16.0 feet) bgs, 6.1 to 6.2 m (20.0 to 20.5 feet) bgs, 7.9 to 8.1 m (26.0 to 26.5 feet) bgs, 8.8 to 9.0 m (29.0 to 29.5 feet) bgs, 9.6 to 9.8 m (31.5 to 32.0 feet) bgs, 10.4 to 10.5 m (34.0 to 34.5 feet) bgs, and 11.1 to 11.3 m (36.5 to 37.0 feet) bgs. During CMT well installation, field personnel cut the recovered soil cores into 0.61 m (2 foot) sections, capped each section, and placed them in coolers on ice for storage and transport to the Tufts ESL. While awaiting analysis, the soil cores were stored at 4ºC to minimize microbial activity and the volatilization of compounds in the soils.

In September 2016, prior to implementing the pilot test, 4 additional wells were installed in the vicinity of CMT-1 (Figure M.3.6). Three of these wells (DHT-1, DHT-2, and DHT-4) were 5.1 cm (2-inch) diameter PVC-wells, screened between 10.1 and 10.7 m (33.0 and 35.0 feet) bgs to deliver amendments into and collect samples from the depths of the aquifer with high TCE and *cis*-DCE concentrations. The fourth well, CMT-6, had a similar construction to the existing CMT wells with 6 screened intervals between 6.2 and 6.4 m (20.5 and 21.0 feet) bgs, 7.9 to 8.1 m (26.0 to 26.5 feet) bgs, 8.8 to 9.0 m (29.0 to 29.5 feet) bgs, 9.6 to 9.8 m (31.5 to 32.0 feet) bgs, 10.4 to 10.5 m (34.0 to 34.5 feet) bgs, and 11.1 to 11.3 m (36.5 to 37.0 feet) bgs. CMT-6, situated 5 m upgradient of CMT-1, allowed monitoring of constituents entering the pilot test area. Well DHT-1 was located 3 m upgradient of CMT-1 and was used as an injection well for bioaugmentation and biostimulation. The third well (DHT-2) is 2.0 m upgradient of CMT-1 and served as an extraction well during recirculation and a monitoring well afterward. This configuration allowed CMT-1 to be used as an extraction well during the pilot test. Soil cores collected during well installation were capped, stored, and transported as described above.

All wells were developed by rapidly pumping (400 mL/min) more than three well volumes (approximately 3.0 L) of water from the well after installation and at least 72-hours prior to sampling to remove fine materials from the well screen and any water that was introduced during drilling.

II.3.2.2. Groundwater Monitoring and Sampling

Site-wide groundwater elevations were measured using a Model 101 or Model 102 water level meter (Solinst; Georgetown, ON). Measurements were collected at 35 existing site groundwater wells in August 2014 with additional measurements prior to and during groundwater sampling events. Groundwater samples were collected using U.S. Environmental Protection Agency (EPA)

low-flow sampling protocols for most wells and using a modified low-flow protocol for CMT-wells. The modified protocol limited purging to the slowest flow rate, approximately 100 mL/min, for a maximum of 25 minutes and omitted turbidity measurements. Water was removed from the wells using a Geopump 2 peristaltic pump (Geotech; Denver, CO) and high-density polyethylene (HDPE) tubing. Water quality parameters (temperature, pH, dissolved oxygen, and specific conductivity) were measured using a 556 MPS or Professional Plus 1060 meter (YSI; Yellow Springs, OH). During the August 2014 sampling, turbidity was measured with a microTPW Handheld Turbidity Meter (HF Scientific; Fort Meyers, FL).
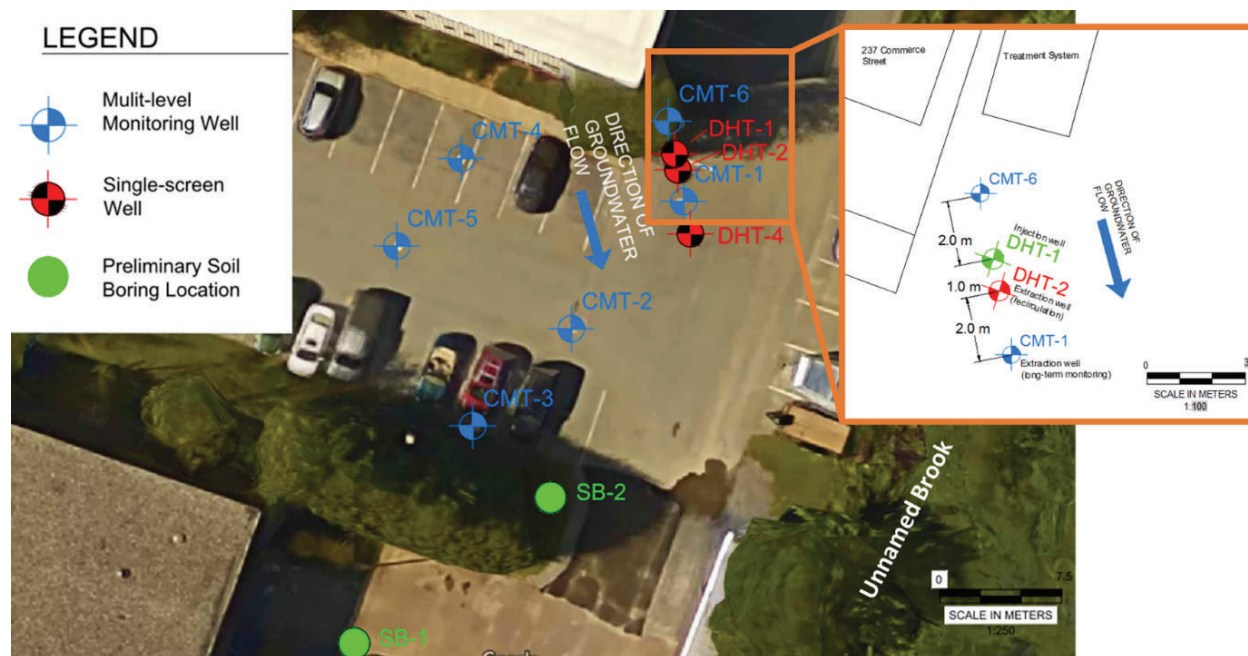
Figure M.3.6. Well locations.

Samples for chlorinated ethene and ethene analysis were collected in 40 mL glass VOA sampling vials with septa caps, completely filled to eliminate headspace; additional sample from select VOA vials was used for VFA, DOC, dissolved metals, and anion analysis. Samples for biological analysis were collected in 1.0 L HDPE bottles (Fisher Scientific; Agawam, MA) for laboratory filtration using a 0.22 μm pore size filter funnel (MoBio Laboratories; Carlsbad, CA). Alternatively, 0.3 to 2.0 L of groundwater was filtered in the field using a 0.2 μm pore size Sterivex filter cartridge (Millipore; Burlington, MA). Sterivex filters to be used for RNA analysis were preserved by injecting 3.0 mL of RNAlater solution (Invitrogen-ThermoFisher; Waltham, MA) into the filter cartridge after the sample was collected. All samples were collected in triplicate, stored on ice, and transported to Tufts ESL for storage and analysis. VOA vials were stored at 4°C, then sampled and analyzed within 72-hours. Additional samples were stored at 4°C and biological samples were stored at -80°C prior to analysis.

Prior to implementing the pilot test, groundwater samples were collected from 9 previously installed site monitoring wells in August 2014, from the 5 CMT-wells (all 7 depths) in September 2014, from select CMT-well depths in October 2015 (chloroethene and biological sampling only), and from select CMT-well depths in September 2016 (chloroethene sampling only). Immediately preceding and throughout the pilot test, groundwater samples were collected from CMT-6, CMT-1, DHT-1, and DHT-2 twice per month for chloroethene and VFA analysis and monthly for biological analysis.

II.4. Laboratory Experiments

II.4.1. Batch Reactor and Microcosm Experimental Methods

Batch reactor (no porous media) and microcosm (with porous media) experiments are often used to determine the capability of microbial populations to transform chlorinated solvents, to assess the need for biostimulation amendments, and to determine microbial transformation rates (Duhamel et al., 2002; Major et al., 2002; Stroo et al., 2013; Stroo and Ward, 2010).

A series of batch reactor and microcosm experiments were performed with material from the Commerce Street Site in order to design aquifer cell experiments and the DHT pilot test, specifically to determine the need for bioaugmentation and biostimulation amendments. These experiments were also used to obtain initial parameters for models of microbial reductive dechlorination.

Batch reactor and microcosm experiments were performed in 160 mL glass serum bottles capped with butyl rubber stoppers and aluminum crimp caps. All reactors were prepared at room temperature in an anaerobic chamber containing an atmosphere of 97% N_2/3% H_2 (Coy Laboratory Products; Grass Lake, MI).

Porous media used in microcosms were derived from cores collected during the installation of CMT and DHT wells as described in Section II.3.2.1 above. Cores used in microcosms were opened and stored in the anoxic chamber prior to use. Reactors were prepared with 0.0 to 20 mL of porous media (0.0 to 15 g) and 80 to 100 mL of liquid for a total volume of approximately 100 mL. The liquid phase consisted of an anoxic growth medium prepared according to (Löffler et al., 2005), unamended site groundwater, anoxic site groundwater prepared as described in Section II.1 above, or a combination of groundwater and growth medium (Table M.4.1).

Reactors were amended with 0.10 to 0.48 mM TCE and a subset of reactors were amended with 5 to 10 mM sodium DL-lactate (60%v/v solution) as electron donor and/or 0.1 mL of Wolin vitamin solution (Wolin et al., 1963); select reactors were bioaugmented with BDI-SZ or KB-1® inoculum (Table M.4.1). Abiotic control reactors were prepared with sterilized growth medium and sterilized porous media to identify possible chlorinated ethene losses caused by abiotic processes, including adsorption to rubber stoppers. Each configuration (see Table M.4.1) was prepared in triplicate for a total of 123 reactors. This matrix of microcosm reactors was used to determine the ability of the native microbial community to breakdown TCE with or without electron donor addition and to assess the need for bioaugmentation.

Table M.4.1. Microcosm and batch reactor configuration.

Microcosm	Start Date	Porous Media	GW Source	Growth Medium	Initial TCE concentration (mM)	Lactate addition	Vitamin addition	Bioaugmentation culture
A1	1/14/2016	CMT-4 10.7-11.3m(Fall 2014)	None	Yes	0.48	No	Yes	None
A1-no soil	1/14/2016	none	None	Yes	0.45	No	Yes	None
C4G-noED	1/14/2016	none	CMT-4 D7 (October 2015)	No	0.44	No	No	None
C4-noED	1/14/2016	CMT-4 10.7-11.3m(Fall 2014)	CMT-4 D7 (October 2015)	No	0.44	No	No	None
C4G	1/14/2016	none	CMT-4 D7 (October 2015)	No	0.44	Yes	No	None
C4-oldGW	1/14/2016	CMT-4 10.7-11.3m(Fall 2014)	CMT-4 D7 (October 2015)	No	0.44	Yes	No	None
C5GM	1/14/2016	none	CMT-4 D7 (October 2015)	Yes	0.46	Yes	Yes	None
C4M-oldGW	1/14/2016	CMT-4 10.7-11.3m(Fall 2014)	CMT-4 D7 (October 2015)	Yes	0.46	Yes	Yes	None
AC5	2/8/2016	none	CMT-5 D7 (October 2015)	No	0.24	No	No	None
BC5GM	2/8/2016	none	CMT-5 D7 (October 2015)	Yes	0.29	Yes	No	BDI
BC5	2/8/2016	CMT-4 10.7-11.3m(Fall 2014)	CMT-5 D7 (October 2015)	No	0.22	Yes	No	BDI
BC5M-oldGW	2/8/2016	CMT-4 10.7-11.3m(Fall 2014)	CMT-5 D7 (October 2015)	Yes	0.20	Yes	Yes	BDI
C5M-oldGW	2/8/2016	CMT-5 10.7-11.3m(Fall 2014)	CMT-1 D7 (October 2015)	Yes	0.20	Yes	Yes	None
C1	2/25/2016	CMT-5 10.7-11.3m(Fall 2014)	CMT-1 D7 (2/22/16)	No	0.21	Yes	No	None
C1M	2/25/2016	CMT-5 10.7-11.3m(Fall 2014)	CMT-1 D7 (2/22/16)	Yes	0.20	Yes	Yes	None
C3	2/25/2016	CMT-5 10.7-11.3m(Fall 2014)	CMT-3 D7 (2/22/16)	No	0.18	Yes	No	None
C3M	2/25/2016	CMT-5 10.7-11.3m(Fall 2014)	CMT-3 D7 (2/22/16)	Yes	0.20	Yes	Yes	None
C4	2/25/2016	CMT-5 10.7-11.3m(Fall 2014)	CMT-4 D7 (2/22/16)	No	0.18	Yes	No	None
C4M	2/25/2016	CMT-5 10.7-11.3m(Fall 2014)	CMT-4 D7 (2/22/16)	Yes	0.18	Yes	Yes	None
C5	2/25/2016	CMT-5 10.7-11.3m(Fall 2014)	CMT-5 D7 (2/22/16)	No	0.16	Yes	No	None
C5M	2/25/2016	CMT-5 10.7-11.3m(Fall 2014)	CMT-5 D7 (2/22/16)	Yes	0.18	Yes	Yes	None

Microcosm	Start Date	Porous Media	GW Source	Growth Medium	Initial TCE concentration (mM)	Lactate addition	Vitamin addition	Bioaugmentation culture
C5G	2/25/2016	none	CMT-5 D7 (2/22/16)	No	0.23	Yes	No	None
C5GM	2/25/2016	none	CMT-5 D7 (2/22/16)	Yes	0.22	Yes	Yes	None
C5-noEd	2/25/2016	CMT-5 10.7-11.3m(Fall 2014)	CMT-5 D7 (2/22/16)	No	0.19	No	No	None
C5M-noEd	2/25/2016	CMT-5 10.7-11.3m(Fall 2014)	CMT-5 D7 (2/22/16)	Yes	0.16	No	Yes	None
C5G-noED	2/25/2016	none	CMT-5 D7 (2/22/16)	No	0.17	No	No	None
AC5	2/25/2016	CMT-5 10.7-11.3m(Fall 2014)	CMT-5 D7 (2/22/16)	Yes	0.15	Yes	No	None
AC5G	2/25/2016	none	CMT-5 D7 (2/22/16)	No	0.15	Yes	No	None
BC5M	2/25/2016	CMT-5 10.7-11.3m(Fall 2014)	CMT-5 D7 (2/22/16)	Yes	0.11	Yes	Yes	BDI
KPC	5/6/2016	none	None	Yes	0.22	Yes	Yes	KB-1
KC4G	5/6/2016	none	CMT-4 D7 (2/20/16)	No	0.17	No	No	KB-1
KC4	5/6/2016	CMT-4 10.4-10.7m (Fall 2014)	CMT-4 D7 (2/20/16)	No	0.23	No	No	KB-1
KC4GM	5/6/2016	none	CMT-4 D7 (2/20/16)	Yes	0.19	Yes	Yes	KB-1
KC4M	5/6/2016	CMT-4 10.4-10.7m (Fall 2014)	CMT-4 D7 (2/20/16)	Yes	0.24	Yes	Yes	KB-1
C4M_2	5/6/2016	CMT-4 10.4-10.7m (Fall 2014)	CMT-4 D7 (2/20/16)	Yes	0.22	Yes	Yes	None
KC4M-noED	5/6/2016	CMT-4 10.4-10.7m (Fall 2014)	CMT-4 D7 (2/20/16)	Yes	0.16	No	No	KB-1
AC4	5/6/2016	CMT-4 10.4-10.7m (Fall 2014)	CMT-4 D7 (2/20/16)	No	0.14	No	No	None
KC4-vitamins	5/9/2016	CMT-4 10.4-10.7m (Fall 2014)	CMT-5 D7 (2/20/16)	No	0.19	Yes	Yes	KB-1
D2	2/24/2017	DHT-2 10.4-10.7m (Fall 2016)	Anoxic GW	No	0.21	Yes	No	None
KD2	2/24/2017	DHT-2 10.4-10.7m (Fall 2016)	Anoxic GW	No	0.20	Yes	No	KB-1
AD2	2/24/2017	DHT-2 10.4-10.7m (Fall 2016)	Anoxic GW	No	0.10	Yes	No	None

II.4.2. Aquifer Cell Transformation Studies; Experimental methods

II.4.2.1. Aquifer Cell 1

Although bioaugmentation and biostimulation have been implemented as effective remedial strategies, many sites exhibit incomplete dechlorination to dichloroethene isomers (DCE) and/or VC or exhibit rebound of contaminant concentrations when active biostimulation ceases (Kielhorn et al., 2000; Lendvay et al., 2003; Major et al., 2002; Stroo and Ward, 2010; Tillotson and Borden, 2017). Contaminant rebound is exacerbated by subsurface heterogeneity, which enables contaminant retention as aqueous and sorbed phases in low permeability porous media, allowing for the slow release of the compounds over time (McGuire et al. 2006; Sale et al. 2013; Stroo and Ward 2010). Subsurface heterogeneity also complicates bioremediation as most bioremediation amendments are delivered through groundwater injection and do not effectively distribute into low permeability regions (Sale et al., 2013; Stroo et al., 2013).

Despite these limitations, bioremediation can be effective in heterogeneous systems (Damgaard et al., 2013b; Scheutz et al., 2010). Biological reductive dechlorination of TCE and PCE adjacent to NAPL source zones is known to increase the dissolution rate by dechlorinating dissolved contaminants to more water soluble compounds and by increasing the concentration gradient between the NAPL and the surrounding fluid, thus reducing source longevity (Amos et al., 2009; Cápiro et al., 2015; Sleep et al., 2006; Yang and McCarty, 2000). Similarly, biological activity in higher permeability zones where bioremediation amendments are more easily distributed can facilitate the back diffusion of compounds from low permeability into higher flow regions by increasing the mass transfer driving force (Chambon et al., 2010; Lima and Sleep, 2007; Scheutz et al., 2010).

Numerical models can serve as predictive tools to guide site management and decision-making, and have been demonstrated to provide accurate assessment of multi-dimensional systems involving permeability heterogeneity and back diffusion at the field- and bench-scales (Chapman et al., 2012; Chapman and Parker, 2005; Parker et al., 2008; Rodriguez, 2006). However, these studies do not account for changes to the driving force and contaminant properties (e.g. diffusivity, sorptive capacity, volatility) caused by biological transformation. Further, there are limited studies that have utilized numerical models to quantify the extent of back diffusion when enhanced by biotransformation.

Due to their important role in attenuating releases from low-permeability media and influence contaminant rebound rates, understanding the distribution of dechlorinating organisms in heterogeneous porous media and quantifying their contribution to enhanced mass flux is essential to designing effective remedies for chlorinated solvent contamination in real-world systems. Quantifying Rdase genes has become a useful tool for identifying *Dhc* stains and assessing the dechlorination capability of a microbial community (Damgaard et al., 2013b; Lee et al., 2008; Ritalahti et al., 2006; Van Der Zaan et al., 2010). In addition to understanding the distribution of organisms at the genus or species level in heterogeneous systems, examining the distribution of specific *Dhc* strains (i.e., cells harboring specific Rdase genes) is necessary to gain a complete picture of dechlorination potential.

This research was undertaken to improve our understanding of microbial growth and distribution within heterogeneous porous media and the contribution of these microbes to increasing the flux of contaminants from low permeability and highly sorptive materials. The influence of permeability and substrate (electron donor and acceptor) availability on the distribution of *Dhc* 16S rRNA and Rdase genes and how these conditions influence the roles of microorganisms was examined using a laboratory-scale, multi-dimensional aquifer cell system. This experiment

(hereafter referred to as Aquifer Cell 1) was performed in an aquifer cell packed with five porous media with permeabilities ranging from 0.03 to 10.2 m/day. An abiotic study of the diffusion of TCE from low permeability regions was completed and compared to results of a subsequent biotic experiment in which the aquifer cell system was bioaugmented with KB-1® (SiREM, Guelph, ON). Spatial and temporal distributions of *Dhc*, Rdase genes, and TCE daughter product formation were monitored within the aquifer cell system using side sampling ports.

A numerical model (Section II.5) capable of simulating abiotic contaminant transport, including diffusion and sorption, was calibrated using data gathered in the abiotic phases of the experiment. This model was then used to compare a prediction of abiotic contaminant transport to the actual contaminant transport observed during the biotic experiment.

II.4.2.1.1. Aquifer Cell 1: Setup and Preparation

The aquifer cell measured 63.5 cm (length) × 38 cm (height) × 1.4 cm (thickness) and was constructed with two 1.4 cm thick glass panels held in an aluminum frame configured with sampling ports aligned in four vertical columns (Cápiro et al., 2015). A layer of clay collected from the Commerce Street Superfund Site (Williston, VT) was emplaced in the bottom 3 cm of the aquifer cell to create a lower confining layer. The clay was dried, ground with a mortar and pestle, and re-saturated with a 0.76 mM TCE solution prior to emplacement. Above the clay, the aquifer cell was packed under water saturated conditions with ASTM Standard 20/30 sand (US Silica Company; Ottawa, IL) as the background with four 5 cm (height) x 14 cm (length) emplaced lenses positioned with sampling ports downgradient of each. The lens materials consisted of: Webster soil (Iowa State University Agricultural Experiment Station; Ames, IA), Appling soil (University of Georgia Agricultural Experiment Station; Eastville, GA), F-95 low permeability sand (Fisher Scientific; Hampton, NH), and loamy sand collected from the Commerce Street site in Williston, VT (Figure M.4.1) with material properties detailed in Table M.1.1. After packing, flow was established in the aquifer cell using a constant head influent system as described by (Cápiro et al., 2015). Influent solutions were prepared in a 5.0 L Mariotte bottle and the flow rate was maintained between 0.10 and 2.60 mL/min by adjusting the heights of the influent and effluent. Flow rates correspond to a seepage (pore-water) velocity of 7.47 to 82.5 cm/day and a residence time of 0.77 to 8.5 days.

II.4.2.1.2. Tracer and Abiotic Desorption Experiment

A tracer test was performed in the aquifer cell using a 10 mM sodium bromide (Fisher Scientific; Hampton, NH) and 0.075 mM sodium fluorescein (Sigma Aldrich; St. Louis, MO) solution at a flow rate of 2.3 to 2.6 mL/min (200-227 cm/day seepage velocity). After a 750 mL pulse of this solution (approximately 0.66 PVs), the influent was changed to the background electrolyte solution of 10 mM sodium chloride. Effluent samples were collected continuously in 19-minute fractions using a CF-2 fraction collector (Spectrum Laboratories; Rancho Dominguez, CA). Additional 0.6 mL samples were collected from 12 of the sampling ports throughout the tracer experiment approximately once every 90 minutes. Effluent sample bromide concentration was measured using a bromide combination electrode; port sample bromide concentrations were measured by IC as described in Section II.2.2. Black light, time-lapse photographs were taken with an EOS Rebel T2 digital camera (Canon; Melville, NY) throughout the tracer experiment to visually verify the flow of fluorescein through the aquifer cell.
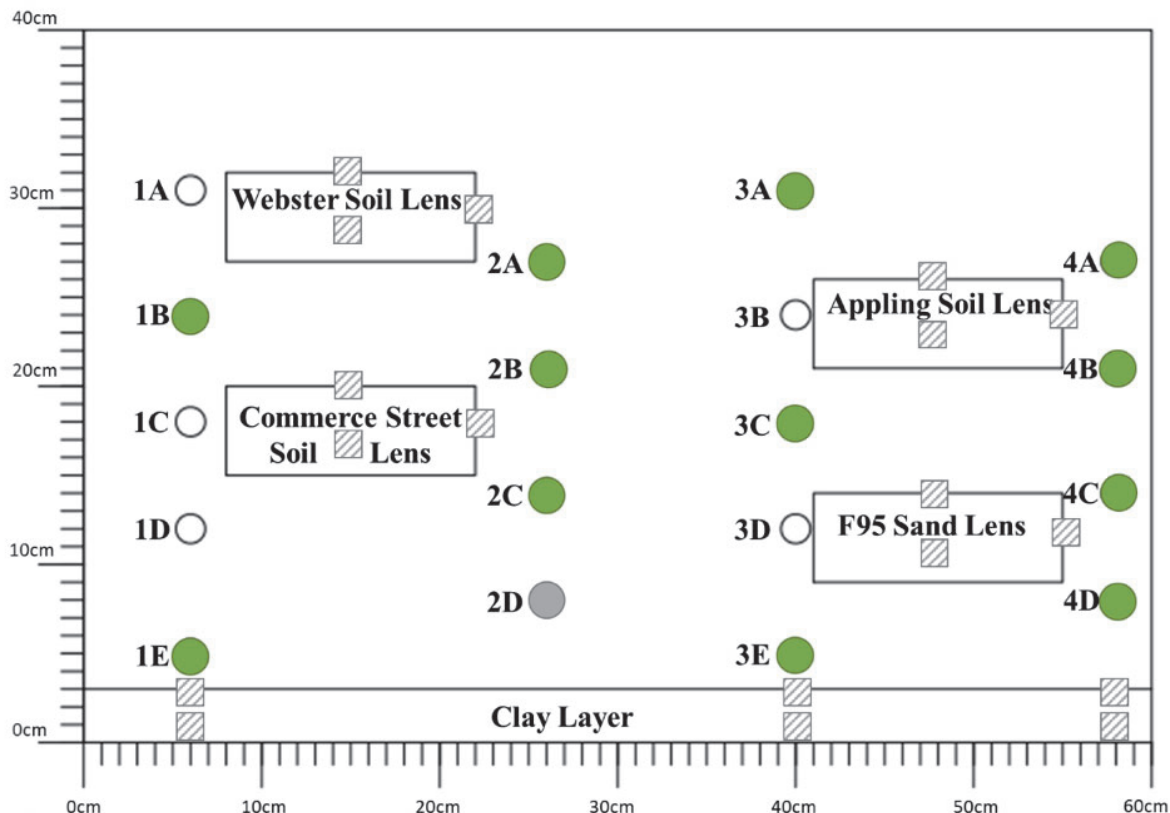
Figure M.4.1. Aquifer cell layout and sample locations. Aqueous sampling ports sampled throughout experiment ⬤ , final 7 rounds only ⬤ , and additional soil sample locations ▨.

After the tracer experiment, the aquifer cell was flushed with a 0.5 mM TCE and 10 mM sodium bromide solution, as summarized in Table M.4.2. When measured TCE concentrations in each of the sampling ports were greater than 0.39 mM, the influent was changed to 10 mM sodium chloride solution without TCE to unload TCE from the cell (Table M.4.2). During this period, 1.6 mL samples were collected from 12 sample ports using a syringe pump to draw samples at a rate of 0.1 mL/min (10% of the background flow rate); 1.6 mL effluent samples were collected from a sampling bulb in the effluent line. Ports were selected for sampling based upon their locations relative to the clay and soil lenses and to provide a sampling port downgradient of each lens; preliminary modeling results suggested that these locations would be most affected by the soil lenses. Sample aliquots (1.0 mL) were used to measure chlorinated ethene (TCE, *cis*-DCE, and VC) and ethene concentrations by GC with FID and the remaining sample volume (0.6 mL) was analyzed for bromide concentration by IC. Details of analytical methods are provided in Section II.2.2.

II.4.2.1.3. Biotic Degradation Experiment

Following the abiotic desorption experiment, the aquifer cell was again loaded with a 0.5 mM TCE influent in three phases (Table M.4.2). Anoxic conditions were then established by changing the influent solution to a reduced mineral salts medium prepared according to Cápiro et al. (2015), and containing 10 mM sodium lactate solution and 0.5 mM TCE. The flow rate was subsequently reduced to approximately 0.25 mL/minute (18 cm/day seepage velocity; 3.4-day residence time) to provide additional time for biodegradation reactions to be observed. The aquifer cell was then bioaugmented with KB-1® inoculum (SiREM; Guelph, Ontario). The SiREM-provided inoculum

was diluted in sterile, reduced mineral salts medium, then 20 mL of dilute inoculum was injected into each of the 18 sampling ports using a syringe pump at a rate of 0.1 mL/min to provide target of approximately 10^4 *Dhc* gene copies/mL of pore water, the cell density suggested to yield acceptable degradation rates (Adrian et al. 2016).

Table M.4.2. Aquifer cell 1 experimental parameters. (L = Loading, U = Unloading)

Phase	Bromide Tracer L	Bromide Tracer U	Abiotic Experiment L	Abiotic Experiment U	Biotic Experiment L I	L II	L III	Phase I	Phase II	Phase III
Avg. Flow Rate (mL/min)	2.4	2.4	1.0	0.93	0.51	0.71	0.39	0.27	0.21	0.16
Duration (PVs)	0.63	2.3	15.9	8.9	12.9	6	3.7	2.6	5.8	1.5
Duration (days)	0.21	0.79	13	8	21	7	8	8	23	8
Influent Solution (mM)	10 mM sodium bromide and 0.075 mM sodium fluorescein	10 mM sodium chloride	10 mM sodium bromide	10 mM sodium chloride	10 mM sodium chloride	Mineral Salts Medium with 10 mM sodium lactate				
Influent TCE (mM)	0	0	0.5	0 mM	0.5	0.5	0.5	0.5	0.04	0.01

Subsequent to bioaugmentation, the influent solution of mineral salts medium, lactate, and TCE was maintained (Phase I), after which the influent TCE concentration was reduced to 0.04 mM (Phase II) (Table M.4.2). For the final Phase (III), the influent TCE concentration was lowered to 0.01 mM TCE. Samples of 1.0 to 2.6 mL were collected from the 12 side ports and from the effluent throughout each stage of the experiment and analyzed for chlorinated ethenes and ethene as described above; after bioenhanced diffusion was observed, an additional port (Port 2D) was sampled during the final 7 rounds of aqueous sampling, beginning 25 days (6.6 PVs) after bioaugmentation. Sample aliquots of 0.5 mL were also analyzed for VFAs by HPLC and the remaining sample volumes were centrifuged and frozen for microbial quantification according to Cápiro et al. (2015). Details of DNA extraction and microbial quantification via qPCR under TaqMan-based chemistry are provided in Section II.2.3. (Ritalahti et al. 2006).

II.4.2.1.4. Soil Sampling and Analysis

Following collection of the final round of aqueous samples from the side ports, the aquifer cell was placed on its side, and one pane of glass was removed. Soil samples were collected from the porous media corresponding to the 13 ports where aqueous samples were collected with an additional 3 samples collected from each of the soil lenses and 6 samples collected from the clay confining layer (Figure M.4.1). Each sample was immediately placed in a sterile container and frozen at -80°C for future DNA extraction and microbial quantification. An additional thirty-five samples (5 of background sand, 5 of each lens, and 10 of the clay confining layer) were collected and analyzed for TCE using the methanol extraction procedure described in Section II.2.1.

II.4.2.2. Aquifer Cell 2

The reliability of model predictions for contaminant biodegradation and field cleanup time depend on the characterization of reaction processes and, more importantly, the use of relevant degradation rates (NRC, 2013). Due to the difficulty in assessing field-scale degradation rates, laboratory estimated parameters and reference values, most commonly derived from microcosm batch studies, have commonly been used for field-scale simulations (Scheutz et al. 2010). However, studies (Ding et al. 2017; Phanikumar et al. 2005) have demonstrated that field scale models using degradation rates from laboratory experiments over-predict the contaminants degradation by up to several orders of magnitude. Incomplete mixing of reagents induced by field heterogeneity has identified to be the main reason for smaller reaction rates in the field (e.g., Dentz et al., 2011; NAVFAC, 2013). Supporting this hypothesis, Haest et al., (2011) demonstrated the effect of mass transport limitations by comparing batch dechlorination rates with rates in column experiments but did not compare their results with a field-scale system.

Dechlorination rates of VOCs depend on numerous properties including: environmental conditions, species present, heterogeneities in porous media, and mass transfer rate limitations. Values derived for one system and microbial community may not be appropriate for different systems or populations. Furthermore, despite the progress made in applying numerical models for field scale dechlorination (e.g., Chambon et al., 2010; McCarty et al., 1998), there is, to date, no numerical study comparing the dechlorination rates from batch to intermediate scale to field scale. Although there are multiple studies of bioremediation at the field scale (Schaefer et al. 2010; Semkiw and Barcelona 2011), none of these studies includes comparisons to both batch and 2-dimensional flow systems using the same materials and methods.

To compare dechlorination rates across experiments of increasing complexity, an aquifer cell experiment (hereafter referred to as Aquifer Cell 2) was designed to recreate as closely as possible the conditions of the planned pilot (DHT) test. All porous media and groundwater were obtained from the Commerce Street Superfund Site in Williston, VT as described in Section II.1. Dechlorination rates derived from the microcosm experiments (Section II.4.1) were used to predict the performance of the aquifer cell using a numerical model incorporating transport of contaminants and electron donors coupled with a model of microbial reductive dechlorination (Section II.5). The performance of the aquifer cell experiment was also compared to the DHT pilot test to assess the suitability of laboratory-derived dechlorination rates on field-scale applications (Section IV).

II.4.2.2.1. Aquifer Cell Setup and Preparation

The second 63.5 cm (length) × 38 cm (height) × 1.4 cm (thickness) aquifer cell was constructed in the same frame described in Section II.4.2.2.1 above. Site clay (borehole CMT-2, 12.2 to 12.8 m [40 to 42 feet] bgs) was dried, ground with a mortar and pestle, then resaturated with a 0.76 mM TCE solution and emplaced in the bottom 3 cm of the aquifer cell to create a lower confining layer. Above the clay, the aquifer cell was packed under water saturated conditions with site soil collected from the 9.4 to 10.4 (31 to 34 feet) bgs cores of borehole DHT-2, collected and stored as described above. For the cores used in the aquifer cell, the acetate sleeves were opened in an anoxic chamber and separated into sections representing 15 cm (6-inches) of borehole depth. Each discrete section was homogenized by mixing with a scoop, placed in Ziploc® bags, then packed in the aquifer cell within 1 hour to maintain the native microbial population. The discrete sections of soil cores were placed in 4 to 6 cm layers in the aquifer cell to recreate the stratigraphy of the field site (Figure M.4.2).

After packing, flow was established in the aquifer cell using a constant head influent system as described by (Cápiro et al. 2015). Anoxic site groundwater was prepared in a 5.0 L Mariotte bottle and the flow rate was controlled by adjusting the heights of the influent and effluent to maintain a flow rate between 0.10 and 0.20 mL/min; a corresponding seepage (pore-water) velocity of 12.5 to 25 cm/day and a residence time of 4.8 to 9.5 days.
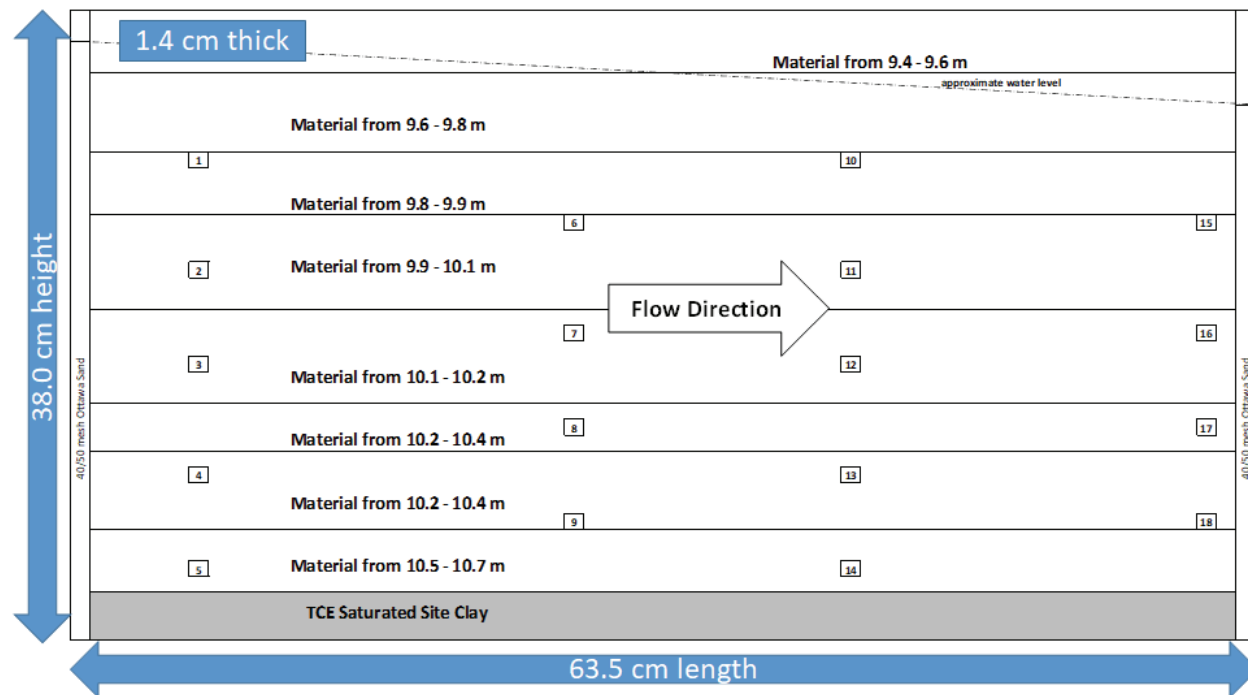
Figure M.4.2. Second Aquifer Cell configuration.

II.4.2.2.2. Aquifer Cell Operation

A tracer test was performed in the aquifer cell using a 385 mL (approximately 1/3 pore volume) pulse of 10 mM sodium bromide and 0.06 mM (50 mg/L) erioglaucine A (blue dye) solution at a flow rate of approximately 0.15 mL/min. Effluent samples were collected continuously in 75 minute fractions using a CF-2 fraction collector (Spectrum Laboratories; Rancho Dominguez, CA) and bromide concentrations were measured using a bromide combination electrode (Cole Parmer; Vernon Hills, IL). Time-lapse photographs were taken with an EOS Rebel T2 digital camera (Canon; Melville, NY) throughout the tracer experiment to visually verify the flow of erioglaucine A tracer through the aquifer cell.

After the tracer experiment, the aquifer cell was flushed with a solution of 0.3 mM TCE in anoxic site groundwater for a period of 32 days at a flow rate of 0.2 mL/min (25 cm/day seepage velocity) to establish a uniform background contaminant concentration. The aquifer cell was then reconfigured to a recirculation system where the effluent was removed with a peristaltic pump (Cole Parmer; Vernon Hills, IL) at a rate of 0.1 mL/min (12.5 cm/day seepage velocity), amended with 100 mM lactate stock at 0.01 mL/min to achieve a concentration of 10 mM lactate, and reinjected into the aquifer cell. After 10-days of recirculation, the aquifer was bioaugmented with KB-1® inoculum (SiREM; Guelph, Ontario). The SiREM provided inoculum was diluted 1:320 in anoxic site groundwater amended with 10 mM lactate and 20 mL of dilute inoculum was injected into each of the 5 sampling ports in the first column using a syringe pump at a rate of 1 mL/min to provide target of approximately 10^6 *Dhc* cells/L of pore water, the cell abundance that indicates

complete transformation to ethene is likely (Lu et al. 2006; Ritalahti et al. 2010b; a; Stroo et al. 2013). Recirculation with lactate amendment continued for an additional 14 days following bioaugmentation to distribute the inoculum throughout the aquifer cell. After recirculation, the aquifer was converted back to a head-driven flow system without recirculation. Flushing of anoxic groundwater with 0.3 mM TCE continued at a flow rate of approximately 0.1 mL/min for 88 days, after which the flow rate was reduced to 0.05 mL/min and maintained for an additional 64 days (Table M.4.3).

After the recirculation phase, three pulses of lactate were introduced into the aquifer cell by changing the influent solution to anoxic groundwater amended with 0.3 mM TCE and 5 mM lactate. Each pulse consisted of 1.0 L, approximately 1 PV, of lactate-amended influent solution. The first two pulses contained 10 mM lactate and were injected over the course of 7 days at a flow rate of 0.1 mL/min, the final pulse contained 5 mM lactate and was injected over 14 days at 0.05 mL/min. The pulses began 17.7, 59.7, and 101.6 days following the end of recirculation.

Table M.4.3. Aquifer cell 1 experimental parameters.

Phase	Bromide Tracer/ TCE loading	Lactate Recirculation	Bioaug-mentation	Lactate/ Biomass Recirculation	Long-term Monitoring	Monitoring w/ Reduced Flow Rate
Duration (days)	37	10	1	14	88	64
Pore Water Velocity (cm/d)	15	15	7.5	7.5	7.5	3.75
Residence Time (days)	4	4	8	8	8	16
Injections	10 mM bromide; 0.06 mM erio-glaucine A (blue dye); 0.3 mM TCE	0.3 mM TCE; 10 mM lactate	100 mL of dilute KB-1® in first column of ports	0.3 mM TCE; 10 mM lactate	0.3 mM TCE; 2 pulses of 10 mM lactate (7 days each)	0.3 mM TCE; 1 pulse of 5 mM lactate (14 days)

Throughout the experiment, 1.6 mL samples were collected from 10 of the sample ports using a syringe pump to draw a sample at a rate of 0.1 mL/min (10% of the background flow rate); effluent samples were collected from a 10 mL sampling bulb in the effluent tubing. Chlorinated ethene (TCE, *cis*-DCE, and VC) and ethene concentrations were measured using by GC with FID. Sample aliquots were also analyzed for VFAs by HPLC and additional sample volumes were centrifuged and frozen for microbial quantification according to (Cápiro et al. 2015).

II.4.2.2.3. Soil Sampling and Analysis

Following collection of the final round of aqueous samples from the side ports, the aquifer was placed on its side, and one pane of glass was removed. Soil samples were collected from the porous media corresponding to all 18 ports with an additional 6 samples collected from the clay confining layer. Each sample was divided in half with one portion immediately placed in a sterile container and frozen at -80°C for future DNA extraction and microbial quantification and the remaining sample immediately placed in methanol for TCE and *cis*-DCE analysis using the methanol extraction procedure described in Section II.2.1.

II.5. Multiphase Flow and Reactive Transport Modeling Framework

II.5.1. Introduction – Modeling DNAPL Mass Release, Transformation, and Persistence in Heterogeneous Environments

At aged DNAPL contamination sites, as concentrations in the more transmissive zones decline, contaminants sequestered in low permeability zones are released back into the mobile plume. This process is often referred to as "back diffusion" (BD) (Mackay and Cherry 1989). Along with DNAPL dissolution, BD has been increasingly recognized as an important process that sustains chlorinated solvent plumes (Abriola et al., 2012; NRC, 2013; Sale et al., 2013, 2008; Stroo et al., 2012).

A number of studies have employed numerical models to capture diffusive mass transport into low permeability zones and to predict persistence of plume tailing due to BD (Chapman et al., 2012; Chapman and Parker, 2005; Maghrebi et al., 2015, 2014; Matthieu et al., 2014; Parker et al., 2008). In general, these previous numerical simulation studies have been implemented on idealized domains. At real field sites, however, variability of permeability at the small scale can range over several orders of magnitude. Maghrebi et al. (2015) is the only previous numerical modeling investigation of BD that incorporated a heterogeneous permeability field generated by a geostatistical model.

Although sorption is an important process within many low permeability units and can influence mass transfer, the influence of sorption on the mass rebound process in chlorinated solvent source zones has not generally been as well-recognized as that of diffusion. While a few previous modeling studies (Maghrebi et al., 2014, 2015; Rodriguez, 2006) have incorporated sorption and explored the effect of sorption properties on plume tailing, most have emphasized the effect of diffusion. In addition, these studies have typically assumed local equilibrium and isotherm linearity. Many experimental studies, however, have demonstrated that the linear equilibrium assumption fails to capture observed behavior. Thus, sorption processes in the subsurface are generally characterized as nonlinear and/or rate-limited, particularly over the wide range of concentrations encountered within DNAPL source zones. Furthermore, the use of simplified configurations of permeability heterogeneity in previous simulation studies also resulted in limited spatial variation of sorption parameters. It is widely recognized, however, that heterogeneity of sorption properties can substantially influence solute transport and result in asymptotic concentration tailing (e.g., Aksoy & Culver, 2004; Rabideau & Miller, 1994).

Most of the previous simulation studies of mass emanating from DNAPL source zones simplified source functions as constant sources (Chapman and Parker, 2005; Maghrebi et al., 2015, 2014; Parker et al., 2008) or as time varying expressions based on known data (Chapman and Parker, 2005; Rodriguez, 2006) and did not explicitly incorporate DNAPL dissolution processes. Thus, researchers did not include heterogeneous DNAPL saturation distributions as model inputs. However, it is now widely recognized that the distribution of DNAPL within a source zone (also known as DNAPL architecture), developed under the influence of a number of site-specific conditions (e.g. Dekker and Abriola, 2000; Lemke et al., 2004a), can be quite complex (e.g. Kueper et al., 1993; Mercer and Cohen, 1990), and that this DNAPL architecture will largely control the behavior and longevity of dissolved mass plumes (e.g. Christ et al., 2010, 2006; Lemke et al., 2004b; Parker and Park, 2004; Phelan et al., 2004). Thus, it is important to consider the spatial distribution of DNAPL in any investigation of BD and plume persistence in heterogeneous source zones.

In addition, most of the previous simulations investigating BD have been performed in 2-D domains, with only a few conducted in 3-D (Maghrebi et al., 2015, 2014). Reduced dimensionality

simulations, however, may not be able to completely capture flow by-passing effects or accurately predict the magnitude and penetration depth of mass in lower permeability zones. Thus, plume persistence may vary with model dimensionality, and it will be important to compare concentration rebound predictions in two and three dimensions.

Microbial reductive dechlorination has been shown to accelerate source zone mass removal and to potentially reduce persistence of toxic plumes by enhancing mass transfer from the nonaqueous to the aqueous phase (e.g., Amos et al., 2008; Cápiro et al., 2015; Sleep et al., 2006). Although attractive as a standalone or complementary remediation technology, there is an urgent need to improve our understanding of dechlorination processes in heterogeneous environments, especially in low permeability zones, due to their important role in determining remediation efficacy (Stroo et al., 2012). Subsurface heterogeneity can affect the distribution and mass flux of fermentable substrates and electron donors between transmissive zones and flow-inaccessible regions. Sequestered substrates in low permeability zones may sustain long-term release of donor mass for dechlorination within or outside of the low permeability zones (Adamson et al., 2011; Adamson and Newell, 2009), potentially altering spatial biomass distributions. Additionally, heterogeneity can influence solute residence times in reactive zones. Previous studies (Amos et al., 2008; Chen et al., 2013) have shown that residence time is a key factor to the determination of the extent of dechlorination.

While select studies have utilized numerical models to assess dechlorination rates in laboratory-scale homogeneous batch (e.g., Bagley, 1998; Fennell and Gossett, 1998; Huang and Becker, 2011; Lee et al., 2004; Sabalowsky and Semprini, 2010a; Yu and Semprini, 2004) and column systems (e.g., Chen et al., 2013; Haest et al., 2010; Sabalowsky and Semprini, 2010b; Schaefer et al., 2009), there are markedly fewer modeling studies of multidimensional laboratory systems (e.g., Chu et al., 2003; Haest et al., 2012). Although field scale modeling of reductive dechlorination has been conducted in a few studies (e.g., Becker and Seagren, 2009; Christ and Abriola, 2007; Manoli et al., 2012; Widdowson, 2004), assessment of dechlorination performance under heterogeneous conditions has been very limited (Hammond et al., 2005). As stated in II.4.2.3, field-scale models using laboratory dechlorination rates have tended to overpredict contaminant degradation.

The following sections describe the development and implementation of a mathematical modeling framework employed in this research to explore the influence of dissolution, sorption, microbial transformation and diffusion process coupling on source longevity, plume evolution, and remedial performance in complex geologic environments. This model was also employed to design and interpret microcosm (section III.2), and aquifer cell experiments (section III.3), to develop training and test data for DRF and FOSM model development (sections III.6 and 7), and to design and assess the DHT (section IV).

II.5.2. Modeling DNAPL Infiltration

Heterogeneous permeability fields and DNAPL saturations were generated numerically for applications to coupled processes exploration (III.4.), geostatistical modeling (III.6.), and sensitivity/optimization modeling (III.7.). Permeability field realizations were constructed based on an real heterogeneous aquifer for which a high-resolution analog dataset is available (Bayer et al. 2011; Heinz et al. 2003). This formation was selected as representative of a structured heterogeneous unconsolidated depositional aquifer environment. Aquifer materials in this formation were grouped into four dominant lithofacies (Table M.5.1) based on the aquifer analog and measured permeability values, following the method by Maji (2005). A series of 3-D realizations of categorical fields were conditionally generated based on synthetic 'boreholes' using

a transition-probability-based Markov Chain (TP/MC) method (Carle 1999). 2-D realizations were then extracted from the x-z cross section of the 3-D domains (Figure M.5.1).

Table M.5.1. Porous medium properties and capillary pressure-saturation parameters.

	GS-x	Gcm	S-x	bGcm,I
Description	Sandy gravel (Silty sand, coarse-grained silt)	Poorly-sorted gravel	Well-sorted sand	Cobble-and-boulder-rich gravel
Volumetric Proportion[a]	29%	57%	6%	6%
Hydraulic Conductivity[a] (m/s)	4.50E-05 (4.50E-06)	2.30E-04	1.00E-03	1.30E-01
Median Grain Size[b] (mm)	0.38 (0.038)	0.44	0.36	0.57
Uniformity Index[b]	1.75	1.66	2.38	1.67
Air Entry Pressure[c] (Pa)	3770.37	1667.73 (Reference)	799.82	70.15

a. Maji, (2005), b. Heinz et al. (2003), c. Fit with method of Haverkamp and Parlange (1986).
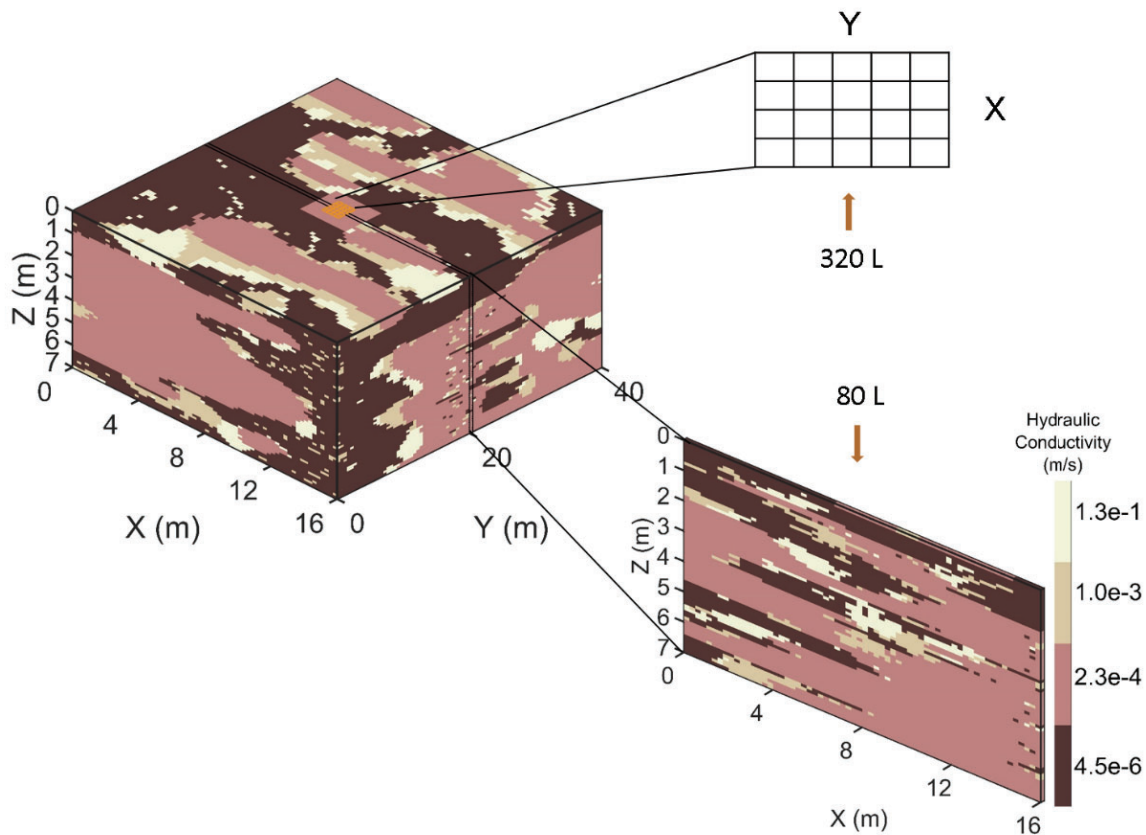
Figure M.5.1. Construction of 3-D and 2-D domain and conceptualization for 3-D and 2-D DNAPL release for hypothetical field 1.

Migration and entrapment of DNAPL was simulated by solution of coupled two phase (organic (o), water (w)) mass balance equations, incorporating a modified Darcy expression (Abriola et al., 1992),

$$\frac{\partial}{\partial t}(\phi s_i \rho_i) = \nabla \cdot (\frac{K k_{ri}}{\mu_i} \nabla(P_i - \rho_i g z)) + q_i \qquad \text{(M.5.1)}$$

where ρ_i is the density of i-phase, K is the soil intrinsic permeability tensor, k_{ri} is the relative permeability of i-phase fluid ($i=o,w$), μ_i is the dynamic viscosity, P_i is the i-phase fluid pressure, and q_i represents the external sources/sinks. The coupled equations (M.5.1) were discretized and solved using the multiphase flow simulators Michigan Vertical and Lateral Organic Redistribution (MVALOR) (2-D) (Abriola et al. 1992) and University of Texas Chemical Compositional Simulator (UTCHEM) (3-D) (Delshad et al. 1996). The framework developed by Kaluarachchi and Parker (1992) was employed to account for entrapment hysteresis effects. This approach uses an apparent effective water saturation that is a function of effective water saturation and immobile organic phase saturation. The Brooks-Corey-Burdine formulations (Brooks and Corey 1964; Burdine 1953) were adopted for modeling two phase capillary pressure-saturation and relative permeability relations. A detailed description of these constitutive relations can be found in Rathfelder and Abriola, (1998). The coupled, nonlinear mass balance equations, along with the constitutive relations and the constraint, $S_a + S_n = 1.0$, constitute a well-posed problem. Details of the numerical implementation and solution algorithms in 2- and 3-D can be found in Abriola et al. (1992) and Delshad et al. (1996), respectively.

In this work, the above multiphase flow models were used to create initial DNAPL distributions for subsequent reactive transport model simulations (II.5.3.3). The decoupling of infiltration and transport simulations is based on the assumption that the time scales of infiltration and plume development are vastly different (weeks to months versus decades). A similar decoupled modeling approach was employed by Lemke et al. (2004) and Christ et al. (2006) to study plume evolution from DNAPL dissolution.

PCE was selected as a representative DNAPL for model simulations. Tables M.5.1 and M.5.2 summarize the input parameters used in the DNAPL infiltration simulations for aquifer properties, fluid properties and capillary pressure-saturation relations. Air entry pressures and pore size index values for each aquifer material are listed in Table M.5.1. Because it comprises the largest volumetric portion of the formation, Gcm was selected for estimation of the reference air entry pressure and pore size index (grain size distribution curves obtained from Heinz et al. (2003)) by employing the Haverkamp and Parlange (1986) method. Leverett scaling was used to determine the capillary entry pressure for the other three lithofacies. For simplicity and in the absence of data, the pore size index, maximum residual DNAPL saturation, and irreducible water saturation parameters were assumed uniform for the four materials (Table M.5.2).

The ensembles of 2-D PCE saturation distributions were generated by simulating infiltration events using MVALOR. A specific volume of PCE was released at a specified rate from a four-node area ($0.5 m^2$) in the top layer of the modeled domain (Figure M.5.1). 3-D DNAPL infiltration simulations were conducted using UTCHEM. In these simulations PCE DNAPL was released at a constant rate from a central location in the top grid layer across a 5×4 grid block area of ($2.5 m^2$) (Figure M.5.1). Here the spill volume per nodal area corresponded to that spilled in the 2-D simulations. Impermeable boundaries were specified for the bottom boundaries of the domains; constant pressure and saturation boundaries were specified for the side boundaries and top boundaries. The resulting non-uniform saturation distributions were then used as inputs to the transport model.

Table M.5.2. DNAPL spill simulation input parameters.

Description	Parameter		Unit
Fluid Properties	Water	PCE	
Density[a]	9.990E+05	1.625E+06	gr/m^3
Dynamic viscosity[a]	1.121E-03	8.90E10-04	Pa $\cdot$ s
Compressibility[a]	4.40E-10	0	Pa^{-1}
Residual saturation	0.08[a]	0.235[b] (Uniform)	
Initial saturation	1	0	
Aqueous Solubility[d]	-	150	gr/m^3
Aqueous Diffusivity[e]	-	7.500E-06	cm^2/s
Capillary pressure-saturation parameters			
Uniform porosity[c]	0.23		
Pore size index[c]	2.33		
Matrix Properties			
Longitudinal Dsp[f]	0.05		m
Horizontal Dsp[f]	0.01		m
Vertical Dsp[f]	0.001		m
Solid Bulk Density[f]	1.625E+06		gr/m^3

a. Set to be uniform in the domain (Christ et al., 2005).
b. Fit to match data of Hoag and Marley (1986).
c. Set to be uniform in the domain (Wang, 2013).
d. Montgomery (2007).
e. Lucius et al. (1992).
f. Maji and Sudicky (2008).

II.5.3. Modeling Reactive Transport at the Laboratory and -and Field Scales

II.5.3.1. Governing Equations

The aqueous transport of a dissolving DNAPL component can be represented as:

$$\frac{\partial}{\partial t}(\phi s_a C_i^a) + \boldsymbol{\nabla} \cdot (\phi s_a C_i^a \underline{v}^a) - \boldsymbol{\nabla} \cdot (\phi s_a \boldsymbol{D}_h^a \cdot \boldsymbol{\nabla} C_i^a) = E_i^{an} + E_i^{as} + R_i^a \qquad (\text{M.5.2})$$

where ϕ is the porosity of the aquifer material (dimensionless), s_a is the aqueous phase saturation (dimensionless), C_i^a is the mass concentration in aqueous phase (ML^{-3}), $\underline{v}^a$ is the aqueous phase linear pore water velocity (LT^{-1}), $\boldsymbol{D}_h^\alpha$ is the hydrodynamic dispersion tensor in the aqueous phase (L^{2}T^{-1}), and E_i^{an} represents the interphase mass exchange between the nonaqueous and aqueous phases. E_i^{as} is the mass transfer between the sorbed and aqueous phases:

$$E_i^{as} = -\rho_b \frac{\partial s_i}{\partial t} \qquad (\text{M.5.3})$$

where ρ_b is the bulk density of the porous medium (ML^{-3}) and S_i is the sorbed concentration of the component with respect to the solid mass (MM^{-1}). R_i^a represents biotransformation/production of component i in the aqueous phase.

Three types of sorption models are incorporated in the model: (a) linear equilibrium sorption, $S_i = K_d C_i^a$, (b) Freundlich equilibrium sorption, $S_i = K_f (C_i{}^a)^{n_f}$, and (c) non-equilibrium sorption characterized by a first-order reversible kinetic expression, $-\rho_b \partial S_i / \partial t = -\beta (C_i^a - S_i/K_d)$, where K_d is the distribution coefficient (L^{3}M^{-1}), K_f is the Freundlich constant ((L^{3}M^{-1})^n), n_f is Freundlich exponent (dimensionless), and β is the first-order mass transfer rate between the aqueous and solid phases (T^{-1}).

Dissolution is represented by a linear driving force expression, consistent with numerous previous modeling and laboratory investigations (e.g., Christ et al., 2006; Parker and Park, 2004):

$$E_i^{an} = \kappa^{an}(C_{i,eq}^a - C_i^a) \tag{M.5.4}$$

where κ^{an} is a lumped mass transfer rate coefficient (T^{-1}) and $C_{i.eq}^a$ is the aqueous solubility of the DNAPL (ML^{-3}). Here $C_{i,eq}^a$ is assumed to approximate the aqueous phase concentration of the component at the DNAPL and bulk aqueous interface. A number of Gilland-Sherwood correlation expressions have been developed in the literature to quantify the lumped mass transfer rate coefficient (e.g. Imhoff et al., 1994; Miller et al., 1990; Powers et al., 1994). These correlations are generally a function of DNAPL saturation, grain size information and flow velocity. For the simulations reported herein, the lumped mass transfer coefficient is computed according to the following correlation (Powers et al., 1994),

$$\kappa^{an} = 4.13 \frac{D_m^a}{d_{50}^2} Re'^{0.598} \left(\frac{d_{50}}{d_m}\right)^{0.673} U_i^{0.369} \left(\frac{s_n}{s_{ni}}\right)^{0.518 + 0.114 \frac{d_{50}}{d_m} + 0.10 U_i} \tag{M.5.5}$$

where d_{50} is the median grain size (L), D_m^a is the aqueous phase molecular diffusivity of the component (L^{2}T^{-1}), Re' is a modified Reynolds number expressed in terms of linear pore water velocity, d_m is the diameter of a "medium-size" sand grain according to the ASTM particle size classification (L), U_i represents the uniformity index (dimensionless), a measure of the grain size distribution ($U_i = d_{60}/d_{10}$), and s_{ni} is the initial DNAPL saturation.

The mathematical model for reductive dechlorination used in this research tracks the transformations and growth of two dechlorinator populations. Previous microbial studies with the KB-1 culture (Duhamel et al. 2002; Duhamel and Edwards 2006, 2007; Haest et al. 2010b) showed that two dominant species, *Geo* and *Dhc,* were responsible for degrading the majority of TCE to cis-DCE and converting cis-DCE to ethene, respectively. This modeling approach, i.e., considering two microbial groups with different dechlorinating functions, has been used in previous studies that modeled biotransformation by laboratory-cultivated cultures (Bagley 1998; Chambon et al. 2010; Chen et al. 2013; Christ and Abriola 2007; Clapp et al. 2004; Haest et al. 2010b; Haston and McCarty 1999; Lee et al. 2004). Hydrogen is assumed as the only direct electron donor for dechlorination and is produced from fermentation of the added organic substrate (i.e., lactate). A few previous studies (e.g., Clapp et al., 2004; Fennell and Gossett, 1998; Malaguerra et al., 2011) have modeled multi-step fermentation processes, including intermediate production of short-chain VFAs. However, the development of a more complex fermentation model requires an understanding and characterization of fermentation pathways, fermenter communities, and thermodynamics (Chambon et al. 2013). In addition, computational efficiency can potentially be compromised by introducing more chemical components into the complex system. Thus, the simplified model was selected. Although the model includes a competitor species, competition for electron donor from other microorganisms, including methanogens, iron-reducers and sulfate-reducers, was not considered in the aquifer cell simulations, as these microbial populations made up a minor fraction of the entire populations in the KB-1 culture (Duhamel and Edwards 2006).

Donor consumption from microorganisms other than dechlorinators could play a role in influencing the effectiveness of *in situ* dechlorination in the DHT.

Based upon the above conceptual model, a dual Monod kinetics model (Chen et al. 2013; Christ and Abriola 2007; Clapp et al. 2004; Lee et al. 2004), which accounts for competitive inhibition, hydrogen utilization, and biomass growth, is applied to describe reductive dechlorination. The mathematical expressions for each chlorinated solvent component are given as:

$$r_{TCE}^a = \frac{k_{max,TCE} C_{TCE}^a X_{GEO}}{K_{s,TCE} I_{TCE} + C_{TCE}^a} \times \frac{C_H^a - C_{H,th,GEO}^a}{K_{s,H,GEO} + \left(C_H^a - C_{H,th,GEO}^a\right)} \tag{M.5.6}$$

$$r_{DCE}^a = \frac{k_{max,DCE} C_{DCE}^a X_{DHC}}{K_{s,DCE} I_{DCE} + C_{DCE}^a} \times \frac{C_H^a - C_{H,th,DHC}^a}{K_{s,H,DHC} + \left(C_H^a - C_{H,th,DHC}^a\right)} \tag{M.5.7}$$

$$r_{VC}^a = \frac{k_{max,VC} C_{VC}^a X_{DHC}}{K_{s,VC} I_{VC} + C_{VC}^a} \times \frac{C_H^a - C_{H,th,DHC}^a}{K_{s,H,DHC} + \left(C_H^a - C_{H,th,DHC}^a\right)} \tag{M.5.8}$$

where r_i^a is the mass rate of dechlorination of component i in the aqueous phase (ML^{-3}T^{-1}), $k_{max,i}$ is the maximum utilization rate for component i (MM$_{bio}^{-1}$T^{-1}), X_j is the concentration (M$_{bio}$L^{-3}) of attached active cell for the TCE dechlorinator ($j = GEO$) and the cis-DCE and VC dechlorinator ($j = DHC$), $K_{s,i}$ is the half saturation constant for component i (ML^{-3}), I_i is the competitive inhibition by different electron acceptors (dimensionless), C_H^a is the aqueous H$_2$ concentration (ML^{-3}), $C_{H,th,j}^a$ is the threshold concentration of H$_2$ for dechlorinating polulation j (ML^{-3}), $K_{s,H,j}$ is the half saturation constant of H$_2$ for dechlorinator j (ML^{-3}).

Here the traditional Monod kinetics equation is multiplied by a hydrogen utilization term, which accounts for the energy constraints to maintain a minimum H$_2$ concentration (Clapp et al. 2004; Fennell and Gossett 1998). The reaction rate, r_i^a, is set to zero when aqueous H$_2$ concentration is less than $C_{H,th,j}^a$. Competitive inhibition, I_i, accounts for the reduction of dechlorination rates originated from shift of degradation priority by dechlorinating populations, and the inhibition caused by the presence of high concentration parent chlorinated ethenes (e.g., Cupples et al., 2004; Garant and Lynd, 1998; Haest et al., 2010; Lee et al., 2004; Yu et al., 2005). I_i takes the general form of $1 + \sum_i C_i^a / K_{I,i}$, where $K_{I,i}$ is the inhibition constant for component i (ML^{-3}). The inhibitory relation among chlorinated ethenes and the values $K_{I,i}$ vary among studies due to experimental conditions and modeling approaches (Chambon et al. 2013). However, inhibition on cis-DCE and VC transformation has been commonly observed. Here, the inhibition is assumed to follow:

$$I_{TCE} = 1; \tag{M.5.9}$$

$$I_{DCE} = 1 + C_{VC}^a / K_{I,VC} \tag{M.5.10}$$

$$I_{VC} = 1 + C_{TCE}^a / K_{I,TCE} + C_{DCE}^a / K_{I,DCE} \tag{M.5.11}$$

Transport and biological reaction of the primary substrate, lactate, as well as the electron donor, H$_2$ are modeled. Lactate is assumed to be fermented through a single-step pathway to produce H$_2$, which is immediately available as electron donor for dechlorination. The stoichiometry can be expressed by the following equation (Ohnishi et al. 2012),

$$CH_3CHOHCOOH + 3H_2O \rightarrow 3CO_2 + 6H_2 \tag{M.5.12}$$
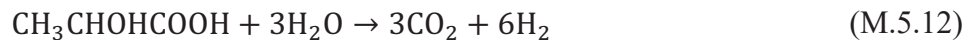
The kinetic model used for lactate transformation by the fermentative population (X_{FEM}) is as follows:

$$r_{LAC}^a = \frac{k_{max,LAC} C_{LAC}^a X_{FEM}}{K_{S,LAC} + C_{LAC}^a} \tag{M.5.13}$$

By combining the equations above, the term R_i^a in equation (M.5.2) for all components can be formalized as: $R_{TCE}^a = -r_{TCE}^a$, $R_{DCE}^a = -r_{DCE}^a + r_{TCE}^a$, $R_{VC}^a = -r_{VC}^a + r_{DCE}^a$, $R_{ETH}^a = r_{VC}^a$ and $R_{LAC}^a = -r_{LAC}^a$. Then, $R_{H_2}^a$ for H2 production and consumption can be written as:

$$R_{H_2}^a = \frac{x_{LAC}}{mw_{LAC}} r_{lac}^a - \left(\frac{x_{TCE}}{mw_{TCE}} r_{TCE}^a + \frac{x_{DCE}}{mw_{DCE}} r_{DCE}^a + \frac{x_{VC}}{mw_{VC}} r_{VC}^a\right) \tag{M.5.14}$$

where x_i is the molar reducing equivalence of H2 that is generated or demanded during transformation of one mole component c_i^a, mw_i is the molecular weight for component i. It is to be noted that the computation in the model was performed based on gram mass. Here, the coefficients x_i for lactate ($x_{LAC} = 6$) and chlorinated ethenes ($x_{TCE} = x_{DCE} = x_{VC} = 1.41$) are obtained from the literature (Christ and Abriola 2007; Ohnishi et al. 2012).

The growth rate of biomass is modeled separately for each population as a function of substrate transformation rate, the yield coefficient, Y_i ($M_{bio}M^{-1}$), for component i, and the first order endogenous decay coefficient, $k_{b,j}$ (T^{-1}), for X_j:

$$\frac{dX_{GEO}}{dt} = Y_{TCE} r_{TCE}^a - k_{b,GEO} X_{GEO} \tag{M.5.15}$$

$$\frac{dX_{DHC}}{dt} = Y_{DCE} r_{DCE}^a + Y_{VC} r_{VC}^a - k_{b,DHC} X_{DHC} \tag{M.5.16}$$

$$\frac{dX_{FEM}}{dt} = Y_{LAC} r_{LAC}^a - k_{b,FEM} X_{FEM} \tag{M.5.17}$$

In this modeling effort, the following assumptions, pertaining to biomass growth and function are also employed: 1) only attached (not planktonic) biomass is active for reductive dechlorination; 2) the biophase is fully penetrated (no mass transfer resistance); 3) attached bacteria are not mobile; 4) the influence of microbial growth on aqueous flow is insignificant (low growth environment); and 5) growth of attached biomass is bounded by a minimum and maximum biomass concentration. Non-attached-to-total cell ratio of 14% (*Geo*) and 24% (*Dhc*) are assumed in this study, based upon measurements in a similar chlorinated solvent aquifer cell system that was bioaugmented with organohalide-respiring mixed cultures (Cápiro et al. 2015).

II.5.3.2 Model Implementation in MT3DMS

Transport simulations were performed using a modified version of the modular three dimensional transport simulator MT3DMS (Zheng and Wang 1999), previously adapted to incorporate rate limited dissolution from an entrapped DNAPL source zone and transient groundwater flow associated with changes in DNAPL saturation (Christ et al. 2006, 2010; Parker and Park 2004).

In the modified MT3DMS, MODFLOW (Harbaugh et al. 2000) is coupled with the transport model to account for the change in the aqueous flow field caused by DNAPL dissolution. The coupling is implemented by introducing the water relative permeability k_{rw} (ML-1) into the groundwater flow equation,

37

$$\nabla(Kk_{rw}\nabla h) = S_{sp}\frac{\partial h}{\partial t}$$ (M.5.18)

where K is the principal component of the hydraulic conductivity tensor (LT-1), h is the hydraulic head (L), S_{sp} is the specific storage of the aquifer (L-1). For the simulations presented herein, the water relative permeability is linked to the DNAPL saturation by the Brooks and Corey (1964) function:

$$k_{rw} = (\frac{1 - s_n - s_w^{min}}{1 - s_w^{min}})^{\frac{2+3\lambda}{\lambda}}$$ (M.5.19)

where λ is pore size index (dimensionless), s_w^{min} is the irreducible water saturation (dimensionless). The flow is frequently adjusted by updating water relative permeability as a function of the newly computed DNAPL saturation values. DNAPL depletion results in an increase in aqueous phase mobility and subsequently groundwater flow velocity, which in turn drives a faster mass exchange between the DNAPL and aqueous phases.

In this research, to ensure mass conservation for nonlinear (Freundlich) sorption simulations, calculation of the retardation factor, $R_f = 1 + \frac{\rho_b}{\theta s_a}\frac{\partial S}{\partial C^a}$, was modified in MT3DMS to employ a standard chord slope method, $\partial S/\partial C^a = \frac{S_{t+1}-S_t}{C_{t+1}^a-C_t^a}$, where S_t and C_t^a are solute concentration and sorbed concentration in the preceding iteration (Rathfelder and Abriola 1994).

Following Christ and Abriola (2006), MT3DMS was further adapted to incorporate multi-order Monod kinetics coupled with microbial growth model to account for biotransformation of multiple components by multiple microbial populations under isothermal conditions (M.5.2 and M.5.3). Variations in fluid density and viscosity were considered negligible. A Monod kinetics subroutine was added to the simulator and stepwise/accumulative mass budget subroutines for six chemical components: TCE, cis-DCE, VC, ethene, lactate and H2. In order to solve the fully coupled transport equations of the six components, the r_i^a terms are calculated by lagging c_i^a and X_j one time step,

$$r_{i,t}^a = \frac{k_{max,i}\ C_{i,t-1}^a\ X_{j,t-1}}{K_{s,i}I_i + C_{i,t-1}^a} \times \frac{C_{H,t-1}^a - C_{H,th,j}^a}{K_{s,H,j} + (C_{H,t-1}^a - C_{H,th,j}^a)}$$ (M.5.20)

In the model, an adaptive time step procedure is applied to account for the error introduced by using an explicit solution scheme for r_i^a so that discrepancy between old and new solutions is constrained within a tolerable range. Furthermore, the following mass discrepancy indicators (Zheng and Wang 1999) are used to evaluate the accuracy of the model solutions for chlorinated ethenes and ethene:

$$Accumulative\ Discreapancy(\%) = \frac{(\sum Source + M_0) - (\sum Sink + M_t)}{0.5[(\sum Source + M_0) + (\sum Sink + M_t)]}$$ (M.5.21)

$$Stepwise\ Discreapancy(\%) = \frac{(Source + M_{t-1}) - (Sink + M_t)}{0.5[(Source + M_{t-1}) + (Sink + M_t)]}$$ (M.5.22)

where M_0 is the total molar mass of carbon bond in chlorinated ethenes and ethene (aqueous and sorbed) in the domain at the initial time step, M_t and M_{t-1} are the total molar mass at time step t and its previous time step, $Source$ and $Sink$ are the total molar mass into/out of the domain from external sources/sink for all chlorinated ethenes and ethene at time step t, while $\sum Source$ and

$\sum Sink$ are cumulative mass exchange terms summed for all time steps. Note that the $Source$ and $Sink$ include mass exchange at constant concentration, constant head, and constant flux boundaries. In general, the global mass balance calculated for simulated time duration using equation (M.6.22) was controlled for the simulations conducted in this research between 0.05% - 0.1%. The biomass (M.5.15-17) is updated after each transport step by the following analytical solution of equations,

$$X_{j,t} = X_{j,t-1}\exp\left(\sum_i \frac{Y_i r_{i,t}^a}{X_{j,t-1}} - k_{b,j}\right) \qquad \text{(M.5.23)}$$

II.5.3.3 Model Parameters for Coupled Process Exploration and Geostatistical Modeling Tool Development

For the transport simulations described in sections III.5, 7, and 8, a natural hydraulic gradient of 0.01 was imposed on the domain, producing average linear groundwater velocities of approximately 0.9 m/day in the majority of the domain, and 0.02 m/day in lower permeable zones. All simulations consisted of two consecutive stages: a 'loading stage', during which PCE DNAPL dissolves, but no change in saturation is permitted, and a flushing stage, with DNAPL dissolution progressing until a specified stopping criterion is satisfied. For both stages, adsorption and solute transport (advection and dispersion) were computed. Since solute transport and interphase mass transfer were not simulated during DNAPL release and infiltration, the first stage was designed to create conditions that are similar to untreated source zones where contaminants have accumulated over a period of years. The second stage is of primary interest in this research, representing the natural restoration or remediation process, during which contaminant infiltration has ceased, and groundwater flushes the contaminated zone under natural or induced gradient conditions until specified target goals are reached.

The physicochemical parameters used in the simulations are listed in Table M.5.2. Dispersivity parameters and solid bulk density were taken from a modeling study of DNAPL dissolution in a similar hydrogeological setting Maji and Sudicky (2008).

Table M.5.3 lists sorption-related parameters used in the simulations. These were estimated from the literature, since sorptive property information for the field materials was not available. In the absence of measured data, the linear equilibrium sorption of solutes to aquifer solids can be estimated using a distribution coefficient, $K_d = K_{oc}f_{oc}$, where K_{oc} (L^3M^{-1}) is the partition coefficient to organic carbon, and f_{oc} is mass fractional of soil organic carbon. Estimated values of K_{oc} for PCE range from 200 ml/g to 600 ml/g (Mackay and Boethling, 2000; Vermeulen, 1991). A K_{oc} value of 400 L/kg was employed here. Based on sedimentary studies of the prototype aquifer in southwestern Germany (Heinz et al., 2003; Kleineidam et al., 1999b; a), lithofacies Gcm, S-x and bGcm were treated as low organic carbon content deposits with f_{oc} of 0.035%. The finest material, GS-x was treated as the most sorptive in the transport simulations, with a f_{oc} approximately one order of magnitude larger. This relatively high value was selected so that the influence of a strongly sorptive medium on DNAPL source zone persistence could be explored. The value is consistent with other f_{oc} values reported for fine materials in the literature (ranging from 0.1% to 2%) (Delle Site, 2001; Domenico and Schwartz, 1997). For consistency and to further facilitate the study of desorption and back diffusion, the hydraulic conductivity and grain size were reduced for this lowest permeability material (GS-x) (bracketed values in Table M.5.1) in the transport simulations to better reflect hydraulic characteristics consistent with a highly sorptive material. For the nonlinear equilibrium sorption model, the Freundlich exponent, n_f was

selected from within the range 0.8-0.9 (Rivett et al., 2006). The Freundlich coefficient K_f was then calculated to ensure comparability with the corresponding linear isotherm for each material by minimizing the difference in total sorbed mass between the linear and nonlinear models over an aqueous concentration range of 0 to the PCE solubility value. A first order mass transfer coefficient for solute PCE sorption from GS-x materials was selected within the range of reported literature values. In published field scale simulations, these vary over several orders of magnitude, from 10^{-4} to 10^{-2} day^{-1} (Aksoy and Culver, 2000, 2004; Goltz and Roberts, 1986, 1988). The other three materials were treated as less sorptive materials, and thus, assigned higher mass transfer rate values.

3-D domains ($16 \times 40 \times 7$ m) were discretized into 373,815 cells, with a resolution of $0.25 \times 0.5 \times 0.1$ m in the x, y, and z directions. The same grid spacing in the x and z directions was used for 2-D domains (16×7 m). An adaptive time step procedure, with an initial time step, maximum time step, and a time-step multiplier, was implemented to handle the high concentration gradient near the DNAPL source at early times, and the relatively mild concentration change at later stages. Balancing computational efficiency and numerical stability, an implicit finite difference method with upstream weighting was chosen as the numerical solution technique. The spatial grid discretization was consistent with those used in the DNAPL spill simulations. Wang (2013) showed that this level of grid resolution sufficiently resolved DNAPL pathways and pool locations, consistent with finer grid spacing. Furthermore, this resolution was consistent with the development of the permeability field, which was conditioned on 18 hypothetical boreholes with 0.25 m spacing in the vertical direction.

Table M.5.3. Formation sorption properties.

Lithofacies	f_{oc} (%)	Distribution Coefficient (m^3/g)	Freundlich Coefficient ($g^{-nf} m^{3nf}$)	Freundlich Exponent (-)	First Order Kinetic Rates (day^{-1})
GS-x	0.50	2.00E-06	5.06E-06	0.80	1.00E-03
Gcm	0.035	1.40E-07	2.23E-07	0.90	1.00E-01
S-x	0.035	1.40E-07	2.23E-07	0.90	1.00E-01
bGcm,I	0.035	1.40E-07	2.23E-07	0.90	1.00E-01

II.5.4. Modeling Biotransformation in Microcosm Scale

In this research, a MATLAB (The MathWorks Inc. 2016) code was developed to model the dechlorination process (TCE to DCE to VC to ethene) in the microcosms as a batch process. In this code a coupled system of eight simultaneous ordinary differential equations (ODEs) are solved for:

- the aqueous phase concentration (mM) of three chloroethenes and ethene (TCE, C_{TCE}^a; DCE, C_{DCE}^a; VC, C_{VC}^a; and ethene, C_{ETH}^a; equation M.5.6-M.5.8)

- the aqueous phase biomass concentration of Geobacter in mg-cells per liter (X_{GEO}, Equation M.5.15)

- the aqueous phase biomass concentration of Dehalococcoides in mg-cells per liter (X_{DHC}, equation M.5.16)

- the volume of aqueous phase present in the microcosm (V^a, equation M.5.26)

- the volume of gas phase present in the microcosm (V^g, equation M.5.27)

It is assumed that the chemical species in the microcosm exist in three phases: as a solute in the groundwater (aqueous phase, a), as a vapor in the head space (gas phase, g), or as a sorbate on the surface of the soil particles (sorbed phase, s). Equilibrium and linear partitioning at all times between the three phases is assumed. Furthermore, it is assumed that the mass of chemical species i in the microcosm can only change in three ways:

1. Chemical species i is converted into another chemical species via dechlorination.

2. Chemical species i is removed from the microcosm when samples of the aqueous phase are taken.

3. Chemical species i in the gas phase escapes from the microcosm via the septum. The abiotic microcosm experiments suggested that this diffusion process could be adequately modeled as first-order, dependent on the concentration of chemical species i in the aqueous phase.

The mass balance equation for chemical species i in a microcosm is then given by:

$$\frac{d}{dt}(V^a C_i^a) + \frac{d}{dt}(V^g C_i^g) + \frac{d}{dt}(q_i M_s) = V^a R_i^a + Q^a C_i^a + k_i^e C_i^a \tag{M.5.24}$$

where C_i^g is the concentration of chemical species i in the gas phase (mM), q_i is the moles of chemical species i sorbed per mass of soil (mmol per g), M_s is the mass of soil (g), R_i^a is the transformation or production rate of chemical species i in the aqueous phase (mM/d), Q^a is the rate of aqueous phase sampling averaged over the duration of the experiment (L/d, negative value), and k_i^e is a rate constant for gas escape from the microcosm (1/d, negative value). Using linear sorption parameters measured in this study and Henry's law, functions of the aqueous phase concentration C_i^a can be substituted for q_i and C_i^g in Equation (M.5.24) and the ODE for chemical species i can be rearranged to form

$$\frac{d}{dt}(C_i^a) = \frac{V^a R_i^a + \dfrac{Q^a C_i^a}{H_i RT} + k_i^e C_i^a}{V^a + \dfrac{V^g}{H_i RT} + K_{d,i} M_s} \tag{M.5.25}$$

where H_i is the Henry's law constant for chemical species i (mmol/m³ Pa), R is the gas constant (J/K mmol), T is the temperature (293 K), and $K_{d,i}$ is the linear sorption constant for chemical species i (L/g).

The transformation or production rates R_i^a for TCE, DCE, VC, and ethene are presented in section II.5.3.1. Based upon the experimental conditions, hydrogen (electron donor) was assumed in excess at all times. Inhibition was modeled by equations M.5.9-11. It is assumed that all dechlorinating bacteria remain in the aqueous phase (i.e., they do not sorb to soil particles) and all dechlorination occurs in the aqueous phase. Growth equations for the two dechlorinator populations are given in M.5.15-16.

To close the system, volume balance equations are also needed:

$$\frac{d}{dt}(V^a) = Q^a \tag{M.5.26}$$

$$\frac{d}{dt}(V^g) = -Q^a \tag{M.5.27}$$

Where Q^a is the aqueous phase sampling rate.

Initial values for the dependent variables in each of the eight ODEs described above were determined as follows:

- For the aqueous phase concentration of the four chemical species (C_{TCE}^a, C_{DCE}^a, C_{VC}^a, and C_{ETH}^a), the initial concentration was set equal to the first set of aqueous phase concentration measurements.

- For the biomass concentration of Dehalococcoides (X_{DHC}), the initial value $X_{DHC,initial}$ was calculated from (1) Dehalococcoides biomass measurements taken from samples of KB-1 inoculum and (2) the total volume of KB-1 inoculum added.

- For the biomass concentration of Geobacter (X_{GEO}), the initial value $X_{GEO,initial}$ was calculated by assuming that (1) the initial concentration of Geobacter cells (cells/L, not mg-cells/L) in KB-1 inoculum is the same as that for Dehalococcoides (Roberts 2017) and (2) Geobacter cells have a mass that is 3.8 times greater than the mass of Dehalococcoides cells (He et al. 2005; Sung et al. 2006). The initial biomass concentration of Geobacter was therefore $X_{GEO,initial} = 3.8\, X_{DHC,initial}$.

- The initial volumes of aqueous phase and gas phase (V^a and V^g) were taken from measurements made at the start of the microcosm trials.

Using the model for microbial dechlorination in a microcosm (Equations M.5.20, M.5.23-27), a MATLAB fitting routine was written that iteratively solved the system's ODEs while varying the three maximum substrate utilization rates ($k_{TCE,max}$, $k_{DCE,max}$, and $k_{VC,max}$) until the modeled aqueous phase concentrations of each chemical species were acceptably close to measured values collected during the microcosm experiments. The objective function for this fitting routine was the sum of squared residuals

$$SSR = \sum_{i=1}^{4} \sum_{j=1}^{n} \left(C_{ij,modeled}^a - C_{ij,measured}^a \right)^2 \tag{M.5.28}$$

where i is the index of the chemical species (either TCE, DCE, VC, or ethene), j is the index of the collected aqueous phase sample (as well as the corresponding modeled aqueous phase concentration at that time), and n is the total number of aqueous phase samples taken.

An iterative model fitting procedure was used where the two yield coefficients were first adjusted manually to match biomass concentration measurements and then the three maximum substrate utilization rates were fit via a MATLAB optimization routine so modeled chemical concentrations matched measured values. The fitting routine was run several times, adjusting the DCE yield coefficient Y^{DCE} and VC yield coefficient Y^{VC} manually each time until modeled Dehalococcoides biomass concentration X_{DHC} values were close to X_{DHC} measurements for all three microcosm trials D2K-1, D2K-2, and D2K-3.

II.6. Parameter Upscaling and Screening Model Tools

II.6.1. Regressed Models for Multi-Rate Mass Transfer in Heterogeneous Media

II.6.1.1. Introduction

In DNAPL source zones, dissolved and sorbed species sequestered in zones of low conductivity can act as a long-term source of contamination to the flowing groundwater. This mass sequestration can lead to long cleanup times and is associated with non-Fickian transport with pronounced breakthrough curve tailing (Adams and Gelhar 1992; Gouze et al. 2008; Haggerty et al. 2000; Mackay et al. 1986; Riva et al. 2008). Failure to properly account for such mass transfer limitations in numerical simulations employed to assess the outcome of different remedial strategies would provide a poor decision basis for stakeholders. However, there is often a large discrepancy in scale between the observation scale (field-scale), typically on the order of meters to tens of meters, and the smallest length scale associated with heterogeneous medium properties (centimeters to tens of centimeters). In these cases, direct numerical simulations become computationally prohibitive.

One goal of this research was to explore the upscaling of aqueous phase transport of a sorbing solute in heterogeneous media, with a focus on developing effective field-scale mass transfer parameters at the meter scale. Here the emphasis was on the desorption and back diffusion of solutes from low-permeability zones at later times, representative of long-term plume persistence. Multi-rate mass transfer (MRMT) models (Carrera et al. 1998; Haggerty and Gorelick 1995) are a promising approach for this upscaling application, due to their efficiency, ease of implementation, and ability to capture late-time tailing. This method is an extension of the dual-domain concept that has long been applied in the sorption literature (van Genuchten and Wierenga 1976). The domain is decomposed into mobile and immobile regions that are defined at each point in space. Advective and dispersive fluxes occur within the mobile region, and the diffusive transfer between the mobile and immobile regions is described in terms of a distribution of first-order rates. This distribution depends on the medium and fluid properties. Brusseau et al. (1989), Valocchi (1990), Sardin et al. (1991) and Villermaux (1990, 1987) developed models accounting for multi-rate processes between regions of different mobility. Building on these investigations, Haggerty and Gorelick (1995) developed an MRMT model, in which immobile zones are connected in parallel to one mobile zone. They showed that the multi-rate model, using an infinite sum of first-order terms, exactly describes the diffusion between mobile and immobile zones and that a truncated series, consisting of only a few terms, provides a very good approximation. In addition, these investigators developed analytical expressions for the first-order rates for idealized geometries of the immobile zones, such as spheres.

Natural porous media, however, cannot usually be described in terms of idealized geometries, and thus, analytical expressions cannot often be directly employed in real applications. Instead, upscaled parameters are typically fitted to breakthrough curves obtained from heterogeneous laboratory or field experiments, or from fine-scale numerical simulations. This parameter fitting, however, is complicated by the complex coupling of reactions and physical transport limitations, precluding the independent upscaling of reaction and physical heterogeneity (Dentz et al. 2011) and necessitating the performance of multiple experiments (e.g. varying flow rates or solute diffusivities (Carrera et al. 1998)).

Fernàndez-Garcia et al. (2009) compared the performance of MRMT models and fine-scale models in heterogeneous two-dimensional domains. Simulations demonstrated that the so-called double-rate and truncated power law mass transfer models could predict the average behavior of the fine scale effluent mass flux. However, the variability of the multi-rate simulations was smaller than

that of the reference fine-scale solutions. This behavior was mainly attributed to the fitting procedure, which used a one-dimensional solution assuming all particles leave the domain across the downstream face. Li et al. (2011) extended this work to three dimensions, and performed a more elaborate upscaling of the hydraulic conductivity, so-called "Laplacian with-skin". In this way, the variability as well as the mean behavior could be reproduced. Note that the latter approach requires input both on the cell to be upscaled and the surrounding cells, and hence cannot be used for regressions of conductivity with respect to local parameters, as is of interest in the present work.

To apply the MRMT model without the need to perform fine-scale simulations or laboratory or field tests, upscaled parameters must be regressed to properties that can be estimated *a priori*. Although a few studies have explored the dependence of upscaled parameters for single-rate models on a few properties, such as the volumetric portion of immobile zones (Pedretti et al.,2014) and permeability field geostatistical parameters (Flach 2012; Zinn and Harvey, 2003), these studies have been limited to reduced dimensionality and scale and to non-sorbing solutes. To date, no regressed model for the estimation of MRMT parameters has been presented for application to three-dimensional heterogeneous media at the field scale.

This research focused on the development of field-scale regressed models for estimation of MRMT parameters. An ensemble of 1 m cube permeability fields was created and for each field, fine-scale simulations of flow and transport were performed for imposed horizontal and vertical hydraulic gradients. Input parameters to MRMT were then fit by comparison of breakthrough curves from the fine-scale simulations with analytical one-dimensional MRMT solutions. To reduce problems with non-uniqueness (Deutsch and Journel, 1998), a step-wise fitting procedure is developed. Consistent with (Fernàndez-Garcia et al. 2009), a double-rate model is shown to produce good fits to fine-scale results. By varying flow rates, geostatistical input parameters, and (linear) sorption coefficients, their links to the parameters of the double-rate model were established. The model problem set-up, multi-rate equations, and regression techniques are described below.

II.6.1.2. Model Problem

The model problem is defined here in terms of the fine-scale equations, initial and boundary conditions, and properties of the heterogeneous medium and the fluid. The upscaled model using multi-rate equations is then introduced.

Fine-scale simulations were carried out in order to obtain transport data to which the upscaled model could be fitted and verified. Single-phase flow with transport and sorption of one solute was modeled by

$$\nabla \cdot \mathbf{u} \ = \ 0, \tag{M.6.1}$$

$$\mathbf{u} \ = \ -\mathbf{K}\,\nabla h, \tag{M.6.2}$$

$$\phi \frac{\partial c}{\partial t} + \rho_b K_d \frac{\partial c}{\partial t} \ = \ -\mathbf{u} \cdot \nabla c + \phi\,\nabla \cdot (\mathbf{D} \cdot \nabla c). \tag{M.6.3}$$

Here, $\mathbf{u}$ denotes the (stationary) Darcy flux, $\mathbf{K}$ the hydraulic conductivity tensor, h the hydraulic head, ϕ the porosity, c the aqueous concentration and $\mathbf{D}$ the full local hydrodynamic dispersion tensor. The pore velocity is $\mathbf{v} = \mathbf{u}\,/\,\phi$. In the flow direction, $D = \alpha_l\,\mathbf{v} + D_m\,\tau$, where α_l is the longitudinal dispersivity, D_m is the molecular diffusivity and $\tau < 1$ is the tortuosity factor. The transverse dispersivity α_t is assumed to be the same in the two transverse directions.

The second term in (M.6.3) describes linear equilibrium sorption, with bulk density ρ_b and sorption distribution coefficient K_d. This term depends on the porosity through $\rho_b = \rho_p (1 - \phi)$ where ρ_p is the particle density. This is made explicit by writing

$$(\phi + \rho_p K_d (1 - \phi)) \frac{\partial c}{\partial t} = -\mathbf{u} \cdot \nabla c + \phi \nabla \cdot (\mathbf{D} \cdot \nabla c) \Rightarrow \tag{M.6.4}$$

$$\phi R \frac{\partial c}{\partial t} = -\mathbf{u} \cdot \nabla c + \phi \nabla \cdot (\mathbf{D} \cdot \nabla c), \tag{M.6.5}$$

$$R = 1 + \rho_p K_d (1/\phi - 1). \tag{M.6.6}$$

Here, R is the retardation factor caused by sorption.

Simulations were carried out in heterogeneous domains $\Omega = \{0 \leq (x; y; z) \leq 1\text{m}\}$. One example is shown in Figure M.6.1a. Two sets of initial and boundary conditions were applied for the simulations with horizontal hydraulic gradient, depending on the purpose of simulations.
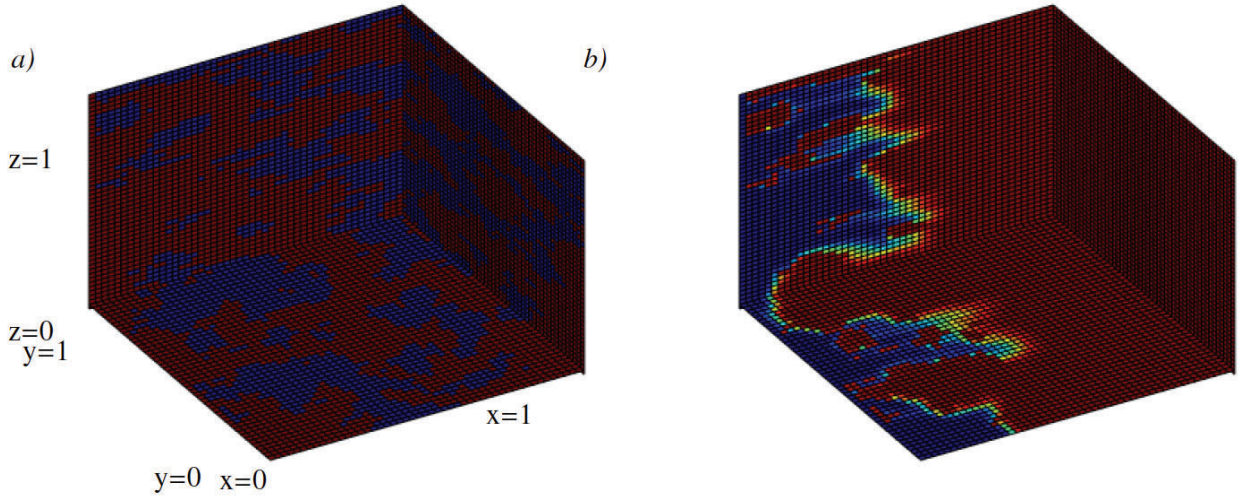
Figure M.6.1. a) High and low-permeability zones in red and blue, respectively. b) Concentration of the solute between zero (blue) and 1 (red), after 1.2 days. Pure water is flushing the domain from left at x=0, displacing water with initial concentration one through the effluent boundary at x=1. All other boundaries are closed. Geostatistical parameters are $a_h = 0{:}22$ m, $a_v = 0{:}10$ m and $f_{im} = 0{:}34$.

Step 1. Dirac delta pulse injection

$$c = 0, \quad \text{for } t = 0, (x > 0, y, z) \in \Omega, \tag{M.6.7}$$

$$h = h_0, (\mathbf{u}c - \phi \mathbf{D} \cdot \nabla c) \cdot \mathbf{n} = \delta(t), \quad \text{for } t > 0, (x, y, z) \in \Gamma_1, \tag{M.6.8}$$

$$h = h_1, (\phi \mathbf{D} \cdot \nabla c) \cdot \mathbf{n} = 0, \quad \text{for } t > 0, (x, y, z) \in \Gamma_2, \tag{M.6.9}$$

$$\mathbf{u} \cdot \mathbf{n} = 0, (\mathbf{u}c - \phi \mathbf{D} \cdot \nabla c) \cdot \mathbf{n} = 0, \quad \text{for } t \geq 0, (x, y, z) \in \Gamma_3, \tag{M.6.10}$$

where $\mathbf{n}$ is the outside normal vector of $\partial\Omega$, $\Gamma_1 = \{\partial\Omega \,|\, x = 0\}$, $\Gamma_2 = \{\partial\Omega \,|\, x = 1\}$ and $\Gamma_3 = \{\partial\Omega \,|\, y = 0, y = 1, z = 0, z = 1\}$. The values of the hydraulic head at the left and right boundaries are discussed in Section II.6.1.3 in terms of the hydraulic gradient. Dirac delta pulse simulations were also performed using a vertical hydraulic gradient. Here, the same set of initial and boundary conditions was applied but with interchanged meaning of x and z.

Step 2. 1-Heaviside condition

$$c = c_0, \quad \text{for } t = 0, \ (x,y,z) \in \Omega, \tag{M.6.11}$$

$$h = h_0, \ c = 0, \quad \text{for } t > 0, \ (x,y,z) \in \Gamma_1, \tag{M.6.12}$$

$$h = h_1, \ (\phi\mathbf{D} \cdot \nabla c) \cdot \mathbf{n} = 0, \quad \text{for } t > 0, \ (x,y,z) \in \Gamma_2, \tag{M.6.13}$$

$$\mathbf{u} \cdot \mathbf{n} = 0, \ (\mathbf{u}c - \phi\mathbf{D} \cdot \nabla c) \cdot \mathbf{n} = 0, \quad \text{for } t \geq 0, \ (x,y,z) \in \Gamma_3. \tag{M.6.14}$$

The value of c_0 is not important, since the equations are linear in the concentration. Here, we used c_0= 1 kg/m^3.

Of particular interest are unconsolidated media that have a connected permeable medium (e.g. sand) as well as inclusions of lower-permeability material such as silt or clay. At late times, back-diffusion from the material with lower permeability acts as a source to the mobile zone. Because initial results showed that transport in three-dimensional domains could not be well represented by two-dimensional simulations, full three-dimensional permeability fields were studied. The inclusions were distributed in the domain using Sequential Indicator Simulations in the software GSLIB (Deutsch and Journel 1998) with two classes of soil and a spherical semivariogram model

$$\gamma(h) = \left(1.5\frac{h}{a} - 0.5\left(\frac{h}{a}\right)^3\right), \quad h \leq a \tag{M.6.15}$$

$$\gamma(h) = 1, \quad h > a \tag{M.6.16}$$

Here $\gamma(h)$ is half of the expected variance between points separated by distance h. The horizontal and vertical directions are parameterized separately. Values of $a = a_h$, a_v describe the range, or the typical size of inclusions. In addition, the total volume fraction of clay f_{im} is prescribed. The permeability, porosity and sorption distribution coefficients are constant for each material and the local permeability is assumed isotropic. Figure M.6.1 depicts one realization with a_h=0.22 m, a_v=0.10 m and 34 % of the volume occupied by the low-permeability material.

Parameter values that are constant for all simulations are presented in Table M.6.1. Several parameters were chosen from Chapman et al. (2012), who studied back diffusion in a sandbox of similar size as the domain size of our fine-scale simulations. However, they investigated 2D flow, used other solutes than the one of interest here, and did not fit dispersivity. Local dispersivity values used here were those fitted in Rathfelder et al. (2001), based on tracer test effluent breakthrough curve in a 0.6 x 0.3 m 2D sandbox. A similar longitudinal dispersivity was fitted from tracer tests in a sand column by Wang et al., (2012). Several parameters varied between simulations, so that regression of upscaled parameters could be accomplished, see Table M.6.2. In total, 700 simulation sets using Step 1 and Step 2 with a horizontal hydraulic gradient, and 300 simulations of Step 1 using a vertical hydraulic gradient (3 x 10 x 10), were used as a basis for the regressions.

II.6.1.3. Multi-rate Equations

Here, rather than discretizing immobile zones such as low-permeability inclusions, the concentration in the mobile and immobile regions is treated by explicit state variables (averages over the coarse 1 m cube grid block), and the transport between these zones in each coarse grid cell is modeled by first-order exchange terms. Transfer between coarse grid blocks of the upscaled model is assumed to occur only in the mobile zone. As noted by Haggerty and Gorelick (1995), multiple first-order rates may in general be needed to accurately account for diffusive mass transfer between the mobile and immobile zones. When dealing with real heterogeneous media, where all rates must be regressed, it is important to use the simplest model that describes the tailing.

Table M.6.1. Parameter values used in all simulations.

Parameter	Value	Motivation
ρ_p	2.65 g/ml	[*Freeze and Cherry*, 1979]
D_m	$7.9 \cdot 10^{-5}$ m^2/day	Value for TCE from [*USEPA*, 1996]
τ	0.5	Commonly 0.01-0.5 [*Freeze and Cherry*, 1979]. $\phi \approx 0.5$.
α_l	10^{-3} m	[*Rathfelder et al.*, 2001; *Wolfand*, 2011]
α_t	10^{-4} m	[*Rathfelder et al.*, 2001; *Wolfand*, 2011]
Permeable:		
K_m	20 m/day	Similar to [*Chapman et al.*, 2012] ($\log(K) = 1.3, \ln(K) = 3.00$)
ϕ_m	0.4	Similar to [*Chapman et al.*, 2012]
R_m	1	
Low-perm.:		
K_{im}	$1.0 \cdot 10^{-5}$ m/day	Similar to [*Chapman et al.*, 2012] ($\log(K) = -5.0, \ln(K) = -11.5$)
ϕ_{im}	0.5	Similar to [*Chapman et al.*, 2012]

Table M.6.2. Variable parameter values. Each case is tested for all combinations of hydraulic gradient, but variability in each of the three top parameters are performed with the other two at the base-case value indicated in bold. Examples of fraction of organic matter, f_{oc}, are calculated using $f_{oc} = K_d = K_{oc}$ with K_{oc}=85 ml/g, which is the mean value for TCE from Delle Site (2001) (range 34-200 ml/g).

Parameter	Value	Comment
$\partial h / \partial x$	0.005, **0.01**, 0.02	
f_{im}	0.1, 0.2, **0.3**	
R_{im}	1, **6**, 11	$K_d = 0$, 1.89, 3.77 ml/g
		$f_{oc} = 0$, 0.022, 0.044
a_h	0.10, 0.14, 0.18, 0.22 m	
a_v	0.10, 0.14, 0.18, 0.22 m	

Preliminary simulations conducted in this research, as well as results presented by (Fernàndez-Garcia et al. 2009), showed that two rates, α_1 and α_2, could describe breakthrough curves very well. The upscaled transport equation is then written as

$$\phi_m R_m \frac{\partial c_m}{\partial t} + \sum_{j=1}^{2} \phi_{imj} R_{im} \frac{\partial c_{imj}}{\partial t} = -\phi_m \mathbf{v}^{eff} \cdot \nabla c_m + \phi_m \nabla \cdot (\mathbf{D}^{eff} \cdot \nabla c_m) \quad \text{(M.6.17)}$$

$$R_m = 1 + \rho_p K_d (1/\phi_{mobile} - 1) \quad \text{(M.6.18)}$$

$$R_{im} = 1 + \rho_p K_d (1/\phi_{immobile} - 1) \quad \text{(M.6.19)}$$

Here, the effective velocity and the effective dispersion tensor are upscaled to account for presence of the immobile zones and $\mathbf{D}^{eff} = \alpha_l^{eff} v^{eff}$. We denote the volume fraction of mobile material by f_m, and the volume fractions of the immobile zones f_{im1} and f_{im2} such that $\sum f = 1$. The modified porosities used above represent the volume fraction of pores in each zone relative to the bulk volume

$$\phi_m = f_m \phi_{mobile}, \quad \text{(M.6.20)}$$

$$\phi_{imj} = f_{imj} \phi_{immobile}. \quad \text{(M.6.21)}$$

Here, ϕ_{mobile} and $\phi_{immobile}$ are the porosities of the high- and low-permeability media. We have that $\phi_m + \phi_{im}$ is the total porosity. The transport equation is supplemented by equations that describe the first-order mass transfer between the mobile and the immobile zones

$$\phi_{imj}R_{im}\frac{\partial c_{imj}}{\partial t} = \phi_{imj}\alpha_j(c_m - c_{imj}). \tag{M.6.22}$$

Defining $\beta_j = \phi_{imj} / \phi_m$, we get upscaled equations

$$R_m\frac{\partial c_m}{\partial t} + \sum_{j=1}^{2}\beta_j R_{im}\frac{\partial c_{imj}}{\partial t} = -\mathbf{v}^{eff}\cdot\nabla c_m + \nabla\cdot(\mathbf{D}^{eff}\cdot\nabla c_m), \tag{M.6.23}$$

$$\frac{\partial c_{imj}}{\partial t} = \alpha'_j(c_m - c_{imj}), \tag{M.6.24}$$

$$\alpha'_j = \frac{\alpha_j}{R_{im}}. \tag{M.6.25}$$

With knowledge of the first-order rates and the corresponding volume fractions, as well as the upscaled flow and dispersion terms, the equations can be discretized and solved.

To estimate the effective conductivity and dispersivity, as well as the first order rates and their corresponding volume fractions, fine-scale simulation results were compared with an analytic solution to a 1-D approximation of equations (M.6.23) - (M.6.25). The derivation is similar to that of (Fernàndez-Garcia et al. 2009), but with the addition of sorption and with more flexible initial- and boundary conditions. The resulting solute mass flux at distance L from the inlet, at time t is the inverse Laplace transform of

$$\tilde{m}(L,p)_D = \exp\left\{\left(\frac{1}{2\alpha_l^{eff}} - \sqrt{\frac{1}{4(\alpha_l^{eff})^2} + \frac{\tilde{\psi}_r(p)}{\alpha_l^{eff}v^{eff}}}\right)L\right\}, \tag{M.6.26}$$

$$\tilde{m}(L,p)_{1-H} = \frac{1}{p}(1 - \tilde{m}(L,p)_D), \tag{M.6.27}$$

$$\tilde{\psi}_r(p) = pR_m + p\beta_1\frac{\alpha_1}{p + \alpha'_1} + p\beta_2\frac{\alpha_2}{p + \alpha'_2}. \tag{M.6.28}$$

Here, p is the Laplace variable, $m(L, p)_D$ is the Laplace transform of the mass flux with Delta pulse injection and $m(L, p)_{1-H}$ is the mass flux with 1-$H(t)$ injection.

II.6.1.4. Numerical Solution and Regression Procedure

In this work, MODFLOW (Harbaugh et al. 2000) and MT3DMS (Zheng and Wang 1999) were used to solve the fine-scale stationary flow and transport problems, respectively. A second-order central difference scheme was applied for space discretization and the linear problems were solved with the Conjugate Gradient Method, applying a Modified Incomplete Cholesky pre-conditioner. The size of the cross section perpendicular to flow was chosen to mimic a reasonable size for large-scale use of the MRMT model (1 x 1 m^2). The domain size along the flow (1 m) is large enough such that fitted parameters based on the effluent mass flux provide a good representation of the average behavior. The selected grid size (2 x 2 x 2 cm^3) is similar to previous tracer test simulations in heterogeneous media that were successfully compared with experimental results (Rathfelder et al. 2001), and provides a good match to the analytical solution using homogeneous sand. The upscaled problem was solved with the same numerical framework, employing a small modification to MT3DMS. Here, the mass transfer terms were lagged one time-step from the advection and dispersion in the mobile zone, using a sufficiently small time-step size for convergence. Focus was not on efficiency of this implementation but rather on applicability of the method and establishment of regressions.

Upscaled parameters were fitted such that the difference between the theoretical (m_t) and simulated fine-scale (m_s) mass flux at the effluent boundary was minimized. Initial investigations revealed that stable parameter fits could be obtained by splitting the fit into two steps. In the first step, α_l^{eff} and v^{eff} were fit to the early-time breakthrough of a Dirac pulse. The effective conductivity K^{eff} was then calculated from v^{eff}. These parameters account for the dispersion and delay of the flow caused by the immobile zones acting as barriers. In this step, the immobile porosity was set to zero. The objective function is

$$SSE_1 = (m_t(t_1) - m_{s1}(t_1))^2 + ... + (m_t(t_N) - m_{s1}(t_N))^2 \qquad (M.6.29)$$

where the simulation time, corresponding to two pore volumes, is split into $N = 400$ periods of equal size. Because the initial mass in place is not equal to one, the mass is scaled by the initial mass before fitting using equation (M.6.26).

The second step was performed to fit α_j and $b = \beta_1 / (\beta_1 + \beta_2)$ with focus on mass flux at late times, i.e. back-diffusion. For this purpose, the $1 - H(t)$ condition was applied using porous immobile zones. To capture small mass flux at late times, the logarithm of mass flux was used in the fitting

$$SSE_2 = (\log m_t(t_1) - \log m_{s2}(t_1))^2 + ... + (\log m_t(t_N) - \log m_{s2}(t_N))^2. \qquad (M.6.30)$$

In order to also obtain a good fit during breakthrough, the logarithm of time was split into $N = 400$ periods of equal size. These simulations were run for 400 pore volumes or until the effluent mass flux was a factor 10^{-4} lower than the initial flux, whichever occurred first. Because the initial simulated mass flux was not equal to one, the flux was scaled by the initial flux before fitting using equation (M.6.27).

As explained in Fernàndez-Garcia et al. (2009), the type 1 and 2 regions in the MRMT model do not correspond exactly to physical regions. In our simulations, we saw that stagnant water forms in sand regions partly surrounded by clay. Therefore, at first, β_1 and β_2 were fitted independently. However, we found that the resulting $\beta_1 + \beta_2$ was close to the theoretical value based on the pore volume of immobile material. Therefore, we imposed this theoretical value and only fitted the relation $\beta_1 / (\beta_1 + \beta_2)$, to reduce the number of fitted variables and hence problems with non-uniqueness.

Before regression, fitted flow and transport parameters were non-dimensionalized, as follows : K^{eff} / K_{sand}, $\alpha_l^{eff} / \alpha_1$, $Sha = \alpha_1 \alpha_h^2 / D$, and $Sh = \alpha_2 \alpha_h^2 / D$. Here, D is the effective diffusion coefficient, and Sha and Sh are Sherwood numbers for the higher and lower first-order mass transfer rates, defined in terms of a length scale representing the horizontal range ("size") of the low-permeability inclusions. This length scale was chosen because it was observed that the first-order rates were more sensitive to the horizontal range than to the vertical range. We chose not to scale with the retardation factor, because the results are not linear with respect to this factor.

Hypotheses regarding the controlling non-dimensional parameters and functional forms were posed based on an understanding of the relevant processes and on the literature. The validity of these hypotheses was first examined by plotting the parameters against the data and the most relevant functional forms and parameters were then further tested using regressions of increasing complexity and number of parameters. For each parameter, a final regression model was chosen as the least complex model that has $R^2 > 0.8$ and an increase in R^2 from the previous model of at least 0.04. One exception was the effective longitudinal dispersivity, where R^2 of the chosen model is 0.70. There is a large spread in this parameter among different realizations of one geostatistical model. Another exception was the effective hydraulic conductivity, where a very accurate model

(R^2=0.99) was chosen, because this parameter influences the regression of transport parameters through the Peclet number, Pe=u $a_h/D=K_2^{eff} \nabla h$ a_h/D, where K_2^{eff} is the regressed effective hydraulic conductivity using "model 2" as explained below. Although the focus of this work was on horizontal flow, the applicability of the regressed models was also tested on simulations with vertical flow.

II.6.2. Bioenhanced Dissolution Screening Tool Development

II.6.2.1. Introduction

In-situ bioremediation is an attractive strategy for the economical long-term management of subsurface contamination emanating from dense non-aqueous phase liquid (DNAPL) or low-permeability source zones (*e.g.*, NRC, 2005; Scheutz et al., 2010; Stroo et al., 2012). Several studies (Lebrón et al. 2007; McGuire et al. 2006; Sleep et al. 2006) have shown that stimulation of indigenous or augmented microorganisms near source zones enhances contaminant dissolution, reducing source longevity and, potentially, contaminant flux. Early efforts to quantify dissolution enhancements due to microbial activity focused on dissolution from fully saturated DNAPL pools (Chu et al. 2003, 2004; Gupta and Seagren 2005; Reitsma and Dai 2001; Seagren et al. 1993, 1994). However, source-zone characterization studies have highlighted the importance of quantifying dissolution from complex source zones comprised of both high-saturation pools and low-saturation ganglia (*e.g.*, Lemke and Abriola, 2006). Thus, there is a need to quantify potential dissolution enhancement from ganglia-contaminated source zone regions.

Enhanced dissolution due to microbial activity (*i.e.*, *bioenhanced* dissolution) is generally defined as the ratio of contaminant mass flux eluting from a DNAPL-contaminated region when microbial activity is present to the contaminant mass flux in the eluate when no microbes are active (Adamson et al. 2004; Amos et al. 2008, 2009; Carr et al. 2000; Cope and Hughes 2001; Da Silva et al. 2006; Schaefer et al. 2009a; Sleep et al. 2006; Yang and McCarty 2000, 2002). Experimental column results have demonstrated an average two- to six-fold enhancement in the rate of dissolution from residual DNAPL (Amos et al. 2008; Christ et al. 2005), with dissolution enhancement reaching as high as a factor of 20 relative to the abiotic case (Amos et al. 2009). Variability in the magnitude of bioenhanced dissolution has been attributed to factors that influence the rate of biotransformation such as low pH (e.g., Cope and Hughes, 2001; Adamson *et al*., 2004) and accumulation of toxic remediation by-products (e.g. Amos et al., 2007a; Yu et al., 2005), as well as hydrologic factors such as insufficient contact time and non-uniform saturations (Amos et al. 2008, 2009; Glover et al. 2007). Although these column results provide much-needed insight into the factors controlling dissolution enhancement, they are not readily applicable to the prediction of dissolution enhancement under a wide variety of subsurface site conditions.

Previous efforts to predict dissolution enhancement due to microbial activity have generally assumed a simple geometry, with a fully saturated DNAPL pool located along the domain boundary. Seagren et al. (1994) were the first to employ a solution to the advection-dispersion-reaction equation (ADRE) in a two-dimensional domain with one-dimensional flow parallel to a DNAPL pool. This study modeled dissolution as a diffusion process away from the fully saturated DNAPL boundary. Using this simplified model, they determined a biotransformation rate threshold, above which dissolution enhancement will take place, and demonstrated that the enhancement scales linearly with biotransformation rate on a log-log plot (Seagren et al., 1994). Chu et al. (2004, 2003) employed a similar mathematical framework to investigate favorable conditions for bioenhanced dissolution in tetrachloroethene (PCE)-contaminated domains. They used their model to explore the influence of electron-donor limitations and bio-clogging on microbial enhancements to dissolution and developed a simplified expression to quantify

bioenhanced dissolution. This simplified expression was similar in form to the original expression developed by Seagren et al. (1994), and again assumed dissolution from a DNAPL pool. In a later work, Chu et al. (2004) extended their model to consider multiple pools placed along the domain boundaries to better simulate a more heterogeneous DNAPL- contaminated region. They showed that enhanced dissolution often had an upper bound, due to competition for an electron donor, the effect of toxic byproduct accumulation on dechlorination kinetics, and DNAPL configuration in the source zone. Follow-up experimental studies using a similar conceptual model (*i.e.*, distinct DNAPL pool zones overlain by uncontaminated groundwater) have likewise demonstrated limitations in enhanced dissolution (Glover et al. 2007; Philips et al. 2011), although Glover et al. (2007) did observe dissolution enhancement factors as high as 13, depending on the sharpness of the interface separating the NAPL contaminated and uncontaminated zones.

Seagren et al. (1993) employed an analytical solution to the one-dimensional ADRE to quantify dissolution enhancements due to microbial activity in ganglia-dominated systems. By comparing solutions that neglected microbial degradation to solutions that included microbial degradation, they were able to predict dissolution enhancement due to microbial activity. Their formulation predicted an effective dissolution rate relative to the maximum rate of dissolution for the given column conditions rather than a bioenhanced dissolution factor. Christ and Abriola (2007), as part of a numerical modeling study of source zone bioremediation, reformulated the Seagren et al. (1993) approach in terms of a bioenhanced dissolution factor to provide a screening-level check on their numerical predictions. However, this approach was only applied to ganglia-dominated geometries with first-order biotransformation kinetics.

In this research, the bioenhanced dissolution factor presented in Christ and Abriola (2007), which is based on an assumption of first-order biotransformation kinetics, was extended to incorporate zero-order and Monod kinetics and used to quantify the expected level of microbially enhanced dissolution under a variety of physicochemical conditions (*i.e.*, transport processes, interphase mass transfer kinetics, and biotransformation kinetics). The bioenhanced dissolution factor was then applied as a simple screening tool and its predictions compared to published laboratory and field results to demonstrate its utility.

II.6.2.2. Mathematical Model

Dissolution in a one-dimensional, semi-infinite, DNAPL ganglia-contaminated system can be modeled using a steady-state form of an ADRE:

$$\phi S_a D \frac{d^2 C}{dx^2} - \phi S_a v \frac{dC}{dx} + k_l \left(C_{eq} - C \right) - R = 0 \tag{M.6.31}$$

where ϕ is the porosity [L³/L³], S_a is the aqueous-phase saturation [L³/L³], C is the contaminant concentration in the aqueous phase [M/L³], D is the macro-scale hydrodynamic dispersion coefficient [L²/T], v is the pore water velocity [L/T], k_l is the lumped mass transfer coefficient [1/T], C_{eq} is the equilibrium concentration of the contaminant in the aqueous phase [M/L³], and R is the biotransformation reaction term [M/(L³·T)]. The assumption of steady-state bio-enhancement processes is an approximation often applied in field remedies. After initial remedy implementation, there will likely be a period of acclimation before a quasi-steady state is reached, and long-term dissolution and/or by-product accumulation may cause further changes later. However, it is assumed that the screening-level approach described herein is appropriate during the extended quasi-steady state period that exists after an initial period of acclimation.

DNAPL ganglia dissolution is represented in (M.6.31) by a linear driving force model (3rd term), which assumes that diffusion across the boundary layer separating the non-aqueous and aqueous phases is a steady process. The value of the lumped mass transfer coefficient, k_l, is typically estimated using an empirical relationship (*e.g.*, Imhoff et al., 1994; Miller et al., 1990; Powers et al., 1992). The relationships of Powers et al. (1992) and Imhoff et al. (1994) incorporate the effect of decreasing DNAPL saturation on the lumped mass transfer coefficient. Chu et al. (2003) suggest that this lumped mass transfer coefficient may also increase with microbial activity, since biofilm formation can decrease the boundary layer width across which dissolution occurs. However, for the purposes of this work the lumped mass transfer coefficient $\left(k_l\right)$ is assumed constant with respect to time (*i.e.*, independent of changing DNAPL saturation or microbial activity).

A significant amount of work has examined the appropriate expression for the reaction term, *R*, when microbes are active in a multiphase system. This work employs the commonly applied dual-Monod-kinetic model for dehalorespiration (*e.g.*, Chen et al., 2013):

$$R = k_{max} X \frac{C_{ED}}{K_s^{ED} + C_{ED}} \frac{C}{K_s + C}$$ (M.6.32)

where k_{max} is the maximum utilization rate for the contaminant [M/(M$_{cells}$·T)], *X* is the biomass concentration [M$_{cells}$/L³], C_{ED} is the electron donor concentration [M/L³], K_s^{ED} is the electron donor half-saturation constant [M/L³], and K_s is the contaminant half-saturation constant [M/L³]. In most applications, the system is engineered to provide electron donor in excess $\left(C_{ED} \quad K_s^{ED}\right)$ and the biomass is assumed to have reached a steady-state value (*i.e.*, *X* is a constant). Under these conditions, equation (M.6.32) can be approximated as:

$$R = k_{max} X \frac{C}{K_s + C}$$ (M.6.33)

Assuming the reaction term in equation (M.6.31) follows the simplified expression in equation (M.6.33), equation (M.6.31) can be expressed in dimensionless form as:

$$\frac{1}{\mathbf{Pe}} \frac{d^2 C^*}{dx^{*2}} - \frac{dC^*}{dx^*} + \mathbf{Da_1}\left(1 - C^*\right) - \mathbf{Da_2} \frac{C^*}{K_s^* + C^*} = 0$$ (M.6.34)

where $C^* = C/C_{eq}$, the ratio of the aqueous-phase solute concentration to the aqueous-phase solute equilibrium concentration and $x^* = x/L$. $K_s^* = K_s/C_{eq}$, a dimensionless form of the Monod half-saturation constant normalized to the aqueous-phase solute equilibrium concentration. Here $\mathbf{Pe} = vL/D$, the Péclet Number, is the ratio of the rate of advection to the rate of dispersion; $\mathbf{Da_1} = k_l L/v$, an interphase mass transfer-based Group I Damköhler Number, is the ratio of the mass transfer rate to the advection rate, $\mathbf{Da_2} = k_{max} XL/C_{eq}v$, a reaction-based Group I Damköhler Number, is the ratio of the biotransformation rate to the advection rate, and *L* is the length of the DNAPL source zone within which dissolution enhancement may occur.

Dimensionless half-saturation constants $\left(K_s^*\right)$ vary depending on the contaminant (Chen et al., 2013; Clapp et al., 2004). In practice, the local source zone dimensionless contaminant

concentration $\left(C^*\right)$ is either be much less than, or much greater than, the dimensionless half-saturation constants (Amos et al., 2007a; Becker, 2006; Chambon et al., 2013; Clapp et al., 2004; Fennell and Gossett, 1998; Haest et al., 2010a; Huang et al., 2014; Huang and Becker, 2009; Kouznetsova et al., 2010; Schaefer et al., 2009a; Torlapati et al., 2012; Yu and Semprini, 2004). When $C^* \quad K^*$, equation (M.6.34) reduces to a mass balance equation with zero-order kinetics:

$$\frac{1}{\mathbf{Pe}}\frac{d^2 C^*}{dx^{*2}} - \frac{dC^*}{dx^*} + \mathbf{Da_1}\left(1 - C^*\right) - \mathbf{Da_2} = 0 \tag{M.6.35}$$

and, when $C^* \quad K^*$, equation (M.6.34) reduces to a mass balance equation with first-order kinetics:

$$\frac{1}{\mathbf{Pe}}\frac{d^2 C^*}{dx^{*2}} - \frac{dC^*}{dx^*} + \mathbf{Da_1}\left(1 - C^*\right) - \frac{\mathbf{Da_2}}{K_s^*}C^* = 0 \tag{M.6.36}$$

Equations (M.6.34)-(M.6.36) can be solved using a variety of mathematical methods. For example, Seagren et al. (1993) employed an analytical solution developed by van Genuchten and Alves (1982) that uses equation (M.6.36) in conjunction with a Robin condition (type III) at the inlet boundary and a Neumann condition (type II) at the outlet boundary of a one-dimensional semi-infinite column. Although the application to a semi-infinite column is expected to introduce error when applied to a finite length column, Seagren et al. (1993) suggested this error is relatively small, especially for advectively dominated systems (*i.e.*, large **Pe**) (van Genuchten and Alves 1982; van Genuchten and Parker 1984), an error level consistent the screening-level application proposed here.

The Seagren et al. (1993) solution quantified the rate of dissolution in a bioenhanced system as a fraction of the maximum possible rate of dissolution, which was calculated assuming the bulk aqueous phase contaminant concentration $\left(C^*\right)$ was equal to zero. It is relatively straight-forward, however, to rearrange the solutions derived in Seagren et al. (1993) to quantify the steady-state, first-order kinetic, bioenhanced dissolution factor (E_1) as the ratio of the biotic (J_{biotic}) and abiotic ($J_{abiotic}$) dissolution flux (Christ and Abriola, 2007):

$$E_1 = \frac{J_{biotic}}{J_{abiotic}} = \frac{\mathbf{Da_1}\int_0^1\left(1 - C_{biotic}^*\right)dx^*}{\mathbf{Da_1}\int_0^1\left(1 - C_{abiotic}^*\right)dx^*}$$

$$= \frac{\mathbf{Da_1}\left(\mathbf{Da_1} + \frac{\mathbf{Da_2}}{K_s^*}\right)^2 - \mathbf{Da_1^2}\left(\mathbf{Da_1} + \frac{\mathbf{Da_2}}{K_s^*} - \left(1 - e^{\frac{\mathbf{Pe}}{2}\left(1 - \sqrt{1 + \frac{4\left(\mathbf{Da_1} + \frac{\mathbf{Da_2}}{K_s^*}\right)}{\mathbf{Pe}}}\right)}\right)\right)}{\left(\mathbf{Da_1} + \frac{\mathbf{Da_2}}{K_s^*}\right)^2\left(1 - e^{\frac{\mathbf{Pe}}{2}\left(1 - \sqrt{1 + \frac{4\mathbf{Da_1}}{\mathbf{Pe}}}\right)}\right)} \tag{M.6.37}$$

A review of the literature suggests that zero-order kinetics are far more likely than first-order kinetics in a DNAPL source zone (*i.e.*, equation (M.6.35)). Typical half-saturation constant values

for chlorinated ethenes frequently fall within the 0.1-10 µM range. Considering typical equilibrium aqueous-phase solute equilibrium concentrations for chlorinated ethenes (*i.e.*, $C_{eq}^{PCE} = 905$ µM; $C_{eq}^{TCE} = 8370$ µM; $C_{eq}^{cis-DCE} = 36,300$ µM; and $C_{eq}^{VC} = 14,000$ µM; Montgomery, 2007) yields dimensionless half-saturation constant values in the range of $10^{-5} - 10^{-2}$. Thus, for the first-order approximation to Monod kinetics to be valid, aqueous-phase concentrations have to be significantly less than $10^{-5} - 10^{-2}$ times their respective equilibrium concentrations. These low concentrations are unlikely in DNAPL source zones, particularly in regions where bioenhanced dissolution occurs. Additionally, these low concentrations may fall below the specific regulatory criteria that are motivating site remediation. In fact, dimensionless half-saturation constant values in the $10^{-5} - 10^{-2}$ range are far more likely to support a zero-order approximation to Monod kinetics, rather than a first-order approach. Using an approach similar to that employed in Christ & Abriola (2007), a steady-state, bioenhanced dissolution factor (E_0) can be developed for zero-order kinetics:

$$E_0 = \frac{J_{biotic}}{J_{abiotic}} = \begin{cases} \frac{1}{2}\left(2 + \mathbf{Da_2}\left(1 - \frac{2}{\mathbf{Da_1}} - \coth\left(\frac{1}{4}\left(\mathbf{Pe} - \sqrt{\mathbf{Pe}(4\mathbf{Da_1} + \mathbf{Pe})}\right)\right)\right)\right) & \text{if } \mathbf{Da_1} \geq \mathbf{Da_2} \\[2em] \dfrac{\mathbf{Da_1}}{1 - e^{\frac{1}{2}\left(\mathbf{Pe} - \sqrt{\mathbf{Pe}(4\mathbf{Da_1} + \mathbf{Pe})}\right)}} & \text{if } \mathbf{Da_1} < \mathbf{Da_2} \end{cases} \tag{M.6.38}$$

When $\mathbf{Da_2}$ is greater than $\mathbf{Da_1}$, the concentration-independent biotransformation rate is greater than the maximum possible dissolution rate. In effect, contaminant mass is removed from the aqueous phase by biotransformation faster than it dissolves into the aqueous phase. Under these conditions (and the boundary conditions described above), the solution to equation (M.6.35) yields non-physical, negative concentrations over the entire domain. Thus, the value of $\mathbf{Da_2}$ is limited to the value of $\mathbf{Da_1}$, which results in the two-part, C^0-continuous, solution shown in equation (M.6.38).

Development of a bioenhanced dissolution factor that incorporates the full Monod kinetic model is more challenging since an analytical solution to equation (M.6.34) does not exist. This value can be estimated numerically, however. In this work, equation (M.6.34) is solved using a fourth-order-accurate, finite-difference approach implementing the three-stage Lobatto IIIa formula (Kierzenka and Shampine, 2001) with a Type III upgradient boundary condition and a Type II downgradient boundary condition. A spatial discretization of $\Delta x^* = 10^{-4}$ was used and non-linearities introduced by the Monod reaction term were resolved using direct (Picard) iteration with a convergence criterion of 10^{-6}. This numerical model was validated using analytical solutions to the zero- and first-order mass balance equations. Excellent mass balance was achieved. This solution (*i.e.*, C_{biotic}^* on $0 \leq x^* \leq 1$) is then incorporated into the definition of the bioenhanced dissolution factor (*i.e.*, $E = J_{biotic}/J_{abiotic} = \mathbf{Da_1}\int_0^1 \left(1 - C_{biotic}^*\right)dx^* \Big/ \mathbf{Da_1}\int_0^1 \left(1 - C_{abiotic}^*\right)dx^*$) to develop an estimate for E.

Equations (M.6.37) - (M.6.38) and the numerical solution to equation (M.6.34) provide relatively simple models that can be used to estimate the level of bioenhanced dissolution expected for a given set of flow and biodegradation conditions in a ganglia-contaminated, uniform-saturation, source zone.

II.7. Statistical Characterization Tool Development

II.7.1. Modeling Background and Formulation

Despite significant advances in our understanding of chlorinated solvent source zones and the maturation of several *in situ* remediation technologies (e.g., bioremediation), our ability to provide *a priori* predictions of the performance of remediation technologies in the field remains severely limited (Kavanaugh et al., 2003; NRC, 2005; Stroo et al., 2003). This limitation mainly arises from our lack of knowledge of the contaminant source zone architecture and mass (Abriola, 2005; Koch and Nowak, 2015; Kueper et al., 2014; Mercer et al., 2010).

A major challenge in site assessment and the design of remedial technologies is the fact that modeling contamination by NAPLs using multiphase flow and transport models is computationally intensive (Dokou & Pinder, 2009). Furthermore, application of stochastic methods, such as Monte Carlo simulations, to explore the implications of the uncertainty associated with formation properties, contaminant spill scenarios and hydrological boundary conditions, involves the intensive use of such models (Koch & Nowak, 2015). In addition, such forward models are not well-suited to consideration of field-measured data from boreholes or monitoring wells. To overcome this limitation multiple inversion techniques have been proposed over the last decade to predict source zone architecture from field data (e.g. Koch & Nowak, 2016; Michalak & Kitanidis, 2004; Neupauer & Lin, 2006; Neupauer & Wilson, 2005; Saenton & Illangasekare, 2007; Yeh et al., 2007; Zeng et al., 2012; J. Zhang et al., 2015). Although effective in identifying contaminant plume distribution, many of these techniques are highly computationally intensive, do not account for presence of NAPL in the domain, or have strong assumptions relating to the location and geometry of the source zone (Koch & Nowak, 2016).

To address the limitations associated with sparse sampling of the source zone, it is now common practice to employ deterministic and stochastic plume interpolation approaches to estimate contaminant concentration at unsampled locations using available borehole data. Kriging packages (Deutsch and Journel, 1998) are among the stochastic methods that have been extensively used for contaminant plume characterization, to interpolate between point observations of mass concentrations at field sites (e.g., Gilbert & Simpson, 1985; Jones et al., 2005; Wu et al., 2005) in an attempt to estimate contaminant mass. Most kriging applications, however, have focused on aqueous concentration measurements to delineate contaminant plumes (Reed et al., 2000; Wu et al., 2005; Basu et al., 2006; Rivett et al., 2006; Yu et al., 2006; Reed and Minsker, 2004), failing to incorporate consideration of sequestered mass, specifically DNAPL, in their site conceptual model, and potentially leading to gross underestimation of total mass and the associated remedial challenges. Over the past two decades, more sophisticated characterization methods based on Markov chain models (MCM) (Carle & Fogg, 1996, 1997) have been considered for processing sparsely sampled data, including hydraulic conductivity (e.g., Elfeki, 2006a, 2006b; Harp et al., 2008; Harp & Vesselinov, 2010) and source zone mass (Maji et al., 2006) observations. In the latter study, however, DNAPL volume and aqueous-phase mass tended to be underestimated.

The above discussion highlights the urgent need for the development of improved, cost-effective, field characterization methods and associated modeling tools that encompass all source zone mass and facilitate the identification of the most critical source zone properties that govern mass persistence and the performance of remedial options. In this work, a statistical model, employing machine learning methods in conjunction with a limited number of field scale simulations, is developed and used to reproduce distributions of contaminant mass (including NAPL saturation, aqueous and sorbed phase concentrations) within a hydrologic subsurface unit.

This work employs random field models, introduced and widely used in computer vision applications, to model correlations among system variables. In particular, Discriminative Random Field (DRF) models are selected to allow for the use of arbitrary features that can capture long-range information and arbitrarily complex functions of the observed data. Once the models are learned from a set of training data, Monte-Carlo sampling methods are then used to generate realizations that are conditioned on measured borehole data. These realizations are then employed to generate approximations of uncertainty that can inform further sampling for characterization and remediation. Aside from a limited number of forward modeling runs needed to train the model, this approach obviates the need to conduct extensive forward simulations with flow and transport models that would be required in the context of Monte-Carlo analysis. In order to investigate the performance of the proposed model, model results are also compared to those obtained through classical ordinary kriging.

The DRF model is conditional in the sense that it considers the dependence of the unobserved contaminant source zone (i.e. DNAPL saturation and aqueous concentration) distribution given two categories of observed information. Firstly, permeability is assumed to be known everywhere in the domain and this information is used as part of the observed data, or features, of the model, as described further in this report. For a discussion about lifting this assumption, see Section III.6. Secondly, the model is conditioned on observed borehole information (saturation and aqueous concentration), and features required for the specification of the DRF model are calculated based on the values of these quantities at the boreholes. The statistical model presented in this work considers discrete values (herein referred to as *labels*) for saturation and aqueous concentration as determined by binning continuous values of these properties. With discrete labels as the variables of interest, the modeling problem becomes one of classification, i.e., determining the label associated with each pixel for each property. Here the classification problem in discrete values was favored over modeling continuous values through regression models. This can be justified by the fact that concentration and saturation categories (labels), as shown in Section III.6, can provide sufficient information for calculating source zone metrics, such as pool fraction (PF), used to predict source zone longevity. Furthermore, handling discrete valued random fields is more feasible than continuous values, specifically in the case of drawing samples using the Markov Chain Monte Carlo (MCMC) method. The next section provides background to graphical and random field models, specifically discriminative random fields which are used in this work.

II.7.2. Graphical Models

Graphical models (or probabilistic graphical models) provide a tractable framework for describing joint probability distributions with potentially complex dependencies among the random variables. Usually, neighboring pixels are considered to be those vertically and horizontally adjacent, corresponding to a graph defined on a regular grid as shown in Figure M.7.1.a. The usefulness of these models centers on the ability to factorize the joint probability distributions across pixels into products of local functions based on the fact that the joint distributions satisfy some conditional independence properties governed by the structure of the graph or model (Wang et al., 2013).
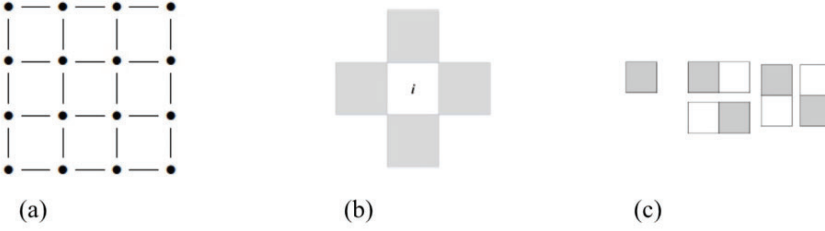
Figure M.7.1. (a) Graphical representation of a random field defined on a regular grid (lattice), (b) First-order neighborhood N_i for site i, (c) First-order cliques: unary and pairwise cliques

Markov Random Fields (MRFs) are perhaps the most widely used class of graphical models. They provide a computationally tractable and relatively flexible means of specifying joint probabilistic models over all pixels in an image that can capture spatial relationships, making use of the assumption that the value of a random variable (such as saturation or concentration), x_i, at pixel (or site) i is independent of all other pixels, except i's neighbors. This assumption is referred to as the local Markov property and can be stated as

$$\forall i \in S, x_i \perp x_{S-\{i\}}|x_{N_i} \tag{M.7.1}$$

where S is the set of pixels or sites in the field, x_i is the random variable of interest (i.e. DNAPL saturation or aqueous concentration) at site i, and N_i is the set of neighbors of site i. For three sets of random variables A, B, and C, the notation $A \perp B|C$ indicates that A and B are statistically independent conditioned on knowledge of C. Using the local Markov property, the Hammersley-Clifford theorem states that the joint probability $p(\mathbf{x})$ can be represented as a Gibbs distribution factorized as a product of positive function of the random variables (Li, 2009). That is,

$$p(\mathbf{x}) \propto \prod_{c \in C} \psi_c(x_c) \tag{M.7.2}$$

where the bold symbol $\mathbf{x}$ represents the vector constructed from the lexicographical ordered pixels i in S, a clique c is a set of mutual neighbors and the clique potential $\psi_c(x_c)$ is a positive-valued function of the variables x_c in the clique. The lowest order random field model that can capture relationships between neighbors consists of two types of cliques, unary, or single-site cliques and pairwise cliques (Figure M.7.1.c). The neighborhood structure defined by such a model is referred to as a first-order neighborhood structure (Figure M.7.1.b). For compactness the representation of clique energy θ_c defined as $\theta_c(x_c) = - \log \psi_c(x_c)$ is adopted so that the joint distribution becomes

$$p(\mathbf{x}) = \frac{1}{Z}\exp\{-E(\mathbf{x})\} \tag{M.7.3}$$

where the energy $E(\pmb{x}) = \sum_{c \in C} \theta_c(\pmb{x}_c)$ is defined as the sum over all clique energies and Z is the normalizing term known as the partition function (Wang et al., 2013).

Now consider constructing a model for $\mathbf{x}$, an unknown quantity to be modeled as a random field, conditioned on observed data, $\mathbf{y}$. Specifically, these observed data $\mathbf{y}$ will be measurements of hydrologic or other physical properties observed in the domain, such as in boreholes, or functions of these measurements. The values of $\mathbf{x}$ represent values of DNAPL saturation or aqueous phase concentration for all pixels in a discretized representation of the source zone.

Unfortunately, our preliminary work indicated that building conditional random fields (CRFs) based on local interactions among the components of $\pmb{x}$, was not suitable for generating realistic realizations of DNAPL saturation or aqueous phase concentration given limited borehole information. As shown in Kaluza et al. (2015), realizations using models based upon the MRF framework tended to overemphasize local data to predict values that may be better informed by

larger scale information. This weakness can be addressed through the use of a modeling approach that can capture more subtle interactions among the random variables and the conditioning data. Of specific interest here are a class of models known as Discriminative Random Fields (DRFs) originally introduced in the computer vision literature for which the clique potentials can take the form of any arbitrary domain-specific discriminative functions, which can capture local, mid-range, or long-range interactions across images (Kumar and Hebert 2006).

II.7.3. DRF Model Formulation

Similar to CRFs, the distribution of x for a DRF is conditioned on the data and is a function of the sum of potential functions. Here however the DRF distribution takes the specific form

$$p(\mathbf{x}|\mathbf{y}) = \frac{1}{Z}\exp\left(\sum_{i\in S} A_i(x_i, \mathbf{y}) + \sum_{i\in S}\sum_{j\in N_i} I_{ij}(x_i, x_j, \mathbf{y})\right) \tag{M.7.4}$$

where $A_i(x_i, \mathbf{y})$ represents the unary, or association, potential and $I_{ij}(x_i, x_j, \mathbf{y})$ represents the pairwise, or interaction, potential. Under the simplifying assumption that the random field to be modeled here are homogeneous and isotropic, these potentials will be equal for all i and j, and therefore the i and j subscripts can be dropped from Equation (M.7.4) (Kumar and Hebert 2006). For the remainder of this discussion, we assume that each site or pixel in an image representing the domain can take on one of discrete set of labels L for each hydrological property (i.e. DNAPL saturation or aqueous phase concentration), where the possible labels for this property at any pixel is given by $k \in L$.

In this work, the association potential $A(x_i, \mathbf{y})$ represents a measure of how likely a pixel i will take label x_i, given the observed borehole and permeability data $\mathbf{y}$, ignoring the effects of other pixels in the image (domain). Following Kumar & Hebert, (2006), the association potential for this multiclass problem takes the form

$$A(x_i, \mathbf{y}) = \sum_{k\in L} \delta(x_i = k) \log P'(x_i = k|\mathbf{y}) \tag{M.7.5}$$

where $\delta(x_i=k) = 1$ when $x_i=k$ and $\delta(x_i=k) = 0$ otherwise, in effect serving as a function to select the appropriate label-dependent parameters in $P'(x_i = k|\mathbf{y})$, which represents an arbitrary discriminative classifier (Kumar & Hebert, 2005). Discriminative classifiers differ from generative classifiers in that they model the conditional distribution $P(x|y)$ rather than the joint distribution $P(x, y)$. In this work, a multinomial logistic regression classifier was used as discriminative classifier, which takes the form

$$P'(x_i = k|\mathbf{y}) = \frac{\exp\left(\mathbf{w}_k^T \mathbf{h}_i(\mathbf{y})\right)}{\sum_{l\in L}\exp\left(\mathbf{w}_l^T \mathbf{h}_i(\mathbf{y})\right)} \tag{M.7.6}$$

where $\mathbf{w}_k$ with $k \in L$ are the coefficients (parameters) for the k-th component of the association potential, and $\mathbf{h}_i(y)$ is a feature vector corresponding to pixel i defined as function of the the observed data y. The specific components of $\mathbf{h}_i$ are defined later in this Section.

The interaction, or pairwise clique, potential $I(x_i, x_j, \mathbf{y})$, considers the interactions between neighboring sites i and j and can be thought as a measure of how the labels at neighboring sites should interact given the observed data $\mathbf{y}$ (Kumar and Hebert 2006). Again, following the ideas in Kumar & Hebert, (2006), the form chosen for the interaction term is

$$I(x_i, x_j, \mathbf{y}) = \sum_{k,l\in L} \mathbf{v}_{kl}^T \boldsymbol{\mu}_{ij}(\mathbf{y})\, \delta(x_i = k)\, \delta(x_j = l) \tag{M.7.7}$$

where $\mathbf{v}_{kl}$ is the coefficient or parameter vector corresponding to the pair of labels k, l and $\boldsymbol{\mu}_{ij}(y)$ represents the pairwise feature vector (Kumar and Hebert 2006), in this work a function of the

feature vectors $\mathbf{h}_i(\mathbf{y})$ and $\mathbf{h}_j(\mathbf{y})$ (specifically $\boldsymbol{\mu}_{ij}(\mathbf{y}) = |\ \mathbf{h}_i(\mathbf{y}) - \mathbf{h}_j(\mathbf{y})\ |$). The first two terms of the function represent a linear regression or inner product of the parameters and the function of feature vectors at neighboring locations i and j. The terms $\delta(x_i = k)$ and $\delta(x_j = l)$ serve as a selection function so that the product between the parameter vector $\mathbf{v}_{kl}$ and the pairwise feature vector is nonzero only when $x_i = k$ and $x_j = l$. In effect, this model consists of one parameter vector $\mathbf{v}_{kl}$ for every unique combination or labels $k,\ l \in L$ and the last two terms in (M.7.7) select the appropriate parameter vector for the specific labels at pixels i and j.

The DRF model (M.7.4-7) is characterized in terms of a collection of parameters, the w and v vectors. To estimate these parameters, a limited number of heterogenous field scale multiphase flow and transport simulations were conducted to generate training and testing datasets. These simulation data were assumed to represent realistic distributions of DNAPL saturations and concentrations across the heterogeneous domains. The DRF model parameters, that is the $\mathbf{w}_k$ and $\mathbf{v}_{kl}$ vectors with $k,l \in L$ were then estimated from these training data. Then, using these parameter vectors and "bore hole" data from the test set, Markov chain Monte-Carlo methods were employed to generate conditional realizations of DNAPL saturation and aqueous phase concentration. The performance of the statistical model was measured by comparing the predicted realizations with the 'true' inter-borehole distributions, as generated in the test set.

The following flow chart (Figure M.7.2) illustrates the sequence of tasks performed to develop the statistical model (hereafter referred to as BRAINS - **B**orehole **R**andom-field **A**utomated **I**nterpolator for **N**APL **S**ource-zones). The procedure for generation of training and test data is described in Section III.6.

Data preparation
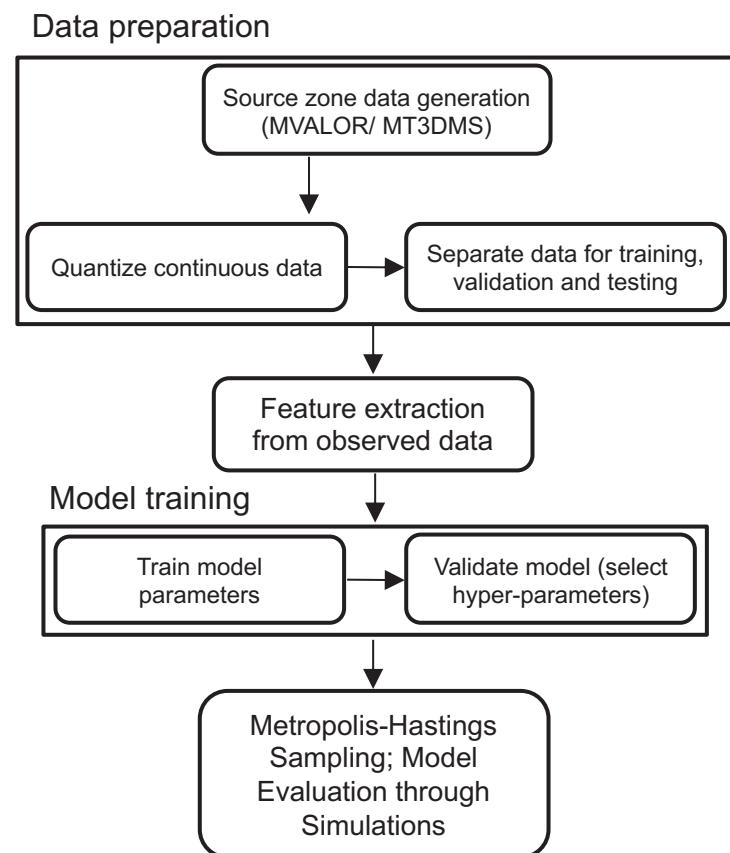
Figure M.7.2. Workflow for BRAINS model

II.8. Sensitivity/Sampling Optimization Modeling

II.8.1. Introduction

Delineation of the down-gradient mass discharge from a contaminant source zone is of particular importance in the estimation of source longevity (e.g., (Christ et al. 2005); (Koch and Nowak 2015), the assessment of long-term impact on groundwater quality (e.g., (Falta et al. 2005a; b; Jawitz et al. 2005), and evaluation of the benefits of source zone remediation at contaminated sites (e.g., (Basu et al. 2006; Falta 2008). Mass discharge and flux averaged concentration (FAC) are receiving increased attention alternative metrics that relate to both source mass removal efficiency and down-gradient plume persistence (e.g., (DiFilippo and Brusseau 2008; Li et al. 2007; Soga et al. 2004; Stroo et al. 2003).

Here, flux averaged concentration is defined as:

$$C_f = \frac{\int KiC_a dA}{\int KidA} \tag{M.8.1}$$

where K is the hydraulic conductivity $[LT^{-1}]$, i is the hydraulic gradient $[-]$, A is the area of control plane $[L^2]$, C_a is the aqueous phase concentration $[ML^{-3}]$. The integral is applied along a down-gradient transect.

Unfortunately, mass discharge or FAC estimates are prone to large uncertainty, due to sparse data and subsurface variability (Kitanidis 1997; Rubin 2003) In addition, because mass discharge integrates uncertain spatial and temporal distributions of varying flow conditions and complex contaminant distributions, estimates of mass discharge suffer from high prediction uncertainty ((Li et al. 2007; Li and Abriola 2009; Troldborg et al. 2010, 2012).

Mass discharge uncertainty quantification has been investigated using the Integral Pumping Test (Chen et al. 2014; Jarsjö et al. 2005), the Passive Flux Meter (Acar et al. 2013; Klammler et al. 2012), and Multilevel Sampling (MLS). MLS measurements of concentration and permeability obtained by indicator Kriging (Li et al. 2007; Li and Abriola 2009) or variogram (Cai et al. 2011) were fitted into certain geostatistical models to estimate the mass discharge uncertainty in terms of probability distributions. Simulations incorporating the physics of flow and transport processes were proposed to account for heterogeneity of permeability and concentration to quantify mass discharge uncertainty, employing numerical transport simulations (Troldborg et al. 2010) or analytical macro-dispersive transport solutions (Troldborg et al. 2012).

Notably, none of the above applications considered the presence of NAPL phase or sorbed mass and their relationship to mass discharge. A few studies incorporated random contaminant sources in transport modeling (Chaudhuri and Sekhar 2006, 2008; Wang and Zheng 2005). However, the physical processes that form DNAPL source zones were neglected. Such simplifications have substantial consequences, since local permeability and flow velocity have significant impacts on emanating mass fluxes (de Barros and Nowak 2010). In addition, it has been demonstrated by numerous laboratory (e.g., (Suchomel and Pennell 2006; Totten et al. 2007) and modeling investigations (e.g., (Christ et al. 2010; Lemke and Abriola 2006; Yang et al. 2018) that the morphology of source zone and sorption properties (e.g., (Maghrebi et al. 2015; Yang et al. 2018) have significant effects on solute transport, DNAPL depletion, and mass discharge prediction. Thus, source zone architecture, DNAPL dissolution, and sorption processes, as well as field-scale heterogeneity, should be taken into account in assessing mass discharge uncertainties.

In addition to the quantification of mass discharge uncertainty, the development of an iterative sampling strategy will be critical to the improvement mass discharge predictions. In order to reduce

uncertainty, additional measurements can be collected and employed, along with statistical models of geologic heterogeneity, to interpolate between unsampled positions. Thus, an optimal sampling design is sought that employs a sampling strategy which applies statistical methods to maximize the expected gain of information, and to reduce the uncertainty associated with a prediction goal (e.g., (Cirpka et al. 2004; Leube et al. 2012; Lu et al. 2018).

Optimal design, performed through data worth analysis, is widely applied in groundwater related problems. Previous studies have focused on reducing prediction uncertainties related to contaminant concentration (e.g., (Herrera and Pinder 2005) and arrival time (e.g., (Nowak et al. 2010), identifying system parameters and the corresponding uncertainties (e.g., (Neuman et al. 2012), and minimizing costs associate with site remediation (e.g., (Liu et al. 2012). In these studies, different utility functions have been developed to explicitly quantify data worth, which include: coefficient of variation (CV) (e.g., Zhang et al., 2005), relative entropy (e.g., (de Barros and Rubin 2008), the trace of the predicted quantity covariance matrix (e.g., (Lu et al. 2012), indicator variable (Nowak et al. 2012), prediction uncertainty reduction (e.g., (de Barros et al. 2012), and monetary terms (e.g., (Feyen and Gorelick 2004).

Assessing the data worth can be accomplished using different statistical methods (Loaiciga et al. 1992). Among the alternative approaches, are those based upon Monte Carlo (MC) sampling, which involved performing a large number of deterministic calculations for random, equally likely realizations and a statistical analysis of results. The MC method, coupled with other statistical techniques, has been widely employed in groundwater modeling and optimal design. Statistical techniques that have been coupled with this approach include the Ensemble Kalman Filter (e.g. (Dai et al. 2016; Herrera and Pinder 2005; Nowak et al. 2010), Bayesian statistical design with bootstrap filter sampling (Liu et al. 2012) or Preposterior Data Impact Assessor (Leube et al. 2012; Nowak et al. 2012), and Bayesian Model Averaging (e.g., (Neuman et al. 2012; Pham and Tsai 2016; Xue et al. 2014). The biggest drawback of the MC based approach is that it is computationally cumbersome, as the MC sample size should be large enough to preserve statistical features.

The first-order second-moment method (FOSM), which uses linear approximations to directly propagate parameter and data uncertainties into system states via sensitivity matrices, is a straightforward and computationally efficient way to estimate mean and variances of dependent quantities. The FOSM approach has been applied to estimate of the influence of permeability uncertainty or recharge rates (Kunstmann et al. 2002); to quantify the uncertainty of capturing plumes by funnel-and-gate systems (Cirpka et al. 2004); and to design optimal groundwater monitoring networks that reduce flux and travel time prediction uncertainties (Fienen et al. 2010) and hyporheic exchange (Wöhling et al. 2016). Vilhelmsen and Ferré (2017) extended FOSM data worth analysis to include simultaneous selection of multiple new measurements and consideration of multiple forecasts.

Previous uncertainty quantification of mass discharge has been investigated either by neglecting the presence of DNAPL or sorbed phase or by assuming simplified DNAPL source zone architecture. Although preliminary assessment of the mass discharge uncertainty can be obtained neglecting mass sources, the result might be biased based on those idealized scenarios. In addition, although groundwater optimal design has been widely explored using different techniques, none of these previous studies have conducted data worth analysis to select additional observations to support a reduction in mass discharge uncertainty, considering heterogeneity in permeability and source mass distributions.

In this research the FOSM is adopted to evaluate the uncertainty of flux averaged concentration predictions. Both aquifer parameters and source zone mass are considered as random variables, to account for aquifer heterogeneity, flow irregularity, source zone morphology, and their interlinkages. In the decision process, data worth analysis is conducted to develop an optimal borehole sampling strategy by selecting the additional measurements that give the largest FAC uncertainty reduction.

II.8.2. Mathematical Formulation

II.8.2.1. FOSM Uncertainty Approximation

Since uncertainty in the hydraulic conductivity field directly influences groundwater flow, DNAPL migration, and solute transport, it is desirable to model the hydraulic conductivity field as a random space function, with uncertainty propagating to other quantities via groundwater flow and contaminant transport simulations. In addition, as source zone architecture and the corresponding DNAPL dissolution and solute transport are mainly controlled by aquifer material heterogeneity, the contaminant mass in different phases (aqueous, DNAPL, and sorbed) are also treated as random variables with their associated uncertainties honoring insufficient site characterization. Porosity is considered as spatially constant and known values for simplicity in this study.

The FOSM propagates uncertainties in system parameters to the model output by applying a linear approximation, which is performed to yield mean values, variances and covariances of all dependent variables. Here hydraulic conductivity, initial aqueous phase concentration, and initial DNAPL saturation were treated as independent random variables. The initial sorbed concentration was related to initial aqueous concentration and texture via an equilibrium relationship. The log conductivity and initial contaminant mass in different phases can be considered as second-order variables with the distribution of $\mathbf{p} \sim N(\overline{\mathbf{p}}, \ \mathbf{C_{pp}})$:

$$\mathbf{p} = \begin{bmatrix} \mathbf{lnK} & C_a{}^0 & S^0 & s_n{}^0 \end{bmatrix}^T \tag{M.8.2a}$$

$$\overline{\mathbf{p}} = E[\mathbf{p}] \tag{M.8.2b}$$

$$\mathbf{C_{pp}}(\mathbf{x_1}, \mathbf{x_2}) = E[(\mathbf{p}(\mathbf{x_1}) - \overline{\mathbf{p}}(\mathbf{x_1}))(\mathbf{p}(\mathbf{x_2}) - \overline{\mathbf{p}}(\mathbf{x_2}))] \tag{M.8.2c}$$

in which lnK is the log conductivity $[LT^{-1}]$, $C_a{}^0$ is the initial aqueous concentration in the domain $[ML^{-3}]$, S^0 is the initial sorbed mass $[MM^{-1}]$, $s_n{}^0$ is the initial NAPL saturation $[-]$, $\overline{\mathbf{p}}$ is the geometric mean of the parameter, E[ ] denote the expected value operator, $\mathbf{C_{pp}}$ is the covariance and cross-covariance function of the parameter fluctuations at location $\mathbf{x_1}$ and $\mathbf{x_2}$, where diagonal elements represent parameter variances, and off-diagonal elements denote interactions between parameter uncertainties. For simplicity, measurement error in these four variables was not considered.

Uncertainty in the dispersion tensor is included implicitly in the analysis in so far as it can be tracked back to uncertainty in the velocity field, which arises from uncertainty in hydraulic conductivity and piezometric head. The uncertainty in the velocity field also propagates uncertainty into the DNAPL dissolution mass transfer coefficient. The down-gradient FAC can also be characterized by its expected value and covariance function since it depends on the random space variable $\mathbf{p}$. The first moment of the FAC prediction is approximated to first-order accuracy by the mean C_f obtained as the solution of coupled flow and transport equations using the ensemble mean values of the four system parameters:

$$E[C_f(\mathbf{p})] = \overline{C}_f = C_f(\overline{\mathbf{p}}) \tag{M.8.3}$$

The propagation of parameter uncertainties into the down-gradient FAC prediction, given by the covariance matrix, are approximated to first-order accuracy by linear error propagation (Dettinger and Wilson 1981):

$$\mathbf{C_{C_f C_f}} = \sigma^2_{C_f} = E[(C_f - \overline{C}_f)](C_f - \overline{C}_f) = \mathbf{H_{C_f} C_{pp} H_{C_f}}^T \tag{M.8.4}$$

where $\mathbf{C_{C_f C_f}}$ is the covariance matrix of down-gradient FAC, $\mathbf{H_{C_f}}$ is the Jacobian matrix containing the sensitivity of down-gradient FAC to an incremental change in each model parameter:

$$\mathbf{H_{C_f}} = \frac{dC_f}{d\overline{\mathbf{p}}^T} \tag{M.8.5}$$

The Jacobian matrix is derived from the adjoint-state sensitivities, which is discussed in section II.8.2.3.

II.8.2.2. Data Worth

Data worth analysis seeks optimal combinations of new, yet to be collected, observations that support a forecast of interest. The worth of existing and new data is evaluated by quantifying their ability to constrain the uncertainty of model predictions (Dausman et al. 2010; Fienen et al. 2010; Leaf 2017; Wöhling et al. 2016). Quantitative criteria are usually developed to rank either individual data point or groups of data points, in an effort to allocate sampling resources efficiently for optimal monitoring network design (Kikuchi 2017). According to FOSM uncertainty propagation, the variance of down-gradient FAC predictions is a product of sensitivities of model outputs to parameters and the parameter covariance matrix. The relative contribution of parameters to model prediction uncertainty, assuming model parameters are fully accessible and measurable, can be evaluated by recomputing variances, replacing new measurement-associated terms in the covariance matrix with zeros, implying perfect knowledge of additional measurements. An estimate of the reduction of down-gradient FAC predictive uncertainty, or data worth, can, thus, be calculated as:

$$\Delta\sigma^2_{C_f} = \sigma^2_{C_{f,base}} - \sigma^2_{C_{f,new}} = \mathbf{H_{C_f} C_{pp} H_{C_f}}^T - \mathbf{H_{C_f} C_{pp,new} H_{C_f}}^T \tag{M.8.6}$$

where $\mathbf{C_{pp,new}}$ is the updated covariance matrix with enhanced parameter knowledge. The reduction in prediction uncertainty can be computed using (M.8.6) for all potential measurement locations and particular measurements to support the identification of the locations with highest expected data worth, where (normalized) data worth expressed as:

$$\text{Normalized Data Worth} = \frac{\sigma^2_{C_{f,new}}}{\sigma^2_{C_{f,base}}} \tag{M.8.7}$$

Here $\sigma^2_{C_{f,new}}$ is the prediction uncertainty with additional sets of observations, and $\sigma^2_{C_{f,base}}$ is the base uncertainty corresponding to existing data only. This normalized quantity ranges between 0 and 1, with the lowest value associated with the largest uncertainty reduction.

The data worth analysis described above is closely related to parameter identifiability, targeted to identify model parameters with high uncertainty, as well as high sensitivity to model predictions. Once these locations/parameters are identified and measurements obtained, new realizations can be generated, and a forward multiphase flow and transport simulation applied to obtain an improved prediction of future states.

II.8.2.3. Evaluation of Sensitivities

For computational efficiency, the adjoint state method (Sun and Yeh 1990; Sykes et al. 1985; Townley and Wilson 1985) was adopted herein to evaluate the sensitivity matrix $\mathbf{H}_{C_f}$. The derivation of the adjoint states equations for the FAC prediction are provided in Supplementary materials. For the selected four random variables (log hydraulic conductivity and contaminant mass in aqueous, sorbed, and DNAPL phase), four adjoint partial differential equations corresponding to four adjoint states were derived with structures similar to the original control equations(Equations M.5.2-M.5.4, M.5.18). Due to the crossover effects between state variables and parameters, the derivation of adjoint states preserves the feature of flow and mass transport coupling. In the adjoint states development, it was assumed that the change of log hydraulic conductivity may affect the velocity field, the dispersion tensor, and the DNAPL dissolution rate. In addition, the DNAPL dissolution rate is also a function of initial DNAPL saturation distribution. Note that, although the impact of DNAPL dissolution on water relative permeability, is considered in the forward flow and transport simulations, this effect is neglected in the calculation of adjoint states to simplify the adjoint state equations. In other words, the water relatively permeability is set as 1, and the flow is assumed to be steady-state in the process of deriving adjoint states equations and marginal sensitivity expressions. Thus, the sensitivity of the water relative permeability with respect to the small change of initial DNAPL saturations is disregarded in this study for simplification.

With the purpose of investigating the sensitivity of down-gradient FAC with respect to the small change of the above mentioned four variables, the performance measure P, which quantifies some state of the system, is defined as the FAC at the down-gradient transect at the time of interest. ς is a functional of the state of the system and is defined accordingly.

$$P = \iint \varsigma\left(\ln K, C_a{}^0, S^0, s_n{}^0, C_f\right) dVdt \tag{M.8.8a}$$

$$\varsigma\left(\ln K, C_a{}^0, S^0, s_n{}^0, C_f\right) = C_f(\mathbf{x}, \tau)\delta(x - x_{mea})\delta(y - y_{mea})\delta(z - z_{mea})\delta(\tau) \tag{M.8.8b}$$

where $\delta(\cdot)$ denotes the Dirac delta function, $\mathbf{x}$ is defined as the location of down-gradient transect, τ is the specific time of interest. After applying the adjoint state theory, the resultant equations for the adjoint states are given as:

$$\nabla \cdot (\mathbf{K}\nabla\Psi_h^*) = \nabla \cdot (\mathbf{K}C_a\nabla\Psi_a^*) - \nabla \cdot (\mathbf{K}E\nabla\Psi_a^*) + \nabla \cdot \left(\mathbf{K}\frac{\partial\hat{k}}{\partial\underline{q}^a}\left(C_a^{eq} - C_a\right)\Psi_a^*\right) - \nabla$$
$$\cdot \left(\mathbf{K}\frac{\partial\hat{k}}{\partial\underline{q}^a}\left(C_a^{eq} - C_a\right)\Psi_n^*\right) - \frac{\partial\varsigma}{\partial h} \tag{M.8.9}$$

$$ns_a\frac{\partial\Psi_a^*}{\partial\tau} = \nabla \cdot \left(\underline{q}^a\Psi_a^*\right) + \nabla \cdot \left(\widetilde{\mathbf{D}}_h^a \cdot \nabla\Psi_a^*\right) + \hat{k}(\Psi_n^* - \Psi_a^*) + K_d\Psi_s^* - \frac{\partial\varsigma}{\partial C_a} \tag{M.8.10}$$

$$n\rho_n\frac{\partial\Psi_n^*}{\partial\tau} = nC_a\frac{\partial\Psi_a^*}{\partial\tau} - \frac{\partial\varsigma}{\partial s_a} \tag{M.8.11}$$

$$\Psi_s^* = -\rho_b\frac{\partial\Psi_a^*}{\partial\tau} - \frac{\partial\varsigma}{\partial S} \tag{M.8.12}$$

with initial and boundary conditions:

$$\left(\mathbf{K}\nabla\Psi_h^* - \mathbf{K}C_a\nabla\Psi_a^* + \mathbf{K}\mathbf{E}\nabla\Psi_a^* - \frac{\partial\hat{k}}{\partial\underline{\mathbf{q}}^a}\mathbf{K}(C_a^{eq} - C_a)\Psi_a^* + \frac{\partial\hat{k}}{\partial\underline{\mathbf{q}}^a}\mathbf{K}(C_a^{eq} - C_a)\Psi_n^* \right) \quad \text{(M.8.13a)}$$

$$\cdot\vec{n} = 0$$

$$\Psi_a^*(\tau = 0) = \Psi_n^*(\tau = 0) = \Psi_S^*(\tau = 0) = 0 \quad \text{(M.8.13b)}$$

$$-(\widetilde{\mathbf{D}}_h^a \cdot \nabla\Psi_a^*) \cdot \vec{n} = 0 \quad \text{(M.8.13c)}$$

Here Ψ_a^*, Ψ_n^*, and Ψ_s^* are adjoint states corresponding to aqueous phase concentration, DNAPL saturation, and sorbed concentration, respectively, Ψ_h^* is the adjoint states corresponding to the hydraulic head. $\tau = t_f - t$ is the backward time, t_f is the final time of simulation. $\mathbf{E}$ is a tensor with components: $E_{ij} = \partial\widetilde{D}_{il}/\partial q_j\,\partial C_a/\partial x_l$, (the summation for $l = x, y, z$ is implied). Thus, the marginal sensitivities corresponding to log hydraulic conductivity field and three initial contaminant mass in different phases can be computed as:

$$\frac{dP}{d\ln K} = \iint_{V,t} \left[\frac{\partial\varsigma}{\partial\ln K} - (\mathbf{K}\nabla h)\cdot\nabla\Psi_h^* + (\mathbf{K}C_a\nabla h)\cdot\nabla\Psi_a^* - (\mathbf{K}\mathbf{F}\nabla C_a)\cdot\nabla\Psi_a^* \right. $$
$$\left. + (\mathbf{K}\nabla h)\frac{\partial\hat{k}}{\partial\underline{q}^a}(C_a^{eq} - C_a)(\Psi_a^* - \Psi_n^*) \right] dVdt \quad \text{(M.8.14a)}$$

$$F_{ij} = \partial\widetilde{D}_{ij}/\partial q_l\,\partial h/\partial x_l \quad \text{(M.8.14b)}$$

$$\frac{dP}{dC_a^0} = \int_V [-ns_a(t = 0)\Psi_a^*(t = 0)]\,dV \quad \text{(M.8.15)}$$

$$\frac{dP}{dS^0} = \int_V [-\rho_b\Psi_a^*(t = 0)]\,dV \quad \text{(M.8.16)}$$

$$\frac{dP}{ds_n^0} = \iint_{V,t} \left[-\frac{\partial\hat{k}}{\partial s_n^0}(C_a^{eq} - C_a)(\Psi_a^* - \Psi_n^*) \right] dVdt$$
$$+ \int_V [nC_a\Psi_a^*(t = 0) - n\rho_n\Psi_n^*(t = 0)]\,dV \quad \text{(M.8.17)}$$

II.8.2.4. Model Framework

The overall procedure for down-gradient FAC prediction, uncertainty quantification, and optimal sampling strategy design is shown in Figure M.8.1. Equiprobable hydraulic conductivity field realizations were first constructed conditioned on existing borehole data. Instead of applying numerical simulations of spilled DNAPL migration to obtain source zone architecture formations, the discriminative random field (DRF) based probabilistic model presented in II.7.3 was employed to generate stochastic realizations of a subsurface source zone, consistent with known, limited site characterization data. The conditional ensemble means of the random fields of log hydraulic conductivity and sequestered contamination were then applied as initial conditions for a coupled groundwater flow (eq. M.5.18-M.5.19) and contaminant transport (eq. M.5.2-M.5.5) simulation coupling DNAPL dissolution, sorption, and dissolved phase transport.

The first-order approximation of FAC at different times (eq. M.8.3) was obtained using a modified version of the MODFLOW (Harbaugh 2005) and MT3DMS (e.g., (Parker and Park 2004; Yang et al. 2018; Zheng and Wang 1999) codes, as described in section II.5. The adjoint states were solved via another modified MT3DMS code (eq. M.8.9-M.8.13). The marginal sensitivities were then computed coupling velocity field, concentration moments, adjoint sates, as well as their

interlinkage via a MATLAB script (eq. M.8.14-M.8.17). The propagation of parameter uncertainties into FAC was then implemented through the FOSM method, with the variance of FAC calculated by coupling the sensitivities and covariance and cross-covariance of four random variables (eq. M.8.4). In the decision process, the new sampling strategy design, taking the form of data worth analysis, was then developed by considering additional measurements at locations with highest variance reduction (eq. M.8.6-M.8.7).
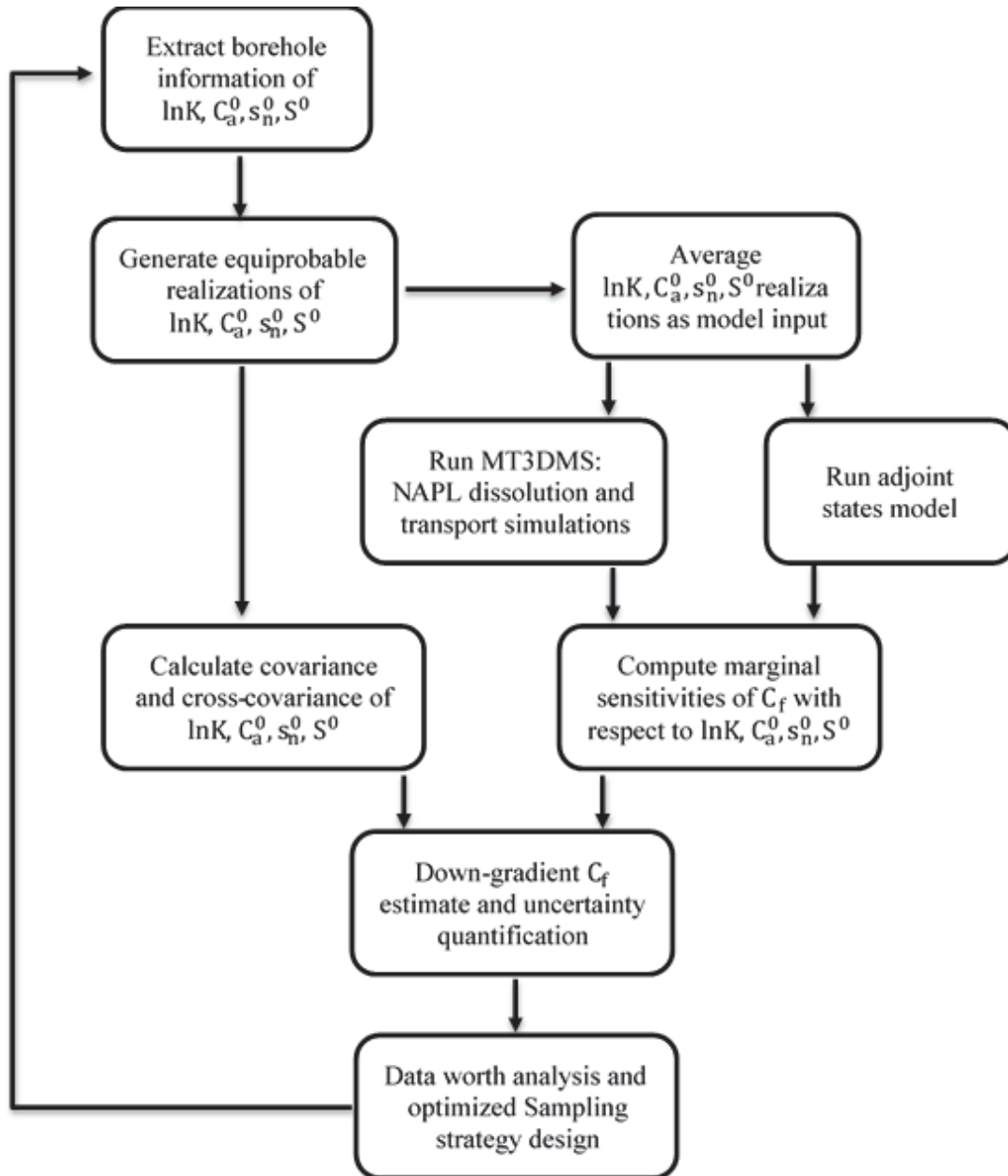
Figure M.8.1. Overall procedure of the optimal sampling network design for prediction of down-gradient FAC and uncertainty quantification.

III. Results and Discussion

III.1. Site Characterization Results

This section describes the results of the preliminary site investigation and materials characterization completed prior to implementation of the DHT. Site groundwater monitoring encompassed water table elevations, water quality parameters, and measurements of, chlorinated ethene, VFA, dissolved organic carbon, dissolved metal, and anion concentrations, and , as well as aqueous *Dhc, Geo*SZ, and RDase gene abundance quantification. Soil characterization included grain size and permeability analyses, total organic carbon measurements, sorption equilibria and rate experiments, soil pH measurements, sorbed chlorinated ethene measurements, and total *Dhc* abundance quantification.

III.1.1. Groundwater Elevation

Site wide groundwater elevations varied from 98.4 to 102.6 m (322.7 to 336.6 feet) above sea level (North American Vertical Datum of 1988) as measured in site monitoring wells in August 2014 (Appendix B.1). Groundwater generally flows north to south with a slight west to east gradient in the pilot test area. The unnamed brook does not appear to influence groundwater flow, with a groundwater elevation of 101.0 m (331.3 ft) on the west side of the brook (MW-06) and 101.1 m (331.6 ft) in a nearby well west of the brook shown on Figure M.3.5 (ASI-05D2).

In the DHT area, groundwater elevations measured in the CMT-wells ranged from 100.9 to 101.1 m (331.2 to 331.8 feet) in September 2014 with no discernable vertical or horizontal gradients. The measured elevations were consistent with the 101.0 m (331.3) foot elevation measured in August 2014 in MW-06, the monitoring well closest to the pilot test area (Figure M.3.3). Similar gradients were observed in October 2015 with slightly higher groundwater elevations ranging from 101.2 to 101.3 m (331.9 to 332.4 feet). In the September 2016 measurements, groundwater elevation in the previously measured CMT-wells ranged from 100.9 to 101.0 m (331.1 to 331.4 feet) with a slight north-south gradient of 0.0012 m/m (0.004 feet/foot). In the newly installed wells, CMT-6, DHT-1, DHT-2 and DHT-4, groundwater elevations were 101.0, 101.0, 100.8, and 101.0 m (331.5, 331.4, 330.8, and 331.4 feet), respectively. A complete table of groundwater elevation measurements at site monitoring wells can be found in Appendix B.1.

III.1.2. Site Groundwater Contaminants

Water sample collected from the site monitoring wells in August 2014 exihibit a large spatial variability in chlorinated ethene concentrations, with high concentrations between Commerce Street and the unnamed stream and low (≤3.03 µM TCE) or undetectable concentrations west of Commerce Street (MW-09D and MW-09M) and east of the stream (ASI-05D2 and ASI-04D2); well locations are shown on Figure M.3.5. Within the plume, TCE concentrations ranged from 119 to 227 µM with lower concentrations of *cis*-DCE (0.50 to 14.4 µM) and ethene (0.32 to 3.82 µM). VC was not detected in any of the monitoring well samples. In monitoring well pair MW-06M and MW-06D, the closest wells to the pilot test area, the concentrations of TCE increased with depth while the concentration of *cis*-DCE decreased. The deeper well, MW-06D had concentrations of TCE and *cis*-DCE of 227 and 5.02 µM, respectively while MW-06M had concentrations of 119 and 14.4 µM. A complete table of groundwater chlorinated ethene and ethene measurements is presented in Appendix B.2.

In the CMT-wells arranged around the pilot test area (Figure M.3.4), the concentrations of TCE were generally lower than the site monitoring wells (up to 117 µM) while the *cis*-DCE concentrations were higher (up to 275 µM), indicating dechlorinating activity by the native

microbial population in this area. The CMT wells facilitated the observation of vertical variations in chlorinated ethene concentrations. For example, in the September 2014 samples, the TCE, *cis*-DCE, VC, and ethene concentrations ranged from non-detect to 0.087 µM, 0.017 to 78.6 µM, non-detect to 0.033 µM, and 1.03 to 2.26 µM, respectively, in the shallowest depth (4.60 to 4.75 m bgs). In the deepest depth (10.94 to 11.09 m bgs), TCE, *cis*-DCE, VC, and ethene concentrations ranged from 0.12 to 1.53 µM, 6.70 to 147 µM, non-detect to 0.27 µM and 0.34 to 2.67 µM, respectively. The highest TCE concentration of 117 µM was in the 9.48 to 9.63 m depth, while the highest *cis*-DCE concentration of 200 µM was measured in deeper groundwater (10.24 to 10.58 m). Subsequent groundwater sampling wells focused on the lower CMT depths where TCE and *cis*-DCE were present at the highest concentrations. In the samples collected in October 2015, TCE was only detected above 0.47 µM in well CMT-1 with concentrations shown in Table R.1.1 while *cis*-DCE was detected in CMT-1 and in the other nearby CMT wells at concentrations up to 139 µM. The high concentrations in CMT-1 and its location in the parking lot led to its selection as the site for the pilot test.

Table R.1.1. Chlorinated ethene and ethene concentrations (µM) measured in CMT-1 samples collected on October 23, 2015.

Depth (m bgs)	TCE concentration	*cis*-DCE concentration	VC concentration	Ethene concentration
6.07 to 6.23	0.505	47.2	0.0162	4.54
7.80 to 7.96	114	40.1	ND	ND
9.48 to 9.63	1.21	134	0.0143	0.228
10.24 to 10.58	0.0393	105	ND	0.0875
10.94 to 11.09	0.489	76.1	0.0124	0.0583

Similar results were observed in the September 2016 samples collected from CMT-1 and the newly installed CMT-6, indicating that the wells were well situated for implementation of the pilot test (Figure M.3.4). In CMT-6, upgradient of the pilot test, the highest TCE and *cis*-DCE concentrations were 81.2, 201, and 195 µM and 140, 134, and 67.9 µM in the 7.92 to 8.01, 8.84 to 8.99, and 9.60 to 9.75 m bgs depths, respectively. All chlorinated ethene and ethene results can be found in Appendix B.2.

III.1.3. Water Quality Parameters

In the monitoring wells sampled in August 2014, the water quality parameters exhibited little variability in pH, ORP, specific conductivity, temperature, dissolved oxygen, and turbidity, ranging from 6.7 to 7.4, -109.1 to 65.2 mv, 735 to 1890 µs/cm, 10.23 to 14.41°C, 0.091 to 0.55 mg/L, and 0.57 to 40.2 NTUs, respectively. Of these parameters, pH and ORP (an indicator of oxygen content) are most critical to successful bioremediation. For biodegradation to occur efficiently, pH should be between 6 and 8 and ORP should be less than -100 mv (Stroo et al. 2013). These conditions are met in MW-05D, a location with a high TCE concentration upgradient of the pilot test area, where pH is 6.87 and ORP is -109.1 mv. In several other locations with high TCE concentrations, the elevated ORP readings (45.8mv in MW-04D, -7.2 mv in MW-06D, and -14.7 in MW-06M) indicate that dechlorination of TCE is unlikely in these areas. All water quality parameter measurements can be found in Appendix B.3.

The CMT-well concentration measurements conducted in September 2014 and October 2015 demonstrate ideal conditions for bioremediation with pH between 6.98 and 8.70 and ORP between -87.2 and -223.4 mv. There were no trends in water quality parameters with depth in the CMT-wells. During the February 2017 sampling event, the ORP measurements were higher than in other sampling rounds, ranging from -150.6 to 29.6 mv. These elevated readings are likely due to the introduction of oxygen due to the large volume of water (4.0 L) collected from these wells for use in microcosm experiments. During the September 2016 sampling event, the groundwater pH measured in CMT-1 ranged from 2.87 to 3.02. Low pH was not observed previously or during the pilot test. It is likely that the pH probe used was not calibrated correctly and these readings are not representative of groundwater conditions at the site.

III.1.4. Groundwater Volatile Fatty Acids and Dissolved Organic Carbon

VFAs were not detected in the site monitoring well or CMT-well samples analyzed. The detection limits for each volatile fatty acid, using the HPLC method described in Section II.2.2, were 0.35 mg/L for fumaric acid and 5 mg/L for all other VFAs. While VFAs are a typical electron donor during active bioremediation, other sources of organic carbon can sustain microbial populations and enable the dechlorination of chlorinated ethenes. Sitewide dissolved organic carbon concentrations ranged from 0.54 to 2.92 mgC/L in the samples collected in August 2014. In the pilot test area CMT-wells sampled in October 2015, dissolved organic carbon concentrations were higher, ranging from 0.89 to 4.9 mgC/L, likely facilitating the dechlorination of TCE to *cis*-DCE observed in the area (Rectanus et al. 2007). Dissolved organic carbon measurements are provided in Table R.1.2.

Table R.1.2. Groundwater dissolved organic carbon (DOC) results (mgC/L) for site monitoring wells (Aug 2014) and CMT-wells (Sep 2014).

Well	Date Sampled	DOC	Well	Date Sampled	DOC
ASI-02D2	8/14/2014	0.79	CMT-2 D3	10/23/2015	1.4
ASI-04D2	8/14/2014	0.82	CMT-2 D4	10/23/2015	0.89
ASI-05D2	8/13/2014	1.11	CMT-2 D5	10/23/2015	3.47
MW-04D	8/14/2014	0.54	CMT-2 D6	10/23/2015	3.19
MW-05D	8/13/2014	1.75	CMT-2 D7	10/23/2015	4.9
MW-06D	8/13/2014	0.8	CMT-3 D4	10/23/2015	1.76
MW-06M	8/14/2014	2.4	CMT-3 D5	10/23/2015	2.88
MW-09D	8/14/2014	2.92	CMT-3 D7	10/23/2015	3.91
MW-09M	8/14/2014	1.57	CMT-4-D5	10/23/2015	2.31
CMT-1 D2	10/23/2015	2.42	CMT-4 D7	10/23/2015	1.27
CMT-1 D3	10/23/2015	1.76	CMT-5 D3	10/23/2015	3.08
CMT-1 D5	10/23/2015	1.64	CMT-5 D5	10/23/2015	2.93
CMT-1 D6	10/23/2015	2.97	CMT-5 D6	10/23/2015	2.66
CMT-1 D7	10/23/2015	2.25	CMT-5 D7	10/23/2015	1.59
CMT-2 D2	10/23/2015	1.98			

III.1.5. Groundwater Dissolved Metals

Concentrations of 21 dissolved metals were measured in groundwater samples collected at the site monitoring wells in August 2014 and in the CMT-well samples collected in September 2014 as shown in Appendix B.4. The metals concentrations observed were consistent with previous rounds of sampling at the site (Nobis Engineering Inc. 2012) and did not indicate any impediments to utilizing bioremediation in the pilot test as shown in Table R.1.3.

Table R.1.3. Average concentrations (range in parentheses) of select dissolved metals measured in site monitoring wells and CMT-wells. All values in µg/L.

Sample Group	Aluminum	Barium	Calcium	Chromium	Copper	Iron
Site Monitoring Wells (2014)	0.12 (ND-0.23)	0.14 (0.09-0.22)	91.5 (62.0-117)	0.003 (ND-0.008)	0.003 (ND-0.01)	1.44 (ND-3.68)
Site Monitoring Wells (NOBIS 2012)	1.54 (ND-7.22)	0.12 (ND-0.20)	102 (59.9-148)	0.019 (ND-0.049)	0.02 (ND-0.05)	15.3 (1.99-36.7)
CMT Wells (2014)	0.033 (ND-0.17)	0.14 (0.05-0.25)	78.5 (29.7-138)	ND	ND	3.07 (0.01-12.6)

Sample Group	Potassium	Magnesium	Manganese	Sodium	Lead	Zinc
Site Monitoring Wells (2014)	3.72 (1.78-6.35)	18.4 (12.6-25.2)	1.05 (0.49-2.09)	343 (45-1316)	0.006 (0.003-0.011)	0.005 (ND-0.03)
Site Monitoring Wells (NOBIS 2012)	2.36 (1.28-4.02)	18.5 (10.4-27.7)	1.66 (0.64-3.27)	84.0 (19.1-310)	0.007 (ND-0.024)	0.049 (ND-0.10)
CMT Wells (2014)	6.16 (1.31-14.4)	13.5 (5.22-25.7)	1.25 (0.11-3.39)	366 (53-1005)	ND	0.001 (ND-0.01)

Notes: 1. Additional metals analyzed but not detected: Arsenic, Cadmium, Cobalt, Molybdenum, Nickel, Selenium, Vanadium. 2. Beryllium not detected by Nobis 2012. 2014 average 0.005, range 0.003-0.009 µg/L.

III.1.6. Groundwater Anions

The samples collected from site-wide monitoring wells in August 2014 were analyzed for anions relevant to bioremediation: chloride, sulfate, nitrite, and nitrate. Similar to previous sampling by (Nobis Engineering Inc. 2012), nitrite and nitrate were not detected across the site while chloride and sulfate were present at the low concentrations shown in Table R.1.4, averaging 6.85 and 7.51 µg/L, respectively. Near the CMT-wells, in MW-06D and MW-06M, the chloride and sulfate concentrations were close to the average values and did not indicate conditions that would impede bioremediation.

Table R.1.4. Groundwater anions, all values in µg/L.

Sample Location	Date Collected	Chloride	Sulfate	Nitrite	Nitrate
ASI-02D2	8/14/2014	18.77424	9.570975	ND	ND
ASI-04D2	8/14/2014	2.756649	7.144461	ND	ND
ASI-05D2	8/13/2014	3.087576	4.902045	ND	ND
MW-04D	8/14/2014	4.693678	7.324914	ND	ND
MW-05D	8/13/2014	5.214537	7.577964	ND	ND
MW-06D	8/13/2014	4.01288	8.860034	ND	ND
MW-06M	8/14/2014	8.553747	9.960891	ND	ND
MW-09D	8/14/2014	3.482385	1.929688	ND	ND
MW-09M	8/14/2014	11.12855	10.34556	ND	ND

Notes: ND=not detected

III.1.7. Groundwater Microbial Abundance

In the biological samples collected from the CMT-wells in September 2014, *Dhc* abundance was generally uniform with a slight increase in cell abundance with depth. The average *Dhc* abundances across the CMT-wells sampled were 1.40×10^6 ($\pm 8.68 \times 10^5$) 16S rRNA gene copies/ L in the deepest two depths (10.2 to 10.6m bgs and 10.9 to 11.1 m bgs), 8.87×10^5 ($\pm 7.46 \times 10^5$) 16S rRNA gene copies/ L in the middle three depths (7.80 to 7.96 m bgs, 8.66 to 8.81 m bgs, and 9.48 to 9.63 m bgs), and 8.89×10^5 ($\pm 1.63 \times 10^5$) 16S rRNA gene copies/ L in the shallowest two depths (4.60 to 4.75 m bgs and 6.07 to 6.22 m bgs). All *Dhc* gene copy counts measured are included as Appendix B.5. *Dhc* abundances exceeding 1×10^6 16S rRNA gene copies/ L are associated with successful transformation of TCE to ethene (Lu et al. 2006; Ritalahti et al. 2010b; a; Stroo et al. 2013).

In the groundwater samples collected in October 2015, samples from two depths (9.48-9.63 m bgs and 10.9-11.1 m bgs) were analyzed to confirm the *Dhc* abundance in the pilot test area. The 16S rRNA gene abundance averaged 1.46×10^6 ($\pm 2.52 \times 10^5$) gene copies/ L in the shallower depth and 2.22×10^6 ($\pm 9.72 \times 10^5$) gene copies/ L in the deeper depth. While these gene abundances suggest a *Dhc* population capable of dechlorination, the RDase genes implicated in ethene formation, *bvcA* and *tceA*, were not detected ($<8.6 \times 10^2$ gene copies/L) in any of the samples analyzed. The lack of *Dhc* cells harboring these RDase genes explains the accumulation of *cis*-DCE observed at the site and the lack of VC and ethene measured in the CMT-wells.

III.1.8. Site Soil Visual Characterization and Grain Size Analysis

Soil boring logs with visual descriptions of the soil cores are included as Appendix B.6. The aquifer generally consists fine grain sand with increasingly fine sands and silts in deeper depths, culminating in a layer of dense, silty clay beginning at 10.7 to 12.2 m (35 to 40 feet) bgs. The water table was generally encountered at approximately 3m (10 feet) bgs. Results of the grain size analysis are included as Appendix B.7 and show the silt and clay content increase with depth. In the pilot test transect well DHT-2 (Figure M.3.6), the shallow depths (> 4.6 m [15 feet] bgs) consisted primarily of fine sand (31.7 to 58.4%) with some medium (10.8% to 33.9%) and very fine sand (3.7% to 44%) but very little clay (0% to 5.6%). Above the water table, the soil contained coarse sand (2.2 to 11.6%) with gravel (16 to 25.3%) identified at 2 depths. Within the aquifer but

above 10.7 m (35 feet) bgs, soil primarily consisted of fine sand (23.4 to 64.8%) and silt/very fine sand (13.6 to 75.4%). Although there was a location containing a higher percentage of clay (26.5%) at 4.6 to 5.3 m (15 to 17.5 feet) bgs, the remainder of the borehole had a lower clay content (1.1 to 6.7%). Between 10.7 and 10.9 m (35 and 35.8 feet) bgs, there is a layer of soil containing primarily silt and very fine sand (81.9 to 88.4%) directly above the confining layer of silt (66.2%) and clay (33.8%) located at 10.9 m (35.8 feet) bgs.

III.1.9. Soil Permeability

Samples from the preliminary borings were analyzed at three depths: shallow water table (4.3 to 4.9 m [14 to 16 feet] bgs), intermediate water table (7.3 to 7.9 m [24 to 26 feet] bgs), and the deep water table (10.4 to 11.0 m [34 to 36 feet] bgs). These data, provided in Table R.1.5, are consistent with the grail size analyses; the shallower depths with a greater proportion of medium grain sands have higher permeability (4.01×10^{-12} m^2 and 3.88×10^{-12} m^2) than the lower depths of finer grain sediments (permeabilities of 9.5×10^{-13} m^2 and 2.32×10^{-12} m^2). Similar results were obtained by analysis of samples collected from the CMT-well and DHT-2 soil borings. In DHT-2, at the screened depth used in the pilot test (10.1 to 10.7 m [33 to 35 feet] bgs), the permeability was 1.01×10^{-13} m^2.

Table R.1.5. Permeability of soil samples collected from soil borings and monitoring wells.

Location	Sample Depth (ft. bgs)	Permeability (m^2)
SB-1	14 to 16	4.01×10^{-12}
SB-1	24 to 26	4.62×10^{-13}
SB-1	34 to 36	9.50×10^{-13}
SB-2	14 to 16	3.88×10^{-12}
SB-2	24 to 26	1.83×10^{-12}
SB-2	34 to 36	2.32×10^{-12}
CMT-1	10.5 to 12	4.70×10^{-12}
CMT-1	17 to 18	2.00×10^{-12}
CMT-4	32 to 34	1.00×10^{-13}
CMT-5	10 to 11	8.10×10^{-12}
CMT-5	18 to 19	2.60×10^{-12}
DHT-2	25 to 27.5	1.02×10^{-12}
DHT-2	27.5 to 30	9.97×10^{-13}
DHT-2	35 to 35.5	1.04×10^{-13}

III.1.10. Soil Organic Carbon

Soil samples from the preliminary soil boring and from CMT-1 were analyzed for total organic carbon with results provided in Table R.1.6. Organic carbon was highest above the water table (> 2.4 m [8 feet] bgs), ranging from 0.46% to 1.54% in CMT-1. Near the water table, organic was detected at low concentrations (0.10% to 0.20%) but was not detected in CMT-1 below 4.0 m (13 feet) bgs. Similarly, in the soil borings, organic carbon was not detected in the sandy aquifer between 7.3 and 11.6 m (24 and 38 feet) bgs. In the single high clay sample analyzed, SB-1 11.6

to 12.2 m (38 to 40 feet) bgs, organic carbon was detected and comprised 0.34% of the sample mass.

Table R.1.6. Soil organic carbon content in preliminary borings and CMT-1.

Location	Sample Depth (ft bgs)	Total Organic Carbon (%)	Location	Sample Depth (ft bgs)	Total Organic Carbon (%)	Location	Sample Depth (ft bgs)	Total Organic Carbon (%)
SB-1	10 to 14	0.21%				CMT-1	2 to 4	1.54%
SB-1	14 to 20	ND	SB-2	14 to 20	0.063%	CMT-1	4 to 6	0.46%
SB-1	20 to 24	0.14%	SB-2	20 to 24	0.064%	CMT-1	8 to 10	0.10%
SB-1	24 to 38	ND	SB-2	24 to 40	ND	CMT-1	10 to 12	0.20%
SB-1	38 to 40	0.34%				CMT-1	13 to 24	ND

Notes: ND = not detected above 0.1 mgC detection limit (~0.012% by mass)

III.1.11. Soil Sorption Capacity and Rate

Adsorption equilibrium experiments were conducted with soils collected from CMT-1 at depths of 2.6 to 2.9 m (8.5 to 9.5 feet) bgs, 2.4 to 3.0 m (8 to 10 feet) bgs, 3.2 to 3.5 m (10.5 to 11.5 feet) bgs, and 12.2 to 1.8 m (40 to 42 feet) bgs. These depths were chosen to assess the effects of particle size and organic carbon on adsorption-desorption processes. The material from depth 3.2 to 3.5 m (10.5 to 11.5 feet) bgs was used for the forward rate to adsorption experiment; this material achieved equilibrium after approximately 90 hours (see Figure R.1.1).
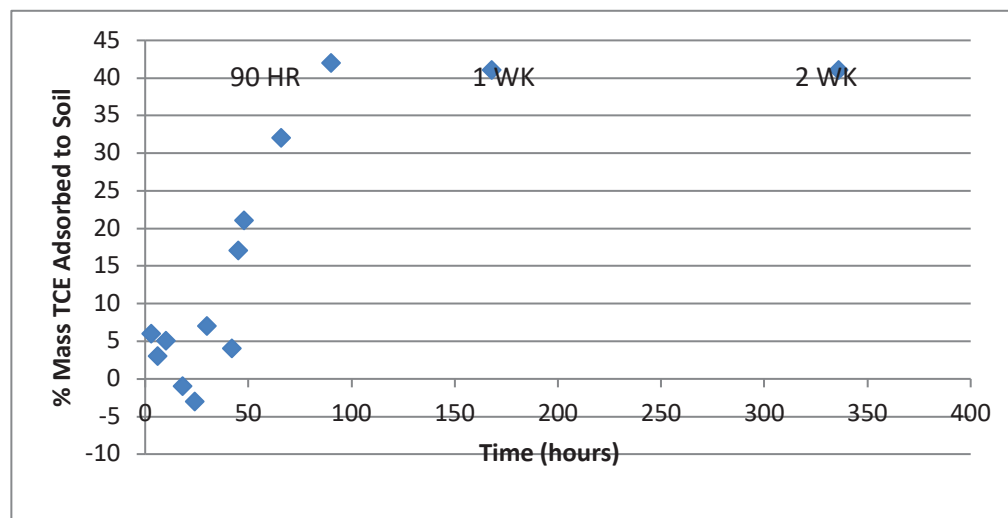
Figure R.1.1. Rate to Adsorption Equilibrium for soil collected from CMT 1 3.2 to 3.5 m (10.5 to 11.5 feet) bgs.

The other three materials were chosen for their range of particle size and organic carbon content. Depth 2.6 to 2.9 m (8.5 to 9.5 feet) bgs consisted of primarily sand (90.5% sand, 7.8% silt, and 1.7% clay) with lowest organic carbon content (0.1% by weight) of the three adsorption isotherm materials tested. The material from this depth also had the lowest sorption equilibrium partitioning coefficient, K_d, (mass of TCE/mass of soil) / (mass of TCE/volume of solution) of the three materials with a value of 1.0×10^{-4} L/g. Similar material from a wider depth range of 2.4 to 3.0 m (8 to 10 feet) bgs, consisted of 73.67% sand, 22.5% silt, 3.5 % clay with a slightly higher organic

carbon content of 0.2% by weight. The K_d for this depth was higher, 4.8×10^{-4} (L/g), due to the increased organic carbon content. A high clay material, collected from the 12.2 to 1.8 m bgs depth of boring CMT-1, consisted of primarily clay (54.9%) and silt (45.1%), with no sand and 0.3% organic carbon by weight. The adsorption isotherm for this depth was also 3.5×10^{-4} (L/g).

A summary of the three adsorption isotherms is shown in Figure R.1.2. The K_d values for each of these isotherms each differ less than a factor of two from their theoretical K_d values, as calculated using the method from Cwiertny and Scherer (2010), shown in Table R.1.7. The small K_d values and relatively similar amount of adsorption among all three materials suggests that contaminant sorption throughout the selected pilot test site is limited and confined to a narrow range. The rate to adsorption equilibrium was found to be the longest for the clay. This might be due to the fact that mass transfer from aqueous to solid phase may be more limited in fine materials.
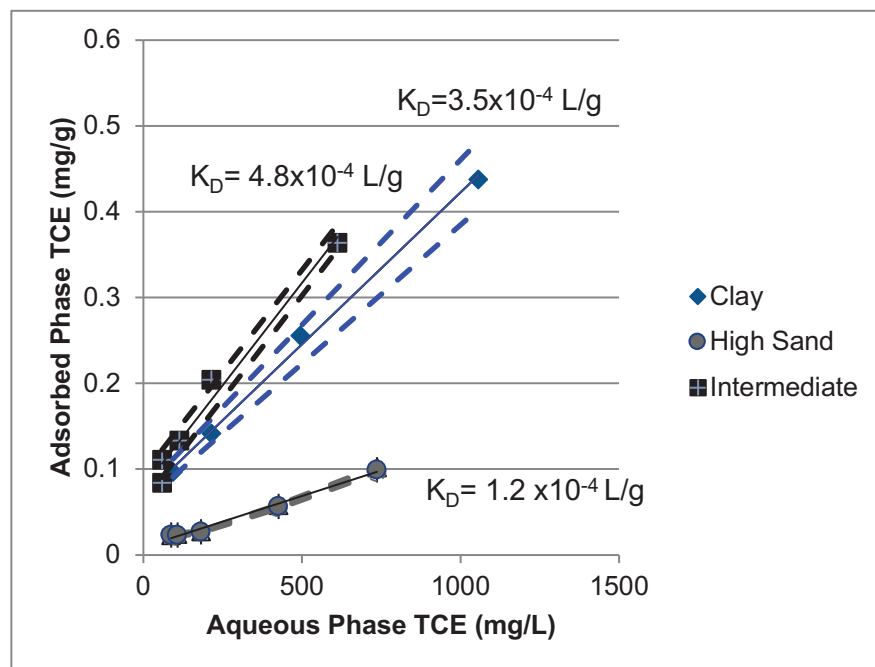
Figure R.1.2. Adsorption Isotherms for soils collected from CMT-1 at depths of 2.6 to 2.9 m bgs (High sand), 2.4 to 3.0 m bgs (Intermediate), and 12.2 to 1.8 m bgs (Clay).

Desorption experiments were completed for soil collected from the 2.4 to 3.0 m bgs and 12.2 to 1.8 m depths of CMT-1. TCE desorbed more quickly from the sandy material (2.4 to 3.0 m bgs) than the clay material (12.2 to 1.8 m bgs) with the time to reach a TCE concentration below the detection limit (< 0.4mg TCE/L) being 3 days and 5 days, respectively.

The data from these experiments were used to calculate 1st order TCE desorption rates for each material type. Results are presented in Table R.1.7). These adsorption-desorption experiments offer insight into the relative rates of mass transfer between the solid and liquid phases. The faster rates of mass transfer within the sandy materials relative to the clay materials indicate higher mobility and shorter contaminant-solid phase interaction times are likely to be observed for materials of larger particle sizes.

III.1.12. Site Soil pH

Site soil pH was measured from samples collected from the CMT-5 borehole. The results, in Table R.1.8, show alkaline soil with pH ranging from 7.71 to 9.44. This soil pH is consistent with the high groundwater pH (up to 8.70) observed during CMT-well sampling.

Table R.1.7. Summary of Materials and Results from Adsorption-Desorption Experiments

Particle Size	Clay Average % Present	High Sand Average % Present	Intermediate Average % Present
Gravel	0.0%	0.0%	0.4%
Coarse Sand	0.0%	0.3%	0.1%
Medium Sand	0.0%	3.5%	4.9%
Fine Sand	0.0%	86.7%	68.7%
Silt	45.1%	7.8%	22.5%
Clay	54.9%	1.7%	3.5%
Total	100.0%	100.0%	100.0%
Total Organic Carbon	0.3%	0.1%	0.2%
K_{oc}	133.33	100.00	200.00
Theoretical K_d (L/g)	4.44E-04	1.48E-04	2.96E-04
Measured K_d (L/g)	3.50E-04	1.00E-04	4.80E-04
Time to Adsorption Equilibrium (hrs)	120	96	24
Time to Desorption Equilibrium (hrs)	120	N/A	72
1st Order Desorption Rate (1/days)	-0.403±0.19	N/A	-0.895±0.42

Notes: 1. Theoretical K_d values calculated according to {Citation} 2. Soils collected from CMT-1 at depths of 2.6 to 2.9 m (8.5 to 9.5 feet) bgs (High sand), 2.4 to 3.0 m (8 to 10 feet) bgs (Intermediate), and 12.2 to 1.8 m (40 to 42 feet) bgs (Clay).

Table R.1.8. Soil pH in samples collected from the CMT-5 borehole.

Depth bgs	Soil pH	Depth (ft bgs)	Soil pH
3.0 to 3.4 m (10 to 11 feet)	7.79	7.3 to 7.6 m (24 to 25 feet)	8.00
3.7 to 4.0 m (12 to 13 feet)	9.63	7.6 to 7.9 m (25 to 26 feet)	8.89
4.9 to 5.2 m (16 to 17 feet)	9.36	9.8 to 10.1 m (32 to 33 feet)	7.71
5.5 to 5.8 m (18 to 19 feet)	8.10	10.1 to 10.4 m (33 to 34 feet)	8.86
6.7 to 7.0 m (22 to 23 feet)	7.81	11 to 11.3 m (36 to 37 feet)	8.08
7 to 7.3 m (23 to 24 feet)	9.44		

III.1.13. Site Soil Contaminants

Soil samples from the preliminary borings were analyzed for volatile organic compounds (VOCs) by a commercial contract laboratory, Test America, Inc. (Burlington, MA). The results, provided in Appendix B.8, showed detectible levels of TCE at depths of 6.1 to 12.2 m (20 to 40 feet) bgs in both locations with the highest TCE concentration, 13,000 µg/kg, at a depth of 9.8 to 10.4 m (32 to 34 feet) bgs in soil boring SB-02. DCE isomers were not detected above the laboratory detection

limit of 5.3 to 230 µg/kg. These results were consistent with the observations in the nearby monitoring wells (MW-06M and MW-06D) where TCE was the primary groundwater contaminant and *cis*-DCE was present at low concentrations (5.02 µM to 14.4 µM).

Soil samples from the CMT-5 soil boring were analyzed in the ESL using an alcohol extraction method and GC-FID as described in Section II.2.1. Due to the high detection limit of this method, TCE and *cis*-DCE were not detected in the CMT-well samples analyzed. Soil samples from the DHT-2 soil boring core were analyzed using alcohol extraction with GC-ECD analysis which had the necessary sensitivity to detect contaminants that desorbed into the extraction solvent. Both TCE and *cis*-DCE were detected in all of the samples collected from the 9.1 to 10.7 m (30 to 35 feet) bgs depth of DHT-2 as shown in Table R.1.9. TCE concentrations ranged from 379.7 to 1839 µg/kg and *cis*-DCE concentrations ranged from 8.77 to 74.27 µg/kg. As with the groundwater sample results, the pilot test area (DHT-2) had lower TCE concentrations and higher *cis*-DCE concentrations than the portion of the site where the preliminary soil borings were conducted.

Table R.1.9. Contaminant concentrations in DHT-2 soil boring samples

Depth (m bgs)	Depth (Ft bgs)	TCE (µg/kg)	*cis*-DCE (µg/kg)
9.1	30	74.3	912
9.3	30.5	40.6	643
9.4	30.8	31.9	1054
9.4	31	48.1	722
9.6	31.5	49.9	380
9.7	31.8	43.3	474
9.8	32	42.2	652
9.9	32.5	53.9	516
10.0	32.8	37.2	841
10.1	33	25.0	840
10.2	33.5	13.4	905
10.3	33.8	13.3	789
10.4	34	14.0	608
10.5	34.5	12.4	920
10.7	35	8.77	1839

III.1.14. Site Soil Microbial Abundance

A single soil sample, from the CMT-4 borehole 10.9 to 11.1 m (35.9 to 36.4 feet) bgs, was analyzed for total *Dhc* abundance. This sample had a total *Dhc* abundance of 1.08×10^7 16S rRNA gene copies/ gram of wet soil. Due to the lack of RDase gene in the groundwater samples analyzed and evidence that bioaugmentation was necessary, no additional analyses of soil microbial abundance were conducted.

III.2. Batch Reactor and Microcosm Experiments and Modeling Results

III.2.1. Experiment Results

Batch reactor and microcosm transformation studies were completed to assess the need to bioaugment the native microbial population at the Commerce Street site. A total of 123 reactors were prepared as described in Section II.4.1 using the combination of materials and amendments detailed in Table M.4.1.

In the 12 microcosms prepared with site soil, groundwater collected more than 1 year prior to use, and amended with TCE and lactate, all of the TCE was transformed to *cis*-DCE over the course of 58.2 (±9.5) days. When 27 similar reactors were prepared with site soil and groundwater collected 3 days prior to use (also amended with TCE and lactate), TCE was completely transformed to *cis*-DCE in an average of 57.6 (±22.9) days. None of these 39 microcosms completely transformed *cis*-DCE to ethene over the course of 140 days, indicating a need to bioaugment the Commerce Street site to achieve dechlorination to ethene over the proposed time-frame of the pilot test. In the reactors prepared with 1-year old CMT-5 groundwater, two reactors produced VC after 82.5 (±3.5) days and one reactor produced ethene after 86 days. These batch experiments were terminated after 95 days. The reactors prepared with 3-day old groundwater from CMT-5 were sampled for 673 days. Over this period, six of the reactors fully transformed TCE to ethene between the 140 day and 588 day sample with VC detectable after an average of 87.2 (±14.8) days. Of the 15 reactors prepared with soil and groundwater from other CMT-wells, 8 showed an increase in ethene concentration from 0.002 mM to 0.016 to 0.44 mM, but still contained mostly *cis*-DCE (68 to 90% of total molar mass) after 673 days.

In batch reactors prepared without soil, transformation of TCE to *cis*-DCE did not occur or required a longer time frame. No transformation was observed in the 6 reactors prepared with 1-year old groundwater during 95 days of sampling. In the 3 reactors prepared with 3-day old groundwater, but no soil and provided with 50% anaerobic growth medium, TCE was completely transformed to *cis*-DCE after 140 days. In the 3 reactors without soil or medium (prepared with 3-day old groundwater), only 1 reactor fully transformed TCE to *cis*-DCE after 588 days. Neither ethene nor VC was detected in any non-augmented reactors prepared without soil. The presence of soil provides a larger initial population of viable dechlorinating microorganisms than the groundwater alone, resulting in more rapid transformation of TCE to *cis*-DCE. The micronutrients and buffering capacity that may be contributed by the soil can also be provided by the anaerobic growth medium, as indicated by a shorter time to full transformation to *cis*-DCE in the groundwater-medium batch reactors than the groundwater only batch reactors.

When lactate was not provided as an electron donor (15 reactors), dechlorination was limited. In the 6 reactors containing CMT-5 groundwater and soil, TCE was fully transformed to *cis*-DCE after 79.9 (±5.4) days but was not transformed to VC or ethene. In the 6 reactors without soil or lactate, only 2 were able to fully transform TCE to *cis*-DCE after 588 days. The remaining 3 reactors without electron donor (prepared with CMT-4 groundwater) were sampled for 95 days and did not demonstrate transformation of TCE to *cis*-DCE. These reactors demonstrate that the organic carbon in the soil and site groundwater provide sufficient electron donor for the microbial species that transform TCE to *cis*-DCE but do not provide the hydrogen necessary for *Dhc* strains to transform *cis*-DCE to VC and ethene. Microcosm and batch reactors bioaugmented with KB-1® or BDI were able to fully transform TCE to ethene over a short timeframe. In the 36 bioaugmented reactors, TCE was reduced to concentrations below detection limits in an average of 7 days (±3.1) days while *cis*-DCE and VC were no longer detected after 33.1 (±18.0) days and 37.0 days (±30.7) days, respectively. In bioaugmented reactors, VC was detected in the earliest samples collected

(<1 day), although it may have been inadvertently introduced with the inoculum. Ethene concentrations increased after 2 to 27 days in bioaugmented reactors.

Figure R.2.1 contains example plots typical of reactor performance for a) native microbial population without lactate, b) native microbial population with lactate electron donor, and c) site materials bioaugmented with BDI. Anaerobic control reactors (21 reactors) did not exhibit transformation of TCE but were used to account for losses of chlorinated solvents through the rubber stopper.
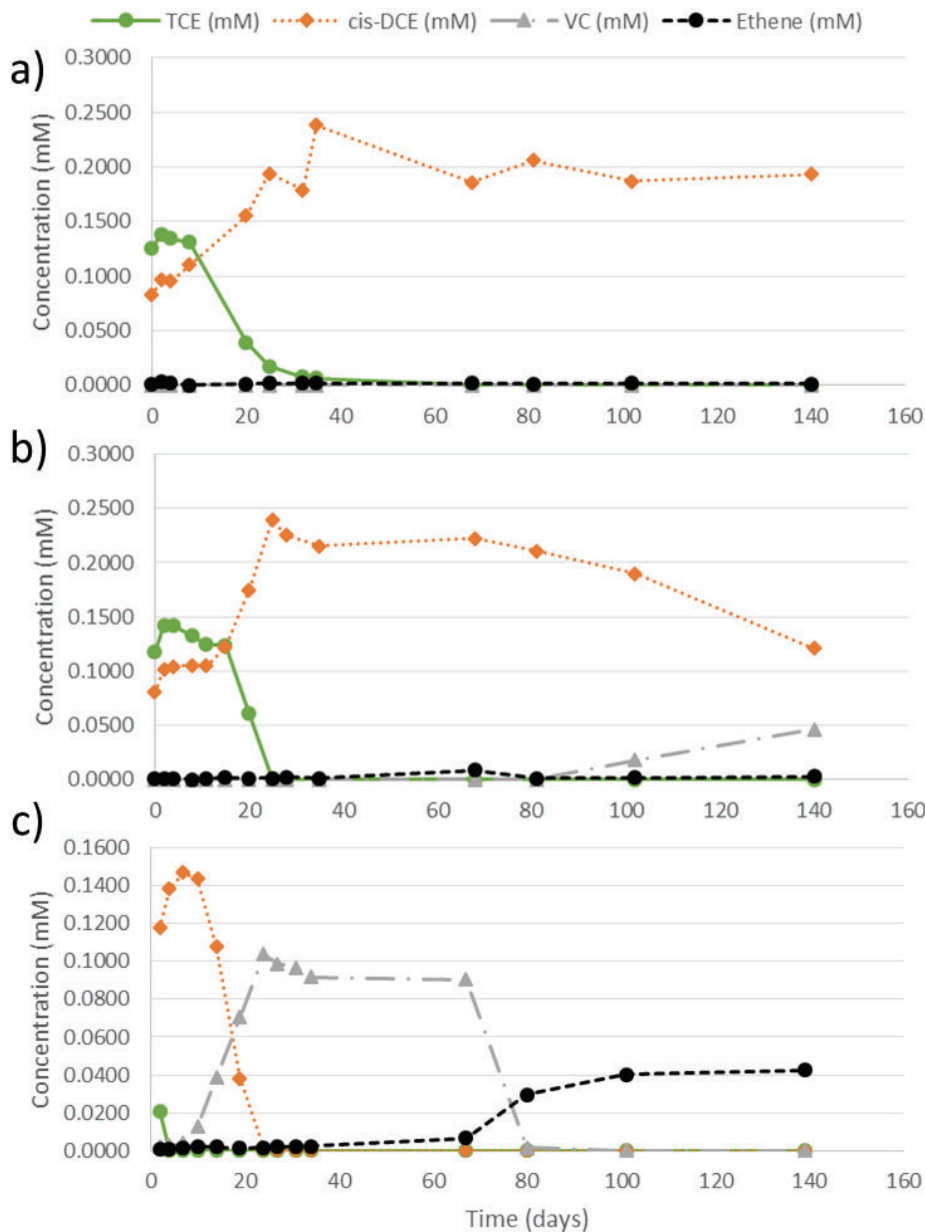
Figure R.2.1. Typical plots of chlorinated ethene and ethene concentrations in microcosms prepared with: a) site soil, site groundwater, and TCE; b) site soil, site groundwater, TCE, and lactate; and c) site soil, site groundwater, TCE, and lactate bioaugmented with BDI.

Additional analysis of the reactors prepared with DHT-2 soil and anoxic site groundwater was performed to develop parameters for modeling the aquifer cell and pilot test experiments. The

lactate added to these microcosms was rapidly fermented to acetate and propionate, providing hydrogen for *Dhc* strains, in microcosm containing native microorganisms and in reactors bioaugmented with KB-1®, but not in the abiotic control reactors (Figure R.2.2).
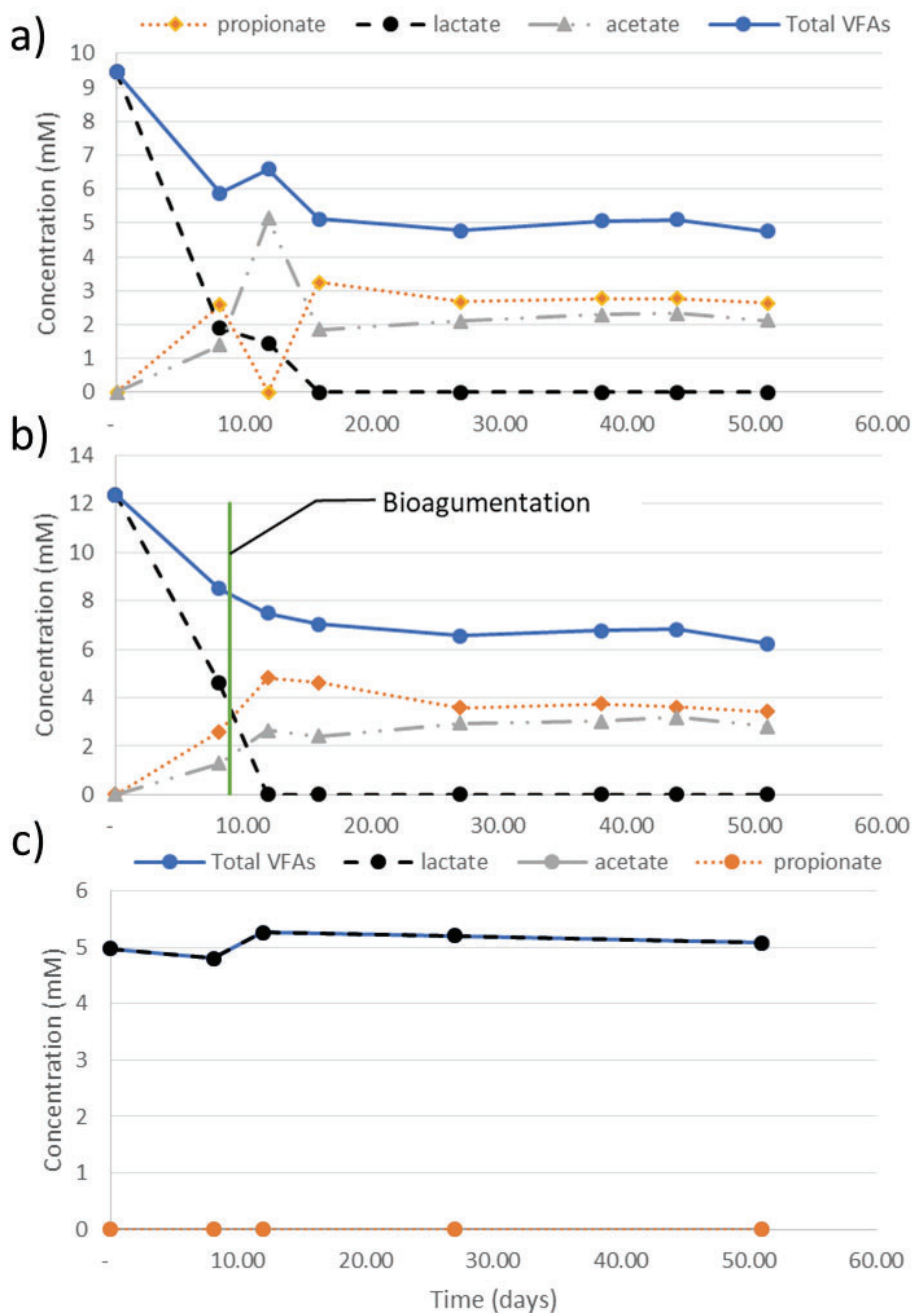
Figure R.2.2. Concentrations of VFAs in microcosms comprised of DHT-2 soil, anoxic groundwater and a) native microbial community, b) bioaugmentation with KB-1® and c) sterilized anoxic control.

After the initial fermentation of lactate, VFA concentrations remained stable as the electron donor was in excess of the molar mass needed to complete dechlorination of TCE to ethene. The chlorinated ethene and ethene concentrations in the DHT-2 microcosms are presented in Figure R.2.3. As in the other microcosm studies prepared with soil and groundwater from the CMT-wells,

the non-bioaugmented reactors stalled at *cis*-DCE, the bioaugmented reactors fully transformed TCE to ethene, and biotic losses of approximately 0.3 mM TCE were observed in the abiotic control reactors. The reactors that were not bioaugmented stalled at *cis*-DCE and did not produce measurable concentrations of VC and ethene, while the bioaugmented reactors fully transformed TCE to ethene.
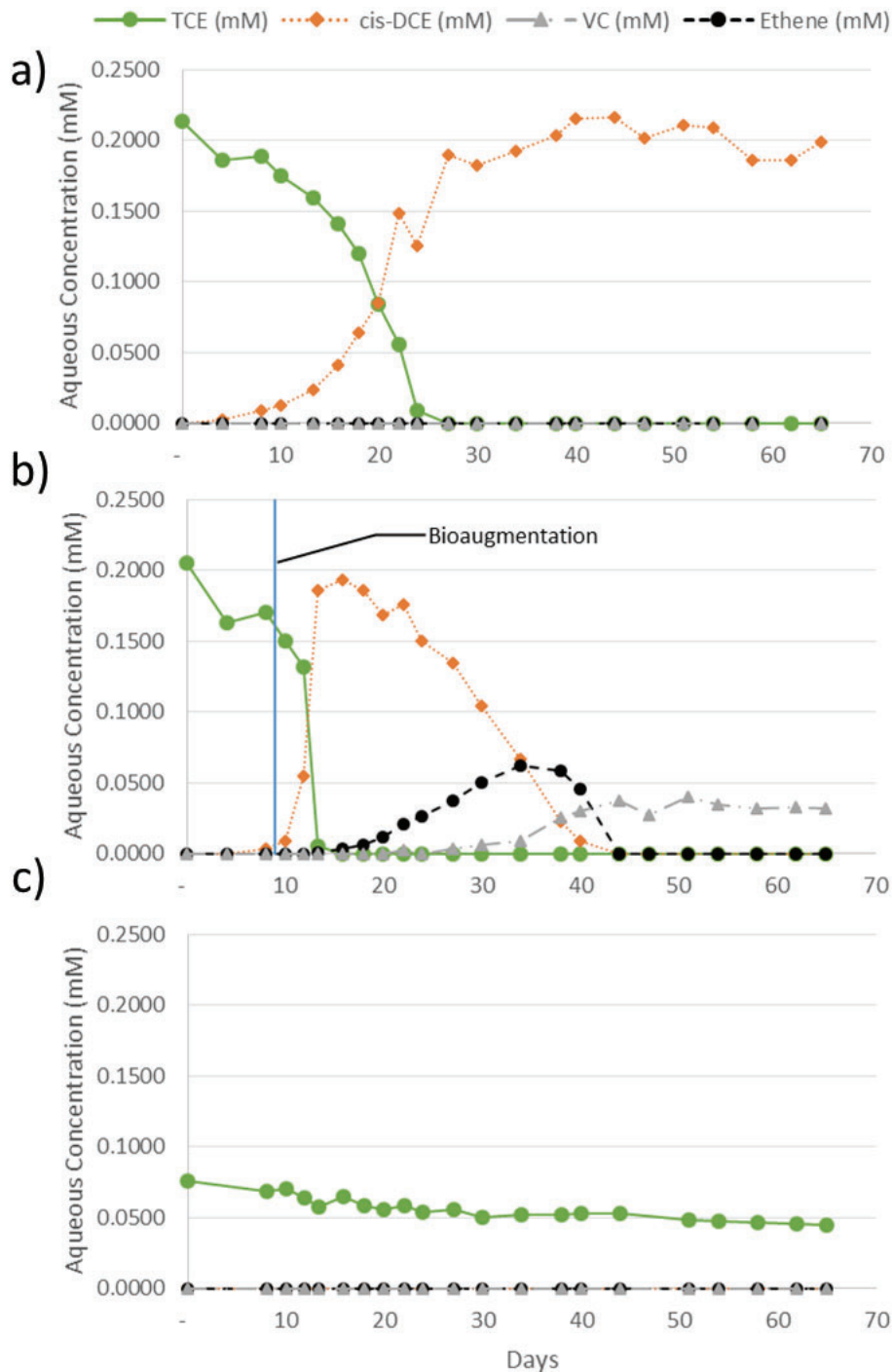
Figure R.2.3. Concentrations of chlorinated ethenes and ethene in microcosms comprised of DHT-2 soil, anoxic groundwater and a) native microbial community, b) bioaugmentation with KB-1® and c) sterilized anoxic control.

The growth of two microbial species, *Dhc* and *Geo*SZ, were monitored in the three DHT-2 soil microcosms bioaugmented with KB-1®. The *Dhc* population increased from an average abundance of 1.33 x 10^8 (±4.00x107) 16S rRNA gene copies/ L after bioaugmentation to a maximum of 1.76 x 10^9 (±1.59 x 10^9) 16S rRNA gene copies/ L after 30 days. The *Dhc* population then declined to 6.20 x 10^8 (±3.27 x 10^8) 16S rRNA gene copies/ L at the end of the experiment (57 days) as the electron acceptor (chlorinated ethenes) had been depleted by day 44 to 51. The *Geo*SZ population increased similarly from an initial abundance of 2.73 x 10^4 gene copies per L (1 reactor; 2 reactors were below the instrument detection limit of 2.50 x 10^4 16S rRNA gene copies/ L) to a maximum of 4.30 x 10^4 (±1.09 x 10^4) 16S rRNA gene copies/ L after 30 days and decreased to below the detection limit after 57 days.

III.2.2. Modeling Results

The model parameter values were taken from the literature and are listed in Table R.2.1.

Table R.2.1. Microcosm Dechlorination Model Parameters.

Symbol	Parameter Name	Value	Reference
$K_{TCE,half}$	TCE half saturation constant	$0.00102\ mM$	(Clapp et al. 2004)
$K_{DCE,half}$	DCE half saturation constant	$0.00192\ mM$	(Clapp et al. 2004)
$K_{VC,half}$	VC half saturation constant	$0.18027\ mM$	(Clapp et al. 2004)
$K_{I,TCE}$	TCE inhibition constant	same as $K_{TCE,half}$	(Christ and Abriola 2007)
$K_{I,DCE}$	DCE inhibition constant	same as $K_{DCE,half}$	(Christ and Abriola 2007)
$K_{I,VC}$	VC inhibition constant	same as $K_{VC,half}$	(Christ and Abriola 2007)
Y^{TCE}	TCE yield coefficient	$9.6\ mg\ cell\ mmol^{-1}$	(Clapp et al. 2004)
k_b	dechlorinator endogenous decay rate	$0.05\ d^{-1}$	(Chen et al. 2013)
k_{TCE}^e	TCE gas escape rate constant	$0.0071\ d^{-1}$	measured
k_{DCE}^e	DCE gas escape rate constant	$0.0083\ d^{-1}$	estimated from k_{TCE}^e
k_{VC}^e	VC gas escape rate constant	$0.0103\ d^{-1}$	estimated from k_{TCE}^e
k_{ETH}^e	ethene gas escape rate constant	$0.0154\ d^{-1}$	estimated from k_{TCE}^e
$K_{d,TCE}$	TCE linear adsorption constant	$1.34 \times 10^{-4}\ L\ g^{-1}$	measured
$K_{d,DCE}$	DCE linear adsorption constant	$4.5 \times 10^{-5}\ L\ g^{-1}$	estimated from $K_{d,TCE}$
$K_{d,VC}$	VC linear adsorption constant	$2.6 \times 10^{-5}\ L\ g^{-1}$	estimated from $K_{d,TCE}$
$K_{d,ETH}$	ethene linear adsorption constant	$8.3 \times 10^{-6}\ L\ g^{-1}$	estimated from $K_{d,TCE}$
Q^a	average aqueous phase sampling rate	$-3.0 \times 10^{-4}\ L\ d^{-1}$	measured

The DCE, VC, and ethene gas escape constants were estimated from the TCE gas escape constant k_{TCE}^e by using Graham's law of effusion

$$k_i^e = k_{TCE}^e \sqrt{\frac{M_{TCE}}{M_i}} \qquad \text{(R.2.1)}$$

where M_{TCE} and M_i are molecular weights.

A measured linear adsorption constant was used for TCE. An approximation (Karickhoff et al. 1979) based on the octanol-water coefficient K_{ow} was used to estimate the linear adsorption constants for DCE, VC, and ethene, using the measured fraction of organic carbon f_{oc} in the soil.

$$K_{d,i} = 6.17 \times 10^{-4} f_{oc} K_{ow} \qquad \text{(R.2.2)}$$

The final adjusted yield coefficient values were $Y^{DCE} = 2.9\ mg\ cell\ mmol^{-1}$ and $Y^{VC} = 1.0\ mg\ cell\ mmol^{-1}$. The corresponding best-fit maximum substrate utilization rates are listed in the following Table R.2.2. An example plot of model results versus measured values is shown in Figure R.2.4-6. The model under-predicts TCE and VC concentrations in some trials, but it successfully matches the overall timing of the dechlorination process.

Table R.2.2. Best-Fit Maximum Substrate Utilization Rates (mmol/mg-cell day), and Mean Square Error (MSE) (mmol^2)

Trial	$k_{TCE,max}$	$k_{DCE,max}$	$k_{VC,max}$	MSE
D2K-1	0.319	0.0903	0.222	0.0054
D2K-2	0.356	0.0742	0.222	0.0009
D2K-3	0.315	0.0774	0.176	0.0027

III.2.3. Conclusions

Microcosm and batch reactor experiments demonstrated the need to bioaugment and biostimulate the site in order to fully transform TCE to ethene. The native microbial population was capable of transforming TCE to *cis*-DCE using the dissolved organic carbon in site groundwater but completed the transformation more quickly when supplied with lactate as an electron donor. When provided with lactate, the native microbial population in a subset of reactors did transform *cis*-DCE to VC and ethene when provided with a suitably long timeframe (>140 days). The absence of continued dechlorination in most reactors indicates a low population of *Dhc* harboring the RDase genes necessary to produce VC and ethene and a non-uniform distribution of organisms at the site. Bioaugmentation of reactors with KB-1® or BDI was successful and allowed TCE to be fully transformed to ethene in an average of 37 days.

A robust numerical model incorporating adsorption of contaminants to soil and partitioning into the bottle headspace was created to simulate microbial reductive dechlorination in the batch reactors and microcosms. The numerical model and Matlab fitting routine were able to match the chlorinated ethene and ethene concentrations observed in the KB-1® bioaugmented microcosms, providing culture-specific yield coefficients and substrate utilization rates that were used in future modeling results.
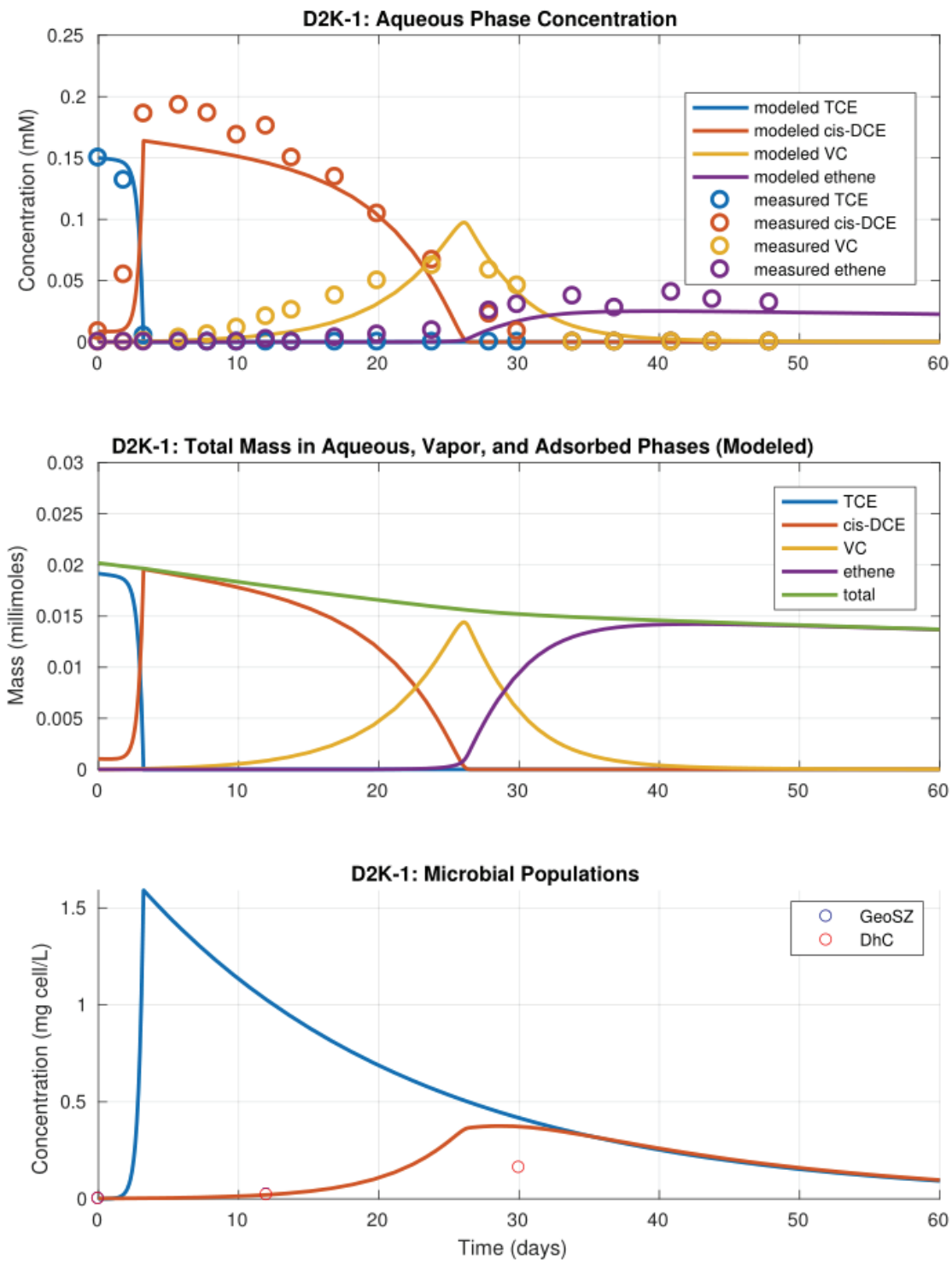
Figure R.2.4. Model Results and Measured Values for Microcosm Trial D2K-1.
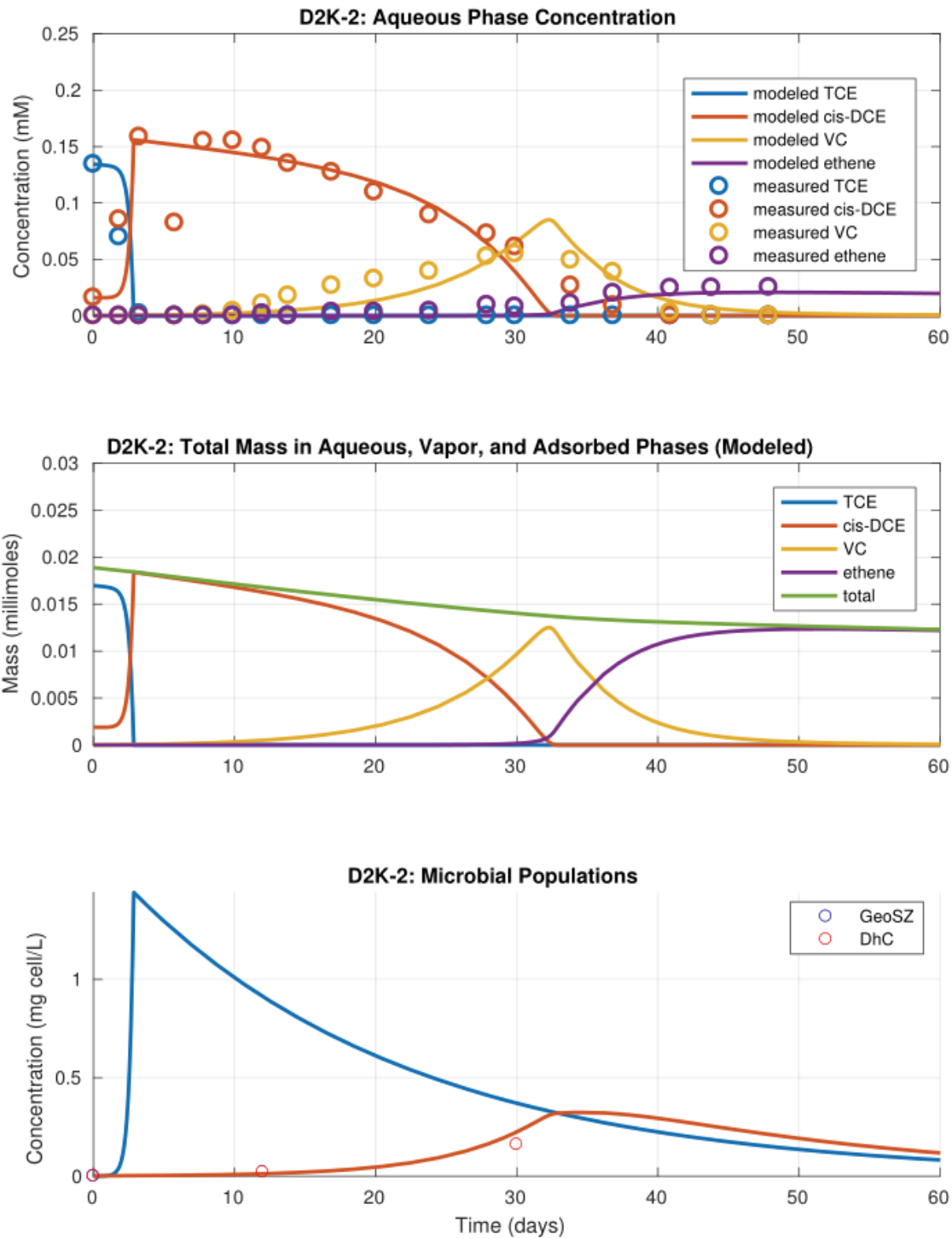
Figure R.2.5. Model Results and Measured Values for Microcosm Trial D2K-2
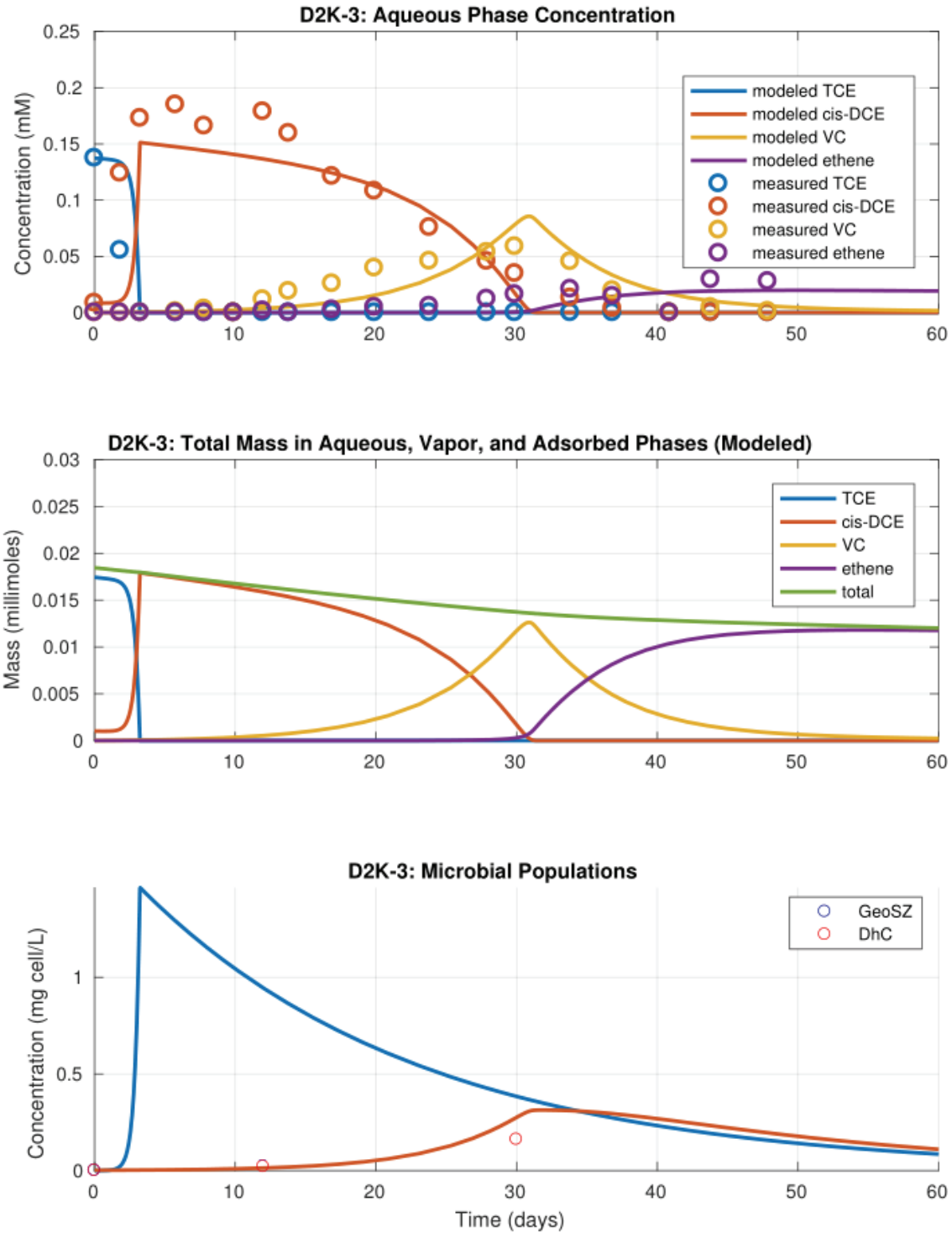
Figure R.2.6. Model Results and Measured Values for Microcosm Trial D2K-3.

III.3. Aquifer Cell Transformation Studies

Two aquifer cell transformation studies were performed as described in Section II.4.2 above. The first aquifer cell contained an ASTM 20/30 background with four lenses of varying hydraulic conductivity and organic carbon content. It was used to quantify the bioenhancement of back diffusion from low permeability zones and to examine the distribution of *Dhc* and associated RDase genes around soil heterogeneities. Results of this research are described in Section III.3.1. The second aquifer cell was constructed with site materials and was used to provide a laboratory scale model of the pilot (DHT) test. This laboratory scale experiment was used to compare numerical model predictions with observations and to develop parameters to model the pilot test. Experimental and modeling results from this aquifer cell experiment are presented in Section III.3.2.

III.3.1. First Aquifer Cell; Experimental and Modeling Results

III.3.1.1. Modeling First Aquifer Cell and Flow Field

To represent the actual experimental conditions of the aquifer cell, the numerical model was implemented to consider all of the experimental features, including the flow and transport properties of the lenses and clay layer, as well as the conditions associated with the influent solution delivery system. Prediction accuracy for compound concentrations in the aquifer cell depends primarily on an accurate simulation of heterogenous flow field. A schematic diagram of the model domain for the aquifer cell is shown in Figure R.3.1.
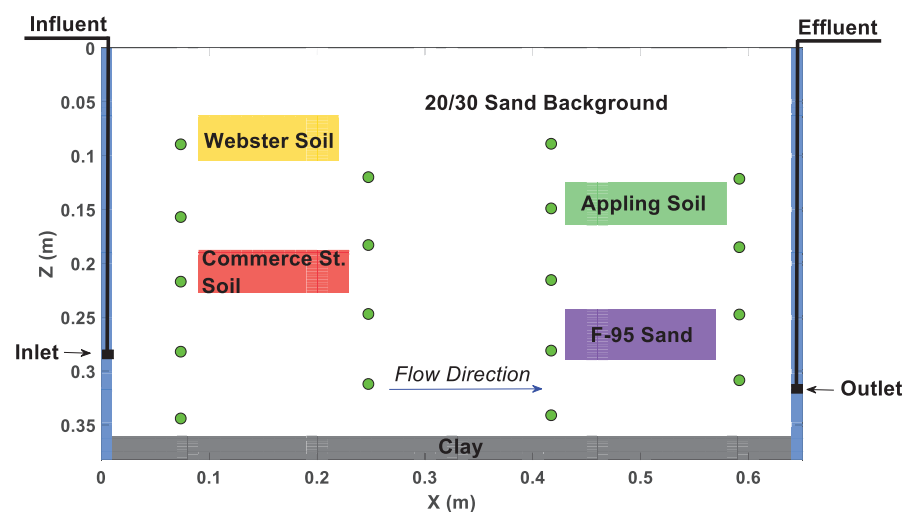
Figure R.3.1. First Aquifer cell construction for numerical simulation

Given the shallow depth of the aquifer cell, it was modeled as a pseudo two-dimensional system, neglecting any parameter variations with depth. . Flow chambers, constructed as slotted stainless steel wells to promote uniform flow distribution into the aquifer cell, were simulated by assigning a hydraulic conductivity 6 orders –of- magnitude higher than that of the background sand to the first and last column of the numerical grid cells. In the experiment, a stainless steel drop tube in the influent chamber was used to supply influent solution from a constant head reservoir to create steady flow field, and an effluent chamber drop tube was opened to the atmosphere at a fixed height. In order to simulate these conditions, the numerical gridblocks associated with the flow tubes in the inlet and outlet chambers (Figure R.3.1) were assigned as constant head cells. A fine spatial discretization was applied to the model domain (grid spacing of 1 cm (length) × 0.25 cm (height)) to adequately capture mass transfer processes (e.g., diffusion) in the vicinity of lenses

86

and clay layers. An implicit finite difference scheme with upstream weighting on advection was used to solve the transport equations, providing computational efficiency and robust numerical solutions. An adaptive temporal discretization was applied to minimize numerical dispersion.

Given the controlled gradient experimental conditions, hydraulic conductivities and dispersivity coefficients were calibrated in the model by matching 1) the average effluent flow rate and 2) the breakthrough curves of the initial bromide tracer test. Here effluent tracer breakthrough curves (BTC) were used to calibrate the hydraulic conductivity of the background sand, while sampling port tracer data were mainly used to fit the hydraulic conductivities of the lenses and the clay layer. The number of adjustable variables in the model prevented the use of a formal parameter optimization procedure. Thus, an iterative parameter updating procedure was used to minimize the root mean square errors between model simulation and BTC observations.

Initial model parameter values listed in Table R.3.1 were obtained from the literature for experiments conducted using the same porous media. These parameters were then adjusted to minimize the differences between model simulation and experimental observation, resulting in the set of calibrated parameters shown in the same table (R.3.1). The subsequent abiotic experiment, involving flushing of a solution of TCE, a sorptive compound, and a non-reactive tracer, bromide, was then simulated using the calibrated parameters, validating the fitted coefficients and facilitating the refinement of the assumed organic carbon content of the materials.

Table R.3.1. Initial and calibrated model parameters for first aquifer cell transport simulations

Porous Media	Hydraulic Conductivity (m/day)		Organic Carbon Content, f_{oc} (%)		Porosity, ϕ (-)
	Calibrated	Initial[a]	Calibrated	Initial[b]	Fixed
ASTM 20/30	200	330	-	0	0.45
Webster Soil	0.6	0.86	3.3	1.96	0.51
Appling Soil	5	10.2	0.75	0.66	0.33
Commerce St. Soil	5	1.7-6.9	0.1	0.1-0.3	0.3
F95 Sand	1	2.5	0.001	0.01	0.28
Commerce St. Clay	0.05	0.08	0.32	0.3	0.78

[a.] Obtained from (Chen et al. 2007; Gaeth et al. 2016; Marcet et al. 2018a; Taylor et al. 2001).
[b.] Obtained from (Gaeth et al. 2016; Marcet et al. 2018a).

Experimental measurements of the total molar sum of chlorinated ethenes and ethene during the biotic experiment were then compared with numerical simulations of sorption, desorption, and diffusion in the absence of microbial reductive dechlorination (MRD) to assess the influence of microbial activity on back diffusion and desorption. Influent TCE concentrations and flow rates were set consistent with experimental conditions (Table M.4.2).

Other input parameters for soil and chemical properties were kept fixed during simulations assuming no/minimal need for adjustment. Porosity was calculated using soil mass and volume emplaced in the aquifer cell and a mid-range value of soil specific gravity. A K_{oc} value of 126 L/kg was used for TCE (Pankow et al. 1996). Free-solution diffusivity of bromide and TCE were taken from (Verschueren 2001) and (Li and Gregory 1974), with values of 2.01E-05 cm^2/s and 7.99E-06 cm^2/s respectively.

III.3.1.2. Bromide Tracer Breakthrough

Calibrated parameters used in the tracer test model are listed in Table R.3.1. Experimental measurements and the associated numerical simulation of the bromide BTC are plotted in Figure R.3.2. Note that the hydraulic conductivity values of the emplaced media were reduced by a factor of 1.5 to 2 from the assumed (literature) initial values to match the measured hydraulic gradient and flow rate. An initial local longitudinal dispersivity value of 0.1 cm and a vertical to longitudinal ratio of 0.1 cm was employed, following (Lyon-Marion et al. 2017). The longitudinal dispersivity was then slightly adjusted to a value of 0.24 cm after calibration in order to match the rise and tailing of the BTC.
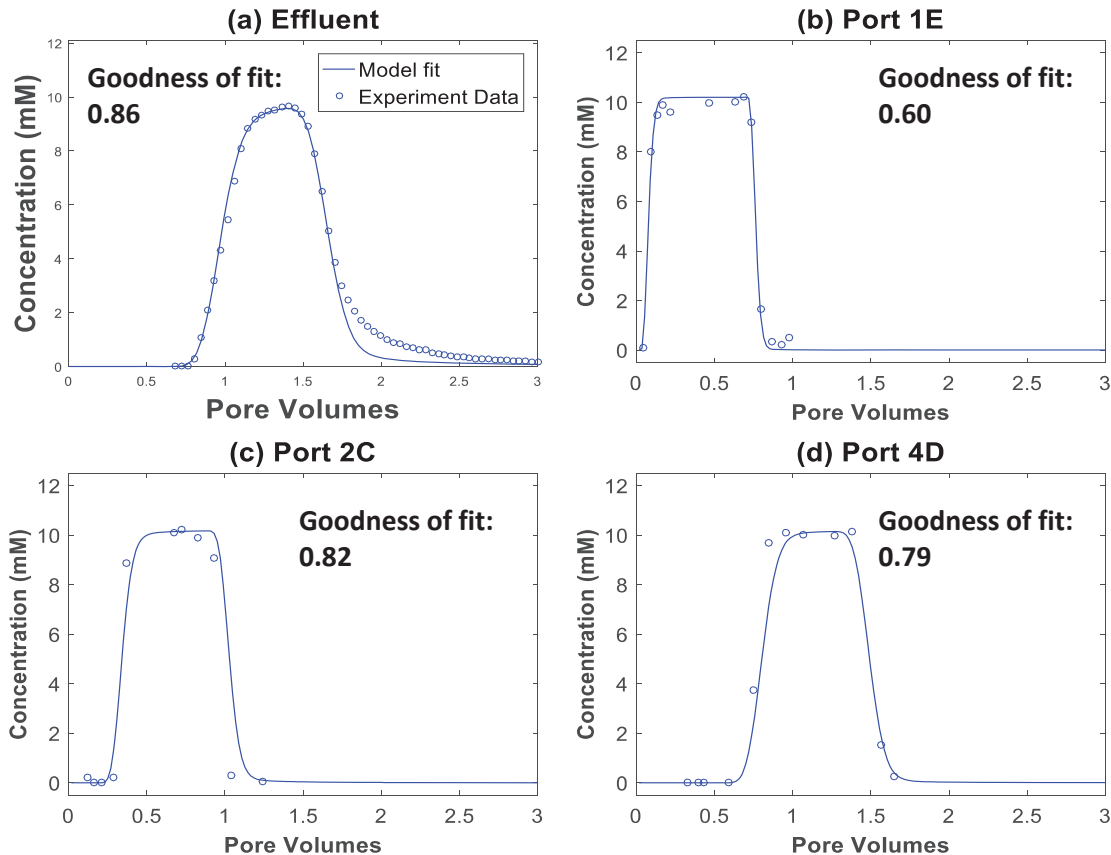
Figure R.3.2. Comparison of bromide tracer concentration measurements (open circles) and model fit (solid lines) in (a) effluent and (b-d) ports.

Using the calibrated parameters, the model matched the experimental BTC with goodness of fit of 0.86, 0.60, 0.82, and 0.79 calculated by "goodnessOfFit" (MATLAB, The Mathworks, Natick, MA) for data collected in effluent, and ports 1E, 2C, and 4D, respectively. An examination of Figure R.3.2 reveals that the model was able to capture the asymmetrical shape of the effluent BTC, but under-predicted the magnitude of the effluent tailing at late times, possibly associated with diffusive mass transport from the clay layer at the bottom of the cell (Figure R.3.3). A mass balance calculation, however, demonstrated that the bromide mass stored in the clay layer would be unable to sustain such a high tailing after the majority of the mass was flushed out. Thus, this high tailing level was attributed to residual bromide from a previous tracer experiment in the cell. Model predictions for side port BTCs provided a close match to the breakthrough times and the plateau maximum concentrations with minor differences in the tail (port 1E) and the width of the

BTCs (ports 2C and 4D), resulting in the slightly lower goodness of fit values mentioned above. In general, the model results displayed good agreement with experimental BTCs in terms of the shape, arrival time, and plateau concentration, demonstrating the capability of the model to simulate the heterogeneous aquifer cell and the suitability of calibrated parameters used in the model.
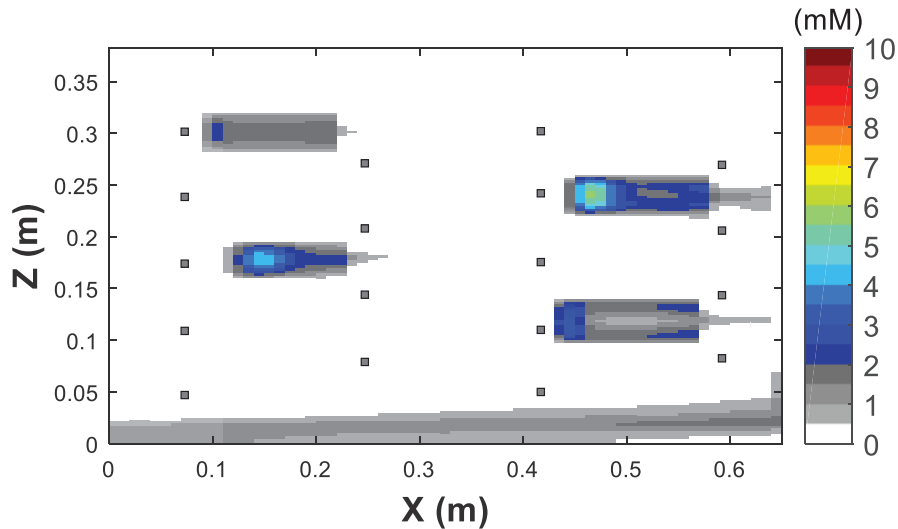
Figure R.3.3. Simulated aqueous concentration of bromide in aquifer cell at PV 1.96 (day 15) of tracer experiment.

III.3.1.3. Desorption and Back Diffusion under Abiotic Conditions

Following the tracer test, an abiotic flushing experiment of TCE and bromide was conducted to investigate sorption-influenced back diffusion in the system. Results of experimental measurements and numerical simulations for the effluent and selected ports during the flushing experiment (PV 0 is the time that the influent TCE and bromide concentrations were reduced to 0 mM) are presented in Figure R.3.4 in both linear and log (inset) scales. The ports above the clay layer (1E) and downgradient of the Commerce Street (2C) and F95 sand (4D) lenses are shown because back diffusion and desorption were most pronounced in these regions, with a more than 28% enhancement of back diffusion for the chlorinated ethene. While the concentration of both solutes dropped when flushing with 0 mM solution began, normalized TCE concentrations remained 3 times and 7 times higher than the bromide concentration in the effluent and selected side ports, respectively. After 9 PVs of flushing with the unamended solution, TCE concentrations dropped to concentrations two orders-of-magnitude lower than the input concentration while bromide concentrations leveled off at three orders-of-magnitude lower than the initial concentration. The agreement between model predictions and experimental measurements shown in Figure R.3.4 reflect a model capable of capturing TCE and bromide breakthrough, with goodness of fits of 0.91 and 0.95 at the effluent, 0.88 and 0.91 at port 1E, 0.99 and 0.86 at port 2C, and 0.98 and 0.84 at port 4D for bromide and TCE, respectively. Although the geometry of the low permeability compartments was digitized based on image of the aquifer cell, it is difficult to numerically capture details introduced during the packing of the aquifer cell, e.g. small-scale variations in lens shape and compaction of the background coarse sand. This uncertainty may partially account for the small discrepancies between model simulations and experimental BTC measurements.
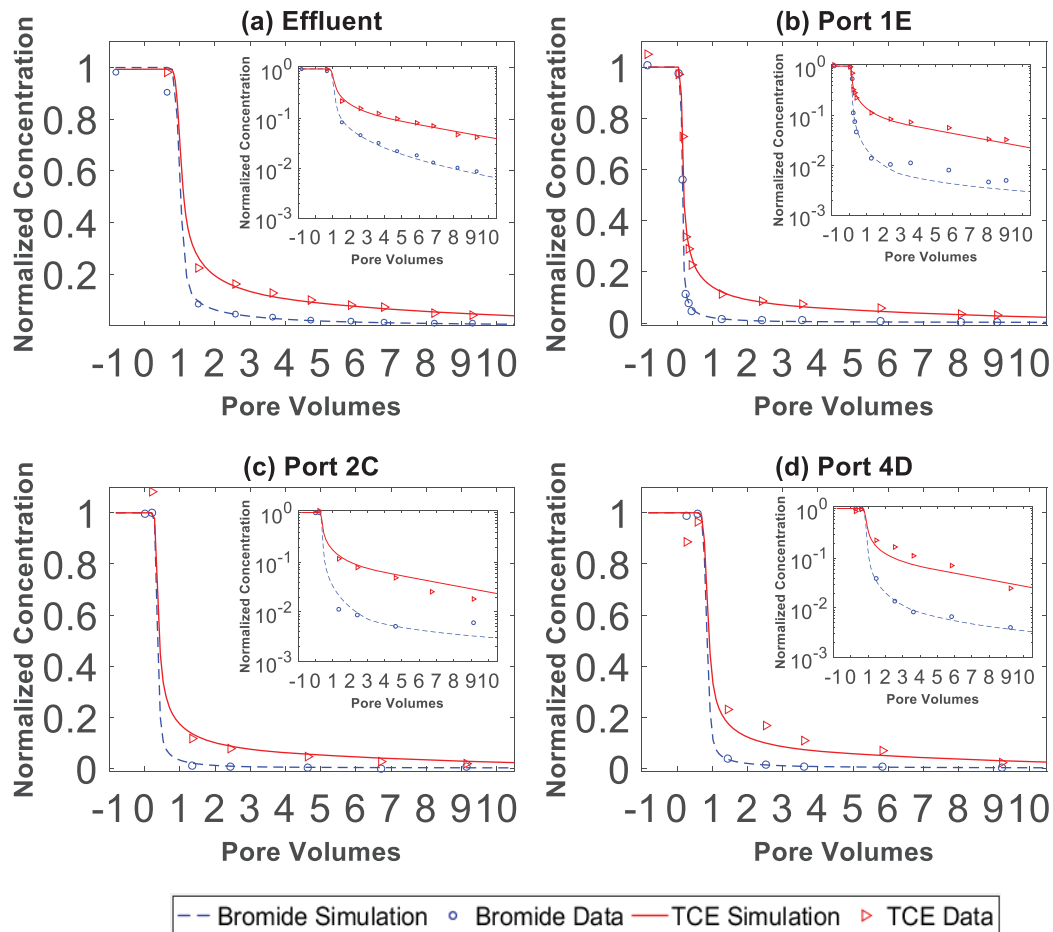
Figure R.3.4. Comparison of experiment observation and model simulation of bromide and TCE concentration plotted in linear and log scale (inset) during abiotic flushing experiment in (a) effluent (b) port 1E (c) port 2C and (d) port 4D. Experiment data: circle—bromide, triangle—TCE; Simulation: dashed line—bromide, solid line—TCE.

III.3.1.4. Biodegradation Results

After bioaugmentation, TCE was rapidly biodegraded with *cis*-DCE detected in the effluent after 0.2 PVs and VC and ethene detected after 2 and 3.4 PVs, respectively. While the influent TCE was maintained at approximately 0.5 mM, before reaching the effluent, all of the TCE was transformed to *cis*-DCE after 2.0 PVs (5.6 days). After lowering the influent TCE concentration to 0.04 mM (2.6 PVs, day 8.4), transformation of TCE yielded an effluent molar composition of 90% *cis*-DCE and 10% VC (Figure R.3.5). The proportion of VC and ethene in the effluent increased to 33% and 27%, respectively after 4.4 PVs (13.8 days following bioaugmentation), after which the proportion of *cis*-DCE and VC decreased and the proportion of ethene continued to increase. Approximately 6.1 PVs (19.8 days) after bioaugmentation, 3.4 PVs (11 days) after lowering the influent TCE concentration, ethene was the only analyte detected in the effluent. At this point in the experiment, *cis*-DCE continued to be detected in the side sampling ports at concentrations of 0.07 - 0.08 mM in ports 1A and 1E (near the influent, Figure M.4.1) and concentrations of 0.02 – 0.03 mM in downgradient ports (columns 2 and 3, Figure M.4.1). When the influent TCE concentration was further reduced to 0.01 mM (9 PVs, 29 days after bioaugmentation), ethene continued to be detected in the effluent at a concentration of 0.04 to 0.06 mM, indicating continued back diffusion and desorption from the low permeability lenses and clay

layer. In the sampling ports, ethene continued to be detected at concentrations of 0.01 – 0.02 mM with the exception of ports impacted by the underlying clay and the higher organic carbon lenses that measured higher concentrations (Figure R.3.5). The highest concentrations, 0.04 to 0.06 mM, were measured in the lowest ports (ports 1E and 3E) where TCE continued to be released from the underlying clay layer; see Figure R.3.5 (b) and (d). Downgradient of the high organic carbon Webster and Appling lenses (ports 3A, 4A, and 4B), ethene was detected at concentrations up to 0.03 mM.

At the conclusion of the experiment, soil samples were analyzed for TCE and *cis*-DCE using the methanol extraction procedure described in Section II.2.1. TCE was detected in the clay layer, Webster lens, and Appling lens with concentrations averaging 1.94 µg/g (±0.57 µg/g), 0.022 µg/g (±0.016 µg/g), and 0.37 µg/g (±0.19 µg/g), respectively. Due to the high detection limit for *cis*-DCE (0.0026 mM), it was only detected in the clay with an average concentration of 49 µg/g (±23 µg/g).
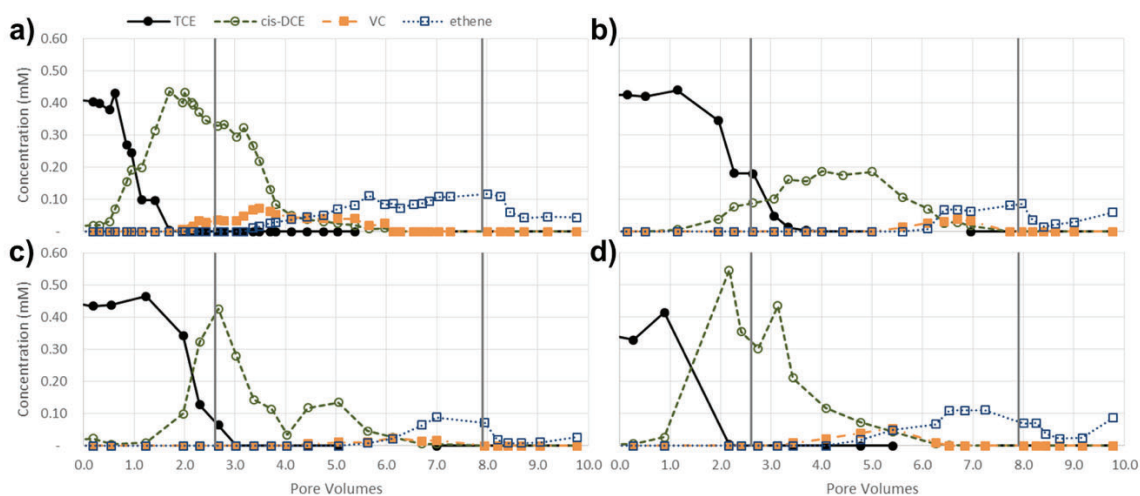
Figure R.3.5. Chlorinated ethene concentrations during biotic experiment in (a) effluent, (b) port 1E, (c) port 2C, and (d) port 4D. Bioaugmentation occurred at PV 0 (day 0). Vertical lines represent the reduction of influent TCE concentration from 0.5 mM to 0.04 mM and from 0.04 mM to 0.01 mM, respectively.

III.3.1.5. Desorption and Back Diffusion under Abiotic and Biotic Conditions

To explore the influence of MRD on solute transport, the abiotic flushing of TCE was predicted by numerical simulation using the input and flow conditions for the biotic experiment and compared with measurements made during the biotic experiment. Differences in magnitude and shape of the data and simulated curves can then be attributed to microbially enhanced back diffusion. Predicted and experimentally measured concentrations of total chlorinated ethenes and ethene in the effluent and selected ports are plotted in Figure R.3.6. The simulated curves (in the absence of MRD) generally follow the trends of the biotic experiment curves. This similarity is attributed to the use of a coarse sand background, which results in advection-dominated transport in which the flow rate and input concentration are the primary determinants of concentration. Biotransformation of TCE to lesser-chlorinated products, which have different physical and chemical properties (i.e., diffusivity in water and sorption to solid phase organic carbon), affects rates of loading into and release from the low permeability lenses, and thus, the elution curve. For example, sampling ports directly impacted by mass transfer out of low permeability layers, displayed more pronounced differences from the abiotic simulation than the effluent BTC (Figure R.3.6), which integrates the effect over the whole aquifer cell.

91
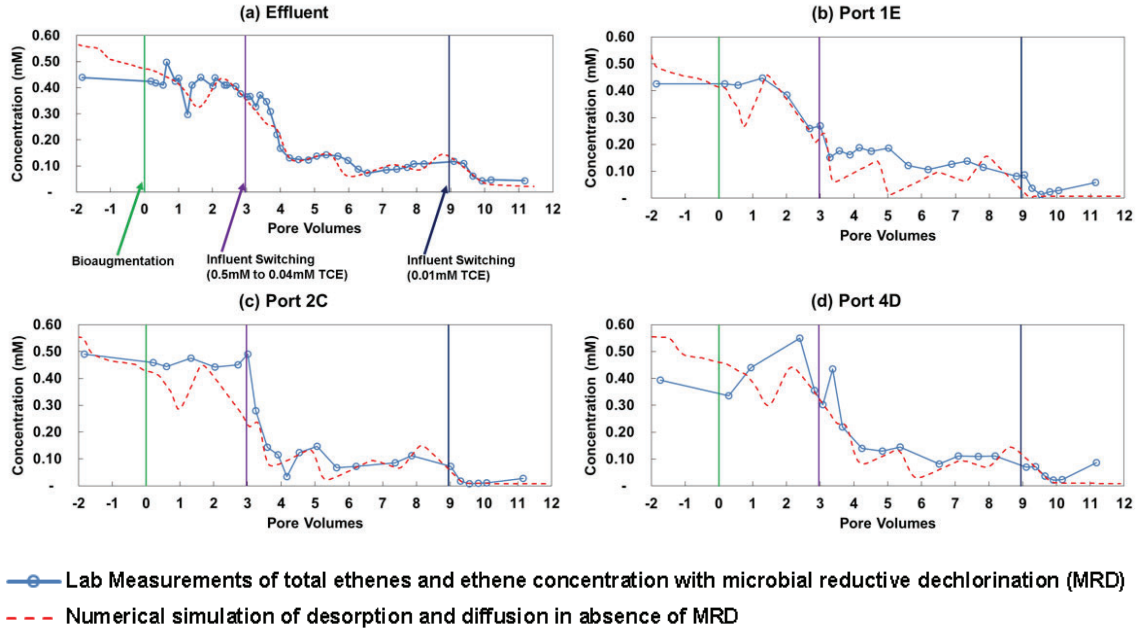
Figure R.3.6. Total molar concentration of chlorinated ethenes and ethene during biotic experiment compared with model simulation of abiotic flushing in (a) effluent (b) port 1E (c) port 2C and (d) port 4D. Bioaugmentation: PV 0 (day 0); influent switched to 0.04mM: PV 2.9 (day 8); influent switched to 0.01mM: PV 8.9 (day 29).

To quantify the extent of bioenhanced back diffusion, cumulative mass was calculated and compared between experimental data and the model simulation with the following expression:

$$\delta_{MRD} = \frac{CM_{exp} - CM_{sim}}{CM_{sim}} \times 100\% \qquad \text{(R.3.1)}$$

where δ_{MRD} represents the percent enhancement by biotransformation, CM_{exp} is the cumulative mass calculated using experiment data for a specific location, CM_{sim} is the cumulative mass calculated using the model simulation at the same location. The δ_{MRD} was calculated for effluent and side port BTCs (Figure R.3.7) during the period from the lowering of the influent TCE concentration (PV 2.9, day 8) to the end of experiment, as greater enhancement was expected when a concentration gradient between the lenses and background was present. The δ_{MRD} for each port over the entire biotic experiment are shown in brackets in Figure R.3.7. The extent of localized bioenhancement calculated was higher than the 12% bioenhancement calculated for the effluent for all locations except port 4B. The highest enhancements of 40% and 53% were observed at two ports, 1E and 3E, located in close proximity to the bottom clay layer (lowest permeability with higher sorption capacity than the background sand). The ports immediately downgradient of the Webster, Commerce Street and F-95 soil lenses were associated with notable amounts of bioenhanced mass transport, ranging from 20-35%, indicating the impact of biotransformation on back diffusion and desorption of contaminants around/within low permeability zones. However, lower δ_{MRD} was observed at the port 4B, immediately downgradient of the Appling soil lens, which could be attributed to volatilization losses of the higher volatility of TCE biodegradation products (*cis*-DCE, VC, and ethene) (this port is located near the free surface in the aquifer cell).
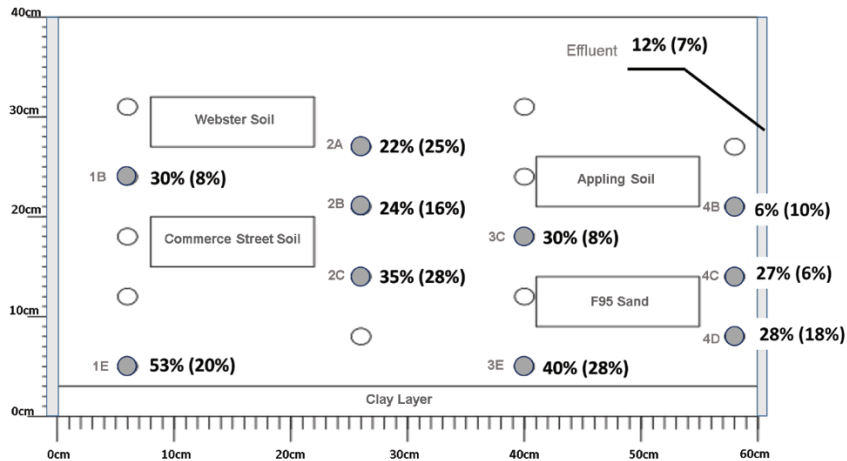
Figure R.3.7. Bioenhancement of back diffusion, δ_{MRD} (%) in effluent and selected port.

III.3.1.6. Growth of *Dehalococcoides* Population

Total *Dhc* abundance increased by greater than two orders-of-magnitude over the course of the experiment from an average over the 12 ports sampled of 2.84×10^5 ($\pm4.43\times10^5$) gene copies/mL following bioaugmentation to 3.78×10^7 ($\pm1.50\times10^7$) gene copies/mL at the conclusion of the experiment (Figure R.3.8, Appendix B.9). Although the population was uniformly distributed across the sampling ports at the beginning and end of the biotic experiment, at intermediate sampling time, 5.2 PVs (6 days) after bioaugmentation, *Dhc* cells were more abundant in downgradient ports (columns C and D) where less chlorinated ethenes (*cis*-DCE and VC) were present than in the upgradient ports (columns A and B); average *Dhc* abundances of 9.64×10^6 ($\pm6.12\times10^6$) gene copies/mL and 7.07×10^7 ($\pm4.6\times10^7$) gene copies/mL were measured in upgradient and downgradient ports, respectively. Where TCE is present, i.e. at the upgradient ports, *Geo* cells are more efficient than *Dhc* cells at transforming TCE to *cis*-DCE and outcompete *Dhc* (Amos et al. 2009; Duhamel and Edwards 2007). When *cis*-DCE and VC are the available electron acceptors, the *Dhc* population faces no competition for those election acceptors, resulting in the higher abundances observed in downgradient ports (Figure R.3.8). The uniform *Dhc* population at the conclusion of the experiment indicates a lack of competition by *Geo* in the last phase of the experiment (lowest TCE influent) as the populations were limited by a lack of electron acceptor.

In soil samples collected at the conclusion of the experiment, total *Dhc* abundance was uniform in the background sand samples (aligned near the sampling ports), averaging 6.58×10^7 ($\pm1.44\times10^8$) gene copies/4.82 g of wet soil (the mass of soil containing 1 mL of pore water). Within the lenses, Dhc abundances were 2.39×10^8 ($\pm1.49\times10^8$) gene copies/6.38g, 1.26×10^8 ($\pm7.28\times10^7$) gene copies/3.54g, 1.09×10^7($\pm1.03\times10^6$) gene copies/7.17g, 1.71×10^7($\pm5.24\times10^6$) gene copes/7.81g, and 4.06×10^6 ($\pm2.23\times10^6$) gene copies/2.14 g throughout the Appling lens, Webster lens, Commerce Street lens, F-95 sand lens, and clay layer, respectively (Appendix B.9). At the sampling port locations, the cell abundances measured in the aqueous sample and soil sample could be used to determine the number of cells attached to the soil phase. In all but 3 locations, 77 – 100% of the cells were associated with the aqueous phase. This finding is typical of cells lacking necessary growth substrates and is expected as electron acceptors (chlorinated ethenes) were depleted by the end of the experiment (Cápiro et al. 2014). Downgradient of the Webster and Appling lenses (port 4B), lenses which continued to release electron acceptor through back diffusion and desorption, 53% of the Dhc 16S rRNA gene copies measured were associated with

93

the solid phase rather than the aqueous phase. Near the influent (ports 1B and 1E), where TCE had been introduced throughout the experiment, most of the cells (90% and 74%, respectively) were attached to the solid phase as there was still sufficient electron acceptor present.
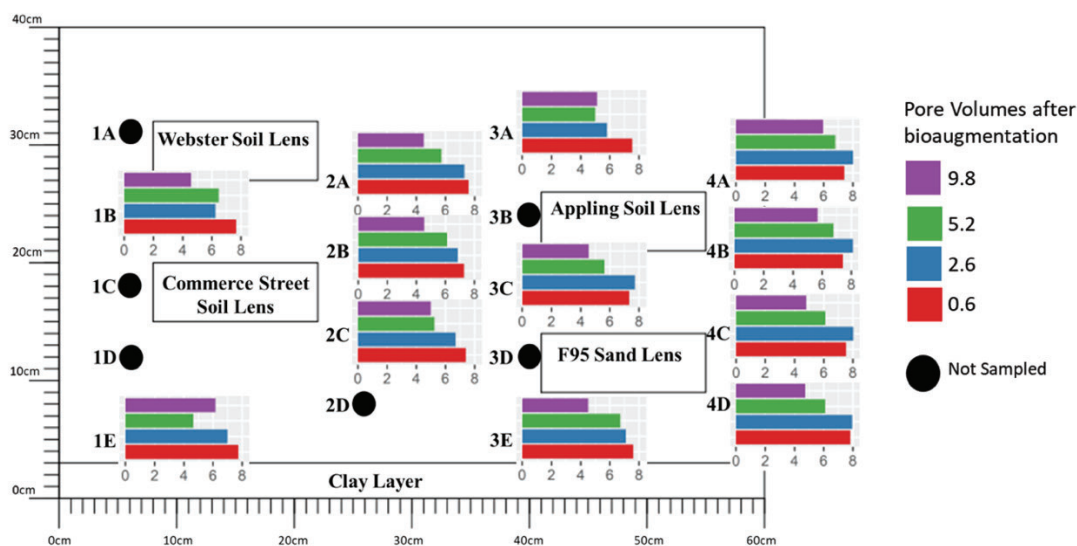
Figure R.3.8. Log aqueous Dhc abundance (gene copies/mL) in sampling ports for samples collected 0.6, 2.6, 5.2, and 9.8 PVs (2-, 8-, 16-, and 37-days) following bioaugmentation.

III.3.1.7. Distribution of RDase Genes

The *Dhc* RDase gene abundance measured in the aqueous samples varied with the type and availability of chlorinated ethenes serving as an electron acceptor as shown in Figures R.3.9. Shortly after bioaugmentation, while the influent TCE concentration was 0.5 mM, samples collected from the first column of ports, near the influent, showed a higher proportion of cells harboring the *tceA* gene (43 – 99%) while the downgradient ports consisted primarily of cells harboring the *vcrA* gene (62 – 99%), all values as percentage of total RDase genes. In the subsequent samples, 2.6 PVs (8 days) following bioaugmentation and prior to reducing the concentration of TCE in the influent to 0.04 mM, samples from ports where TCE was predominant (1B, 1E, 2A, 2B, 2C, 3C, 4D) contained cells harboring a combination of all three RDase genes (28-54% *vcrA*, 27-53% *bvcA*, 12-45% *tceA*) while ports where *cis*-DCE and VC concentrations were highest (3E, 4A, 4B) mostly contained cells harboring the *vcrA* gene (70-95% *vcrA*, 4-30% *bvcA*, 0-3% *tceA*). The remaining two ports (3A, 4C) had not yet formed measurable concentrations of VC and contained a higher abundance of cells harboring *tceA* (67-85%) at the expense of *vcrA*. After reducing the influent TCE concentration, in samples collected 5.2 PVs (16 days) after bioaugmentation (Figure R.3.9), cells harboring the *bvcA* and *tceA* were in excess of 35% of the total cells harboring *Dhc* RDase genes only in the first column of ports (1B, 1E) and immediately downgradient of the organic carbon-containing Webster and Commerce Street soil lens (ports 2A, 2C), locations where TCE and *cis*-DCE were present in the highest concentrations.

94
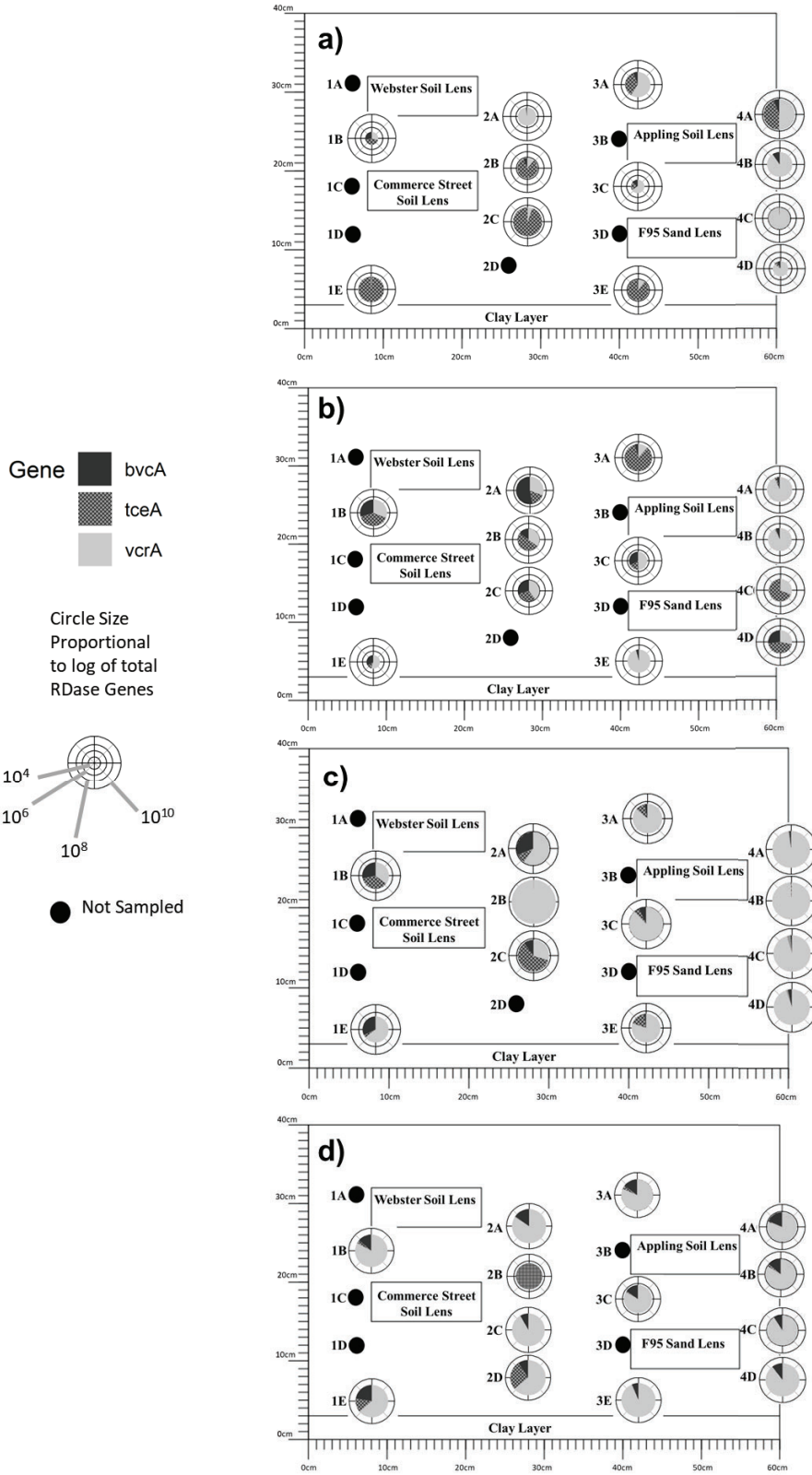
Figure R.3.9. Aqueous RDase abundance and composition(a) 0.6 PVs (2 days) following bioaugmentation (b) 2.6 PVs (8 days), (c) 5.2 PVs (16 days) following bioaugmentation, and (d) final aqueous samples, 9.8 PVs (37 days) following bioaugmentation.

95

By the end of the experiment, 9.8 PVs (37 days) following bioaugmentation and 1.8 PVs (8 days) after lowering the influent TCE to 0.01 mM, aqueous samples collected in all but 2 ports had a similar proportion of cells harboring the *bvcA* and *vcrA* genes (81-92% *vcrA,* 6-18% *bvcA,* 0-4% *tceA*). In the samples above the clay layer (1E, 2D), where TCE continued to diffuse out, cells harboring *tceA* continued to make up a larger proportion of RDase genes than in the other port locations (14-27%) while those harboring the *vcrA* gene made up a smaller proportion than in the other port locations (64%).

The presence of and associated mass transfer from the lenses impacted the growth of specific *Dhc* strains and the associated detection of predominant RDase genes by altering the transport and mass transfer of chlorinated ethenes. In locations where TCE was present, cells harboring the *tceA* gene were detected early in the experiment, then, as the terminal electron acceptor shifted to less chlorinated ethenes, cells harboring the *vcrA* gene predominated over other strains. The proportion of cells harboring the *bvcA* gene varied from 0 to 53% of the total RDase genes. The relative abundance of cells harboring *bvcA* was greater in locations where *cis*-DCE was available as an electron acceptor, downgradient of the low permeability lenses when influent TCE was high (0.5 mM) and near the influent when influent TCE was reduced to 0.04 mM. Overall, the abundance of RDase genes exceeded the abundance of *Dhc* 16S rRNA genes by an average of 3.64-fold ($\pm$5.61) as has been observed previously (Cápiro et al. 2015; Damgaard et al. 2013a; Van Der Zaan et al. 2010).

In soil samples collected at the conclusion of the experiment, nearly all of the cells in the background porous media harbored the *vcrA* gene (75-100%) (shown in Figure R.3.10), consistent with the findings in the aqueous sampling ports. In ports 2B (near the Commerce Street lens) and 2E (above the clay layer), cells harboring the *tceA* gene made up a larger proportion of the total (27-36% *vcrA*, 1-2% *bvcA,* 62-73% *tceA*). There were variations in the proportions of RDase genes detected within the various porous media. In the clay layer, cells harboring *bvcA* were predominant (13-45% *vcrA,* 47-83% *bvcA*, 2-6% *tceA*). In the deep clay sample near the influent chamber, the location with the highest TCE and *cis*-DCE concentrations (2.7 and 95 µg/g, respectively), *tceA* was the only RDase gene detected at the conclusion of the experiment. *Dhc* cells harboring the *bvcA* gene were also predominant along the top and downgradient edges of the Commerce Street (94-96%) and F-95 sand lenses (44-73%), both low permeability lenses with low organic carbon. The downgradient edge of the Appling soil lens also had a higher proportion of cells (32%) harboring the *bvcA* gene than the samples collected from the background sand around the lens (0.02% to 14%). In the middle of the Webster, Commerce Street, and F-95 lenses, cells harboring *tceA* were present at the end of the experiment consisting of 15%, 19%, and 45% of the total RDases in each lens, respectively. The total gene copies contained in each sample are presented in Appendix B.9.

The spatial variation in the proportion of cells harboring each RDase gene can be explained in terms of the hydraulic and sorptive properties of the lens materials and the effect of these properties had on the mass transfer of electron acceptors (i.e. chlorinated ethenes). The Webster and F-95 lenses had the lowest hydraulic conductivity, impeding the flushing of TCE from these lenses and resulting in longer exposure of cells to TCE and *cis*-DCE, thus favoring cells harboring the *tceA* and *bvcA* gene. Although Appling soil has a hydraulic conductivity comparable to the Commerce Street material, its position downgradient of the influent caused TCE to be flushed from the lens rapidly, favoring *Dhc* cells harboring the *vcrA* gene (87%). The overall abundance of RDase genes was approximately 1 order-of-magnitude lower in the clay, 2.53×10^6 ($\pm 1.3 \times 10^6$) gene copies/g, when compared with the background porous media and lenses (2.52×10^7 ($\pm 4.9 \times 10^7$) gene copies/g), likely due to the slower diffusion of electron donor into the clay and the probability of

a smaller initial biomass due to limited penetration of the inoculum into the clay during bioaugmentation.
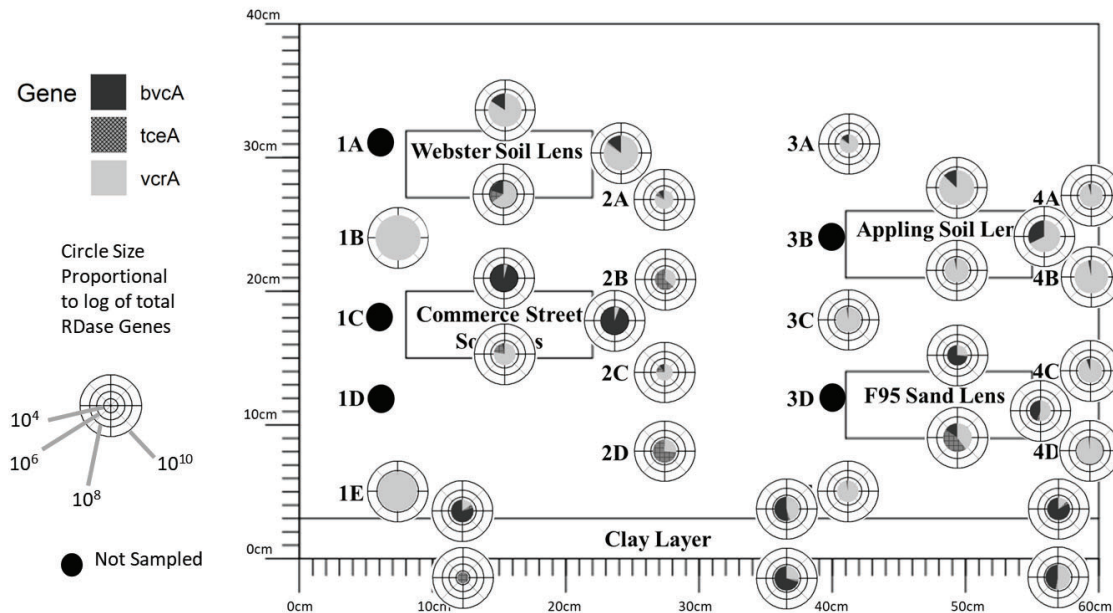
Figure R.3.10. RDase abundance and composition in soil samples at end of experiment, 9.8 PVs (37 days) following bioaugmentation.

As with the total *Dhc* abundance, nearly all of the *vcrA* and *bvcA* genes measured at port sample locations were associated with the aqueous phase samples (93% to 100%) with a few exceptions. In ports 1B, 1E, and 4B, 45% to 87% of the *vcrA* genes detected were associated with the solid phase, likely due to the accessibility of electron acceptor near the influent and to that desorbing from the organic carbon in the Webster soil lens. Cells harboring the *tceA* gene were associated with the solid phase (31% to 100% attached) in all locations but four, indicating that cells harboring *tceA* may be able to remain attached even when lacking a growth substrate. In ports 1B, 2B, 4C, and 4D, only 0% to 7% of the *tceA* genes measured were associated with the solid phase. These are locations that are not impacted by the clay or high organic carbon lenses, had the lowest total ethene, and were regions facing the greatest electron acceptor limitation.

III.3.2. Second Aquifer Cell; Experiment and Modeling Results

III.3.2.1. Modeling of the Second Aquifer Cell and Flow Field

The second aquifer cell domain (Figure R.3.11) was constructed to incorporate the experimental multi-layer packing configuration, as well as the flow distribution system, using the same approach employed for the first aquifer cell experiment, described in Section III.3.1 above. Higher hydraulic conductivity (6 orders-of-magnitude lower than that of the Commerce Street soil) was assigned to the first and last column of the numerical grid cells, which represented the flow chambers. In order to simulate the controlled head gradient created by drop tubes in the influent and effluent chambers, the numerical grids at the inlet and outlet locations of the tubes were assigned as constant head/concentration cells. A refined uniform grid spacing (5 mm (length) × 2 mm (height)) was applied in the upstream-weighting implicit finite difference scheme to resolve transport processes, ensure computational stability, and improve predictive accuracy.
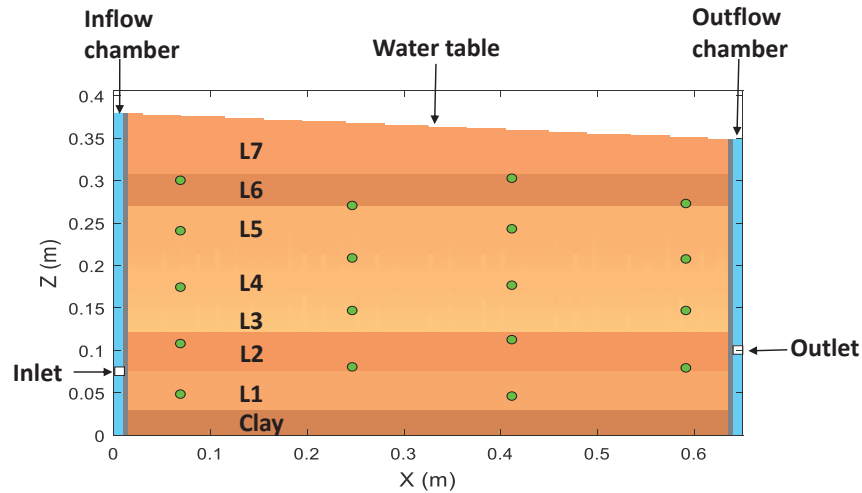
Figure R.3.11. Second Aquifer cell construction for numerical simulation

Experimental data from the non-reactive tracer experiment were used in conjunction with the numerical model to characterize the flow field. Porosities were estimated by using soil mass and soil volume emplaced in the aquifer cell. A set of hydraulic conductivities was initially estimated by using the time-lapse tracer images of concentration front travel distance, in conjunction with, head gradient measurements. The estimated material properties are provided in Table R.3.2. A longitudinal dispersivity of 0.1 cm and a vertical to longitudinal dispersivity ratio of 0.1 were employed, following Lyon-Marion et al. (2017). The simulated results were compared qualitatively with the experimental effluent BTC and visually with photographed tracer images to examine the suitability of these parameters.

Table R.3.2. Parameters for soil properties used in 2nd aquifer cell modeling

Porous Media	Hydraulic Conductivity (m/day)	Porosity, ϕ(-)
L7	1.16	0.45 (0.51)[a]
L6	0.58	0.51
L5	1.47	0.45
L4	2.31	0.45
L3	2.79	0.45
L2	0.69	0.4
L1	1.47	0.5
Clay	0.11	0.56

[a] The porosity of L7 was adjusted to fit tracer data. The adjusted value in the parentheses was used in the model.

A few other chemical property parameters were obtained from literature and kept fixed in the model (Table R.3.3). $K_{d,TCE}$ was set as as 0.12 L/kg and 0.35 L/kg for upper layer materials and the clay, respectively, consistent with batch sorption measurements in section III.1.11 (Gaeth 2017). The $K_{d,DCE}$ and $K_{d,VC}$ were obtained by scaling $K_{d,TCE}$ based on the ratio of $K_{oc,i}/K_{oc,TCE}$, where $K_{oc,i}$ is organic carbon partitioning coefficient (L^3/M) for component i. Ethene, lactate, and H$_2$ were assumed to be non-sorptive constituents.

Table R.3.3. Chemical component properties for 2nd aquifer cell modeling

Properties	mw^a (gram/mole)	$D_m{}^a$ (m²/day)	$K_{oc}{}^b$ (L/kg)
TCE	131.4	6.90e-5	126
DCE	96.94	7.80e-5	48
VC	62.5	9.20e-5	26
ETH	28.05	1.16e-4	-
LAC	89.07	1.27e-4	-
H₂	2.01	3.32e-e	-

[a] D_m is the molecular diffusivity. Parameters from Christ and Abriola (2007) and Chen et al. (2013).
[b] From Mackay et al., 2006.
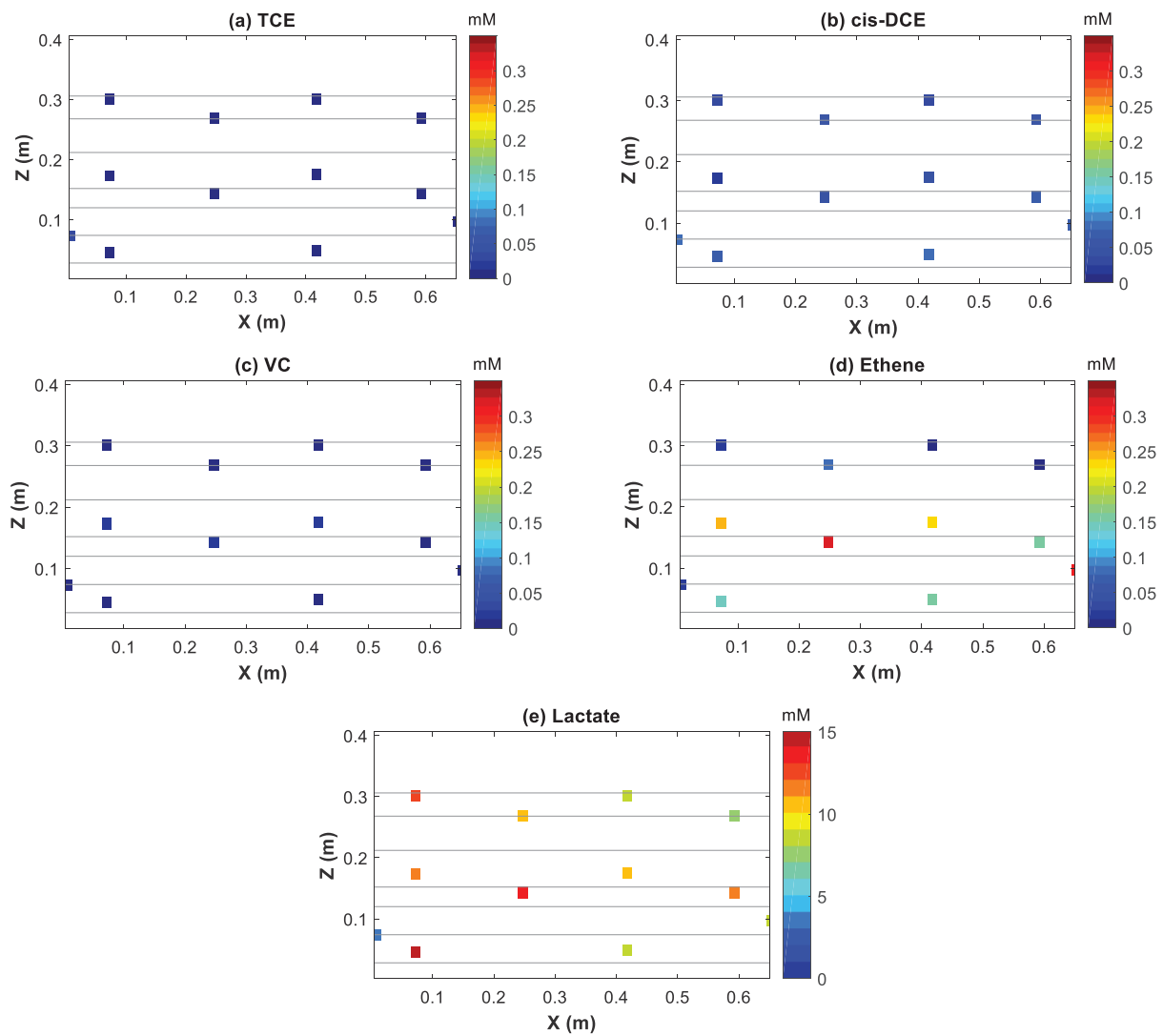
Figure R.3.12. Measured initial ports concentration for chemical components, (a) TCE, (b) cis-DCE, (c) VC, (d) ethene, and (e) lactate.

Table R.3.4. Batch-calibrated parameters used in the Monod kinetics model for reductive dechlorination.

Parameter	Microcosm	Literature[d]
$k_{max,i}$ (μmol/(mg-cell d))		
TCE	330	2.4-366
DCE	80	1.7-48
VC	210	2.6-48
LAC	60[a]	120
$K_{s,i}$ (μM)		
TCE	1.0	0.54-1.5
DCE	1.9	0.54-3.3
VC	180.0	0.54-360
H_2-GEO	0.1[c]	0.015-0.1
H_2-DHC	0.1[c]	0.015-0.1
LAC	2.5[b]	2.5
$K_{I,i}$ (μM)		
TCE	$= K_{S,TCE}$	-
DCE	$= K_{S,DCE}$	-
VC	$= K_{S,VC}$	100-500
Y_i (mg-cell/mmol)		
TCE	9.6	3.3-22.6
DCE	2.9	3.3-9.8
VC	1	3.3-9.8
LAC	4[b]	1.5-6.3
$C_{H,th,j}^{a}$ (nM)		
GEO	2[c]	-
DHC	2[c]	-
$k_{b,j}$ (1/day)		
GEO	0.05	0.05-0.1
DHC	0.05	0.05-0.1
FEM	0.05	0.05-0.1

[a] Not simulated in the microcosm model. Fitted in the aquifer cell model.
[b] Not simulated in the microcosm model. Taken from Fennell and Gossett (1998), adjusted form 35 °C to laboratory temperature.
[c] Not simulated in the microcosm model. Taken from Christ and Abriola (2007).
[d] Taken from Clapp et al. (2004), Lee et al. (2004), Christ and Abriola (2007), and Chen et al. (2013). Literature values for lactate were taken from Fennell and Gossett (1998) and Chen et al. (2013).

For the second aquifer cell model, the initial time was set to be the end of the recirculation phase or the beginning of the flushing period (Table M.4.3). Transformation rate parameters, half saturation constants ($K_{s,i}$), inhibition constants ($K_{I,i}$) and microbial yield coefficients (Y_i) were adopted from the microcosm modeling (section III.2.2) and used as initial values in the aquifer cell

model. The average of $k_{max,i}$ for the three microcosm trials was used for initial simulations (Table R.3.4). The fermentation process was not simulated in the microcosm model, as electron donor was assumed to be in excess. Thus, rate parameters for lactate transformation in the aquifer cell were obtained from the literature ($K_{s,LAC}$, and Y_{LAC}) or fit to match the experimental lactate concentration ($k_{max,LAC}$). Side port measurements of chemical and biomass concentrations (Figure R.3.12 and R.3.13) were processed by using a 2-D scatter data interpolation algorithm, "griddata" (MATLAB, The Mathworks, Natick, MA), to obtain initial concentration contours used in the aquifer cell model (Figure R.3.14 and R.3.15).
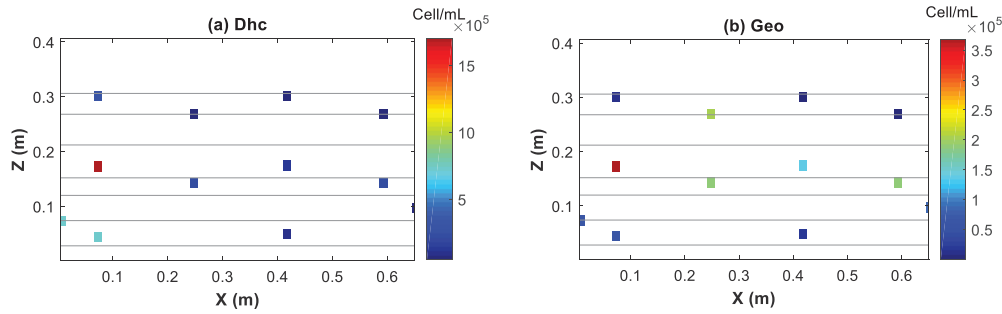
Figure R.3.13. Measured initial ports biomass concentration for dechlorinators: (a) Geo, and (b) Dhc
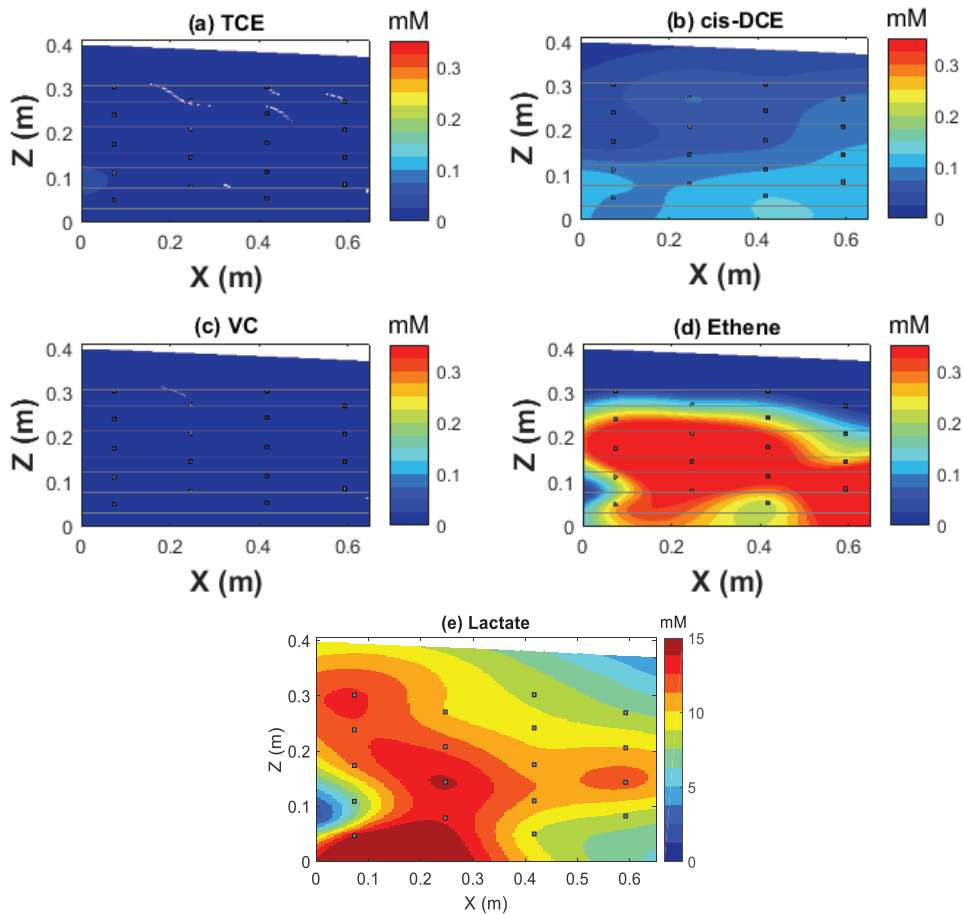
Figure R.3.14. Interpolated initial concentration for chemical components, (a) TCE, (b) cis-DCE, (c) VC, (d) ethene, and (e) lactate.
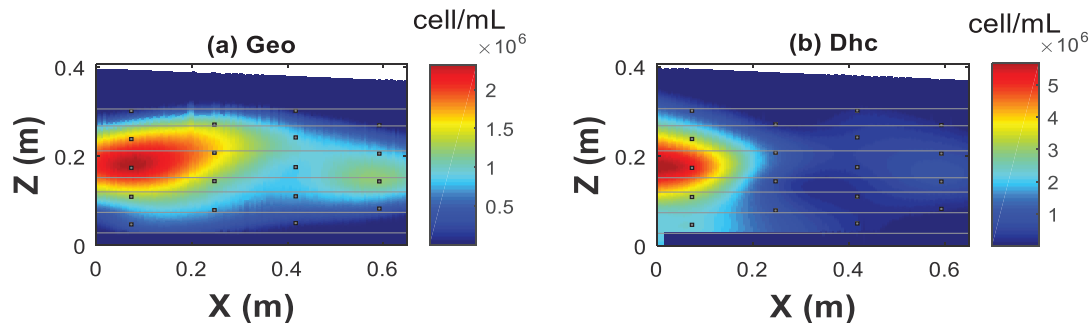
Figure R.3.15. Interpolated initial biomass concentration for dechlorinators: (a) Geo, and (b) Dhc.

III.3.2.2. Modeling the Bromide Tracer Test

The bromide tracer test data exhibited significant tailing in the effluent samples (Figure R.3.16) and a maximum bromide concentration of 40% of the influent concentration. Photographs of the erioglaucine A (blue dye) tracer experiment revealed the existence of a layer of higher permeability in the center of the aquifer cell, corresponding to soil from the 33 to 34 ft bgs depth of borehole DHT-2 (Figure R.3.17). Transport through this higher permeability layer was assumed to have created the early peak in the effluent bromide tracer curve and subsequent tailing, as bromide was slowly flushed from the lower permeability layers above and below it. Using the set of the estimated parameters, the model was able to provide a reasonable fit to the experimental BTC with a calculated normalized root mean square error of 32% (Figure R.3.16).
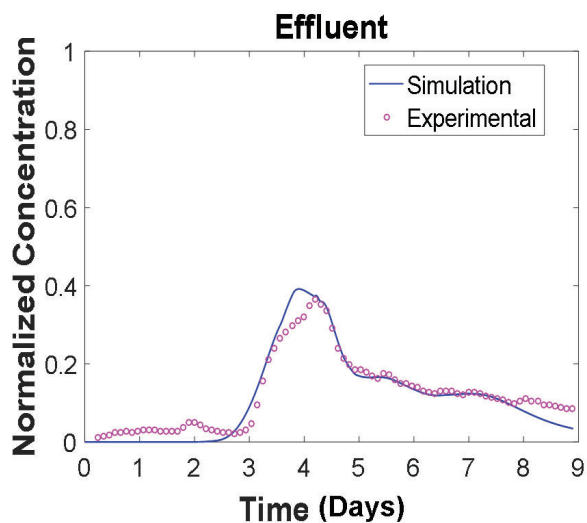
Figure R.3.16. Comparison of experimental and model simulated effluent BTC. Experimental data: pink circle; Model simulation: blue solid line.

The simulated BTC matched the general shape and arrival time of experimental BTC but displayed discrepancies in terms of peak concentration and tailing concentration at the end, possibly due to variations in layer configuration. It is difficult for the model to numerically characterize the detailed changes of layer shape introduced during the packing processes. The mismatch in early time concentration before tracer breakthrough was likely caused by a preferential flow pathway allowing a small proportion of influent solution to bypass the porous media. A small area of blue dye (erioglaucine A) was observed at the bottom of the effluent screen in a photo taken 5.4 hours after beginning the tracer test (Figure R.3.17). The adequacy of the estimated parameters was confirmed by a visual inspection between simulated and photographed concentrations (Figure

R.3.17). Minor adjustment was made to the porosity of L7 to improve the goodness of fit, associated with possible loose packing and air entry in the top (Table R.3.2). In summary, the simulation results displayed good agreement with experiment data, ensuring the credibility for follow-up simulations of reductive dechlorination.
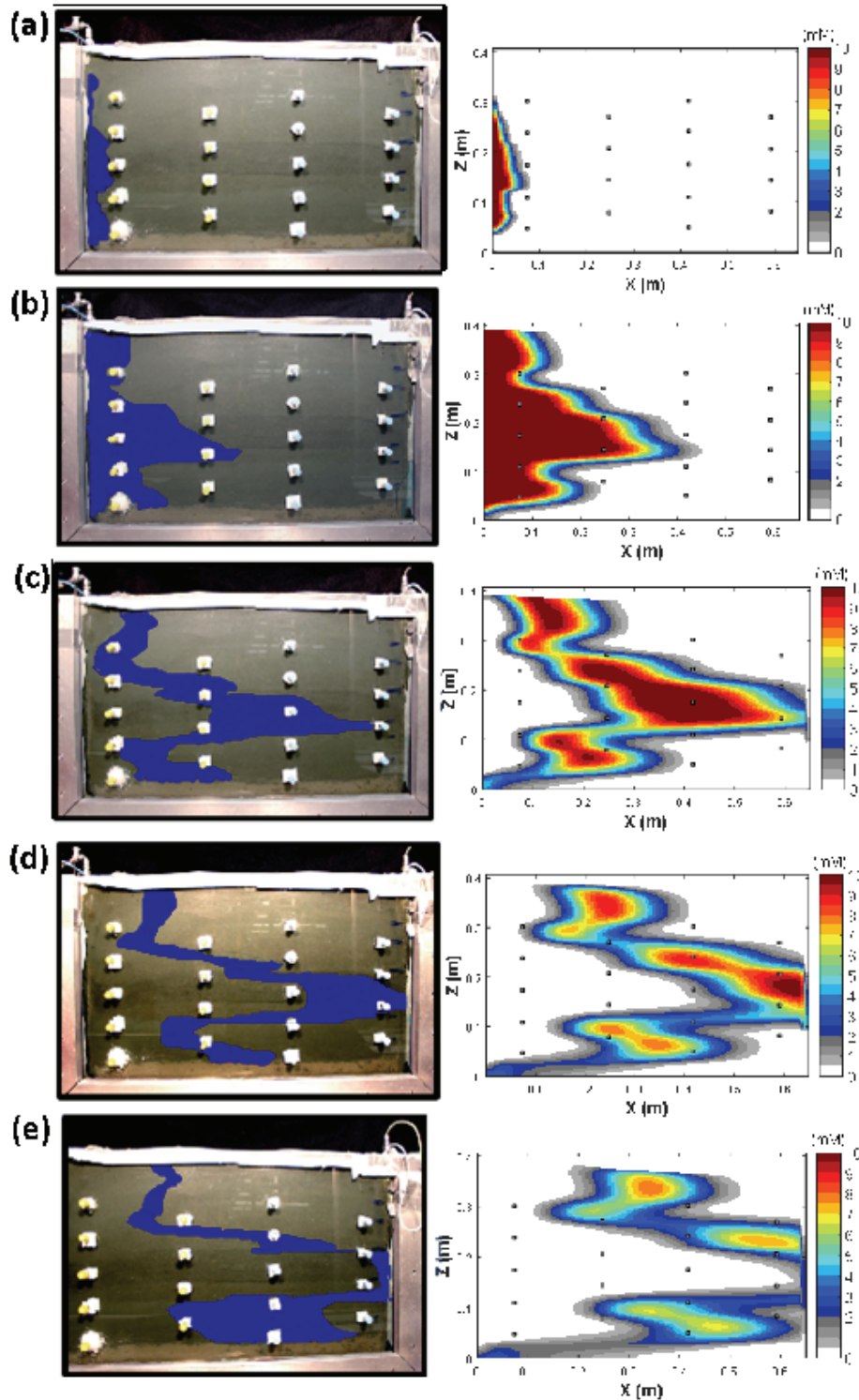
Figure R.3.17. Photographed (left) and simulated (right) tracer concentration for selected time: (a) hour 5.4, (b) day 1.8, (c) day 3.1, (d) day 4.1, and (e) day 4.9. Color in the photos is enhanced.

III.3.2.3. VOC and VFA Results

The chlorinated ethene and ethene concentrations measured in aquifer cell effluent samples are shown on Figure R.3.18. As soon as lactate was introduced to the aquifer cell, at the beginning of recirculation, TCE was transformed to *cis*-DCE by the native microbial population, similar to the results of the microcosm experiments. After bioaugmentation, TCE was no longer detected and effluent ethene concentrations began to increase. The ethene concentration peaked at the end of the recirculation phase as chlorinated ethenes were reintroduced in the influent as *cis*-DCE and VC and had additional time to be dechlorinated. After recirculation, when lactate was no longer being introduced, effluent ethene concentrations dropped and *cis*-DCE and VC concentrations began to increase.
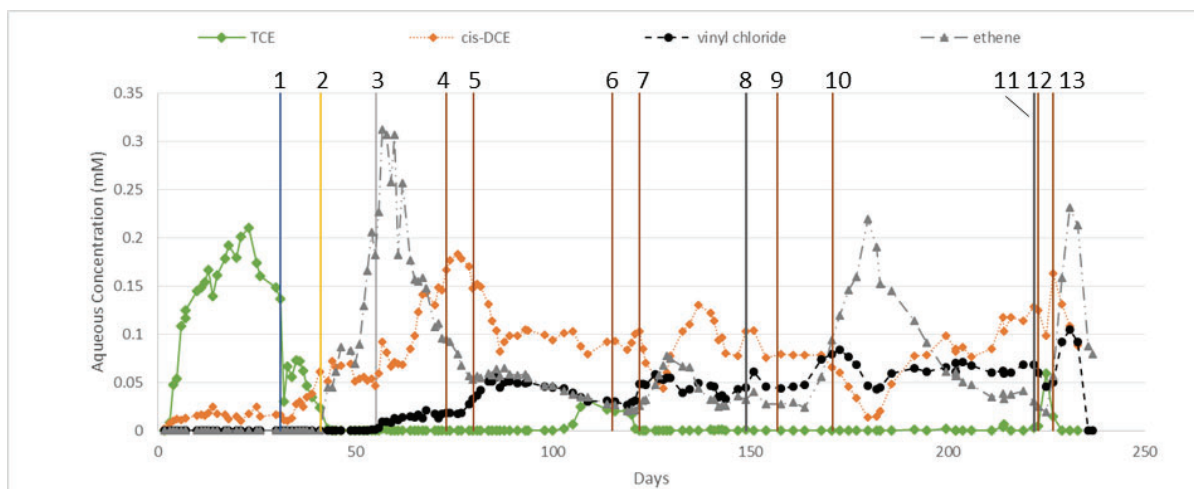
Figure R.3.18. Chlorinated ethene and ethene concentrations in Commerce Street Aquifer Cell effluent. Vertical lines represent, from left to right: 1. Beginning of recirculation with lactate; 2. Bioaugmentation 3. End of recirculation; 4. Beginning of lactate pulse; 5. End of lactate pulse; 6. Beginning of lactate pulse; 7. End of lactate pulse; 8. Decrease in flow rate; 9. Beginning of lactate pulse; 10. End of lactate pulse; 11. Increase in flow rate; 12. Beginning of lactate pulse; 13. End of lactate pulse.

After each lactate pulse, *cis*-DCE was partially transformed to VC and ethene. When the aquifer cell rate flow rate was reduced to 0.05 mL/min (16 day residence time), more of the influent TCE was transformed to ethene with effluent concentrations of 5% *cis*-DCE, 17% VC, and 78% ethene on a molar basis compared to 60% *cis*-DCE, 23% VC, and 17% ethene when the residence time was 37 days (0.1 mL/min flow rate). The flow rate was then increased to 0.15 mL/min for 16 days to complete a final bromide tracer test. A 5 mM lactate pulse was introduced concurrent with the bromide tracer. With the faster flow rate and shorter residence time (25 days), the proportion of ethene in the effluent decreased to 54% while the VC and *cis*-DCE proportions increased to 23% and 22%, respectively. VC and ethene concentrations peaked approximately 1 PV after each lactate pulse, then declined as electron donor became limited. Between the first and second lactate pulses, 35 days (approximately 5 pore volumes) elapsed allowing a small amount of TCE (up to 18% on a molar basis) to past through the aquifer cell untransformed. The fact that a majority of the TCE introduced into the aquifer cell was transformed into *cis*-DCE, VC, and ethene after each lactate pulse suggests that electron donor was present in the background groundwater solution as organic carbon. Analysis of VFAs in the aquifer cell effluent revealed large spikes in VFA concentration, primarily acetate, lasting 1 to 2 pore volumes after each lactate pulse, after which VFAs were no longer detected, providing further evidence that other forms of organic carbon are serving as an electron donor (Figure R.3.19).
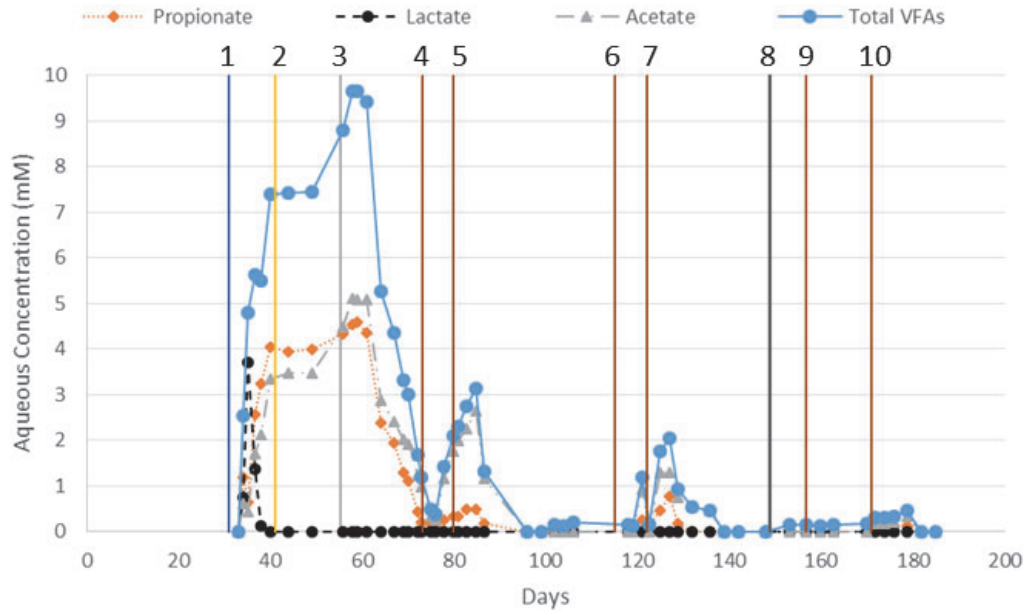
Figure R.3.19. VFA concentrations in Commerce Street aquifer cell effluent. Vertical lines represent, from left to right: 1. Beginning of recirculation with lactate; 2. Bioaugmentation 3. End of recirculation; 4. Beginning of lactate pulse; 5. End of lactate pulse; 6. Beginning of lactate pulse; 7. End of lactate pulse; 8. Decrease in flow rate; 9. Beginning of lactate pulse; and 10. End of lactate pulse.

III.3.2.4. Modeling Reductive Dechlorination in the Second Aquifer Cell

The set of hydrogeological parameters obtained from calibration to the tracer test was used, in conjunction with dechlorination rates from the microcosm experiments, as inputs for the enhanced version of MT3DMS to simulate dechlorination after recirculation. Modeling results (Figure R.3.20) revealed that application of microcosm-derived parameters did not yield good agreement (average relative error of 108%) with aquifer-cell observations of chlorinated ethenes and ethene concentrations. Specifically, production of VC was overpredicted by a factor of 4 and production of ethene was underpredicted by a factor of 5. The predicated behavior was associated with the competitive inhibition imposed on VC transformation.
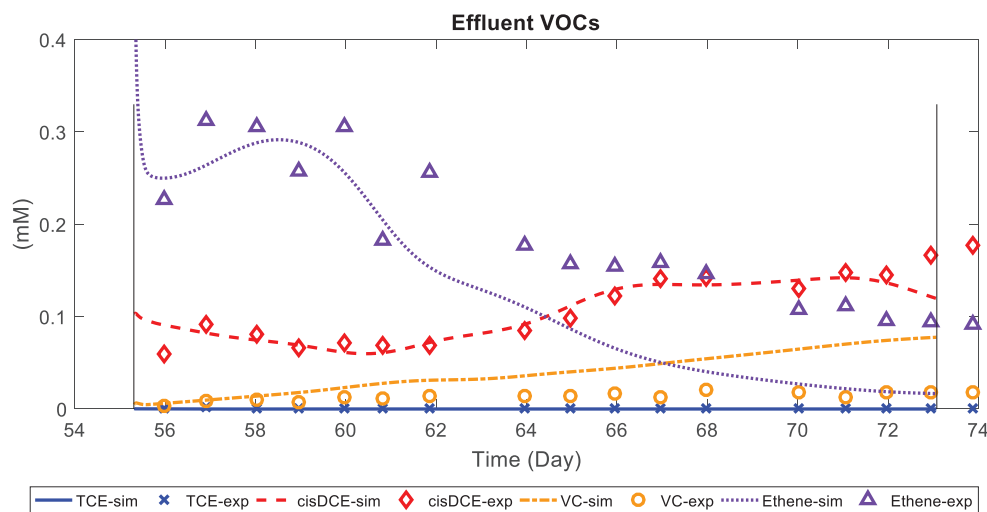
Figure R.3.20. Comparison between simulated and experimental effluent concentrations for chlorinated ethenes and ethene by using Mircrocosm-fitting parameters.

105

A better fit to the experimental observations was obtained with relative errors of 16%, 19%, 40% and 20% for *cis*-DCE, VC, ethene and lactate by removing the competitive inhibition on transformation of *cis*-DCE and VC (Figure R.3.21). A close match to the experimental concentration of *cis*-DCE and ethene was achieved through the simulated period, while ethene concentration was under-predicted, but came close to the observed data at the end. The large predictive error for ethene could be attributed to the uncertainty in interpolating the initial ethene and biomass concentrations. Specifically, the lack of sampling ports in L7 and the clay layer could have potentially led to underprediction of the total initial mass of ethene and dechlorinators. Prediction of *cis*-DCE and VC was likely less sensitive to their initial concentrations which were lower than that of ethene. Fitting of the lactate concentration confirmed the appropriateness of the parameters used in fermentation Monod kinetics.
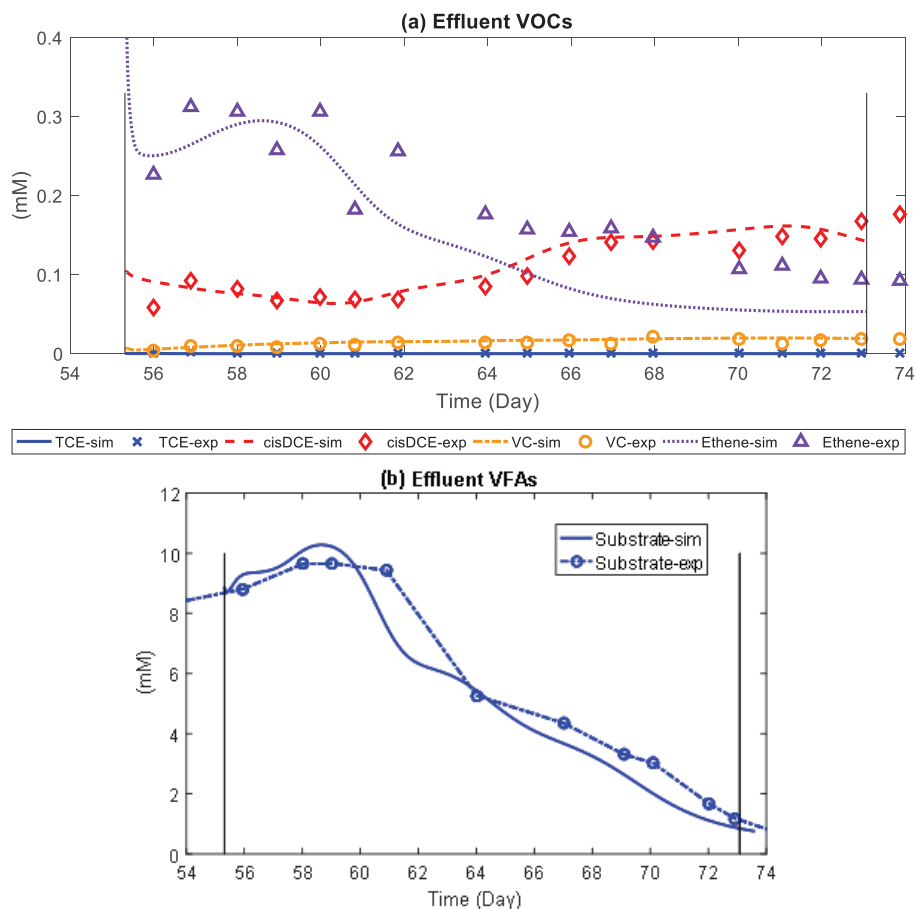
Figure R.3.21. Comparison between simulated and experiment effluent concentrations for (1) chlorinated ethenes and ethene components, and (b) lactate. Competitive inhibition in the Monod kinetics was removed in this simulation.

The simulation results displayed little sign of inhibition between chlorinated products, which was contrary to the batch experimental observations. The aquifer cell system with a realistic ratio of porous media to aqueous phase may provide microenvironments to protect microbial cells from inhibitory high concentrations, while the microcosm system with a lower ratio of soil to water could potentially expose microbial cells to sudden changes of conditions in the aqueous phase. Microcosm simulation with removal of inhibition did not yield good matches to the experimental data (Figure R.3.22), which further supports the hypothesis of different inhibition behavior in the well-mixed, aqueous dominated and more complex, porous media-dominated systems.
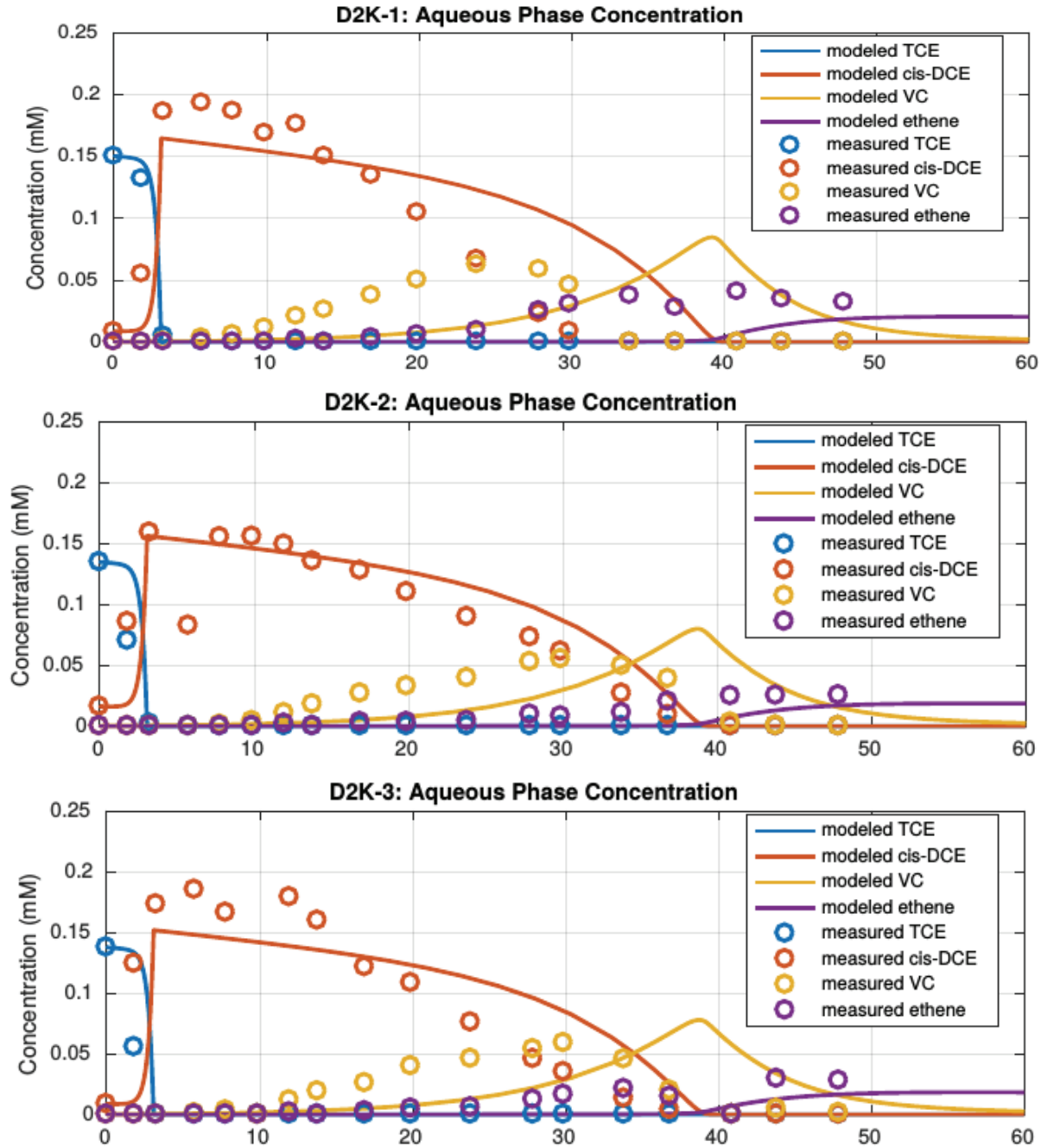
Figure R.3.22. Microcosm simulation with removal of competitive inhibitions for a triplet experiment of the KB-1 culture.

III.3.2.5. Modeling the Influence of Heterogeneity on Reductive Dechlorination

An additional simulation was conducted for a homogeneous domain, with averaged hydraulic conductivities, and porosities to explore the influence of soil heterogeneity on reductive dechlorination. Comparison of simulation results for models employing both heterogeneous and uniform domain properties, incorporating the same domain size and transformation rate parameters, reveals that ethene production was under-predicted by the uniform property model (Figure R.3.23). *cis*-DCE concentrations were first under-predicted and then over-predicted.

Coupling of laboratory observations with these modeling results suggests that transformation to ethene varied spatially within the domain, primarily associated with low permeability layers (Figure R.3.24). On one hand, the low permeability zones provided longer residence times for complete dechlorination, which was rate-controlled. On the other hand, they acted as reservoirs to supply electron donor when substrates in the permeable zones were depleted. This variation in transformation productions between the two simulations demonstrates the influence of local heterogeneity on dechlorination prediction accuracy. The results also suggest that sparse sampling at field sites will necessarily result in models that use average soil properties and will increase prediction uncertainty
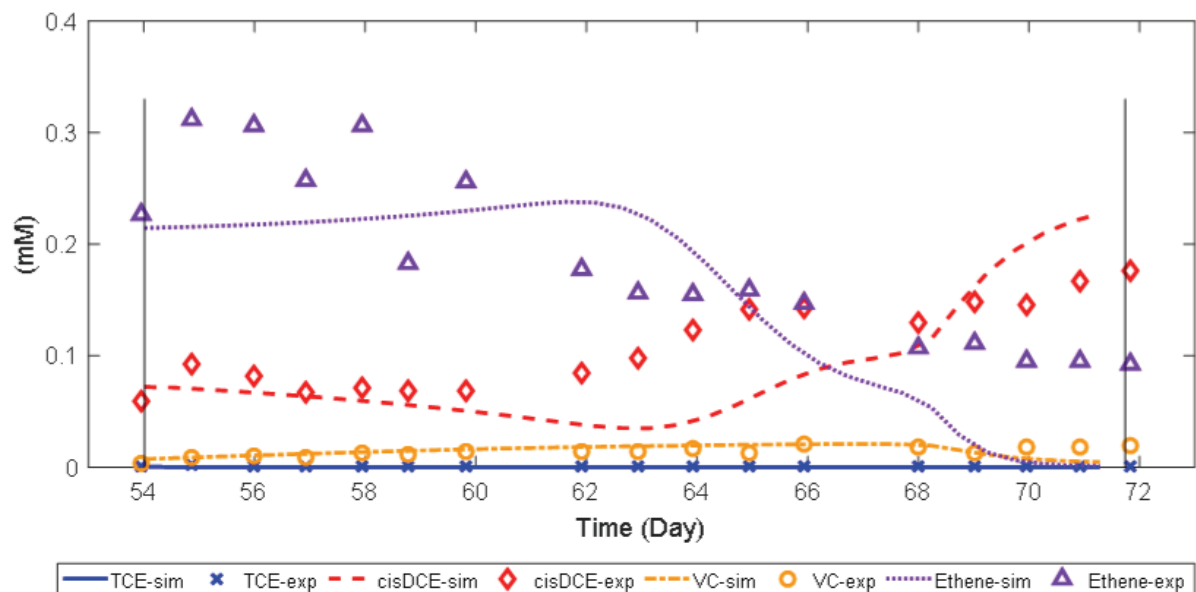
Figure R.3.23. Model prediction in homogeneous domain with uniform soil properties.

III.3.2.6. Growth of *Dehalococcoides* Population

Dhc abundance was measured in aqueous samples collected from the sample ports at three times during the aquifer cell experiment: 1 to 2 days before the end of recirculation, 20 to 25 days after the first lactate pulse, and at the conclusion of the experiment. These data exhibit little change in the total *Dhc* abundance, with an average across the ports of 3.26×10^8 ($\pm 5.02 \times 10^8$), 7.80×10^8 ($\pm 1.68 \times 10^9$), and 2.69×10^8 ($\pm 2.59 \times 10^8$) 16S rRNA gene copies/L in each round of sampling, respectively (Figure R.3.25). The data suggest that a sufficient population of *Dhc* was distributed throughout the aquifer cell during recirculation and remained relatively constant over the course of the experiment. Although there may have been an increase in *Dhc* abundance during lactate pulses, the samples analyzed did not include these time points.
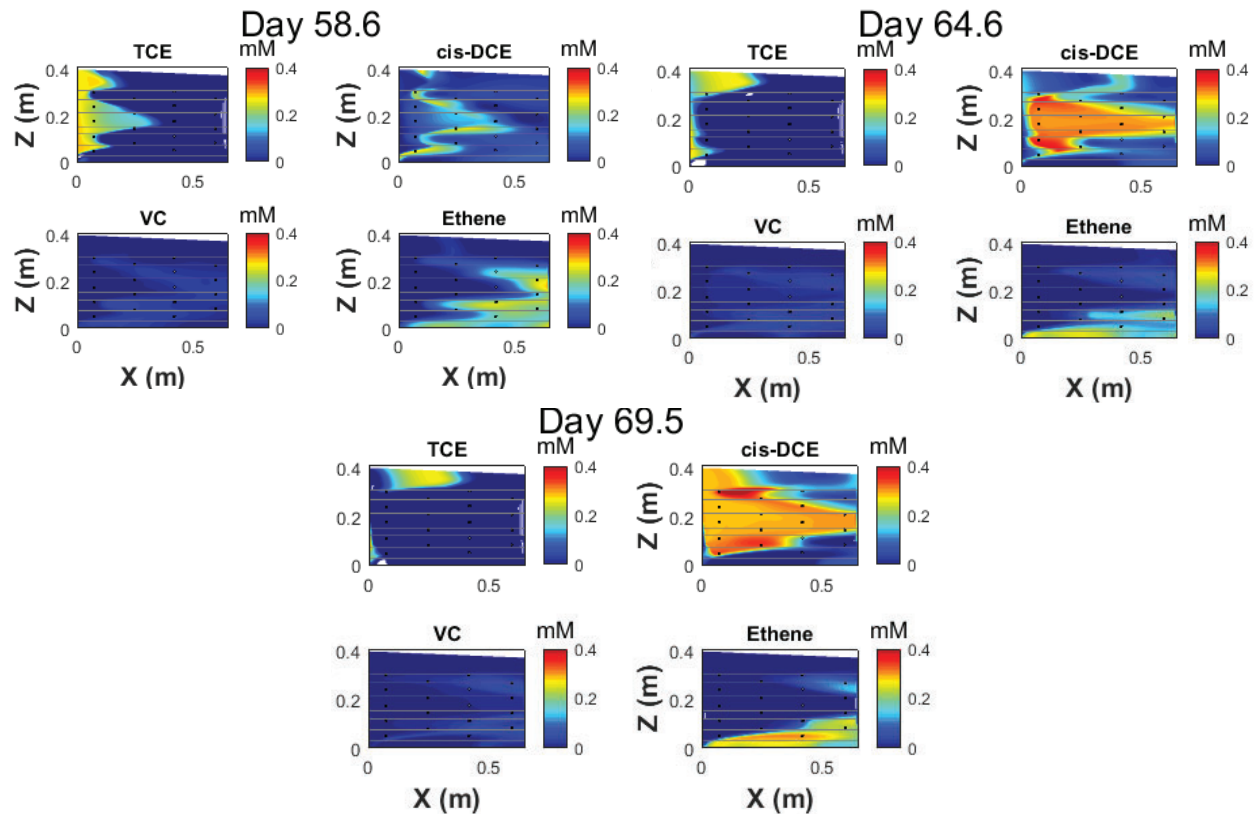
Figure R.3.24. Simulated concentrations for chlorinated ethenes and ethene in heterogeneous domain at day 58.6, day 64.6 and day 69.5.
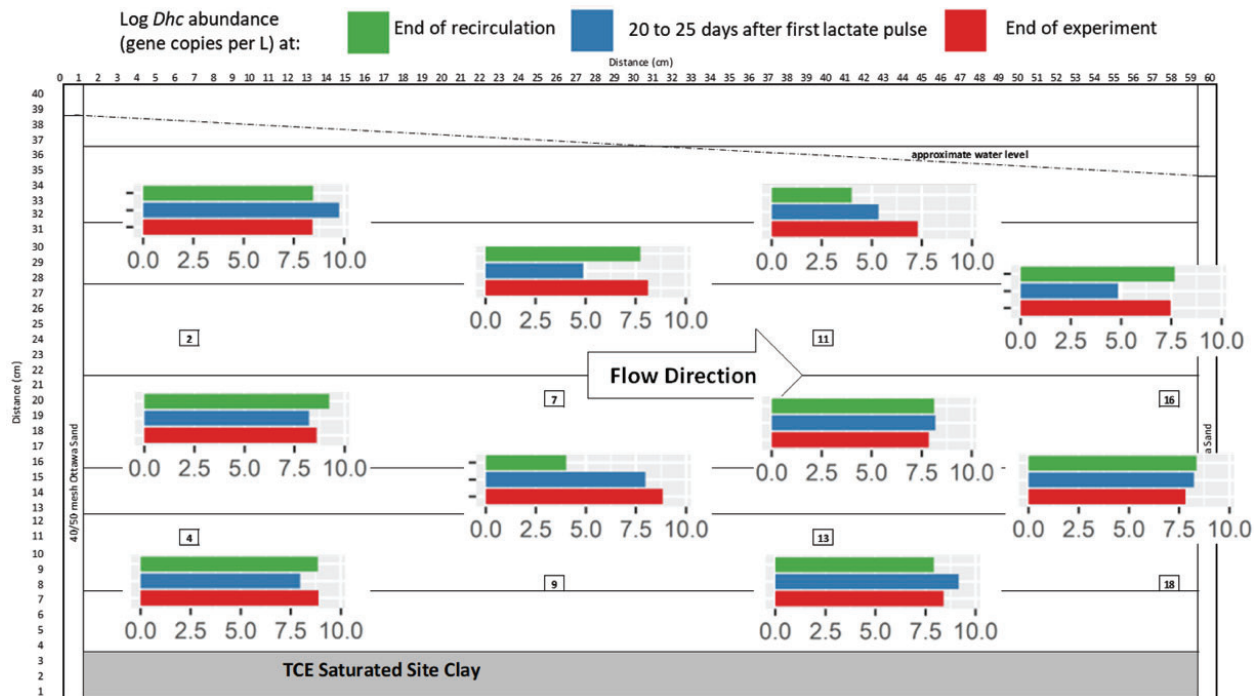
Figure R.3.25. Commerce street aquifer cell Log Dhc abundance (16S rRNA gene copies per L) in port aqueous sample 1 to 2 days before the end of recirculation, 20 to 25 days after the first lactate pulse, and at the end of the experiment.

III.3.3. Conclusions

This first aquifer cell experiment quantified the contribution of bioenhanced back diffusion to the overall mass flux of chlorinated solvents from porous media, knowledge that will allow predictions of bioremediation performance to incorporate bioenhanced desorption and back diffusion and, thus, improve the accuracy of predicting cleanup times. By accounting for this bioenhancement, predicted cleanup times will be reduced and bioremediation can be proposed as a remedy for sites where chlorinated solvent mass is stored in low permeability or highly sorptive materials.

The shift in the predominant strain of *Dhc* with changes in electron acceptor abundance demonstrates the importance of maintaining a robust dechlorinating community harboring multiple RDase genes. If the necessary genes are present, the microbial population is able to adapt to changes in electron acceptor availability caused by the transport of chlorinated ethenes out of low permeability and highly sorptive soils, even if these locations have not been identified due to the paucity of samples, typical of field applications. These population shifts will allow efficient transformation of chlorinated solvents to ethene over the course of a bioremediation application.

The successful implementation of bioaugmentation and biostimulation in an aquifer cell packed with porous media lens with a range of hydraulic permeabilities and organic carbon content revealed that:

- Heterogeneity in hydraulic conductivity and organic carbon content affected the rate of contaminant mass transfer, especially the rate and capacity for contaminant sorption, controlling the back diffusion of sequestered mass from low permeability zones.

- Organohalide respiring bacteria were able to enhance the mass transfer of TCE out of the low permeability regions, when compared with abiotic processes alone, thus enhancing mass flux of chlorinated ethenes from the domain.

- *Dhc* cells were capable of penetrating low permeability porous media including clays.

- The distribution of specific *Dhc* strains was influenced by the availability of electron acceptors within and near soils of differing physical properties.

In the second aquifer cell experiment, TCE was transformed to a combination of *cis*-DCE, VC, and ethene.

o The numerical modeling studies of the VOCs and VFAs further showed that:

- Observed aquifer cell microbial transformation rates were consistent with batch-fitted values, when permeability variations were accounted for and competitive inhibitions were removed.

- Multi-dimensional models with uniform properties or 1-D models, using microcosm dechlorination rates, were unable to predict aquifer cell performance.

Heterogeneity in soil properties influences the complete dechlorination of TCE to ethene. Inclusion of heterogeneity in numerical modeling is crucial to predictive accuracy of reductive dechlorination.

III.4. Modeling the influence of coupled mass transfer processes on mass flux down-gradient of heterogeneous DNAPL source zones

Motivated by the aquifer cell observations (Section III.3) and the background literature review presented in Section II.5.1, a series of transport simulations was undertaken for a suite of DNAPL source zone realizations in 2- and 3-D heterogeneous domains to more comprehensively explore the influence of dissolution, sorption, and diffusion process coupling on source longevity and near-source plume persistence in complex geologic environments. The sections below describe results of these simulations. Modeling methodology and simulation parameters can be found in Sections II.5.2-3.

III.4.1. DNAPL Infiltration Simulations

Representative simulated 2-D and 3-D PCE-DNAPL saturation distributions are shown in Figure R.4.1 and Figure R.4.2, respectively. Examination of these figures reveals that the low permeability layers act as capillary barriers to vertical migration. Until a new vertical pathway is encountered, the PCE DNAPL continues to accumulate and extend horizontally. Visual inspection of the permeability fields reveals that the occurrence of very high DNAPL saturations (>0.7) is associated with infiltration into high permeability media that are surrounded by low permeability media, which prevent the DNAPL from moving horizontally or vertically.

In comparison to the 2-D simulations, the 3-D simulations exhibit different migration pathways, with less vertical penetration and more extensive lateral movement of the DNAPL. The difference between maximum saturations in the 2- and 3-D simulations is, however, small (<2.2%), which suggests a relatively small influence of dimensionality in determining maximum DNAPL saturation. On the other hand, a comparison of (a) and (b) in Figures R.4.1 and R.4.2 reveals that DNAPL distributions for fields 1 and 2 differ markedly, attributed to the locations of low permeability layers in the domain. For field 2 simulations, much of the DNAPL spreads and pools above low permeability layers at the bottom of the domain. For field 1 simulations, the DNAPL either resides in the top part of the domain, or penetrates down and accumulates on the bottom boundary.
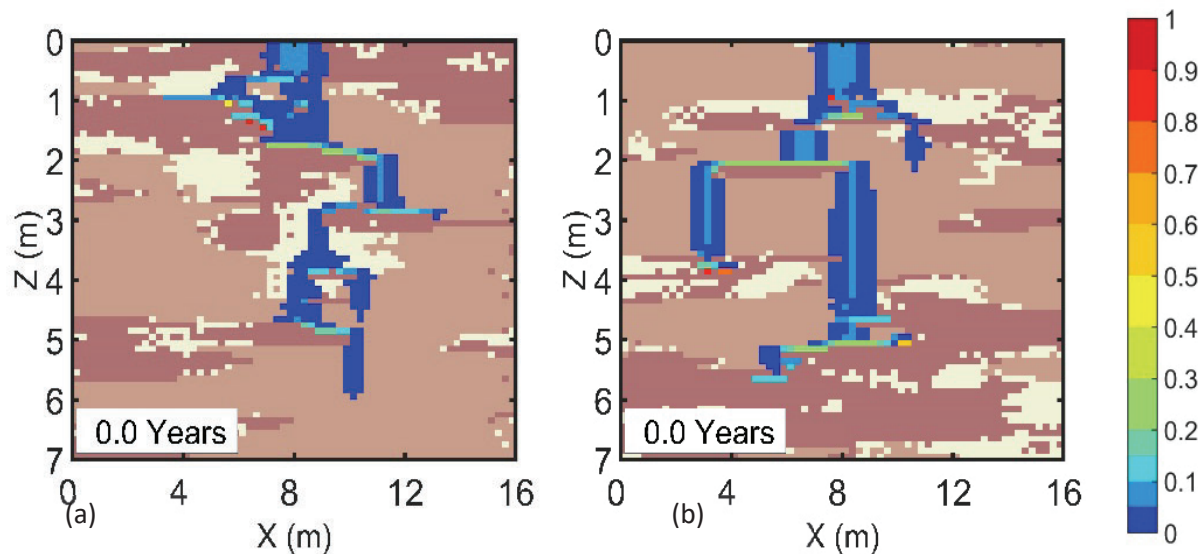
Figure R.4.1. Selected realizations of PCE-DNAPL source zones for field 1 (a) and field 2 (b) with color map for DNAPL saturation, copper color map for background permeability field.

(a)   (b)
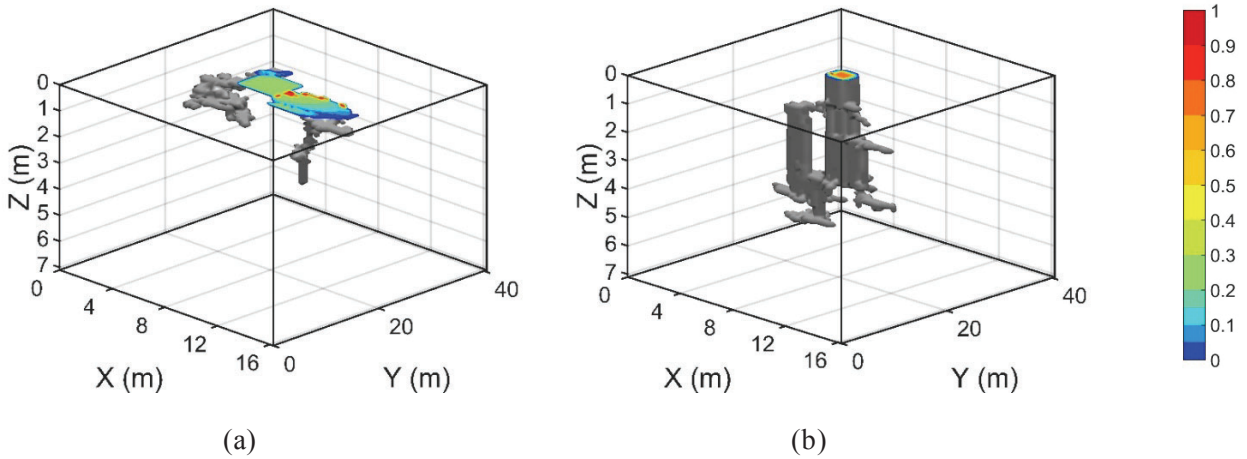
Figure R.4.2. Initial PCE-DNAPL saturation distribution in 3-D for field 1 (a) and field 2 (b).

A comparison of initial DNAPL distribution (Table R.4.1) shows that 3-D simulations exhibit fewer pools/high saturation cells than those in 2-D, attributed to the greater lateral spreading, and field 1 has more DNAPL pools than field 2, attributed to the low permeability layer configuration. The slight reduction in average DNAPL mass compared to the initial release volume is attributed to DNAPL migration out of the domain across vertical boundaries during the infiltration simulation.

Table R.4.1. 2-D and 3-D DNAPL spill distribution statistics.

	DNAPL Mass (kg)	Domain-averaged Saturation	PF	Distribution (%) of cells containing DNAPL mass at four saturation levels			
				10^{-6}-0.15	0.15-0.3	0.3-0.7	0.7-1
2-D Field #1	128.62 ($\pm$0.15)	0.0062 ($\pm$7.3e^{-6})	0.56 ($\pm$0.11)	89.62 ($\pm$3.87)	5.31 ($\pm$2.40)	0.99 ($\pm$1.80)	4.08 ($\pm$2.58)
				33.33 ($\pm$8.75)	16.83 ($\pm$19.06)	5.80 ($\pm$8.45)	52.25 ($\pm$19.59)
2-D Field #2	129.66 ($\pm$0.03)	0.0062 ($\pm$1.6e^{-6})	0.44 ($\pm$0.13)	92.54 ($\pm$2.97)	4.20 ($\pm$2.52)	0.92 ($\pm$1.39)	2.34 ($\pm$1.26)
				46.39 ($\pm$9.86)	14.89 ($\pm$8.93)	7.07 ($\pm$7.70)	37.76 ($\pm$13.59)
3-D Field #1	516	2.96e^{-4}	0.44	70.72	24.43	1.40	3.44
				27.95	44.31	4.07	28.94
3-D Field #2	515	2.95e^{-4}	0.30	97.71	0.65	0.46	1.18
				66.75	2.95	5.54	28.07

The 2-D results represent the ensemble mean with the standard deviation in parentheses.

112

III.4.2. 2-D Transport Simulations

Three restoration metrics, total plume longevity, DNAPL removal time, and post-DNAPL plume longevity, were considered to evaluate the influence of DNAPL dissolution and sorption-retarded diffusion on near-source plume behavior for 2-D and 3-D transport simulations. Total plume longevity is defined as the period during which contaminant concentration along a transect of compliance (located 8 meters down-gradient of the PCE-DNAPL infiltration location) is sustained above 0.001 mg/L, excluding the 30-year loading period. DNAPL removal time measures the time for removal of 99.99% of the initial DNAPL. Post-DNAPL plume longevity is calculated by subtracting DNAPL removal time from total plume longevity; it represents the period during which plume tailing is sustained by sequestered mass (sorbed and aqueous phase) only. Flux averaged concentration and maximum concentration at down-gradient transects of compliance were used to determine total plume and post-DNAPL plume longevity. The pool fraction (PF) metric, defined as the fraction of DNAPL mass in pool regions, was used to quantify the evolution of the DNAPL mass distribution and to study the interplay between DNAPL dissolution and transport processes This metric can be calculated by separating (or categorizing) source zone mass spatially into ganglia (i.e., residual or finger) ($s_n \leq s_{nr}^{max}$) and pool regions ($s_n > s_{nr}^{max}$), using the maximum residual DNAPL saturation (s_{nr}^{max}) as the ganglia–pool saturation threshold. Metrics and metric statistics were evaluated for the ensemble of 2-D simulations, and for 3-D simulations for four sorption cases: no sorption (nosp), linear sorption (kdsp), Freundlich sorption (kfsp) and rate-limited sorption (rlsp). In total, 160 numerical simulations were conducted for the 2-D fields, and 8 numerical simulations for the 3-D fields.

III.4.2.1. Influence of Sorption on Restoration Metrics in 2-D

The simulation results for the ensemble of 20 realizations for hypothetical field 1 were used to investigate the coupled effect of sorption and BD on near-source plume tailing. Figure R.4.3 presents median ensemble statistics calculated based on the flux averaged concentration along the down-gradient boundary. Inspection reveals that the presence of sorption substantially increases plume persistence; total plume persistence increases by 22%, 52%, and 55% for the cases with linear, nonlinear, and rate-limited sorption, respectively. However, the median DNAPL removal time for the three sorption cases is only 2-3% higher than that of the no sorption case, indicating a small influence of sorption on the DNAPL dissolution process. Thus, the effect of sorption on total plume persistence is attributed primarily to its influence on post-DNAPL plume persistence. Indeed, the median post-DNAPL persistence is 6 times larger for the linear sorption case, and the other two sorption cases exhibit even more persistent post-DNAPL plumes, with persistence times a factor of 10 larger than those observed for the no sorption case. Extreme outliers for the two metrics of total plume longevity and DNAPL removal time are observed for all of the four cases, while there are no outliers for the metric of post-DNAPL plume longevity. Under almost all simulation conditions, DNAPL removal time represents more than half of the total plume longevity. Thus, the large variances in total plume longevity and DNAPL removal time can be attributed to the heterogeneity (in space and magnitude) of the initial DNAPL saturation distribution. The metric outliers are generally associated with persistent DNAPL in certain parts of the domain.

Inspection of Table R.4.2 reveals that the metric means for the four cases follow the trends observed for the metric medians. Note that the variance of total plume longevity decreases as the sorption model changes, from no sorption, to linear sorption, to nonlinear sorption, to rate-limited sorption. This reduction in the variance of total plume longevity is associated with a reduction in its range, as the minimum longevity values increase more than the maximum. In contrast, for the

post-DNAPL plume longevity, the range (and variance) increases with sorption complexity. This observation suggests that the sorbed mass has a larger influence on concentration tailing under conditions where the DNAPL source doesn't persist. This apparent effect can be explained by considering that, while the remaining DNAPL mass is dissolving in a small part of the domain, the plume is being sustained by BD and desorption in other parts. The DNAPL dissolves away at different rates. Depletion of one cluster of DNAPL pools initiates mass discharge from low permeability layers, which is controlled by sorption and diffusion.
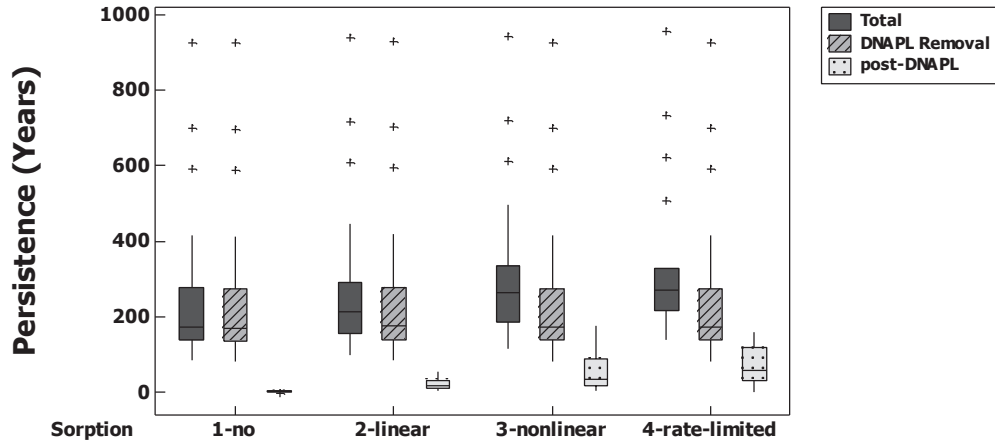
Figure R.4.3. Boxplot comparing flux averaged concentration based on total plume longevity, DNAPL removal time and post-DNAPL plume longevity for the no sorption, linear sorption, nonlinear sorption and rate-limited sorption cases for 20 source zone realizations of field 1 (The bottom and top of the box represent the first and third quartiles, and the band in the box is the median. The lower and upper ends of the whiskers represent the minimum and maximum data within the interquartile range (IQR) from the bottom and top of the box. Outliers are plotted as asterisks).

Table R.4.2. Statistics for flux averaged concentration based and maximum concentration (in parentheses) based total plume longevity, DNAPL removal time and post-DNAPL plume in the no sorption, linear sorption, nonlinear sorption and rate-limited sorption cases for 20 source zone realizations of field 1.

	Sorption	Mean	StD	Minimum	Maximum
Total plume longevity (Years)	nosp	268.4 (270.2)	223.8 (223.7)	83.6 (84.9)	925.0 (926.3)
	kdsp	291.5 (311.8)	220.5 (218.7)	96.7 (107.2)	939.8 (953.9)
	kfsp	322.8 (428.6)	211.4 (209.5)	115.9 (167.9)	941.6 (1029.0)
	rlsp	336.8 (397.1)	208.4 (210.8)	137.2 (178.9)	953.9 (1028.8)
Post-DNAPL plume longevity (Years)	nosp	2.8 (4.6)	1.9 (1.5)	-2.9 (1.9)	5.9 (7.3)
	kdsp	21.2 (41.5)	13.5 (18.6)	4.1 (8.4)	55.1 (81.2)
	kfsp	54.2 (159.9)	48.0 (63.0)	5.1 (33.2)	174.7 (324.7)
	rlsp	68.4 (128.7)	48.4 (39.0)	1.1 (39.1)	157.7 (204.4)
DNAPL removal time (Years)	nosp	265.6	223.6	80.4	923.6
	kdsp	270.3	224.1	83.6	929.5
	kfsp	268.7	223.2	83.0	925.5
	rlsp	268.4	223.3	82.4	925.5

For the simulations with a persistent DNAPL, sequestered mass in low permeability layers in the vicinity of depleted DNAPL pools may have sufficient time to fully diffuse into transmissive zones. Thus, the existence of persistent DNAPL influences not only the removal rate of DNAPL but also the duration of the post-DNAPL period. For the 20 simulations, faster DNAPL removal is usually associated with a longer post-DNAPL tailing period and vice versa. Figure R.4.4 illustrates mass discharge from low permeability layers as the DNAPL mass is dissolved, demonstrating that local mass transfer behavior is governed by different processes in different parts of the domain.
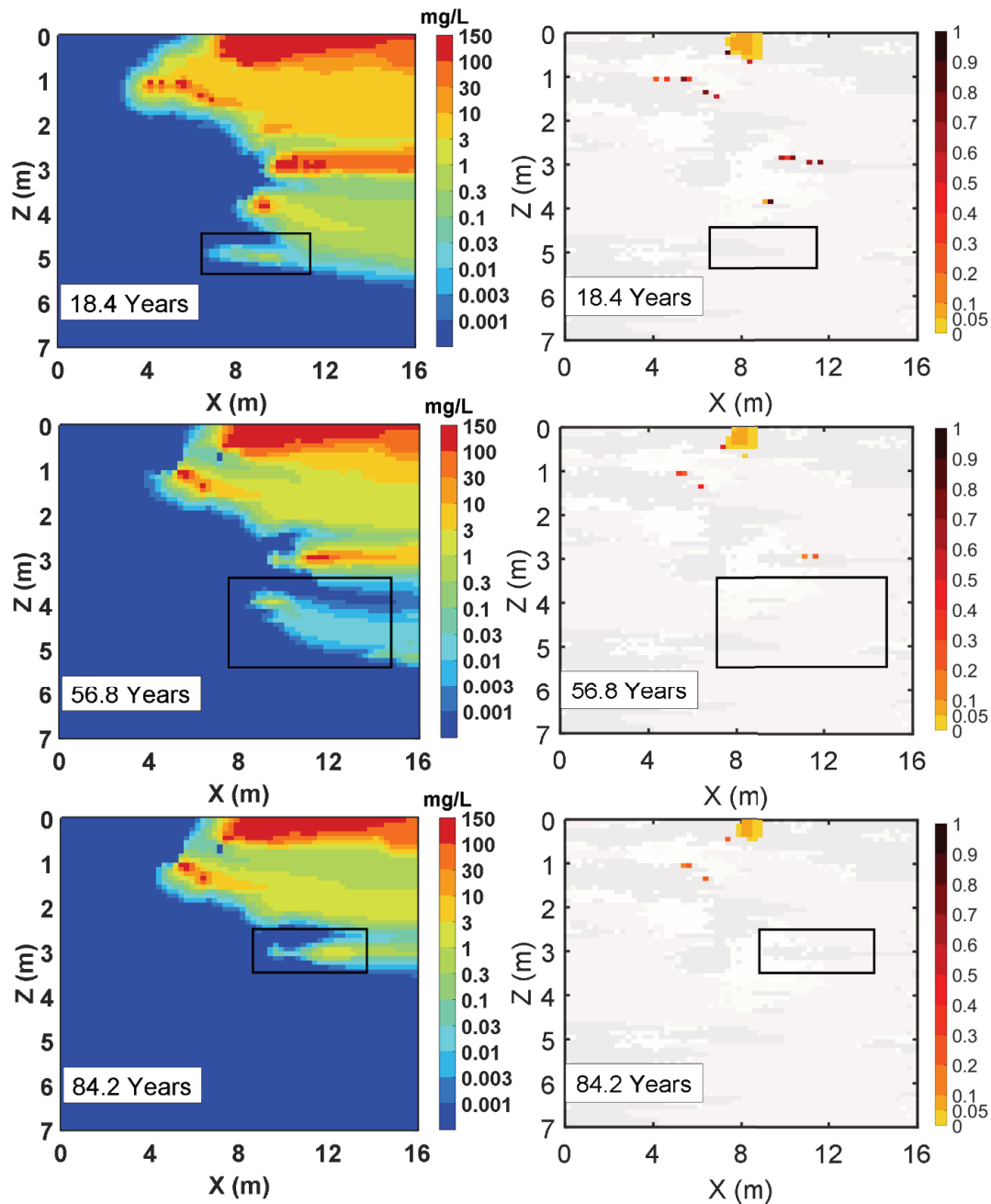
Figure R.4.4. Aqueous concentration contour (left column) and DNAPL saturation distribution (right column) at selected times for the example simulation of field 1. The boxed areas show plumes sustained by sequestered mass in low permeability layers.

The total longevity, DNAPL removal time, and post-DNAPL longevity, as determined by maximum concentration along the down-gradient boundary, are presented within parentheses in Table R.4.2. In comparison to the flux averaged concentration, the maximum concentration is linked to local mass transfer behavior. The negative minimum values reported for post-DNAPL persistence in the no sorption case are attributed to meeting the maximum concentration target prior to complete DNAPL depletion.

To further understand the interplay between DNAPL dissolution, sorption, and BD, it is illustrative to examine a representative simulation. Figure R.4.5(a) presents the initial DNAPL saturation distribution for a selected example, along with the corresponding permeability field.
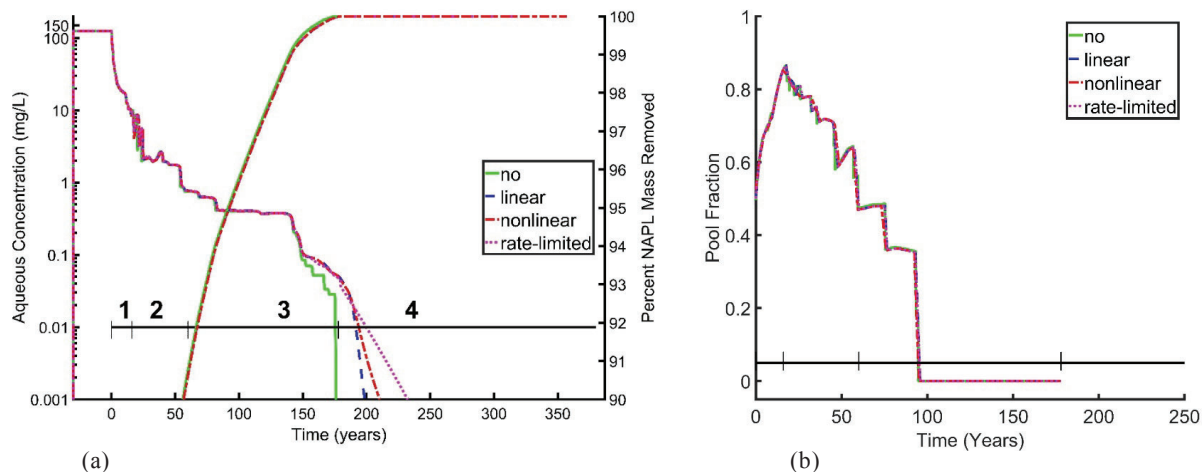
Figure R.4.5. Flux averaged concentration through effluent boundary (a) and temporal change of pool fraction in the domain (b) for the example simulation shown in Figure R.4.1(a) of field 1.

The evolution of flux averaged concentrations along the down-gradient boundary and DNAPL pool fraction are plotted in Figures R.4.5 (a) and (b) for the four sorption cases. The right y-axis in Figure R.4.5(a) plots the associated % removal for the final 10% of the entrapped DNAPL mass. The curves are divided into four segments, corresponding to four regimes, each dominated by a different mass transfer process. The first regime is associated with the dissolution of low saturation ganglia (<0.23) and is characterized by a sharp decrease in down-gradient concentration and a steep rise in pool fraction. The second regime is associated with the dissolution of high saturation DNAPL pools and exhibits a decreasing concentration trend with several 'bumps'. Here, as the pool fraction decreases, localized high concentrations are emitted from pool areas and travel down-gradient creating concentration spikes which characterize the second regime. The pool fraction continues to decrease until the pools become ganglia, dissolution of which then results in a small increase in pool fraction. The depletion rate for individual pools varies with size and accessibility. Thus, pool fraction displays a decreasing trend with a series of small peaks during the second regime. In the third regime, the down gradient concentration is governed by the slow depletion of persistent or flow inaccessible DNAPL, resulting in concentration plateaus. The pool fraction during this third regime exhibits a "stepped" decrease. Each "step" represents slow dissolution of one cluster of DNAPL saturations existing in the domain. The final "step" associated with a pool fraction of 0, persists for a long period of time. In this realization, the last remaining DNAPL ganglia are either trapped in low permeability layers or enclosed by low permeability materials. Due to the similar initial DNAPL release location and the presence of a low permeability zone at this location for each of the field 1 realizations, the entrapped DNAPL tended to create long

116

plateaus in most simulations for field 1. The presence of these small inaccessible DNAPL zones is also the reason for the outliers observed in Figure R.4.3. The complete removal of DNAPL depends on the dissolution rate of this flow-inaccessible mass for the field 1 ensemble. The fourth and last regime is the post-DNAPL period, during which the down-gradient plume is influenced solely by mass diffusing out from low permeability zones. The concentration curves for the four sorption cases begin to deviate from each other during this final regime.

III.4.2.2. Influence of Permeability Field

To investigate the general validity of the findings presented above for a different permeability configuration within the release zone, transport simulations were conducted for the ensemble of field 2 PCE source realizations. In these field 2 simulations, the PCE is released within a more permeable material and tends to penetrate much further into the domain. The boxplot in Figure R.4.6 presents data for flux averaged concentration-based and maximum concentration-based metrics. The trends of the median total plume persistence, DNAPL removal time and post-DNAPL plume persistence follow the pattern of simulation results for field 1, with the shortest longevity for the no sorption case and the longest for the rate-limited sorption case.
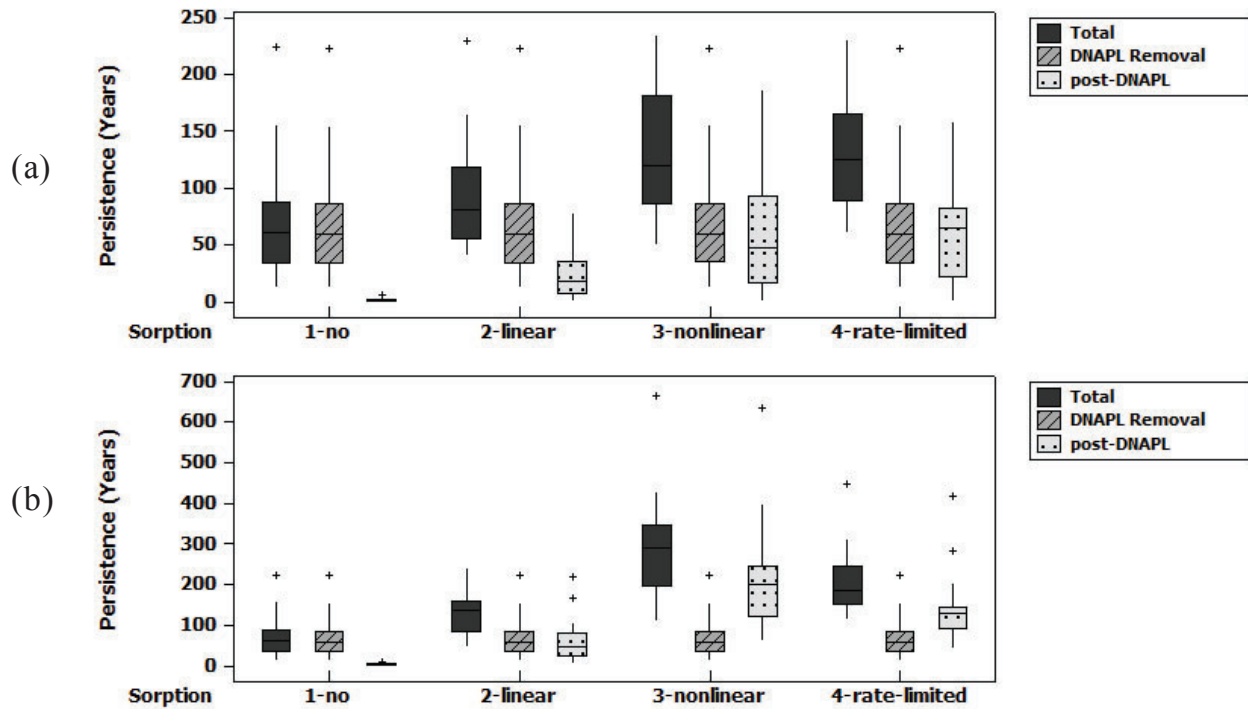
Figure R.4.6. Boxplot for (a) flux averaged concentration-based and (b) maximum concentration based total plume longevity, DNAPL removal time and post-DNAPL plume longevity for the no sorption, linear sorption nonlinear sorption and rate-limited sorption cases for 20 source zone realizations of field 2.

The time scales for plume evolution in these two different scenarios, however, differ substantially; the median total plume persistence for the field 2 ensemble simulations is halved and the median DNAPL persistence is reduced by 2/3 in comparison with the field 1 values. This difference is attributed to the existence of a lower pool fraction and less DNAPL mass entrapment in low permeability zones in the field 2 scenario, which were examined in section III.5.1. The median post-DNAPL plume longevity increases by several years (<10) for field 2. This behavior is attributed to three factors: 1) the increased storage capacity for aqueous and sorbed mass in the thick low permeability zone at the bottom of the domain that has pooled DNAPL above; 2) the

reduced flow accessibility to sequestered mass in the thick low permeability zones compared with those in the more distributed low permeability layers for realizations of field 1; and 3) the greatly shortened DNAPL removal time (regime 3). The comparison of these two scenarios suggests that the configuration of low permeability regions is a fundamental determinant of plume persistence. We observed a major dependence of source zone configuration on locations of low permeability layers with extensive horizontal correlation length (Wang, 2013).

III.4.2.3. Influence of Dissolution Mass Transfer

There are two factors potentially contributing to the determination of dissolution rate in the kinetic dissolution model (equation M.5.4): 1) the lumped mass transfer coefficient, κ^{an} and 2) the solubility, C_{eq}^a. In this study, κ^{an} is calculated by the Powers et al (1994) correlation (equation M.5.5). This correlation was developed from column dissolution experiments for $s_n < 0.18$; this saturation range encompasses saturations present in the majority of cells for the 2-D (81.07%-97.51%), and 3-D (74.70% and 97.87%) simulations. It is noted, however, that none of the Sherwood number correlations (e.g., Imhoff et al., 1994; Miller et al., 1990; Nambi and Powers, 2003; Powers et al. 1994) available in the literature has been developed for as wide a range of initial DNAPL saturations as that observed in this study (trace to 0.9). Among the available correlations, the Nambi and Powers (2003) correlation is valid for a slightly wider range of condition ($s_n < 0.35$). Comparison of simulations conducted using the Nambi and Powers (2003) and the Powers et al. (1994) (not shown here) revealed that predicted plume longevities were not very sensitive to the choice of correlation. Additional tests (not shown here) were conducted by increasing the magnitude of the lumped mass transfer coefficient to approximate equilibrium dissolution. The results were similar to the original ones simulated by the Powers et al. (1994). Christ et al. (2006) showed that the selection of a mass transfer correlation for DNAPL dissolution has more influence on late time mass transfer (>95% DNAPL removal) and suggested that use of a ganglia-based mass transfer correlation may predict faster DNAPL removal and shorter source longevity. Our simulation results, however, showed that longer DNAPL persistence is not necessarily linked to longer post-NAPL plume persistence. Plume persistence in this study was found to be the result of the interaction between DNAPL dissolution, diffusion, and sorption.

Solubility is another property that has been shown to influence source longevity (e.g., Seyedabbasi et al., 2012). To explore this factor, post spill transport simulations were conducted for a higher solubility DNAPL, with properties consistent with that of TCE, to compare with behavior observed in the previous PCE simulations. Input properties for the DNAPL included: a solubility of 1000 mg/L, density of 1466 kg/m³, aqueous phase diffusivity of 9.1E-6 cm²/sec, and K_{oc} of 126 L/kg (three times smaller than that of PCE). The cases with no sorption and linear sorption were simulated for a release in one selected realization for fields 1 and 2. Simulations results (Table R.4.3) reveal that the total longevity decreased dramatically for the TCE plume, attributed to faster DNAPL dissolution. While the post-DNAPL period was sustained for a longer time for TCE in the linear sorption cases, the no sorption case simulations exhibited slightly shorter post-DNAPL longevity for TCE than for PCE. In the no sorption cases with TCE, it is likely that the higher concentration gradient between transmissive and low permeability zones drives faster release of the sequestered mass from low permeability zones. For the linear sorption cases with TCE, two factors are most likely contributing to longer post-DNAPL times: 1) larger quantities of dissolved mass in the inaccessible zones in the domain and 2) the more rapid DNAPL dissolution relative to the period of desorption and BD, which are occurring at rates similar to that of PCE. Thus, the relative contribution of sorbed and low permeability sequestered mass to contaminant persistence increases as the contaminant solubility increases. These simulation results also indicate that the loading and release of stored mass in low permeability zones are very sensitive to the inclusion

and simulation of sorption. It should be noted here, that the TCE DNAPL spill distribution was assumed to be the same as that for PCE in these simulations. If the actual spill release were simulated, TCE spills would not be expected to penetrate as deep vertically due the smaller density, which would significantly impact the mass distribution and persistence simulation results.

Table R.4.3. Comparison of downgradient mass flux persistence for TCE and PCE.

	Compound	Sorption	DNAPL removal	Post-DNAPL	Total Persistence	Loaded Mass	Initial DNAPL Mass
			(Years)	(Years)	(Years)	(kg)	(kg)
Field 5	PCE	no	174.6	2.6	177.2	130.7	129.8
	PCE	linear	179	20.7	199.7	134.2	129.8
	TCE	no	23.6	1.9	25.5	122.9	117.3
	TCE	linear	27.7	29.5	57.2	146.4	117.3
Field 7	PCE	no	72.8	0.4	73.2	130.7	129.8
	PCE	linear	72.4	7	79.4	136.1	129.8
	TCE	no	9.7	0.2	9.9	124.6	117.3
	TCE	linear	9.7	29.1	39.0	160.4	117.3

III.4.3. 3-D Transport Simulations

To explore the influence of model dimensionality on remedial metrics, simulations were conducted on two selected 3-D saturation realizations (one for each of the fields), with the four different sorption treatments. Again, the three flux-averaged concentration based metrics were examined (Figure R.4.7). The 3-D results generally follow the trends predicted in the "2d mean" simulations: (1) the inclusion of sorption results in prolonged plume persistence (i.e., total and post-DNAPL), the extent of which depends on the sorption complexity; (2) the total plume persistence is greater in field 1 than field 2; (3) the DNAPL removal time is not sensitive to sorption type, and varies within 6% of the no sorption case; and (4) the DNAPL removal time is greater in the field 1 scenario than in the field 2 scenario. The post-DNAPL removal time varies within a certain range for both fields in each sorption case, appearing to be negligibly affected by the field configuration. The consistency of trends observed between the 2-D and 3-D simulations supports conclusions reached above relating to the importance of sorption and permeability field heterogeneity in the source zone to the accurate prediction of plume persistence.

Despite the similarities, 2-D models tended to predict longer plume persistence than 3-D in these simulations. The "2-D mean" total plume persistence and DNAPL removal time are approximately two fold greater than the corresponding metrics in 3-D in all four sorption cases for both fields. The differences between "2-D mean" and 3-D, however, could be an artifact of the single realization associated with the 3-D DNAPL infiltration simulation. To further explore the influence of dimensionality, additional transport simulations were performed for the four sorption cases and both fields in 2-D with DNAPL spills and permeability fields extracted from the center x-z cross section in the 3-D spill scenarios. Results of these simulations (labeled '2d in 3d') are also presented in Figure R.4.5. Although closer to the 3D simulations than those of the 2D mean, these additional simulations produced longer total plume and DNAPL persistence times for both fields in comparison with the 3-D simulations. Trends in post-DNAPL persistence time, however, were less clear.

Although the same volume (80L) of DNAPL was released in the center slice of the 3-D domain as the 2-D domain, only a small portion of DNAPL was eventually retained in the center cross section of the 3-D domain. Consequently, horizontal migration and spreading of DNAPL in the 3-D simulation resulted in increased access of the DNAPL to groundwater flow and an acceleration of dissolution. The spreading also resulted in access of dissolved mass to a larger medium volume but did not necessarily lead to more mass sequestration. The sequestration of mass depends on the spatial distribution of the sorptive properties of the medium. Therefore, the post-DNAPL persistence can be longer (field 2 case) or shorter (field 1 case) in 3-D than persistence in the 2D in 3D simulations. In a heterogeneous domain, the 2D in 3D or 2D simulations may not be representative of real conditions, as the center of mass of the DNAPL and sequestered mass may not be in the transect where the source is released.

To further explore the contribution of sequestered mass to near-source plume persistence, the ratio (percent) of post-DNAPL time to total plume persistence was calculated (Figure R.4.7).
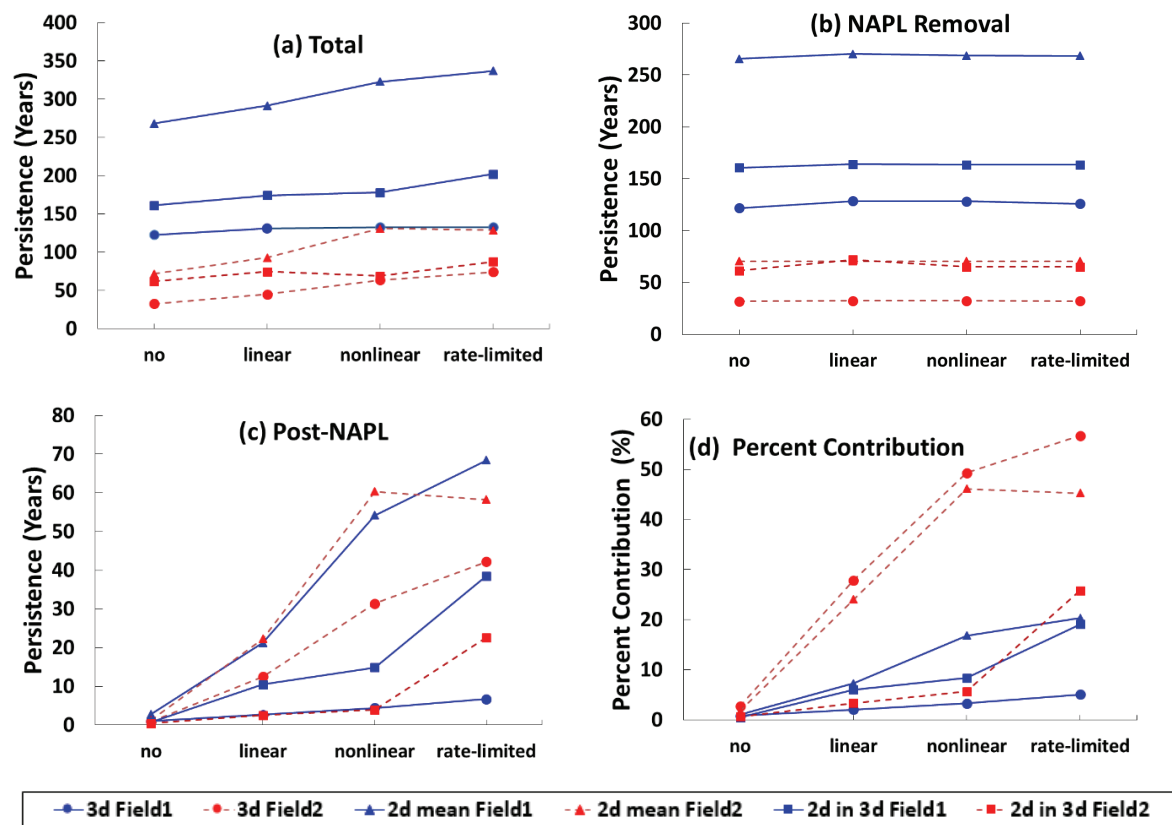
Figure R.4.7. Flux averaged concentration-based (a) total plum longevity, (b) DNAPL removal time, (c) post-DNAPL time, and (d) percent of BD to total plume persistence for the four sorption cases. "3d" represents 3-D infiltration and restoration simulation results; "2d mean" represents the mean metrics for a suite of 2-D infiltration and restoration simulation in section 3.1; "2d in 3d" represents 2-D restoration simulation results by extracting NAPL saturation distribution and permeability field from the center cross-section of 3-D simulation.

Comparison of the results for fields 1 and 2 shows that the influence of sequestered mass on plume persistence is highly dependent on the configuration of the permeability field in both 2-D and 3-D. Field 1 appears to be DNAPL-dominated while field 2 is the opposite. In addition, the influence of the sequestered mass on plume persistence is also associated with the sorption complexity of media. Figure R.4.7 shows that there is little or no effect of sequestered mass and BD on plume

tailing in the no sorption case, regardless of model dimension. Sequestered mass becomes a more important contributor to plume tailing when sorption is a present (e.g., in the linear, nonlinear and rate-limited sorption cases). Thus, BD alone appears to be only a minor factor in sustaining downgradient plumes compared to DNAPL dissolution when low permeability layers are thin and not very sorptive. Conversely, predictions based upon assumptions of no sorption or linear sorption could be mistakenly optimistic about plume persistence times when the sorption properties of site media are complex. In addition, the discrepancies between 2-D and 3-D predictions of post-DNAPL time become larger as sorption is included. This suggests that model dimensionality and sorption representation together can play important roles when predicting plume longevity for a heterogeneous field that is highly sorptive or has nonideal sorption in low permeability zones. Use of 3-D simulations may be more appropriate for sites with nonideal sorption, where spreading in the transverse (lateral) direction will affect mass exchange between transmissive and low permeability zones.

Discrepancies between 2- and 3-D simulations can be also understood in the context of the influence of reduced dimensionality on PCE migration vertical pathways (Wang, 2013). The DNAPL spill simulations demonstrated that 2-D releases resulted in deeper penetration than the 3-D cases. For mildly heterogeneous permeability fields, Christ et al. (2005) came to the same conclusion for vertical spreading in 2-D and 3-D. They also reported smaller GTP values in 2-D than in 3-D, which means that simulations in 2-D scenarios were associated with more pooling and, consequently, longer persistence of down-gradient plumes. Thus, for both mildly and highly heterogeneous fields, these results suggest that 2-D predictions cannot represent 3-D ones. The initial averaged saturation per bulk volume calculated for 3-D is smaller than 2-D, which could partially contribute to the more rapid cleanup in the 3-D simulations. A thorough study that includes the whole ensemble of 3-D simulations would be needed to reach a more general conclusion.

III.4.4. Discussion and Conclusions

Simulations conducted herein reveal that accurate representation of sorption processes in transport models is crucial to the accurate prediction of plume longevity, especially for the prediction of post-DNAPL dissolution longevity. While diffusive mass rebound or back diffusion has been heavily emphasized in previous investigations (e.g., Ball et al., 1997; Chapman et al., 2012; Chapman and Parker, 2005; Liu and Ball, 2002; Matthieu et al., 2014; Parker et al., 2008; Seyedabbasi et al., 2012), the results of this study suggest that sorption processes will dominate the rate of mass release to transmissive zones.

Simulations that neglected the storage capacity of low permeability compartments for sorbed contaminants, tended to substantially underestimate the mass loading in low permeability compartments during the pre-remediation period. These results indicate that the achievement of remediation objectives would likely be compromised by "optimistic predictions" of plume longevity, if sorption processes are neglected or an inappropriate sorption model is assumed. Note, however, that the simulations conducted herein revealed a very limited effect of sorption on the rate of DNAPL dissolution. Chemical or biological transformations were not included in the modeling studies presented here. If such reactions were simulated, the longevity of DNAPL and the aqueous source contaminant would likely be reduced. The transformation products, however, would contribute to down gradient flux and plume persistence.

Simulation results also demonstrated a strong influence of source zone complexity (e.g., heterogeneity of the permeability field, DNAPL architecture, process coupling) on source zone mass transport and near-source plume persistence. Results suggest that the presence of DNAPL

tends to control the clean-up rate in the near source area in most cases. Simulations demonstrate how small, isolated, pockets of DNAPL can evolve and persist in heterogeneous domains. The removal of the last few percent of the DNAPL or trace DNAPL mass is especially important in terms of reducing plume tailing time, since this part of the DNAPL mass usually represents the most persistent source. Although neat phase DNAPL is not typically detected at most sites, this work suggests that trace amounts of DNAPL source mass present in the field can be as influential as sequestered sorbed and dissolved mass in controlling plume tailing, and that these small quantities of DNAPL mass can be difficult to differentiate from the diffused and sorbed mass without exhaustive characterization. Thus, by neglecting consideration of the influence of DNAPL architecture and dissolution, previous studies would presumably have tended to over-emphasize the importance of BD and may have been relatively inaccurate in their predictions of plume behavior and longevity.

The simulations presented herein also demonstrate that the evolving plume is directly linked to the spatial heterogeneity of the medium, source mass distribution, and sorption properties. The inclusion of DNAPL dissolution, sorption, and diffusion allows the model to capture the interplay between these processes in aged heterogeneous source zones. Due to the presence of heterogeneity, different regimes within the domain, where local mass behavior is governed by different processes (i.e., dissolution and BD), were shown to exist before complete NAPL removal from the domain. In other words, the release of sequestered mass does not begin at the same time at every spatial location. A common method used to model a DNAPL source in previous studies has been to use a source loading function, followed by period during which this loading is halted to allow for BD. Using this approach, the spatial variations of source zone DNAPL architecture are greatly simplified; this approach cannot capture the interplay between different transport processes at the local scale that has been demonstrated here to be crucial in determining down-gradient concentrations in highly heterogeneous sites. In addition, the large variability among the predicted longevity metrics of the simulations in this work also points to the importance of source zone heterogeneity in plume longevity predictions. The location of low permeability layers, especially thick and laterally persistent layers, is controlling for both the formation of the source zone architecture and the solute plume. In sum, these results imply that simplified models that idealize subsurface stratigraphy/or neglect process coupling will be unable to adequately predict plume persistence.

The conclusions drawn above are associated with the specific simulation conditions assumed in this work, i.e., the selected DNAPL, permeability, and associated media sorption characteristics. The low permeability zones in this work were consistent with a silty sand or coarse-grained silt. The hydraulic conductivity of these materials, however, are one to two orders of magnitude higher than those of clays, which have been considered as low permeability zones in previous studies. If a smaller hydraulic conductivity material were used for low permeability zones, the discharge of stored mass out of the low permeability zones would be expected to be slower. However, the penetration depth and the amount of mass loaded into these zones would also likely be reduced. For the lower conductivity materials, longer DNAPL persistence might also be possible due to more areas of flow bypassing. Thus, further work would be useful to explore behavior in other depositional environments.

This study showed that reduced dimensionality has a substantial impact on predictions of plume longevity. Although results from the limited number of 3-D simulations presented are not exhaustive, the large discrepancies observed between plume longevity predicted by the 3-D and 2-D simulations suggest that 2-D simulations, although computationally efficient, are only useful for examining trends in plume metrics in highly heterogeneous formations. It is likely that predictions

obtained by 2-D simulations will be most misleading in cases where strong nonideal sorption is present. A more quantitative comparative analysis would require additional simulations in 3-D.

All of the scenarios considered here explored near-source zone (within 10 m of the DNAPL zone) plume evolution. An examination of transport at larger distances down gradient of a DNAPL source zone is a topic that is worthy of further investigation. The complex interplay of heterogeneity and sorption/BD processes will likely also be important at this larger plume scale. For example, relative to DNAPL mass, the influence of sorption and BD would be expected to become more significant along transects further down-gradient from a source zone, as the plume encounters more opportunities for sorption and diffusion into low permeability zones (NRC, 2005). However, plume concentrations would also be more diluted by mixing with transport further down gradient, reducing concentration gradients for mass sequestration into less permeable zones. In addition, concentration rebound and BD fluxes depend on the local contrasts between concentrations in the more mixed transmissive zones and the less permeable zones, suggesting that BD rates and flux averaged concentrations would be greatly affected by local heterogeneity.

Based upon the simulation comparisons for no sorption, linear sorption, nonlinear sorption and rate-limited sorption models presented above, it is anticipated that the plume tailing sustained by the sequestered mass will vary with different specifications of Koc and sorption mass transfer rate; it is likely that the effect of BD and sorption on plume tailing will be less significant with smaller Koc and faster mass transfer. The importance of including sorption and using a field-specific sorption model and associated parameters may also depend on the heterogeneity of the permeability field, as has been suggested in previous studies (Rivett et al. 2006; Rodriguez 2006). Thus, it will be important for site managers to explore sensitivity to sorption parameters for the permeability fields and properties representative of their particular field site and release conditions.

III.5. Parameter Upscaling and Screening Model Tools

III.5.1. Regressed Models for Multi-rate Mass Transfer in Heterogeneous Media

III.5.1.1. Parameters Sensitivity

Prior to the fitting of the upscaled model to the fine-scale model simulations, it is helpful to explore the behavior of the upscaled system of equations (M.6.23) - (M.6.25). To this end, a parameter sensitivity analysis was undertaken. Figure R.5.1 illustrates the influence of the different upscaled parameters on solute breakthrough, when they are increased or reduced by a factor of ten. Increased velocity (increased effective conductivity K^{eff}) naturally gives faster breakthrough. Another impact of increased flow rate is reduced late-time tailing. This can be explained by the larger concentration gradients induced between the sand and clay, which result in faster diffusion out of the clay. In addition to this, the flow rate has an impact on several of the other parameters (Section III.5.1.2), but for this illustration, only one parameter at a time is modified. The effective longitudinal dispersivity α_l^{eff} has little effect on the long term behavior, but early breakthrough is smoother when it is increased. With good communication between the sand and the "surface of the clay", i.e. large first-order rate α_1, the breakthrough is smoother, since the solute diffuses faster out of the clay. A similar effect is obtained if there is more of the clay that has good communication with the sand (larger capacity ratio β_1). When the communication between the interior of the clay and the sand is good (large α_2), more of the solute is flushed out at early times, which substantially reduces the cleanup time. On the other hand, if there is more of this clay (larger β_2), the cleanup time is delayed. In summary, the largest impacts on late-time tailing are due to the smaller of the two first-order rates, α_2, and the corresponding capacity ratio β_2, in addition to the flow rate.

time (days)
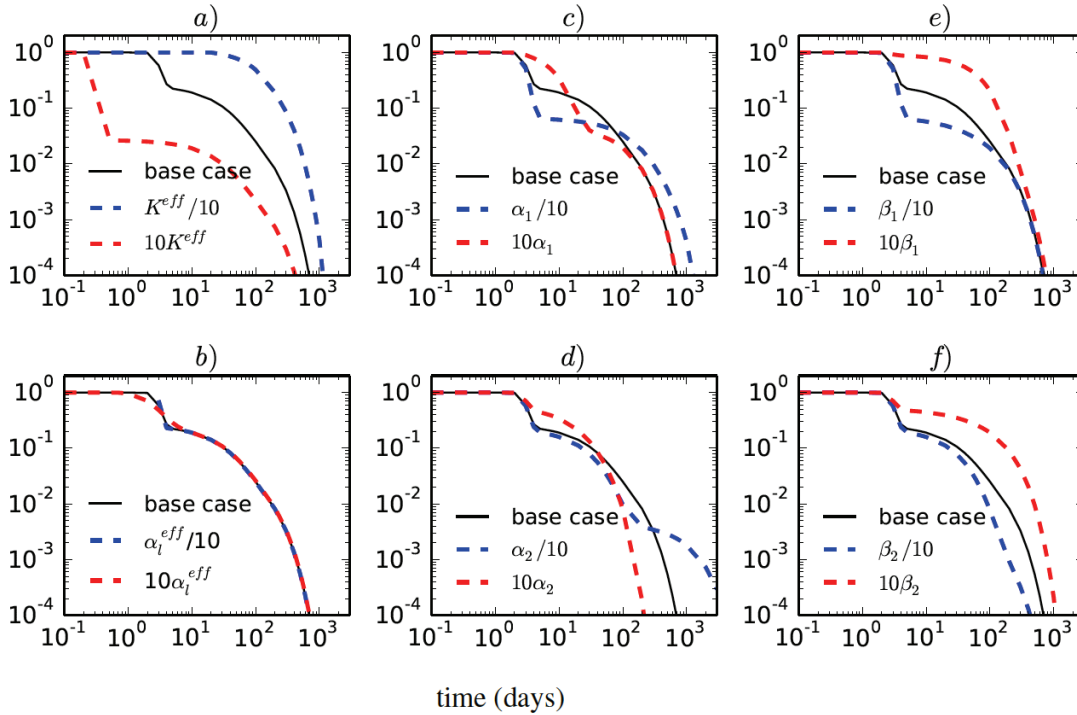
Figure R.5.1. Illustration of the impact of upscaled parameters on the scaled effluent mass flux (breakthrough curve), in a domain of initially uniform concentration that is being flushed with pure water. Only one parameter at a time was changed from this case. We used $f_{im} = 0.31$; $a_h = a_v = 0.1$ m and $R_{im} = 6$.

III.5.1.2. Fitted parameters

Figure R.5.2(a) presents goodness of fit results for each individual fine scale simulation. A review of the figure reveals that cases with large retardation factors and large Peclet numbers are best fit. Figure R.5.2(b) illustrates break through curves corresponding to the best and worst fits. The best fit is indistinguishable from the simulation result, and the worst fit also displays small errors compared with differences between cases. Based upon their relatively small size, fitting errors are neglected in the discussion below.
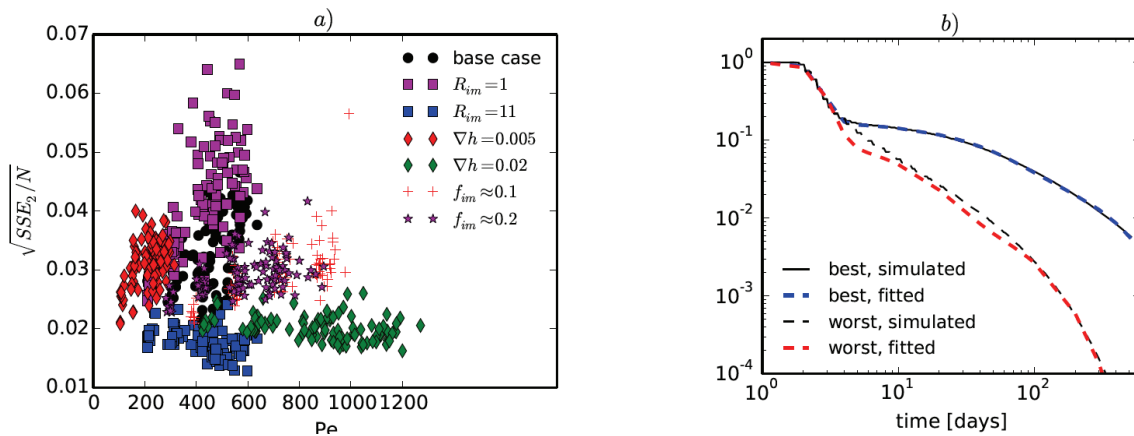
Figure R.5.2. a) Goodness of fit, b) Scaled effluent mass flux corresponding to the best and the worst fit. The best fit is for one of the simulations applying $R_{im} = 11$; $a_h = 0.22$ m and $a_v = 0.14$ m. The worst fit is for one of the simulations applying $R_{im} = 1$; $a_h = 0.22$ m and $a_v = 0.18$ m. Other parameters are as defined for the base case.

124

The uniqueness of the fit was tested for two simulation cases that have $f_{im} = 0.3$; $a_v = 0.1$ m and $a_h = 0.1$ m respectively $a_h = 0.22$ m. Three sets of initial guesses were applied, involving a base case, initial guesses a factor of two smaller, and initial guesses a factor of two larger. The fitted parameters vary within a few percent from the base case, which is small compared to the difference between cases, cf. Section III.5.1.3.

III.5.1.3. Regressions

Based upon the fitted parameters, regression expressions were sought. Tested regression expressions and coefficients of the chosen models are presented in Tables R.5.1 and R.5.2, respectively. The range of validity of these models is given by the range of tested parameters (Table M.6.2). Figure R.5.3 illustrates the performance of the chosen regression models (bolded models in Table R.5.1.

As demonstrated by the high R^2 of the first effective hydraulic conductivity model ($K^{eff} / K_{sand})_0$ (Table R.5.2), the scaled effective hydraulic conductivity is proportional to the volumetric fraction of low-permeability material, and explained very well with only this parameter. Because the low-permeability inclusions have negligible conductivity, model 0 would represent a weighted average if $\lambda_0 = -1$, i.e. the upscaling that would be expected for layers parallel to the flow. The λ_0 model value of -1.67 indicates a faster rate of permeability reduction, and was expected, since the inclusions are not parallel to the flow. The model allowing for a constant not strictly 1 (model 1) gave no improvement and was therefore disregarded. Model 2, incorporating the geometry of clay inclusions, $a_v = a_h$, together with the volumetric fraction of clay, fit the effective conductivity very well, with high R^2 and all points in Figure R.5.3(a) close to the ideal line. This model was chosen.

As shown in Figure R.5.1, the breakthrough curves (especially at late times) are not very sensitive to the effective dispersivity. Nevertheless, for completeness, this parameter was also regressed. There is a large spread in its values and the regression is not as good as for the other effective parameters (Figure R.5.3(b)). The effective dispersivity scaled by the fine-scale dispersivity is expected to be larger than one, and tending to one when $f_{im} \circledR 0$.

Model 1 allows for this but is not significantly better than model 0, which allows the parameter to tend to zero. Again, taking into account the geometrical properties (model 2) improves the result, as could be expected. The effective dispersivity is approximately proportional to square root of a_v/a_h for a given f_{im}. A comparison of models 2 and 3 show that there is negligible gain in allowing for a nonlinear dependence on f_{im}. Therefore, model 2 was chosen.

The Sherwood numbers were found to increase with increasing Peclet number. Allowing for a nonlinear dependence on the Peclet number yielded an improvement for Sh, corresponding to the lower first-order rate, but not for Sha. In addition, faster transfer was obtained with increasing sorptive capacity, i.e. larger R_{im}. For Sha, corresponding to the higher rate, model 3 was chosen, incorporating the Peclet number and R_{im}. For Sh it was important to include the geometrical properties (model 5). The relative proportion of low-permeability material corresponding to the faster rate, b, was found to increase with reduced retardation factor, reduced volumetric clay fraction and reduced Peclet number. It also slightly increased with reduced a_v/a_h, i.e. flatter inclusions have relatively more of the clay represented by the faster rate. Although models 3 and 4 have the same R^2, the Peclet number is modeled by addition because model 4 has a more even distribution of errors between low and high values of b. Thus this form was kept in the chosen model (5), which also takes geometrical factors into consideration.

The regressed model for K^{eff} can also be applied for vertical flow. Note that the inverse relation between a_v and a_h is used.

Table R.5.1. Regression models numbered by subscripts. R^2 of the chosen models are marked in bold.

Model	R^2
$(K^{eff}/K_{sand})_0 = 1 + \lambda_0 f_{im}$	0.95
$(K^{eff}/K_{sand})_1 = \lambda_0 + \lambda_1 f_{im}$	0.95
$(K^{eff}/K_{sand})_2 = 1 + \lambda_0 f_{im}(a_v/a_h)^{\lambda_1}$	**0.99**
$(\alpha_l^{eff}/\alpha_l)_0 = \lambda_0 f_{im}$	0.58
$(\alpha_l^{eff}/\alpha_l)_1 = \lambda_0 + \lambda_1 f_{im}$	0.60
$(\alpha_l^{eff}/\alpha_l)_2 = \lambda_0 f_{im}(a_v/a_h)^{\lambda_1}$	**0.70**
$(\alpha_l^{eff}/\alpha_l)_3 = \lambda_0 + \lambda_1 f_{im}^{\lambda_2}(a_v/a_h)^{\lambda_3}$	0.73
$Sha_0 = \lambda_0 Pe$	0.74
$Sha_1 = \lambda_0 Pe^{\lambda_1}$	0.74
$Sha_2 = \lambda_0 + \lambda_1 Pe^{\lambda_2}$	0.74
$Sha_3 = \lambda_0 Pe R_{im}^{\lambda_1}$	**0.84**
$Sha_4 = \lambda_0 Pe R_{im}^{\lambda_1}(a_v/a_h)^{\lambda_2}$	0.85
$Sha_5 = \lambda_0 Pe^{\lambda_1} R_{im}^{\lambda_2}(a_v/a_h)^{\lambda_3}$	0.85
$Sh_0 = \lambda_0 Pe$	0.67
$Sh_1 = \lambda_0 Pe^{\lambda_1}$	0.71
$Sh_2 = \lambda_0 + \lambda_1 Pe^{\lambda_2}$	0.71
$Sh_3 = \lambda_0 Pe R_{im}^{\lambda_1}$	0.75
$Sh_4 = \lambda_0 Pe R_{im}^{\lambda_1}(a_v/a_h)^{\lambda_2}$	0.80
$Sh_5 = \lambda_0 Pe^{\lambda_1} R_{im}^{\lambda_2}(a_v/a_h)^{\lambda_3}$	**0.88**
$b_0 = \lambda_0 + \lambda_1 R_{im}$	0.44
$b_1 = \lambda_0 + \lambda_1 R_{im} f_{im}$	0.52
$b_2 = \lambda_0 + \lambda_1 R_{im} f_{im}^{\lambda_2}$	0.52
$b_3 = \lambda_0 + \lambda_1 R_{im} f_{im} Pe^{\lambda_2}$	0.78
$b_4 = \lambda_0 + \lambda_1 R_{im} f_{im} + \lambda_2 Pe^{\lambda_3}$	0.78
$b_5 = \lambda_0 + \lambda_1 R_{im} f_{im} + \lambda_2 Pe^{\lambda_3}(a_v/a_h)^{\lambda_4}$	**0.83**

Table R.5.2. Coefficients and R^2 of regressed models.

Parameter	λ_0	λ_1	λ_2	λ_3	λ_4	R^2
K^{eff}/K_{sand}	-1.748	0.1802				0.99
α_l^{eff}/α_l	87.90	0.4822				0.70
Sha	0.2122	0.3929				0.84
Sh	0.2539	0.6940	0.2528	-0.4457		0.88
b	0.7176	-0.0661	-0.005800	0.5567	0.3650	0.83
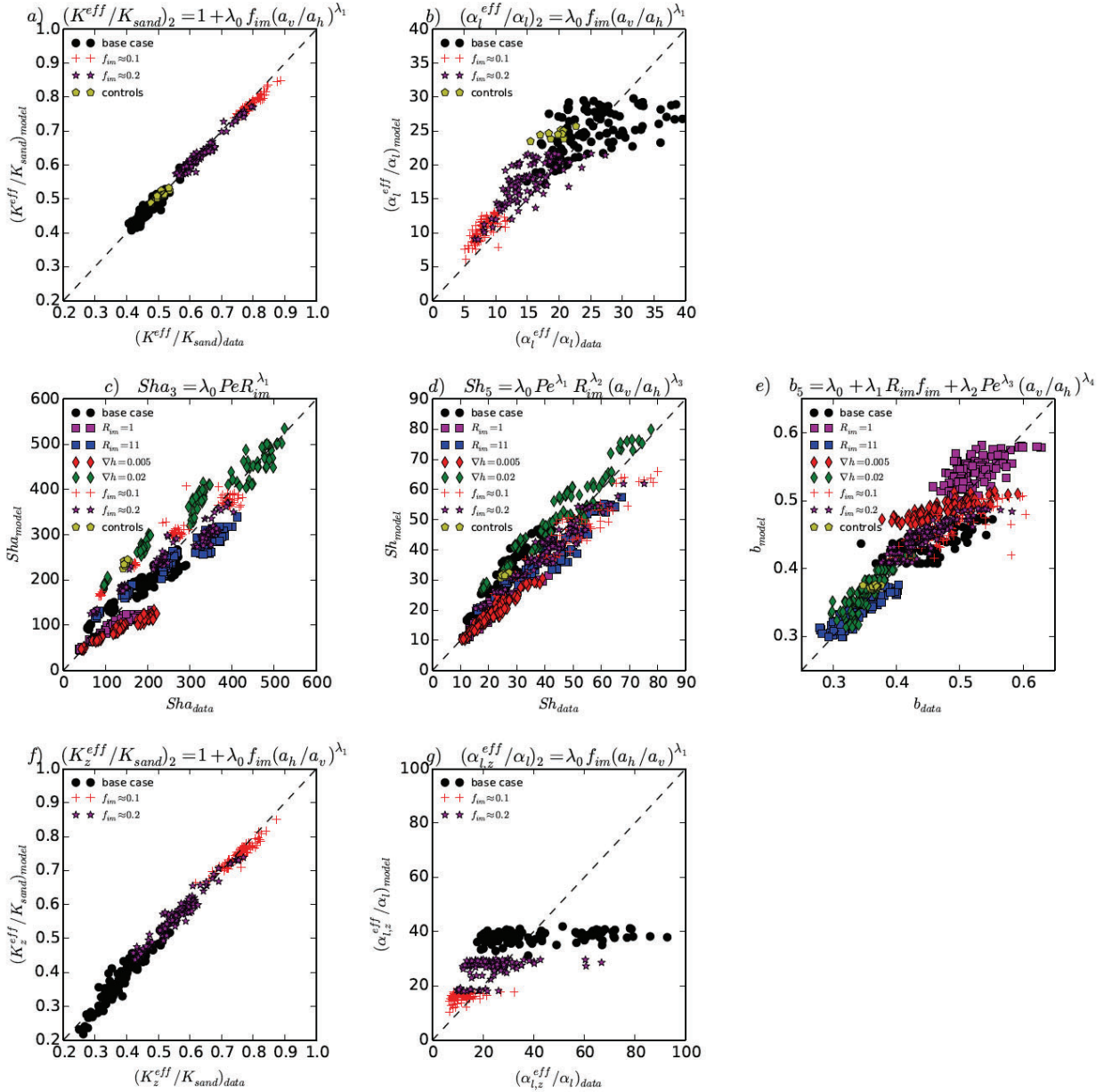
Figure R.5.3. Regression performance for a) scaled effective hydraulic conductivity, b) scaled effective dispersivity, c) Sherwood number for the higher first-order rate, d) Sherwood number for the lower first-order rate, and e) fraction of low-permeability material corresponding to the faster rate. Model numbers are indicated in the titles and the different cases used for the regression are explained in the captions. Subfigures f) and g) show the applicability of regressed models to simulations with vertical flow.

Although fitting to the analytical model does not give an effective transverse dispersivity, the implemented model at large scale must also provide this parameter. For comparison, the regressed model obtained with horizontal flow was applied to simulation results with vertical flow, again interchanging the meaning of a_v *and* a_h. There is a large spread in dispersivities that is not explained by the model. However, given the small impact of the longitudinal dispersivity on tailing, it may be anticipated that the transverse dispersivity also has relatively small impact on the late-time tailing.

127

III.5.1.4. Model Verification

All regressions were obtained using the boundary and initial conditions described in Section II.6.2.2 and other properties as defined in Tables M.6.1-2. In this section, the fitted and regressed parameters are tested for other initial and boundary conditions, and other geostatistical properties.

Ten control simulations were run with R_{im} = 9, a_v=a_h = 0.12 m, delta(h) = 0.015 and other properties as the base case. These were not used as data for the regressions. Applying the regressions to these simulations yielded good results (see Figure R.5.3). Simulations were also performed to test the impact of initial and boundary conditions on the utility of the regression expressions. In these simulations, R_{im} = 6, a_v=a_h = 0.1 m, f_{im}= 0.31 and delta(h) = 0.01. The fitted parameters are K^{eff} = 9.060 m/ day, α_l^{eff} = 0.01841 m, α_1 = 0.2471 day^{-1} , α_2= 0.05477 day^{-1}, β_1= 0.2997 and β_2 = 0.2709. The fitted Peclet number is 229.

Figure R.5.4(a) shows the fine-scale breakthrough curve and the analytical multi-rate solution that is fitted to this curve. Here, the initial- and boundary conditions of the base case (Step 2) were used. Inspection of the figure reveals that the fit is very good. The fitted parameters were also used in a numerical simulation of the multirate model, which yielded the same breakthrough curve and similar square root of SSE_2/N. In Figure R.5.4(b), rather than flushing the domain with pure water at t > 0, the solute concentration of the influent water is zero only for the first 100 days, and later it is equal to the initial concentration. Also here, the fine-scale solution agrees well with the simulated multi-rate solution. Figure R.5.4(c) shows the breakthrough curve for a Dirac pulse injection. This scenario is quite different from the scenario that was used for fitting of parameters, and the errors are larger than for the previous cases. Nevertheless, the late-time tailing, which is the main focus here, is well described using the same fitted upscaled parameters. Figures R.5.4(d-f) present simulations corresponding to those of Figures R.5.4(a-c), but here, parameters were obtained from the regression expressions (Figure R.5.3) rather than the fitted parameters. Again, breakthrough curves are close to the fine-scale solutions, confirming the usefulness of the regressed parameters.

The stability of the models with respect to the initial condition was also explored. Figure R.5.5 displays the fine-scale concentration after 1.2 days when the solute (concentration 1 kg/ m^3) was initially placed in the zone between x= 0.24-0.50 m. Other conditions are as in Figure R.5.4(a). The solute concentration in clay is highest where the solute was initially placed, whereas the concentration in the sand is larger downstream of this location.

Figure R.5.6(a) presents concentrations averaged over y and Figure R.5.6(b) shows the corresponding breakthrough curves. MRMT results are in good agreement with the fine-scale simulations.

III.5.1.5. Discussion

As discussed by Carrera et al. (1998), when studying breakthrough in an aquifer, it may be challenging to distinguish between the effects of physical mass transfer and sorption, because both produce tailing. In addition, the impacts of mechanical dispersion may be confounded with the former two. In this work, the different effects were separated as a part of the fitting procedure. We used zero porosity of low-conductive zones when fitting dispersivity and effective conductivity, and we used these fitted parameters together with an assumed known sorption capacity when fitting mass transfer parameters. Upscaled simulations were run using parameters that were regressed to the geostatistical parameters, hydraulic gradient (via the Peclet number) and sorption capacity. The upscaling of dispersion has been an extensive topic of previous work, see e.g. the review by Gelhar et al. (1992). The effective dispersivity has often been expressed as dependent

on the overall scale of observation. This is not accounted for in our fitting, as the domain size was fixed to reflect an anticipated typical cell size of large-scale simulations. Use of our regressed values produced good agreement with fine-scale breakthrough curves using both the analytical solution and a discretized model with centimeter size cells in the flow direction. This may be partly due to the low impact of effective dispersivity on our results. Applications using very different grid sizes should consider previous work on dispersion but be careful if those investigations accounted for mass-transfer in effective dispersion coefficients.
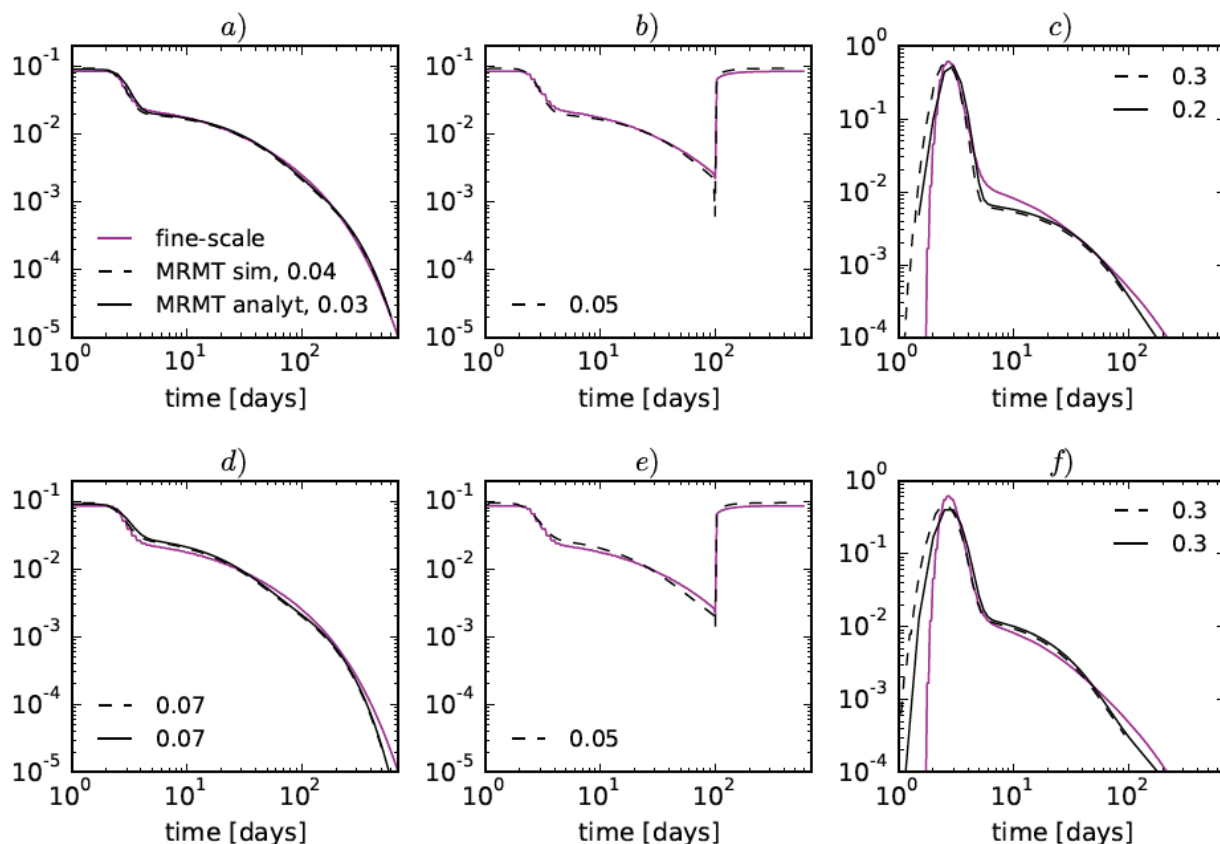
Figure R.5.4. Effluent mass flux (kg/m²day) using fitted parameters (top row) and regressed parameters (bottom row). The three columns represent inlet boundary conditions 1 - H(t) (left), step function (center) and Dirac pulse (right). Numbers in the legends represent square root of SSE_2/N, although here no scaling of the flux was performed. For the Dirac pulse, the error was calculated based on 4 orders of magnitude range in the breakthrough curve, including the largest value.

Previous investigations have shown that parameter fitting to a single-rate model produces a first-order rate that varies with the duration of solute exposure and experimental time (Flach, 2012; Guan et al., 2008; Maraqa, 2001). In contrast, we are able to obtain good matches using constant-in-time first-order rates that are relatively insensitive to the initial and boundary conditions such as exposure time. The success of this approach may be attributed to our two-stage fitting procedure, as well as, the ability to resolve early and late-time diffusion with respectively the faster and the slower of the two first-order rates. We can also compare our results with the analytical multi-rate expressions derived by (Haggerty and Gorelick, 1995), which were developed to represent diffusion between a well-mixed mobile zone and a sphere or layer of negligible conductivity. These authors scaled the first-order rates, as well as, the diffusion coefficient with Rim .

129
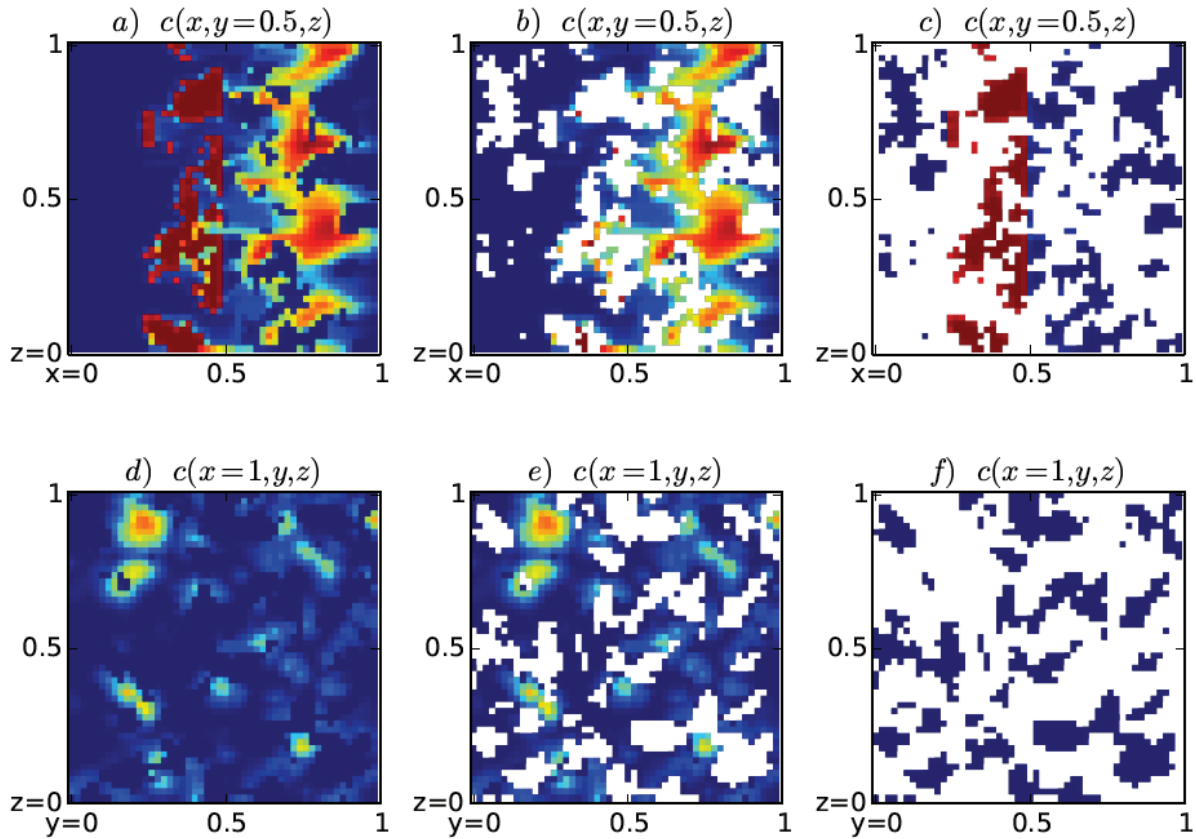
Figure R.5.5. Fine-scale concentration after 1.2 days, along the flow direction (top row) and at the effluent boundary (bottom row). Values are in the range 0-1 kg/m3 as represented by colors blue to red. The center and right columns shows results restricted to the high respectively low-permeability zones. See error measure description in Figure R.5.4, here measured at t > 1.
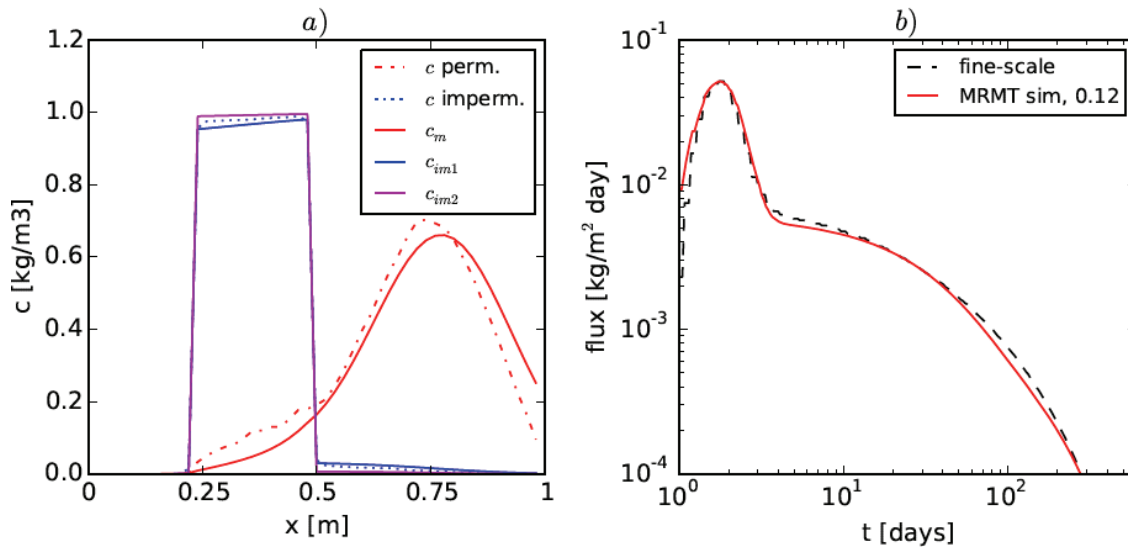
Figure R.5.6. a) Concentration along the flow direction at 1.2 days (1.16 days fine-scale and 1.24 days MRMT), averaged over y, and b) effluent mass flux (kg/m^{2}day). For error measure in label, cf. caption to Figure R.543, here with t > 1. The results are from fine-scale simulation and an MRMT simulation using regressed parameters.

130

They showed that the slowest Sherwood number is a factor 4 smaller than the second slowest Sherwood number for spherical inclusions. For layers, their two Sherwood numbers differed by a factor of 9. The relation between our faster and slower Sherwood numbers, when using a truncated series, varies over a larger range (3-10) but the present work suggests a greater influence of other parameters in comparison with the geometries of inclusions.

Contrary to the analytical results of (Haggerty and Gorelick 1995), the Sherwood numbers obtained here are sensitive to the Peclet number. In fact, the faster of the two Sherwood numbers increases linearly with Pe, whereas the slower rate is slightly less sensitive to Pe. Also, it is shown that there is a nonlinear dependence on R_{im} , and that only the slower rate is significantly affected by the geometry of inclusions. These results are more similar to the work of (Powers et al. 1994) who regressed a Sherwood number for a first-order dissolution model. Their regression takes into account the flow rate (Reynolds number) and parameters representing the dynamic interfacial area between phases. This further confirms that Sherwood numbers are affected by the flow field in real media with complex geometries and non-uniformity of mobile concentrations. This dependence on Pe applies also to the ratio between the pore volumes representative of the different Sherwood numbers. The use of MRMT models in large domains with varying flow conditions in space or time should make use of this by applying the local and current Pe when calculating the upscaled parameters.

III.5.1.6. Conclusions

The robustness of the regressed model was verified against fine-scale simulations with inputs and initial- and boundary conditions differing from those used in the regression process. The regressed models developed in this work can, thus, be used for performing MRMT simulations without the need for time-consuming fine-scale simulations. Based on the results presented herein, the following observations can be made:

- An MRMT model with two constant-in-time first-order rates can successfully reproduce fine-scale breakthrough curves in three-dimensional heterogeneous sorptive media.
- To capture the average behavior and ensemble variability of the full three-dimensional system, it is necessary to base the upscaling on three-dimensional simulations.
- Uniqueness of the fits with respect to the initial guess was demonstrated when using step-wise fitting.
- The fitted parameters and the regressed models were shown to be robust with respect to initial and boundary conditions.
- Consistent with the results of (Dentz et al., 2011), we found that physical mass transfer cannot be upscaled independently of reactive transport.
- For parameter ranges outside the scope of this work, a similar approach could be used to regress parameters and subsequently use them in upscaled simulations.

III.5.2. Bioenhanced Dissolution Screening Tool Development (based on Phelan et al. 2015)

III.5.2.1. Comparison of Measured and Predicted Bioenhancement Factors

To assess its suitability as a screening-level predictive tool, the developed model (Equations M.6.37-38) was applied to published bioenhanced dissolution laboratory column studies. Here the goal was to provide better than order-of-magnitude estimates of bioenhanced dissolution, aiding in remedial design. To this end, the model was employed to predict the dissolution enhancement observed in four experiments, performed by (Amos et al., 2009 and Yang and McCarty, 2002). In these experiments, packed sand columns were contaminated with PCE-DNAPL and augmented

with microbial cultures capable of dechlorinating PCE to lesser-chlorinated daughter products. Table R.5.3 presents the associated experimental parameters.

Table R.5.3. Experimental Parameters.

Column		Flow Rate (mL/min)	Porosity (-)	Column Cross-sectional Area (cm²)	DNAPL Source Zone Length (cm)	Average Initial Saturation (%)
Author	Substrates					
Yang & McCarty, 2002	pentanol	3.2	0.340	4.91	30	2
	oleate					
	1:1 v/v PCE:olive oil					4
Amos *et al.*, 2009	3:1 PCE:hexadecane	0.25	0.375	1.81	10	23.7

Figures R.5.7 and R.5.8 present column effluent data for PCE and associated biotransformation products for the (Amos et al., 2009, Yang and McCarty, 2002) columns, respectively. The authors of both studies do not compute bioenhancement factors for their experiments, although Amos *et al.* (2009; Figure 1) present a cumulative bioenhancement factor, but they define that value as the ratio of eluted masses as opposed to the ratio of steady-state mass fluxes described in equation (M.6.35). To estimate bioenhancement factors from the data reported in both studies, a steady-state (or, a pseudo-steady-state) regime for each experiment (both biotic and abiotic) must first be identified. The steady-state bioenhancement factor is then computed as the time-averaged ratio of the steady-state effluent concentration to the steady-state effluent concentration measured in an abiotic control column under the same flow conditions.
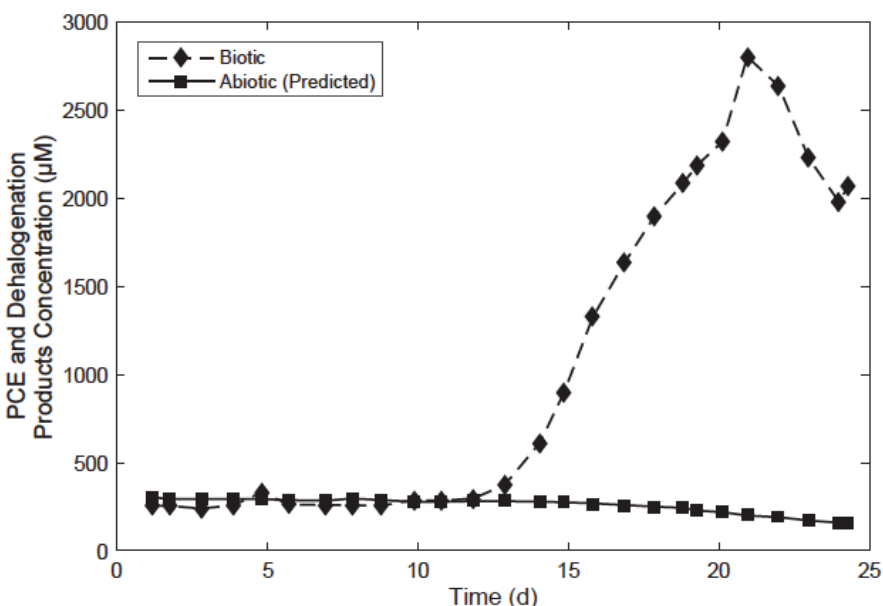
Figure R.5.7. Bioenhancement factor estimated by Amos et al. (2009) from column data. The approximate steady-state portion of this curve is denoted by the square symbols (occurring after about 29 pore volumes.
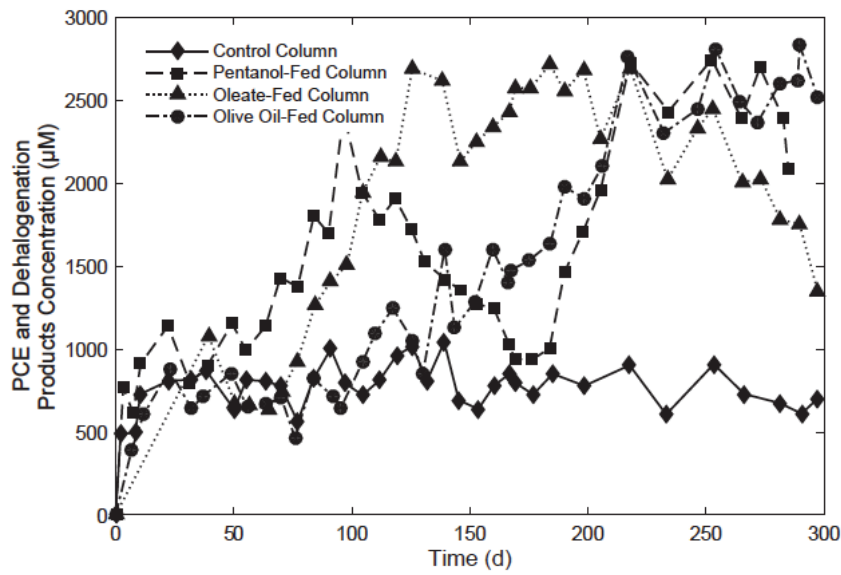
Figure R.5.8. Total effluent chloroethene and ethene concentrations measured by Yang & McCarty (2002).

To help identify the steady-state regime for each column, the effluent data were processed through several smoothing algorithms (kernel smoothing, local regression smoothing, median smoothing, and adaptive smoothing (Parametric Technology Corporation, 2010). The temporal concentration derivative (*i.e.*, dC/dt) was then calculated from these smoothed data using a second-order-accurate finite-difference approximation. These analyses for the (Yang & McCarty, 2002) columns suggest that steady-state conditions exist for the control column from about 100 days to the end of the experiment, from about 100 to 115 days for the pentanol column, from about 170 to 210 days for the oleate column, from about 280 days to the end of the experiment for the olive oil column (although only data up to 300 days will be used), and from about 20 days to 25 days for Amos et al.'s (2009) hexadecane column. The corresponding time-averaged bioenhancement factors (and corresponding 95% confidence intervals) are 2.44 ± 0.24, 3.24 ± 0.09, 4.08 ± 0.18, and 13.1 ± 0.80 for the pentanol, oleate, olive oil, and hexadecane columns, respectively.

As described in section II.6.2, the bioenhancement factors are nonlinear functions of the Damköhler 1 and 2 Numbers (**Da₁** and **Da₂**), the Péclet Number (**Pe**), and the dimensionless half-saturation constant $\left(K_s^*\right)$. The following sections describe how these four dimensionless parameters were estimated for the selected column experiments.

The Damköhler 1 Number $\left(k_l L/v\right)$ requires quantification of the pore velocity (v) and the lumped interphase mass transfer coefficient $\left(k_l\right)$. The pore velocity varies slightly over time and distance along the column due to changes in DNAPL saturation (S_n) as dissolution proceeds. Table R.9.2 presents the spatially averaged DNAPL saturations and the calculated pore velocities (see Table R.9.1 for flow rate and porosity data). The velocity reported in Table R.9.2 is averaged over the range of saturations observed, *i.e.*, $v = \int_{S_n^{begin}}^{S_n^{end}} \left[Q/\phi\left(1-S_n\right)A \right] dS_n \bigg/ \left(S_n^{begin} - S_n^{end} \right)$, to reflect a representative velocity value over the course of the column experiment. Here S_n^{begin} and S_n^{end}

133

denote the DNAPL saturations at the beginning and end of the pseudo-steady-state portion of each experiment, respectively. This averaging procedure is used when reporting all quantities that depend, usually through pore velocity, on non-aqueous phase saturation (*i.e.*, **Re**, **Sh**, k_l, **Da₁**, **Da₂**, *D*, **Pe**, and **E**).

Table R.5.4. Initial and final DNAPL saturations and average pore velocities.

Substrate	Steady-state S_n (%)		v (cm/d)
	begin	end	
pentanol	1.91	1.91	1.96
oleate	1.83	1.78	1.96
olive oil	3.74	3.71	1.99
hexadecane	22.9	22.4	11.4

It should be noted that neither set of authors measured the non-aqueous phase saturations at the beginning and end of the steady-state periods as presented in Table R.5.4. Rather, these values were calculated by scaling the initial non-aqueous phase saturations by the total mass of chlorinated ethenes remaining in the column divided by the initial mass of PCE in the columns.

The Sherwood Number correlation of (Powers et al. 1994) was used to estimate the lumped mass transfer coefficient, as it incorporates aqueous-phase velocity, soil texture, and changing DNAPL saturation:

$$\textbf{Sh} = 4.13\textbf{Re}^{0.598} \left(\frac{d_{50}}{d_M}\right)^{0.673} U_i^{0.369} \left(\frac{S_n}{S_n^{begin}}\right)^{\alpha} \tag{R.5.1}$$

where **Sh** is the Sherwood Number is given as:

$$\textbf{Sh} = \frac{k_l d_{50}^2}{D_m} \tag{R.5.2}$$

Here d_{50} is the mean grain size of the porous media and D_m is molecular diffusion coefficient (8.70×10^{-6} cm²/s for PCE; (Montgomery 2007)). The Reynolds number is:

$$\textbf{Re} = \frac{v \rho_w d_{50}}{\mu_w} \tag{R.5.3}$$

where ρ_w and μ_w are the density and dynamic viscosity of water, here assumed to be taken at 20°C (ρ_w = 998 kg/m³ and μ_w = 1.02×10⁻³ Pa·s; (Mott and Untener 2014)). Other quantities in equation (R.5.1) include d_M, the diameter of a "medium" sand grain (0.5 mm) as defined by the United States Department of Agriculture (Driscoll 1986), U_i is the uniformity coefficient of the porous media, $S_n^{initial}$ is the initial DNAPL saturation (see Table R.5.3), and the exponent α incorporates the effect of porous medium texture on the DNAPL interfacial area:

$$\alpha = 0.518 + 0.114 \frac{d_{50}}{d_M} + 0.1 U_i \tag{R.5.4}$$

Table R.5.5 summarizes values for grain size parameters, and the saturation-averaged Reynolds number, mass transfer coefficients, and Damköhler 1 Numbers.

Table R.5.5. Damköhler 1 Number Development.

Substrate	d_{50} (mm)	U_i (-)	**Re** ($\times 10^4$)	α	**Sh**	k_l (d^{-1})	**Da$_1$**
pentanol			6.04		0.478	4.83	74.1
oleate	2.73^1	22.1^1	6.03	3.35	0.459	4.65	71.4
olive oil			6.15		0.481	4.87	73.2
hexadecane	0.32	1.86^2	4.14	0.777	0.0362	26.5	23.2

[1]Harmon et al. (1992)
[2]Chen et al. (2013)

The Damköhler 2 Number $\left(k_{max}XL/C_{eq}v\right)$ requires estimation of several parameters, the most challenging of which is the biomass concentration (X). Yang and McCarty (2002) stated that each column had about 1 mg of biomass per 100 mL of pore volume. It is reasonable to assume that not all of this biomass is active so a value one- to two-orders-of-magnitude (*i.e.*, 1.5-orders-of-magnitude) lower will be used for this analysis. Amos et al. (2009) estimated an active dehalogenating (PCE to *cis*-DCE and *cis*-DCE to ethene) biomass concentration of 16.6×10^9 cells in the pore volume of their column and a typical cell density of 10^{-12} g/cell. The sensitivity of bioenhancement factor values to these assumptions will be explored below.

Table R.5.6. summarizes the batch experiment-derived kinetic parameters, the biotransformation rate constants, and the resulting **Da$_2$** values. Note that a large range of **Da$_2$** values is represented, reflecting the wide variation in experimental systems.

Table R.5.6. Damköhler Number 2 Development.

Substrate	k_{max} (μmol/mg·d)	X (mg/L)	K_s (μM)	C_{eq} (μM)	K_s^*	**Da$_2$**
pentanol				900	2.22×10^{-4}	1.97
oleate	366^1	0.316	0.2^1			
olive oil				819	2.44×10^{-4}	2.13
PCE/HD	0.094^2	40.8	0.54^2	300	1.80×10^{-3}	11.2

[1]Lee et al. (2004)
[2]Chen et al. (2013)

The Péclet Number $\left(vL/D\right)$ requires estimation of the longitudinal hydrodynamic dispersion coefficient. The conventional approach for estimating this parameter was employed (Bear 1988)

$$D = \alpha_x v + \tau D_m \tag{R.5.5}$$

where α_x is the longitudinal dispersivity coefficient, assumed to be 1 cm for column experiments of this size (Chen et al., 2013; Gelhar et al., 1992) and τ is the tortuosity, assumed to be ⅔ (Bear 1988). Table R.5.7 summarizes the transport parameters for these experiments and the resulting Péclet Numbers.

Table R.5.7. Péclet Number Development.

Substrate	a_x (cm)	τ (-)	D (cm²/d)	Pe
pentanol			2.46	23.9
oleate	1	⅔	2.46	23.9
olive oil			2.50	24.0
hexadecane			11.9	9.58

Figure R.5.9 compares the observed and predicted bioenhancement factors. Error bars for the observed bioenhancement factors reflect the experimental standard deviation. The error bars on the predicted bioenhancement factors reflect the variability resulting from time-variant, spatially averaged DNAPL saturation over the course of the experiments. There is relatively good agreement, often within *one-tenth* of one order of magnitude, between the experimental bioenhancement factors and the zero-order and Monod predictions (relative errors range from about approximately 10% to 25%). Differences in the predicted and observed factor may be due to (i) poor characterization of the mass transfer rate coefficient $\left(k_l \right)$, (ii) differences in microbial activity (*i.e.*, k_{max} and K_s) reported by (Lee et al. 2004) and observed in the columns, and (iii) a lack of information on the biomass concentration (X) in the column source zone. The order-of-magnitude over-prediction of the (Yang & McCarty, 2002) bioenhancement factors (*i.e.*, pentanol, oleate, and olive oil) derived with first-order kinetics is not surprising, considering that the steady-state effluent concentrations of PCE are between two- and four-orders-of-magnitude greater than the half-saturation constant. Although expected, it is important to note this over-prediction, since it is not uncommon in field applications to simplify Monod biotransformation processes with a pseudo-first-order kinetic approach. Further, the close agreement between the zero-order and Monod kinetics predictions indicates that this process can successfully be modeled as a zero-order process for these experimental conditions.
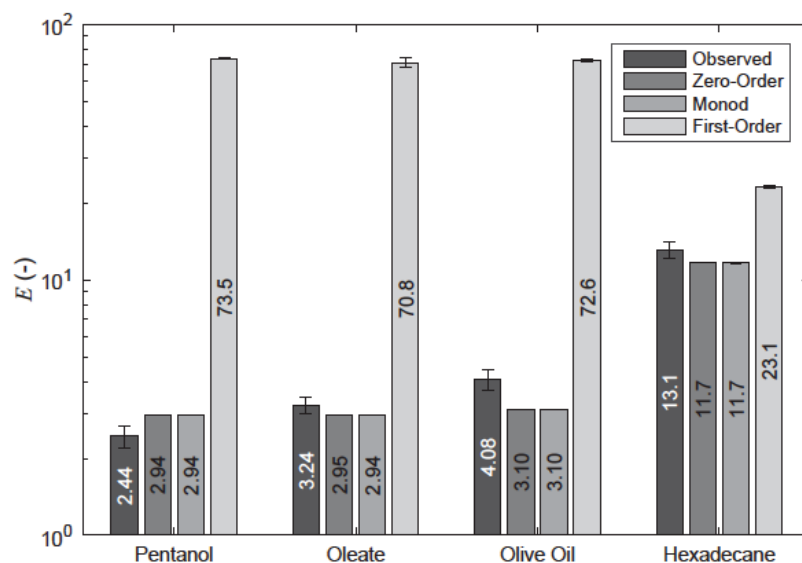
Figure R.5.9. Observed and predicted values for the bioenhancement factors. The height of the observed bar is the bioenhancement factor over the steady-state portion of the experiment; the error bars represent the time-weighted standard deviation. The error bars on the predicted values reflect the variability due to uncertainty in the non-aqueous phase saturation.

III.5.2.2. Sensitivity of Bioenhancement Factor to Biomass Concentration

Successful validation of the bioenhancement factor approach relies on the selection of an appropriate biomass concentration. Both Yang & McCarty (2002) and Amos et al. (2009) reported a biomass value within the experimental columns (based on a measurement of unattached biomass), but these values are subject to a significant level of uncertainty, especially with respect to how much of the reported biomass is actually active and able to take part in biotransformation. For example, Chen et al. (2013) determined that the ratio of total to unattached biomass in the Amos et al. (2009) column ranged from 1 to 20, depending on the organism and location within the column. An analysis was undertaken to explore the sensitivity of the bioenhancement factor predictions to the biomass concentration values. Figure R.5.10 presents predicted bioenhancement factors (using Monod kinetics) over a range of biomass concentrations from 1 µg/L to 1 g/L for the Yang and McCarty (2002) columns.
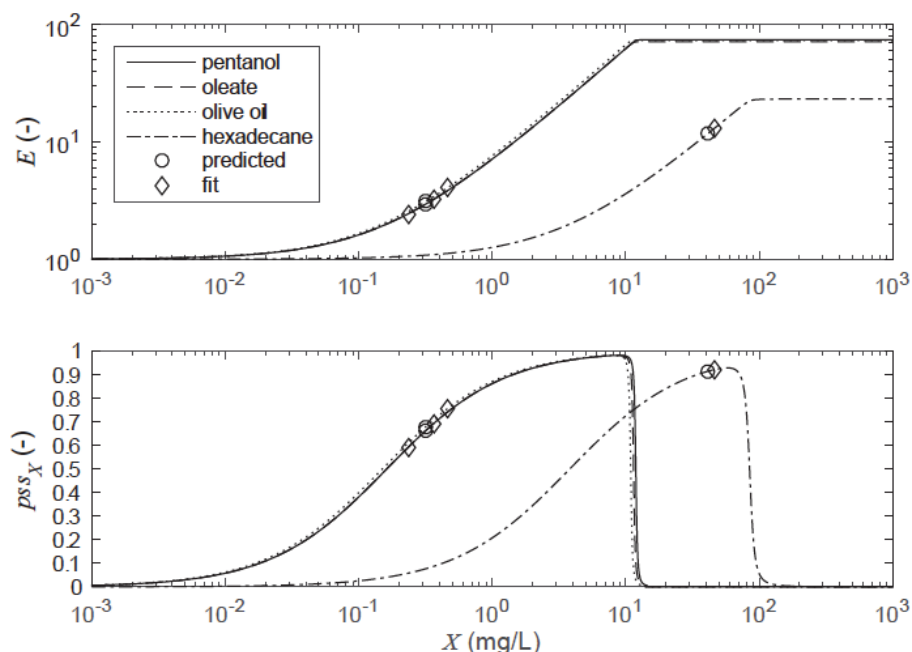
Figure R.5.10. Sensitivity of predicted Monod-kinetics bioenhancement factors to assumed biomass concentration. Symbols indicate predicted and best-fit results from individual column experiments.

The prediction scaled sensitivity of the bioenhancement factor to biomass concentration is also shown. Here the prediction scaled sensitivity (pss_X) is computed as (Hill 1998):

$$pss_X = \frac{\partial E}{\partial X} \frac{X}{100\%} \frac{100\%}{E} \tag{R.5.6}$$

The prediction scaled sensitivity represents the percentage change in the bioenhancement factor produced by a one-percent change in the biomass concentration. Overlain on the bioenhancement factor and prediction scaled sensitivity curves are a set of circular symbols representing the *model-predicted* bioenhancement values and corresponding prediction scaled sensitivities for the assumed biomass concentration in each column. The diamond symbols represent the biomass concentration value required to obtain the bioenhancement factor observed in the experimental results. As might be expected, the bioenhancement factor curve is sigmoid; at low biomass concentrations little bioenhancement is observed due to low biomass (E is asymptotic to one), while at high biomass concentrations bioenhancement is limited by dissolution kinetics. E

137

asymptotically approaches a value dependent on **Pe**, **Da₁**, and K_s^*. An analytical expression of this relationship does not exist, but can be evaluated numerically. Inspection of Figure R.5.10 reveals that the predicted bioenhancement factors for the Yang & McCarty (2002) experiments all fall in a region of moderately high sensitivity to biomass concentration while the prediction for the Amos *et al.* (2009) experiment is very sensitive to biomass concentration. This suggests that careful evaluation of this parameter is necessary when employing this simplified bioenhancement factor approach to field-scale situations. The fact that all experiments demonstrated relatively large values of pss_X suggests that this sensitivity may be more likely the rule than the exception in many engineered bioremediation systems. Field-scale sensitivity to this parameter will be explored in section III.5.2.4.

Additionally, Figure R.5.10 reveals rapid reduction in the magnitude of the parameter scaled sensitivity in the region of a biomass concentration of 10 mg/L (Yang & McCarty (2002) experiments) and 100 mg/L (Amos et al. (2009) experiment). These concentrations are the approximate values required to make **Da₂** (*i.e.*, the biotransformation rate) equal to **Da₁** (*i.e.*, the dissolution rate). This indicates that efforts to increase biomass concentration in an attempt to increase the bioenhancement factor are worthwhile up until the point that the bioenhancement factor becomes strongly limited by the dissolution rate. At this point additional increases in biomass are not effective. It can be observed from Figure R.5.10 that the rate at which this sensitivity reduces from its maximum value to zero is inversely proportional to the half-saturation constant.

III.5.2.3. Model Application

To aid in the application of this screening model, a series of nomographs was developed to provide a simplified tool that can be used for engineering bioremediation systems (Mohamed and Hatfield 2011). The nomographs visually depict the dissolution enhancement one can expect when adjusting engineered parameters such as groundwater velocity (residence time) or biomass concentration. Figure R.5.10 is a three-dimensional surface plot that depicts the behavior of the zero-order bioenhancement factor (E_0) as a function of the three dimensionless numbers, **Pe**, **Da₁**, and **Da₂**. Six isosurfaces are presented for a range of bioenhancement factor values. Inspection of the isosurfaces reveals an increase in bioenhancement (E_0) with increasing mass transfer rate (**Da₁**) and biotransformation rate (**Da₂**). Further, for a given set of transport conditions (**Pe**) and biotransformation rate (**Da₂**), the sensitivity of the bioenhancement factor to dissolution rate (**Da₁**) decreases as the dissolution rate becomes large. An analogous observation can be made for the biotransformation rate (**Da₂**) for a given set of transport conditions (**Pe**) and dissolution rate (**Da₁**). This reflects the fact that as the biodegradation rate becomes larger, bioenhancement begins to be rate-limited by dissolution and vice-versa. Similarly, in advectively dominated systems (*i.e.*, **Pe** values greater than approximately one), the sensitivity of the bioenhancement factor to **Pe** becomes very small. The residence time is simply too short to allow for further bioenhancement. An analogous figure could be developed for the first-order and Monod bioenhancement factors, although generation of the equivalent Monod figure would be very computationally costly.

Figure R.5.11 (and its first-order and Monod analogs) is useful for drawing general conclusions about the behavior of the bioenhancement factor. For example, an increase in pore velocity corresponds to an increase in the Péclet Number and decrease in the Damköhler 1 and 2 Numbers, which leads to a decrease in the bioenhancement factor. Unfortunately, however, the three-dimensional format of Figure R.5.11 makes it difficult to use in the analysis and design of bioremediation systems.

Figure R.5.12 transforms the three-dimensional isosurface plots to a series of contour plots of the zero-order kinetics bioenhancement factor as a function of dissolution rate ($\mathbf{Da_1}$) and biotransformation rate ($\mathbf{Da_2}$) for a selection of different transport regimes (*i.e.*, constant values of **Pe**). The Péclet Number was held constant, as opposed to the Damköhler 1 or 2 Numbers, due to the relationship between pore velocity and the hydrodynamic dispersion coefficient (see equation (R.5.5)), which may make the Péclet Number difficult to control in an engineered system. Note the discontinuity in slope (*i.e.*, $\partial E_0/\partial \mathbf{Da_1}$ and $\partial E_0/\partial \mathbf{Da_2}$) along the line $\mathbf{Da_1} = \mathbf{Da_2}$ resulting from the piecewise nature of equation (M.6.38).
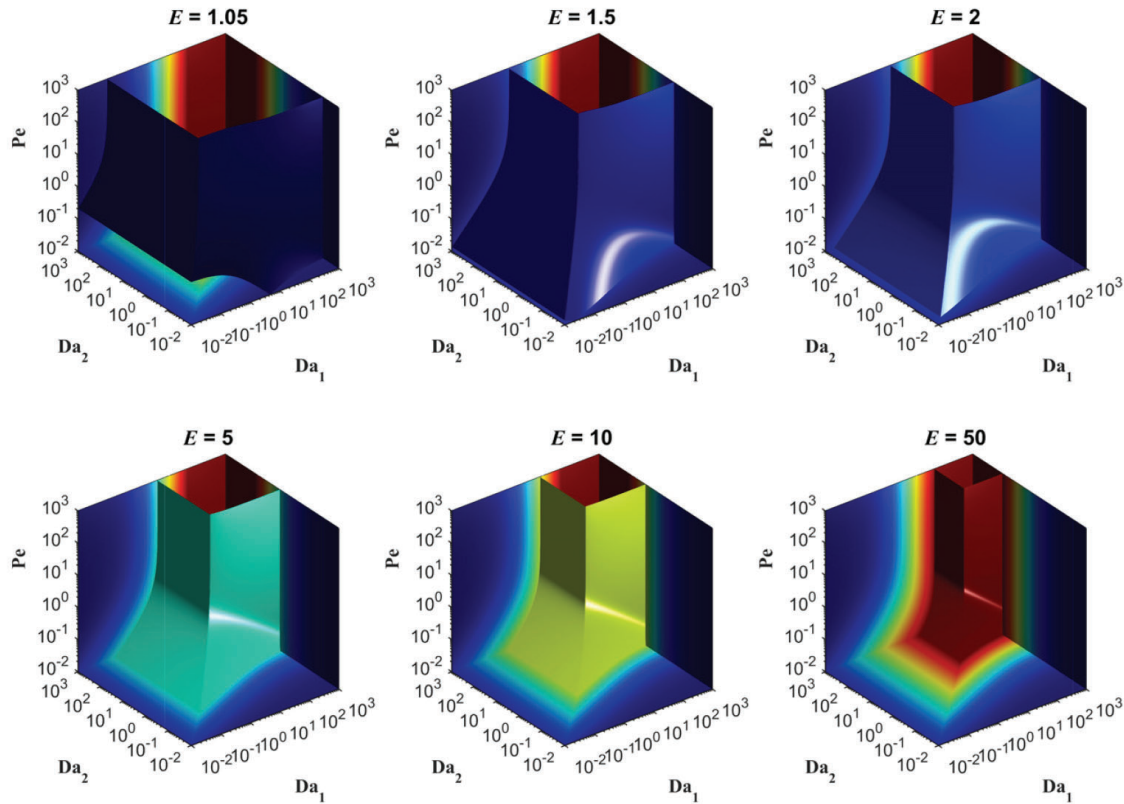
Figure R.5.11. Isosurfaces plots depicting the bioenhancement factor as a function of Péclet and Damköhler Numbers assuming zero-order kinetics.

For situations where first-order kinetics may be appropriate, Figure R.5.13 presents the corresponding set of contours for first-order kinetics. Here the behavior of E_1 is varies smoothly in the vicinity of the line $\mathbf{Da_1} = \mathbf{Da_2}$. The numerical Monod bioenhancement factor simulator described previously was used to examine dimensionless half-saturation constants ranging from 10^{-6}, reflective of an actual half-saturation constant six-orders below the equilibrium solubility (typical of an analytical detection limit for a compound like PCE), to 1, reflective of an actual half-saturation constant on the order of the equilibrium solubility. As an example, Figure R.5.14 depicts the contours for a dimensionless half-saturation constant of 10^{-1}; the supplemental information contains the corresponding plots for Monod kinetics given a range of these dimensionless half-saturation constants. Note that bioenhancement factor plots for dimensionless half-saturation constant values less than 10^{-4} are visually indistinguishable from the zero-order plots. These figures (*i.e.*, Figures R.5.12 – R.5.14) are useful from a remedial design perspective; through a set of simple calculations, anticipated enhancements in mass removal can be estimated graphically.
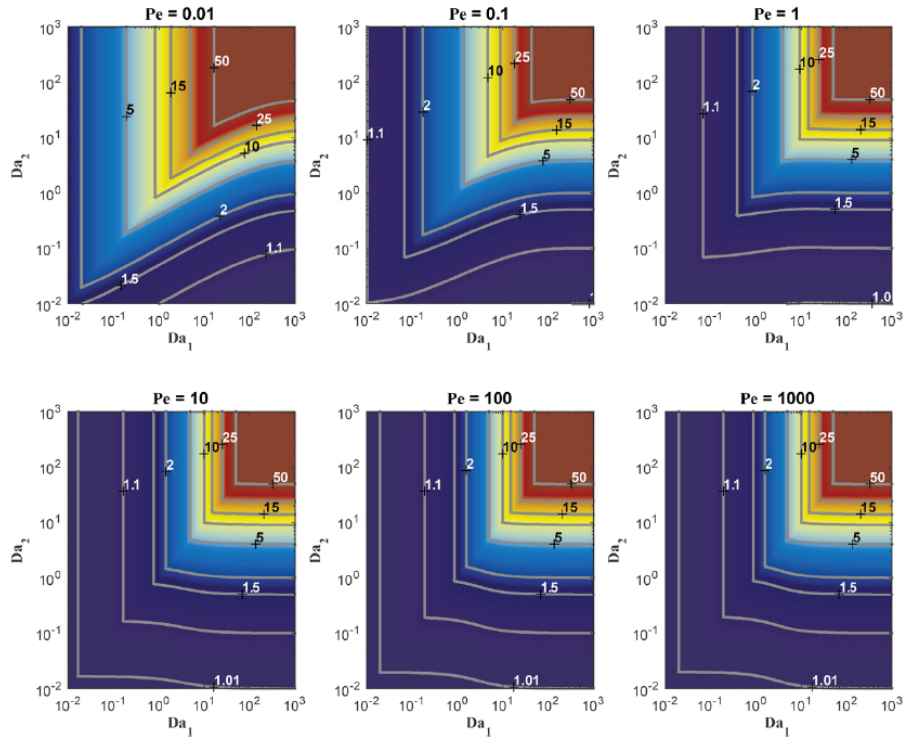
Figure R.5.12. Contour plots of the zero-order-kinetics bioenhancement factor as a function of Damköhler 1 and 2 Numbers. Each individual plot represents bioenhancement factor values at different Péclet Number values
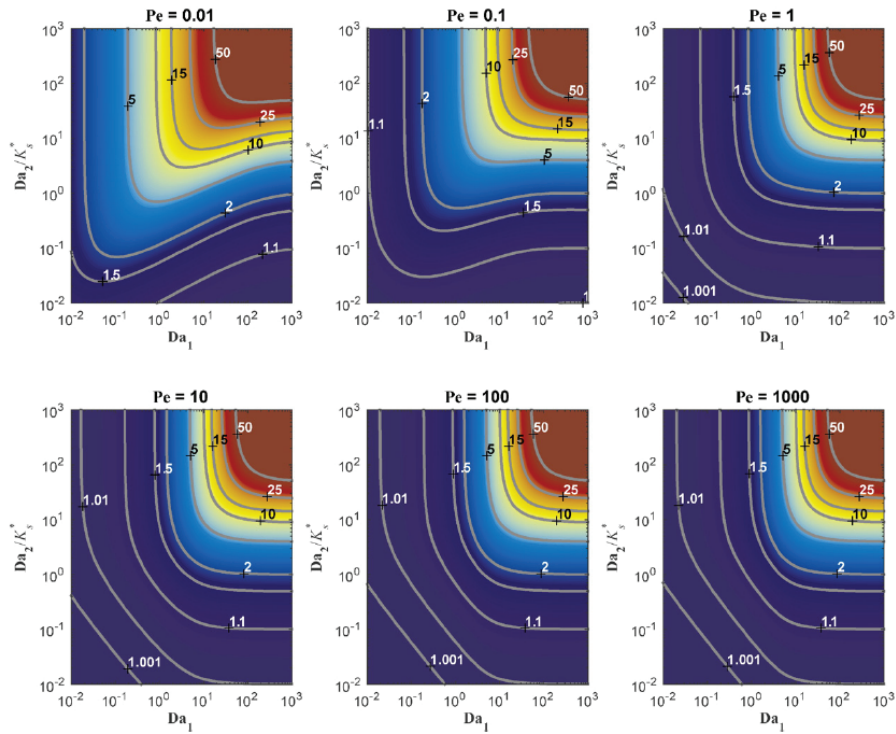
Figure R.5.13. Contour plots of the first-order-kinetics bioenhancement factor as a function of Damköhler 1 and 2 Numbers. Each individual plot represents bioenhancement factor values at different Péclet Number values.
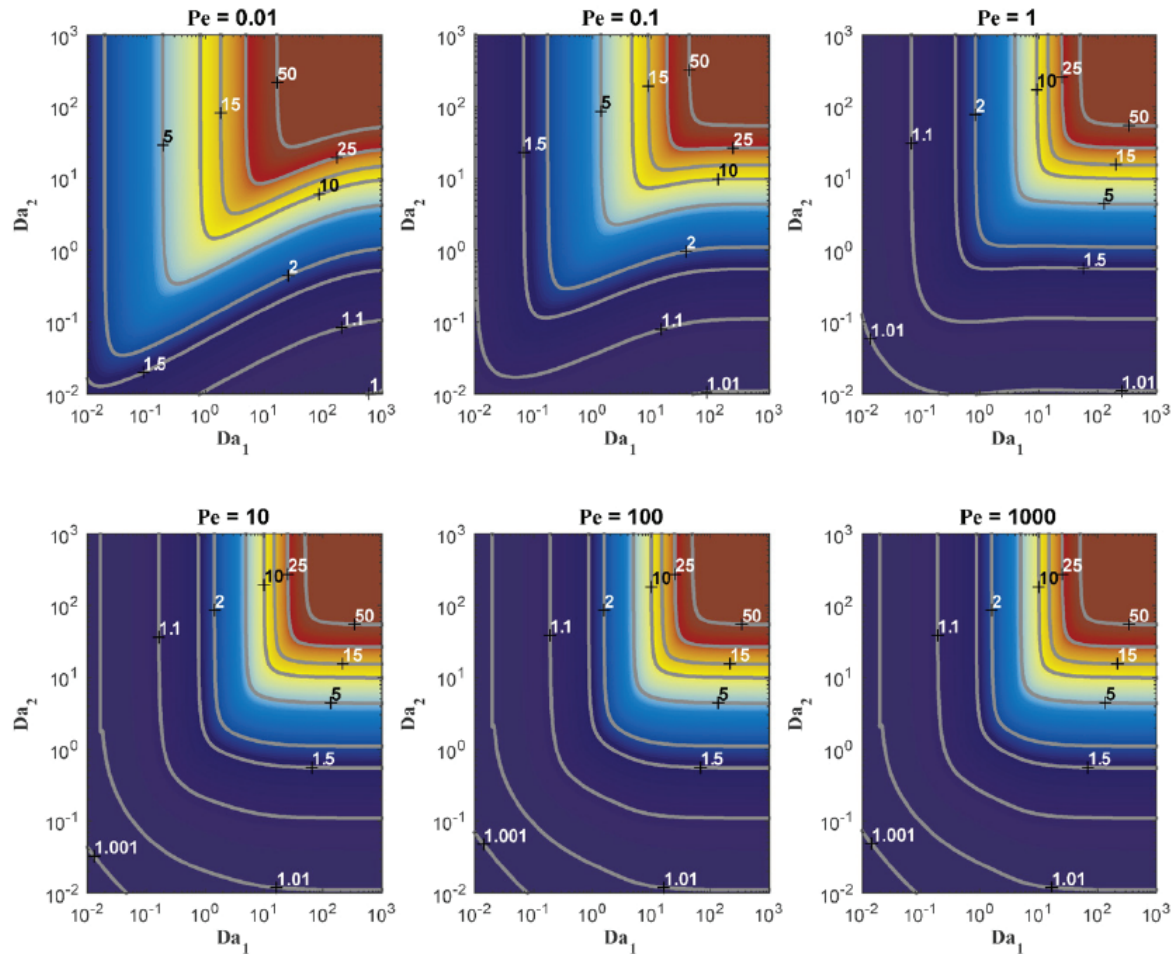
Figure R.5.14. Contour plots of the Monod-kinetics bioenhancement factor as a function of Damköhler 1 and 2 Numbers and a dimensionless half-saturation constant of $K*_s = 10^{-1}$. Each individual plot represents bioenhancement factor values at different Péclet Number values.

III.5.2.4. Application to a Field Site

The SABRE (Source Area Bioremediation) project is a well-known field and laboratory demonstration of *in situ* biotransformation of a trichloroethene-DNAPL source zone (Zeeb and Houlden 2010). Using available data from the literature and realistic assumptions regarding grain size distribution, dispersion parameters, and temperature, summarized in Table R.5.8, estimates of the four dimensionless numbers were developed as **Da₁** = 109, **Da₂** = 0.437, **Pe** = 12.5, and $K_s^* = 9.56 \times 10^{-4}$. Source-zone TCE concentrations are initially in the 1700-1900 µM range (Wilson and Cia 2012; Zeeb and Houlden 2010), which are significantly higher than the half-saturation constant of 8.00 µM reported by (Cupples et al. 2004b). This suggests that the kinetics operative at the SABRE site can likely be modelled with a zero-order assumption. Using Figure R.5.12 yields an estimated bioenhancement factor of 1.4, which is in relatively close agreement with the value of 1.6 developed from the ratio of post-biostimulation flux to pre-biostimulation flux data at the site (Zeeb and Houlden 2010).

Table R.5.8. Parameter Used to Estimate Bioenhancement Factor for SABRE Site.

Dimensionless Number	Parameter	Value	Reference	Comments	Dimensionless Number Value
Péclet	v	7.72×10^{-6} m/s	Zeeb & Houlden (2010)		$\mathbf{Pe} = 12.5$
	L	12.5 m			
	α	1 m	Gelhar et al. (1992)	Assumed	
	τ	⅔		Assumed	
	D_m	10^{-5} cm²/s	Kresic, (2006)		
	D	0.077 cm²/s	N/A	Computed using equation (13)	
Damköhler 1	d_{50}	8 mm	N/A	Assumed for fine to medium gravel	$\mathbf{Da_1} = 109$
	U_i	1	N/A	Assumed	
	ρ_w	1000 kg/m³	Mott and Untener, (2014)	Assumed for 10°C	
	μ_w	1.30×10^{-3} Pa·s			
	S_n	3.5%	Rivett et al., (2010)		
	k_l	5.82 d⁻¹	N/A	Computed using equation (10)	
Damköhler 2	X	50 mg/L	Harkness and Fisher, (2013)		$\mathbf{Da_2} = 0.437$
	k_{max}	3.90 µmol/mg·d	Cupples et al. (2004)	Estimated from batch experiments.	
	K_s	8.00 µM			
	C_{eq}	8.37×10^3 µM	Wilson & Cai (2012)		
Dimensionless Half-Saturation Constant					$K_s^* = 9.56\times10^{-4}$

As previously stated, analysis of the Yang & McCarty (2002) and Amos et al. (2009) data suggests that bioenhancement number predictions are sensitive to biomass concentration estimates (see Figure R.5.10). A similar analysis was undertaken here to explore the sensitivity of the bioenhancement factor estimated for the SABRE site to the biomass concentration. Figure R.5.15, similar to Figure R.5.10, depicts the bioenhancement factor obtained using the parameters in Table R.5.8 and biomass concentrations ranging from 10^{-1} to 10^5 mg/L. The parameter scaled sensitivity to biomass concentration (pss_X) is presented as well. The circle and diamond symbols indicate the bioenhancement factor and parameter scaled sensitivity values, respectively, for the SABRE site. Inspection of Figure R.5.15 reveals that the bioenhancement number predicted for the SABRE site is moderately sensitive to the biomass concentration ($pss_X \approx 0.3$), although not as sensitive as the bioenhancement number predictions for the Yang & McCarty (2002) and Amos et al. (2009) experiments (*see* Figure R.5.10). This emphasizes the importance of representative biomass concentration measurements in remedial efforts. Further, Figure R.5.15 suggests that the predicted bioenhancement factor can be substantially increased with an increased biomass concentration; the

bioenhancement factor does not become insensitive to biomass concentration until concentrations exceed 10,000 mg/L. The magnitude of this biomass concentration value suggests that the system may not ever become mass-transfer limited.
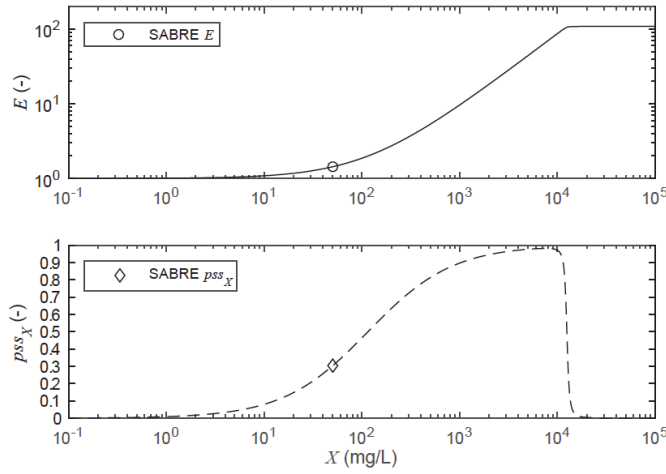
Figure R.5.15. Sensitivity of predicted Monod-kinetics bioenhancement factors to assumed biomass concentration. Symbols indicate predicted and best-fit results from individual column experiments.
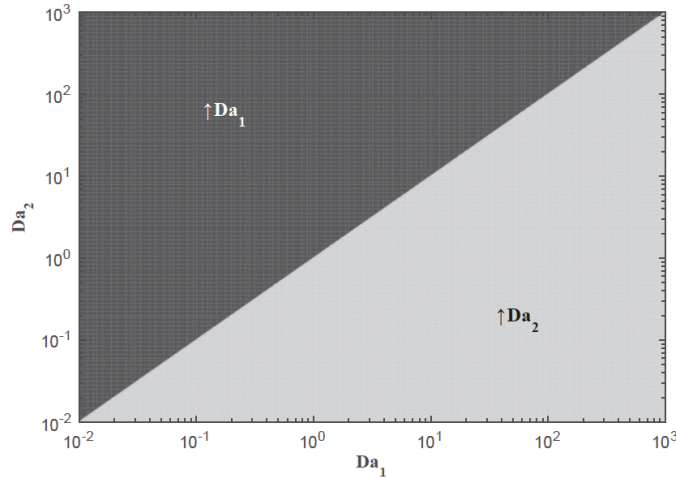
Figure R.5.16. Regions of dominant parameter-scaled sensitivity for zero-order kinetics. The zero-order kinetic bioenhancement factor is never more sensitive to the Péclet Number than the Damköhler Numbers.

The SABRE results suggest that when optimizing remedial approaches that exploit bioenhanced dissolution, it can be helpful to identify if a given system is most sensitive to transport mechanisms (**Pe**), mass transfer (**Da$_1$**), or biotransformation kinetics (**Da$_2$**). Stated alternatively, will the largest increase in bioenhancement be realized by attempting to alter the Péclet or Damköhler Numbers? This can be assessed by identifying the largest parameter scaled sensitivity among these three dimensionless numbers,

$$pss_{max} = \max\left(\left|\frac{\partial E}{\partial \mathbf{Pe}}\frac{\mathbf{Pe}}{100\%}\frac{100\%}{E}\right|, \left|\frac{\partial E}{\partial \mathbf{Da_1}}\frac{\mathbf{Da_1}}{100\%}\frac{100\%}{E}\right|, \left|\frac{\partial E}{\partial \mathbf{Da_2}}\frac{\mathbf{Da_2}}{100\%}\frac{100\%}{E}\right|\right) \quad \text{(R.5.7)}$$

Figure R.5.16 presents a region plot that identify regions where the Damköhler 1 and Damköhler 2 Numbers have their respective maximum parameter scaled sensitivities for zero-order kinetics. For the zero-order kinetics case, the biotransformation factor is always more sensitive to the

143

Damköhler Numbers than the Péclet Number and, in fact, the regions of maximum parameter scaled sensitivity ($pss_{max} = pss_{\mathbf{Da}_1}$ vs. $pss_{max} = pss_{\mathbf{Da}_2}$) are independent of the magnitude of the Péclet Number.
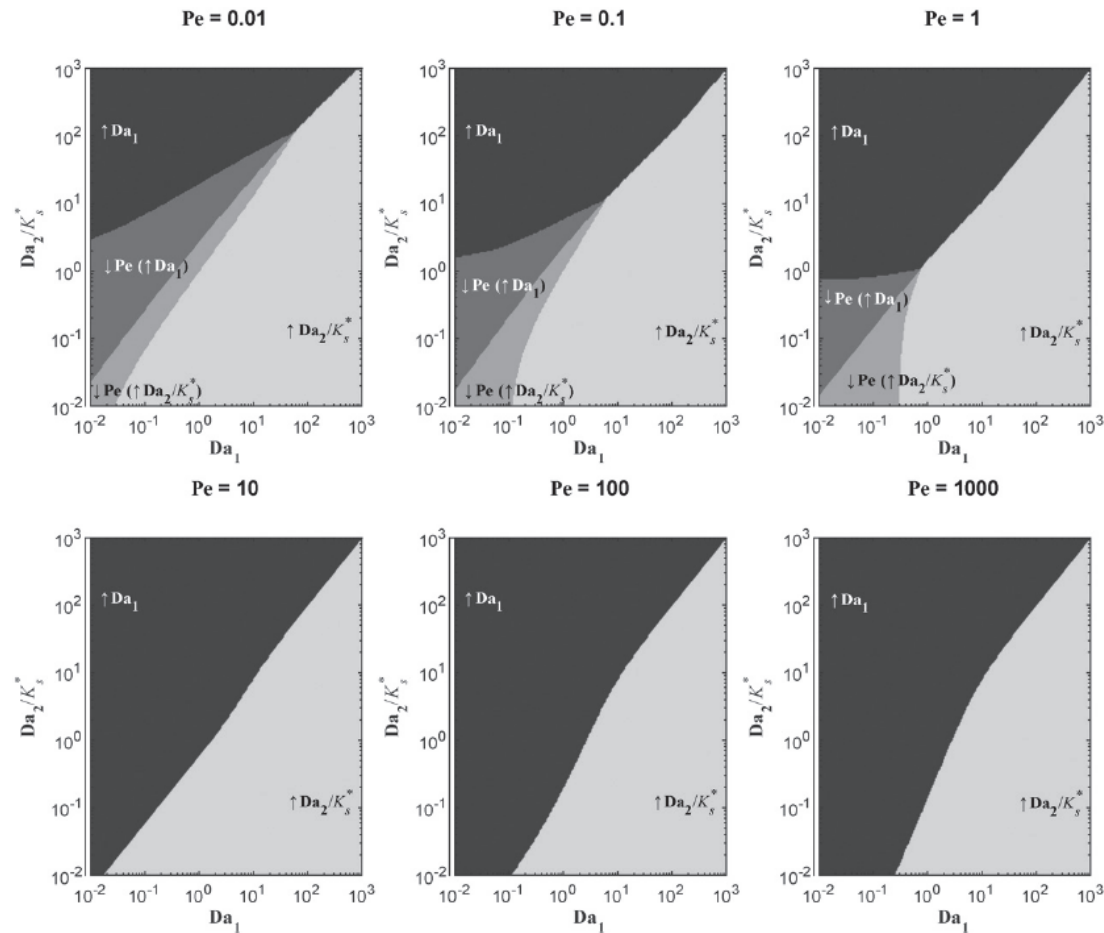
Figure R.5.17. Regions of dominant parameter-scaled sensitivity for first-order kinetics. Unlike the zero-order kinetic model, the first-order bioenhancement factor has regions where it is sensitive to the Péclet Number. In general, designs that try to equalize the Damköhler Numbers yield the greatest bioenhancement factors.

For potential situations where first-order kinetics are appropriate, Figure R.5.17 reveals regions where decreasing the Péclet Number (less advectively dominated), increasing the Damköhler 1 Number (increased mass transfer kinetics), or increasing the Damköhler 2 Number (increased biotransformation kinetics) leads to the greatest increase in the bioenhancement factor. Due to the difficulty in controlling the Péclet Number in engineered systems, owing to the nature of hydrodynamic dispersion in porous media, the Péclet Number region is subdivided into two regions that indicate the dimensionless number (**Da₁** or **Da₂**) with the second-highest parameter scaled sensitivity. Fortunately, the region where the bioenhancement factor is most sensitive to transport processes (*i.e.*, Péclet Number) is relatively small and only occurs when transport is not advectively dominated (**Pe** < 1 in Figure R.5.17). Inspection of Figures R.5.16 and R.5.17 further reveals that, in general, optimizations that attempt to equalize the Damköhler 1 and Damköhler 2 Numbers (*i.e.*, equalize mass transfer and biotransformation rates) will yield the greatest increase in bioenhancement factor. Put simply, if a remedial system is biotransformation-rate limited (*i.e.*,

$Da_1 > Da_2$) the design should be modified to increase the biotransformation rate (Da_2) or, conversely, if a remedial system is mass transfer rate limited (*i.e.*, $Da_1 < Da_2$) the design should be modified to increase the mass transfer rate (Da_1). Although the figures are not presented here, a similar analysis of the Monod kinetics parameter scaled sensitivities yields the same conclusion. For example, at the SABRE site ($Da_1 = 109$, $Da_2 = 0.437$), designing a remediation strategy that increases Da_2 (*i.e.*, increasing the biotransformation rate constant) will lead to an increase in the bioenhancement factor. This conclusion is consistent with the results of the biomass concentration sensitivity analysis described earlier. One way this could be achieved is through additional bioaugmentation efforts. Alternatively, at a hypothetical site with $Pe = 10$, $Da_1 = 0.1$, and $Da_2 = 10$ and first-order kinetics, increasing the mass transfer rate (Da_1) will lead to an increase in the bioenhancement factor. The Powers *et al*. (1994) correlation suggests that the most practical way to increase Da_1 would be to reduce the pore velocity. However, reducing the pore velocity will also increase Da_2, as both Da_1 and Da_2 are inversely proportional to this quantity. Thus, steps may have to be taken to maintain Da_2 values while attempting to increase Da_1.

III.5.2.5. Conclusions

In this work, the first-order bioenhancement factor described in Christ and Abriola (2007) was extended to incorporate zero-order and Monod kinetics. The zero-order bioenhancement factor can be computed through a closed-form expression that is slightly more complex than the first-order expression presented in Christ and Abriola (2007). Both the zero-order and first-order bioenhancement factor expressions can be cumbersome and time consuming to use, involving evaluation of complicated exponential and hyperbolic trigonometric functions. Therefore, a pair of nomographs was presented to facilitate graphical solution of the bioenhancement factor expressions. Further, a closed-form expression for the Monod bioenhancement factor does not exist; in this work, it is computed numerically and presented as a series of nomographs, similar to the zero- and first-order bioenhancement factor nomographs, that can be useful in the analysis and design of remedial systems. The ability of these tools to quantify the expected benefits of bioenhanced dissolution was assessed using four sets of relatively well-described column experiments. Results indicate that bioenhancement factors estimated directly from laboratory data match very well with those values computed using experimental parameters (well within an order of magnitude). Considerable uncertainty in bioenhancement factor predictions is due to uncertainty in biomass concentrations, which is often difficult to predict when designing remedial approaches that exploit bioenhanced dissolution. Sensitivity results suggest that bioenhancement factor predictions are sensitive to the estimated value of biomass concentration and that uncertainty in this parameter must be considered during the design stage. The ability of these tools to estimate the bioenhancement factor for a well-described field site was also evaluated. Results indicated that this approach could match the field data very well – the bioenhancement factors computed using the nomographs under-predicted the bioenhancement factor estimated from field data by approximately 12.5%. This is considered good agreement, especially considering the uncertainty introduced by the heterogeneous, multi-dimensional nature of a field site. Similar to the column experiments, this prediction was found to be sensitive to biomass concentration. The implications of biomass concentration uncertainty notwithstanding, the bioenhancement factor approach can be of value in the design and operation stages of a given site remedy. When evaluating bioenhancement factor behavior as a function of the Péclet and Damköhler Numbers, practitioners can use either the equations (for zero- and first-order kinetics) or the contour plots. These plots allow practitioners to estimate bioenhancement factors of existing or proposed site remedies and identify potential operating or design changes that will lead to increased bioenhanced dissolution and, ideally, more rapid site cleanup and closure.

III.6. Statistical Characterization Tool Development and Application

III.6.1. Data Preparation

In this work, the statistical model, BRAINS, based on Equations M.7.4-7, was trained using mass distribution data generated from multiphase flow and transport model simulations in heterogeneous permeability fields. A detailed description of the infiltration and transport simulations, as well as summaries of the input parameters used in TPROGs, M-VALOR and MT3DMS simulations, can be found in Section II.5 (Yang et al., 2018). These MVALOR/MT3DMS simulation results provided the raw data for preprocessing as input data for the statistical model. Six time points (i.e. t=1, 3, 4, 6, 7, 10 years after a spill loading time of 1 year) were taken from each MT3DMS simulation, for an ensemble of 40 hypothetical permeability fields. In order to properly evaluate the statistical model, these selected realizations were partitioned into training, cross-validation, and test sets. The train-validation-test set split ratio was 40:10:50. Each of the selected time points were treated as independent observations. However, simulation data were kept together when splitting the data into training, cross validation and testing data sets. That is, all 6 time points of any single MT3DMS simulation (i.e. single permeability realization) were kept in the same data set (either train, cross validation or test). This was done to assure that the model was trained, validated and tested with data from all available time regimes. The process of model training, cross validation and testing are explained in detail below.

The two hydrological quantities of interest, DNAPL saturation and aqueous concentration, were quantized into discrete labels by binning continuous values of these properties. Saturation values which fall between 0 and 1 were discretized into 4 categories or labels. For concentration, the values span over a wider range between 0 and 150 [mg/L], where the distinctions in lower values are important, as well as capturing values on the high end of the range. Therefore, concentration values were binned into seven categories of labels, split into roughly logarithmic ranges. Table R.6.1 presents the upper lever boundary for each of these saturation and concentration categories.

Table R.6.1. Upper level limits for concentration and saturation categories.

Categories	0	1	2	3	4	5	6
Concentration (mg/L)	1.0E-3	1.0E-2	1.0E-1	1	10	100	150
Saturation	1.0E-3	0.15	0.6	1	-	-	-

III.6.2. Model Features

The features $\mathbf{h}_i(\mathbf{y})$ used in the models are based on saturation and concentration borehole data from MT3DMS simulations and permeability values at each pixel. Features are measurable properties calculated from the raw data that can help us build a predictive model. For example, a feature could be the average value of some quantity in a region of the image. Each pixel in the image that represents the domain will have a feature vector, a vector of calculated or extracted features that corresponds to that pixel. It is desirable to use as few features as possible that can produce an informative model, as more features result in more parameters to optimize. The following quantities were extracted from borehole data for each pixel i and used as intermediate calculations for more complex final features that were ultimately used in the model:

- d_U, d_D: distance between pixel i and the closest up-gradient and down-gradient boreholes.
- $\bar{C}_U, \bar{C}_D$: mean aqueous concentration at closest up-gradient and down-gradient boreholes respectively over a window centered on the elevation of pixel i in the borehole (See Figure R.6.1). The length of this averaging window is proportional to transverse dispersion length

scale ($l_{VT} = \sqrt{4\alpha_V d_{U,D}}$), which is related to vertical transverse dispersivity (α_V) and distance from pixel i to the closest up-gradient or down-gradient borehole (d_U, d_D). This length was specifically chosen to consider the effect of vertical transverse dispersion in the model.

- $\bar{S}_U, \bar{S}_D$: mean saturation at closest up-gradient and down-gradient boreholes respectively, over a 3-pixel window centered at the elevation of pixel i.
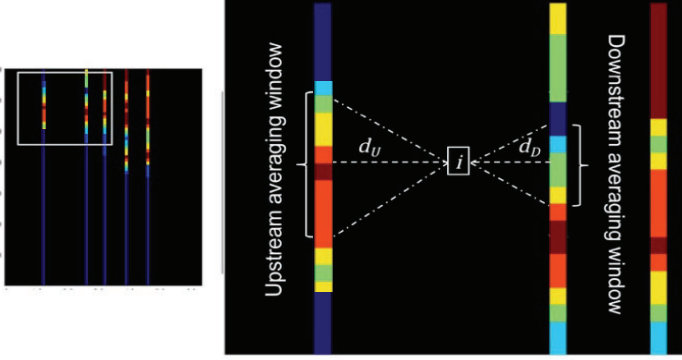
Figure R.6.1. Illustration of borehole features for a pixel between two borehole columns.

The averages over the borehole windows were then weighted based on how close the boreholes are to the pixel for which the features are being calculated. In particular, the features for borehole saturation and aqueous concentration are distance-weighted averages of the values of the quantities at the closest boreholes on either side of each pixel as shown in (M.6.1).

$$f_U(X_i) = \bar{X}_U\left(1 - \frac{d_U}{d_U+d_R}\right) ; f_D(X_i) = \bar{X}_D\left(1 - \frac{d_D}{d_U+d_R}\right) ; \; where \; X: C \; or \; S \qquad (R.6.1)$$

Using these quantities, the features that comprise the feature vector $h_i(\mathbf{y})$ are listed in Table R.6.2. These features can be summarized as a bias term always equal to 1; distance weighted average of saturation values at up-gradient and down-gradient boreholes at site i ($f_U(S_i)$, $f_D(S_i)$); distance weighted average of aqueous concentration at up-gradient and down-gradient boreholes at site i ($f_U(C_i)$, $f_D(C_i)$); the difference in average concentrations at up-gradient and down-gradient boreholes ($\bar{C}_D - \bar{C}_U$); the value of permeability at pixel i ($\log(k_i)$); and lastly the ratio between the observed permeability at site i and the pixel just below it ($\log\{k(\text{row}_i, \text{column}_i) / k(\text{row}_i+1, \text{column}_i)\}$).

Table R.6.2. List of final features used in the model.

FEATURE NO.	SATURATION	CONCENTRATION
1	Bias term; 1	Bias term; 1
2	$\log(k_i)$	$\log(k_i)$
3	$\log\{k(\text{row}_i, \text{column}_i) / k(\text{row}_i+1, \text{column}_i)\}$	$\log\{k(\text{row}_i, \text{column}_i) / k(\text{row}_i+1, \text{column}_i)\}$
4	$f_U(S_i) + f_D(S_i)$	$f_U(S_i)$
5	$\bar{C}_D - \bar{C}_U$	$f_D(S_i)$
6	$f_U(C_i)$	$f_U(C_i)$
7	$f_D(C_i)$	$f_D(C_i)$

These set of features were mainly selected considering the physical processes involved in this

problem such as advection, dispersion and capillarity. Furthermore, the selection of model features occurred over a process of trial and error by testing the model over multiple set of candidate features to optimize the model performance. Due to different processes involved in DNAPL infiltration and dissolution, slightly different sets of features were used for predicting NAPL saturation and aqueous concentration distributions. For example, the difference between average concentrations at downstream and upstream boreholes ($\bar{C}_D - \bar{C}_U$) could be a good indicator of the presence of DNAPL between those two boreholes, however it might not give any valuable information about the aqueous phase concentration between boreholes.

III.6.3. Parameter Estimation; Model Training

Let $\theta = \{w_k, v_{kl}\}\ k, l \in L$ be the set of parameter vectors for the association and interaction terms involved in the DRF model defined in Section II.7 (Equations M.7.4-7). Since there is one w_k vector for each possible label, there will be $|L|$ association parameter vectors, each of length N, where N is the number of features in the feature vector. Each v_{kl} parameter vector corresponds to a pair of labels where $v_{kl} = v_{lk}$, so there will be $\binom{|L|+2-1}{2} = \binom{|L|+1}{2} = \frac{(|L|+1)|L|}{2}$ interaction parameter vectors of length N to account for every combination of pairs of labels neighboring pixels can take.

Estimating these parameters requires calculating the partition function in (M.7.4), which is an intractable problem [Li, 2009]. However, this calculation can be avoided by solving for the pseudolikelihood rather than the likelihood so that the parameters are estimated as:

$$\hat{\theta}^{ML} \approx \underset{\theta}{\operatorname{argmax}} \prod_{m=1}^{M} \prod_{i \in S} P(x_i^m | \mathbf{x}_{N_i}^m, y^m, \theta) \tag{R.6.2}$$

where m indicates an image in the training set M. Lastly as in (Kumar and Hebert 2006) a regularization term is introduced to keep the interaction potential parameters from dominating the function. With this final regularization term and by combining (M.7.4) and (R.6.2), (R.6.2) becomes

$$\hat{\theta} = \underset{\theta}{\operatorname{argmax}} \sum_{m=1}^{M} \sum_{i \in S} \{A_i(x_i, \mathbf{y}) + \sum_{j \in N_i} I_{ij}(x_i, x_j, \mathbf{y}) - \log z_i\} - \frac{1}{2\tau^2} \mathbf{v}^2 \tag{R.6.3a}$$

$$z_i = \sum_{x_i \in L} \exp\left(A(x_i, \mathbf{y}) + \sum_{j \in N_i} I(x_i, x_j, \mathbf{y})\right) \tag{R.6.3b}$$

where z_i is the ith component of normalization term corresponding to pixel i and τ is the model hyperparameter, which is trained through cross validation. Cross validation is a hyperparameter optimization method, which involves reserving a particular sample of the dataset (here 10% of the dataset) for use in cross validation set subsequent to training. In this technique the model parameters (i.e. $\theta = \{w_k, v_{kl}\}$) are trained for different values of τ, using the training data set. Later the cross-validation set is used, as an independent dataset, to find the optimal hyperparameter (τ) which minimizes the objective cost function (i.e. maximizes the pseudolikelihood) as described in section III.6.5.

To estimate the model parameters, the $\mathbf{w}_k$ parameters are initialized using a multinomial logistic regression classifier where $\mathbf{v}_{kl}$ are set to zero everywhere. This initialization provides a starting point to achieve a more local optimization than would be attained by using a random or zero initialization approach. For each value of τ, the parameter vectors $\mathbf{w}_k$ and $\mathbf{v}_{kl}$ are trained sequentially by successively fixing one set of parameters and estimating the other through stochastic gradient descent (Jones et al., 2001).

III.6.4. Metropolis-Hastings Sampling; Simulations

Once the model is trained on the forward simulation data, realizations from the model can be obtained through sampling. In particular, we use Metropolis-Hastings sampling, described by the following algorithm (Table R.6.3), where the cost of assigning a specific label refers to the negative pseudolikelihood as described in (R.6.3a and R.6.3b). The Metropolis-Hastings (MH) method is one of the most popular and widely applied forms of Markov Chain Monte Carlo (MCMC) algorithms used to simulate nonstandard, complex multivariate distributions (Hastings 1970; Martino and Elvira 2017; Metropolis et al. 1953; Robert 2015).

Table R.6.3. Metropolis-Hastings Sampling Algorithm

1:	*Initialize domain as a uniform distribution across all possible labels*
2:	**for** *each pixel i in the domain (except the borehole pixels) do*
3:	*Propose new label from uniform distribution across possible labels*
4:	**if** *proposed label does not equal current label at pixel i then*
5:	*Calculate current cost (using current label)*
6:	*Calculate proposed cost (using proposed label)*
7:	*Accept new label with probability P_{accept} = min {1, exp(current cost - proposed cost)}*
	That is, if P(proposed label) $\geq$ P(current label), proposed label is accepted and if
	P(proposed label) < P(current label), the proposed label is accepted with probability P_{accept}
8:	*end **if***
9:	*end **for***
10:	*repeat 2-9 for N=2000 times, where N is the number of equiprobable realizations*

III.6.5. Results and Discussion

After training and validating the model parameters in BRAINS, the simulator was used to estimate DNAPL saturation and aqueous concentration distributions from borehole measurements and permeability data for realizations in the test data set. Figure R.6.2 presents examples of the ensemble mean (Figure R.6.2(d)) and variance (Figure R.6.2(e)) of 2000 equiprobable DNAPL saturation and aqueous concentration realizations at two different times for the input permeability field shown in Figure R.6.2(a) and input borehole data shown in Figure R.6.2(b). The MT3DMS simulation results (i.e. true labels) are presented in Figure R.6.2(c). These simulations were performed based on the knowledge of 7 equally spaced boreholes in the domain.

Inspection of these and similar model results indicate that BRAINS (i.e. Figure R.6.2(d)) can reconstruct the general structure and distribution of contaminant mass observed in the true results (Figure R.6.2(c)), producing realistic saturation and aqueous concentration fields given the permeability and input borehole data. By visually comparing the model predictions (Figure R.6.2(d)) with true labels (Figure R.6.2(c)) we can infer that the joint probabilistic model performs best in the prediction of aqueous concentration labels. This behavior can be explained by the continuous nature of aqueous phase concentration, in comparison to the sparse and discontinuous saturation distribution, especially at later times (Figure R.6.2.III). However, as shown in Figures R.6.2.I and R.6.2.III, BRAINS is capable of modeling the presence of highly saturated pooled DNAPL on top of low permeability layers, associated with highly heterogeneous aquifers that contain continuous stratigraphy and sufficient textural contrast. The modeling of these high saturated DNAPL pools is mainly achieved by concurrent utilization of two saturation model

features: average concentration difference at up-gradient and down-gradient boreholes ($\bar{C}_D - \bar{C}_U$), and the ratio between the observed permeability at site i and the pixel just below it ($\log\{k(\text{row}_i, \text{column}_i) / k(\text{row}_{i+1}, \text{column}_i)\}$).
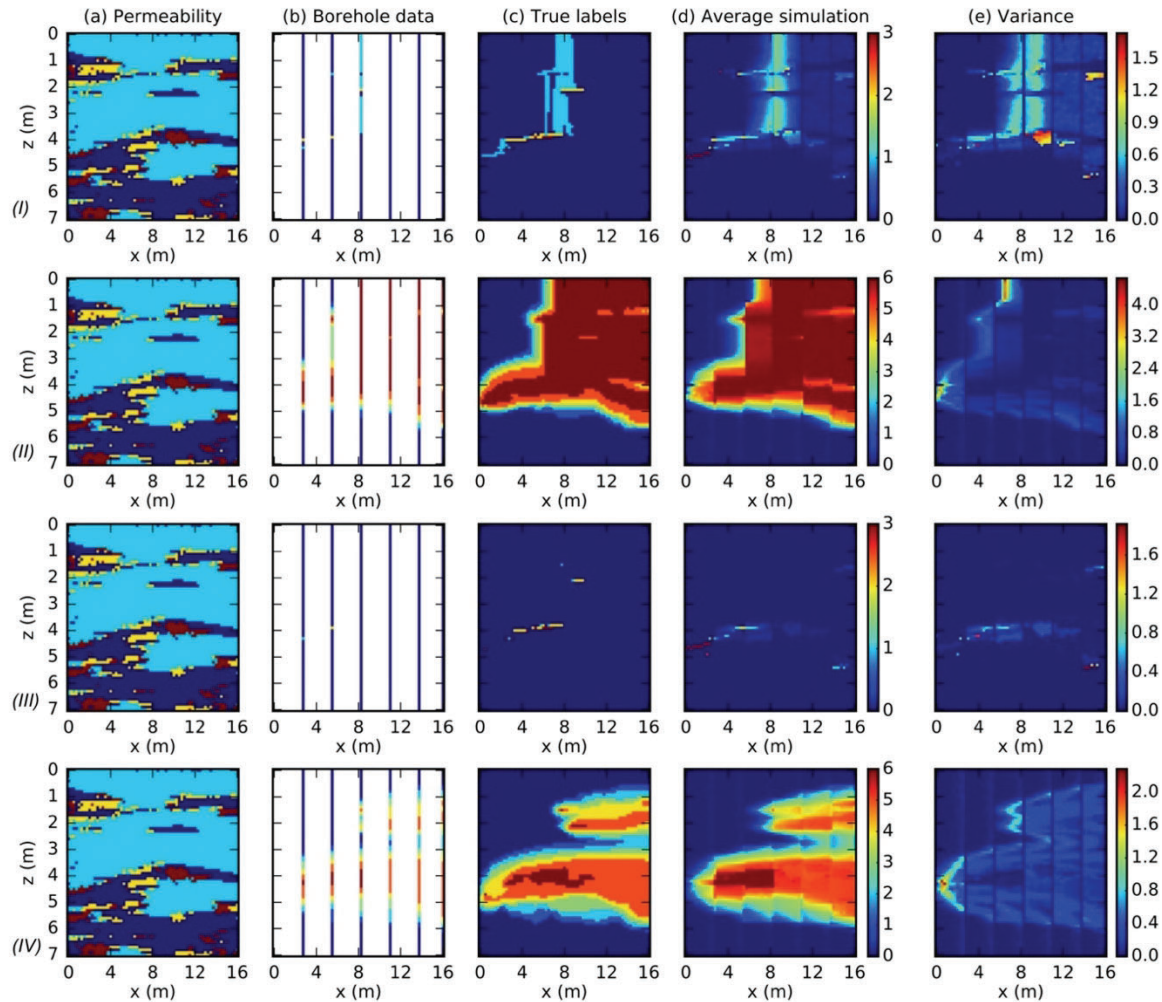
Figure R.6.2. Example of saturation (I, III) and concentration (II, IV) prediction results at (I, II) t = 1 year and (III, IV) t = 10 years after spill. (a) Input permeability, (b) Input borehole data, (c) MT3DMS results (i.e. true labels), (d) average and, (e) variance of 2000 equiprobable realizations.

The variability among realizations of the model (Figure R.6.2(e)) can be used as a measure of uncertainty at every point in the domain. That is, for each pixel in an image, the variability in the values of saturation and concentration across realizations provides insight into the uncertainty of the model, given the observed borehole data. These uncertainty fields (Figure R.6.2(e)) could be used to design optimal sampling strategy inferring the statistically optimal location for additional borehole measurements to characterize source zones under realistic field conditions.

Despite the successful performance of BRAINS model in predicting DNAPL source zone architecture and distribution, two major sources of error (i.e. type I and type II errors) are involved in these models and can be observed in Figures R.6.2.I and R.6.2.III. Type I error (i.e., false positive) is the incorrect prediction of DNAPL (either pool or ganglia) in a specific region of the domain where no DNAPL actually exists. Some examples of type I error can be seen in the down-gradient (i.e. right hand) side of Figures R.6.2.I(d) and R.6.2.III(d). These false positive errors

often occur at interfaces of lower permeability beneath high permeability regions and are associated with higher uncertainty (variance) as evident in Figures R.6.2.I(e) and R.6.2.III(e). Type II error (i.e. false negative) refers to a failure to reproduce DNAPL source zones that are present in the true image (e.g. top half of Figure R.6.2.III(d)). These types of errors are usually caused by insufficient borehole data and often observed at later times.

Ensemble mean results for saturation and concentration fields simulated by BRAINS are compared below (Figure R.6.3) with the realizations obtained from classical ordinary kriging approach (Krige 1951; Matheron 1963). The kriging packages from SURFER software (version 15.0, Golden Software Inc., Golden, CO, USA) were used to calculate the experimental semivariograms and estimate the saturation and aqueous phase plume architectures. First, for each saturation and concentration realization, the experimental semivariograms obtained from sampled borehole data were fit to two-dimensional exponential models. These exponential variogram models were then used as the input for kriging to generate saturation and concentration realizations based on observed borehole data.
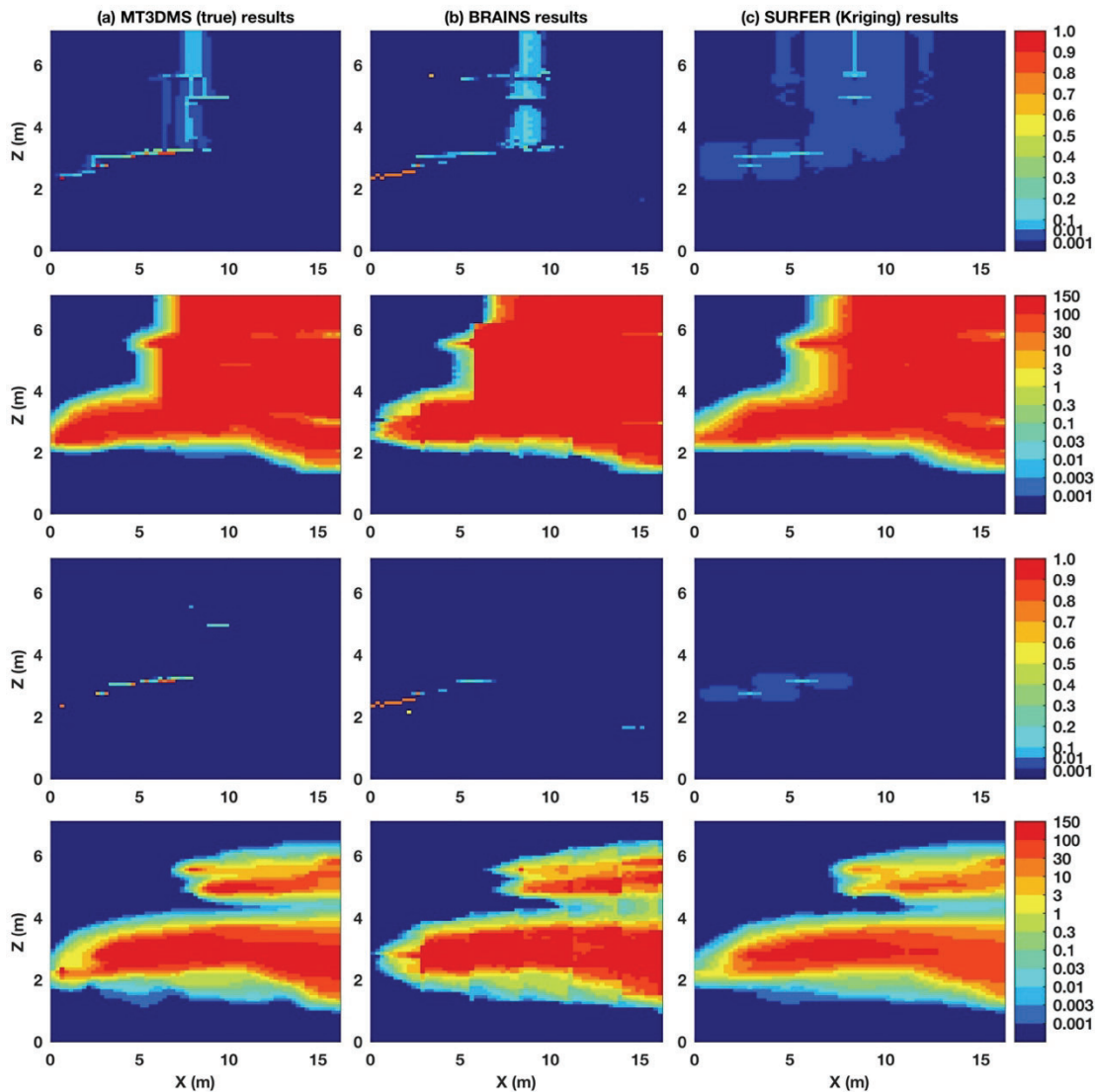
Figure R.6.3. Comparison of Saturation and Concentration results from ordinary kriging and joint probabilistic models

For these comparisons, the predicted categorical labels from BRAINS (i.e. {0,1,2,3} for saturation and {0,1,…,6} for concentration) had be converted into a true range of continuous values (i.e. between 0 to 1 for saturation and 0 to 150 mg/L for concentration). Based upon a logarithmic scale of saturation and concentration category limits (Table R.6.1), the following procedure was chosen for this conversion. As the first step, the ensemble means of 2000 predicted categorized saturation and concentration realizations for each permeability field and at each specific time were calculated. As shown in Figure R.6.2(d) saturation and concentration values in these average realizations range continuously between 0 to the maximum number of categories (i.e. 3 for saturation and 6 for concentration). To convert these average realizations into true ranges of saturation and concentration values, a representative value from the true range of values was assigned to each saturation and concentration category. These representative values were determined from a representative forward MT3DMS simulation result by extracting the pixels belonging to each category and calculating the average value (i.e. saturation or concentration) of those groups of pixels as a representative value for that specific category (e.g. for example the representative value for saturation category 1 and 2 were assigned to be 0.053 and 0.245, respectively). Consecutively the mean categorized realizations were converted (by logarithmic transformation) to the true range of continuous values using these representative values.

It is clear from Figure R.6.3 that the concentration results from kriging (i.e. Figures R.6.3.II(c) and IV(c)) are similar to BRAINS model results (i.e. Figures R.6.3.II(b) and IV(b)), qualitatively match the MT3DMS (true) results (i.e. Figures R.6.3.II(a) and IV(a)). As before, this is attributed to the continuous nature of concentration data. However, the BRAINS model produces a more realistic DNAPL saturation field both at early and late times (i.e. Figures R.6.3.I(b) and III(b)). Similar to results presented by Maji R. et al., (2006), the kriging method tends to smooth out the sharp spatial variations observed and expected in DNAPL source zone architecture (i.e. Figures R.6.3.I(c) and III(c)). In other words, the kriging approach predicts a higher mass of low saturation DNAPL (i.e. ganglia) around observed borehole data, while it is not successful in reconstructing the higher saturated pooled DNAPL in the domain. This smoothing tendency is likely to result in lower predicted pool fractions compared to realistic (true) DNAPL architecture.

To better evaluate the performance of both models, the saturation and concentration metrics for predicted and true results are compared at different times. Seven different metrics are calculated for the true and predicted concentration and saturation fields at 4 different time points for each permeability realization in the test data set and plotted in Figures R.6.4 and R.6.5, respectively for BRAINS and the kriging model. These metrics include total DNAPL mass (Figures R.6.4(a), R.6.5(a)), total aqueous and sorbed mass with linear equilibrium sorption assumption (Figures R.6.4(b), R.6.5(b)), pool fraction (PF) (Figures R.6.4(c), R.6.5(c)), x and z center (Figures R.6.4(d), R.6.4(e), R.6.5(d), R.6.5(e)) and spread (Figures R.6.4(f), R.6.4(g), R.6.5(f), R.6.5(g)) of mass. The coefficient of determination, R^2, is a measure of correlation between predicted and true metric values.
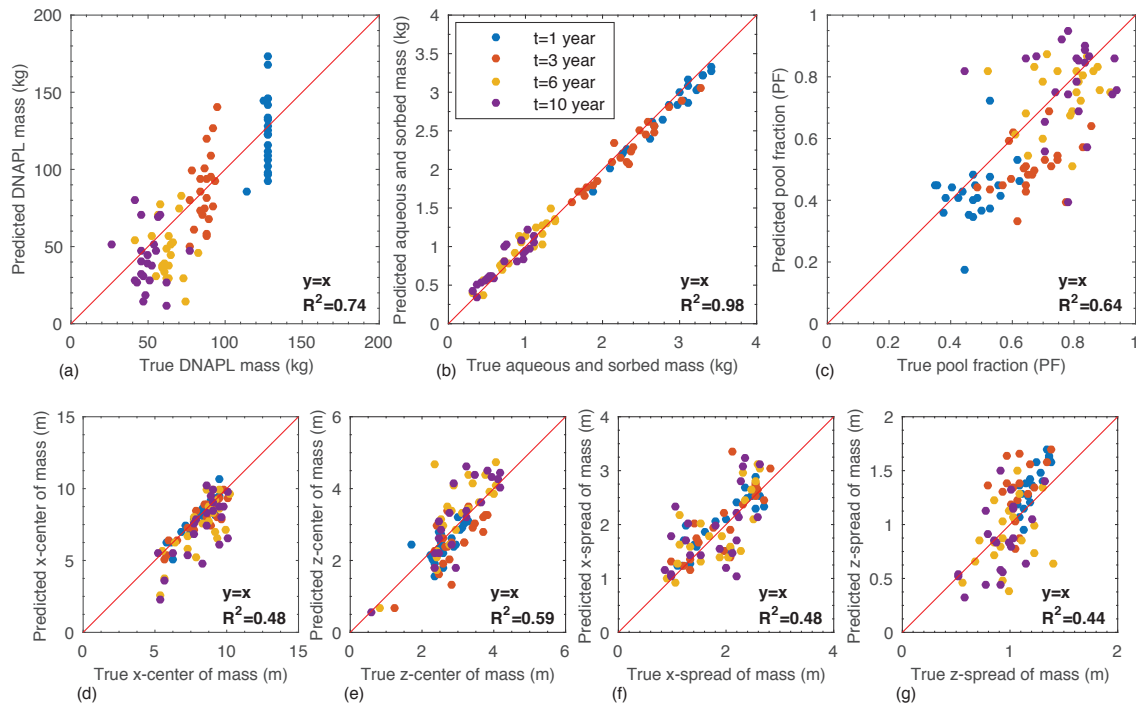
Figure R.6.4. Saturation and concentration metrics, predicted vs. true for BRAINS model. (a) Total DNAPL mass, (b) Total aqueous and sorbed mass (linear equilibrium sorption assumption), (c) Pool fraction (PF), (d) x-center of mass, (e) z-center of mass, (f) x-spread of mass, (g) z-spread of mass. R^2 values are calculated with respect to x=y line and is the measure of correlation between predicted and true metric values.
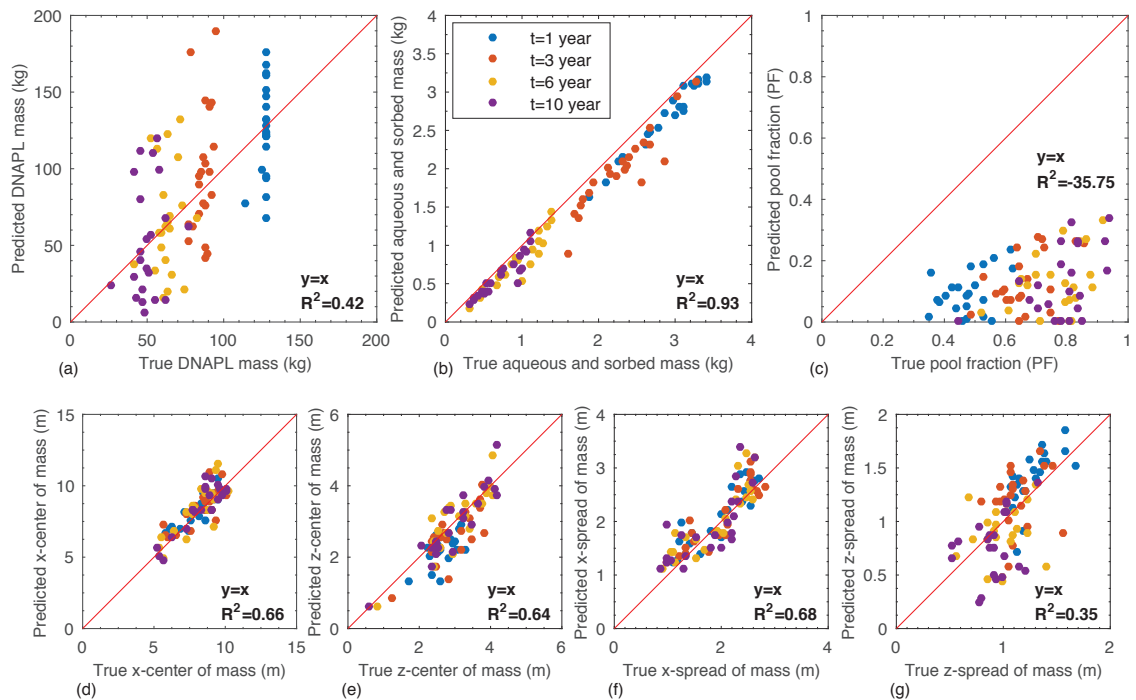
Figure R.6.5. Saturation and concentration metrics, predicted vs. true for kriging approach. (a) Total DNAPL mass, (b) Total aqueous and sorbed mass (linear equilibrium sorption assumption), (c) Pool fraction (PF), (d) x-center of mass, (e) z-center of mass, (f) x-spread of mass, (g) z-spread of mass. Negative R^2 value in (c) implies that a horizontal line fits the data better than x=y line.

These results indicate that both models can provide reasonable reconstruction of aqueous and sorbed phase mass distributions based on borehole data. However, recognizing that most of the contaminant mass is stored in the DNAPL phase, a major drawback of the kriging method is its performance in predicting DNAPL saturation architecture. This disadvantage mainly arises due to failure of ordinary kriging to capture localized peaks at unsampled locations, and to the smoothing nature of kriging algorithm. (Maji et al. 2006) also observed similar behavior, for both kriging and TP/MC models, while reconstructing contaminant source zones using limited borehole data. Comparison of Figures R.6.4(c) and R.6.5(c) shows that the BRAINS model performs favorably in estimating realistic pool fraction, while kriging tends to greatly under-predict the pool fraction. This is specifically important as recent studies (e.g., Christ et al., 2006, 2010) have shown that the distribution of DNAPL between ganglia and pool regions, indicated by pool fraction, controls the DNAPL dissolution characteristics and therefore can serve as a useful metric to predict source zone longevity. It is also evident from Figures R.6.4(a) and R.6.5(a), that both models under-predict the total DNAPL mass at later times due to sparse and limited saturation borehole data at those time regimes. This behavior is more pronounced in the case of the kiging model (Figure R.6.5(a)).

With the goal of validating and examining the robustness of the joint probabilistic model, the trained BRAINS model was tested to explore its performance with borehole spacing configurations different from those used in the model training (i.e. base case or Case 1). Accordingly, two more sets of simulations (Case 2-3) with different saturation and concentration borehole configurations were performed over the 80 realizations (i.e. 20 permeability realizations at 4 time points) in the test data set. For Cases 2 and 3, 6 and 5 equally spaced boreholes, respectively, were selected. It should be noted that the test data sets in these two cases were the same as those for Case 1. In other words, permeability realizations and the true saturation and concentration distributions in these sets were the same as the base case scenario and only the number and location of concentration and saturation boreholes were different from the Case 1.

In addition to different borehole configurations the model was also tested for various spill scenarios. For this purpose, realistic spatial distributions of DNAPL and aqueous phase contaminants under 4 different spill scenarios (Case 4-7) were generated using numerical simulation (i.e. "true" results). These simulations were conducted with the original 20 permeability realizations (test data set). The trained model was then applied to predict the DNAPL and aqueous phase contaminant mass distributions for each of the new spill scenarios using the saturation and concentration borehole observations in conjunction with the known permeability fields. Table 4 presents the spill rate and initial volume of PCE DNAPL for each spill scenario including the base case (i.e. the case used in the model training).

Table R.6.4. DNAPL spill scenarios.

Spill Scenarios	Case 1 (base)	Case 4 (higher rate)	Case 5 (lower rate)	Case 6 (higher volume)	Case 7 (lower volume)
Spill rate (L/day)	2	**20**	**0.5**	2	2
Spill Volume (L)	80	80	80	**160**	**40**

Finally, BRAINS performance was also tested using a different set of 20 permeability field realizations. These realizations were taken from the "field 1" ensemble simulations in Yang et al. (2018). In contrast to the permeability fields used as training data (i.e. field 2 scenario, Figure 5.a) the low permeability layers in these realizations (i.e. field 1) are mostly present in the top part of the domain (see Figure 1 in Yang et al., 2018). Note that both of these hypothetical permeability

fields, however, share the same geostatistical characteristics (i.e. consistent transition probability matrices and volumetric portion of lithofacies). The PCE release rate in the new simulations was the same as that of Case 5 (i.e. 0.5 L/day, lower rate than the base case).The contaminant borehole configuration was the same as Case 1 (i.e. 7 equally spaced boreholes).

The relative performance of BRAINS for each of these cases was evaluated using normalized root mean square error (NRMSE) for each of the metrics shown in Figure R.6.4. NRMSE, defined as the root mean square error (RMSE) normalized by the mean value of the observed metric, ranges between 0 and 1 and facilitates the comparison of model performance for metrics with different scales. The expression for NRMSE for each saturation or concentration metric is given as:

$$\text{NRMSE} = \frac{1}{\overline{m_a}} \sqrt{\frac{1}{n} \sum_{i=1}^{n} \left[(m_p)_i - (m_a)_i \right]^2} \tag{R.6.4}$$

where n is the number of realizations in the test data set (i.e. n=80 for 20 permeability realizations and 4 time points), $(m_p)_i$ and $(m_a)_i$ are the predicted and actual (true) metrics respectively for the ith realization, and $\overline{m_a}$ is the mean value of saturation or concentration metric for the actual realizations. The NRMSE values for each of the metrics shown in Figure R.6.4 is listed in Tables R.6.5 and R.6.6 for different borehole configurations and various spill scenarios. In addition, Table R..6.5 includes the kriging simulation results (with borehole configurations similar to Case 1) for the base case spill scenario.

Table R.6.5. NRMSE estimation of different metrics for various borehole configuration vs. kriging approach results for the base case spill scenario.

Borehole configuration	Kriging (7 boreholes)	Case 1 (7 boreholes)	Case 2 (6 boreholes)	Case 3 (5 boreholes)
Total DNAPL mass	0.44	0.28	0.36	0.33
Total aqueous and sorbed mass	0.14	0.07	0.08	0.12
Pool fraction	0.85	0.23	0.26	0.18
x-center of mass	0.10	0.15	0.17	0.17
z-center of mass	0.17	0.21	0.19	0.21
x-spread of mass	0.18	0.24	0.26	0.29
z-spread of mass	0.27	0.24	0.24	0.29

It is clear from Table R.6.5 that BRAINS in general outperforms the kriging approach even in the cases with fewer boreholes (i.e. Cases 2 and 3), although as would be expected, the performance of BRAINS is sensitive to borehole numbers and locations. These results also indicate that kriging can capture the spatial moments of the contaminant plume slightly better than BRAINS, however this approach performs poorly in predicting total DNAPL mass and pool fraction.

Table R.6.6 suggests that BRAINS performance is robust for a wider range of spill rate and spill volume conditions than those used in the training data. The exception is for Case 7, where a lower accuracy in predicting DNAPL plume architecture was observed. This lower accuracy was attributed to the lower spill volume and associated sparse saturation observations in the selected boreholes for this case. The NRMSE results for Case 8 indicate that the trained model can reasonably predict contaminant mass distribution independent of the permeability field structure (i.e. location of low permeability layers in the domain).

Table R.6.6. NRMSE estimation of different metrics for different spill scenarios

Spill Scenarios	Case 1 (base)	Case 4 (higher rate)	Case 5 (lower rate)	Case 6 (higher volume)	Case 7 (lower volume)	Case 8 (field 1, lower rate)
Total NAPL mass	0.28	0.28	0.31	0.26	0.36	0.37
Total aqueous and sorbed mass	0.07	0.07	0.09	0.09	0.08	0.06
Pool Fraction	0.23	0.28	0.18	0.24	0.29	0.22
x-center of mass	0.15	0.11	0.13	0.13	0.12	0.13
z-center of mass	0.21	0.19	0.18	0.10	0.29	0.26
x-spread of mass	0.24	0.28	0.21	0.17	0.38	0.23
z-spread of mass	0.24	0.26	0.20	0.17	0.47	0.36

III.6.6. Summary and Conclusions

This section has described the development and successful application of a discriminative random field model for contaminant source zone characterization and uncertainty quantification. The main advantage of the DRF model over more traditional MRF/CRF-type methods is its ability to capture a broader range of dependencies over longer spatial scales between the conditioning data (borehole observations and perm field) and variables to be modeled (maps of NAPL saturation and aqueous phase concentrations). Furthermore, the DRF method contrasts starkly with a 'brute force' (stochastic) MC approach, which would require running an abundant number of forward flow and transport simulations for various spill scenarios, hydrological boundary conditions, and permeability realizations. In addition, accounting for the measured borehole data in such stochastic forward simulations is not straightforward. The DRF model, in contrast, is completely characterized by a collection of parameters (i.e. w and v vectors), and need only be trained once. Although the training data are obtained from forward model simulations of NAPL entrapment and subsequent dissolution via groundwater flow, it is important to emphasize that far (i.e. at least 2 orders of magnitude) fewer forward simulations are needed than would be required for a traditional MC approach (e.g. Koch & Nowak, 2015, 2016). Once the DRF parameters are determined, the model can be used to generate realizations of the NAPL saturation and aqueous phase concentration using off-the-shelf Metropolis sampling methods.

By comparing the predicted and true metrics for contaminant mass distributions, it was shown above that the trained DRF model (BRAINS) produced realistic saturation and concentration fields conditioned to borehole data for different NAPL spill scenarios at different times. The predicted concentration and saturation results from BRAINS were also compared with those obtained from a widely used ordinary kriging approach. This comparison clearly illustrated that BRAINS outperformed the kriging approach significantly in reconstructing NAPL saturation distribution and architecture. Specifically, the kriging approach fails to predict the pool fraction of NAPL mass in the domain successfully. This can be explained by the smoothing nature of kriging method as well as the fact that kriging fails to capture localized peaks in NAPL saturation in unsampled locations.

It is important to note that, in this work, the permeability was assumed known at all pixels in the domain. However, in real-world applications only a few measurements of permeability are typically available from borehole logs and core sampling. This assumption of perfect knowledge can be lifted by generating stochastic realizations of the permeability field, conditioned on

measured permeability borehole data and based on some general geostatistical knowledge of the subsurface domain. Then BRAINS can be applied to these permeability realizations to generate equiprobable realizations of the contaminant source zone, conditioned to concentration and saturation borehole measurements. The ensemble averages over realizations of this stochastic process represent the expected values for concentration and saturation fields, while the variances provide a quantifiable measure of the uncertainty associated with the permeability and contaminant source zone mass distribution. These uncertainty measurements can help to infer the optimal locations for further borehole sampling.

Assessing computational effort, the methodology presented in this paper is significantly more efficient than other stochastic (forward or inversion) approaches. For example, for the 2D problem presented herein, approximately 30 minutes was required to generate 2000 saturation and concentration realizations for 100 equiprobable permeability fields (2×10^5 realizations) using the trained DRF model. These computations employed 100 CPU cores, in parallel, each with 128 GB of memory. It is anticipated that a stochastic approach, based on forward flow and transport models and similar to that presented in Koch & Nowak (2016), would require more than 10^5 transport model runs prior to application of rejection sampling for conditioning the source zone distribution on borehole data. This large number of forward simulations would demand more than 20 days of computation time using the computational resources applied in the current study.

In conclusion, this study demonstrates the successful development of a discriminative random field model as a promising method for contaminant source zone characterization and uncertainty quantification. The developed model, however, can be further optimized to reduce the type I and II errors observed in NAPL saturation reconstruction, either by adopting a more advanced machine learning methods such as *generative adversarial networks* (GANs) or application of permeability-based features that carry more information about the permeability of surrounding and neighboring pixels. Future work should focus on exploring the performance of the trained DRF model under different geologic environments and across different scales of heterogeneity. It is anticipated that, while the developed features and model structure are robust, the DRF model itself will need to be retrained for applications to different depositional environments. Thus, the present study should be viewed as a proof of principle for the application of this modeling approach and as the first step in generating a 3D characterization tool (i.e. library of models) that can be applied over a wide range of conditions observed at contaminated sites.

III.7. Predictive Modeling of Field-Scale Remediation, Optimization and Uncertainty - Sensitivity/Sampling Optimization Modeling

III.7.1. Synthetic Test Cases

The uncertainty quantification/optimal sampling design approach described in Figure M.8.1, was demonstrated through application to two numerically generated source zone scenarios, one with architecture dominated by ganglia, with a pool fraction (PF) of 0.44 (case 1), and the other dominated by pools with PF equal to 0.73 (case 2). The forward flow and transport model setup and the generation of realizations of the four random variables are briefly discussed below. All simulations of DNAPL infiltration, dissolution, and solute transport were conducted on two-dimensional (2-D) domains, with the intention of illustrating and assessing the performance of our approach in the design of sampling networks for FAC uncertainty reduction. A two-dimensional implementation was selected both to reduce computational time and to make use of the DRF algorithm for generating realizations of the initial aqueous concentrations and DNAPL saturations.

III.7.1.1. Permeability fields

The approach discussed in section II.5.2 was applied to generate a series of 100 equiprobable three-dimensional (3-D) permeability realizations conditioned on 22 synthetic borehole measurements with the same discretization. X-z cross section center slices of the 3-D realizations were extracted to form 2-D domains, where one borehole was located at the down-gradient transect and another three boreholes were located within the modeled domain, equi-distant from each other. Among the 100 realizations, one permeability domain was selected as the "true" case (Figure R.7.1). This domain was then used to generate "true" initial distributions of DNAPL, aqueous and sorbed mass.

As the FOSM method propagates the uncertainties in system parameters into the results to first-order accuracy, the mean FAC can be obtained by employing the solution of the flow and transport equations for the mean of the realizations. The average log conductivity of the 100 2-D conductivity realizations and the corresponding variance are shown in Figure R.7.2. Comparison of the "true" and averaged conductivity fields reveals that the averaged conductivity field captures the general horizontal stratigraphy in the formation, with some fine detail lost due to smoothing at locations without observations.
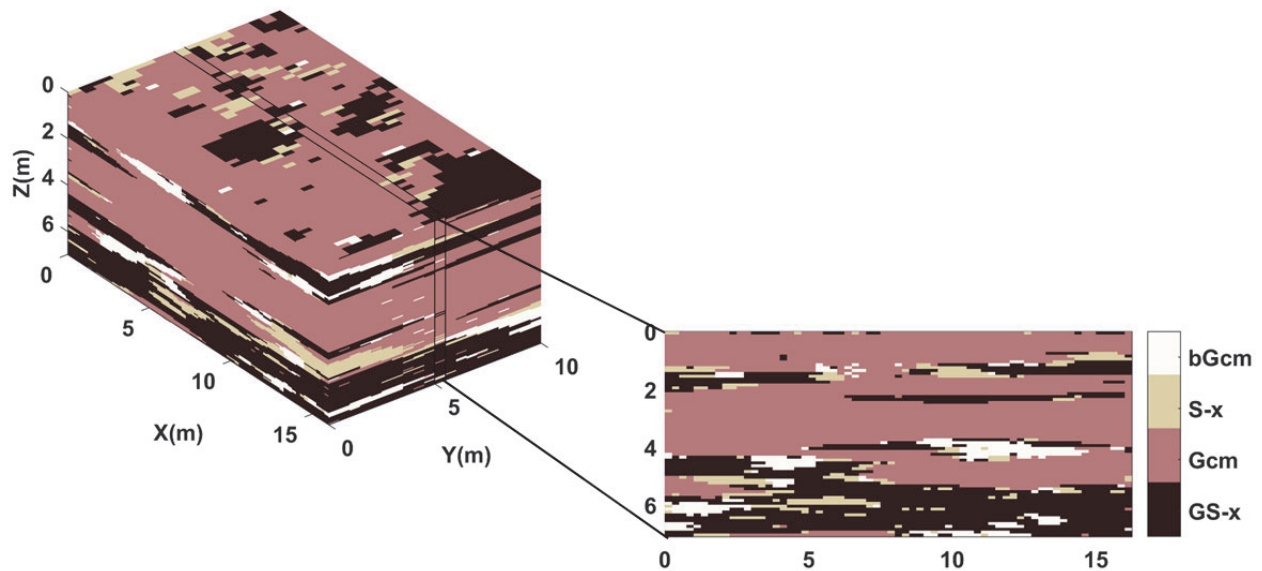
Figure R.7.1. True 3-D conductivity field and selected 2-D x-z plane center slice.
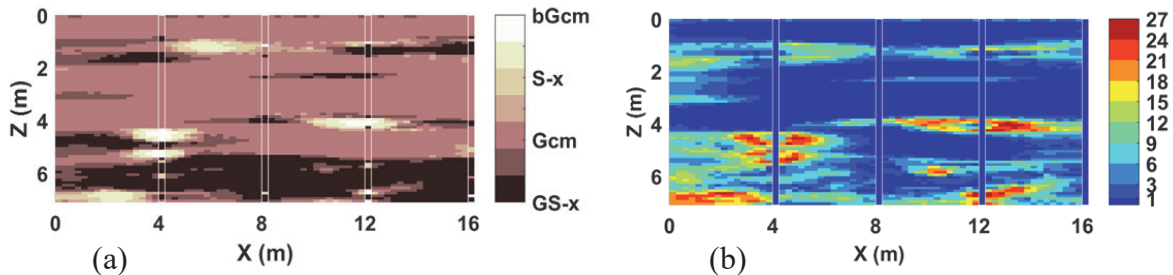
Figure R.7.2. Statistical properties of the 2-D log conductivity fields. (a) Averaged 2-D log conductivity field over 100 realizations; (b) variance of the 100 2-D log conductivity realizations. White rectangles indicate the four borehole locations

III.7.1.2. True Initial Conditions

DNAPL release and migration were modeled using the approach presented in section II.5.2. After the initial DNAPL distribution was obtained (Figure R.7.3(a)), transport modeling was conducted to obtain the "true" initial aqueous and sorbed concentrations. A detailed description of transport model set up is presented in sections II.5.2 and II.5.3.3.
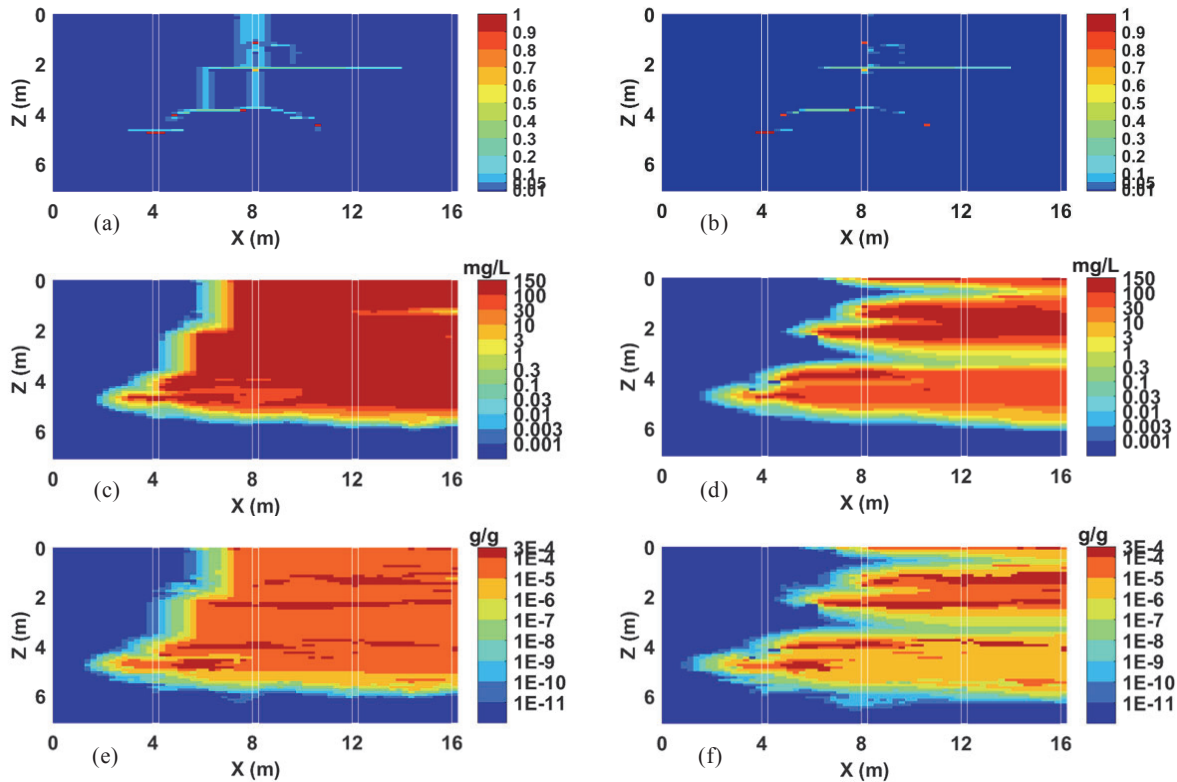
Figure R.7.3. True PCE-DNAPL source zone, initial aqueous concentration, and sorbed concentration of ganglia-dominated case (left (a), (c), (e)) and pool-dominated case (right (b), (d), (f)), respectively

Consistent with the two-stage simulations, a 1 year "loading stage" was first simulated, during which PCE DNAPL dissolved, but no change in saturation was permitted. Linear equilibrium sorption was assumed. The aqueous and sorbed concentrations at the end of the loading stage were considered as the "true" initial distributions of aqueous and sorbed concentrations corresponding to case 1 (Figure R.7.3(c), (e)). The change of DNAPL saturation was then allowed, and the DNAPL dissolution and solute transport were simulated for approximately 4.7 years. The DNAPL saturation, aqueous, and sorbed concentration distributions at 4.7 years were selected as the "true" initial conditions for case 2 (Figure R.7.3(b), (d), (f)). In Figure R.7.3, borehole locations are those used for generation of the permeability realizations.

III.7.1.3. Realizations of Initial DNAPL Saturation, Aqueous, and Sorbed Concentration Distributions

The DRF model (BRAINS), incorporating full knowledge of the conductivity field, as well as the "true" aqueous concentrations and DNAPL saturations in the four boreholes, were then used to generate 2000 realizations of aqueous concentration and DNAPL saturation for each conductivity field. The sorbed concentration distribution was obtained by assuming equilibrium with the aqueous concentration. Averaged aqueous concentration, DNAPL saturation, and sorbed

concentration distributions for the 200,000 realizations, as well as the corresponding variances, are shown in Figure R.7.4 for both cases. Visual inspection of the averaged contaminant mass in the different phases reveals that the realizations generated by the DRF method are qualitatively consistent with the "true" initial concentrations.
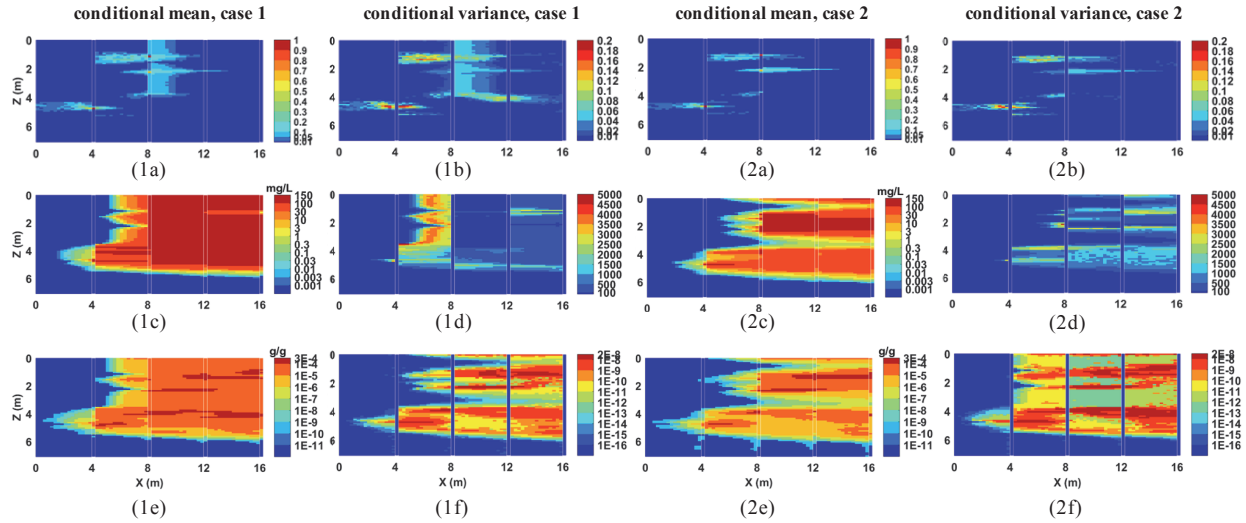
Figure R.7.4. Conditional mean and variance of DNAPL saturation (1a-1b for case1, 2a-2b for case 2), conditional mean and variance of aqueous concentration (1c-1d for case 1, 2c-2d for case 2), and conditional mean and variance of sorbed concentration (1e-1f for case 1, 2e-2f for case 2).

III.7.2. Sensitivities of Down-Gradient FACs to System Properties

The sensitivity analysis results, which form the basis for the data worth analysis, are discussed in this section. The sensitivities S_{ij}, which represent the FAC change due to an incremental change in each model parameter, have different units for each parameter. So that the sensitivities can be readily compared to each other, a scaled, dimensionless local sensitivity coefficient can be introduced:

$$S_{ij} = \left. \frac{\partial C_{fi}}{\partial p_j} \right|_{\mathbf{p}^*} \tag{R.7.1}$$

$$\bar{S}_{ij} = S_{ij} \cdot \frac{\sigma_{p_j}}{\sigma_{C_{fi}}} \tag{R.7.2}$$

where σ_{p_j} is the parameter scaling factor, and $\sigma_{C_{fi}}$ is the FAC prediction scaling factor. In the context of data worth analysis for the prediction phase, the parameter scaling factor is defined as the expected parameter uncertainty, while the prediction scaling factor is chosen as the acceptable prediction uncertainty (Finsterle 2015).

Computed sensitivities of down-gradient FACs with respect to log hydraulic conductivity, initial aqueous concentration, initial sorbed concentration, and initial DNAPL saturation for the ganglia dominated case corresponding to selected times (1 year, 5 years, 10 years, and 20 years) are presented in Figure R.7.5. Inspection of the sensitivity results reveal that largest sensitivities propagate from down-gradient to up-gradient as time increases and that local hydraulic conductivity values have the greatest impact on the FAC predictions. At the same distance from

160

the down-gradient transect, locations with lower hydraulic conductivities are associated with larger sensitivities over longer time periods. This is consistent with the fact that the hydraulic conductivity field is the major factor controlling the flow and transport processes, as well as the sorption capacity and DNAPL dissolution. Furthermore, initial aqueous and sorbed concentrations have a major effect on FAC predictions at early times, while the influence of initial DNAPL saturation persists for longer periods. Notably, sensitivities of down-gradient FAC predictions with respect to initial DNAPL saturations are significant as the DNAPL dissolves away. This is attributed to the fact that, with the presence of DNAPL, a small change in DNAPL saturation only leads to minor changes in the DNAPL dissolution rate, and, thus has a small impact on down-gradient FAC. When the DNAPL dissolves away, however, a small addition of DNAPL makes a large contribution to the FAC.

The sensitivities of down-gradient FAC with respect to the four random variables corresponding to the pool-dominated case are not shown here, as the results display similar patterns as those presented above.
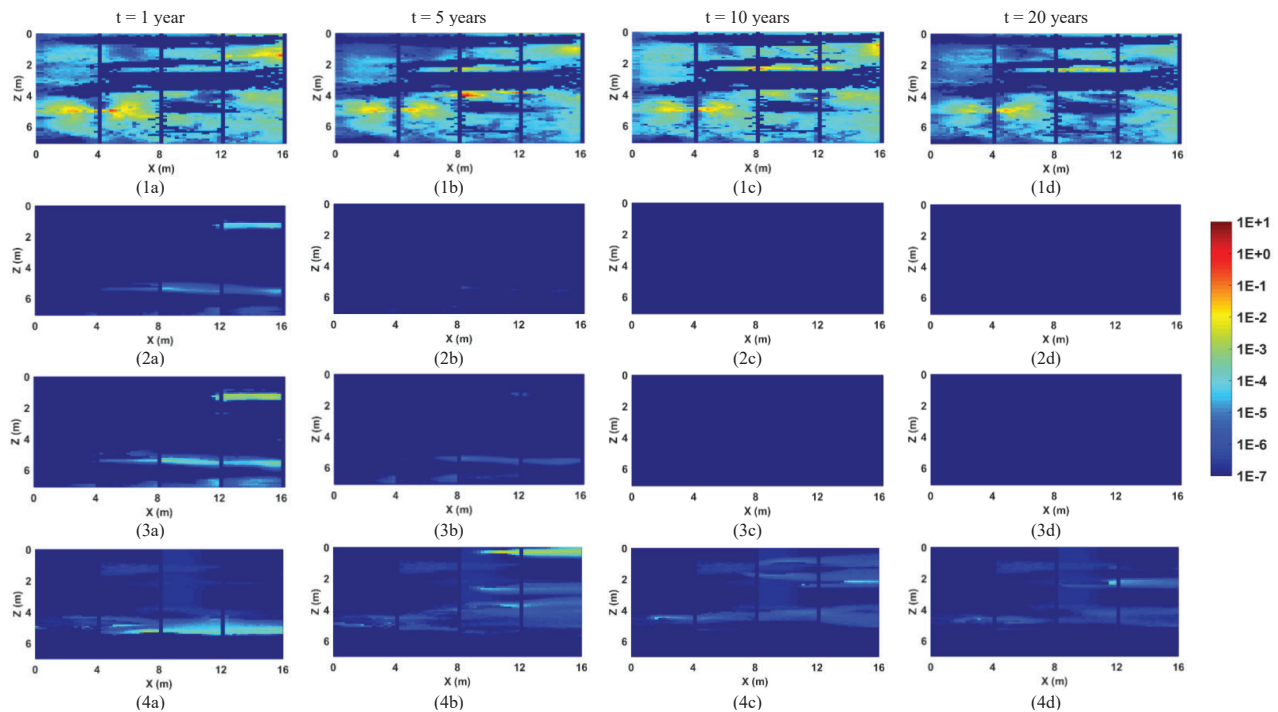
Figure R.7.5. Absolute local sensitivities of down-gradient FAC with respect to log conductivity (1a-1d), initial aqueous concentration (2a-2d), initial sorbed concentration (3a-3d), and initial DNAPL saturation (4a-4d) at selected times

III.7.3. Assessment of the First-round Sampling

The above averaged log conductivity and contaminant mass distributions served as inputs for the modified groundwater flow and transport model. Down-gradient FACs were estimated at 1, 5, 10 and 20 years for both cases. Covariance matrices corresponding to four random variables were calculated from the 200,000 equiprobable realizations. The uncertainties in FAC predictions were then be evaluated via the FOSM method, coupling sensitivities and covariances.

III.7.3.1. Down-gradient FAC Predictions

Conditional means and variances of FACs are presented in Table R.7.1. Here the CV (the standard

deviation over the mean), which is an integral outcome of prediction precision and extension of variability, was adopted to quantify the uncertainties associated with the predictions. The true FACs, conditional means, and corresponding error bounds $E[C_f] \pm \sigma_{C_f}$, are presented in Figure R.7.6 and Table R.7.1 for both cases.

Table R.7.1. true, conditional mean, standard deviation, and coefficient of variation of down-gradient FACs (mg/L)) at selected times (years) for both cases

time	"true"	Mean (mg/L)			StD (mg/L)				CV		
		1st [a]	2nd-FOSM [b]	2nd-uniform [c]	1st	Expected [d]	2nd-FOSM	2nd-uniform	1st	2nd-FOSM	2nd-uniform
					ganglia dominated case						
1	10.97	11.49	10.77	11.66	8.08	5.24	3.02	6.74	0.70	0.28	0.58
5	1.96	7.79	6.10	8.03	9.68	6.84	6.06	9.07	1.24	0.99	1.13
10	1.13	4.29	3.75	1.83	3.61	1.23	3.17	4.02	0.84	0.84	2.20
20	1.01	0.89	1.05	1.14	2.72	0.70	2.06	2.39	3.05	1.96	2.09
					pool dominated case						
1	2.98	5.57	4.61	4.28	4.27	1.24	4.13	4.09	0.77	0.90	0.96
5	1.18	3.86	2.28	2.23	5.42	1.23	2.21	3.10	1.40	0.97	1.39
10	1.01	1.29	1.23	1.26	3.45	0.79	1.98	1.66	2.67	1.61	1.32
20	0.84	0.62	0.69	0.54	2.28	0.61	1.02	1.44	3.67	1.47	2.67

[a] first-round sampling based on four borehole measurements
[b] second-round sampling based on six borehole measurements, two additional boreholes were selected based on FOSM and data worth analysis
[c] second-round sampling based on six borehole measurements, two additional boreholes were located evenly at the center of the domain
[d] expected standard deviation reduction before conducting second-round sampling

Comparison of the true value and prediction at 1 year reveals that, for case 1, the mean FAC of 11.49 mg/L is very close to the true value of 10.97 mg/L. The relatively small standard deviation and the good estimate lead to a CV smaller than 1, indicating reasonable prediction accuracy. The FACs at 5 and 10 years (7.79 mg/L and 4.29 mg/L), however, are 3-4 times higher than the true values (1.96 mg/L and 1.13 mg/L), with the true FACs lying close to the lower error bounds of the predictions. This overestimation, along with large standard deviations and increased CVs, can be attributed primarily to the poor estimation of initial DNAPL mass and the continuous dissolution of DNAPL. As the estimated initial DNAPL mass is much higher than the true value, higher aqueous concentrations emitted from ganglia and pools arrive at the down-gradient boundary over longer time periods, resulting in higher FACs. Inspection of the FAC prediction of 0.89 mg/L at 20 years indicates good agreement with the true value of 1.01 mg/L. This better agreement at later time is attributed to the fact that FAC is mainly controlled by the dissolution of DNAPL pools at later times and that the DNAPL saturation hot spots (close to 0.9) are well-reproduced by the model.

The predictions of FACs at selected times corresponding to case 2, however, exhibit a different trend. In this pool dominated case, the ganglia dissolve rapidly, resulting in a sharp decrease in down-gradient FAC, and the initial aqueous concentrations in most of the region are smaller than

the solubility. The initial DNAPL saturation distribution, thus, makes the most contribution to FAC predictions at early times. Since the conditional mean of the initial DNAPL source zone incorporates more low saturation ganglia than the true distribution, the predicted FACs at 1 and 5 years (5.57 mg/L and 3.86 mg/L), are much higher than the true values (2.98 mg/L and 1.18 mg/L). At later stages, the FACs are mainly governed by the dissolution of high saturation pools and the slow depletion of persistent or flow inaccessible DNAPL, resulting in concentration plateaus. As both true and predicted FACs reach this regime, the FAC forecasts corresponding to the pool dominated case of 1.29 mg/L and 1.62 mg/L at 10 and 20 years are comparable to the true values of 1.01 mg/L and 0.84 mg/L.

It is noteworthy that the CV increases as time goes by; in other words, the uncertainties associated with the FAC predictions become more significant. This can be attributed to the uncertainty propagation that occurs with time. Although the mean forecast at 20 years is comparatively accurate, with the predicted FAC of 0.89 mg/L and 0.62 mg/L compared to the true FAC of 1.01 mg/L and 0.89 mg/L for ganglia- and pool-dominated case, respectively, the uncertainties associated with the predictions are still obvious with the CV larger than 1 (3.05 and 3.67), indicating additional site investigation is required to ensure prediction precision.
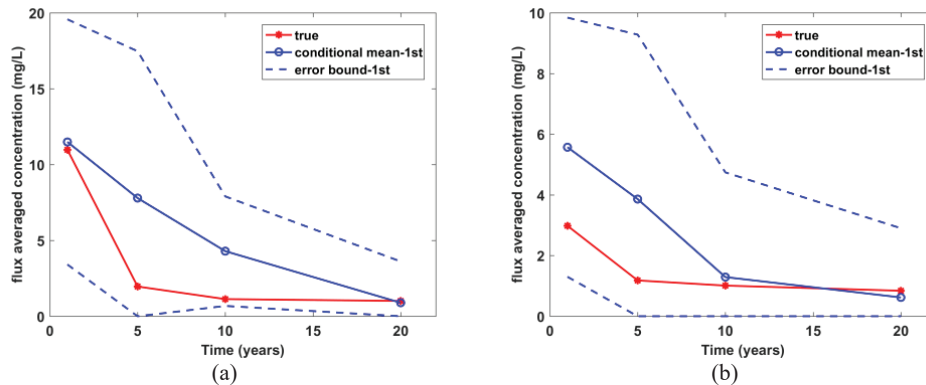
Figure R.7.6. True, first-round conditional mean, and the error bound of FACs at selected times for ganglia dominated (a) and pool dominated (b) cases.

III.7.3.2. Sampling Strategy Design

The data worth analysis introduced in section II.8.2.2 was then applied to guide the optimal sampling network design. Here the cost of additional measurements was justified by the difference in the FAC uncertainty before and after extra data collection. Thus, observations associated with the highest expected data worth, i.e., the largest uncertainty reduction, were selected for additional measurements. Consistent with the first phase sampling patterns, measurements of hydraulic conductivity and initial contaminant mass in different phases were evaluated along vertical lines (boreholes). The expected data worth of additional measurements for the prediction of FAC at four selected times of case 1 are shown in Figure R.7.7.

After calculating the expected variance reduction, which quantifies how the measurements along additional individual boreholes could reduce the variance of the prediction, two more boreholes were selected for sampling (white rectangles in Figure R.7.7). The expected variance reduction for each column measurements, calculated based on Equation M.8.7 are shown in Figure R.7.8. As can be seen, the model guided sampling strategy recommends additional sampling locations that vary with the prediction time window. In general, the additional selected sampling locations are further down-gradient for early time predictions and move up-gradient with prediction time. This

trend can be explained by considering the fact that DNAPL dissolution and contaminant transport closer to the down-gradient boundary have an earlier impact on FAC; the up-gradient entrapped and sequestered contaminant mass, in contrast, affect down-gradient FAC at later times.
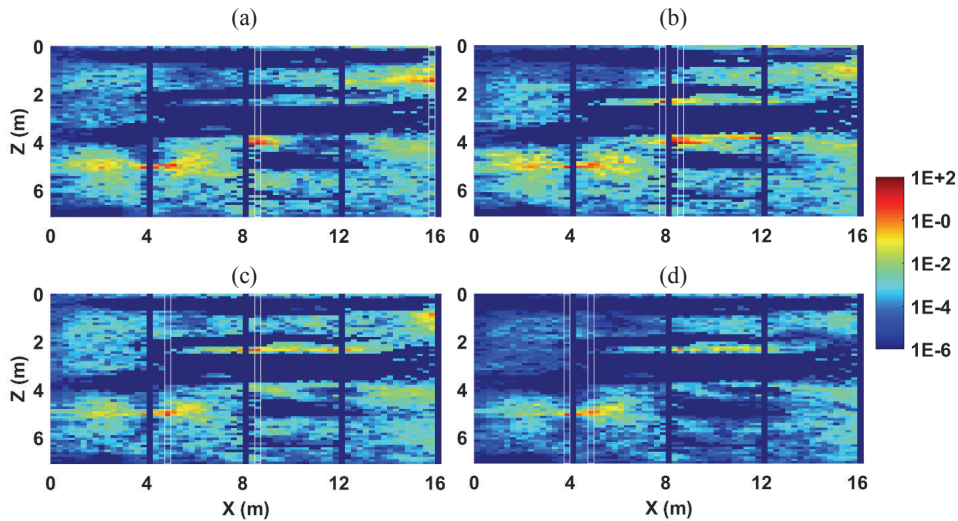
Figure R.7.7. Data worth of additional log conductivity, initial aqueous concentration, sorbed concentration, and DNAPL saturation measurements for flux averaged concentration prediction at 1 year (a), 5 years (b), 10 years (c), and 20 years (d) for the ganglia dominated case.

The two more sampling locations for phase 2 together with the expected values and conditional variances of the four parameters for case 1 are shown in Figure R.7.9 and R.7.10, respectively.
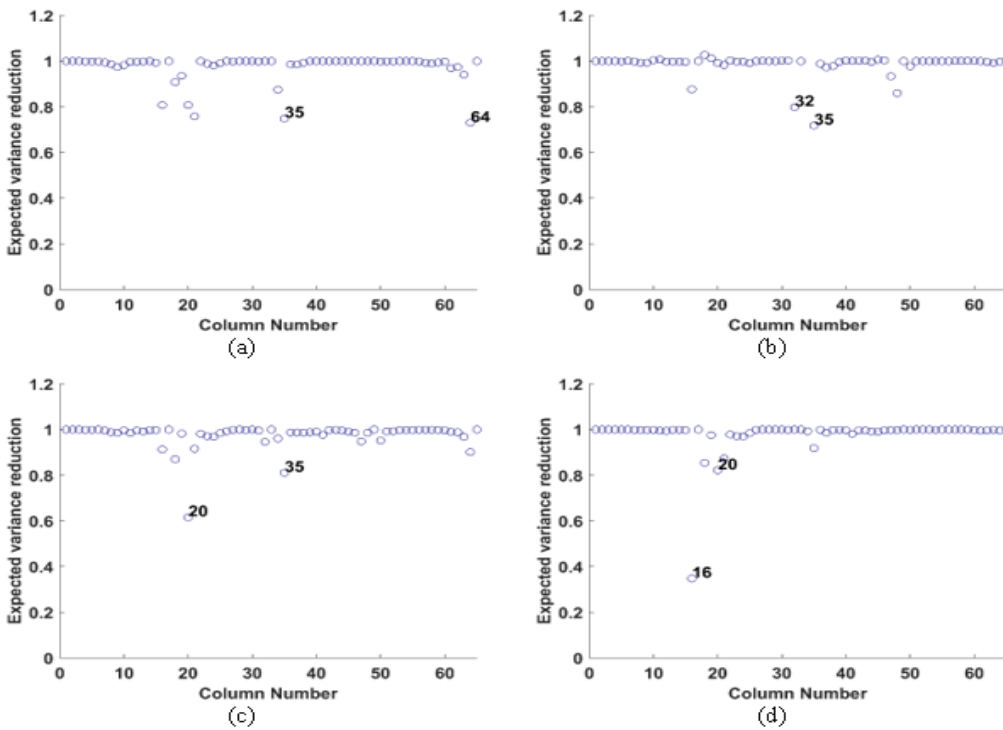
Figure R.7.8. Expected variance reduction of additional log conductivity, initial aqueous concentration, sorbed concentration, and DNAPL saturation borehole measurements for FAC prediction at 1 year (a), 5 years (b), 10 years (c), and 20 years (d) for the ganglia dominated case

164
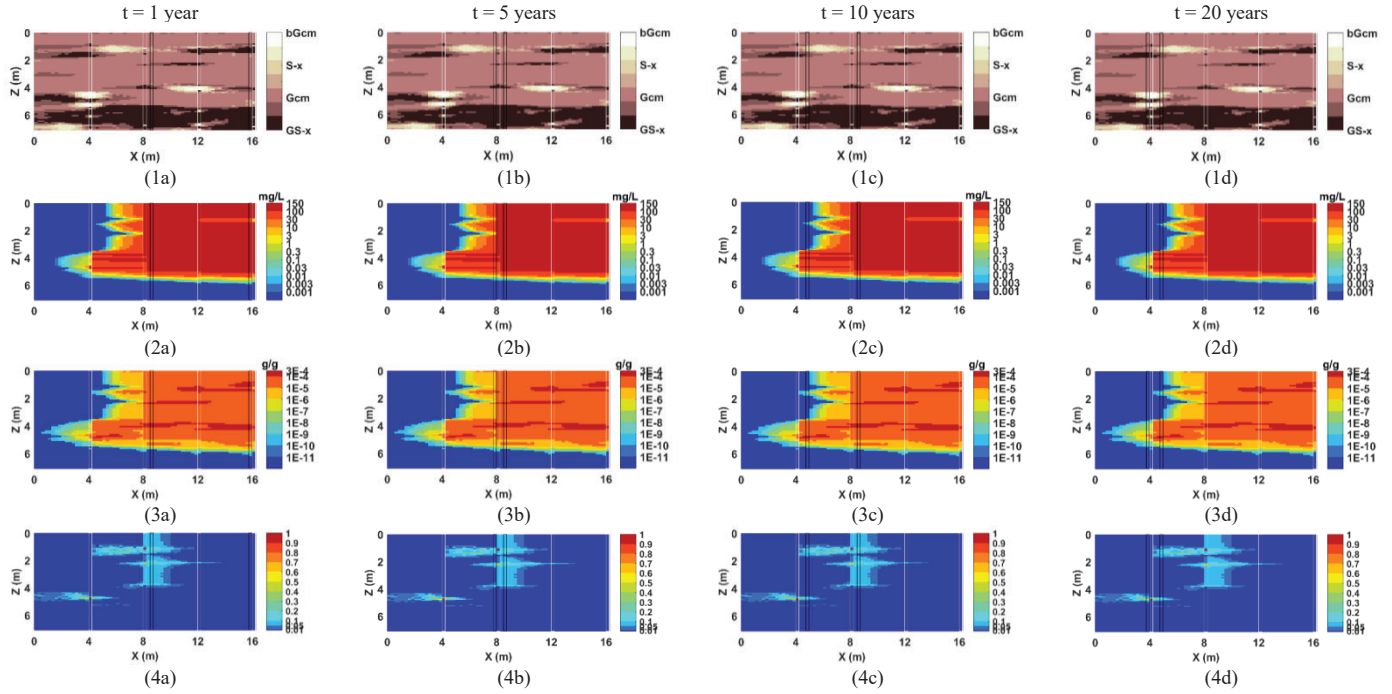
Figure R.7.9. Sampling results with conditional means of log conductivity (1a-1d), initial aqueous concentration (2a-2d), initial sorbed concentration (2a-3d), and initial DNAPL saturation (4a-4d) for FAC predictions at selected times of ganglia dominated case. White rectangles represent 1st round sampling locations, black rectangles represent 2nd round sampling boreholes
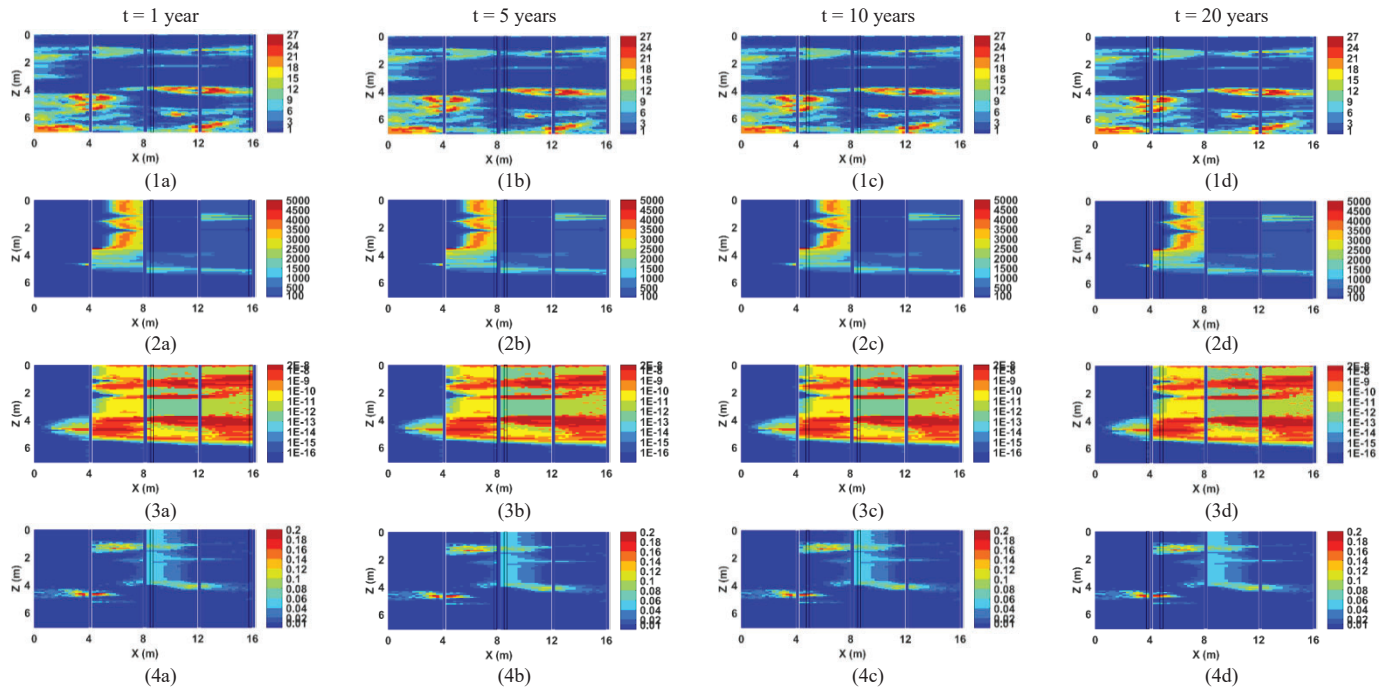
Figure R.7.10. Sampling results with conditional variances of log conductivity (1a-1d), initial aqueous concentration (2a-2d), initial sorbed concentration (2a-3d), and initial DNAPL saturation (4a-4d) for FAC predictions at selected times of ganglia dominated case. White rectangles represent 1st round sampling locations, black rectangles represent 2nd round sampling boreholes

Inspection of the sampling patterns reveals that locations with low hydraulic conductivities are good potential candidates for additional measurements. Since lower hydraulic conductivities are associated with lower velocities, larger residence times, and larger potential for DNAPL entrapment, it is apparent that lower hydraulic conductivities have stronger impact on the FAC predictions. In addition, the dissolution of DNAPL mass makes the greatest contribution to the evolution of FAC. Consequently, locations with high saturations are chosen with priority. Based on the DNAPL infiltration and formation mechanics, high saturation pools will be formed where vertically migrating DNAPL encounters lower permeable strata and starts to spread laterally. The chosen high DNAPL saturation measurements together with the underlying low permeability layers, thus, are highly informative since they provide information not only about the volumetric flow rate through the source area, but also the source zone longevity, the total contaminant mass flux, and the plume evolution further down-gradient. In addition to the significant impact of hydraulic conductivities and DNAPL saturations on the FAC predictions, the potential borehole measurements are also linked to high parameter variances, reflecting the propagation of large parameter uncertainties to the FAC prediction.

The resulting data worth and variance reduction of the additional borehole measurements for FAC predictions corresponding to the pool dominated source zone are depicted in Figures R.7.11 and R.7.12. Similar to the ganglia-dominated case, the migration of selected sampling locations from down-gradient to up-gradient was observed for different prediction windows, except for FAC prediction at 10 years. This inconsistency at 10 years may be attributed to the large sensitivities of the FAC to the low hydraulic conductivity lens, which are about two orders of magnitude larger than the sensitivities at other locations. It is noteworthy that, comparing the data worth plot with the variance of log conductivity field, the low data worth locations are associated with the low hydraulic conductivity variances, which further demonstrates the dominant control of hydraulic conductivity on FAC predictions.
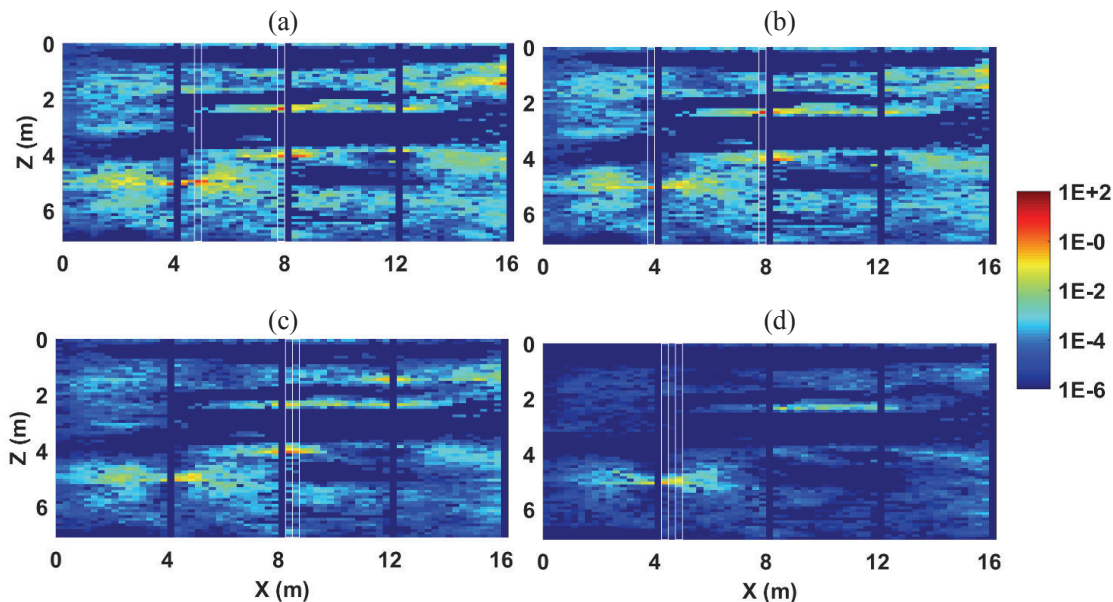
Figure R.7.11. Data worth of additional log conductivity, initial aqueous concentration, sorbed concentration, and DNAPL saturation measurements for FAC prediction at 1 year (a), 5 years (b), 10 years (c), and 20 years (d) for the pool dominated case

166
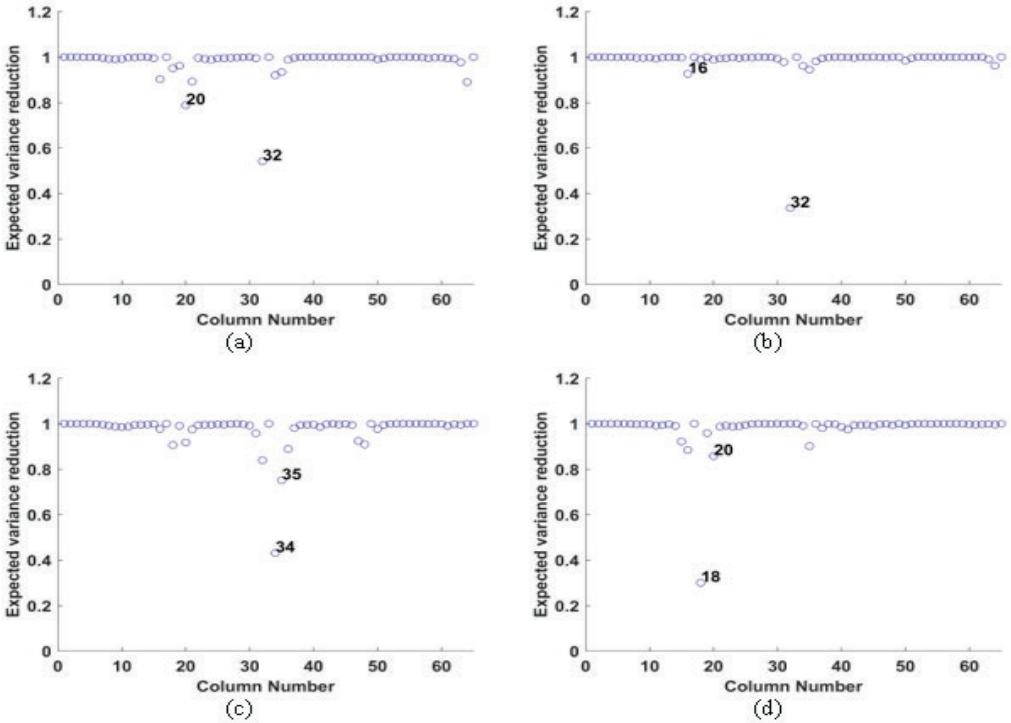
Figure R.7.12. Expected variance reduction of additional log conductivity, initial aqueous concentration, sorbed concentration, and DNAPL saturation borehole measurements for FAC prediction at 1 year (a), 5 years (b), 10 years (c), and 20 years (d) for the pool dominated case

Figures R.7.13 and R.7.14 present the two selected borehole locations for phase 2 sampling with conditional means and variances of the four random variables for the pool-dominated case.

The concentration and DNAPL saturation measurements in the selected boreholes are associated with the positions of large variances, which then translate to a better source zone characterization and a reduced FAC variance at early times. The borehole selections also exhibit a tendency to place additional measurements in low hydraulic conductivity regions for all prediction targets, which can be attributed to the combined effects of high variance and large sensitivity impact. The resulting measurements at these locations help to better capture the flow field through the source area and characterize the DNAPL source zone architecture.
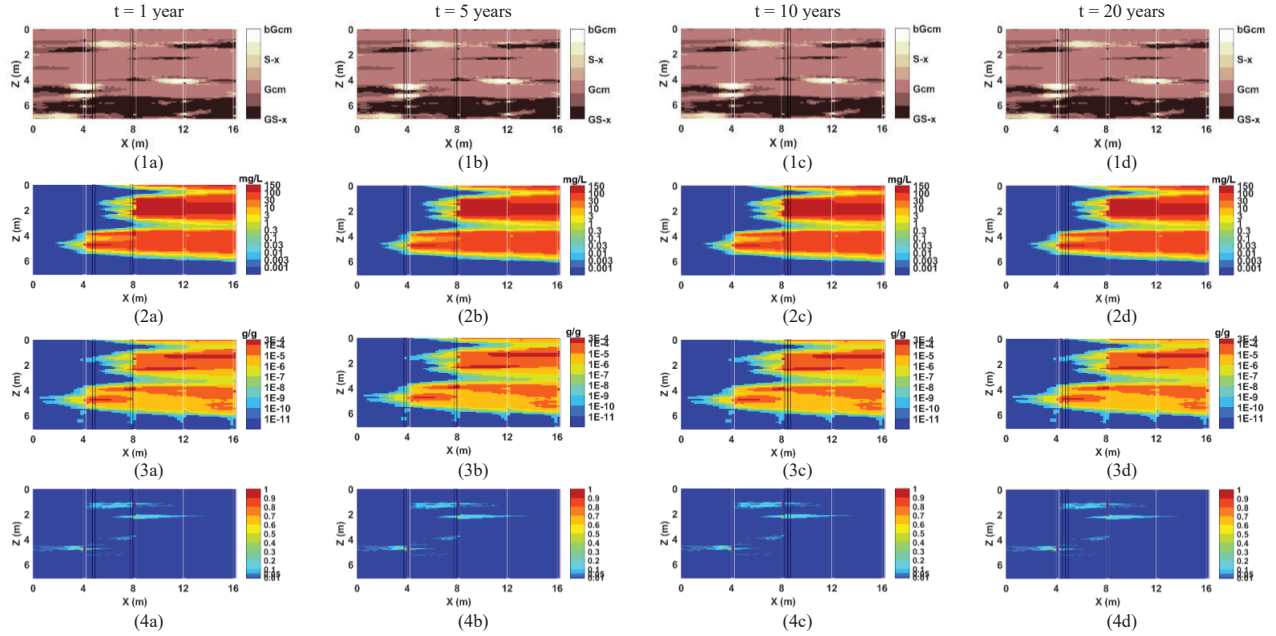
Figure R.7.13. Sampling results with conditional means of log conductivity (1a-1d), initial aqueous concentration (2a-2d), initial sorbed concentration (2a-3d), and initial DNAPL saturation (4a-4d) for FAC predictions at selected times of pool dominated case. White rectangles represent 1st round sampling locations, black rectangles represent 2nd round sampling boreholes
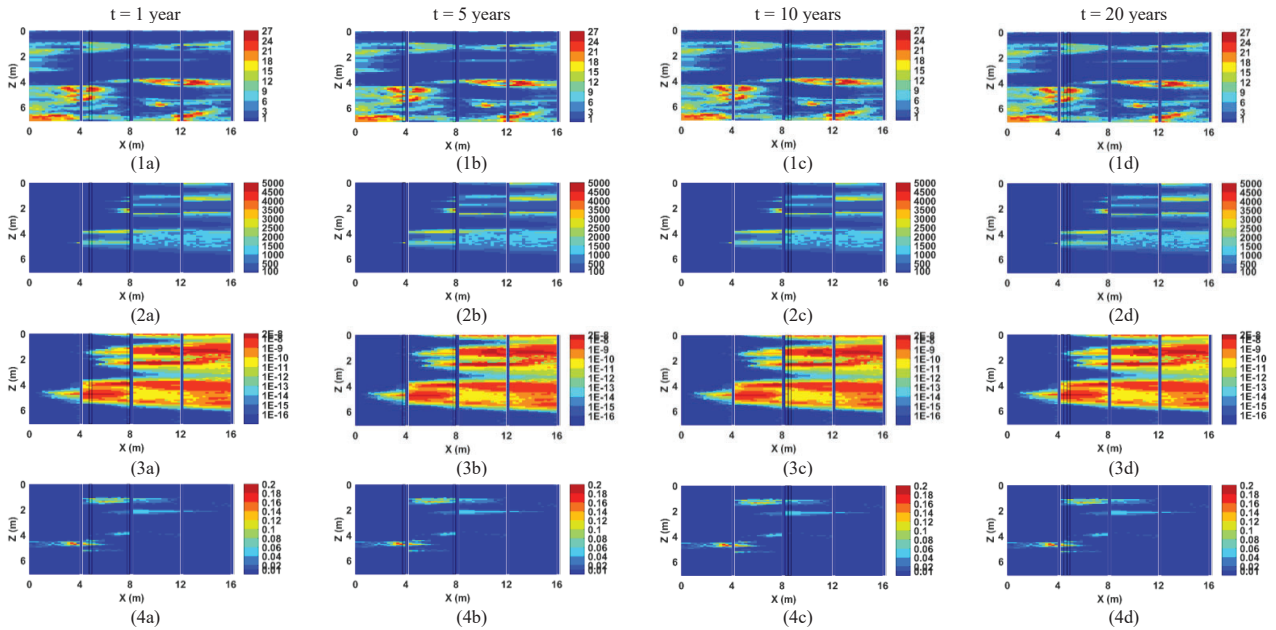
Figure R.7.14. Sampling results with conditional variances of log conductivity (1a-1d), initial aqueous concentration (2a-2d), initial sorbed concentration (2a-3d), and initial DNAPL saturation (4a-4d) for FAC predictions at selected times of pool dominated case. White rectangles represent 1st round sampling locations, black rectangles represent 2nd round sampling boreholes

III.7.4. Assessment of the Second-round Sampling

The precise worth of additional observations can only be quantified after performing the measurements. Recall that, to identify the new sampling locations, it was assumed that the most

likely values of the measurements were their expected values and that linearization about the last prediction was appropriate (eq. M.8.3). To explore the appropriateness of these assumptions and the effectiveness of the modeling framework for identification of optimal sampling locations, the second-round borehole measurements were used as the basis for generation of new parameter realizations with the DRF model and subsequent FOSM analyses. Implementing the DRF model including these new sampling locations resulted in four new sets of conditional means and variances of hydraulic conductivity field and initial contaminant mass distributions for each case based on different prediction targets. These results are shown in Figure R.7.15-R.7.22. The flow and transport model were then applied using the mean distributions to yield new FAC predictions at the selected times.
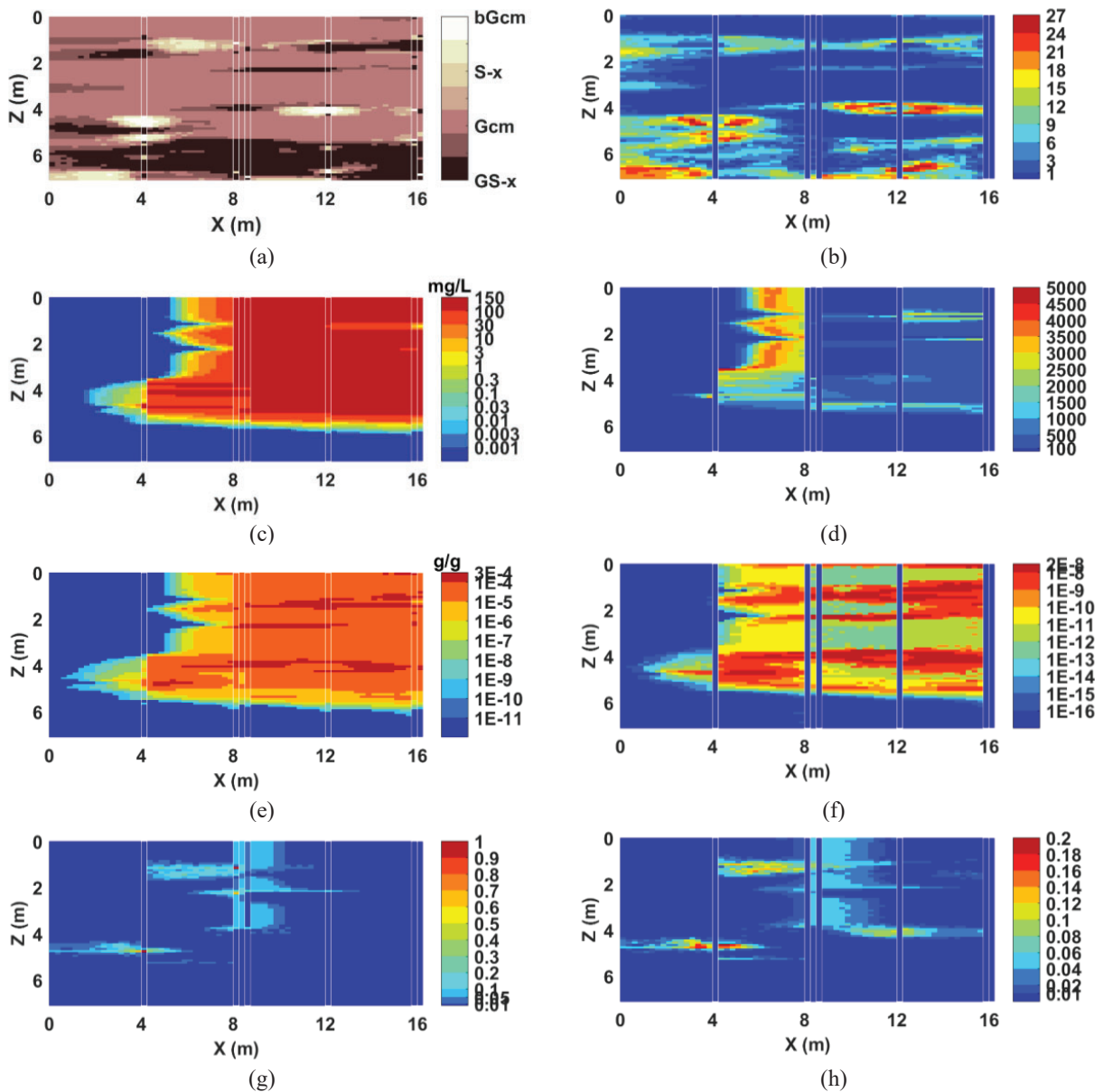
Figure R.7.15. Conditioned means and variances of log permeability field (a,b), initial aqueous concentration (c,d), initial sorbed concentration (e,f), and initial DNAPL saturation (g,h) for second-round FAC prediction at 1 year of ganglia dominated case
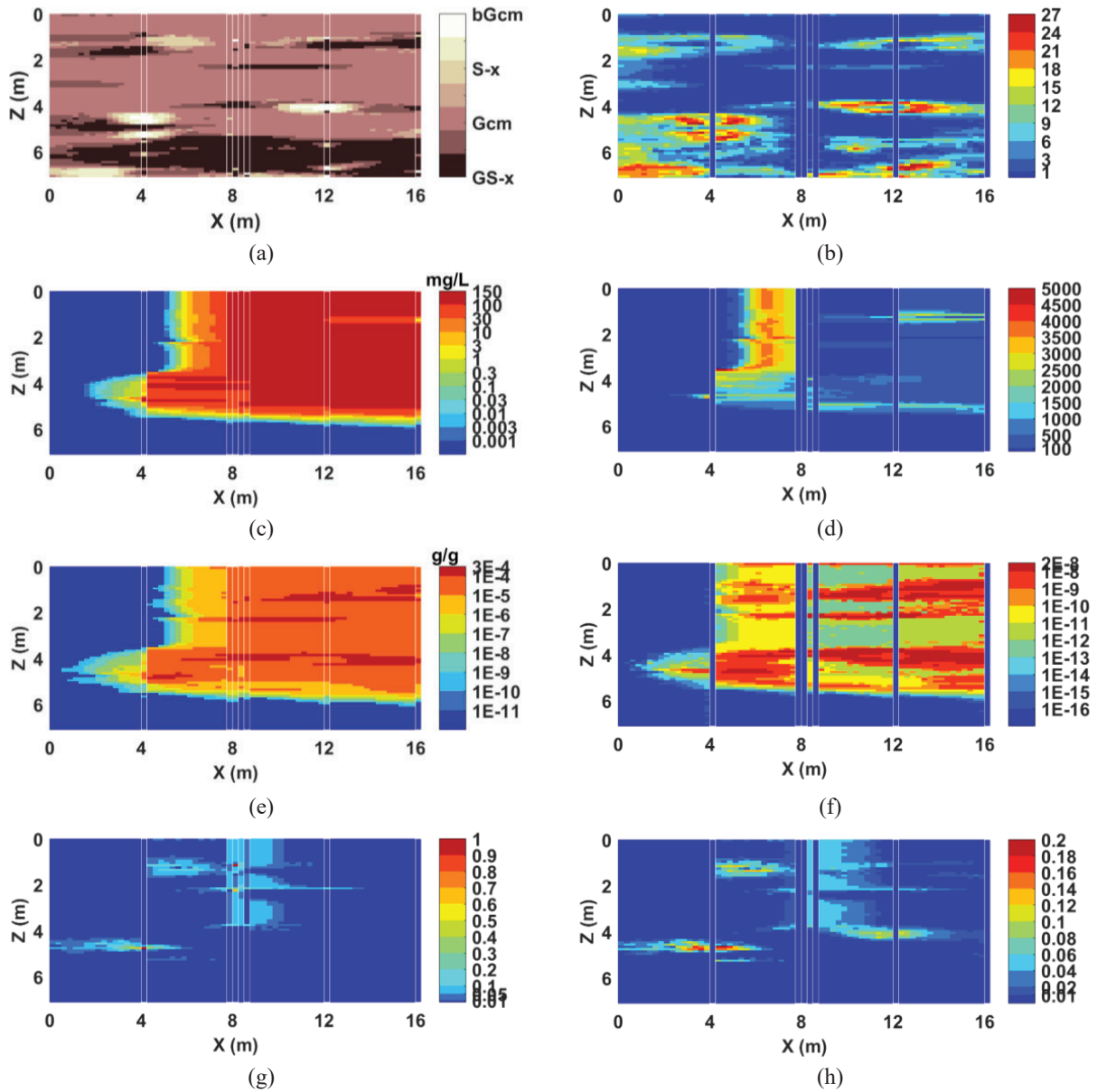
Figure R.7.16. Conditioned means and variances of log permeability field (a,b), initial aqueous concentration (c,d), initial sorbed concentration (e,f), and initial DNAPL saturation (g,h) for second-round FAC prediction at 5 years of ganglia dominated case

170
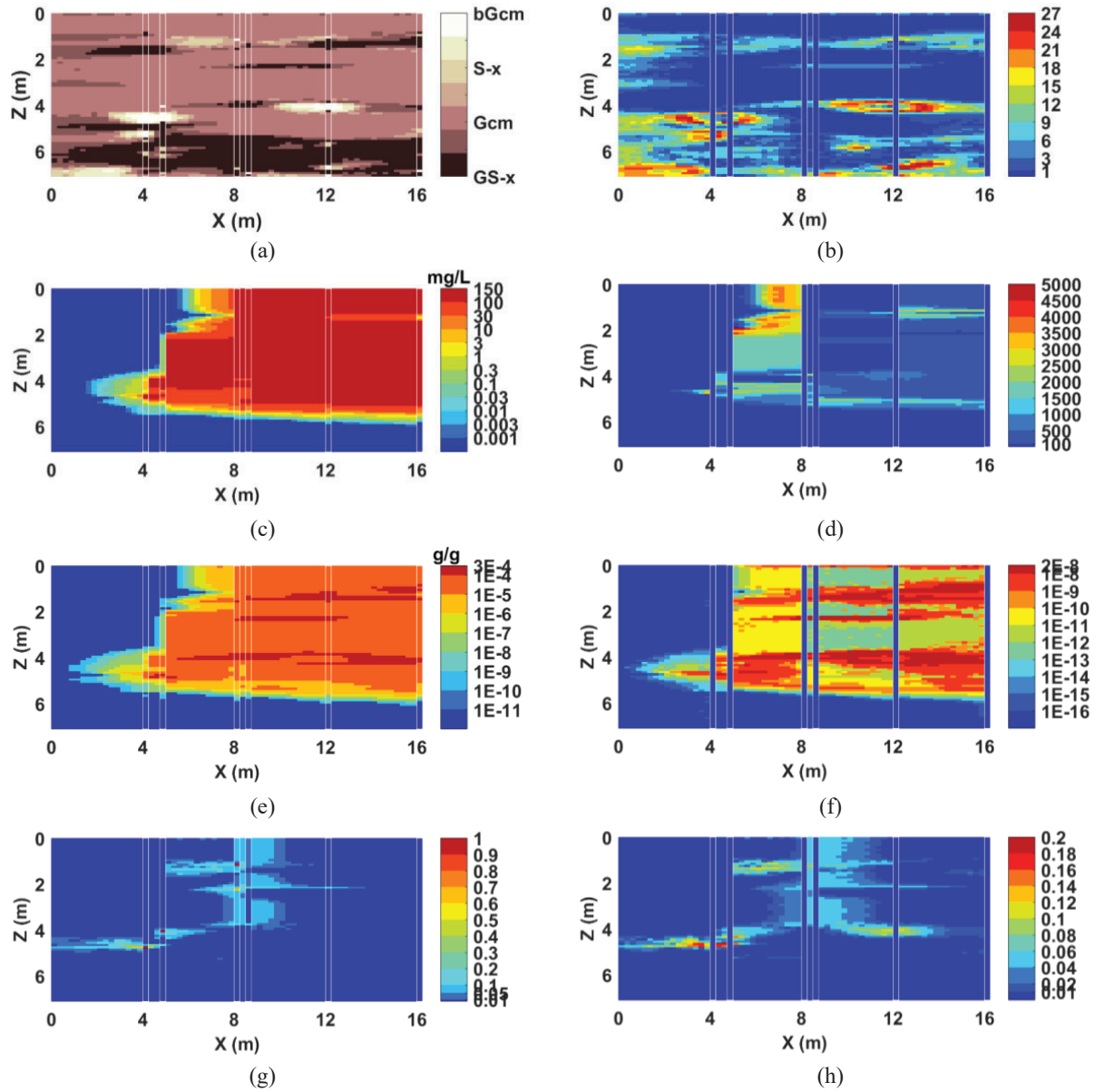
Figure R.7.17. Conditioned means and variances of log permeability field (a,b), initial aqueous concentration (c,d), initial sorbed concentration (e,f), and initial DNAPL saturation (g,h) for second-round FAC prediction at 10 years of ganglia dominated case
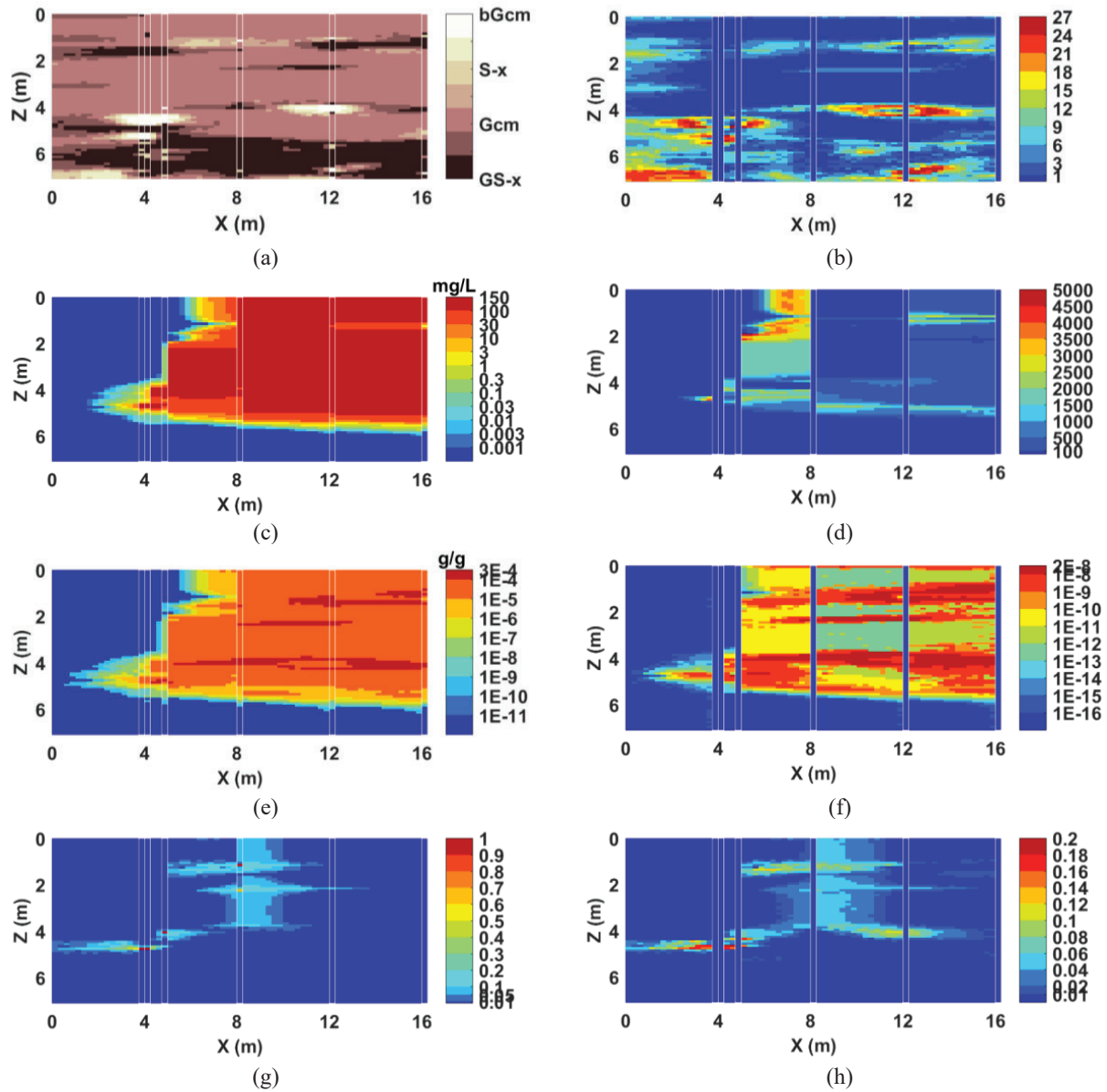
Figure R.7.18. Conditioned means and variances of log permeability field (a,b), initial aqueous concentration (c,d), initial sorbed concentration (e,f), and initial DNAPL saturation (g,h) for second-round FAC prediction at 20 years of ganglia dominated case

172
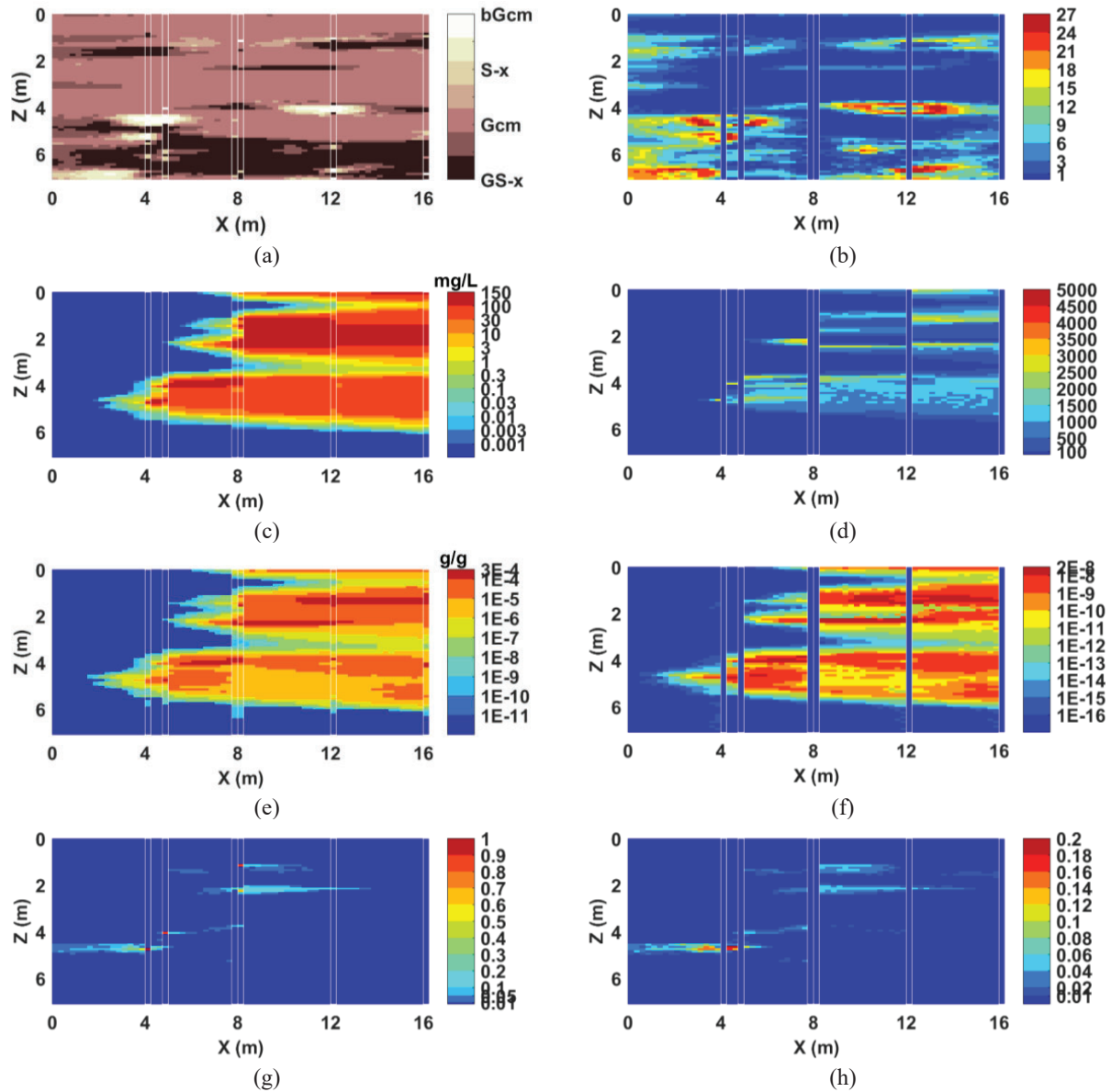
Figure R.7.19. Conditioned means and variances of log permeability field (a,b), initial aqueous concentration (c,d), initial sorbed concentration (e,f), and initial DNAPL saturation (g,h) for second-round FAC prediction at 1 year of pool dominated case
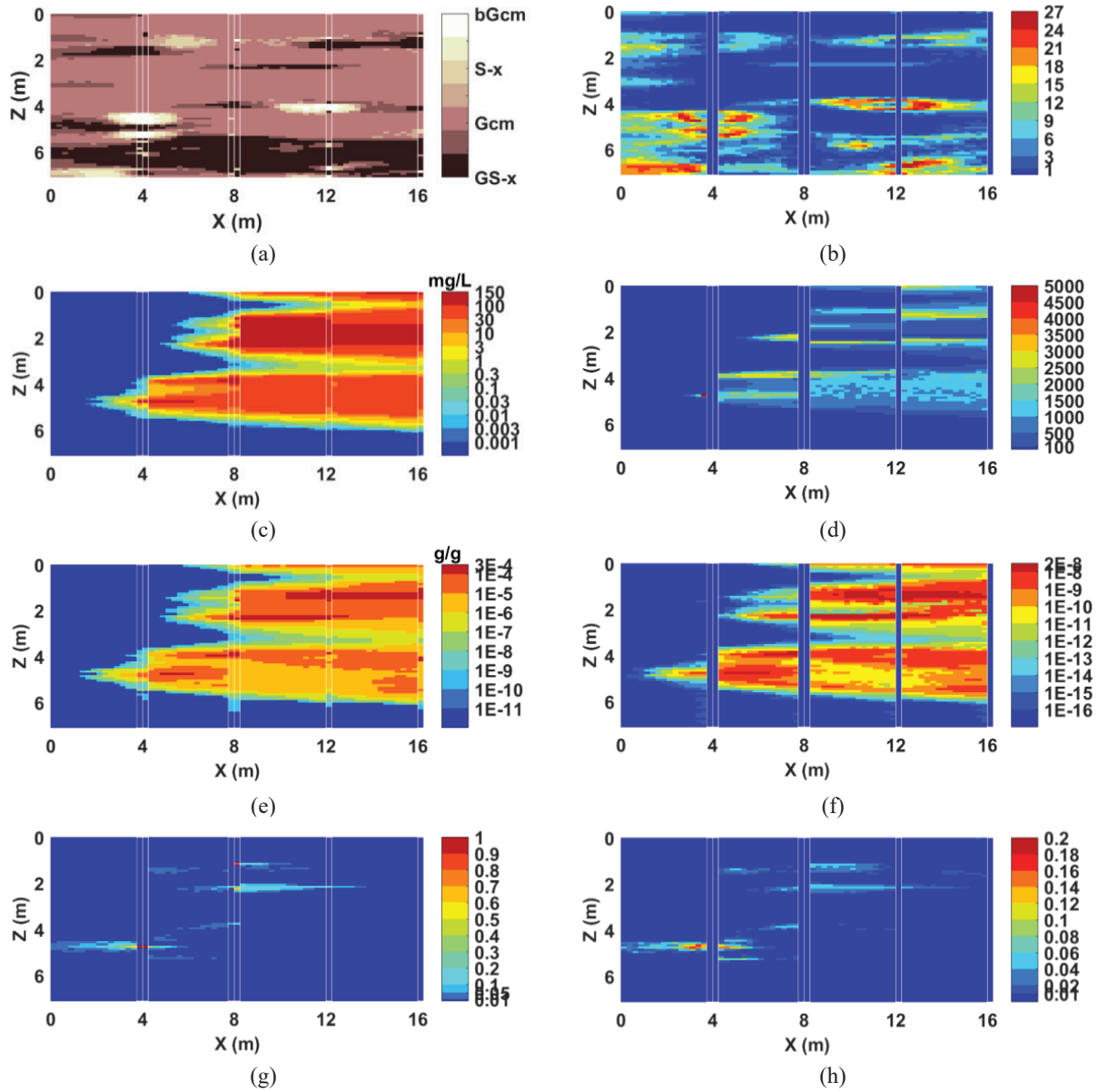
Figure R.7.20. Conditioned means and variances of log permeability field (a,b), initial aqueous concentration (c,d), initial sorbed concentration (e,f), and initial DNAPL saturation (g,h) for second-round FAC prediction at 5 years of pool dominated case
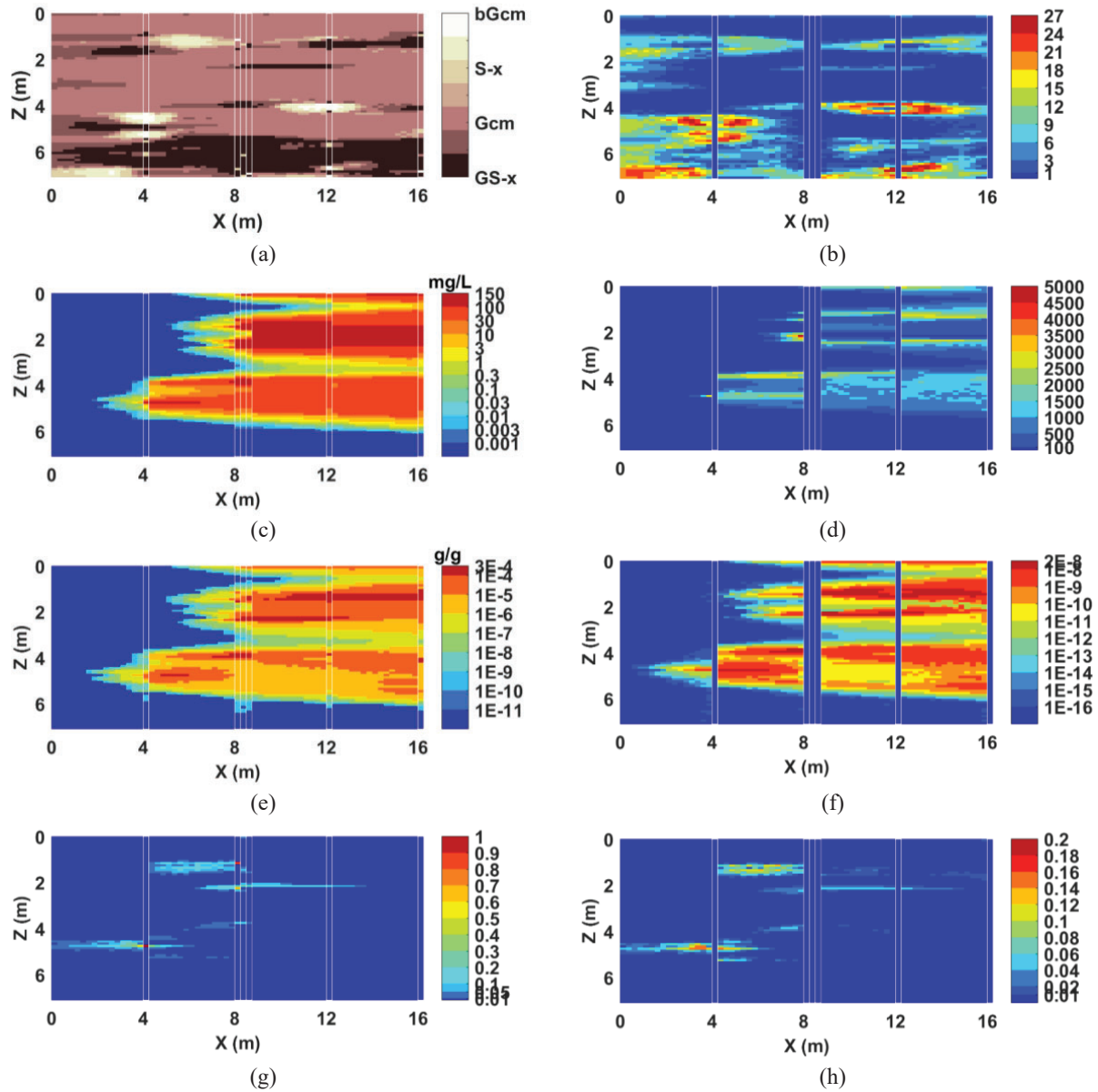
Figure R.7.21. Conditioned means and variances of log permeability field (a,b), initial aqueous concentration (c,d), initial sorbed concentration (e,f), and initial DNAPL saturation (g,h) for second-round FAC prediction at 10 years of pool dominated case

175
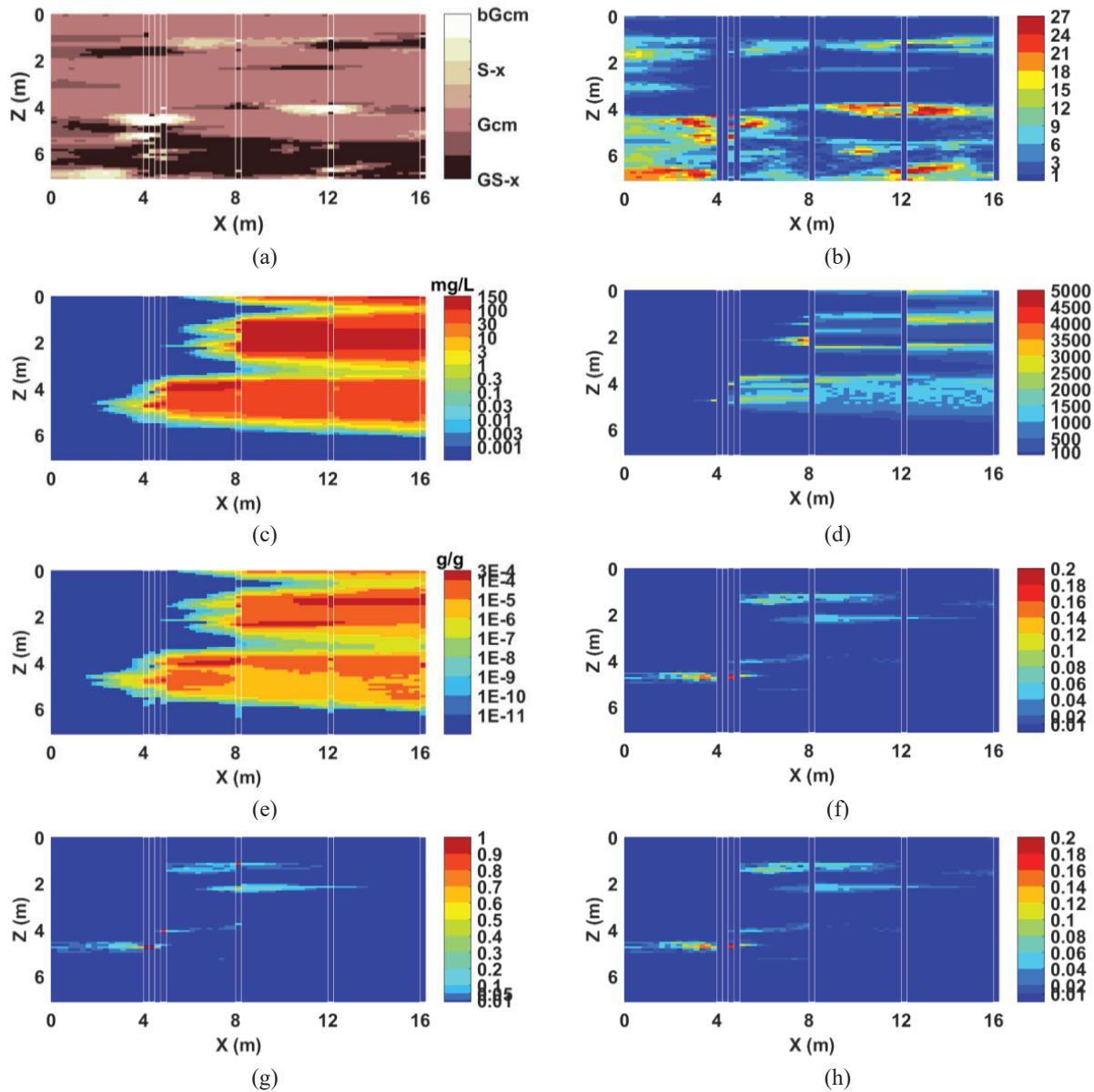
Figure R.7.22. Conditioned means and variances of log permeability field (a,b), initial aqueous concentration (c,d), initial sorbed concentration (e,f), and initial DNAPL saturation (g,h) for second-round FAC prediction at 20 years of pool dominated case

III.7.4.1. Down-gradient FAC predictions

Figure R.7.23 compares the means and error bounds of FAC predictions for both sampling campaigns. Examination of the figure reveals a closer agreement with the true fluxes and a significant reduction in the variances, as well as the CVs for both cases after performing second-round sampling, indicating reduced uncertainties in the FAC predictions. With enhanced characterization of the hydraulic conductivity field and initial contaminant mass distributions, the relative error of the predicted mean FAC at selected times decreased by 2.6%, 86.23%, 47.79%, and 7.92% for the ganglia dominated case, and by 32.21%, 133.9%, 5.94%, and 8.33% for the pool dominated case, respectively. Detailed numbers are given in Table R.7.1.

Comparison of the true aquifer properties with the new generated conditional statistics indicates

176

improved characterization of source zone architecture. The new source zones exhibit reduced total mass, resulting in more reasonable FAC predictions at early times for both cases. At later stages (20 years), the suggested sampling locations that target low hydraulic conductivity lenses and high DNAPL saturation pools, lead to prediction of slower flow and DNAPL dissolution rates, thus producing higher FAC predictions that are closer to the true values.

The expected and real variance reductions after the second-round sampling, however, display a slightly different trend than anticipated (Table R.7.1). In the data worth analysis (eq. M.8.6), perfect knowledge was assumed by setting the true additional measurements to the expected values and the variances to zero. When the site investigation is actually performed, however, the true measurements may differ from their conditional means. Hence, different sensitivity effects of FAC predictions to parameters can be anticipated from the first-round sampling. Due to the differences between the expected and real sensitivities of FAC after executing the second-round sampling, the expected and real FAC variance reductions are different. With DNAPL saturation hot spots and low hydraulic conductivity lenses being captured in and around new boreholes after performing the second-round sampling, larger impacts of parameters on FAC predictions can be expected.

(a)   (b)
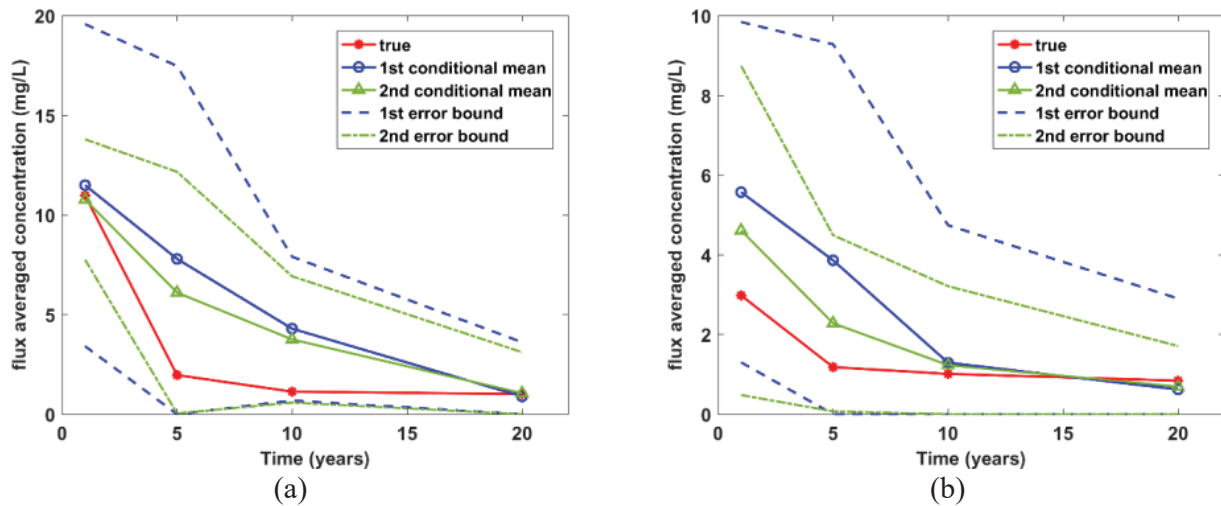
Figure R.7.23. True, first and second round FOSM conditional mean, and the error bound of FACs at selected times for ganglia dominated (a) and pool dominated (b) cases

III.7.4.2. Sampling Patterns for Further Assessment

Subsequent to the second-round sampling, a data worth analysis was again performed. The resulting data worth of additional measurements together with the location of two more optimal sampling boreholes (outlined in white) are shown in Figures R.7.24 and R.7.25 for both cases. The ganglia-dominated case exhibits sampling patterns that reflect measurements down-gradient and at locations with high DNAPL ganglia saturation uncertainties due to their early time effects on FAC predictions. Low hydraulic conductivity samples are again targeted for later time FAC predictions. The lower the hydraulic conductivity under the source zone, the higher potential for DNAPL persistence and the longer impact on down-gradient FACs. Therefore, the plume is far more likely to maintain concentration plateaus over longer times, resulting in more reasonable FAC predictions at later times.

Sampling patterns corresponding to the pool dominated case display similar trends compared to previous sampling phase. The early time sampling locations support the impact of initial aqueous concentration by selecting the measurements with large concentration uncertainties. Hydraulic

conductivity and DNAPL saturation measurements exploring the source zone architecture and the highly irregular flow pattern are still the focus of further site investigation, since these parameters are associated with the largest sensitivity impact and maximum uncertainty reduction. The coupling of these two parameters controls DNAPL dissolution rate, sorption capacity, and plume longevity, as well as the down-gradient FAC.
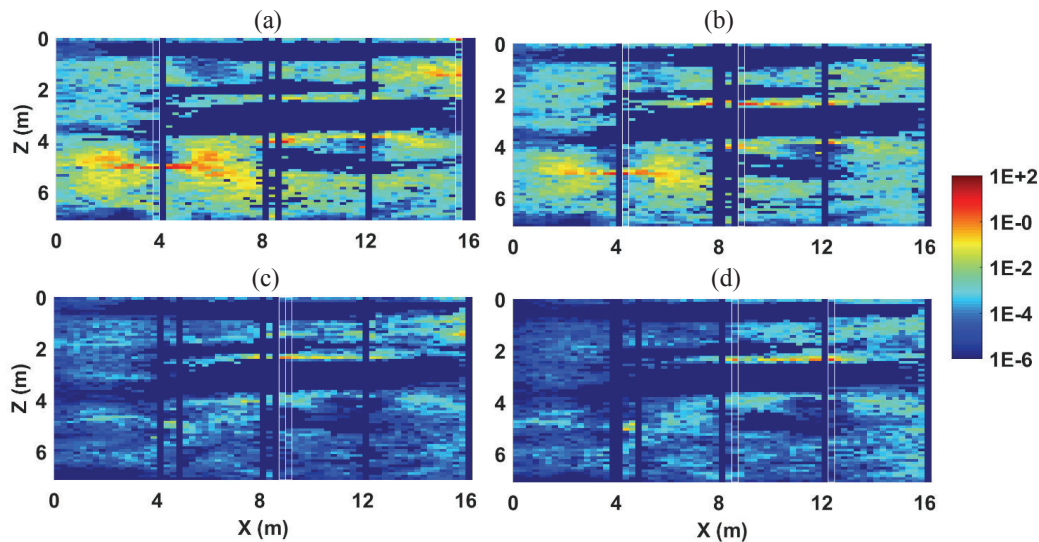
Figure R.7.24. Data worth of additional log conductivity, initial aqueous concentration, sorbed concentration, and DNAPL saturation measurements for flux averaged concentration prediction at 1 year (a), 5 years (b), 10 years (c), and 20 years (d) for the ganglia dominated case
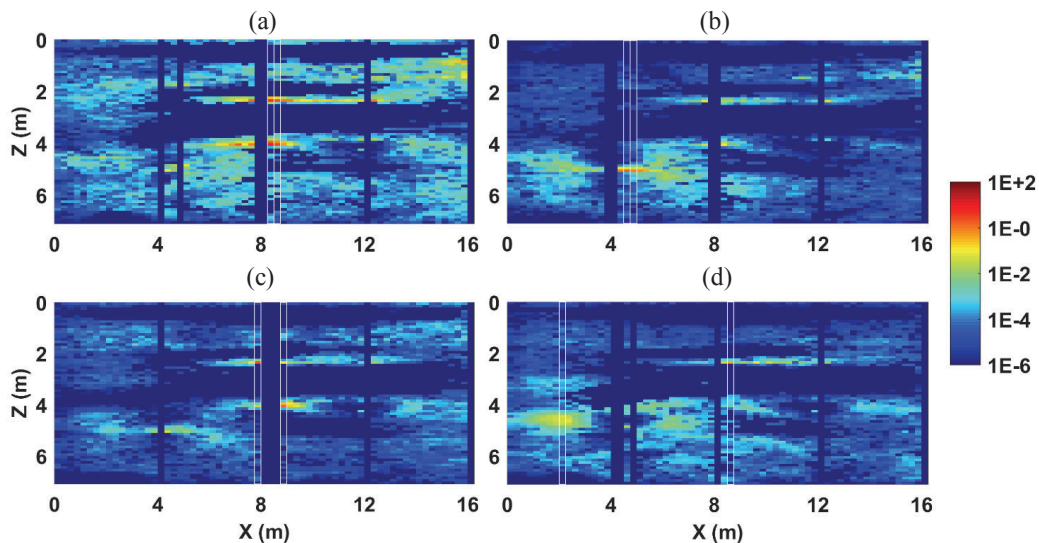
Figure R.7.25. Data worth of additional log conductivity, initial aqueous concentration, sorbed concentration, and DNAPL saturation measurements for flux averaged concentration prediction at 1 year (a), 5 years (b), 10 years (c), and 20 years (d) for the pool dominated case

III.7.5. Comparison to Alternative Sampling Approaches

To further explore the usefulness of the FOSM-guided sampling approach, FAC predictions were compared to those obtained using a uniform sampling approach, where the two additional boreholes were evenly spaced between previous sampling locations. In addition, in order to

confirm the time-specific optimization of an individual sampling pattern, the optimal sampling design corresponding to a single time prediction was applied to the other three times for both cases.

Conditional means, standard deviations, CVs, and error bounds of FACs based on FOSM-selected and uniform spacing for second-round sampling are presented in Table R.7.1 and Figure R.7.26. The resulting FAC predictions and the corresponding standard deviations and CVs, employing the time-specific sampling patterns for other simulation times, are summarized in Table R.7.2 and R.7.3 for the ganglia- and pool-dominated cases, respectively.

Inspection of Tables R.7.1 to R.7.3 reveal that the predicted FACs of case 1 based on the FOSM method are closer to the true values, compared to those obtained from other sampling patterns, for all but one time (10 years) (where the best estimate is obtained with the uniform sampling approach). Since the FOSM sampling design takes into account the changing sensitivity of FAC to various parameters with time, more accurate FAC predictions can be expected compared to other sampling approaches. The uniform sampling strategy, however, resulted in a lower pool fraction estimate than did the optimal sampling strategy. This lower pool fraction led to a more rapid dissolution rate, with a sharper decrease in FACs compared to optimal sampling patterns. Thus, the FAC prediction at 10 years was more comparable to the true value essentially by coincidence.

The FAC prediction at 1 year for case 2 is slightly higher in comparison to the uniform sampling result. As discussed above, the criterion for estimation of the optimal sampling pattern is based upon expected values. However, the FOSM guided sampling locations provide parameter information different from the expected values. In this case, sampling encountered low flow and high DNAPL saturation zones, resulting in higher FAC at early time. The similar predictions at 5 and 10 years can be explained by predicted transport reaching a concentration plateau. In the uniform sampling approach, the high DNAPL saturation pools were not encountered, and a lower prediction was achieved in comparison to both true and FOSM estimates at 20 years. Compared to the conditional mean FACs after applying time-specific sampling patterns to other prediction goals, more accurate results were achieved with the FOSM based optimal sampling patterns for case 2 at the four selected times.

A comparison of the standard deviations of FACs based on the optimal and alternative sampling approaches for both cases indicates that the lowest standard deviations were achieved when performing the optimal sampling patterns for all the selected times. As expected, the standard deviations and CVs of second-round FAC predictions based on the FOSM sampling patterns, are smaller for all selected times, in comparison with those that result from the uniform sampling, indicating decreased uncertainty and better confidence in the predictions.

The uncertainty reductions of FAC predictions (i.e., the standard deviation differences before and after the second-round sampling at four simulation times), are quantified in Figures R.7.27 for both cases. Collecting new data based on the time-specific optimal sampling pattern results in the greatest uncertainty reduction of FAC predictions for that time. The uniform sampling pattern did not consider interaction between different parameters and the FACs spatially and temporally, hence, valuable information about better source zone characterization was neglected, leading to less accurate predictions. The FOSM method achieves 0.98%-46.04% more uncertainty reduction with the same number of sampling positions than the uniform sampling approach for FAC predictions.

The worst performance of mean FAC prediction was found for pattern 2d when applied to predict case 2b, while the largest FAC uncertainty was found for pattern 1b when applied predict case 1a. This can be explained by the fact that these two patterns lay their focus on opposed features in

their respective design objectives. Improved ganglia characterization and reduced parameter uncertainties were focused for early time predictions, in contrast, high saturation pools with the low hydraulic conductivity lens underlaying were preferred for later time estimates. These comparisons further demonstrate the dominant influence of site characterization on FAC predictions.

These examples have demonstrated that the coupling of FOSM uncertainty quantification with the data worth analyses can provide reasonable FAC predictions together with the corresponding uncertainties. The FOSM-based optimal sampling patterns outperform the alternative sampling approaches for most of the prediction goals with more accurate estimates and better confidence intervals.

(a) (b)
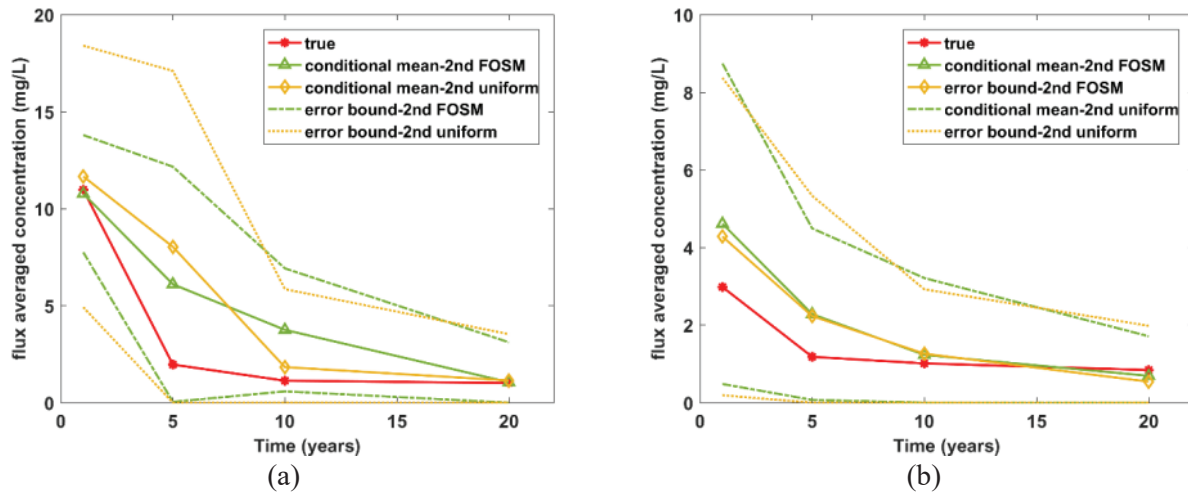
Figure R.7.26. True, second round uniform and FOSM conditional mean, and the error bound of FAC at selected times for ganglia dominated (a) and pool dominated (b) cases

(a) (b)
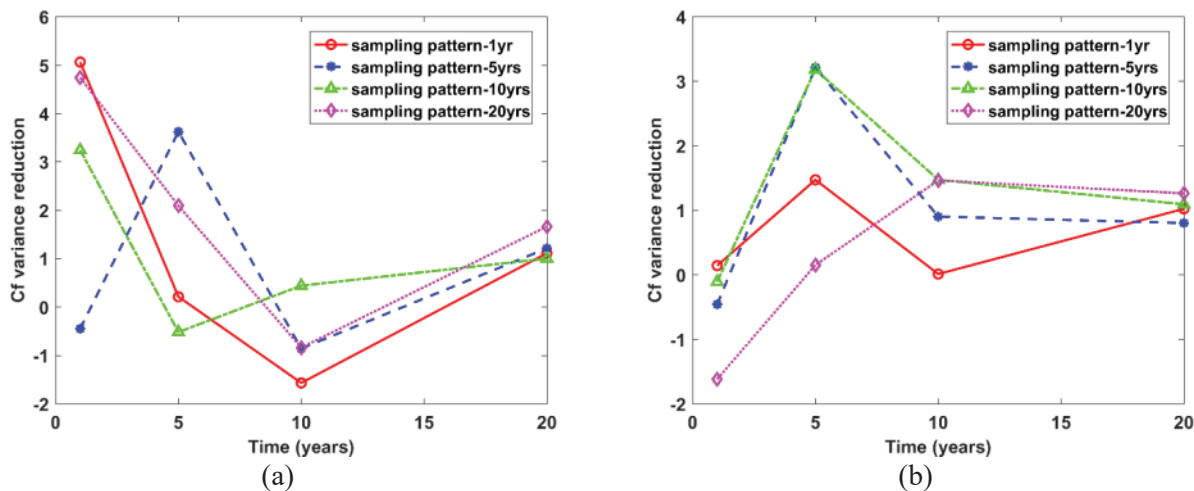
Figure R.7.27. Reduced variance of FAC predictions based on prediction targeted sampling patterns for ganglia dominated (a) and pool dominated (b) cases

180

Table R.7.2. Conditional mean (mg/L), standard deviation (mg/L), and coefficient of variation of down-gradient FACs for every sampling design when applying to different prediction goals for the ganglia dominated case

Pattern	Case 1a			Case 1b			Case 1c			Case 1d		
	Mean	StD	CV	Mean	StD	CV	Mean	StD	CV	Mean	StD	CV
1a	10.77	3.02	0.28	6.44	9.47	1.47	3.75	5.18	1.38	0.49	1.61	3.28
1b	11.22	8.53	0.76	6.10	6.06	0.99	3.44	4.47	1.30	0.44	1.51	3.44
1c	12.74	4.84	0.38	8.57	10.20	1.19	3.75	3.17	0.84	0.75	1.72	2.29
1d	12.37	3.34	0.27	8.53	7.59	0.89	4.44	4.45	1.01	1.05	2.06	1.96

Table R.7.3. Conditional mean, standard deviation, and coefficient of variation of down-gradient FACs for every sampling design when applying to different prediction goals for the pool dominated case

Pattern	Case 2a			Case 2b			Case 2c			Case 2d		
	Mean	StD	CV	Mean	StD	CV	Mean	StD	CV	Mean	StD	CV
2a	4.61	4.15	0.90	2.95	3.95	1.34	1.72	3.44	2.00	0.50	1.26	2.52
2b	5.25	4.73	0.90	2.28	2.21	0.97	1.14	1.55	1.36	0.61	1.48	2.42
2c	5.21	4.38	0.84	3.29	2.24	0.68	1.23	1.98	1.61	0.49	1.19	2.43
2d	5.66	5.89	1.04	3.96	5.27	1.33	1.79	1.99	1.11	0.69	1.01	1.47

III.7.6. Discussion and Conclusions

An efficient FOSM method, honoring borehole observations and designed to estimate the FAC and its corresponding variance at distinct times, was presented and validated. Data worth analyses were performed to provide more accurate mean FAC predictions and to reduce uncertainty to the maximum extent, thereby ensuring a maximum return on investment in future data acquisition. Unlike Monte Carlo simulations, which have large computational demands, the FOSM method, coupling adjoint state theory, is computationally efficient.

By considering the process coupling of DNAPL dissolution, sorption, diffusion, and mass transport, simulation results in this study indicate that among the four system parameters considered, hydraulic conductivity dominates the FAC predictions, as the hydraulic conductivity values affect the velocity field, which further governs the concentration distribution down-gradient. Spatial heterogeneity of the DNAPL mass distribution, in addition, was also demonstrated to influence the FAC, with the presence of DNAPL tending to control the source plume persistence through dissolution.

Data worth assessments were conducted to investigate the usefulness of the proposed model framework for guiding acquisition of additional data that can most efficiently predict the FACs. Because of the nonlinear dependence of FACs on log hydraulic conductivities, as well as the initial contaminant mass, predictions with high variances may be biased. It is of particularly import to explore to which extent the effectiveness of FOSM method may be compromised by nonlinear model behavior. Simulation results suggested that the linearity assumption underlying the methodology does not invalidate its usefulness in evaluating data worth as it pertains to predictions of future FACs. In general, although observation worth outcomes varied to some extent for predicting FACs at different times based on widely varying parameter fields, the relative worth of

additional measurements of the same type were typically consistent, with potential locations associated with low hydraulic conductivity regions, as well as high DNAPL saturation pools.

It was demonstrated that potential measurement candidates vary with different prediction time windows, with selected locations closer to the down-gradient transect for early time predictions, but moving upgradient when the prediction of FAC at later times is targeted. The resulting optimal sampling patterns are consistent with the heterogeneous flow field, associated varying DNAPL dissolution rates. A comparison with alternative sampling approaches verified the effectiveness and superiority of the FOSM method for FAC predictions, and also demonstrated the importance of considering spatial heterogeneity and the interplay between different transport processes at the local scale.

The analysis in this study was restricted to 2-D to reduce the computational burden. Although it was demonstrated by Yang et al. (2018) that reduced dimensionality has a crucial impact on predictions of plume longevity, 2-D simulation results are useful for examining trends in plume metrics. Since the post-DNAPL removal regime was not considered in this study, and the relative importance of different system parameters for FAC predictions, as well as the optimal sampling network design, were the primary concern, the 2-D simulations were still capable of demonstrating the utility of the approach, quantifying data worth in reducing prediction uncertainty and developing an optimal sampling network.

The model framework proposed herein, although demonstrated on 2-D synthetic cases, has been shown capable of ranking yet-to-be acquired data in order of its importance for making predictions of future system behavior. Simulation comparisons of the optimal sampling network corresponding to FOSM method with alternative sampling approaches, demonstrated that the method can provide valuable guidance in selecting additional borehole measurement locations. Overall, the developed sampling strategy, coupling sensitivity analysis and uncertainty quantification, demonstrates promise for enhancement of the ability to guide characterization of source zones under realistic field conditions.

IV. Design and Implementation of Pilot Downhole Treatability Test

IV.1. Design and Implementation

As discussed in Section II.4.2.3, laboratory studies tend to overestimate potential treatment effectiveness. For example, a comparison of 138 chlorinated solvent bioremediation field and laboratory studies revealed that median laboratory rate constants were consistently higher (up to one order-of-magnitude) than the observed field rate constants (Suarez and Rifai 1999). Most laboratory treatability studies do not adequately mimic mass transfer processes, such as rate-limited dissolution, diffusion and desorption, that may control system performance at a heterogeneous field site. The underlying premise for the pilot (DHT) test methodology proposed herein is the recognition that: (a) even advanced assessment tools, such as molecular probes, fail to provide the reaction rate information necessary to predict the extent of remediation in complex subsurface environments, and (b) the tool or method should provide information that is relevant at the field scale and can be readily incorporated into model(s) that are able to simulate remediation performance and account for uncertainty.

The pilot (DHT) test was designed to test the application of effective rate parameters in the performance assessment of field-scale remediation technologies. In conjunction with the microcosm transformation studies (Section III.2) and the aquifer cell experiments (Section III.3), the pilot test allowed the comparison of MRD rate parameters across systems of increasing complexity.
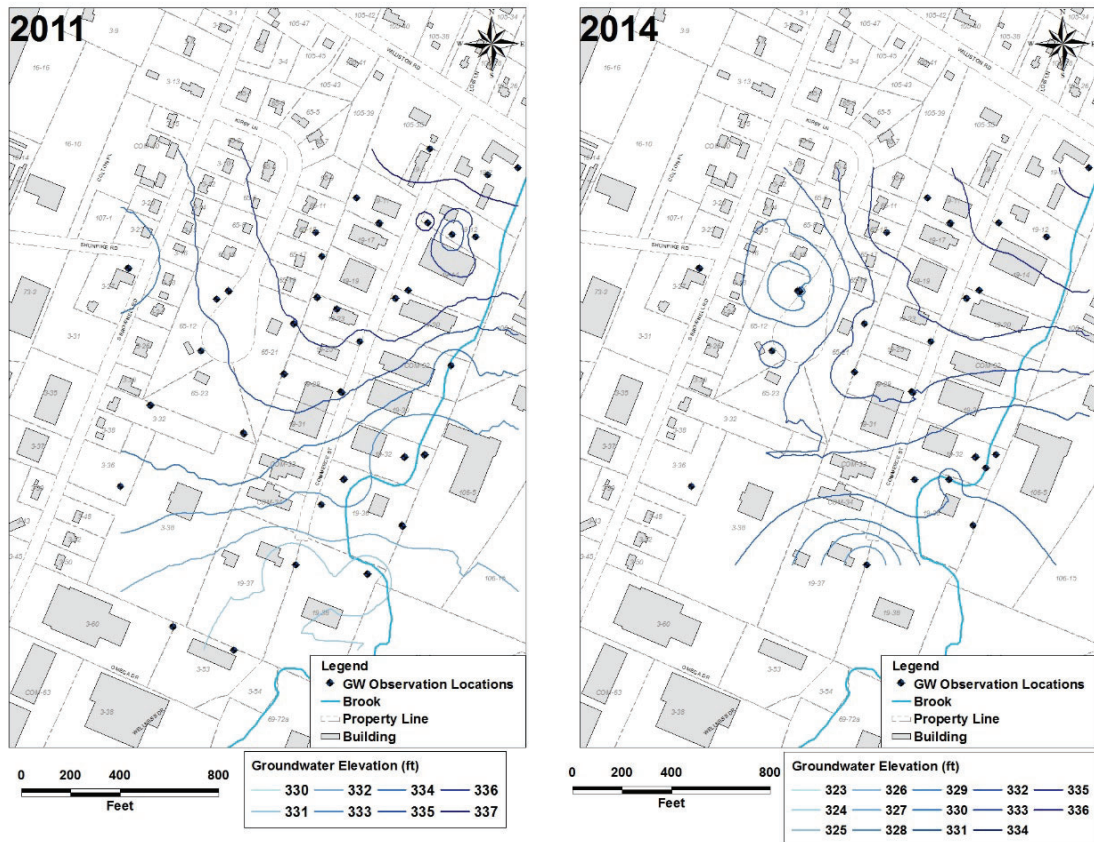
Figure P.1.1. Interpolated head contours in 2011 (left) and 2014 (right). The interpolation was based on available head measurements from wells displayed in the maps.

183

Prior to designing the pilot test, efforts centered on analyzing available site data and selecting the optimal location(s) for installation of a multi-level well transect, down gradient of the main source area. This selection was based on concentration and head observations which provided evidence of the source location, groundwater flow direction, plume evolution, and accessibility considerations. Inspection of available data revealed a complex source zone, characterized by non-uniform groundwater flow, a number of high concentration areas, and multiple chlorinated solvent plumes. Measurements of groundwater contamination and hydraulic head were inspected and interpolated with the software ArcGIS using two methods; the Inverse Distance Weighted method and the Empirical Bayesian Kriging method. The two methods yielded similar interpolations. Contours developed using the Inverse Distance Weighted method are shown in Figures P.1.1 (hydraulic head) and P.1.5 (concentration) and discussed below.

The contaminated sand unit is approximately 12.2 m (40 ft.) deep. It is relatively homogeneous, but with a slightly fining trend downwards, and is bounded below by a consistent clay layer. Recorded (interpolated) groundwater levels display a small gradient from the northern part of the site towards both the southwest and the southeast (Figure P.1.1). While the southeasterly flow follows the surface topology in that direction, the southwesterly flow component is thought to originate from intermittent sump pumping in residential buildings on the western part of the site, performed to mitigate basement flooding. The rate of pumping is unknown. There is a shallow brook to the southeast of the transect locations, with low flow.

IV.1.1. Site Groundwater Flow Model Development

A site groundwater flow model was developed based on site data using Visual MODFLOW Flex, encompassing a domain that is considerably larger than the DHT study area. The elevations of the ground surface and clay layer were prescribed based on existing topographical and geophysical data (Figure P.1.2). Heterogeneous hydraulic conductivity fields corresponding to different depths below ground surface were generated using a Kriging interpolation method based on permeability measurements in CMT-1 and CMT-5 (Figure P.1.3). The measured values vary within one order-of-magnitude. To account for the formation layering, modeled vertical conductivities were set one order-of-magnitude lower than those in the horizontal direction. Prescribed heads were set at all lateral boundaries in the modeling process. These values were first obtained based on the interpolated groundwater elevation contour at the boundaries, and then calibrated to better fit the measured and interpolated groundwater levels within the domain. Natural recharge was prescribed based upon the available hydrologic data, while no-recharge boundary conditions were prescribed at the locations of paved roads and buildings. The small brook was treated as a very shallow and narrow river with a riverbed conductivity one order of magnitude lower than the average measured horizontal hydraulic conductivity. In addition, two pumping wells with different screen depths and pumping rates were included at the western and southern parts of the site (Figure P.1.4), to capture the effect of intermittent sump pump discharge. The flow model was calibrated to approximate measured groundwater levels. The sump pump discharge rates were used as another fitting parameter to capture the measured drawdown at these locations. In general, the simulation reproduces the interpolated groundwater elevation contours quite well and the normalized root mean squared error of the simulated versus observed head is small (Figure P.1.4).
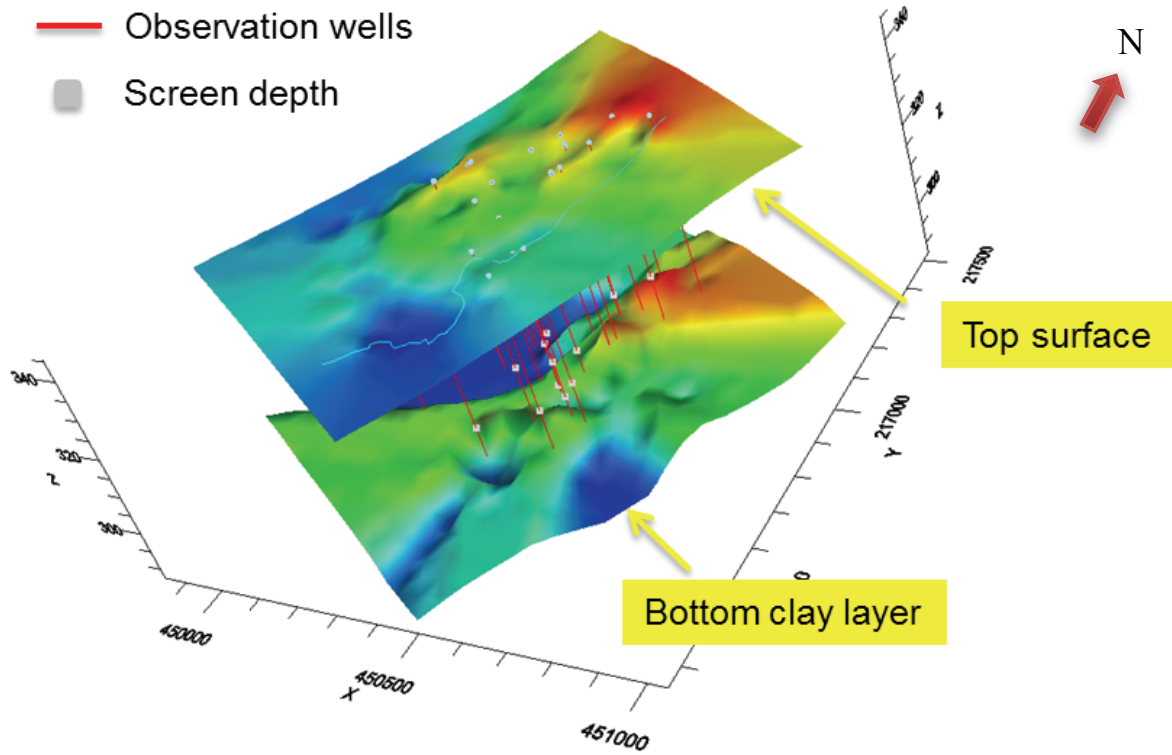
Figure P.1.2. Top and bottom layer formation of site flow model
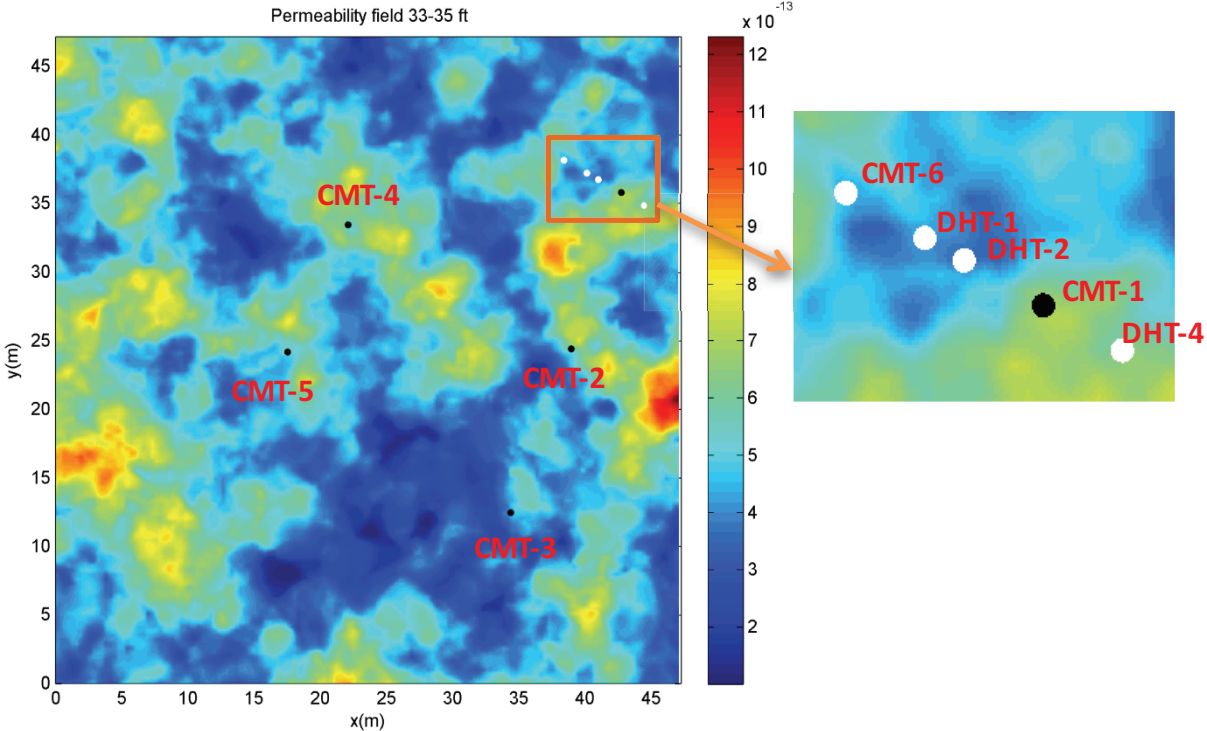
Figure P.1.3. Permeability (m^2) field focused on the DHT test and transect area at 33-35 ft. bgs
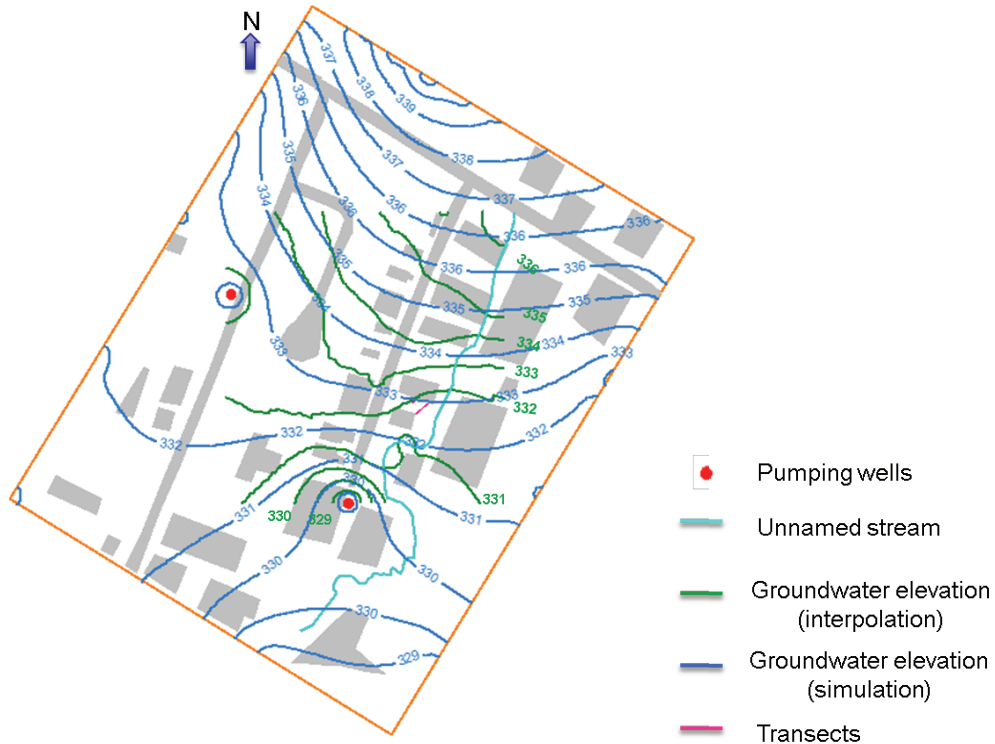
Figure P.1.4. Comparison of interpolated groundwater elevation contour based on well observations and the simulated groundwater elevation contour

IV.1.2. Downhole Treatment (DHT) Transect Locations

Inspection of available site contaminant concentration data revealed the presence of a complex source zone, characterized by a number of high concentration areas, and multiple chlorinated solvent plumes, see Figure P.1.5. Contoured data suggested the existence of more than one source area at the site. A persistent high concentration area (source) close to Commerce Street was chosen as the focus of this project, see Figure P.1.6. Head observations in this area indicate that vertical groundwater flow is negligible and that the lateral flow direction in the proximity of this source area is towards the southeast. In addition, comparison of plume contours between the years 2000 and 2011 (Figure P.1.5) revealed that plume spreading occurred towards the southeast in this period, consistent with the head data. Based on the concentration and head observations, which provided evidence of the source location, groundwater flow direction, and plume evolution, and based on accessibility considerations, optimal locations for installation of two multi-level well transects were selected. These locations were down gradient (southeast) of the source area and perpendicular to the estimated groundwater flow, see Figure P.1.6. The up-gradient and down-gradient transects are approximately 18.3 and 36.6 m (60 and 120 feet) long, respectively, and located within the properties labeled 19-30 and 19-32, where previously measured TCE concentrations range from 5-50 mg/L.
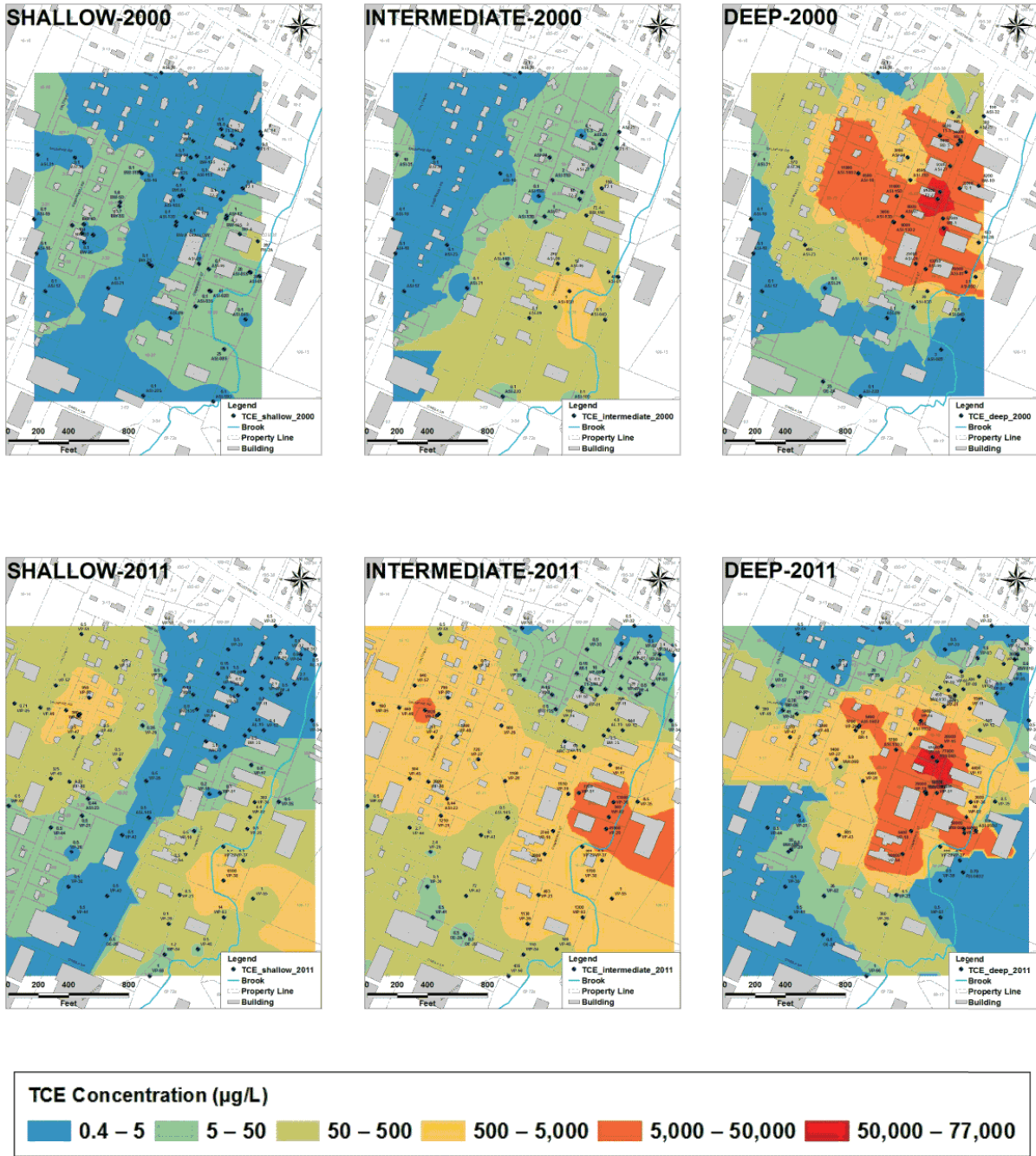
Figure P.1.5. Interpolated TCE concentrations (μg/L) in the years 2000 (top) and 2011 (bottom). The concentration is shown for the shallow (0-20 ft below surface), intermediate (20-30 ft below surface), and deep (>30 ft below surface) portions of the aquifer. The interpolation was based on available concentration measurements from wells displayed in the maps.
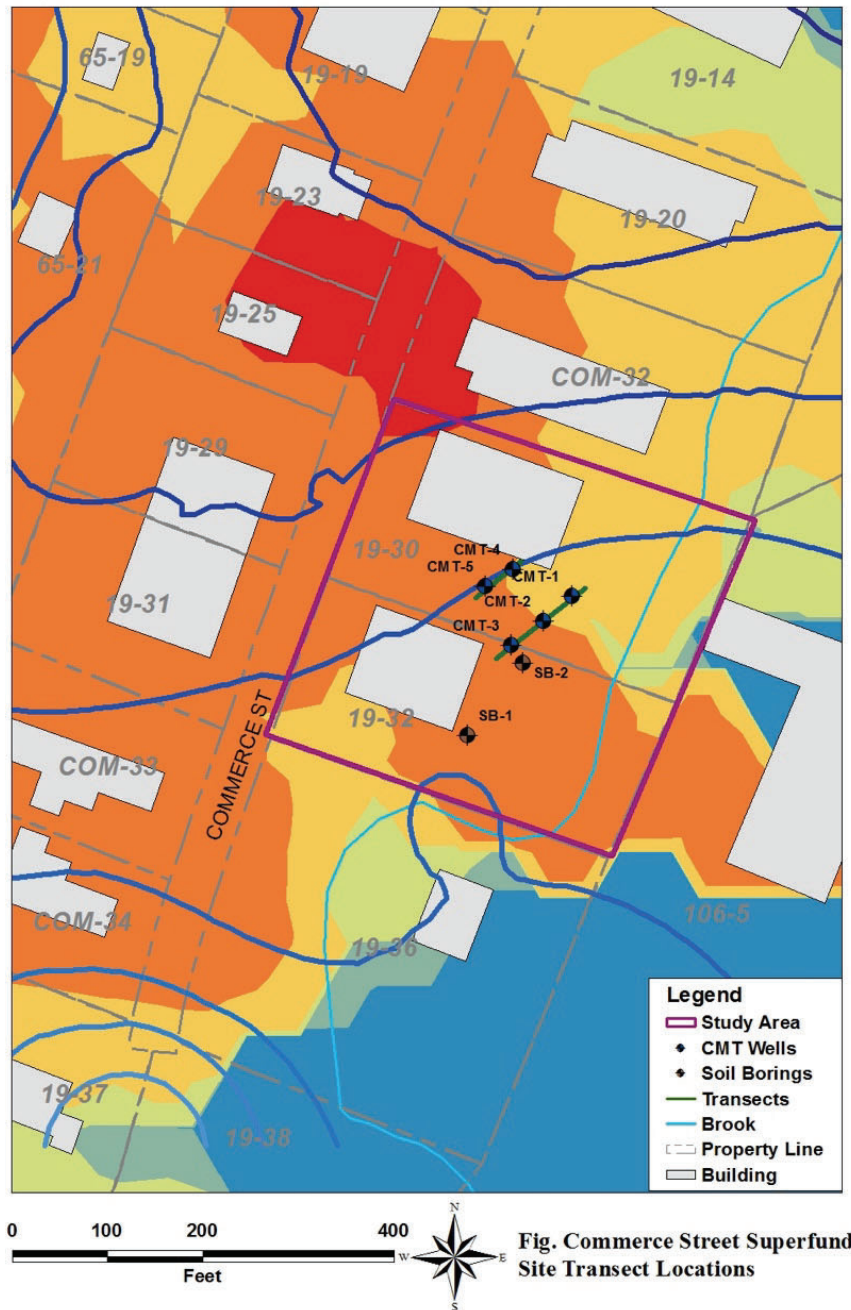
Figure P.1.6. Study area with positioning of new soil borings (#1 and #2) and transects with multi-level (CMT) wells. The figure also shows interpolated head contours (cf. legend in Figure P.1.4) and the interpolated TCE concentration in 2011 (depth >30 ft, cf. legend in Figure P.1.5).

IV.1.3. Pilot Test Treatment System

The treatment system consisted of four pumps and two tanks housed in a treatment trailer with tubing connected to wells DHT-1, DHT-2, and CMT-1 (Figure P.1.7). Three Masterflex peristaltic pumps (Cole Parmer; Vernon Hills, IL) were used to extract groundwater from DHT-2 and CMT-1 as described below. A Series I HPLC pump (Scientific Systems Inc; State College, PA) was used to inject amendments into DHT-1. A 75.7 L (20-gallon) polyethylene plastic tank (Ace Roto-mold-Den Hartog Industries; Hospers, IA) was used to mix batches of groundwater and amendments.

Additional batches of amendments were prepared in 40 L polyethylene totes. The second polyethylene plastic tank, with a capacity of 284 L (75 gallons [Ace Roto-mold-Den Hartog Industries; Hospers, IA]), was used to collect and hold extracted groundwater prior to on-site treatment and discharge. The effluent treatment system consisted of a submersible pump, a 10 micron bag filter, a 0.1 micron bag filter, and a 208 L (55 gallon) vessel of activated carbon. After treatment, extracted water was discharged to the unnamed brook east of the site. During operation of the pilot test, groundwater samples from the extraction wells were collected from a sample port in the treatment trailer connected to the extraction tubing without additional purging.
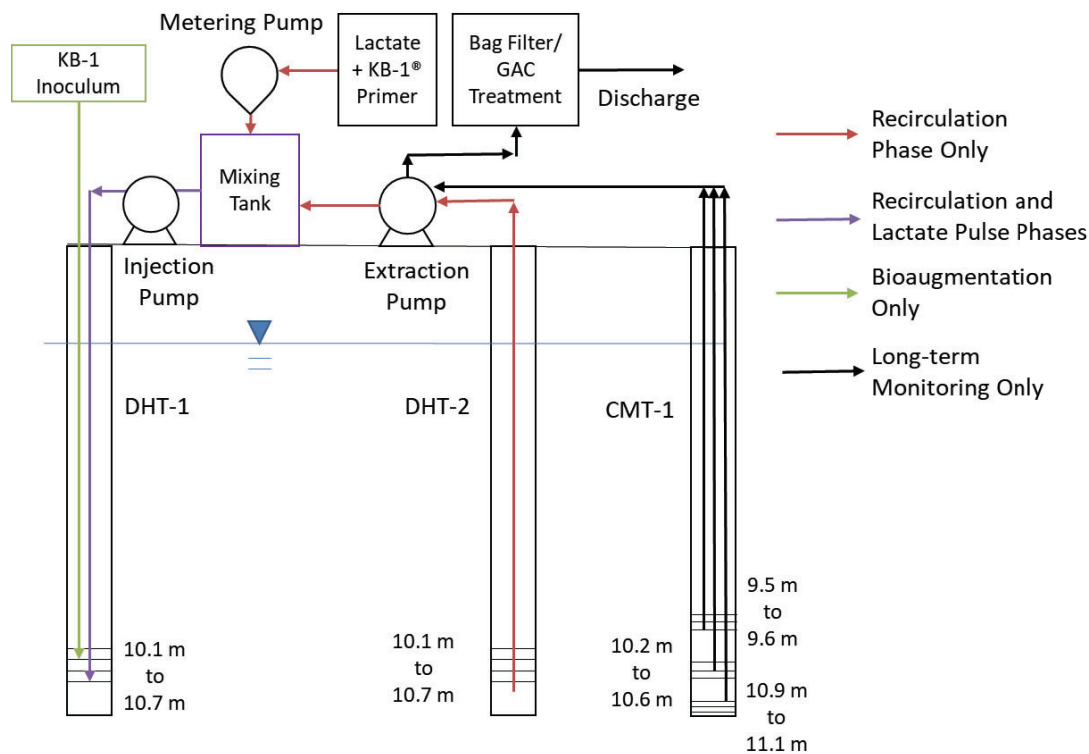
Figure P.1.7. Pilot Test System Configuration.

IV.1.4. Pilot Test Operation

The pilot test system was operated in three configurations over the course of the experiment as described below and show in Table P.1.1.

Table P.1.1. Pilot Test Operation.

	Phase:	Bromide Tracer/lactate loading	Lactate Recirculation	Bioaugmen-tation	Lactate/ Biomass Recirculation	Long-term Monitoring	Monitoring w/ Reduced Flow Rate
DHT Test	Duration (days)	4	3	1	14	62	44
	Pore Water Vel. (cm/d)	14.3	14.3	14.3	7.15	7.15	4.76
	Residence Time (days)	7	7	7	14	14	21
	Injections	10 mM bromide; 5mM lactate; 0.85 g/L KB-1 Primer®	5mM lactate; 0.85 g/L KB-1 Primer®	1.5 L of KB-1® inoculum	5mM lactate; 0.85 g/L KB-1 Primer®	1 pulse of 13.1 mM lactate (14 days)	1 pulse of 37 mM lactate (22 days)

Step 1 – Lactate Injection (Establish Bioactive Zone)
During Step 1, groundwater was extracted from DHT-2 and reinjected into well DHT-1 at a target flow rate of 16.5 mL/min (0.004 gallons per minute [gpm]) to achieve a target residence time of 7 days. A 38 L pulse containing 16.5 mM sodium bromide (conservative tracer), 5 mM lactate (a microbial electron donor source), and 0.85 g/L KB-1 Primer® (used to create more ideal conditions for bioaugmentation, e.g., neutral pH, dissolved oxygen below 0.5 mg/L and ORP below -150 mV [SiREM, Guelph, ON]) was delivered over 1.5 days at approximately 17 mL/min (seepage velocity of 14 cm/day) as shown in Table 1. Here the volume and concentration of the injected bromide tracer were chosen based on flow and transport model simulations employing a range of longitudinal dispersivities. Following the 38 L pulse, extracted groundwater was amended with 5 mM lactate and 0.85 g/L of KB-1 Primer® prior to reinjection. A bromide probe (Cole Parmer; Vernon Hills, IL) was placed in the flow stream from the DHT-2 pump to monitor the breakthrough of the bromide pulse. Additional bromide and VFA samples were collected from the extracted water to quantify the breakthrough of injected fluids. Step 1 continued for 7 days to ensure that lactate passed through the target zone, anoxic conditions were established, and electron donor was available for the PCE-to-ethene dechlorinating consortia, introduced in Step 2.

Step 2 – Bioaugmentation (Distribute Microorganisms)
Step 2, bioaugmentation, encompasses inoculation of the site and maintenance of conditions suitable for the growth of the dechlorinating consortia. During Step 2, the recirculation system continued to operate between wells DHT-1 and DHT-2. On day 8, 1.5 L of a PCE-to-ethene microbial inoculum, KB-1® (SiREM; Guelph, ON), was delivered into well DHT-1 to establish an initial *Dhc* population of approximately 10^6 cells/L within the 1 m treatment zone. Continued recirculation with lactate electron donor and KB-1 Primer® amendment followed bioaugmentation to further promote conditions conducive to organohalide respiration of the TCE plume. The system continued to operate with a 7-day residence time (17 mL/min) in a recirculation mode in an effort to create an anoxic zone conducive to the growth and activity of the introduced KB-1® inoculum. Following the completion of bromide tracer measurements in the downgradient well (DHT-2 located 1 m from the injection at DHT-1), system operation was continued in a recirculation mode for an additional week at a decreased flow rate of 8.5 mL/min, which corresponds to a seepage velocity of 7 cm/day and a doubled residence time of 14 days (Table P.1.1). This longer residence time within the treatment zone was selected to promote complete detoxification of TCE to ethene.

Step 3 – Pumping and Monitoring (Assess Performance)
Following Step 2, the target zone between DHT-1 and DHT-2 had a well-established community of dechlorinating organisms and conditions suitable for organohalide respiration. At this time, the recirculation system was disconnected and wells DHT-1 and DHT-2 were used for groundwater monitoring. During Step 3, groundwater was extracted from the lowest three depths of CMT-1 at approximately 450 mL/min to maintain hydraulic control of the contaminant plume and ensure that VOC-impacted groundwater migrated into the bioactive zone and was captured by the monitoring wells (Table P.1.1). At this flow rate, the residence time for groundwater between DHT-1 and DHT-2 was approximately 14 days (7.15 cm/day pore water velocity). Extracted water was discharged through the treatment system to the unnamed stream east of the site. After 62 days (76 days following bioaugmentation), the extraction rate was reduced to 300 mL/min to provide a longer residence time of 21 days between DHT-1 and DHT-2 (4.76 cm/day pore water velocity).

During Step 3, 2 pulses of lactate and KB-1 Primer® were introduced into DHT-1 to maintain conditions suitable to biotransformation of TCE to ethene. The first pulse of 75 L of 13.1 mM lactate and 0.85 g/L KB-1 Primer® was injected at 3.5 mL/min over the course of 14 days beginning 16 days after bioaugmentation. The second pulse was also 75 L, containing 37 mM

lactate and 3.4 g/L KB-1 Primer® injected at 2.8 mL/min over the course of 23 days beginning 48 days after bioaugmentation. The lactate concentrations were selected to maintain a concentration of at least 5 mM lactate in the groundwater flowing through the injection well.

During Step 3, groundwater samples were collected periodically (1-2 times per month) from CMT-6 (upgradient of bioactive zone), DHT-1 (bioactive zone), and DHT-2 (bioactive zone), and from at least three levels in CMT-1 (downgradient of the bioactive zone). Samples from CMT-6, DHT-1, and DHT-2 were collected using the modified low-flow sampling protocol described in Section II.3.2.2 above; samples from CMT-1 were collected at sampling ports in the treatment system. Groundwater samples were analyzed for chlorinated ethenes, ethene, and VFAs using the methods described in Section II.2.2 with additional samples collected monthly for biological analysis.

IV.2. Pilot (Downhole Treatability) Test Results (Task III.1 and III.2)

The following subsections contain the results of the Commerce Street pilot test including the bromide tracer results, field parameter and VFA results, chlorinated ethene and ethene results, and microbial abundance.

IV.2.1. Pilot Test Bromide Tracer

At the inception of the pilot test, bromide injected into DHT-1 was detected in DHT-2 approximately 9 days after beginning the injection, peaking after 11 days (Figure P.2.1). The pulse was injected over the course of 4 days indicating a residence time of approximately 7 days between DHT-1 and DHT-2. The successful detection of bromide in DHT-2 indicated good hydraulic connectivity between the wells.

IV.2.2. Pilot Test Field Parameters and VFAs

Prior to beginning injections of lactate and KB-1® primer, the field parameters measured in pilot test wells DHT-1 and DHT-2 were comparable to those in the CMT-wells. ORP was -110.8 and -138.7 mv in DHT-1 and DHT-2 respectively and pH was 7.2 and 7.4 (Appendix B.9). Although these conditions are suitable for bioremediation, the addition of KB-1® primer reduces ORP and maintains a neutral pH as microbial reductive dechlorination is stimulated by the addition of lactate. At the end of the 21-day recirculation phase (during which lactate and KB-1® primer were introduced into DHT-1), the ORP in DHT-1 and DHT-2 was reduced to -330.0 and -225.2 mv, respectively, while the pH was slightly reduced to 6.8 and 6.9. ORP and pH remained at their target concentrations throughout the pilot test, although pH decreased to a low of 6.55 in DHT-2 as *cis*-DCE was dechlorinated. Beginning in October 2017, high dissolved oxygen readings (>10 mg/L) were recorded. As a negative ORP value was also recorded at these times, it is impossible for the dissolved oxygen concentration to be as high as the measurements recorded. The water quality meter's dissolved oxygen probe was likely malfunctioning so dissolved oxygen values were no longer recorded.
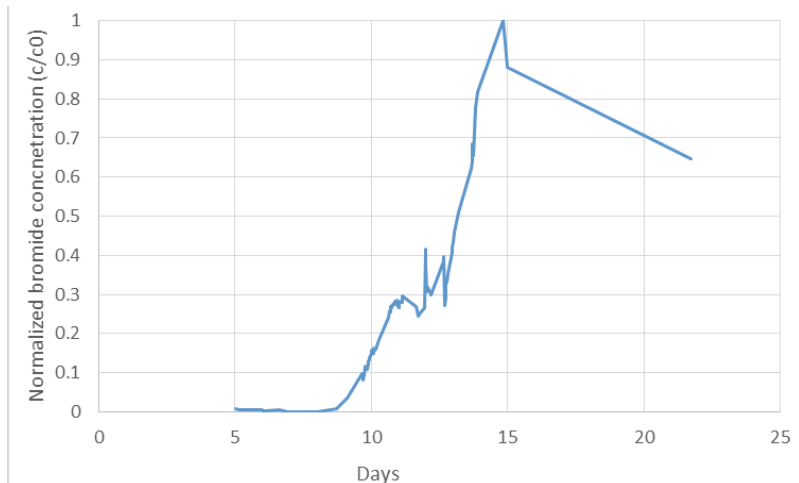
Figure P.2.1. Bromide breakthrough curve in downgradient well DHT-2.

At the end of recirculation, VFA analysis of samples collected from DHT-1 and DHT-2 contained lactate, acetate, and propionate with a total VFA concentration of 12.8 mM in the injection well and 6.0 mM in downgradient well DHT-2 as shown on Figure P.2.2. During subsequent lactate pulses, lactate and acetate were measured in the injection well while only acetate and propionate were measured downgradient. This mixture of acetate and propionate (lactate fermentation products) indicated an active microbial community and distribution of electron donor throughout the pilot test area. In well DHT-2, VFA concentrations decreased after each pulse but remained at concentrations above 0.28 mM total VFAs in all samples collected, indicating sufficient mixing of VFAs in the pilot test area to maintain conditions suitable for microbial reductive dechlorination.
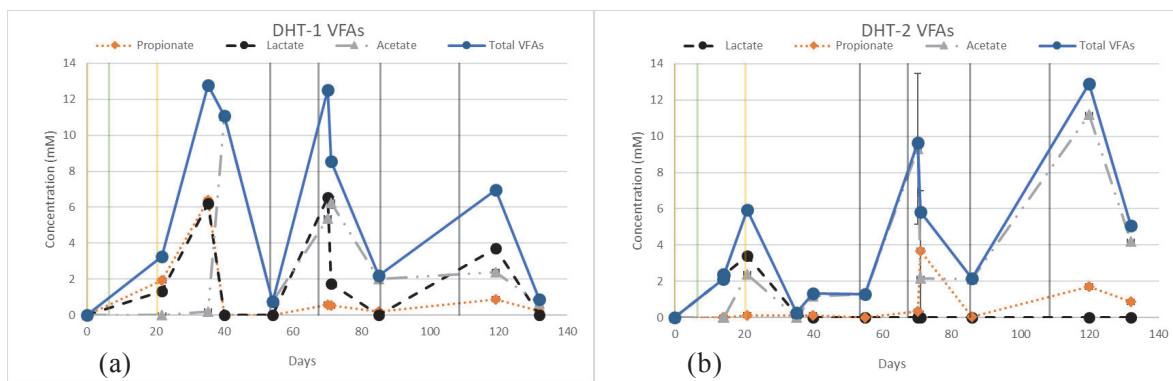
Figure P.2.2. VFA concentrations in injection well DHT-1 and downgradient well DHT-2 during pilot test. Vertical lines in each panel represent, from left to right: 1. Beginning of recirculation with lactate; 2. Bioaugmentation 3. End of recirculation; 4. Beginning of lactate pulse; 5. End of lactate pulse; 6. Beginning of lactate pulse; and 7. End of lactate pulse.

IV.2.3. Pilot Test Contaminant Concentrations

Prior to beginning the pilot test, *cis*-DCE was the only chlorinated ethene detected in the pilot test area with a concentration of 0.14 mM upgradient of the pilot test in well CMT-1 depth 2 and 0.11 mM in DHT-2, the downgradient pilot test well monitored throughout the experiment. Over the course of the pilot test, the *cis*-DCE concentration upgradient (CMT-6) remained steady but slightly higher than the initial sample, averaging 0.17 ($\pm$0.013) mM. Downgradient of the pilot test, VC and ethene were first detected 14 days after bioaugmentation, the residence time between DHT-1 and DHT-2 during this phase, reaching concentrations of 0.015 mM VC and 0.006 mM

ethene after 33.5 days. After an additional 15 days, the VC and ethene concentrations remained nearly unchanged (0.021 and 0.005 mM, respectively). Because groundwater quality parameters, including ORP and pH remained stable, the likely explanation for the lack of continued dechlorination was decreasing electron donor availability. This conclusion is supported by VFA sample results showing low levels of VFAs in DHT-2 14 days after ending the lactate recirculation phase.

After the first lactate pulse, VC and ethene concentrations continued to increase reaching concentrations of 0.046 and 0.017 mM, respectively, 79.4 days after bioaugmentation with the *cis*-DCE concentration decreasing slightly from a peak of 0.15 mM to 0.13mM. In order to assess the effect of residence time on the extent of dechlorination, 75 days following bioaugmentation and coinciding with the beginning of the second lactate pulse, the extraction rate in DHT-1 was reduced to increase groundwater residence time in the pilot test area from 14 to 21 days (4.8 cm/day pore water velocity). The maximum ethene concentration of 0.10 mM observed during the pilot test occurred 113.3 days following bioaugmentation (38 days after reducing the flow rate and 5 days after the end of the second lactate pulse) while the VC concentration remained steady at 0.04 mM and the *cis*-DCE concentration decreased to 0.053 mM. In the final samples collected 12 days later, the ethene concentration in DHT-2 began to decrease slightly while VC and *cis*-DCE concentrations increased, once again indicating a decrease in electron donor availability.
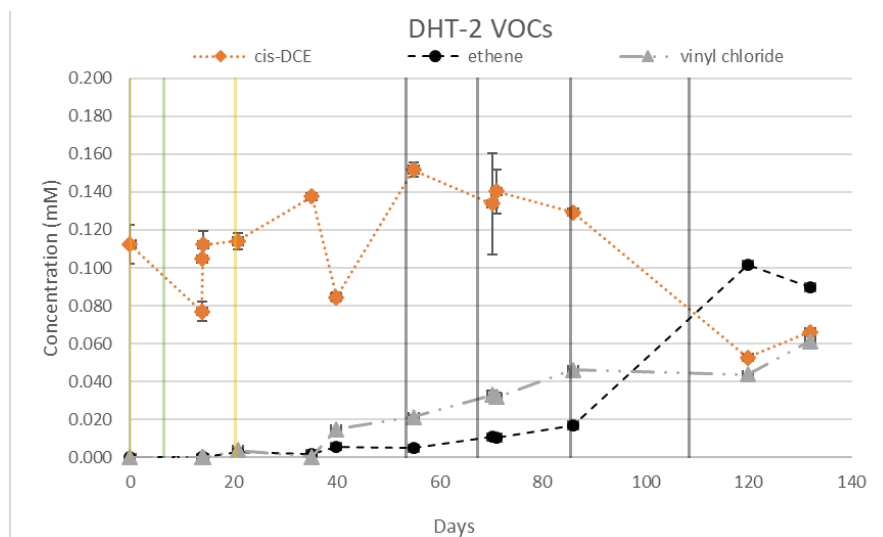
Figure P.2.3. Chlorinated ethene and ethene concentrations in DHT-2, downgradient of injection well. Vertical lines represent, from left to right: 1. Beginning of recirculation with lactate; 2. Bioaugmentation 3. End of recirculation; 4. Beginning of lactate pulse; 5. End of lactate pulse; 6. Beginning of lactate pulse; and 7. End of lactate pulse.

By reducing the extraction rate to increase residence time by 50%, the proportion of ethene in the downgradient well increased from approximately 5% of total ethenes to 46% while the proportion of *cis*-DCE declined from 79% to 28%, demonstrating the importance of maintaining sufficient residence time to achieve complete dechlorination of TCE to ethene.

IV.2.4. Pilot Test Microbial Abundance

Total *Dhc* abundance, measured in samples collected from wells DHT-1 and DHT-2 during the pilot test, increased from 6.2×10^4 and 4.9×10^4 16S rRNA gene copies/ L, respectively prior to bioaugmentation to 1.8×10^8 and 2.7×10^6 16S rRNA gene copies/ L at the end of the recirculation phase (Figure P.2.4). After an additional 32 days, *Dhc* abundance in DHT-1 and

DHT-2 were nearly identical at 5.0×10^8 16S rRNA gene copies/ L. The *Dhc* abundance remained constant until the flow rate was reduced, after which it continued to increase to a maximum abundance of 1.8×10^{10} and 1.6×10^{10} 16S rRNA gene copies/ L in samples collected from DHT-1 and DHT-2, respectively.
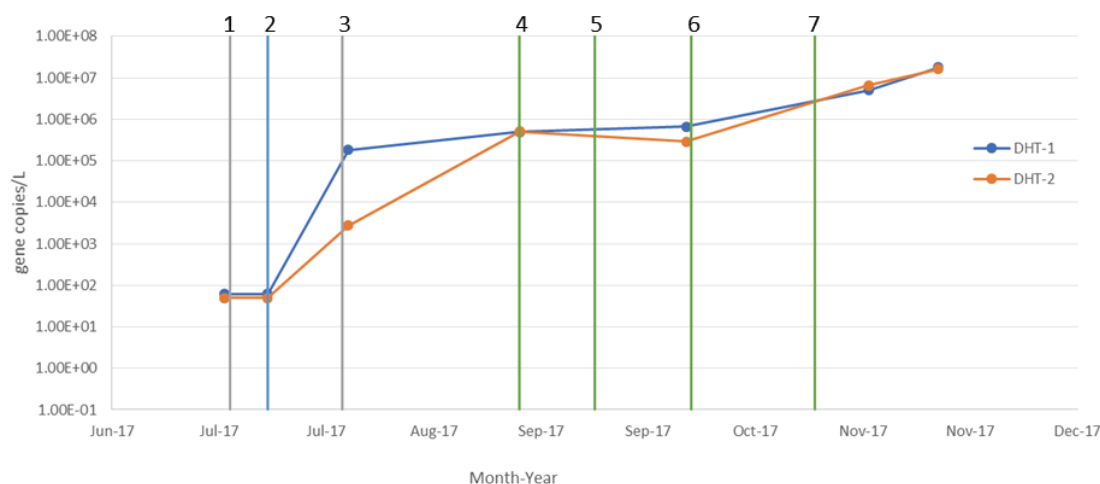
Figure P.2.4. Dhc abundance during pilot test in injection well DHT-1 and downgradient well DHT-2. Vertical lines represent, from left to right: 1. Beginning of recirculation with lactate; 2. Bioaugmentation 3. End of recirculation; 4. Beginning of lactate pulse; 5. End of lactate pulse; 6. Beginning of lactate pulse; and 7. End of lactate pulse.

Bioaugmentation with KB-1® successfully provided a large, viable *Dhc* population capable of transforming *cis*-DCE to ethene over the duration of the pilot test as seen in the chlorinated ethene and ethene results (Figure P.2.3). The lactate pulses were rapidly fermented (Figure P.2.2.) and provided a growth substrate to increase the *Dhc* population (Figure P.2.4) although growth stalled when the residence time of lactate in the pilot test area was insufficient to increase the degree of *cis*-DCE dechlorination. Reducing the pumping rate in CMT-1 increased the residence time of contaminants and amendments in the region between DHT-1 and DHT-2, increasing the extent of transformation of *cis*-DCE to ethene and allowing the *Dhc* population to continue to increase in abundance.

IV.3. Pilot (downhole treatability) Test Modeling Results

The laboratory-calibrated transport model was used to simulate the post-bio-recirculation portion of the field-scale biotransformation study. Recall that the DHT comprised a bio-recirculation phase and a long-term monitoring phase. The first phase was designed to create the active treatment zone. The latter one was of main interest and selected for the simulation study.

The flow field used in the transport model with a dimension of 12 m (Y) × 9.5 m (X) ×13 m (Z) was extracted from the site flow model simulated by Visual MODFLOW Flex (Figure P.3.1). Table P.3.1 shows the estimated hydraulic conductivities used in the flow model. Based upon the very small water table slope in the selected treatment zone, the influence of the natural groundwater gradient on contaminant transport was considered to be negligible. Groundwater flow during this phase of the DHT was driven by pumping in the downgradient CMT 1 well. Based on the knowledge of groundwater flow, concentration data of VOCs and lactate (Table P.3.2), and preliminary mathematical modeling, an active treatment zone with uniform initial cis-DCE (0.18 mM) and lactate (1.1 mM) concentrations was established. A baseline concentration of 0.01 mM was assigned to the other chemical components. Based on measurements from an upgradient CMT

194

6 well, a constant source of 0.165 mM cis-DCE was introduced into the domain though simulation. The model, parametrized with temperature-adjusted laboratory calibrated $k_{max,i}$ rates (Table P.3.3), was used to explore the transferability and applicability of the laboratory-scale parameters to a field scale system, as the size of the treatment zone and the aquifer cell are comparable.

Here, numerical simulation of the field-scale biotransformation was conducted for the last phase of the DHT, during which a slower flow/ longer residence time was imposed (Table P.1.1). Results indicate that observed transformation rates were not consistent with temperature-adjusted batch-estimated parameters (Figure P.3.2). Predicted ethene concentrations in DHT-2 were substantially higher than those observed in the field test, which is likely attributed to the upscaling effect on laboratory measured local rate parameters. While the field model used coarser spatial resolution and average soil properties for the numerical grid blocks, the aquifer cell (section III.3.2) was modeled with more detailed heterogeneities and fine grid blocks. Specifically, the variation of hydraulic conductivities differs: with a range of 0.28-0.36 m/day for the treated depth (two layers, 2 ft) in the field model; with a range of 0.1-2.7 m/day for the active zone (203 layers, 1.3 ft) in the aquifer cell. As have shown in the aquifer cell experiments (section III.3.2), transformation rates were influenced by the local residence time. The presence of high permeable layers in the aquifer cell reduced the transformation of cis-DCE to ethene due to shorter residence time (2.9 days, 10.3 days for the whole cell). The modeling results showed that the "effective" transformation rates might be influenced by heterogeneity of soil properties, and further suggested the need to consider the heterogeneous effect and upscaling when applying laboratory biodegradation results to interpret field-scale remediation performance of biotransformation.
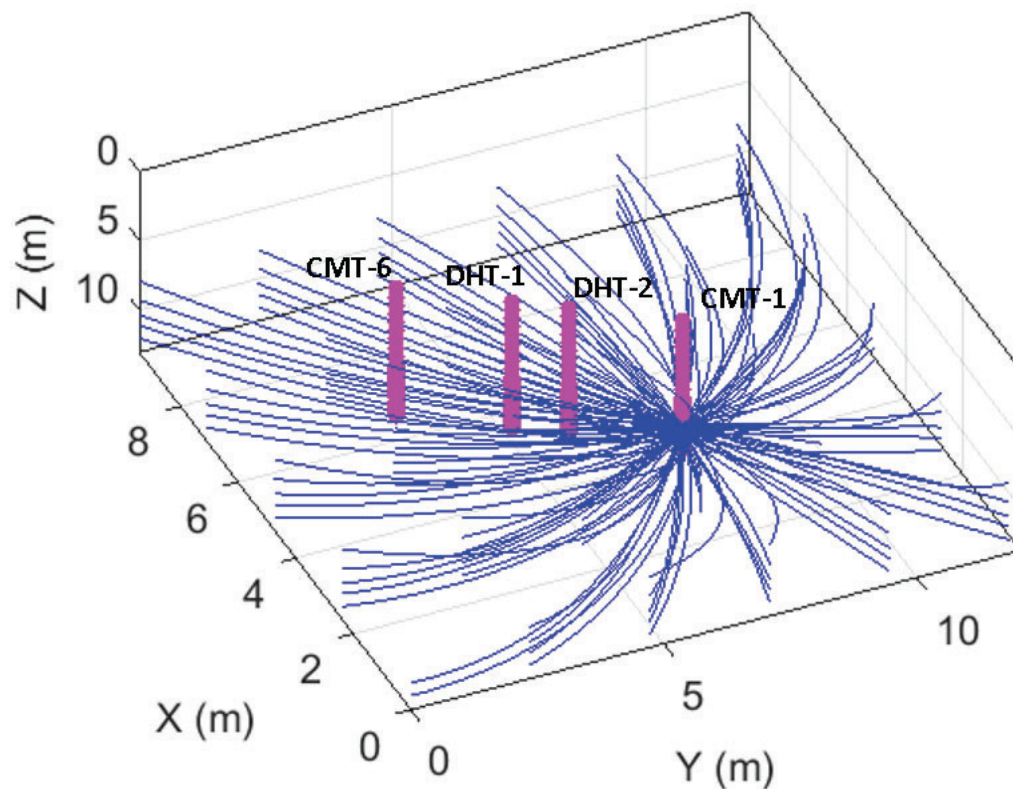
Figure P.3.1. Pumping at wells downgradient of the treatment zone after the recirculation phase.

Table P.3.1. Hydraulic conductivities estimated for field. Values are bolded for the depth of DHT 1 and 2.

Depth bgs (ft)	Hydraulic conductivity (m/d)
0--10	3.4471
10--12	5.6667
12--14	7.5503
14-16	4.4221
16-18	1.1475
18-20	1.2263
20-22	1.2239
22-24	1.0420
24-26	2.1358
26-28	0.4982
28-28.5	0.6869
28.5-29	0.6869
29-29.5	0.6869
29.5-30	0.6869
30-30.5	0.8076
30.5-31	0.8076
31-31.5	0.8076
31.5-32	0.3917
32-32.5	0.3917
32.5-33	0.4030
33-33.5	**0.3621**
33.5-34	**0.3621**
34-34.5	**0.2836**
34.5-35	**0.2836**
35-35.5	0.2288
35.5-36	0.2285
36-36.5	0.2019
36.5-37	0.2019
37-37.5	0.2313
37.5-38	0.2313
38-38.5	0.2313
38.5-39	0.2313
39-39.5	0.2313
39.5-40	0.2313
40-bottom	0.1310

Table P.3.2. Initial concentrations (mM) measured in the wells.

Component	CMT-6	DHT-1	DHT-2	CMT-1
TCE	5.2E-02	0.0E+00	0.0E+00	0.0E+00
cis-DCE	1.5E-01	1.6E-01	1.3E-01	2.9E-01
VC	0.0E+00	6.3E-03	4.6E-02	9.6E-04
Ethene	4.0E-03	5.7E-03	1.7E-02	2.2E-03
Lactate	0.0E+00	2.2E+00	2.2E+00	4.2E-02

Table P.3.3. Rate parameters used in the Monod kinetics model for field simulations.

Parameter	Microcosm (20-23°C)	Field[a] (17°C)
$k_{max,i}$ (μmol/(mg cell*d))		
TCE	330	223
Cis-DCE	80	53
VC	210	171
Lactate	60	47

[a] Estimated based on studies by Friis et al., 2007.
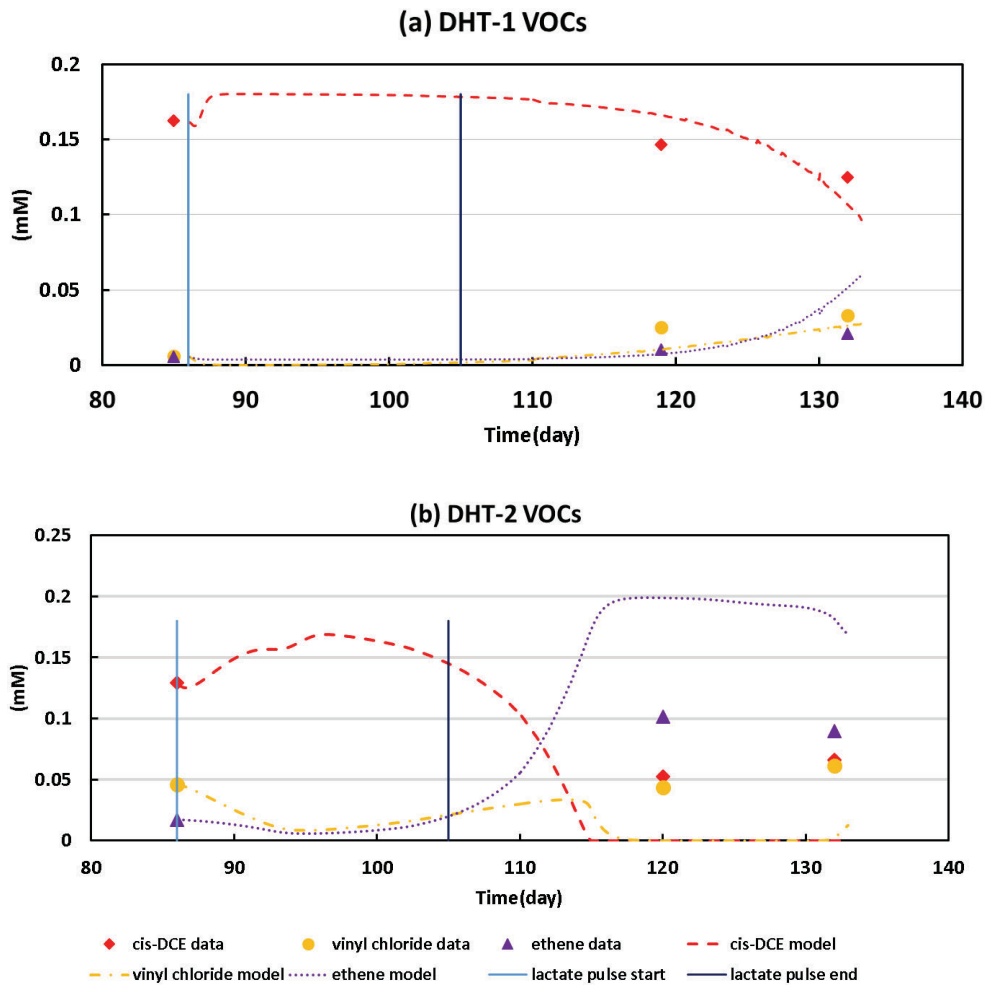
Figure P.3.2. Comparison of field-measured and model simulated results for chlorinated ethenes and ethene in DHT-1 and DHT-2.

V. Conclusions and Implications for Future Research / Implementation

Sections III and IV of this report detail the results of research conducted to develop and demonstrate a remediation design and performance protocol that couples characterization of the contaminant source with down-hole treatability testing and mathematical modeling to efficiently assess the suitability of a remediation technology to estimate remedial performance (e.g., mass removal/destruction) and the uncertainty associated with such predictions. It should be noted that, although the mathematical tools developed in this research were applied herein to *in situ* reductive dechlorination scenarios, these models and their associated implementation protocols are equally applicable to a range of remedial technologies (e.g., *in situ* oxidation, natural attenuation) for which successful application may be hindered by heterogeneous mass distributions.

Appendix VII.A presents a straightforward framework for implementation of the mathematical models developed here for near source site characterization and plume response prediction. The framework couples the 2D BRAINS model, described in sections II.7 and III.6 of this report, with an existing upscaled mass transfer model previously developed under SERDP sponsorship (Christ et al., 2010). The trained BRAINS model is used to generate a set of 2D representations of contaminant mass distributions along a plume centerline. These representations are then used to quantify effective, or upscaled, source characterization metrics along with estimations of their uncertainty, which can be employed in the screening model to forecast interactions between the source zone and long-term plume behavior, potentially facilitating adaptive site management (ASM).

The modeling framework presented in Figure A.1.1 represents the work flow for site characterization and screening-level down gradient flux assessment. Here, once a DNAPL source zone site has been identified, available data on the site geology/stratigraphy are collected and matched to a representative site subsurface permeability model. The permeability models are then linked to a library of machine learning characterization tools (i.e. BRAINS library). The research summarized in Sections II.7 and III.6 demonstrated both the feasibility and methodology for the development of the trained BRAINS model. If a characterization library that is consistent with the subject site is not available, the methodology developed and presented in Sections II.7 and III.6 could be implemented to develop a site-specific characterization tool. Such an exercise, however, would be simulation intensive and likely require additional site data collection.

After a site-matched characterization tool is obtained, site managers employ BRAINS, along with measured borehole data to estimate effective source zone metrics. It is important to note that this procedure requires only the field-measured borehole data (permeability, saturation, sorption and aqueous concentration) as inputs, as well as some geostatistical characteristics of the subsurface domain. The borehole contaminant mass data should be obtained from the vicinity of the plume centerline. This requirement arises from the fact that the BRAINS model was developed and validated in 2D in this research. The requirement could be relaxed in the future by extending and training the BRAINS model in 3D.

The framework developed and presented in this research is applicable to bench-, pilot-, and field-scale scenarios that would generally be modeled using a traditional advection-dispersion-reaction equation. Similar to the case study presented in Appendix VII.A, it is expected that this framework will provide a reasonable order-of-magnitude flux-averaged concentration estimate by bracketing the range of mass recovery behavior for most realistic source zone scenarios that are comprised of a combination of NAPL pools and ganglia regions. ESTCP-supported research may provide an avenue for extending the framework to a wider array of sites, and for determining framework limitations that may be encountered in the field.

Beyond this framework, high level conclusions associated with each phase of the research (as presented in Figure B.1.1) are presented below.

V.1. Phase I Conclusions

Phase I research focused on the development and demonstration of new mathematical characterization tools that use borehole observations of contaminant mass and porous medium texture/sorption properties to estimate the spatial distribution of contaminant mass within the source zone, averaged metrics (e.g., average saturation, pool fraction, total mass). and their associated uncertainties. Here, the specific objective was to develop a protocol and software tools that employ measured field data to produce realizations of a real (heterogeneous) subsurface source zone that capture the features controlling source longevity and remedial performance. The developed model, however, could be further optimized to reduce the errors observed in NAPL saturation reconstruction, either by adopting more advanced machine learning methods such as *generative adversarial networks* (GANs) (Goodfellow et al., 2014; Sun, 2018) or application of permeability-based features that carry more information about the permeability of surrounding and neighboring pixels. Future work should focus on exploring the performance of the trained DRF model under different geologic environments and across different scales of heterogeneity. It is anticipated that, while the developed features and model structure are robust, the DRF model itself will need to be retrained for applications to different depositional environments. Thus, the present study should be viewed as a proof of principle for the application of this modeling approach and as the first step in generating a 3D characterization tool (i.e. library of models) that can be applied over a wide range of conditions observed at contaminated sites.

- **A discriminative random field (DRF) model (BRAINS) was developed and implemented for contaminant source zone characterization and uncertainty quantification.** The DRF model is completely characterized by a small collection of parameters (w and v vectors). These parameters are determined within the model through a 'training' process, employing a set of source zone spill data specific to the selected DNAPL contaminant and geologic environment. Once the DRF parameters are determined, the model is used to generate realizations of the DNAPL saturation and aqueous phase concentration using off-the-shelf Metropolis sampling methods. This methodology is far superior to Monte Carlo approaches, which require extensive flow and transport simulations to generate a similar set of realizations and cannot easily account for measured data. .

- **Ensemble averages over realizations of the DRF model represent the expected values for concentration and saturation fields, while the variances provide a quantifiable measure of the uncertainty associated with permeability and contaminant source zone.** These uncertainty measurements were used in Phase III to identify optimal locations for further borehole sampling.

- Model performance was assessed by comparing estimated and 'true' metrics for contaminant mass distributions in a structured heterogeneous unconsolidated depositional aquifer environment. **The trained DRF model produced realistic saturation and concentration fields, conditioned to borehole data for a range of NAPL spill scenarios (release rates, spill ages, pool fractions). Comparison with a traditional kriging approach clearly demonstrated the superiority of BRAINS in reconstructing DNAPL saturation distributions and associated DNAPL architecture metrics.**

V.2. Phase II Conclusions

Phase II research focused on batch and bench-scale laboratory testing, and upscaled mathematical

model development to support the design and implementation of a field remediation strategy. The performance of microbial reductive dechlorination was evaluated in heterogeneous aquifer cells, representative of field conditions. Collected microcosm and aquifer cell data were employed, in conjunction with an enhanced transport model, to assess the suitability of batch-measured parameters and transformation rates for larger scale performance predictions. Mathematical modeling was also used to estimate effective (upscaled) mass transfer rates for sorbed and sequestered mass, as well as bioenhanced dissolution, and to elucidate the processes controlling mass persistence and plume evolution under realistic conditions at the field scale.

- **A robust numerical model incorporating adsorption of contaminants to soil, gas-water partitioning, and septa losses was created and implemented to simulate microbial reductive dechlorination in batch reactor and microcosm experiments.** The model was successfully used to fit media- and culture-specific substrate utilization rates and yield coefficients.

- **An industry-standard groundwater transport simulator, MT3DMS, was adapted in this research to incorporate multi-order Monod kinetics coupled with a microbial growth model to account for biotransformation of multiple components by multiple microbial populations** under isothermal conditions. A Monod kinetics subroutine was added to the simulator and stepwise/accumulative mass budget subroutines for six chemical components: TCE, cis-DCE, VC, ethene, lactate and H_2. This model was used to simulate all aquifer cell experiments, as well as the down hole test (Phase III).

- **Bioenhanced desorption and back diffusion of chlorinated solvents play an important role in mass release in heterogeneous formations.** For the examined experimental conditions, the magnitude of this enhancement was observed to vary spatially and temporally (range of 6-55%), with the largest enhancement measured at interfaces with fine-textured, highly sorptive media. These results suggest that bioenhanced desorption/back diffusion can significantly reduce plume persistence and remedial cleanup time frames. The experimental observations also point to the need for upscaled mass transfer parameters that can account for local scale heterogeneity.

- **Temporal and spatial population shifts in the predominant strain of *Dhc* are observed with changes in electron acceptor abundance.** These observations demonstrate the importance of maintaining a robust dechlorinating community harboring multiple RDase genes. When the necessary genes are present, the microbial population is able to adapt to changes in electron acceptor availability associated with varying up gradient concentrations or the back diffusion of chlorinated ethenes from low permeability and highly sorptive materials. Thus, even if the locations of sequestered mass cannot be explicitly identified, due to the incomplete characterization typical of field applications, these population shifts will allow efficient transformation of chlorinated solvents to ethene over the course of a bioremediation application.

- *Dhc* **cells are capable of penetrating low permeability porous media, including clays.**

- **Multi-dimensional models with uniform properties or 1-D models, employing microcosm-measured dechlorination rates, were unable to accurately predict aquifer cell performance.** However, **observed aquifer cell microbial transformation rates *were* consistent with microcosm-fitted values, when permeability variations were incorporated** in the model.

- **Models must incorporate heterogeneity to make accurate predictions of dechlorination** Heterogeneity in material properties has a substantial influence on the rate and extent of dechlorination of TCE to ethene. The extent of ethene formation is highly dependent on hydraulic residence time (controlled by local permeability) and the availability of electron donor (controlled by sorption capacity of and diffusion from low permeability layers).

- **Competitive inhibition was found to be of little significance in heterogeneous-packed formations,** attributed to microenvironments in the aquifer cell and differences in soil/water ratios between microcosm and aquifer cell experiments.

- **Accurate representation of sorption processes (i.e., extent, rate limitations, and nonlinearity) in transport models is crucial to the accurate prediction of plume longevity,** particularly for the prediction of post-DNAPL dissolution longevity; **(de)sorption processes were observed to dominate the rate of mass release (back diffusion) to transmissive zones, following DNAPL dissolution.** Sorption was shown to have little influence on the rate of DNAPL dissolution.

- Simulation results also demonstrated a strong influence of source zone complexity (e.g., heterogeneity of the permeability field, DNAPL architecture, process coupling) on source zone mass transport and near-source plume persistence. Although neat phase DNAPL is not typically detected at most sites, this work suggests that **trace amounts of DNAPL source mass present in the field can be as influential as sequestered sorbed and dissolved mass in controlling plume tailing, and that these small quantities of DNAPL mass can be difficult to differentiate from the diffused and sorbed mass without exhaustive characterization.**

- Due to the presence of heterogeneity, different regimes exist in which local mass release behavior is governed by different processes (i.e., dissolution versus back diffusion). **Simplified source loading and back diffusion models cannot capture the interplay between different transport processes at the local scale that are crucial to the determination of down-gradient concentrations and plume longevity at heterogeneous sites.**

- **An upscaled model was developed and parameterized to describe effective mass transfer (desorption) rates in three dimensional heterogeneous systems.** This Multi-Rate Mass Transfer (MRMT) model, with two constant-in-time first-order rates, was shown to successfully reproduce fine-scale breakthrough curves. Correlation expressions were developed and implemented for calculation of effective model parameters from general geometric, flow, and sorption properties. The model was shown to be robust with respect to initial and boundary conditions.

- **A screening level model was developed and implemented to estimate bioenhancement of DNAPL dissolution.** Nomographs were presented to facilitate graphical estimation of bioenhancement factor expressions for zero-order, first-order, and full Monod transformation kinetics as a function of the Péclet and Damköhler Numbers. These nomographs can be useful in the analysis and design of remedial systems. Results suggest that bioenhancement factor predictions are sensitive to the estimated value of biomass concentration and that uncertainty in this parameter must be considered during the design stage.

V.3. Phase III Conclusions

In this phase, a downhole treatability test was conducted at the selected field site (Commerce Street

Superfund Site, Williston, VT) to estimate effective *in situ* transformation/reaction rates and to support the design and assessment of site remediation strategies. A mathematical model, refined and validated in Phase II, was employed to estimate effective field transformation rates. Estimated rates were compared to aquifer cell-measured rates to shed light on the processes controlling remediation at the field scale. A comprehensive transport/adjoint sensitivity model and associated protocol for its application were also developed and demonstrated in this phase to quantify field-scale transport model prediction uncertainty (based upon mathematical characterization tools developed in Phase I) and to identify optimal borehole sampling locations for follow-on site characterization work to facilitate the more accurate prediction of down gradient mass flux at future times.

- **In this work, a first-order second-moment (FOSM) uncertainty analysis modeling framework was developed and implemented to estimate variance in predicted flux averaged concentration (FAC) along a transect down gradient of a DNAPL source zone.** The method honors borehole observations and enables consideration of the coupling among aquifer heterogeneity, flow irregularity, and source zone mass distribution (morphology). In the framework, an adjoint state method was adopted to evaluate the sensitivity matrix (representing the sensitivities of down-gradient FAC to incremental changes in initial mass and permeability distributions). Results show that the FOSM method is a computationally efficient means to provide reliable conditional means of FAC and its corresponding variances.

- **Application of the FOSM method to numerically generated, field-scale, source zone scenarios revealed that hydraulic conductivity variations and DNAPL saturation distributions tend to dominate FAC predictions.**

- **The FOSM model was coupled with data worth assessments and implemented in the modeling framework to guide acquisition of additional site data.** Model applications revealed that selected borehole locations varied with the prediction time window, tending to move up gradient as later prediction times were targeted. The selected locations for additional borehole measurements were also generally associated with low hydraulic conductivity regions and/or locations of high DNAPL saturation pools. A comparison with alternative borehole sampling approaches verified the effectiveness and superiority of the FOSM method for identifying additional borehole sampling locations to improve FAC predictions.

- **Down Hole Test results were consistent with trends observed in the aquifer cell experiment.** Bioaugmentation with KB-1® successfully provided a large, viable *Dhc* population capable of transforming *cis*-DCE to ethene over the duration of the pilot test. Lactate pulses were rapidly fermented and provided a growth substrate to increase the *Dhc* population. Growth stalled when the residence time in the pilot test area was insufficient to increase the degree of *cis*-DCE dechlorination. By reducing the pumping rate, the residence time increased, increasing the extent of transformation of *cis*-DCE to ethene and allowing the *Dhc* population to continue to increase in abundance.

- **Mathematical modeling results indicate that observed transformation rates were not consistent with temperature-adjusted batch-estimated and aquifer-cell validated parameters. Predicted ethane concentrations were substantially higher than those observed in the field test.** This failure to predict DHT performance is likely due to inadequate model resolution of formation heterogeneity in the treatment zone. While the field model used coarser spatial resolution and average soil properties for the numerical grid blocks, the aquifer cell was modeled with more detailed heterogeneities and fine grid blocks. Transformation rates

were likely strongly influenced by the presence of low permeability layers in the treatment zone, which inhibited mixing.

VI. Literature Cited

Abriola, L. M. (2005). "Guest Editorial: Contaminant Source Zones: Remediation or Perpetual Stewardship?" *Environmental Health Perspectives*, 113(7), A438–A439.

Abriola, L. M., Christ, J. A., Pennell, K. D., and Ramsburg, C. A. (2012). "Source Remediation Challenges." *Delivery and Mixing in the Subsurface*, SERDP ESTCP Environmental Remediation Technology, Springer, New York, NY, 239–276.

Abriola, L. M., Rathfelder, K., Maiza, M., and Yadav, S. (1992). *VALOR code version 1.0: A PC code for simulating immiscible contaminant transport in subsurface systems. Final report*. Electric Power Research Inst., Palo Alto, CA (United States); Michigan Univ., Ann Arbor, MI (United States). Dept. of Civil and Environmental Engineering.

Acar, Ö., Klammler, H., Hatfield, K., Newman, M. A., Annable, M. D., Cho, J., Parker, B. L., Cherry, J. A., Pehme, P., Quinn, P., and Kroeker, R. (2013). "A stochastic model for estimating groundwater and contaminant discharges from fractured rock passive flux meter measurements." *Water Resources Research*, 49(3), 1277–1291.

Adams, E. E., and Gelhar, L. W. (1992). "Field study of dispersion in a heterogeneous aquifer: 2. Spatial moments analysis." *Water Resources Research*, 28(12), 3293–3307.

Adamson, D. T., Lyon, D. Y., and Hughes, J. B. (2004). "Flux and product distribution during biological treatment of tetrachloroethene dense non-aqueous-phase liquid." *Environmental Science & Technology*, 38(7), 2021–2028.

Adamson, D. T., McGuire, T. M., Newell, C. J., and Stroo, H. (2011). "Sustained treatment: Implications for treatment timescales associated with source-depletion technologies." *Remediation Journal*, 21(2), 27–50.

Adamson, D. T., and Newell, C. J. (2009). "Support of Source Zone Bioremediation through Endogenous Biomass Decay and Electron Donor Recycling." *Bioremediation Journal*, 13(1), 29–40.

Adrian, L., and Löffler, F. E. (Eds.). (2016). *Organohalide-Respiring Bacteria*. Springer-Verlag, Berlin Heidelberg.

Aksoy, A., and Culver, T. B. (2000). "Effect of Sorption Assumptions on Aquifer Remediation Designs." *Groundwater*, 38(2), 200–208.

Aksoy, A., and Culver, T. B. (2004). "Impacts of Physical and Chemical Heterogeneities on Aquifer Remediation Design." *Journal of Water Resources Planning and Management*, 130(4), 311–320.

Amos, B. K., Christ, J. A., Abriola, L. M., Pennell, K. D., and Löffler, F. E. (2007a). "Experimental Evaluation and Mathematical Modeling of Microbially Enhanced Tetrachloroethene (PCE) Dissolution." *Environmental Science & Technology*, 41(3), 963–970.

Amos, B. K., Daprato, R. C., Hughes, J. B., Pennell, K. D., and Löffler, F. E. (2007b). "Effects of the nonionic surfactant tween 80 on microbial reductive dechlorination of chlorinated ethenes." *Environmental Science and Technology*, 41(5), 1710–1716.

Amos, B. K., Suchomel, E. J., Pennell, K. D., and Löffler, F. E. (2008). "Microbial activity and distribution during enhanced contaminant dissolution from a NAPL source zone." *Water Research*, 42(12), 2963–2974.

Amos, B. K., Suchomel, E. J., Pennell, K. D., and Löffler, F. E. (2009). "Spatial and temporal distributions of Geobacter lovleyi and Dehalococcoides spp. during bioenhanced PCE-NAPL dissolution." *Environmental Science and Technology*, 43(6), 1977–1985.

Bagley, D. M. (1998). "Systematic Approach for Modeling Tetrachloroethene Biodegradation." *Journal of Environmental Engineering*, 124(11), 1076–1086.

Ball, W. P., Liu, C., Xia, G., and Young, D. F. (1997). "A diffusion-based interpretation of tetrachloroethene and trichloroethene concentration profiles in a groundwater aquitard." *Water Resources Research*, 33(12), 2741–2757.

de Barros, F. P. J., Ezzedine, S., and Rubin, Y. (2012). "Impact of hydrogeological data on measures of uncertainty, site characterization and environmental performance metrics." *Advances in Water Resources*, 36, 51–63.

de Barros, F. P. J., and Nowak, W. (2010). "On the link between contaminant source release conditions and plume prediction uncertainty." *Journal of Contaminant Hydrology*, 116(1–4), 24–34.

de Barros, F. P. J., and Rubin, Y. (2008). "A risk-driven approach for subsurface site characterization." *Water Resources Research*, Wiley-Blackwell, 44(1).

Basu, N. B., Rao, P. S. C., Poyer, I. C., Annable, M. D., and Hatfield, K. (2006). "Flux-based assessment at a manufacturing site contaminated with trichloroethylene." *Journal of Contaminant Hydrology*, 86(1–2), 105–127.

Bayer, P., Huggenberger, P., Renard, P., and Comunian, A. (2011). "Three-dimensional high resolution fluvio-glacial aquifer analog: Part 1: Field study." *Journal of Hydrology*, 405(1), 1–9.

Bear, J. (1988). *Dynamics of Fluids in Porous Media*. Dover Publications, New York.

Becker, J. G. (2006). "A modeling study and implications of competition between Dehalococcoides ethenogenes and other tetrachloroethene-respiring bacteria." *Environmental Science & Technology*, 40(14), 4473–4480.

Becker, J. G., and Seagren, E. A. (2009). "Modeling the Effects of Microbial Competition and Hydrodynamics on the Dissolution and Detoxification of Dense Nonaqueous Phase Liquid Contaminants." *Environmental Science & Technology*, 43(3), 870–877.

Brooks, R. H., and Corey, A. T. (1964). *Hydraulic Properties of Porous Media*. Hydrology papers, Colorado State University, Fort Collins, Colorado.

Brusseau, M. L., Jessup, R. E., and Rao, P. S. C. (1989). "Modeling the transport of solutes influenced by multiprocess nonequilibrium." *Water Resources Research*, 25(9), 1971–1988.

Burdine, N. T. (1953). "Relative Permeability Calculations From Pore Size Distribution Data." *Journal of Petroleum Technology*, 5(03), 71–78.

Cai, Z., Wilson, R. D., Cardiff, M. A., and Kitanidis, P. K. (2011). "Increasing Confidence in Mass Discharge Estimates Using Geostatistical Methods." *Ground Water*, 49(2), 197–208.

Cai, Z., Wilson, R. D., and Lerner, D. N. (2012). "Assessing TCE Source Bioremediation by Geostatistical Analysis of a Flux Fence." *Groundwater*, 50(6), 908–917.

Cápiro, N. L., Löffler, F. E., and Pennell, K. D. (2015). "Spatial and temporal dynamics of organohalide-respiring bacteria in a heterogeneous PCE-DNAPL source zone." *Journal of Contaminant Hydrology*, 182, 78–90.

Cápiro, N. L., Wang, Y., Hatt, J. K., Lebron, C., Pennell, K. D., and Löffler, F. E. (2014). "Distribution of organohalide-respiring bacteria between solid and aqueous phases." *Environmental Science and Technology*, 48(18), 10878–10887.

Carle, S. F. (1999). *T-PROGS: Transition Probability Geostatistical Software, version 2.1*. University of California, Davis.

Carle, S. F., and Fogg, G. E. (1996). "Transition probability-based indicator geostatistics." *Mathematical Geology*, 28(4), 453–476.

Carle, S. F., and Fogg, G. E. (1997). "Modeling Spatial Variability with One and Multidimensional Continuous-Lag Markov Chains." *Mathematical Geology*, 29(7), 891–918.

Carr, C. S., Garg, S., and Hughes, J. B. (2000). "Effect of Dechlorinating Bacteria on the Longevity and Composition of PCE-Containing Nonaqueous Phase Liquids under Equilibrium Dissolution Conditions." *Environmental Science & Technology*, 34(6), 1088–1094.

Carrera, J., Sánchez-Vila, X., Benet, I., Medina, A., Galarza, G., and Guimerà, J. (1998). "On matrix diffusion: formulations, solution methods and qualitative effects." *Hydrogeology Journal*, 6(1), 178–190.

Chambon, J. C., Bjerg, P. L., Scheutz, C., Baelum, J., Jakobsen, R., and Binning, P. J. (2013). "Review of reactive kinetic models describing reductive dechlorination of chlorinated ethenes in soil and groundwater." *Biotechnology and Bioengineering*, 110(1), 1–23.

Chambon, J. C., Broholm, M. M., Binning, P. J., and Bjerg, P. L. (2010). "Modeling multi-component transport and enhanced anaerobic dechlorination processes in a single fracture–clay matrix system." *Journal of Contaminant Hydrology*, 112(1–4), 77–90.

Chapman, S. W., and Parker, B. L. (2005). "Plume persistence due to aquitard back diffusion following dense nonaqueous phase liquid source removal or isolation." *Water Resources Research*, 41(12).

Chapman, S. W., Parker, B. L., Sale, T. C., and Doner, L. A. (2012). "Testing high resolution numerical models for analysis of contaminant storage and release from low permeability zones." *Journal of Contaminant Hydrology*, 136–137, 106–116.

Chaudhuri, A., and Sekhar, M. (2006). "Stochastic modeling of solute transport in 3-D heterogeneous porous media with random source condition." *Stochastic Environmental Research and Risk Assessment*, Springer-Verlag, 21(2), 159–173.

Chaudhuri, A., and Sekhar, M. (2008). "Modelling of solute transport in a mild heterogeneous porous medium using stochastic finite element method: Effects of random source conditions." *International Journal for Numerical Methods in Fluids*, Wiley-Blackwell, 56(5), 557–586.

Chen, L., Miller, G. A., and Kibbey, T. C. G. (2007). "Rapid pseudo-static measurement of hysteretic capillary pressure-saturation relationships in unconsolidated porous media." *Geotechnical Testing Journal*, 30(6), 474–483.

Chen, M., Abriola, L. M., Amos, B. K., Suchomel, E. J., Pennell, K. D., Löffler, F. E., and Christ, J. A. (2013). "Microbially enhanced dissolution and reductive dechlorination of PCE by a

mixed culture: Model validation and sensitivity analysis." *Journal of Contaminant Hydrology*, 151, 117–130.

Chen, X., Brooks, M. C., and Wood, A. L. (2014). "The uncertainty of mass discharge measurements using pumping methods under simplified conditions." *Journal of Contaminant Hydrology*, 156, 16–26.

Chen, X., and Jawitz, J. W. (2009). "Convergence of DNAPL Source Strength Functions with Site Age." *Environmental Science & Technology*, 43(24), 9374–9379.

Christ, J. A., and Abriola, L. M. (2007). "Modeling metabolic reductive dechlorination in dense non-aqueous phase liquid source-zones." *Advances in Water Resources*, Biological processes in porous media: From the pore scale to the field, 30(6–7), 1547–1561.

Christ, J. A., Lemke, L. D., and Abriola, L. M. (2005). "Comparison of two-dimensional and three-dimensional simulations of dense nonaqueous phase liquids (DNAPLs): Migration and entrapment in a nonuniform permeability field." *Water Resources Research*, 41(1).

Christ, J. A., Ramsburg, A. C., Pennell, K. D., and Abriola, L. M. (2006). "Estimating mass discharge from dense nonaqueous phase liquid source zones using upscaled mass transfer coefficients: An evaluation using multiphase numerical simulations." *Water Resources Research*, 42(11).

Christ, J. A., Ramsburg, A. C., Pennell, K. D., and Abriola, L. M. (2010). "Predicting DNAPL mass discharge from pool-dominated source zones." *Journal of contaminant hydrology*, 114(1–4), 18–34.

Chu, M., Kitanidis, P. K., and McCarty, P. L. (2003). "Effects of biomass accumulation on microbially enhanced dissolution of a PCE pool: a numerical simulation." *Journal of Contaminant Hydrology*, 65(1–2), 79–100.

Chu, M., Kitanidis, P. K., and McCarty, P. L. (2004). "Possible factors controlling the effectiveness of bioenhanced dissolution of non-aqueous phase tetrachloroethene." *Advances in Water Resources*, 27(6), 601–615.

Cirpka, O. A., Bürger, C. M., Nowak, W., and Finkel, M. (2004). "Uncertainty and data worth analysis for the hydraulic design of funnel-and-gate systems in heterogeneous aquifers." *Water Resources Research*, 40(11), 1–12.

Clapp, L. W., Semmens, M. J., Novak, P. J., and Hozalski, R. M. (2004). "Model for In Situ Perchloroethene Dechlorination via Membrane-Delivered Hydrogen." *Journal of Environmental Engineering*, 130(11), 1367–1381.

Cope, N., and Hughes, J. B. (2001). "Biologically-Enhanced Removal of PCE from NAPL Source Zones." *Environmental Science & Technology*, 35(10), 2014–2021.

Cupples, A. M., Spormann, A. M., and McCarty, P. L. (2004a). "Vinyl Chloride and *cis* -Dichloroethene Dechlorination Kinetics and Microorganism Growth under Substrate Limiting Conditions." *Environmental Science & Technology*, 38(4), 1102–1107.

Cupples, A. M., Spormann, A. M., and McCarty, P. L. (2004b). "Comparative evaluation of chloroethene dechlorination to ethene by Dehalococcoides-like microorganisms." *Environmental Science & Technology*, 38(18), 4768–4774.

Cwiertny, D. M., and Scherer, M. M. (2010). "Abiotic Processes Affecting the Remediation of Chlorinated Solvents." 69–108.

Da Silva, M. L. B., Daprato, R. C., Gomez, D. E., Hughes, J. B., Ward, C. H., and Alvarez, P. J. J. (2006). "Comparison of bioaugmentation and biostimulation for the enhancement of dense nonaqueous phase liquid source zone bioremediation." *Water Environment Research: A Research Publication of the Water Environment Federation*, 78(13), 2456–2465.

Dai, C., Xue, L., Zhang, D., and Guadagnini, A. (2016). "Data-worth analysis through probabilistic collocation-based Ensemble Kalman Filter." *Journal of Hydrology*, 540, 488–503.

Damgaard, I., Bjerg, P. L., Bælum, J., Scheutz, C., Hunkeler, D., Jacobsen, C. S., Tuxen, N., and Broholm, M. M. (2013a). "Identification of chlorinated solvents degradation zones in clay till by high resolution chemical, microbial and compound specific isotope analysis." *Journal of Contaminant Hydrology*, Elsevier B.V., 146, 37–50.

Damgaard, I., Bjerg, P. L., Jacobsen, C. S., Tsitonaki, A., Kerrn-Jespersen, H., and Broholm, M. M. (2013b). "Performance of Full-Scale Enhanced Reductive Dechlorination in Clay Till." *Ground Water Monitoring & Remediation*, 33(1), 48–61.

Das, B. M. (1997). "5 Hydrometer Analysis." *Soil Mechanics Laboratory Manual. 5th ed.*, Austin, 23–34.

Dausman, A. M., Doherty, J., Langevin, C. D., and Sukop, M. C. (2010). "Quantifying Data Worth Toward Reducing Predictive Uncertainty." *Ground Water*, 48(5), 729–740.

Dekker, T. J., and Abriola, L. M. (2000). "The influence of field-scale heterogeneity on the infiltration and entrapment of dense nonaqueous phase liquids in saturated formations." *Journal of Contaminant Hydrology*, 42(2), 187–218.

Delle Site, A. (2001). "Factors Affecting Sorption of Organic Compounds in Natural Sorbent/Water Systems and Sorption Coefficients for Selected Pollutants. A Review." *Journal of Physical and Chemical Reference Data*, 30(1), 187–439.

Delshad, M., Pope, G. A., and Sepehrnoori, K. (1996). "A compositional simulator for modeling surfactant enhanced aquifer remediation, 1 formulation." *Journal of Contaminant Hydrology*, 23(4), 303–327.

Dentz, M., Le Borgne, T., Englert, A., and Bijeljic, B. (2011). "Mixing, spreading and reaction in heterogeneous media: A brief review." *Journal of Contaminant Hydrology*, Reactive Transport in the Subsurface: Mixing, Spreading and Reaction in Heterogeneous Media, 120–121, 1–17.

Dettinger, M. D., and Wilson, J. L. (1981). "First order analysis of uncertainty in numerical models of groundwater flow part: 1. Mathematical development." *Water Resources Research*, 17(1), 149–161.

Deutsch, C. V., and Journel, A. G. (1998). *GSLIB : geostatistical software library and user's guide*. New York ; Oxford : Oxford University Press.

DiFilippo, E. L., and Brusseau, M. L. (2008). "Relationship between mass-flux reduction and source-zone mass removal: Analysis of field data." *Journal of Contaminant Hydrology*, 98(1–2), 22–35.

DiFilippo, E. L., and Brusseau, M. L. (2011). "Assessment of a simple function to evaluate the relationship between mass flux reduction and mass removal for organic-liquid contaminated source zones." *Journal of Contaminant Hydrology*, 123(3–4), 104–113.

Ding, D., Benson, D. A., Fernàndez-Garcia, D., Henri, C. V., Hyndman, D. W., Phanikumar, M. S., and Bolster, D. (2017). "Elimination of the Reaction Rate 'Scale Effect': Application of the Lagrangian Reactive Particle-Tracking Method to Simulate Mixing-Limited, Field-Scale Biodegradation at the Schoolcraft (MI, USA) Site: FIELD-SCALE REACTIVE PARTICLE TRACKING." *Water Resources Research*, 53(12), 10411–10432.

Dokou, Z., & Pinder, G. F. (2009). Optimal search strategy for the definition of a DNAPL source. *Journal of Hydrology*, *376*(3), 542–556. https://doi.org/10.1016/j.jhydrol.2009.07.062

Domenico, P. A., and Schwartz, F. W. (1997). *Physical and Chemical Hydrogeology*. Wiley, New York.

Driscoll, F. G. (1986). *Groundwater and Wells*. Johnson Screens, St. Paul, Minn.

Duhamel, M., and Edwards, E. A. (2006). "Microbial composition of chlorinated ethene-degrading cultures dominated by Dehalococcoides: Quantitative PCR of dechlorinating cultures." *FEMS Microbiology Ecology*, 58(3), 538–549.

Duhamel, M., and Edwards, E. A. (2007). "Growth and Yields of Dechlorinators, Acetogens, and Methanogens during Reductive Dechlorination of Chlorinated Ethenes and Dihaloelimination of 1,2-Dichloroethane." *Environmental Science & Technology*, 41(7), 2303–2310.

Duhamel, M., Mo, K., and Edwards, E. a. (2004). "Characterization of a Highly Enriched Dehalococcoides -Containing Culture That Grows on Vinyl Chloride and." *Applied Environmental Microbiology*, 70(9), 5538–5545.

Duhamel, M., Wehr, S. D., Yu, L., Rizvi, H., Seepersad, D., Dworatzek, S., Cox, E. E., and Edwards, E. a. (2002). "Comparison of anaerobic dechlorinating enrichment cultures maintained on tetrachloroethene, trichloroethene, cis-dichloroethene and vinyl chloride." *Water Research*, 36(17), 4193–4202.

Elfeki, A. M. M. (2006a). "Reducing concentration uncertainty using the coupled Markov chain approach." *Journal of Hydrology*, 317(1), 1–16.

Elfeki, A. M. M. (2006b). "Prediction of contaminant plumes (shapes, spatial moments and macrodispersion) in aquifers with insufficient geological information." *Journal of Hydraulic Research*, 44(6), 841–856.

Falta, R. W. (2008). "Methodology for Comparing Source and Plume Remediation Alternatives." *Ground Water*, Wiley/Blackwell (10.1111), 46(2), 272–285.

Falta, R. W., Basu, N., and Rao, P. S. (2005a). "Assessing impacts of partial mass depletion in DNAPL source zones: II. Coupling source strength functions to plume evolution." *Journal of Contaminant Hydrology*, Elsevier, 79(1–2), 45–66.

Falta, R. W., Rao, P. S., and Basu, N. (2005b). "Assessing the impacts of partial mass depletion in DNAPL source zones: I. Analytical modeling of source strength functions and plume response." *Journal of Contaminant Hydrology*, 78(4), 259–280.

Fennell, D. E., and Gossett, J. M. (1998). "Modeling the Production of and Competition for Hydrogen in a Dechlorinating Culture." *Environmental Science & Technology*, 32(16), 2450–2460.

Fernàndez-Garcia, D., Llerar-Meza, G., and Gómez-Hernández, J. J. (2009). "Upscaling transport with mass transfer models: Mean behavior and propagation of uncertainty." *Water Resources Research*, 45(10).

Feyen, L., and Gorelick, S. M. (2004). "Reliable groundwater management in hydroecologically sensitive areas." *Water Resources Research*, Wiley-Blackwell, 40(7).

Fienen, M. N., Doherty, J. E., Hunt, R. J., and Reeves, H. W. (2010). "Using Prediction Uncertainty Analysis to Design Hydrologic Monitoring Networks: Example Applications from the Great Lakes Water Availability Pilot Project Scientific Investigations Report 2010–5159."

Finsterle, S. (2015). "Practical notes on local data-worth analysis." *Water Resources Research*, 51(12), 9904–9924.

Flach, G. P. (2012). "Relationship between dual-domain parameters and practical characterization data." *Ground Water*, 50(2), 216–229.

Friis, A. K., Heimann, A. C., Jakobsen, R., Albrechtsen, H.-J., Cox, E., and Bjerg, P. L. (2007). "Temperature dependence of anaerobic TCE-dechlorination in a highly enriched Dehalococcoides-containing culture." *Water Research*, 41(2), 355–364.

Fure, A. D., Jawitz, J. . W., and Annable, M. D. (2006). "DNAPL source depletion: Linking architecture and flux response." *Journal of Contaminant Hydrology*, 85(3), 118–140.

Gaeth, S. P. (2017). "Examining Reactive Minerals, Sulfide, and Bioremediation Interactions for Improved Chlorinated Solvent Detoxification." 155.

Gaeth, S. P., Cápiro, N., Pennell, K. D., and Ramsburg, A. C. (2016). "Examining Reactive Minerals, Sulfide, and Bioremediation Interactions for Improved Chlorinated Solvent Detoxification." (February 2016).

Garant, H., and Lynd, L. (1998). "Applicability of competitive and noncompetitive kinetics to the reductive dechlorination of chlorinated ethenes." *Biotechnology and Bioengineering*, 57(6), 751–755.

Gelhar, L. W., Welty, C., and Rehfeldt, K. R. (1992). "A critical review of data on field-scale dispersion in aquifers." *Water Resources Research*, 28(7), 1955–1974.

van Genuchten, M. T., and Alves, W. J. (1982). *Analytical Solutions of the One-Dimensional Convective-Dispersive Solute Transport Equation*. Technical Bulletins, United States Department of Agriculture, Economic Research Service.

van Genuchten, M. T., and Parker, J. C. (1984). "Boundary conditions for displacement experiments through short laboratory soil columns [Dispersion coefficients]." *Journal of the Soil Science Society of America (USA)*.

van Genuchten, M. T., and Wierenga, P. J. (1976). "Mass Transfer Studies in Sorbing Porous Media I. Analytical Solutions1." *Soil Science Society of America Journal*, 40(4), 473.

Gilbert, R. O., and Simpson, J. C. (1985). "Kriging for estimating spatial pattern of contaminants: Potential and problems." *Environmental Monitoring and Assessment*, 5(2), 113–135.

Glover, K. C., Munakata-Marr, J., and Illangasekare, T. H. (2007). "Biologically enhanced mass transfer of tetrachloroethene from DNAPL in source zones: experimental evaluation and influence of pool morphology." *Environmental Science & Technology*, 41(4), 1384–1389.

Golden Software, LLC. (-). *Surfer*. Golden Software, LLC., Golden, Colorado.

Goltz, M. N., Kim, S., Yoon, H., and Park, J. (2007). "Review of Groundwater Contaminant Mass Flux Measurement." *Environmental Engineering Research*, 12(4), 176–193.

Goltz, M. N., and Roberts, P. N. (1986). "Interpreting organic solute transport data from a field experiment using physical nonequilibrium models." *Journal of Contaminant Hydrology*, Transport and Transformations of Organic Contaminants, 1(1), 77–93.

Goltz, M. N., and Roberts, P. V. (1988). "Simulations of physical nonequilibrium solute transport models: Application to a large-scale field experiment." *Journal of Contaminant Hydrology*, 3(1), 37–63.

Gouze, P., Melean, Y., Le Borgne, T., Dentz, M., and Carrera, J. (2008). "Non-Fickian dispersion in porous media explained by heterogeneous microscale matrix diffusion: Non-Fickian Dispersion and Heterogeneous Diffusion." *Water Resources Research*, 44(11), n/a-n/a.

Guan, J., Molz, F. J., Zhou, Q., Liu, H. H., and Zheng, C. (2008). "Behavior of the mass transfer coefficient during the MADE-2 experiment: New insights." *Water Resources Research*, 44(2).

Gupta, S., and Seagren, E. A. (2005). "Comparison of Bioenhancement of Nonaqueous Phase Liquid Pool Dissolution with First- and Zero-Order Biokinetics." *Journal of Environmental Engineering*, 131(1), 165–169.

Haest, P. J., Philips, J., Springael, D., and Smolders, E. (2011). "The reactive transport of trichloroethene is influenced by residence time and microbial numbers." *Journal of Contaminant Hydrology*, 119(1–4), 89–98.

Haest, P. J., Springael, D., Seuntjens, P., and Smolders, E. (2012). "Self-inhibition can limit biologically enhanced TCE dissolution from a TCE DNAPL." *Chemosphere*, 89(11), 1369–1375.

Haest, P. J., Springael, D., and Smolders, E. (2010a). "Dechlorination kinetics of TCE at toxic TCE concentrations: Assessment of different models." *Water Research*, 44(1), 331–339.

Haest, P. J., Springael, D., and Smolders, E. (2010b). "Modelling reactive CAH transport using batch experiment degradation kinetics." *Water Research*, 44(9), 2981–2989.

Haggerty, R., and Gorelick, S. M. (1995). "Multiple-Rate Mass Transfer for Modeling Diffusion and Surface Reactions in Media with Pore-Scale Heterogeneity." *Water Resources Research*, 31(10), 2383–2400.

Haggerty, R., McKenna, S. A., and Meigs, L. C. (2000). "On the late-time behavior of tracer test breakthrough curves." *Water Resources Research*, 36(12), 3467–3479.

Hammond, G. E., Valocchi, A. J., and Lichtner, P. C. (2005). "Application of Jacobian-free Newton–Krylov with physics-based preconditioning to biogeochemical transport." *Advances in Water Resources*, 28(4), 359–376.

Harbaugh, A. W. (2005). *MODFLOW-2005, The U.S. Geological Survey Modular Ground-Water Model-the Ground-Water Flow Process*.

Harbaugh, A. W., Banta, E. R., Hill, M. C., and McDonald, M. G. (2000). *MODFLOW-2000, The U.S. Geological Survey Modular Ground-Water Model - User Guide to Modularization Concepts and the Ground-Water Flow Process*. Open-File Report, USGS Numbered Series, Geological Survey (U.S.).

Harkness, M., and Fisher, A. (2013). "Use of emulsified vegetable oil to support bioremediation of TCE DNAPL in soil columns." *Journal of Contaminant Hydrology*, 151, 16–33.

Harmon, T. C., Semprini, L., and Roberts, P. V. (1992). "Simulating Solute Transport Using Laboratory-Based Sorption Parameters." *Journal of Environmental Engineering*, 118(5), 666–688.

Harp, D. R., Dai, Z., Wolfsberg, A. V., Vrugt, J. A., Robinson, B. A., and Vesselinov, V. V. (2008). "Aquifer structure identification using stochastic inversion." *Geophysical Research Letters*, 35(8).

Harp, D. R., and Vesselinov, V. V. (2010). "Stochastic inverse method for estimation of geostatistical representation of hydrogeologic stratigraphy using borehole logs and pressure observations." *Stochastic Environmental Research and Risk Assessment*, 24(7), 1023–1042.

Hastings, W. K. (1970). "Monte Carlo Sampling Methods Using Markov Chains and Their Applications." *Biometrika*, 57(1), 97–109.

Haston, Z. C., and McCarty, P. L. (1999). "Chlorinated Ethene Half-Velocity Coefficients (K_S) for Reductive Dehalogenation." *Environmental Science & Technology*, 33(2), 223–226.

Haverkamp, R., and Parlange, J. Y. (1986). "Predicting the Water-Retention Curve from Particle-Size Distribution: 1. Sandy Soils without Organic Matter1." *Soil Science*, 142(6), 325.

He, J., Holmes, V. F., Lee, P. K. H., and Alvarez-Cohen, L. (2007). "Influence of vitamin B12 and cocultures on the growth of Dehalococcoides isolates in defined medium." *Applied and Environmental Microbiology*, 73(9), 2847–2853.

He, J., Ritalahti, K. M., Aiello, M. R., and Löffler, F. E. (2003). "Complete detoxification of vinyl chloride by an anaerobic enrichment culture and identification of the reductively dechlorinating population as a Dehalococcoides species." *Applied and Environmental Microbiology*, 69(2), 996–1003.

He, J., Sung, Y., Krajmalnik-Brown, R., Ritalahti, K. M., and Löffler, F. E. (2005). "Isolation and characterization of Dehalococcoides sp. strain FL2, a trichloroethene (TCE)- and 1,2-dichloroethene-respiring anaerobe." *Environmental Microbiology*, 7(9), 1442–1450.

Heinz, J., Kleineidam, S., Teutsch, G., and Aigner, T. (2003). "Heterogeneity patterns of Quaternary glaciofluvial gravel bodies (SW-Germany): application to hydrogeology." *Sedimentary Geology*, 158(1), 1–23.

Herrera, G. S., and Pinder, G. F. (2005). "Space-time optimization of groundwater quality sampling networks." *Water Resources Research*, Wiley-Blackwell, 41(12).

Hill, M. C. (1998). *Methods and Guidelines for Effective Model Calibration*. Water-Resources Investigations Report, USGS Numbered Series, U.S. Geological Survey : Branch of Information Services [distributor],.

Hoag, G. E., and Marley, M. C. (1986). "Gasoline Residual Saturation in Unsaturated Uniform Aquifer Materials." *Journal of Environmental Engineering*, 112(3), 586–604.

Huang, D., and Becker, J. G. (2009). "Determination of intrinsic monod kinetic parameters for two heterotrophic tetrachloroethene (PCE)-respiring strains and insight into their application." *Biotechnology and Bioengineering*, 104(2), 301–311.

Huang, D., and Becker, J. G. (2011). "Dehalorespiration Model That Incorporates the Self-Inhibition and Biomass Inactivation Effects of High Tetrachloroethene Concentrations." *Environmental Science & Technology*, 45(3), 1093–1099.

Huang, D., Lai, Y., and Becker, J. G. (2014). "Impact of initial conditions on extant microbial kinetic parameter estimates: application to chlorinated ethene dehalorespiration." *Applied Microbiology and Biotechnology*, 98(5), 2279–2288.

Hug, L. A., Beiko, R. G., Rowe, A. R., Richardson, R. E., and Edwards, E. A. (2012). "Comparative metagenomics of three Dehalococcoides-containing enrichment cultures: the role of the non-dechlorinating community." *BMC Genomics*, 13(1), 327.

Imhoff, P. T., Jaffé, P. R., and Pinder, G. F. (1994). "An experimental study of complete dissolution of a nonaqueous phase liquid in saturated porous media." *Water Resources Research*, 30(2), 307–320.

ITRC. (2003). "Technology Overview: An Introduction to Characterizing Sites Contaminated with DNAPLS." The Interstate Technology & Regulatory Council, Washington, DC.

ITRC. (2004). "Strategies for Monitoring the Performance of DNAPL Source Zone Remedies." The Interstate Technology & Regulatory Council, Washington, DC.

ITRC. (2011). "Integrated DNAPL Site Strategy." The Interstate Technology & Regulatory Council, Washington, DC.

Jarsjö, J., Bayer-Raich, M., and Ptak, T. (2005). "Monitoring groundwater contamination and delineating source zones at industrial sites: Uncertainty analyses using integral pumping tests." *Journal of Contaminant Hydrology*, Elsevier, 79(3–4), 107–134.

Jawitz, J. W., Fure, A. D., Demmy, G. G., Berglund, S., and Rao, P. S. C. (2005). "Groundwater contaminant flux reduction resulting from nonaqueous phase liquid mass reduction." *Water Resources Research*, 41(10).

Jones, E., Oliphant, T., and Peterson, P. (2001). *{SciPy}: Open source scientific tools for {Python}*.

Jones, N. L., Davis, R. J., and Sabbah, W. (2005). "A Comparison of Three-Dimensional Interpolation Techniques for Plume Characterization." *Groundwater*, 41(4), 411–419.

Kaluarachchi, J. J., and Parker, J. C. (1992). "Multiphase flow with a simplified model for oil entrapment." *Transport in Porous Media*, 7(1), 1–14.

Kaluza, M. C. D. P., Miller, E. L., and Abriola, L. M. (2015). "Markov random field models for quantifying uncertainty in subsurface remediation." *2015 IEEE International Geoscience and Remote Sensing Symposium (IGARSS)*, 4296–4299.

Karickhoff, S. W., Brown, D. S., and Scott, T. A. (1979). "Sorption of hydrophobic pollutants on natural sediments." *Water research*, 13(3), 241–248.

Kavanaugh, M. C., Suresh, P., and Rao, C. (2003). *THE DNAPL REMEDIATION CHALLENGE: IS THERE A CASE FOR SOURCE DEPLETION?* U.S. ENVIRONMENTAL PROTECTION AGENCY, Office of Research & Development, WASHINGTON, DC.

Kaye, A. J., Cho, J., Basu, N. B., Chen, X., Annable, M. D., and Jawitz, J. W. (2008). "Laboratory investigation of flux reduction from dense non-aqueous phase liquid (DNAPL) partial source zone remediation by enhanced dissolution." *Journal of Contaminant Hydrology*, 102(1–2), 17–28.

Kielhorn, J., Melber, C., Wahnschaffe, U., Aitio, a, and Mangelsdorf, I. (2000). "Vinyl chloride: still a cause for concern." *Environmental health perspectives*, 108(7), 579–588.

Kikuchi, C. (2017). "Toward Increased Use of Data Worth Analyses in Groundwater Studies." *Groundwater*, 55(5), 670–673.

Kitanidis, P. K. (1997). "Introduction to Geostatistics: Applications in Hydrogeology." (2018).

Klammler, H., Hatfield, K., Guimarães da Luz, J. A., Annable, M. D., Newman, M., Cho, J., Peacock, A., Stucker, V., Ranville, J., Cabaniss, S. A., and Rao, P. S. C. (2012). "Contaminant discharge and uncertainty estimates from passive flux meter measurements." *Water Resources Research*, 48(2).

Kleineidam, S., Rügner, H., and Grathwohl, P. (1999a). "Influence of petrographic composition/organic matter distribution of fluvial aquifer sediments on the sorption of hydrophobic contaminants." *Sedimentary Geology*, 129(3), 311–325.

Kleineidam, S., Rügner, H., Ligouis, B., and Grathwohl, P. (1999b). "Organic Matter Facies and Equilibrium Sorption of Phenanthrene." *Environmental Science & Technology*, 33(10), 1637–1644.

Koch, J., and Nowak, W. (2015). "Predicting DNAPL mass discharge and contaminated site longevity probabilities: Conceptual model and high-resolution stochastic simulation." *Water Resources Research*, 51(2), 806–831.

Koch, J., and Nowak, W. (2016). Identification of contaminant source architectures-A statistical inversion that emulates multiphase physics in a computationally practicable manner. *Water Resources Research*, *52*(2), 1009–1025. https://doi.org/10.1002/2015WR017894

Kouznetsova, I., Mao, X., Robinson, C., Barry, D. A., Gerhard, J. I., and McCarty, P. L. (2010). "Biological reduction of chlorinated solvents: Batch-scale geochemical modeling." *Advances in Water Resources*, 33(9), 969–986.

Kram, M. L., Keller, A. A., Rossabi, J., and Everett, L. G. (2002). "DNAPL Characterization Methods and Approaches, Part 2: Cost Comparisons." *Groundwater Monitoring & Remediation*, 22(1), 46–61.

Kresic, N. (2006). *Hydrogeology and Groundwater Modeling*. CRC Press, Boca Raton, Fla.

Krige, D. G. (1951). "A statistical approach to some mine valuation and allied problems on the Witwatersrand." Thesis.

Kueper, B. H., Redman, D., Starr, R. C., Reitsma, S., and Mah, M. (1993). "A Field Experiment to Study the Behavior of Tetrachloroethylene Below the Water Table: Spatial Distribution of Residual and Pooled DNAPL." *Groundwater*, 31(5), 756–766.

Kueper, B. H., Stroo, H. F., Vogel, C. M., and Ward, C. H. (Eds.). (2014). *Chlorinated Solvent Source Zone Remediation*. Springer New York, New York, NY.

Kumar, S., and Hebert, M. (2005). "A hierarchical field framework for unified context-based classification." *Tenth IEEE International Conference on Computer Vision (ICCV'05) Volume 1*, 1284-1291 Vol. 2.

Kumar, S., and Hebert, M. (2006). "Discriminative Random Fields." *International Journal of Computer Vision*, 68(2).

Kunstmann, H., Kinzelbach, W., and Siegfried, T. (2002). "Conditional first-order second-moment method and its application to the quantification of uncertainty in groundwater modeling." *Water Resources Research*, 38(4), 6-1-6–14.

Leaf, A. T. (2017). "Using Models to Identify the Best Data: An Example from Northern Wisconsin." *Groundwater*, 55(5), 641–645.

Lebrón, C. A., McHale, T., Young, R., Williams, D., Bogaart, M. G., Major, D. W., McMaster, M. L., Tasker, I., and Akladiss, N. (2007). "Pilot-scale evaluation using bioaugmentation to enhance PCE dissolution at dover AFB national test site." *Remediation Journal*, 17(2), 5–17.

Lee, I. S., Bae, J. H., Yang, Y., and McCarty, P. L. (2004). "Simulated and experimental evaluation of factors affecting the rate and extent of reductive dehalogenation of chloroethenes with glucose." *Journal of Contaminant Hydrology*, 74(1), 313–331.

Lee, P. K. H., Macbeth, T. W., Sorenson, K. S., Deeb, R. a., and Alvarez-Cohen, L. (2008). "Quantifying genes and transcripts to assess the in situ physiology of 'Dehalococcoides' spp. in a trichloroethene-contaminated groundwater site." *Applied and Environmental Microbiology*, 74(9), 2728–2739.

Lemke, L. D., and Abriola, L. M. (2006). "Modeling dense nonaqueous phase liquid mass removal in nonuniform formations: Linking source-zone architecture and system response." *Geosphere*, 2(2), 74–82.

Lemke, L. D., Abriola, L. M., and Goovaerts, P. (2004a). "Dense nonaqueous phase liquid (DNAPL) source zone characterization: Influence of hydraulic property correlation on predictions of DNAPL infiltration and entrapment." *Water Resources Research*, 40(1).

Lemke, L. D., Abriola, L. M., and Lang, J. R. (2004b). "Influence of hydraulic property correlation on predicted dense nonaqueous phase liquid source zone architecture, mass recovery and contaminant flux." *Water Resources Research*, 40(12).

Lendvay, J. M., Löffler, F. E., Dollhopf, M., Aiello, M. R., Daniels, G., Fathepure, B. Z., Gebhard, M., Heine, R., Helton, R., Shi, J., Krajmalnik-Brown, R., Major, C. L., Barcelona, M. J., Petrovskis, E., Hickey, R., Tiedje, J. M., and Adriaens, P. (2003). "Bioreactive barriers: A comparison of bioaugmentation and biostimulation for chlorinated solvent remediation." *Environmental Science and Technology*, 37(7), 1422–1431.

Leube, P. C., Geiges, A., and Nowak, W. (2012). "Bayesian assessment of the expected data impact on prediction confidence in optimal sampling design." *Water Resources Research*, 48(2), 1–16.

Li, K. B., and Abriola, L. M. (2009). "A multistage multicriteria spatial sampling strategy for estimating contaminant mass discharge and its uncertainty." *Water Resources Research*, 45(6), 1–15.

Li, K. B., Goovaerts, P., and Abriola, L. M. (2007). "A geostatistical approach for quantification of contaminant mass discharge uncertainty using multilevel sampler measurements." *Water Resources Research*, 43(6), 1–14.

Li, L., Zhou, H., and Gómez-Hernández, J. J. (2011). "Transport upscaling using multi-rate mass transfer in three-dimensional highly heterogeneous porous media." *Advances in Water Resources*, 34(4), 478–489.

Li, S. Z. (2009). *Markov Random Field Modeling in Image Analysis*. Springer Publishing Company, Incorporated.

Li, Y.-H., and Gregory, S. (1974). "Diffusion of ions in sea water and in deep-sea sediments." *Geochimica et Cosmochimica Acta*, 38(5), 703–714.

Lima, G. P., and Sleep, B. E. (2007). "The spatial distribution of eubacteria and archaea in sand-clay columns degrading carbon tetrachloride and methanol." *Journal of Contaminant Hydrology*, 94(1–2), 34–48.

Liu, C., and Ball, W. P. (2002). "Back Diffusion of Chlorinated Solvent Contaminants from a Natural Aquitard to a Remediated Aquifer Under Well-Controlled Field Conditions: Predictions and Measurements." *Groundwater*, 40(2), 175–184.

Liu, X., Lee, J., Kitanidis, P. K., Parker, J., and Kim, U. (2012). "Value of Information as a Context-Specific Measure of Uncertainty in Groundwater Remediation." *Water Resources Management*, 26(6), 1513–1535.

Loaiciga, H. A., Charbeneau, R. J., Everett, L. G., Fogg, G. E., Hobbs, B. F., and Rouhani, S. (1992). "Review of Ground-Water Quality Monitoring Network Design." *Journal of Hydraulic Engineering*, 118(1), 11–37.

Löffler, F. E., Sanford, R. A., and Ritalahti, K. M. (2005). "Enrichment, cultivation, and detection of reductively dechlorinating bacteria." *Methods in Enzymology*, 397(1996), 77–111.

Löffler, F. E., Yan, J., Ritalahti, K. M., Adrian, L., Edwards, E. A., Konstantinidis, K. T., Müller, J. A., Fullerton, H., Zinder, S. H., and Spormann, A. M. (2013). "Dehalococcoides mccartyi gen. nov., sp. nov., obligately organohalide-respiring anaerobic bacteria relevant to halogen cycling and bioremediation, belong to a novel bacterial class, Dehalococcoidia classis nov., order Dehalococcoidales ord. nov. and family Dehalococcoidaceae fam. nov., within the phylum Chloroflexi." *International Journal of Systematic and Evolutionary Microbiology*, 63(2), 625–635.

Lovley, D. R., Stolz, J. F., Jr, G. L. N., and Phillips, E. J. P. (1987). "Anaerobic production of magnetite by a dissimilatory iron-reducing microorganism." *Nature*, 330(6145), 252–254.

Lu, D., Ricciuto, D., and Evans, K. (2018). "An efficient Bayesian data-worth analysis using a multilevel Monte Carlo method." *Advances in Water Resources*, Elsevier, 113(January), 223–235.

Lu, D., Ye, M., Neuman, S. P., and Xue, L. (2012). "Multimodel Bayesian analysis of data-worth applied to unsaturated fractured tuffs." *Advances in Water Resources*, 35, 69–82.

Lu, X., Wilson, J. T., and Kampbell, D. H. (2006). "Relationship between Dehalococcoides DNA in ground water and rates of reductive dechlorination at field scale." *Water Research*, 40(16), 3131–3140.

Lucius, J. E., Olhoeft, G. R., Hill, P. L., and Duke, S. K. (1992). *Properties and hazards of 108 selected substances*. Open-File Report, USGS Numbered Series, U.S. Dept. of the Interior, Geological Survey,.

Lyon-Marion, B. A., Becker, M. D., Kmetz, A. A., Foster, E., Johnston, K. P., Abriola, L. M., and Pennell, K. D. (2017). "Simulation of magnetite nanoparticle mobility in a heterogeneous flow cell." *Environmental Science: Nano*, Royal Society of Chemistry, 4(7), 1512–1524.

Mackay, D. M., and Boethling, R. S. (Eds.). (2000). *Handbook of Property Estimation Methods for Chemicals: Environmental Health Sciences*. CRC Press, Boca Raton.

Mackay, D. M., and Cherry, J. A. (1989). "Groundwater contamination: pump-and-treat remediation." *Environmental Science & Technology*, 23(6), 630–636.

Mackay, D. M., Freyberg, D. L., Roberts, P. V., and Cherry, J. A. (1986). "A natural gradient experiment on solute transport in a sand aquifer: 1. Approach and overview of plume movement." *Water Resources Research*, 22(13), 2017–2029.

Mackay, D., Shiu, W. Y., Ma, K.-C., and Lee, S. C. (Eds.). (2006). *Handbook of physical-chemical properties and environmental fate for organic chemicals*. CRC/Taylor & Francis, Boca Raton, FL.

Maghrebi, M., Jankovic, I., Allen-King, R. M., Rabideau, A. J., Kalinovich, I., and Weissmann, G. S. (2014). "Impacts of transport mechanisms and plume history on tailing of sorbing plumes in heterogeneous porous formations." *Advances in Water Resources*, 73, 123–133.

Maghrebi, M., Jankovic, I., Weissmann, G. S., Matott, L. S., Allen-King, R. M., and Rabideau, A. J. (2015). "Contaminant tailing in highly heterogeneous porous formations: Sensitivity on model selection and material properties." *Journal of Hydrology*, Groundwater flow and transport in aquifers: Insights from modeling and characterization at the field scale, 531, 149–160.

Maji, R. (2005). "Conditional stochastic modelling of DNAPL migration and dissolution in a high-resolution aquifer analog." PhD Thesis, University of Waterloo, Waterloo, Ont.

Maji, R., and Sudicky, E. A. (2008). "Influence of mass transfer characteristics for DNAPL source depletion and contaminant flux in a highly characterized glaciofluvial aquifer." *Journal of Contaminant Hydrology*, Partial Source Zone Removal, 102(1), 105–119.

Maji, R., Sudicky, E. A., Panday, S., and Teutsch, G. (2006). "Transition Probability/Markov Chain Analyses of DNAPL Source Zones and Plumes." *Ground Water*, 44(6 Understanding), 853–863.

Major, D. W., McMaster, M. L., Cox, E. E., Edwards, E. a., Dworatzek, S. M., Hendrickson, E. R., Starr, M. G., Payne, J. A., and Buonamici, L. W. (2002). "Field demonstration of successful bioaugmentation to achieve dechlorination of tetrachloroethene to ethene." *Environmental Science and Technology*, 36(23), 5106–5116.

Malaguerra, F., Chambon, J. C., Bjerg, P. L., Scheutz, C., and Binning, P. J. (2011). "Development and Sensitivity Analysis of a Fully Kinetic Model of Sequential Reductive Dechlorination in Groundwater." *Environmental Science & Technology*, 45(19), 8395–8402.

Manoli, G., Chambon, J. C., Bjerg, P. L., Scheutz, C., Binning, P. J., and Broholm, M. M. (2012). "A remediation performance model for enhanced metabolic reductive dechlorination of chloroethenes in fractured clay till." *Journal of Contaminant Hydrology*, 131(1–4), 64–78.

Maraqa, M. A. (2001). "Prediction of mass-transfer coefficient for solute transport in porous media." *Journal of Contaminant Hydrology*, 50(1–2), 1–19.

Marcet, T. F. (2014). "Secondary Impacts of In Situ Chlorinated Solvent Remediation Due to Metal Sulfide Preceipitation and Thermal Treatment." Tufts University.

Marcet, T. F., Cápiro, N. L., Morris, L. A., Hassan, S. M., Yang, Y., Löffler, F. E., and Pennell, K. D. (2018a). "Release of Electron Donors during Thermal Treatment of Soils." *Environmental Science and Technology*, 52(6), 3642–3651.

Marcet, T. F., Cápiro, N. L., Yang, Y., Löffler, F. E., and Pennell, K. D. (2018b). "Impacts of low-temperature thermal treatment on microbial detoxification of tetrachloroethene under continuous flow conditions." *Water Research*, 145, 21–29.

Martino, L., and Elvira, C. (2017). "Metropolis Sampling." *arXiv:1704.04629 [stat]*.

Matheron, G. (1963). "Principles of geostatistics." *Economic Geology*, 58(8), 1246–1266.

Matthieu, D. E., Brusseau, M. L., Guo, Z., Plaschke, M., Carroll, K. C., and Brinker, F. (2014). "Persistence of a Groundwater Contaminant Plume after Hydraulic Source Containment at a Chlorinated-Solvent Contaminated Site." *Groundwater Monitoring & Remediation*, 34(4), 23–32.

McCarty, P. L., Goltz, M. N., Hopkins, G. D., Dolan, M. E., Allan, J. P., Kawakami, B. T., and Carrothers, T. J. (1998). "Full-Scale Evaluation of In Situ Cometabolic Degradation of Trichloroethylene in Groundwater through Toluene Injection." *Environmental Science & Technology*, 32(1), 88–100.

McGuire, T. M., McDade, J. M., and Newell, C. J. (2006). "Performance of DNAPL Source Depletion Technologies at 59 Chlorinated Solvent-Impacted Sites." *Groundwater Monitoring & Remediation*, 26(1), 73–84.

Mercer, J. W., and Cohen, R. M. (1990). "A review of immiscible fluids in the subsurface: Properties, models, characterization and remediation." *Journal of Contaminant Hydrology*, 6(2), 107–163.

Mercer, J. W., Cohen, R. M., and Noel, M. R. (2010). "DNAPL Site Characterization Issues at Chlorinated Solvent Sites." *In Situ Remediation of Chlorinated Solvent Plumes*, H. F. Stroo and C. H. Ward, eds., Springer New York, New York, NY, 217–280.

Metropolis, N., Rosenbluth, A. W., Rosenbluth, M. N., Teller, A. H., and Teller, E. (1953). "Equation of State Calculations by Fast Computing Machines." *The Journal of Chemical Physics*, 21(6), 1087–1092.

Michalak, A. M., & Kitanidis, P. K. (2004). Estimation of historical groundwater contaminant distribution using the adjoint state method applied to geostatistical inverse modeling. *Water Resources Research*, *40*(8), 1–14. https://doi.org/10.1029/2004WR003214

Miller, C. T., Poirier-McNeil, M. M., and Mayer, A. S. (1990). "Dissolution of Trapped Nonaqueous Phase Liquids: Mass Transfer Characteristics." *Water Resources Research*, 26(11), 2783–2796.

Miura, T., Yamazoe, A., Ito, M., Ohji, S., Hosoyama, A., Takahata, Y., and Fujita, N. (2015). "The Impact of Injections of Different Nutrients on the Bacterial Community and Its Dechlorination Activity in Chloroethene-Contaminated Groundwater." *Microbes and Environments*, 30(2), 164–171.

Mohamed, M., and Hatfield, K. (2011). "Dimensionless parameters to summarize the influence of microbial growth and inhibition on the bioremediation of groundwater contaminants." *Biodegradation*, 22(5), 877–896.

Montgomery, J. H. (2007). *Groundwater Chemicals Desk Reference*. CRC Press, Boca Raton.

Mott, R. L., and Untener, J. A. (2014). *Applied Fluid Mechanics*. Pearson, Boston.

NAVFAC. (2013). *Best Practices for Injection and Distribution of Amendments*. Technical Report, Battelle Memorial Institute and NAVFAC Alternative Restoration Technology Team, Port Hueneme, California, 81.

Neuman, S. P., Xue, L., Ye, M., and Lu, D. (2012). "Bayesian analysis of data-worth considering model and parameter uncertainties." *Advances in Water Resources*, 36, 75–85.

Neupauer, R. M., & Lin, R. (2006). Identifying sources of a conservative groundwater contaminant using backward probabilities conditioned on measured concentrations. *Water Resources Research*, *42*(3). https://doi.org/10.1029/2005WR004115

Neupauer, R. M., & Wilson, J. L. (2005). Backward probability model using multiple observations of contamination to identify groundwater contamination sources at the Massachusetts Military Reservation. *Water Resources Research*, *41*(2), 1–14. https://doi.org/10.1029/2003WR002974

Nobis Engineering Inc. (2012). "Draft 2012 Data Summary Commerce Street Plume Superfund Site Williston , Vermont.". Lowell, MA.

Nobis Engineering Inc. (2015). *Remedial Investigation, Volume I Commerce Street Plume Superfund Site Williston, Vermont*. US Environmental Protection Agency Region 1, Lowell, MA.

Nobis Engineering Inc. (2018). *Research Study Field Program Technical Memorandum Commerce Street Plume Site Williston, Vermont*. Lowell, MA.

Nowak, W., de Barros, F. P. J., and Rubin, Y. (2010). "Bayesian geostatistical design: Task-driven optimal site investigation when the geostatistical model is uncertain." *Water Resources Research*, 46(3), 1–17.

Nowak, W., Rubin, Y., and de Barros, F. P. J. (2012). "A hypothesis-driven approach to optimize field campaigns." *Water Resources Research*, 48(6), 1–16.

NRC. (2005). *Contaminants in the Subsurface: Source Zone Assessment and Remediation*. The National Academies Press, Washington, DC.

NRC. (2013). *Alternatives for Managing the Nation's Complex Contaminated Groundwater Sites*. The National Academies Press, Washington, D.C.

Ohnishi, A., Hasegawa, Y., Abe, S., Bando, Y., Fujimoto, N., and Suzuki, M. (2012). "Hydrogen fermentation using lactate as the sole carbon source: Solution for 'blind spots' in biofuel production." *RSC Advances*, 2(22), 8332.

Pankow, J. F., Feenstra, S., Cherry, J. A., and Ryan, M. C. (1996). "Dense chlorinated solvents and other DNAPLs in groundwater : background and history of the problem." *Dense Chlorinated Solvents and Other DNAPLs in Groundwater*, J. F. Pankow and J. A. Cherry, eds., Waterloo Press, Guelph, Ontario, Canada, 1–52.

Parker, B. L., Chapman, S. W., and Guilbeault, M. A. (2008). "Plume persistence caused by back diffusion from thin clay layers in a sand aquifer following TCE source-zone hydraulic isolation." *Journal of Contaminant Hydrology*, Partial Source Zone Removal, 102(1), 86–104.

Parker, J. C., and Park, E. (2004). "Modeling field-scale dense nonaqueous phase liquid dissolution kinetics in heterogeneous aquifers." *Water Resources Research*, 40(5).

Pedretti, D., Fernàndez-Garcia, D., Sanchez-Vila, X., Bolster, D., and Benson, D. A. (2014). "Apparent directional mass-transfer capacity coefficients in three-dimensional anisotropic heterogeneous aquifers under radial convergent transport." *Water Resources Research*, 50(2), 1205–1224.

Pham, H. V., and Tsai, F. T.-C. (2016). "Optimal observation network design for conceptual model discrimination and uncertainty reduction." *Water Resources Research*, 52(2), 1245–1264.

Phanikumar, M. S., Hyndman, D. W., Zhao, X., and Dybas, M. J. (2005). "A three-dimensional model of microbial transport and biodegradation at the Schoolcraft, Michigan, site: BIOREMEDIATION AT SCHOOLCRAFT." *Water Resources Research*, 41(5).

Phelan, T. J., Abriola, L. M., Gibson, J. L., Smits, K. M., and Christ, J. A. (2015). "Development and application of a screening model for evaluating bioenhanced dissolution in DNAPL source zones." *Journal of Contaminant Hydrology*, 183, 1–15.

Phelan, T. J., Lemke, L. D., Bradford, S. A., O'Carroll, D. M., and Abriola, L. M. (2004). "Influence of textural and wettability variations on predictions of DNAPL persistence and plume development in saturated porous media." *Advances in Water Resources*, A Tribute to George F. Pinder, 27(4), 411–427.

Philips, J., Springael, D., and Smolders, E. (2011). "A three-layer diffusion-cell to examine bio-enhanced dissolution of chloroethene dense non-aqueous phase liquid." *Chemosphere*, 83(7), 991–996.

Powers, S. E., Abriola, L. M., and Weber, W. J. (1992). "An experimental investigation of nonaqueous phase liquid dissolution in saturated subsurface systems: Steady state mass transfer rates." *Water Resources Research*, 28(10), 2691–2705.

Powers, S. E., Abriola, L. M., and Weber, W. J. (1994). "An experimental investigation of nonaqueous phase liquid dissolution in saturated subsurface systems: Transient mass transfer rates." *Water Resources Research*, 30(2), 321–332.

Rabideau, A. J., and Miller, C. T. (1994). "Two-dimensional modeling of aquifer remediation influenced by sorption nonequilibrium and hydraulic conductivity heterogeneity." *Water Resources Research*, 30(5), 1457–1470.

Rathfelder, K., and Abriola, L. M. (1998). "The influence of capillarity in numerical modeling of organic liquid redistribution in two-phase systems." *Advances in Water Resources*, 21(2), 159–170.

Rathfelder, K. M., and Abriola, L. M. (1994). "Mass conservative numerical solutions of the head-based Richards equation." *Water Resources Research*, 30(9), 2579–2586.

Rathfelder, K. M., Abriola, L. M., Taylor, T. P., and Pennell, K. D. (2001). "Surfactant enhanced recovery of tetrachloroethylene from a porous medium containing low permeability lenses 2. Numerical simulation." *Journal of Contaminant Hydrology*, 24.

Rectanus, H. V., Widdowson, M. A., Chapelle, F. H., Kelly, C. A., and Novak, J. T. (2007). "Investigation of reductive dechlorination supported by natural organic carbon." *Ground Water Monitoring and Remediation*, 27(4), 53–62.

Reed, P. M., and Minsker, B. S. (2004). "Spatial Interpolation Methods for Nonstationary Plume Data." *Groundwater*, 42(2), 190–202.

Reed, P. M., Minsker, B., and Valocchi, A. J. (2000). "Cost-effective long-term groundwater monitoring design using a genetic algorithm and global mass interpolation." *Water Resources Research*, 36(12), 3731–3741.

Reitsma, S., and Dai, Q. L. (2001). "Reaction-enhanced mass transfer and transport from non-aqueous phase liquid source zones." *Journal of contaminant hydrology*, 49(1), 49–66.

Ritalahti, K. M., Amos, B. K., Sung, Y., Wu, Q., Koenigsberg, S. S., and Löffler, F. E. (2006). "Quantitative PCR targeting 16S rRNA and reductive dehalogenase genes simultaneously monitors multiple Dehalococcoides strains." *Applied and Environmental Microbiology*, 72(4), 2765–2774.

Ritalahti, K. M., Hatt, J. K., Lugmayr, V., Henn, K., Petrovskis, E. A., Ogles, D. M., Davis, G. A., Yeager, C. M., Lebrón, C. A., and Löffler, F. E. (2010a). "Comparing On-site to off-site biomass collection for dehalococcoides biomarker gene quantification to predict in situ chlorinated ethene detoxification potential." *Environmental Science and Technology*, 44(13), 5127–5133.

Ritalahti, K. M., Hatt, J. K., Petrovskis, E., and Loffler, F. E. (2010b). "Groundwater Sampling for Nucleic Acid Biomarker Analysis." *Handbook of Hydrocarbon and Lipid Microbiology*, 5(1), 3407–3418.

Riva, M., Guadagnini, A., Fernandez-Garcia, D., Sanchez-Vila, X., and Ptak, T. (2008). "Relative importance of geostatistical and transport models in describing heavily tailed breakthrough curves at the Lauswiesen site." *Journal of Contaminant Hydrology*, 101(1), 1–13.

Rivett, M. O., Dearden, R., and Wealthall, G. (2010). "Streamtube project overview : longitudinal transect assessment of the SABRE site DNAPL source zone." *CL:aire Bulletin*, Resear.

Rivett, M. O., Chapman, S. W., Allen-King, R. M., Feenstra, S., and Cherry, J. A. (2006). "Pump-and-Treat Remediation of Chlorinated Solvent Contamination at a Controlled Field-Experiment Site." *Environmental Science & Technology*, 40(21), 6770–6781.

Robert, C. P. (2015). "The Metropolis-Hastings algorithm." *arXiv:1504.01896 [stat]*.

Roberts, J. (2017). "Optimizing Injection Methods Using High Quality Anaerobic Injection Water and Dealing with Low pH Groundwater During Bioremediation of Chlorinated Solvents." Denver, Colorado.

Rodriguez, D. (2006). "Significance of diffused zone mass storage and rebound in determing the longevity of solute plumes emanating from heterogeneous DNAPL source zones."

Rubin, Y. (2003). *Applied Stochastic Hydrogeology*. Oxford University Press, Oxford ; New York.

Sabalowsky, A. R., and Semprini, L. (2010a). "Trichloroethene and cis-1,2-dichloroethene concentration-dependent toxicity model simulates anaerobic dechlorination at high concentrations: I. batch-fed reactors." *Biotechnology and Bioengineering*, 107(3), 529–539.

Sabalowsky, A. R., and Semprini, L. (2010b). "Trichloroethene and cis-1,2-dichloroethene concentration-dependent toxicity model simulates anaerobic dechlorination at high concentrations. II: Continuous flow and attached growth reactors." *Biotechnology and Bioengineering*, 107(3), 540–549.

Saenton, S., and Illangasekare, T. H. (2007). "Upscaling of mass transfer rate coefficient for the numerical simulation of dense nonaqueous phase liquid dissolution in heterogeneous aquifers." *Water Resources Research*, 43(2).

Sale, T. C., Newell, C., Stroo, H. F., Hinchee, R., and Johnson, P. (2008). *Frequently Asked Questions Regarding Management of Chlorinated Solvents in Soils and Groundwater*. Environmental Security Technology Certification Program Office (DOD). Arlington, Va.

Sale, T., Parker, B. L., Newell, C. J., and Devlin, J. F. (2013). *Management of Contaminants Stored in Low Permeability Zones - A State of the Science Review*. SERDP Project, Fort Collins, Colorado.

Sardin, M., Schweich, D., Leij, F. J., and van Genuchten, M. T. (1991). "Modeling the Nonequilibrium Transport of Linearly Interacting Solutes in Porous Media: A Review." *Water Resources Research*, 27(9), 2287–2307.

Schaefer, C. E., Callaghan, A. V., King, J. D., and McCray, J. E. (2009a). "Dense Nonaqueous Phase Liquid Architecture and Dissolution in Discretely Fractured Sandstone Blocks." *Environmental Science & Technology*, 43(6), 1877–1883.

Schaefer, C. E., Condee, C. W., Vainberg, S., and Steffan, R. J. (2009b). "Bioaugmentation for chlorinated ethenes using Dehalococcoides sp.: Comparison between batch and column experiments." *Chemosphere*, 75(2), 141–148.

Schaefer, C. E., Towne, R. M., Vainberg, S., McCray, J. E., and Steffan, R. J. (2010). "Bioaugmentation for Treatment of Dense Non-Aqueous Phase Liquid in Fractured Sandstone Blocks." *Environmental Science & Technology*, 44(13), 4958–4964.

Scheutz, C., Broholm, M. M., Durant, N. D., Weeth, E. B., Jørgensen, T. H., Dennis, P., Jacobsen, C. S., Cox, E. E., Chambon, J. C., and Bjerg, P. L. (2010). "Field Evaluation of Biological Enhanced Reductive Dechlorination of Chloroethenes in Clayey Till." *Environmental Science & Technology*, 44(13), 5134–5141.

Seagren, E. A., Rittmann, B. E., and Valocchi, A. J. (1993). "Quantitative evaluation of flushing and biodegradation for enhancing in situ dissolution of nonaqueous-phase liquids." *Journal of Contaminant Hydrology*, 12(1–2), 103–132.

Seagren, E. A., Rittmann, B. E., and Valocchi, A. J. (1994). "Quantitative Evaluation of the Enhancement of NAPL-Pool Dissolution by Flushing and Biodegradation." *Environmental Science & Technology*, 28(5), 833–839.

Semkiw, E. S., and Barcelona, M. J. (2011). "Field Study of Enhanced TCE Reductive Dechlorination by a Full-Scale Whey PRB." *Groundwater Monitoring & Remediation*, 31(1), 68–78.

Seyedabbasi, M. A., Newell, C. J., Adamson, D. T., and Sale, T. C. (2012). "Relative contribution of DNAPL dissolution and matrix diffusion to the long-term persistence of chlorinated solvent source zones." *Journal of Contaminant Hydrology*, 134–135, 69–81.

Shang, H. (2015). "Geotechnical laboratory characterization of sand- zeolite mixtures."

Sleep, B. E., Seepersad, D. J., Mo, K., Heidorn, C. M., Hrapovic, L., Morrill, P. L., McMaster, M. L., Hood, E. D., Lebron, C., Lollar, B. S., Major, D. W., and Edwards, E. A. (2006). "Biological enhancement of tetrachloroethene dissolution and associated microbial community changes." *Environmental Science and Technology*, 40(11), 3623–3633.

Soga, K., Page, J. W. E., and Illangasekare, T. H. (2004). "A review of NAPL source zone remediation efficiency and the mass flux approach." *Journal of Hazardous Materials*, Elsevier, 110(1–3), 13–27.

Stroo, H. F., Leeson, A., Marqusee, J. A., Johnson, P. C., Ward, C. H., Kavanaugh, M. C., Sale, T. C., Newell, C. J., Pennell, K. D., Lebrón, C. A., and Unger, M. (2012). "Chlorinated Ethene Source Remediation: Lessons Learned." *Environmental Science & Technology*, 46(12), 6438–6447.

Stroo, H. F., Leeson, A., and Ward, C. H. (2013). *Bioaugmentation for Groundwater Remediation: an Overview. Bioaugmentation for Groundwater Remediation*, Springer, New York, NY.

Stroo, H. F., Unger, M., Ward, C. H., Kavanaugh, M. C., Vogel, C., Leeson, A., Marqusee, J., and Smith, B. P. (2003). "Remediating chlorinated solvent source zones." *Environmental Science & Technology*, 37(11), 224A-230A.

Stroo, H. F., and Ward, C. H. (2010). *In Situ Remediation of Chlorinated Solvent Plumes*.

Suarez, M. P., and Rifai, H. S. (1999). "Biodegradation Rates for Fuel Hydrocarbons and Chlorinated Solvents in Groundwater." *Bioremediation Journal*, 3(4), 337–362.

Suchomel, E. J., and Pennell, K. D. (2006). "Reductions in Contaminant Mass Discharge Following Partial Mass Removal from DNAPL Source Zones." *Environmental Science & Technology*, American Chemical Society, 40(19), 6110–6116.

Sun, N.-Z., and Yeh, W. W.-G. (1990). "Coupled inverse problems in groundwater modeling: 1. Sensitivity analysis and parameter identification." *Water Resources Research*, 26(10), 2507–2525.

Sung, Y., Fletcher, K. E., Ritalahti, K. M., Apkarian, R. P., Ramos-Hernández, N., Sanford, R. A., Mesbah, N. M., and Löffler, F. E. (2006). "Geobacter lovleyi sp. nov. strain SZ, a novel metal-reducing and tetrachloroethene-dechlorinating bacterium." *Applied and Environmental Microbiology*, 72(4), 2775–2782.

Sykes, J. F., Wilson, J. L., and Andrews, R. W. (1985). "Sensitivity Analysis for Steady State Groundwater Flow Using Adjoint Operators." *Water Resources Research*, 21(3), 359–371.

Taylor, T. P., Pennell, K. D., Abriola, L. M., and Dane, J. H. (2001). "Surfactant enhanced recovery of tetrachloroethylene from a porous medium containing low permeability lenses 1. Experimental studies." *Journal of Contaminant Hydrology*, 48(3–4), 325–350.

The MathWorks Inc. (2016). *Matlab*. The MathWorks Inc., Natick, Massachusetts.

Tillotson, J. M., and Borden, R. C. (2017). "Rate and extent of chlorinated ethene removal at 37 ERD sites." *Journal of Environmental Engineering (United States)*, 143(8), 1–10.

Torlapati, J., Clement, T. P., Schaefer, C. E., and Lee, K. K. (2012). "Modeling Dehalococcoides sp. Augmented Bioremediation in a Single Fracture System." *Groundwater Monitoring & Remediation*, 32(3), 75–83.

Totten, Annable, Jawitz, and Delfino. (2007). "Fluid and Porous Media Property Effects on Dense Nonaqueous Phase Liquid Migration and Contaminant Mass Flux." *Environmental Science & Technology*, American Chemical Society, 41(5), 1622–1627.

Townley, L. R., and Wilson, J. L. (1985). "Computationally Efficient Algorithms for Parameter Estimation and Uncertainty Propagation in Numerical Models of Groundwater Flow." *Water Resources Research*, Wiley-Blackwell, 21(12), 1851–1860.

Troldborg, M., Nowak, W., Lange, I. V., Santos, M. C., Binning, P. J., and Bjerg, P. L. (2012). "Application of Bayesian geostatistics for evaluation of mass discharge uncertainty at contaminated sites." *Water Resources Research*, 48(9), 1–19.

Troldborg, M., Nowak, W., Tuxen, N., Bjerg, P. L., Helmig, R., and Binning, P. J. (2010). "Uncertainty evaluation of mass discharge estimates from a contaminated site using a fully Bayesian framework." *Water Resources Research*, 46(12), 1–19.

Valocchi, A. J. (1990). "Use of temporal moment analysis to study reactive solute transport in aggregated porous media." *Geoderma*, 46(1), 233–247.

Vermeulen, N. P. E. (1991). "Handbook of Chemical Property Estimation Methods. W. J. Lyman, W. F. Reehl and D. H. Rosenblatt. American Chemical Society, Washington DC, 1990. 960 pp., US $49.95. ISBN 0-8412-1761-0." *Recueil des Travaux Chimiques des Pays-Bas*, 110(2), 61–61.

Verschueren, K. (2001). *Handbook of environmental data on organic chemicals*. Wiley.

Vilhelmsen, T. N., and Ferré, P. A. "Ty." (2017). "Supplementary material for: Extending data worth analyses to select multiple observations targeting multiple forecasts Linear uncertainty analysis."

Villermaux, J. (1987). "Chemical engineering approach to dynamic modelling of linear chromatography: A flexible method for representing complex phenomena from simple concepts." *Journal of Chromatography A*, 406, 11–26.

Villermaux, J. (1990). "Dynamics of linear interactions in heterogeneous media: A systems approach." *Journal of Petroleum Science and Engineering*, 4(1), 21–30.

Wang, C., Komodakis, N., and Paragios, N. (2013). "Markov Random Field modeling, inference & learning in computer vision & image understanding: A survey." *Computer Vision and Image Understanding*, 117(11), 1610–1627.

Wang, P. P., and Zheng, C. (2005). "Contaminant transport models under random sources." *Ground Water*, Wiley/Blackwell (10.1111), 43(3), 423–433.

Wang, X. (2013). "Dense Nonaqueous Phase Liquid (DNAPL) Source Zone Characterization in Highly Heterogeneous Permeability Fields." Master's thesis, Tufts University.

Wang, Y., Li, Y., Costanza, J., Abriola, L. M., and Pennell, K. D. (2012). "Enhanced Mobility of Fullerene (C60) Nanoparticles in the Presence of Stabilizing Agents." *Environmental Science & Technology*, 46(21), 11761–11769.

Widdowson, M. A. (2004). "Modeling Natural Attenuation of Chlorinated Ethenes Under Spatially Varying Redox Conditions." *Biodegradation*, 15(6), 435–451.

Wilson, R., and Cia, Z. (2012). "Source area DNAPL bioremediation: performance monitoring and assessment. CL:AIRE SABRE Bulletin 6." CL:AIRE.

Wöhling, T., Geiges, A., and Nowak, W. (2016). "Optimal Design of Multitype Groundwater Monitoring Networks Using Easily Accessible Tools." *Groundwater*, 54(6), 861–870.

Wolin, E. A., Wolin, M. J., and Wolfe, R. S. (1963). "Formation of Methane by Bacterial Extracts." *The Journal of biological chemistry*, 238(6), 2882–6.

Wu, J., Zheng, C., and Chien, C. C. (2005). "Cost-effective sampling network design for contaminant plume monitoring under general hydrogeological conditions." *Journal of contaminant hydrology*, 77(1–2), 41–65.

Xue, L., Zhang, D., Guadagnini, A., and Neuman, S. P. (2014). "Multimodel Bayesian analysis of groundwater data worth." *Water Resources Research*, 50(11), 8481–8496.

Yamada, T., Sekiguchi, Y., Hanada, S., Imachi, H., Ohashi, A., Harada, H., and Kamagata, Y. (2006). "Anaerolinea thermolimosa sp. nov., Levilinea saccharolytica gen. nov., sp. nov. and Leptolinea tardivitalis gen. nov., sp. nov., novel filamentous anaerobes, and description of the new classes Anaerolineae classis nov. and Caldilineae classis nov. in the bacterial phylum Chloroflexi." *International Journal of Systematic and Evolutionary Microbiology*, 56(6), 1331–1340.

Yang, L., Wang, X., Mendoza-Sanchez, I., and Abriola, L. M. (2018). "Modeling the influence of coupled mass transfer processes on mass flux downgradient of heterogeneous DNAPL source zones." *Journal of Contaminant Hydrology*, 211, 1–14.

Yang, Y., and McCarty, P. L. (2000). "Biologically Enhanced Dissolution of Tetrachloroethene DNAPL." *Environmental Science & Technology*, 34(14), 2979–2984.

Yang, Y., and McCarty, P. L. (2002). "Comparison between donor substrates for biologically enhanced tetrachloroethene DNAPL dissolution." *Environmental Science & Technology*, 36(15), 3400–3404.

Yeh, H.-D., Chang, T.-H., & Lin, Y.-C. (2007). Groundwater contaminant source identification by a hybrid heuristic approach. *Water Resources Research*, *43*(9). https://doi.org/10.1029/2005WR004731

Yu, S., Dolan, M. E., and Semprini, L. (2005). "Kinetics and Inhibition of Reductive Dechlorination of Chlorinated Ethylenes by Two Different Mixed Cultures." *Environmental Science & Technology*, 39(1), 195–205.

Yu, S., and Semprini, L. (2004). "Kinetics and modeling of reductive dechlorination at high PCE and TCE concentrations." *Biotechnology and Bioengineering*, 88(4), 451–464.

Yu, S. Y., Chae, G. T., Jeon, K. H., Jeong, J. S., and Park, J. G. (2006). "Trichloroethylene Contamination in Fractured Bedrock Aquifer in Wonju, South Korea." *Bulletin of Environmental Contamination and Toxicology*, 76(2), 341–348.

Van Der Zaan, B., Hannes, F., Hoekstra, N., Rijnaarts, H., De Vos, W. M., Smidt, H., and Gerritse, J. (2010). "Correlation of Dehalococcoides 16S rRNA and chloroethene-reductive dehalogenase genes with geochemical conditions in chloroethene-contaminated groundwater." *Applied and Environmental Microbiology*, 76(3), 843–850.

Zeeb, P., and Houlden, L. (2010). "Overview of the SABRE field test. CL:AIRE SABRE Bulletin 5." CL:AIRE.

Zeng, L., Shi, L., Zhang, D., & Wu, L. (2012). A sparse grid based Bayesian method for contaminant source identification. *Advances in Water Resources*, *37*, 1–9. https://doi.org/10.1016/j.advwatres.2011.09.011

Zhang, C., Werth, C. J., and Webb, A. G. (2008). "Investigation of surfactant-enhanced mass removal and flux reduction in 3D correlated permeability fields using magnetic resonance imaging." *Journal of Contaminant Hydrology*, 100(3–4), 116–126.

Zhang, J., Zeng, L., Chen, C., Chen, D., & Wu, L. (2015). Efficient Bayesian experimental design for contaminant source identification. *Water Resources Research*, *51*(1), 576–598. https://doi.org/10.1002/2014WR015740

Zheng, C., and Wang, P. P. (1999). *MT3DMS: A modular three-dimensional multi-species transport model for simulation of advection, dispersion, and chemical reactions of contaminants in ground-water systems. Documentation and user's guide*. Contract Report, U.S. Army Engineer Research and Development, Vicksburg, MS.

Zinn, B., and Harvey, C. F. (2003). "When good statistical models of aquifer heterogeneity go bad: A comparison of flow, dispersion, and mass transfer in connected and multivariate Gaussian hydraulic conductivity fields." *Water Resources Research*, 39(3), 1051.

VII. Appendices

VII.A. Practical Considerations: Implementation of Site Characterization Tool/Screening Model

Recognizing the importance of DNAPL source zone characterization for assessment of remediation effectiveness and prediction of contaminant persistence, several approaches have been developed to link averaged characterization metrics to mass discharge behavior and source zone longevity (Christ et al., 2006, 2010; Jawitz et al., 2005; Saenton & Illangasekare, 2007). However, accurate assessment of such source zone architecture metrics is quite challenging in real-word applications.

This appendix presents a straightforward framework for implementation of mathematical models for near source site characterization and plume response prediction. Application of this modeling framework is illustrated with a hypothetical case study. The framework couples the 2D BRAINS model, described in sections II.7 and III.6 of this report, with an existing upscaled mass transfer model previously developed under SERDP sponsorship (Christ et al., 2010). The trained BRAINS model is used to generate a set of 2D representations of contaminant mass distributions along a plume centerline. The underlying assumption in this approach is that the source zone architecture metrics calculated from these 2D realizations of contaminant mass along the plume centerline are representative of 3D source zone metrics. These results enable the estimation of effective, or upscaled, parameters employed in the screening model, as well as the estimation of the uncertainty associated with screening model predictions.

It is important to note that, in this research, BRAINS was trained specifically for a highly heterogeneous categorical formation. It is anticipated that, while the developed features and model structure are robust, the model itself will need to be retrained for applications to different depositional environments. This training will provide a library of trained models (i.e. BRAINS library) applicable for different types of geological formations and across different scales of heterogeneity. Thus, although the present work focuses on 2D application of the Discriminative Random Field (DRF) model for a specific unconsolidated formation type, it should be viewed as a proof of principle for the application of this modeling framework and as the first step in generating a 3D characterization tool (i.e. library of models) that can be applied over a wide range of conditions observed at contaminated sites.

The modeling framework presented in Figure A.1.1 represents the work flow for site characterization and screening-level down gradient flux assessment. Here, once a DNAPL source zone site has been selected, available data on the site geology/stratigraphy are collected and matched to a representative site subsurface permeability model. The permeability models are then linked to a library of machine learning characterization tools (i.e. BRAINS library). The research summarized in Sections II.7 and III.6 demonstrated both the feasibility and methodology for the development of the trained BRAINS model. If a characterization library is not available, the methodology developed and presented in Sections II.7 and III.6 could be implemented to develop a site-specific characterization tool. Such an exercise, however, would be simulation intensive and likely require additional site data collection.

After a site-matched characterization tool is obtained, site managers employ BRAINS, along with measured borehole data to estimate source zone metrics. It is important to note that this procedure requires only the field-measured borehole data (permeability, saturation, sorption and aqueous concentration) as inputs, as well as some geostatistical characteristics of the subsurface domain. The borehole contaminant mass data should be obtained from the vicinity of the plume centerline.

Figure A.1.1. Flow chart outlining the suggested Modeling Framework

The flow chart contains the following elements:

- Identify site with possible DNAPL contamination
- Assemble/review site geology/stratigraphy data
- Assemble/review contaminant mass data
- Delimit source zone region for analysis/identify data gaps
- Sufficient data are available?
  - no → Collect additional concentration data
  - yes →
- Generate multiple (e.g. 100) conditioned permeability field realizations
- Select site-appropriate tool from BRAINS library
- Generate equiprobable realizations of contaminant mass distribution for each permeability field
- Estimate source zone metrics and uncertainty from average of realizations
- Employ up-scaled screening model to estimate plume response for range of predicted metrics
- Results consistent w/existing CSM?
  - yes →
  - no → Modify existing CSM and examine site management alternatives and "short-term" metrics/objectives
- Re-run Upscaled Model to Rapidly Prototype Alternatives
- Is site amenable to active treatment?
  - yes → Develop site specific model to design treatment
  - no → Recommend Alternative Management Strategy based on Protocol Results
- Implement treatment strategies
- Collect data on treatment progress
- Update Tool with Newly Collected Data
- Protocol Results & associated data support Site Transition/Closure

This requirement arises from the fact that the BRAINS model was developed and validated in 2D in this research. The requirement could be relaxed in the future by extending and training the BRAINS model in 3D.

As discussed in section III.6.6, the first step in applying BRAINS to a real-word problem is to generate multiple realizations of the permeability field, conditioned on measured permeability borehole data and based on geostatistical knowledge of the subsurface domain. Generation of permeability realizations can be accomplished using readily available geostatistical software packages such as GSLIB (Deutsch & Journel, 1998), TPROGs (Carle, 1999) or SURFER (Golden Software, LLC.) depending on the geostatistical characteristics of the formation (e.g. categorical, Gaussian, etc.).

Once the permeability realizations have been generated, the site-appropriate trained BRAINS model is applied to each of these permeability fields to generate a set of equiprobable realizations of contaminant mass distribution along the plume centerline plane. Application of this model ensures that all realizations are conditioned on the borehole data for (DNAPL) saturations and (aqueous and sorbed) concentrations.

As explained in section III.6, a set of source zone characterization metrics, such as DNAPL mass spatial moments and pool fraction (PF), can be calculated from the average (saturation and concentration) realizations for each permeability field. From these metric sets, 95 percentile boundaries for each metric can be computed, as a measure of estimated range, using the mean (μ) and standard deviation (s) of the metric over all permeability realizations (i.e. $\mu \pm 2s$). This procedure provides a simple and straightforward approach to predict the estimated range of characterization metrics across all equiprobable permeability realizations.

Once the estimated ranges for source zone (SZ) metrics have been estimated, the Protocol employs the upscaled screening tool, presented by Christ et al., (2010), to predict mass recovery behavior. This two-domain upscaled mass transfer model was shown to accurately estimate dissolution behavior from ganglia- and pool-dominated source zones representative of the highly non-uniform DNAPL mass distributions typical of real source zones for all levels of mass recovery (Christ et al., 2010). Screening tool output can then guide preliminary site remediation decisions and future in-source data collection.

The two-domain upscaled model (i.e. Equations A.1.1a,b) relates the flux-averaged effluent concentration (C_{out}^{Total}) to a given level of mass removal (M/M_0) using three site-specific parameters: the initial pool fraction (PF_0), the fraction of flux eluting from these pool regions (f_x^p), and the flux-averaged down-gradient contaminant concentration ($\overline{C_0}$).

$$\frac{C_{out}^{Total}}{C_{eq}} = 2 - \left(1 - \frac{f_x^p \overline{C_o}}{C^{eq}}\right)^{\left(\frac{PF \cdot \left(M/M_o\right)}{PF_0}\right)^{0.5}} - \left(1 - \frac{\left(1 - f_x^p\right)\overline{C_0}}{C^{eq}}\right)^{\left(\frac{(1-PF)\left(M/M_o\right)}{1-PF_0}\right)^{1.5\left(\frac{1-PF_0}{PF_0}\right)^{-0.26}}} \quad \text{(A.1.1a)}$$

$$PF = \begin{cases} 1 - \left(1 - PF_0\right)\left(1 - \left(\frac{M}{\left(1-PF_0\right)M_o}\right)^{5.6 \pm 2.6}\right) & if \ \left(\frac{M}{M_o}\right) \leq \left(1 - PF_0\right) \\ 1 \ otherwise \end{cases} \quad \text{(A.1.1b)}$$

where C^{eq} is the equilibrium solubility of the contaminant. Equation A.1.1 is applicable to unconsolidated aquifers contaminated with non-aqueous phase liquids and is expected to provide

a reasonable flux-averaged concentration prediction regardless of the level of heterogeneity in the permeability field.

All the characterization metrics involved in Equation A.1.1 can be determined from BRAINS's predicted average saturation and concentration realizations for each permeability field.

The initial pool fraction (PF_0) metric, defined as the fraction of DNAPL mass in pool regions, can be calculated from the average saturation realizations generated with BRAINS using Equation A.1.2. Here source zone mass is separated (or categorized) spatially into ganglia (i.e., residual or finger)) ($s_n \leq s_{nr}^{max}$) and pool regions ($s_n > s_{nr}^{max}$), using the maximum residual DNAPL saturation (s_{nr}^{max}) as the ganglia-pool saturation threshold:

$$PF = \frac{\sum \rho^n s_n n \Delta x \Delta y \Delta z \forall s_n \geq s_{nr}^{max}}{\sum \rho^n s_n n \Delta x \Delta y \Delta z} = \frac{\sum s_n \forall s_n \geq s_{nr}^{max}}{\sum s_n} \qquad (A.1.2)$$

where ρ^n is the DNAPL density, s_n is the DNAPL saturation, n is the porosity, and Δx, Δy, and Δz are the cell dimensions in the x, y, and z directions, respectively.

The steps for calculating initial fraction of flux attributed to pool dissolution (f_x^p) in a 3D domain is also straightforward (Christ et al., 2010). The idea here is that the fraction of flux emanating from pool regions (f_x^p) is proportional to the projected fraction of these pool areas onto the 2-D down-gradient control plane, oriented perpendicular to regional flow (Figure A.1.2):

$$f_x^p = \frac{A_{projected}^p}{A_{projected}^p + A_{projected}^g} = \frac{\sum \forall \max(s_n(:,y,z)) \geq s_{nr}^{max}}{\sum \forall \max(s_n(:,y,z)) \geq s_{nr}^{max} + \sum \forall \max(s_n(:,y,z)) < s_{nr}^{max}} \qquad (A.1.3)$$

Here $A_{projected}^p$ and $A_{projected}^g$ are the projected areas of DNAPL pools and ganglia onto the down-gradient control plane.
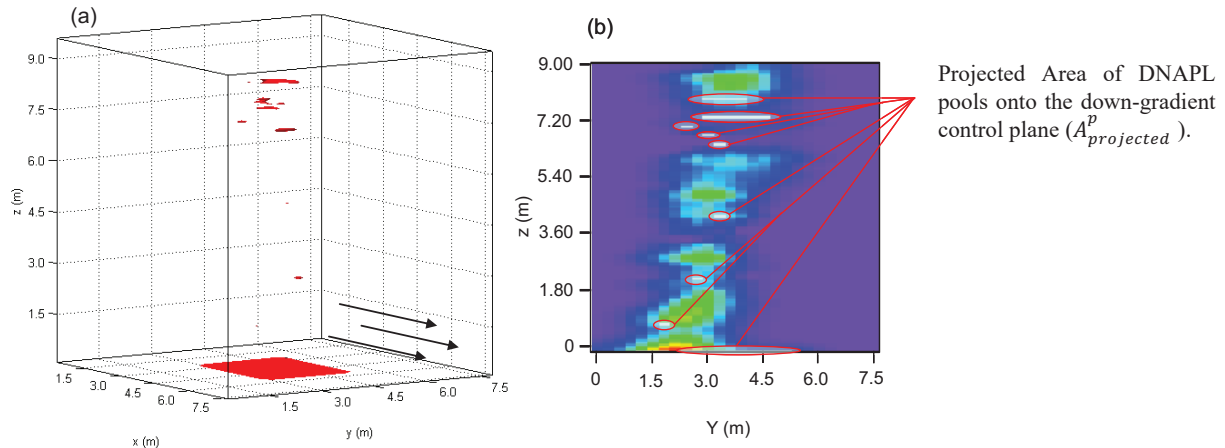
Figure A.1.2. (a) Three-dimensional distribution of pools in a non-uniform source-zone (b) resulting contaminant concentration field at the down-gradient boundary with regions eluting from pool zones ($A_{projected}^p$) highlighted.

A similar approach can be applied to calculate f_x^p in a 2D domain (i.e. average saturation results from BRAINS) by calculating the fraction of projected pool regions across a 1D control line (column) oriented perpendicular to the flow at the down-gradient boundary. Characterization of pool locations within a source zone is achievable using the average saturation results from BRAINS for each permeability realization.

The initial flux-averaged down-gradient concentration ($\overline{C_0}$), can also be determined using the average concentration results from BRAINS. This metric is calculated as the mean aqueous concentration of the grids along the down-gradient column weighted by their permeability values.

$$\overline{C_0} = \frac{\int KiC_a \mathrm{d}A}{\int Ki \mathrm{d}A} = \frac{\sum KC_a \mathrm{d}A}{\sum K \mathrm{d}A} \tag{A.1.4}$$

where K is the hydraulic conductivity $[\mathrm{LT^{-1}}]$, i is the hydraulic gradient $[-]$, A is the area of control plane $[\mathrm{L^2}]$, C_a is the aqueous phase concentration $[\mathrm{ML^{-3}}]$. The integral/summation is applied along a down-gradient transect. It is noteworthy that, alternatively other estimates of flux-averaged concentration, such as transect observations or in-situ flux meters can be employed for calculating initial FAC.

By incorporating the extremes (i.e. 95 percentile boundaries) and expected values of these predicted source zone metrics into the upscaled screening model, the mass recovery behavior can be bracketed for most realistic source zone scenarios.

Case Study

This section presents an application of the modeling framework, including the Site Characterization Tool and Screening Model, for the hypothetical case study described in Section III.7.

As explained in section III.7, a transition-probability-based Markov Chain (TP/MC) approach using TPORGs software (Carle, 1999) was employed to generate a series of 100 equiprobable three-dimensional (3-D) permeability realizations conditioned on synthetic borehole measurements with the same discretization. X-Z cross section center slices of the 3-D realizations were extracted to form 2-D domains, where one borehole was located at a down-gradient transect (assessment location for screening level model predictions) and three other boreholes were installed an equal distance apart. An example of a 2D permeability field reconstruction employing a transition-probability-based Markov Chain (TP/MC) approach using TPROGs software (Carle, 1999) is shown in Figure A.1.3. These permeability field realizations were constructed based on geostatistical characteristics of the T$\ddot{u}$bingen aquifer at the Herten site (Maji, 2005) (Table A.1.1).

Table A.1.1. Soil properties at Herten site.

Lithofacies	Volumetric Proportion	Permeability (m^2)
Gs-x	29%	5.14E-12
GCm	57%	2.63E-11
S-x	6%	1.14E-10
bGcm,i	6%	1.49E-08
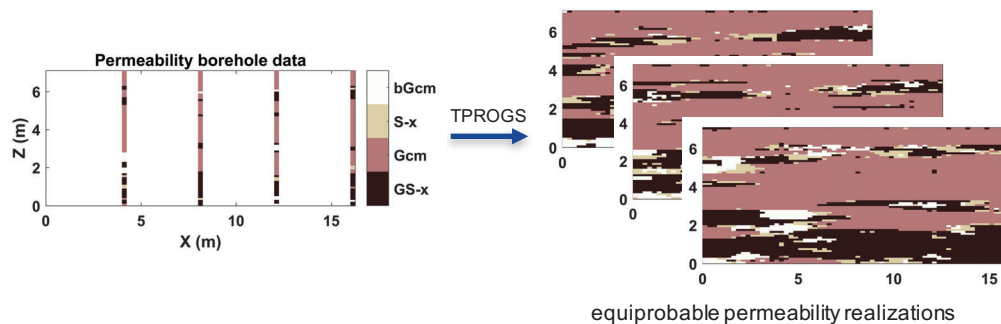
Figure A.1.3. Permeability field reconstruction from four permeability boreholes using TPROGs.

Among these 100 realizations, one permeability domain was selected as the "true" case (Figure A.1.4). This domain was then used to generate "true" initial distributions of DNAPL, aqueous and sorbed mass. DNAPL release, migration and transport was modeled using MVALOR and MT3DMS software to obtain the "true" initial aqueous and sorbed concentrations. A detailed description of DNAPL infiltration and transport model set up is presented in II.5.2 and II.5.3.3.
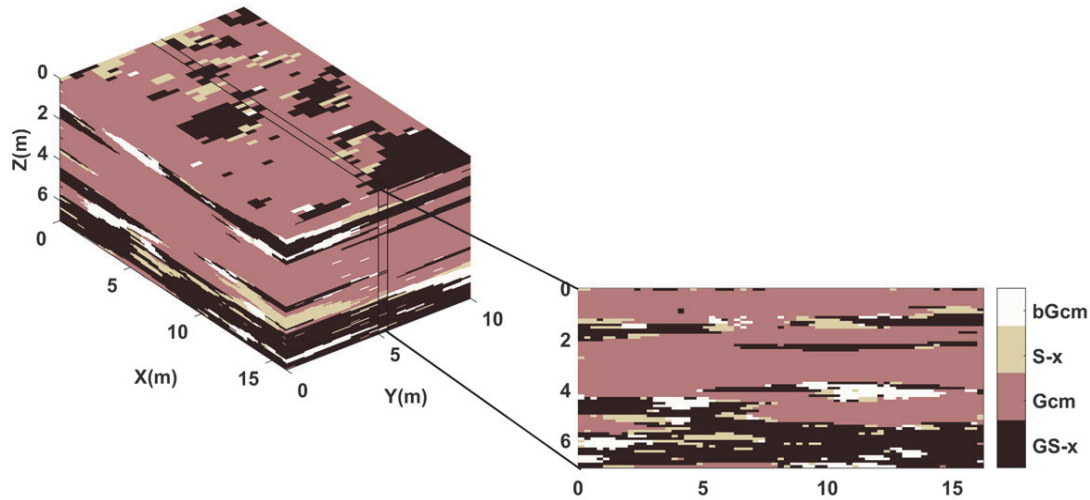
Figure A.1.4. True 3-D conductivity field and selected 2-D x-z plane center slice.

It should be noted that, in this case study the validated MVALOR and MT3DMS simulators were adopted to reconstruct realistic field data. The permeability values, DNAPL distribution, aqueous and sorbed mass concentrations simulated using the methods described above would be obtained directly from the site in a real field application (as described in Figure A.1.1).

Using the "true" aqueous concentrations and DNAPL saturations in the four boreholes, the trained BRAINS model was then applied to generate 2000 realizations of aqueous concentration and DNAPL saturation for each permeability field. The sorbed concentration distribution was obtained by assuming equilibrium with the aqueous concentration. The model outputs an average (saturation and concentration) realization over 2000 equiprobable realizations for each of the 100 permeability fields (i.e. 100 averaged saturation and concentration realizations). Examples of these averaged aqueous concentration and DNAPL saturation distributions are presented in Figure A.1.5.
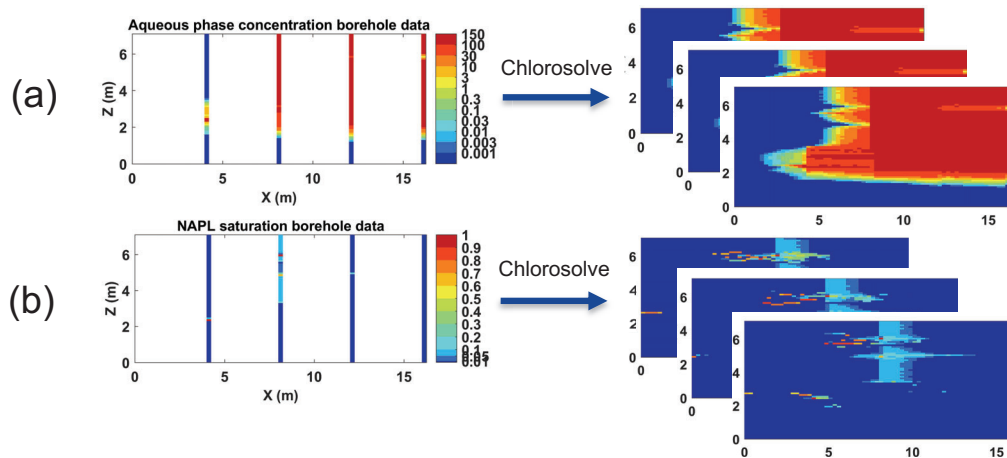
Figure A.1.5. Equiprobable realizations of, (a) aqueous concentration, (b) DNAPL saturation generated from BRAINS.

Source zone characterization metrics can now be calculated for each of these average realizations (Equations A.1.2-4), yielding a predicted range of values for each metric. Table A.1.2 compares the predicted (i.e. from BRAINS) and true values for the two metrics (PF_0 and f_x^p) used in the upscaled screening model (Equation A.1.1). The initial flux-averaged down-gradient concentration ($\overline{C_0}$), was calculated using the down-gradient borehole concentration and permeability data and hence is the same for the true and predicted cases.

Table A.1.2. Comparison of predicted and true metrics used in upscaled screening model

METRICS	PF_0			f_x^p		
	True	Predicted		True	Predicted	
		mean	StD		mean	StD
	0.432	0.487	0.058	0.143	0.234	0.04

The flux-averaged concentration (FAC) at the down-gradient boundary was then calculated by incorporating these predicted source zone architecture metrics into the two-domain upscaled screening model (Equation A.1.1). Figure A.1.6 presents the estimated range for mass recovery behavior calculated using the upscaled screening model based on true metric values (solid green line), as well as the expected and extreme (i.e. 95 percentile boundaries) of source zone metrics determined from BRAINS (solid black and dashed lines). The true mass recovery behavior based on MT3DMS forward simulation results is also presented in this figure (i.e. blue squares).
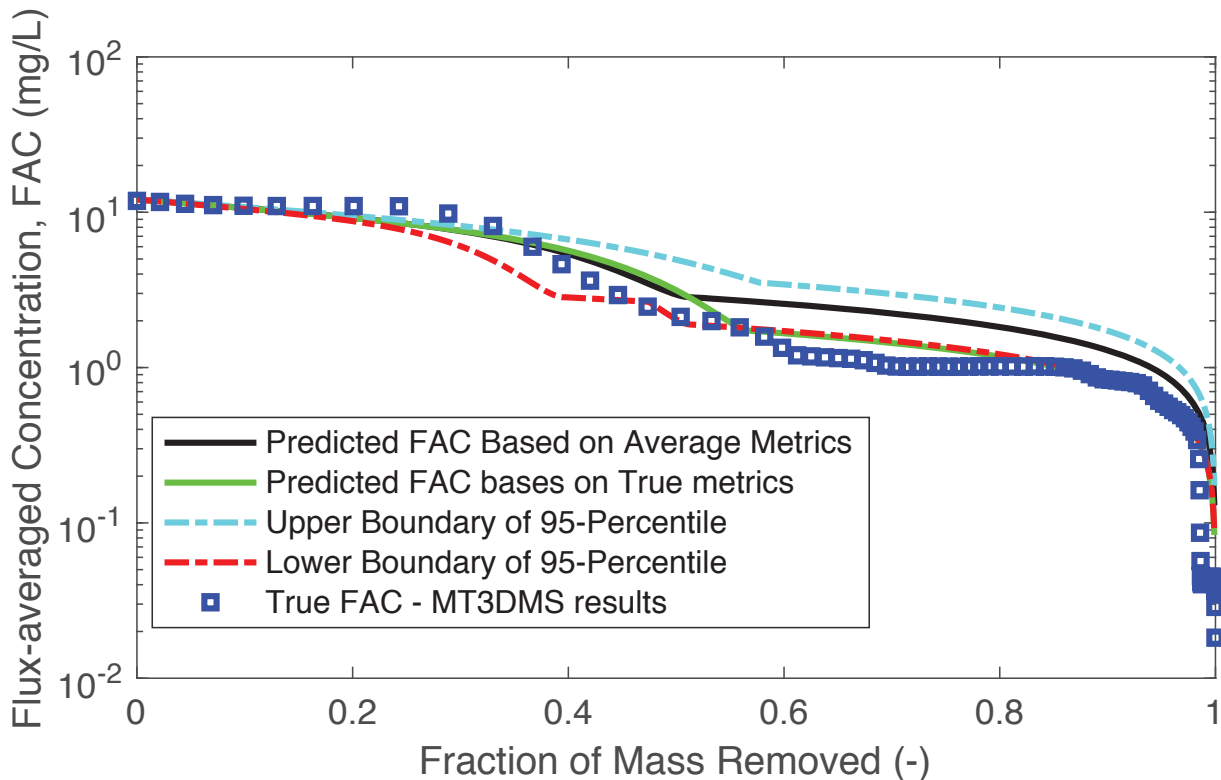
Figure A.1.6. Comparison between predicted range and true mass recovery behavior (flux-averaged concentration as a function of fraction of mass removed).

It is clear from Figure A.1.6 that the upscaled screening model provides realistic mass recovery predictions given the true metric values (i.e. solid green line vs. blue squares). These results also suggest that the FAC values predicted from the screening tool based on expected (average) values of source zone metrics qualitatively match the 'true' results specifically for $M/M_0 <$ PF$_0$. The deviation observed between the predicted (solid black line) and true results (blue squares) for $M/M_0 >$ PF$_0$ can be attributed to the higher f_x^p values estimated using BRAINS compared to the true metric value (i.e. 0.234 vs 0.143). Nonetheless, it is evident from these results that the upscaled screening model can successfully predict the likely behavior of plume response to source mass removal using the estimated source zone characterization metrics from BRAINS. For example, consistent with the true results, the screening model predictions suggest that more than 90% of the contaminant mass must be removed before the flux-averaged concentration at down-gradient boundary drops an order of magnitude, suggesting that this is a poor candidate for remediation technologies that employ flushing. This is mainly due to the fact that most of the contaminant mass in this case is stored in high saturated DNAPL pools.

The framework developed and presented in this research is applicable to bench-, pilot-, and field-scale scenarios that would generally be modeled using the advection-dispersion equation. Similar to the case study presented here, it is expected that this framework will provide a reasonable order-of-magnitude flux-averaged concentration range estimate by bracketing the mass recovery behavior, for most realistic source zone scenarios that are comprised of a combination of NAPL pools and ganglia regions.

VII.B. Supporting Data

VII.B.1. Groundwater Elevations

VII.B.2. Groundwater Chlorinated Ethene and Ethene Measurements

VII.B.3. Groundwater Water Quality Parameters

VII.B.4. Groundwater Dissolved Metals

VII.B.5. Groundwater Microbial Abundance

VII.B.6. Soil Boring Logs

VII.B.7. Soil Grain Size Results

VII.B.8. Soil VOC Results

VII.B.9. Groundwater Water Quality Parameters During Pilot Test

VII.B.10. Derivation of Adjoint States Control Equations and Marginal Sensitivity of Down-Gradient FAC with Respect to *ln(K)*

The control equations of forward flow and transport:

$$\mathbf{\nabla}(\mathbf{K}\nabla h) = 0 \tag{B.10.1}$$

$$\frac{\partial}{\partial t}(ns_a C_a) + \rho_b \frac{\partial S}{\partial t} = -\mathbf{\nabla}\left(\underline{\mathbf{q}}^a C_a\right) + \mathbf{\nabla}\left(\widetilde{\mathbf{D}}_h^a \nabla C_a\right) + \hat{k}\left(C_a^{eq} - C_a\right) \tag{B.10.2}$$

$$\frac{\partial}{\partial t}(ns_n \rho_n) = -\hat{k}\left(C_a^{eq} - C_a\right) \tag{B.10.3}$$

$$S = K_d C_a \tag{B.10.4}$$

Differentiate the control equations with respect to lnK:

$$\mathbf{\nabla}\left(\frac{\partial}{\partial \ln K}(\mathbf{K}\nabla h)\right) = 0 \tag{B.10.5}$$

$$\frac{\partial}{\partial t}\left(\frac{\partial}{\partial \ln K}(ns_a C_a)\right) + \rho_b \frac{\partial}{\partial \ln K}\left(\frac{\partial S}{\partial t}\right)$$
$$= -\mathbf{\nabla}\left(\frac{\partial}{\partial \ln K}\left(\underline{\mathbf{q}}^a C_a\right)\right) + \mathbf{\nabla}\left(\frac{\partial}{\partial \ln K}\left(\widetilde{\mathbf{D}}_h^a \nabla C_a\right)\right) + \frac{\partial}{\partial \ln K}\left(\hat{k}C_a^{eq} - \hat{k}C_a\right) \tag{B.10.6}$$

$$\frac{\partial}{\partial \ln K}\left(\frac{\partial}{\partial t}(ns_n \rho_n)\right) = -\frac{\partial \hat{k}}{\partial \ln K}\left(C_a^{eq} - C_a\right) \tag{B.10.7}$$

$$\frac{\partial S}{\partial \ln K} = \frac{\partial}{\partial \ln K}(K_d C_a) \tag{B.10.8}$$

Let:

$$\frac{\partial h}{\partial \ln K} = \Psi_h \qquad \frac{\partial C_a}{\partial \ln K} = \Psi_a \qquad \frac{\partial s_a}{\partial \ln K} = \Psi_n \qquad \frac{\partial S}{\partial \ln K} = \Psi_S \tag{B.10.9}$$

Thus:

$$\nabla\left(\frac{\partial}{\partial \ln K}(\mathbf{K}\nabla h)\right) = \nabla\left(\mathbf{K}\nabla\frac{\partial h}{\partial \ln K} + \frac{\partial \mathbf{K}}{\partial \ln K}\nabla h\right) = \nabla(\mathbf{K}\nabla\Psi_h + \mathbf{K}\nabla h) = 0 \tag{B.10.10}$$

$$\frac{\partial}{\partial t}(ns_a\Psi_a + nC_a\Psi_n) + \rho_b\frac{\partial\Psi_S}{\partial t}$$
$$= -\nabla\left(\underline{\mathbf{q}}^{\mathbf{a}}\Psi_a + \frac{\partial\underline{\mathbf{q}}^{\mathbf{a}}}{\partial \ln K}C_a\right) + \nabla\left(\widetilde{\mathbf{D}}_h^a\nabla\Psi_a + \frac{\partial\widetilde{\mathbf{D}}_h^a}{\partial \ln K}\nabla C_a\right) \tag{B.10.11}$$
$$+ \frac{\partial\widehat{k}}{\partial \ln K}\left(C_a^{eq} - C_a\right) - \widehat{k}\Psi_a$$

$$\frac{\partial}{\partial t}(-n\rho_n\Psi_n) = -\frac{\partial\widehat{k}}{\partial \ln K}\left(C_a^{eq} - C_a\right) + \widehat{k}\Psi_a \tag{B.10.12}$$

$$\Psi_S = K_d\Psi_a \tag{B.10.13}$$

in which:

$$\frac{\partial\underline{\mathbf{q}}^{\mathbf{a}}}{\partial \ln K} = \frac{\partial}{\partial \ln K}(-\mathbf{K}\nabla h) = -\mathbf{K}\nabla\Psi_h - \mathbf{K}\nabla h \tag{B.10.14}$$

$$\frac{\partial\widetilde{\mathbf{D}}_h^a}{\partial \ln K} = \frac{\partial\widetilde{\mathbf{D}}_h^a}{\partial\underline{\mathbf{q}}^{\mathbf{a}}}\frac{\partial\underline{\mathbf{q}}^{\mathbf{a}}}{\partial \ln K} = \frac{\partial\widetilde{\mathbf{D}}_h^a}{\partial\underline{\mathbf{q}}^{\mathbf{a}}}(-\mathbf{K}\nabla\Psi_h - \mathbf{K}\nabla h) \tag{B.10.15}$$

$$\frac{\partial\widehat{k}}{\partial \ln K} = \frac{\partial\widehat{k}}{\partial\underline{\mathbf{q}}^{\mathbf{a}}}\frac{\partial\underline{\mathbf{q}}^{\mathbf{a}}}{\partial \ln K} = \frac{\partial\widehat{k}}{\partial\underline{\mathbf{q}}^{\mathbf{a}}}(-\mathbf{K}\nabla\Psi_h - \mathbf{K}\nabla h) \tag{B.10.16}$$

Take an inner product of Ψ_h^* with (1) and integrate:

$$\iint_{V,t}\Psi_h^*[\nabla(\mathbf{K}\nabla\Psi_h + \mathbf{K}\nabla h)]\,dVdt = 0 \tag{B.10.17}$$

Take an inner product of Ψ_a^* with (2) and integrate:

$$\iint_{V,t}\Psi_a^*\left[\frac{\partial}{\partial t}(ns_a\Psi_a + nC_a\Psi_n) + \rho_b\frac{\partial\Psi_s}{\partial t} + \nabla\left(\underline{\mathbf{q}}^{\mathbf{a}}\Psi_a - \mathbf{K}\nabla\Psi_h C_a - \mathbf{K}\nabla h C_a\right)\right.$$
$$- \nabla\left(\widetilde{\mathbf{D}}_h^a\nabla\Psi_a - \frac{\partial\widetilde{\mathbf{D}}_h^a}{\partial\underline{\mathbf{q}}^{\mathbf{a}}}\mathbf{K}\nabla\Psi_h\nabla C_a - \frac{\partial\widetilde{\mathbf{D}}_h^a}{\partial\underline{\mathbf{q}}^{\mathbf{a}}}\mathbf{K}\nabla h\nabla C_a\right) \tag{B.10.18}$$
$$\left. - \frac{\partial\widehat{k}}{\partial\underline{\mathbf{q}}^{\mathbf{a}}}(-\mathbf{K}\nabla\Psi_h - \mathbf{K}\nabla h)\left(C_a^{eq} - C_a\right) + \widehat{k}\Psi_a\right]dVdt = 0$$

Take an inner product of Ψ_n^* with (3) and integrate:

$$\iint_{V,t}\Psi_n^*\left[-\frac{\partial}{\partial t}(n\rho_n\Psi_n) + \frac{\partial\widehat{k}}{\partial \ln K}\left(C_a^{eq} - C_a\right) - \widehat{k}\Psi_a\right]dvdt = 0 \tag{B.10.19}$$

Take an inner produce of Ψ_s^* with (4) and integrate:

$$\iint_{V,t} \Psi_S^* [\Psi_S - K_d \Psi_a] dvdt = 0 \tag{B.10.20}$$

A performance measure that quantifies some state of the system is defined as:

$$P = \iint_{V,t} \varsigma(\ln K, h, C_a, S, s_n) \, dVdt \tag{B.10.21}$$

where $\varsigma(\ln K, h, C_a, S, s_n)$ is a functional of the state of the system.

The marginal sensitivity of this performance measure with respect to $\ln K$ is obtained by differentiation equation:

$$\begin{aligned}
\frac{dP}{d\ln K} = \iint_{V,t} &\left[\frac{\partial \varsigma(\ln K, h, C_a, S, s_n)}{\partial \ln K} + \frac{\partial \varsigma(\ln K, h, C_a, S, s_n)}{\partial h} \Psi_h \right. \\
&+ \frac{\partial \varsigma(\ln K, h, C_a, S, s_n)}{\partial C_a} \Psi_a + \frac{\partial \varsigma(\ln K, h, C_a, S, s_n)}{\partial s_a} \Psi_n \\
&\left. + \frac{\partial \varsigma(\ln K, h, C_a, S, s_n)}{\partial S} \Psi_S \right] dVdt
\end{aligned} \tag{B.10.22}$$

Adding these four equations (17), (18), (19), and (20) to the right side of equation (22):

$$\begin{aligned}
\frac{dP}{d\ln K} = \iint_{V,t} &\left\{ \frac{\partial \varsigma(\ln K, h, C_a, S, s_n)}{\partial \ln K} + \frac{\partial \varsigma(\ln K, h, C_a, S, s_n)}{\partial h} \Psi_h \right. \\
&+ \frac{\partial \varsigma(\ln K, h, C_a, S, s_n)}{\partial C_a} \Psi_a + \frac{\partial \varsigma(\ln K, h, C_a, S, s_n)}{\partial s_a} \Psi_n \\
&+ \frac{\partial \varsigma(\ln K, h, C_a, S, s_n)}{\partial S} \Psi_S + \Psi_h^* [\nabla(\mathbf{K}\nabla\Psi_h + \mathbf{K}\nabla h)] \\
&+ \Psi_a^* \left[\frac{\partial}{\partial t} (ns_a \Psi_a + nC_a \Psi_n) + \rho_b \frac{\partial \Psi_S}{\partial t} \right. \\
&+ \nabla \left(\mathbf{q}^a \Psi_a - \mathbf{K}\nabla\Psi_h C_a - \mathbf{K}\nabla h C_a \right) \\
&- \nabla \left(\widetilde{\mathbf{D}}_h^a \nabla\Psi_a - \frac{\partial \widetilde{\mathbf{D}}_h^a}{\partial \underline{\mathbf{q}}^a} \mathbf{K}\nabla\Psi_h \nabla C_a - \frac{\partial \widetilde{\mathbf{D}}_h^a}{\partial \underline{\mathbf{q}}^a} \mathbf{K}\nabla h \nabla C_a \right) \\
&\left. - \frac{\partial \widehat{k}}{\partial \underline{\mathbf{q}}^a} (-\mathbf{K}\nabla\Psi_h - \mathbf{K}\nabla h)(C_a^{eq} - C_a) + \widehat{k}\Psi_a \right] \\
&+ \Psi_n^* \left[-\frac{\partial}{\partial t} (n\rho_n \Psi_n) + \frac{\partial \widehat{k}}{\partial \underline{\mathbf{q}}^a} (-\mathbf{K}\nabla\Psi_h - \mathbf{K}\nabla h)(C_a^{eq} - C_a) - \widehat{k}\Psi_a \right] \\
&\left. + \Psi_S^* [\Psi_S - K_d \Psi_a] \right\} dVdt
\end{aligned} \tag{B.10.23}$$

Because:

$$\begin{aligned}
\Psi_h^* \nabla \cdot (\mathbf{K}\nabla\Psi_h) &= \nabla \cdot (\Psi_h^* \mathbf{K}\nabla\Psi_h) - \nabla\Psi_h^* \cdot \mathbf{K}\nabla\Psi_h \\
&= \nabla \cdot (\Psi_h^* \mathbf{K}\nabla\Psi_h) - \nabla \cdot (\Psi_h \mathbf{K}\nabla\Psi_h^*) + \Psi_h \nabla \cdot (\mathbf{K}\nabla\Psi_h^*)
\end{aligned} \tag{B.10.24}$$

$$\Psi_a^* \frac{\partial}{\partial t}(ns_a\Psi_a) = \frac{\partial}{\partial t}(\Psi_a^* ns_a\Psi_a) - ns_a\Psi_a\frac{\partial\Psi_a^*}{\partial t} \tag{B.10.25}$$

$$\Psi_a^* \frac{\partial}{\partial t}(nC_a\Psi_n) = \frac{\partial}{\partial t}(\Psi_a^* nC_a\Psi_n) - nC_a\Psi_n\frac{\partial\Psi_a^*}{\partial t} \tag{B.10.26}$$

$$\Psi_a^* \rho_b\frac{\partial\Psi_S}{\partial t} = \frac{\partial}{\partial t}(\Psi_a^* \rho_b\Psi_S) - \Psi_S\rho_b\frac{\partial\Psi_a^*}{\partial t} \tag{B.10.27}$$

$$\Psi_a^* \boldsymbol{\nabla}\cdot\left(\underline{\mathbf{q}}^{\mathbf{a}}\Psi_a\right) = \boldsymbol{\nabla}\cdot\left(\Psi_a^*\underline{\mathbf{q}}^{\mathbf{a}}\Psi_a\right) - \boldsymbol{\nabla}\Psi_a^*\cdot\left(\underline{\mathbf{q}}^{\mathbf{a}}\Psi_a\right) \tag{B.10.28}$$

$$\begin{aligned}-\Psi_a^*\boldsymbol{\nabla}\cdot(\mathbf{K}\boldsymbol{\nabla}\Psi_h C_a) &= -\boldsymbol{\nabla}\cdot(\Psi_a^*\mathbf{K}\boldsymbol{\nabla}\Psi_h C_a) + \boldsymbol{\nabla}\Psi_a^*\cdot(\mathbf{K}\boldsymbol{\nabla}\Psi_h C_a)\\ &= -\boldsymbol{\nabla}\cdot(\Psi_a^*\mathbf{K}\boldsymbol{\nabla}\Psi_h C_a) + \boldsymbol{\nabla}\cdot(\Psi_h\mathbf{K}\boldsymbol{\nabla}\Psi_a^* C_a) - \Psi_h\boldsymbol{\nabla}\cdot(\mathbf{K}\boldsymbol{\nabla}\Psi_a^* C_a)\end{aligned} \tag{B.10.29}$$

$$\begin{aligned}-\Psi_a^*\boldsymbol{\nabla}\cdot\left(\widetilde{\mathbf{D}}_h^a\boldsymbol{\nabla}\Psi_a\right) &= -\boldsymbol{\nabla}\cdot\left(\Psi_a^*\widetilde{\mathbf{D}}_h^a\boldsymbol{\nabla}\Psi_a\right) + \boldsymbol{\nabla}\Psi_a^*\cdot\left(\widetilde{\mathbf{D}}_h^a\boldsymbol{\nabla}\Psi_a\right)\\ &= -\boldsymbol{\nabla}\cdot\left(\Psi_a^*\widetilde{\mathbf{D}}_h^a\boldsymbol{\nabla}\Psi_a\right) + \boldsymbol{\nabla}\cdot\left(\Psi_a\widetilde{\mathbf{D}}_h^a\boldsymbol{\nabla}\Psi_a^*\right) - \Psi_a\boldsymbol{\nabla}\cdot\left(\widetilde{\mathbf{D}}_h^a\boldsymbol{\nabla}\Psi_a^*\right)\end{aligned} \tag{B.10.30}$$

$$\begin{aligned}\Psi_a^*\boldsymbol{\nabla}\cdot\left(\frac{\partial\widetilde{\mathbf{D}}_h^a}{\partial\underline{\mathbf{q}}^{\mathbf{a}}}\mathbf{K}\boldsymbol{\nabla}\Psi_h\boldsymbol{\nabla}C_a\right) &= \boldsymbol{\nabla}\cdot\left(\Psi_a^*\frac{\partial\widetilde{\mathbf{D}}_h^a}{\partial\underline{\mathbf{q}}^{\mathbf{a}}}\mathbf{K}\boldsymbol{\nabla}\Psi_h\boldsymbol{\nabla}C_a\right) - \boldsymbol{\nabla}\Psi_a^*\cdot\left(\frac{\partial\widetilde{\mathbf{D}}_h^a}{\partial\underline{\mathbf{q}}^{\mathbf{a}}}\mathbf{K}\boldsymbol{\nabla}\Psi_h\boldsymbol{\nabla}C_a\right)\\ &= \boldsymbol{\nabla}\cdot\left(\Psi_a^*\frac{\partial\widetilde{\mathbf{D}}_h^a}{\partial\underline{\mathbf{q}}^{\mathbf{a}}}\mathbf{K}\boldsymbol{\nabla}\Psi_h\boldsymbol{\nabla}C_a\right) - \boldsymbol{\nabla}\cdot\left(\Psi_h\frac{\partial\widetilde{\mathbf{D}}_h^a}{\partial\underline{\mathbf{q}}^{\mathbf{a}}}\mathbf{K}\boldsymbol{\nabla}\Psi_a^*\boldsymbol{\nabla}C_a\right) + \Psi_h\boldsymbol{\nabla}\\ &\quad \cdot\left(\frac{\partial\widetilde{\mathbf{D}}_h^a}{\partial\underline{\mathbf{q}}^{\mathbf{a}}}\mathbf{K}\boldsymbol{\nabla}\Psi_a^*\boldsymbol{\nabla}C_a\right)\end{aligned} \tag{B.10.31}$$

$$\begin{aligned}\Psi_a^*\frac{\partial\widehat{\mathbf{k}}}{\partial\underline{\mathbf{q}}^{\mathbf{a}}}&(C_a^{eq} - C_a)\mathbf{K}\boldsymbol{\nabla}\Psi_h\\ &= \boldsymbol{\nabla}\cdot\left(\Psi_a^*\frac{\partial\widehat{\mathbf{k}}}{\partial\underline{\mathbf{q}}^{\mathbf{a}}}(C_a^{eq} - C_a)\,\mathbf{K}\Psi_h\right) - \Psi_h\boldsymbol{\nabla}\cdot\left(\frac{\partial\widehat{\mathbf{k}}}{\partial\underline{\mathbf{q}}^{\mathbf{a}}}(C_a^{eq} - C_a)\,\mathbf{K}\Psi_a^*\right)\end{aligned} \tag{B.10.32}$$

$$\begin{aligned}\Psi_n^*\frac{\partial\widehat{\mathbf{k}}}{\partial\underline{\mathbf{q}}^{\mathbf{a}}}&(C_a^{eq} - C_a)\,\mathbf{K}\boldsymbol{\nabla}\Psi_h\\ &= \boldsymbol{\nabla}\cdot\left(\Psi_n^*\frac{\partial\widehat{\mathbf{k}}}{\partial\underline{\mathbf{q}}^{\mathbf{a}}}(C_a^{eq} - C_a)\,\mathbf{K}\Psi_h\right) - \Psi_h\boldsymbol{\nabla}\cdot\left(\frac{\partial\widehat{\mathbf{k}}}{\partial\underline{\mathbf{q}}^{\mathbf{a}}}(C_a^{eq} - C_a)\,\mathbf{K}\Psi_n^*\right)\end{aligned} \tag{B.10.33}$$

$$-\Psi_n^*\frac{\partial}{\partial t}(n\rho_n\Psi_n) = -\frac{\partial}{\partial t}(\Psi_n^* n\rho_n\Psi_n) + n\rho_n\Psi_n\frac{\partial\Psi_n^*}{\partial t} \tag{B.10.34}$$

Thus, the marginal sensitivity becomes:

$$
\begin{aligned}
\frac{dP}{d\ln K} = \iint_{V,t} \Bigg\{ & \frac{\partial \varsigma(\ln K, h, C_a, S, s_n)}{\partial \ln K} + \frac{\partial \varsigma(\ln K, h, C_a, S, s_n)}{\partial h} \Psi_h \\
& + \frac{\partial \varsigma(\ln K, h, C_a, S, s_n)}{\partial C_a} \Psi_a + \frac{\partial \varsigma(\ln K, h, C_a, S, s_n)}{\partial s_a} \Psi_n \\
& + \frac{\partial \varsigma(\ln K, h, C_a, S, s_n)}{\partial S} \Psi_S + \boldsymbol{\nabla}(\Psi_h^* \mathbf{K} \boldsymbol{\nabla} \Psi_h) - \boldsymbol{\nabla}(\Psi_h \mathbf{K} \boldsymbol{\nabla} \Psi_h^*) \\
& + \Psi_h \boldsymbol{\nabla}(\mathbf{K} \boldsymbol{\nabla} \Psi_h^*) + \Psi_h^* \boldsymbol{\nabla}(\mathbf{K} \boldsymbol{\nabla} h) + \frac{\partial}{\partial t}(\Psi_a^* n s_a \Psi_a) - n s_a \Psi_a \frac{\partial \Psi_a^*}{\partial t} \\
& + \frac{\partial}{\partial t}(\Psi_a^* n C_a \Psi_n) - n C_a \Psi_n \frac{\partial \Psi_a^*}{\partial t} + \frac{\partial}{\partial t}(\Psi_a^* \rho_b \Psi_S) - \Psi_S \rho_b \frac{\partial \Psi_a^*}{\partial t} \\
& + \boldsymbol{\nabla}\left(\Psi_a^* \underline{\mathbf{q}}^{\mathbf{a}} \Psi_a\right) - \boldsymbol{\nabla}\Psi_a^*\left(\underline{\mathbf{q}}^{\mathbf{a}} \Psi_a\right) - \boldsymbol{\nabla}(\Psi_a^* \mathbf{K} \boldsymbol{\nabla} \Psi_h C_a) + \boldsymbol{\nabla}(\Psi_h \mathbf{K} \boldsymbol{\nabla} \Psi_a^* C_a) \\
& - \Psi_h \boldsymbol{\nabla}(\mathbf{K} \boldsymbol{\nabla} \Psi_a^* C_a) - \Psi_a^* \boldsymbol{\nabla}(\mathbf{K} \boldsymbol{\nabla} h C_a) - \boldsymbol{\nabla}\left(\Psi_a^* \widetilde{\mathbf{D}}_h^a \boldsymbol{\nabla} \Psi_a\right) \\
& + \boldsymbol{\nabla}\left(\Psi_a \widetilde{\mathbf{D}}_h^a \boldsymbol{\nabla} \Psi_a^*\right) - \Psi_a \boldsymbol{\nabla}\left(\widetilde{\mathbf{D}}_h^a \boldsymbol{\nabla} \Psi_a^*\right) + \boldsymbol{\nabla}\left(\Psi_a^* \frac{\partial \widetilde{\mathbf{D}}_h^a}{\partial \underline{\mathbf{q}}^{\mathbf{a}}} \mathbf{K} \boldsymbol{\nabla} \Psi_h \boldsymbol{\nabla} C_a\right) \\
& - \boldsymbol{\nabla}\left(\Psi_h \frac{\partial \widetilde{\mathbf{D}}_h^a}{\partial \underline{\mathbf{q}}^{\mathbf{a}}} \mathbf{K} \boldsymbol{\nabla} \Psi_a^* \boldsymbol{\nabla} C_a\right) + \Psi_h \boldsymbol{\nabla}\left(\frac{\partial \widetilde{\mathbf{D}}_h^a}{\partial \underline{\mathbf{q}}^{\mathbf{a}}} \mathbf{K} \boldsymbol{\nabla} \Psi_a^* \boldsymbol{\nabla} C_a\right) \\
& + \Psi_a^* \boldsymbol{\nabla}\left(\frac{\partial \widetilde{\mathbf{D}}_h^a}{\partial \underline{\mathbf{q}}^{\mathbf{a}}} \mathbf{K} \boldsymbol{\nabla} h \boldsymbol{\nabla} C_a\right) + \boldsymbol{\nabla} \cdot \left(\Psi_a^* \frac{\partial \widehat{\mathbf{k}}}{\partial \underline{\mathbf{q}}^{\mathbf{a}}}\left(C_a^{eq} - C_a\right) \mathbf{K} \Psi_h\right) - \Psi_h \boldsymbol{\nabla} \\
& \cdot \left(\frac{\partial \widehat{\mathbf{k}}}{\partial \underline{\mathbf{q}}^{\mathbf{a}}}\left(C_a^{eq} - C_a\right) \mathbf{K} \Psi_a^*\right) + \Psi_a^* \frac{\partial \widehat{\mathbf{k}}}{\partial \underline{\mathbf{q}}^{\mathbf{a}}}(\mathbf{K} \boldsymbol{\nabla} h)\left(C_a^{eq} - C_a\right) + \Psi_a^* \widehat{\mathbf{k}} \Psi_a \\
& - \frac{\partial}{\partial t}(\Psi_n^* n \rho_n \Psi_n) + n \rho_n \Psi_n \frac{\partial \Psi_n^*}{\partial t} - \boldsymbol{\nabla} \cdot \left(\Psi_n^* \frac{\partial \widehat{\mathbf{k}}}{\partial \underline{\mathbf{q}}^{\mathbf{a}}}\left(C_a^{eq} - C_a\right) \mathbf{K} \Psi_h\right) \\
& + \Psi_h \boldsymbol{\nabla} \cdot \left(\frac{\partial \widehat{\mathbf{k}}}{\partial \underline{\mathbf{q}}^{\mathbf{a}}}\left(C_a^{eq} - C_a\right) \mathbf{K} \Psi_n^*\right) - \Psi_n^* \frac{\partial \widehat{\mathbf{k}}}{\partial \underline{\mathbf{q}}^{\mathbf{a}}}(\mathbf{K} \boldsymbol{\nabla} h)\left(C_a^{eq} - C_a\right) \\
& - \Psi_n^* \widehat{\mathbf{k}} \Psi_a + \Psi_S^* \Psi_S - \Psi_S^* K_d \Psi_a \Bigg\} dV dt
\end{aligned}
\tag{B.10.35}
$$

$$\frac{dP}{d\ln K} = \iint_{V,t} \left\{ \Psi_h \left[\frac{\partial \varsigma(\ln K, h, C_a, S, s_n)}{\partial h} + \nabla(\mathbf{K}\nabla\Psi_h^*) - \nabla(\mathbf{K}\nabla\Psi_a^* C_a) \right. \right.$$

$$+ \nabla\left(\frac{\partial \widetilde{\mathbf{D}}_h^a}{\partial \underline{\mathbf{q}}^{\mathbf{a}}} \mathbf{K}\nabla\Psi_a^* \nabla C_a \right) - \nabla\cdot\left(\frac{\partial \widehat{k}}{\partial \underline{\mathbf{q}}^{\mathbf{a}}} \left(C_a^{eq} - C_a \right) \mathbf{K}\Psi_a^* \right) + \nabla$$

$$\left. \cdot \left(\frac{\partial \widehat{k}}{\partial \underline{\mathbf{q}}^{\mathbf{a}}} \left(C_a^{eq} - C_a \right) \mathbf{K}\Psi_n^* \right) \right]$$

$$+ \Psi_a \left[\frac{\partial \varsigma(\ln K, h, C_a, S, s_n)}{\partial C_a} - ns_a \frac{\partial \Psi_a^*}{\partial t} - \underline{\mathbf{q}}^{\mathbf{a}}\nabla\Psi_a^* - \nabla\left(\widetilde{\mathbf{D}}_h^a \nabla\Psi_a^*\right) \right.$$

$$\left. + \widehat{k}\Psi_a^* - \widehat{k}\Psi_n^* - K_d\Psi_S^* \right]$$

$$+ \Psi_n \left[\frac{\partial \varsigma(\ln K, h, C_a, S, s_n)}{\partial s_a} - nC_a \frac{\partial \Psi_a^*}{\partial t} + n\rho_n \frac{\partial \Psi_n^*}{\partial t} \right]$$

$$+ \Psi_S \left[\frac{\partial \varsigma(\ln K, h, C_a, S, s_n)}{\partial S} - \rho_b \frac{\partial \Psi_a^*}{\partial t} + \Psi_S^* \right]$$

$$+ \left[\frac{\partial \varsigma(\ln K, h, C_a, S, s_n)}{\partial \ln K} + \nabla(\Psi_h^* \mathbf{K}\nabla\Psi_h) - \nabla(\Psi_h \mathbf{K}\nabla\Psi_h^*) \right. \qquad \text{(B.10.36)}$$

$$+ \Psi_h^* \nabla(\mathbf{K}\nabla h) + \frac{\partial}{\partial t}(\Psi_a^* ns_a\Psi_a) + \frac{\partial}{\partial t}(\Psi_a^* nC_a\Psi_n) + \frac{\partial}{\partial t}(\Psi_a^* \rho_b\Psi_S)$$

$$+ \nabla\left(\Psi_a^* \underline{\mathbf{q}}^{\mathbf{a}}\Psi_a \right) - \nabla(\Psi_a^* \mathbf{K}\nabla\Psi_h C_a) + \nabla(\Psi_h \mathbf{K}\nabla\Psi_a^* C_a)$$

$$- \Psi_a^* \nabla(\mathbf{K}\nabla h C_a) - \nabla\left(\Psi_a^* \widetilde{\mathbf{D}}_h^a \nabla\Psi_a \right) + \nabla\left(\Psi_a \widetilde{\mathbf{D}}_h^a \nabla\Psi_a^* \right)$$

$$+ \nabla\left(\Psi_a^* \frac{\partial \widetilde{\mathbf{D}}_h^a}{\partial \underline{\mathbf{q}}^{\mathbf{a}}} \mathbf{K}\nabla\Psi_h \nabla C_a \right) - \nabla\left(\Psi_h \frac{\partial \widetilde{\mathbf{D}}_h^a}{\partial \underline{\mathbf{q}}^{\mathbf{a}}} \mathbf{K}\nabla\Psi_a^* \nabla C_a \right)$$

$$+ \Psi_a^* \nabla\left(\frac{\partial \widetilde{\mathbf{D}}_h^a}{\partial \underline{\mathbf{q}}^{\mathbf{a}}} \mathbf{K}\nabla h \nabla C_a \right) + \nabla\cdot\left(\Psi_a^* \frac{\partial \widehat{k}}{\partial \underline{\mathbf{q}}^{\mathbf{a}}} \left(C_a^{eq} - C_a \right) \mathbf{K}\Psi_h \right)$$

$$+ \Psi_a^* \frac{\partial \widehat{k}}{\partial \underline{\mathbf{q}}^{\mathbf{a}}} (\mathbf{K}\nabla h)\left(C_a^{eq} - C_a \right) - \nabla\cdot\left(\Psi_n^* \frac{\partial \widehat{k}}{\partial \underline{\mathbf{q}}^{\mathbf{a}}} \left(C_a^{eq} - C_a \right) \mathbf{K}\Psi_h \right)$$

$$\left. \left. - \Psi_n^* \frac{\partial \widehat{k}}{\partial \underline{\mathbf{q}}^{\mathbf{a}}} (\mathbf{K}\nabla h)\left(C_a^{eq} - C_a \right) - \frac{\partial}{\partial t}(\Psi_n^* n\rho_n\Psi_n) \right] \right\} dVdt$$

The arbitrary functions Ψ_h^*, Ψ_a^*, Ψ_n^*, and Ψ_S^* are now defined in order to eliminate the state sensitivities of Ψ_h, Ψ_a, Ψ_n, and Ψ_S, yielding:

$$\frac{\partial \varsigma(\ln K, h, C_a, S, s_n)}{\partial h} + \nabla(\mathbf{K}\nabla\Psi_h^*) - \nabla(\mathbf{K}\nabla\Psi_a^* C_a) + \nabla\left(\frac{\partial \widetilde{\mathbf{D}}_h^a}{\partial \underline{\mathbf{q}}^{\mathbf{a}}} \mathbf{K}\nabla\Psi_a^* \nabla C_a \right) - \nabla$$

$$\cdot\left(\frac{\partial \widehat{k}}{\partial \underline{\mathbf{q}}^{\mathbf{a}}} \left(C_a^{eq} - C_a \right) \mathbf{K}\Psi_a^* \right) + \nabla\cdot\left(\frac{\partial \widehat{k}}{\partial \underline{\mathbf{q}}^{\mathbf{a}}} \left(C_a^{eq} - C_a \right) \mathbf{K}\Psi_n^* \right) = 0 \qquad \text{(B.10.37)}$$

$$\frac{\partial \varsigma(\ln K, h, C_a, S, s_n)}{\partial C_a} - ns_a \frac{\partial \Psi_a^*}{\partial t} - \underline{\mathbf{q}}^{\mathbf{a}}\nabla\Psi_a^* - \nabla\left(\widetilde{\mathbf{D}}_h^a \nabla\Psi_a^*\right) + \widehat{k}\Psi_a^* - \widehat{k}\Psi_n^* - K_d\Psi_S^* = 0 \quad \text{(B.10.38)}$$

240

$$\frac{\partial \varsigma(\ln K, h, C_a, S, s_n)}{\partial s_a} - nC_a \frac{\partial \Psi_a^*}{\partial t} + n\rho_n \frac{\partial \Psi_n^*}{\partial t} = 0 \tag{B.10.39}$$

$$\frac{\partial \varsigma(\ln K, h, C_a, S, s_n)}{\partial S} - \rho_b \frac{\partial \Psi_a^*}{\partial t} + \Psi_S^* = 0 \tag{B.10.40}$$

Define $\tau = t_f - t$ as backward time, the governing equations of the adjoint states are:

$$\frac{\partial \varsigma(\ln K, h, C_a, S, s_n)}{\partial h} + \nabla(K\nabla \Psi_h^*) - \nabla(KC_a \nabla \Psi_a^*) + \nabla\left(K \frac{\partial \widetilde{\mathbf{D}}_h^a}{\partial \underline{\mathbf{q}}^a} \nabla C_a \nabla \Psi_a^*\right) - \nabla$$
$$\cdot \left(\frac{\partial \widehat{k}}{\partial \underline{\mathbf{q}}^a} (C_a^{eq} - C_a) K \Psi_a^*\right) + \nabla \cdot \left(\frac{\partial \widehat{k}}{\partial \underline{\mathbf{q}}^a} (C_a^{eq} - C_a) K \Psi_n^*\right) = 0 \tag{B.10.41}$$

$$\frac{\partial \varsigma(\ln K, h, C_a, S, s_n)}{\partial C_a} + ns_a \frac{\partial \Psi_a^*}{\partial \tau} - \underline{\mathbf{q}}^a \nabla \Psi_a^* - \nabla(\widetilde{\mathbf{D}}_h^a \nabla \Psi_a^*) + \widehat{k}\Psi_a^* - \widehat{k}\Psi_n^* - K_d \Psi_S^* = 0 \tag{B.10.42}$$

$$\frac{\partial \varsigma(\ln K, h, C_a, S, s_n)}{\partial s_a} + nC_a \frac{\partial \Psi_a^*}{\partial \tau} - n\rho_n \frac{\partial \Psi_n^*}{\partial \tau} = 0 \tag{B.10.43}$$

$$\frac{\partial \varsigma(\ln K, h, C_a, S, s_n)}{\partial S} + \rho_b \frac{\partial \Psi_a^*}{\partial \tau} + \Psi_S^* = 0 \tag{B.10.44}$$

The marginal sensitivity turns out to be:

$$\frac{dP}{d\ln K} = \iint_{V,t} \left[\frac{\partial \varsigma(\ln K, h, C_a, S, s_n)}{\partial \ln K} + \nabla(\Psi_h^* K \nabla \Psi_h) - \nabla(\Psi_h K \nabla \Psi_h^*) + \Psi_h^* \nabla(K\nabla h) \right.$$
$$+ \frac{\partial}{\partial t}(\Psi_a^* ns_a \Psi_a) + \frac{\partial}{\partial t}(\Psi_a^* nC_a \Psi_n) + \frac{\partial}{\partial t}(\Psi_a^* \rho_b \Psi_S) + \nabla\left(\Psi_a^* \underline{\mathbf{q}}^a \Psi_a\right)$$
$$- \nabla(\Psi_a^* K \nabla \Psi_h C_a) + \nabla(\Psi_h K \nabla \Psi_a^* C_a) - \Psi_a^* \nabla(K\nabla hC_a)$$
$$- \nabla(\Psi_a^* \widetilde{\mathbf{D}}_h^a \nabla \Psi_a) + \nabla(\Psi_a \widetilde{\mathbf{D}}_h^a \nabla \Psi_a^*) + \nabla\left(\Psi_a^* \frac{\partial \widetilde{\mathbf{D}}_h^a}{\partial \underline{\mathbf{q}}^a} K \nabla \Psi_h \nabla C_a\right)$$
$$- \nabla\left(\Psi_h \frac{\partial \widetilde{\mathbf{D}}_h^a}{\partial \underline{\mathbf{q}}^a} K \nabla \Psi_a^* \nabla C_a\right) + \Psi_a^* \nabla\left(\frac{\partial \widetilde{\mathbf{D}}_h^a}{\partial \underline{\mathbf{q}}^a} K \nabla h \nabla C_a\right) + \nabla$$
$$\cdot \left(\Psi_a^* \frac{\partial \widehat{k}}{\partial \underline{\mathbf{q}}^a} (C_a^{eq} - C_a) K \Psi_h\right) + \Psi_a^* \frac{\partial \widehat{k}}{\partial \underline{\mathbf{q}}^a} (K\nabla h)(C_a^{eq} - C_a) - \nabla$$
$$\cdot \left(\Psi_n^* \frac{\partial \widehat{k}}{\partial \underline{\mathbf{q}}^a} (C_a^{eq} - C_a) K \Psi_h\right) - \Psi_n^* \frac{\partial \widehat{k}}{\partial \underline{\mathbf{q}}^a} (K\nabla h)(C_a^{eq} - C_a)$$
$$\left. - \frac{\partial}{\partial t}(\Psi_n^* n\rho_n \Psi_n) \right] dVdt \tag{B.10.45}$$

Boundary conditions of the forward flow and transport equations are

$$-(K\nabla h) \cdot \vec{n} = 0 \text{ on } \Gamma_1 \tag{B.10.46}$$

$$-(\widetilde{\mathbf{D}}_h^a \nabla C_a) \cdot \vec{n} = 0 \text{ on } \Gamma_1 \tag{B.10.47}$$

$$-\left(\widetilde{\mathbf{D}}_h^a \nabla C_a - \underline{\mathbf{q}}^a C_a\right) \cdot \vec{n} = g(\mathbf{x}, t) \text{ on } \Gamma_2 \tag{B.10.48}$$

Differentiate the boundary equations with respect to lnK:

$$-\frac{\partial}{\partial \ln K}(\mathbf{K}\nabla h)\cdot\vec{n} = (-\mathbf{K}\nabla\Psi_h - \mathbf{K}\nabla h)\cdot\vec{n} = 0 \tag{B.10.49}$$

$$-\frac{\partial}{\partial \ln K}\left(\widetilde{\mathbf{D}}_h^a \nabla C_a\right)\cdot\vec{n} = \left[-\widetilde{\mathbf{D}}_h^a \nabla\Psi_a + \frac{\partial\widetilde{\mathbf{D}}_h^a}{\partial\underline{\mathbf{q}}^a}(\mathbf{K}\nabla\Psi_h^* + \mathbf{K}\nabla h)\nabla C_a\right]\cdot\vec{n} = 0 \tag{B.10.50}$$

$$-\frac{\partial}{\partial \ln K}\left(\widetilde{\mathbf{D}}_h^a \nabla C_a - \underline{\mathbf{q}}^a C_a\right)\cdot\vec{n}$$

$$= -\left[\widetilde{\mathbf{D}}_h^a \nabla\Psi_a - \frac{\partial\widetilde{\mathbf{D}}_h^a}{\partial\underline{\mathbf{q}}^a}(\mathbf{K}\nabla\Psi_h \nabla C_a + \mathbf{K}\nabla h\nabla C_a) - \underline{\mathbf{q}}^a\Psi_a\right.$$

$$\left. + (\mathbf{K}\nabla\Psi_h + \mathbf{K}\nabla h)C_a\right]\cdot\vec{n} = 0 \tag{B.10.51}$$

Take an inner product of Ψ_h^* with (49) and integrate:

$$\iint_{V,t} -\nabla(\Psi_h^* \mathbf{K}\nabla\Psi_h + \Psi_h^* \mathbf{K}\nabla h)\,dVdt = 0 \tag{B.10.52}$$

Take an inner product of Ψ_a^* with (50) and integrate:

$$\iint_{V,t} -\nabla\left[\Psi_a^* \widetilde{\mathbf{D}}_h^a \nabla\Psi_a - \Psi_a^* \frac{\partial\widetilde{\mathbf{D}}_h^a}{\partial\underline{\mathbf{q}}^a}(\mathbf{K}\nabla\Psi_h + \mathbf{K}\nabla h)\nabla C_a\right]dVdt = 0 \tag{B.10.53}$$

Take an inner product of Ψ_a^* with (51) and integrate:

$$\iint_{V,t} -\nabla\left[\Psi_a^* \widetilde{\mathbf{D}}_h^a \nabla\Psi_a - \Psi_a^* \frac{\partial\widetilde{\mathbf{D}}_h^a}{\partial\underline{\mathbf{q}}^a}(\mathbf{K}\nabla\Psi_h + \mathbf{K}\nabla h)\nabla C_a - \Psi_a^*\underline{\mathbf{q}}^a\Psi_a\right.$$

$$\left. + \Psi_a^*(\mathbf{K}\nabla\Psi_h + \mathbf{K}\nabla h)C_a\right]dVdt = 0 \tag{B.10.54}$$

Because:

$$\Psi_h^*\nabla(\mathbf{K}\nabla h) = \nabla(\Psi_h^*\mathbf{K}\nabla h) - \nabla\Psi_h^*(\mathbf{K}\nabla h) \tag{B.10.55}$$

$$-\Psi_a^*\nabla(\mathbf{K}\nabla h C_a) = -\nabla(\Psi_a^*\mathbf{K}\nabla h C_a) + \nabla\Psi_a^*(\mathbf{K}\nabla h C_a) \tag{B.10.56}$$

$$\Psi_a^*\nabla\left(\frac{\partial\widetilde{\mathbf{D}}_h^a}{\partial\underline{\mathbf{q}}^a}\mathbf{K}\nabla h\nabla C_a\right) = \nabla\left(\Psi_a^*\frac{\partial\widetilde{\mathbf{D}}_h^a}{\partial\underline{\mathbf{q}}^a}\mathbf{K}\nabla h\nabla C_a\right) - \nabla\Psi_a^*\left(\frac{\partial\widetilde{\mathbf{D}}_h^a}{\partial\underline{\mathbf{q}}^a}\mathbf{K}\nabla h\nabla C_a\right) \tag{B.10.57}$$

The initial conditions of adjoint states are defined as:

$$\Psi_a^*(\tau = 0) = \Psi_n^*(\tau = 0) = \Psi_S^*(\tau = 0) = 0 \tag{B.10.58}$$

Then:

$$\frac{\partial}{\partial t}(\Psi_a^* n s_a \Psi_a), \frac{\partial}{\partial t}(\Psi_a^* n C_a \Psi_n), \frac{\partial}{\partial t}(\Psi_a^* \rho_b \Psi_S), \frac{\partial}{\partial t}(\Psi_n^* n \rho_n \Psi_n) \text{ terms vanish}$$

The boundary conditions of adjoint states are defined as:

$$-\left(\mathbf{K}\nabla\Psi_h^* - \mathbf{K}C_a\nabla\Psi_a^* + \mathbf{K}\frac{\partial\widetilde{\mathbf{D}}_h^a}{\partial\underline{\mathbf{q}}^a}\nabla C_a\nabla\Psi_a^* - \frac{\partial\widehat{k}}{\partial\underline{\mathbf{q}}^a}\mathbf{K}(C_a^{eq}-C_a)\Psi_a^*\right.$$

$$\left.+\frac{\partial\widehat{k}}{\partial\underline{\mathbf{q}}^a}\mathbf{K}(C_a^{eq}-C_a)\Psi_n^*\right)\cdot\vec{n}=0 \tag{B.10.59}$$

$$-\left(\widetilde{\mathbf{D}}_h^a\nabla\Psi_a^* + \underline{\mathbf{q}}^a\Psi_a^*\right)\cdot\vec{n}=0 \text{ on } \Gamma_1 \tag{B.10.60}$$

$$\left(\widetilde{\mathbf{D}}_h^a\nabla\Psi_a^*\right)\cdot\vec{n}=0 \text{ on } \Gamma_2 \tag{B.10.61}$$

The final expression of marginal sensitivity becomes:

$$\frac{dP}{d\ln K}=\iint_{V,t}\left[\frac{\partial\varsigma(\ln K, h, C_a, S, s_n)}{\partial\ln K}-\nabla\Psi_h^*(\mathbf{K}\nabla h)+\nabla\Psi_a^*(C_a\mathbf{K}\nabla h)\right.$$

$$\left.-\nabla\Psi_a^*\left(\frac{\partial\widetilde{\mathbf{D}}_h^a}{\partial\underline{\mathbf{q}}^a}\mathbf{K}\nabla h\nabla C_a\right)+\frac{\partial\widehat{k}}{\partial\underline{\mathbf{q}}^a}(\mathbf{K}\nabla h)(C_a^{eq}-C_a)(\Psi_a^*-\Psi_n^*)\right]dVdt \tag{B.10.62}$$

VII.B.11. Derivation of Adjoint States Control Equations and Marginal Sensitivity of Down-gradient FAC with Respect to C_a^0

The control equations of forward flow and transport:

$$\nabla(\mathbf{K}\nabla h)=0 \tag{B.11.1}$$

$$\frac{\partial}{\partial t}(ns_aC_a)+\rho_b\frac{\partial S}{\partial t}=-\nabla\left(\underline{\mathbf{q}}^aC_a\right)+\nabla\left(\widetilde{\mathbf{D}}_h^a\nabla C_a\right)+\widehat{k}(C_a^{eq}-C_a) \tag{B.11.2}$$

$$\frac{\partial}{\partial t}(ns_n\rho_n)=-\widehat{k}(C_a^{eq}-C_a) \tag{B.11.3}$$

$$S=K_dC_a \tag{B.11.4}$$

Differentiate the control equations with respect to C_a^0:

$$\nabla\left(\frac{\partial}{\partial C_a^0}(\mathbf{K}\nabla h)\right)=0 \tag{B.11.5}$$

$$\frac{\partial}{\partial t}\left(\frac{\partial}{\partial C_a^0}(ns_aC_a)\right)+\rho_b\frac{\partial}{\partial C_a^0}\left(\frac{\partial S}{\partial t}\right)$$

$$=-\nabla\left(\frac{\partial}{\partial C_a^0}\left(\underline{\mathbf{q}}^aC_a\right)\right)+\nabla\left(\frac{\partial}{\partial C_a^0}\left(\widetilde{\mathbf{D}}_h^a\nabla C_a\right)\right)+\frac{\partial}{\partial C_a^0}\left(\widehat{k}C_a^{eq}-\widehat{k}C_a\right) \tag{B.11.6}$$

$$\frac{\partial}{\partial C_a^0}\left(\frac{\partial}{\partial t}(ns_n\rho_n)\right)=-\frac{\partial\widehat{k}}{\partial C_a^0}(C_a^{eq}-C_a) \tag{B.11.7}$$

$$\frac{\partial S}{\partial C_a^0}=\frac{\partial}{\partial C_a^0}(K_dC_a) \tag{B.11.8}$$

Let:

$$\frac{\partial C_a}{\partial C_a{}^0} = \Psi_a \qquad \frac{\partial s_a}{\partial C_a{}^0} = \Psi_n \qquad \frac{\partial S}{\partial C_a{}^0} = \Psi_S \tag{B.11.9}$$

Thus:

$$\frac{\partial}{\partial t}(ns_a\Psi_a + nC_a\Psi_n) + \rho_b\frac{\partial\Psi_S}{\partial t}$$
$$= -\nabla\left(\underline{q}^a\Psi_a + \frac{\partial\underline{q}^a}{\partial C_a{}^0}C_a\right) + \nabla\left(\widetilde{D}_h^a\nabla\Psi_a + \frac{\partial\widetilde{D}_h^a}{\partial C_a{}^0}\nabla C_a\right) \tag{B.11.10}$$
$$+ \frac{\partial\hat{k}}{\partial C_a{}^0}(C_a^{eq} - C_a) - \hat{k}\Psi_a$$

$$\frac{\partial}{\partial t}(-n\rho_n\Psi_n) = -\frac{\partial\hat{k}}{\partial C_a{}^0}(C_a^{eq} - C_a) + \hat{k}\Psi_a \tag{B.11.11}$$

$$\Psi_S = K_d\Psi_a \tag{B.11.12}$$

Take an inner product of Ψ_a^* with (2) and integrate:

$$\iint_{V,t}\Psi_a^*\left[\frac{\partial}{\partial t}(ns_a\Psi_a + nC_a\Psi_n) + \rho_b\frac{\partial\Psi_s}{\partial t} + \nabla\left(\underline{q}^a\Psi_a\right) - \nabla(\widetilde{D}_h^a\nabla\Psi_a)\right.$$
$$\left. - \frac{\partial\hat{k}}{\partial C_a{}^0}(C_a^{eq} - C_a) + \hat{k}\Psi_a\right]dVdt = 0 \tag{B.11.13}$$

Take an inner product of Ψ_n^* with (3) and integrate:

$$\iint_{V,t}\Psi_n^*\left[-\frac{\partial}{\partial t}(n\rho_n\Psi_n) + \frac{\partial\hat{k}}{\partial C_a{}^0}(C_a^{eq} - C_a) - \hat{k}\Psi_a\right]dVdt = 0 \tag{B.11.14}$$

Take an inner produce of Ψ_s^* with (4) and integrate:

$$\iint_{V,t}\Psi_S^*[\Psi_S - K_d\Psi_a]dVdt = 0 \tag{B.11.15}$$

A performance measure that quantifies some state of the system is defined as:

$$P = \iint_{V,t}\varsigma\left(C_a{}^0, C_a, S, s_n\right)dVdt \tag{B.11.16}$$

where $\varsigma\left(C_a{}^0, C_a, S, s_n\right)$ is a functional of the state of the system.

The marginal sensitivity of this performance measure with respect to $C_a{}^0$ is obtained by differentiation equation:

$$\frac{dP}{dC_a{}^0} = \iint_{V,t}\left[\frac{\partial\varsigma\left(C_a{}^0, C_a, S, s_n\right)}{\partial C_a{}^0} + \frac{\partial\varsigma\left(C_a{}^0, C_a, S, s_n\right)}{\partial C_a}\Psi_a + \frac{\partial\varsigma\left(C_a{}^0, C_a, S, s_n\right)}{\partial s_a}\Psi_n\right.$$
$$\left. + \frac{\partial\varsigma\left(C_a{}^0, C_a, S, s_n\right)}{\partial S}\Psi_S\right]dVdt \tag{B.11.17}$$

Adding these three equations (13), (14), and (15) to the right side of equation (17):

$$\frac{dP}{dC_a^0} = \iint_{V,t} \left\{ \frac{\partial \varsigma(C_a^0, C_a, S, s_n)}{\partial C_a^0} + \frac{\partial \varsigma(C_a^0, C_a, S, s_n)}{\partial C_a} \Psi_a + \frac{\partial \varsigma(C_a^0, C_a, S, s_n)}{\partial s_a} \Psi_n \right.$$

$$+ \frac{\partial \varsigma(C_a^0, C_a, S, s_n)}{\partial S} \Psi_S$$

$$+ \Psi_a^* \left[\frac{\partial}{\partial t}(ns_a \Psi_a + nC_a \Psi_n) + \rho_b \frac{\partial \Psi_S}{\partial t} + \nabla\left(\underline{q}^a \Psi_a\right) - \nabla(\widetilde{\mathbf{D}}_h^a \nabla \Psi_a) \right.$$

$$\left. - \frac{\partial \widehat{k}}{\partial C_a^0}(C_a^{eq} - C_a) + \widehat{k}\Psi_a \right]$$

$$+ \Psi_n^* \left[-\frac{\partial}{\partial t}(n\rho_n \Psi_n) + \frac{\partial \widehat{k}}{\partial C_a^0}(C_a^{eq} - C_a) - \widehat{k}\Psi_a \right]$$

$$\left. + \Psi_S^*[\Psi_S - K_d \Psi_a] \right\} dVdt \tag{B.11.18}$$

Because:

$$\Psi_a^* \frac{\partial}{\partial t}(ns_a \Psi_a) = \frac{\partial}{\partial t}(\Psi_a^* ns_a \Psi_a) - ns_a \Psi_a \frac{\partial \Psi_a^*}{\partial t} \tag{B.11.19}$$

$$\Psi_a^* \frac{\partial}{\partial t}(nC_a \Psi_n) = \frac{\partial}{\partial t}(\Psi_a^* nC_a \Psi_n) - nC_a \Psi_n \frac{\partial \Psi_a^*}{\partial t} \tag{B.11.20}$$

$$\Psi_a^* \rho_b \frac{\partial \Psi_S}{\partial t} = \frac{\partial}{\partial t}(\Psi_a^* \rho_b \Psi_S) - \Psi_S \rho_b \frac{\partial \Psi_a^*}{\partial t} \tag{B.11.21}$$

$$\Psi_a^* \nabla \cdot \left(\underline{q}^a \Psi_a\right) = \nabla \cdot \left(\Psi_a^* \underline{q}^a \Psi_a\right) - \nabla \Psi_a^* \cdot \left(\underline{q}^a \Psi_a\right) \tag{B.11.22}$$

$$-\Psi_a^* \nabla \cdot \left(\widetilde{\mathbf{D}}_h^a \nabla \Psi_a\right) = -\nabla \cdot \left(\Psi_a^* \widetilde{\mathbf{D}}_h^a \nabla \Psi_a\right) + \nabla \Psi_a^* \cdot \left(\widetilde{\mathbf{D}}_h^a \nabla \Psi_a\right)$$
$$= -\nabla \cdot \left(\Psi_a^* \widetilde{\mathbf{D}}_h^a \nabla \Psi_a\right) + \nabla \cdot \left(\Psi_a \widetilde{\mathbf{D}}_h^a \nabla \Psi_a^*\right) - \Psi_a \nabla \cdot \left(\widetilde{\mathbf{D}}_h^a \nabla \Psi_a^*\right) \tag{B.11.23}$$

$$-\Psi_n^* \frac{\partial}{\partial t}(n\rho_n \Psi_n) = -\frac{\partial}{\partial t}(\Psi_n^* n\rho_n \Psi_n) + n\rho_n \Psi_n \frac{\partial \Psi_n^*}{\partial t} \tag{B.11.24}$$

Thus, the marginal sensitivity becomes:

$$\frac{dP}{dC_a{}^0} = \iint_{V,t} \left\{ \frac{\partial\varsigma(C_a{}^0, C_a, S, s_n)}{\partial C_a{}^0} + \frac{\partial\varsigma(C_a{}^0, C_a, S, s_n)}{\partial C_a}\Psi_a + \frac{\partial\varsigma(C_a{}^0, C_a, S, s_n)}{\partial s_a}\Psi_n \right.$$

$$+ \frac{\partial\varsigma(C_a{}^0, C_a, S, s_n)}{\partial S}\Psi_S + \frac{\partial}{\partial t}(\Psi_a^* ns_a\Psi_a) - ns_a\Psi_a\frac{\partial\Psi_a^*}{\partial t}$$

$$+ \frac{\partial}{\partial t}(\Psi_a^* nC_a\Psi_n) - nC_a\Psi_n\frac{\partial\Psi_a^*}{\partial t} + \frac{\partial}{\partial t}(\Psi_a^*\rho_b\Psi_S) - \Psi_S\rho_b\frac{\partial\Psi_a^*}{\partial t} + \boldsymbol{\nabla}$$

$$\cdot \left(\Psi_a^*\underline{\mathbf{q}}^a\Psi_a\right) - \boldsymbol{\nabla}\Psi_a^* \cdot \left(\underline{\mathbf{q}}^a\Psi_a\right) - \boldsymbol{\nabla} \cdot \left(\Psi_a^*\widetilde{\mathbf{D}}_h^a\boldsymbol{\nabla}\Psi_a\right) + \boldsymbol{\nabla} \cdot \left(\Psi_a\widetilde{\mathbf{D}}_h^a\boldsymbol{\nabla}\Psi_a^*\right) \quad \text{(B.11.25)}$$

$$- \Psi_a\boldsymbol{\nabla} \cdot \left(\widetilde{\mathbf{D}}_h^a\boldsymbol{\nabla}\Psi_a^*\right) - \Psi_a^*\frac{\partial\widehat{k}}{\partial C_a{}^0}\left(C_a^{eq} - C_a\right) + \Psi_a^*\widehat{k}\Psi_a$$

$$- \frac{\partial}{\partial t}(\Psi_n^* n\rho_n\Psi_n) + n\rho_n\Psi_n\frac{\partial\Psi_n^*}{\partial t} + \Psi_n^*\frac{\partial\widehat{k}}{\partial C_a{}^0}\left(C_a^{eq} - C_a\right) - \Psi_n^*\widehat{k}\Psi_a$$

$$\left. + \Psi_S^*\Psi_S - \Psi_S^* K_d\Psi_a \right\} dVdt$$

$$\frac{dP}{dC_a{}^0} = \iint_{V,t} \left\{ \Psi_a\left[\frac{\partial\varsigma(C_a{}^0, C_a, S, s_n)}{\partial C_a} - ns_a\frac{\partial\Psi_a^*}{\partial t} - \underline{\mathbf{q}}^a\boldsymbol{\nabla}\Psi_a^* - \boldsymbol{\nabla}(\widetilde{\mathbf{D}}_h^a\boldsymbol{\nabla}\Psi_a^*) + \widehat{k}\Psi_a^* \right.\right.$$

$$\left. - \widehat{k}\Psi_n^* - K_d\Psi_S^* \right] + \Psi_n\left[\frac{\partial\varsigma(C_a{}^0, C_a, S, s_n)}{\partial s_a} - nC_a\frac{\partial\Psi_a^*}{\partial t} + n\rho_n\frac{\partial\Psi_n^*}{\partial t} \right]$$

$$+ \Psi_S\left[\frac{\partial\varsigma(C_a{}^0, C_a, S, s_n)}{\partial S} - \rho_b\frac{\partial\Psi_a^*}{\partial t} + \Psi_S^* \right]$$

$$+ \left[\frac{\partial\varsigma(C_a{}^0, C_a, S, s_n)}{\partial C_a{}^0} + \frac{\partial}{\partial t}(\Psi_a^* ns_a\Psi_a) + \frac{\partial}{\partial t}(\Psi_a^* nC_a\Psi_n) \right. \quad \text{(B.11.26)}$$

$$+ \frac{\partial}{\partial t}(\Psi_a^*\rho_b\Psi_S) + \boldsymbol{\nabla}\left(\Psi_a^*\underline{\mathbf{q}}^a\Psi_a\right) - \boldsymbol{\nabla}(\Psi_a^*\widetilde{\mathbf{D}}_h^a\boldsymbol{\nabla}\Psi_a) + \boldsymbol{\nabla}(\Psi_a\widetilde{\mathbf{D}}_h^a\boldsymbol{\nabla}\Psi_a^*)$$

$$- \Psi_a^*\frac{\partial\widehat{k}}{\partial C_a{}^0}\left(C_a^{eq} - C_a\right) + \Psi_n^*\frac{\partial\widehat{k}}{\partial C_a{}^0}\left(C_a^{eq} - C_a\right)$$

$$\left.\left. - \frac{\partial}{\partial t}(\Psi_n^* n\rho_n\Psi_n) \right] \right\} dVdt$$

The arbitrary functions Ψ_a^*, Ψ_n^*, and Ψ_S^* are now defined in order to eliminate the state sensitivities of Ψ_a, Ψ_n, and Ψ_S, yielding:

$$\frac{\partial\varsigma(C_a{}^0, C_a, S, s_n)}{\partial C_a} - ns_a\frac{\partial\Psi_a^*}{\partial t} - \underline{\mathbf{q}}^a\boldsymbol{\nabla}\Psi_a^* - \boldsymbol{\nabla}(\widetilde{\mathbf{D}}_h^a\boldsymbol{\nabla}\Psi_a^*) + \widehat{k}\Psi_a^* - \widehat{k}\Psi_n^* - K_d\Psi_S^* = 0 \quad \text{(B.11.27)}$$

$$\frac{\partial\varsigma(C_a{}^0, C_a, S, s_n)}{\partial s_a} - nC_a\frac{\partial\Psi_a^*}{\partial t} + n\rho_n\frac{\partial\Psi_n^*}{\partial t} = 0 \quad \text{(B.11.28)}$$

$$\frac{\partial\varsigma(C_a{}^0, C_a, S, s_n)}{\partial S} - \rho_b\frac{\partial\Psi_a^*}{\partial t} + \Psi_S^* = 0 \quad \text{(B.11.29)}$$

Define $\tau = t_f - t$ as backward time, the governing equations of the adjoint states are:

$$\frac{\partial \varsigma\left(C_a{}^0, C_a, S, s_n\right)}{\partial C_a} + ns_a \frac{\partial \Psi_a^*}{\partial \tau} - \underline{\mathbf{q}}^a \nabla \Psi_a^* - \nabla\left(\widetilde{\mathbf{D}}_h^a \nabla \Psi_a^*\right) + \hat{k}\Psi_a^* - \hat{k}\Psi_n^* - K_d \Psi_S^* = 0 \qquad \text{(B.11.30)}$$

$$\frac{\partial \varsigma\left(C_a{}^0, C_a, S, s_n\right)}{\partial s_a} + nC_a \frac{\partial \Psi_a^*}{\partial \tau} - n\rho_n \frac{\partial \Psi_n^*}{\partial \tau} = 0 \qquad \text{(B.11.31)}$$

$$\frac{\partial \varsigma\left(C_a{}^0, C_a, S, s_n\right)}{\partial S} + \rho_b \frac{\partial \Psi_a^*}{\partial \tau} + \Psi_S^* = 0 \qquad \text{(B.11.32)}$$

The marginal sensitivity turns out to be:

$$\begin{aligned}
\frac{dP}{dC_a{}^0} = \iint_{V,t} \Bigg[& \frac{\partial \varsigma\left(C_a{}^0, C_a, S, s_n\right)}{\partial C_a{}^0} + \frac{\partial}{\partial t}\left(\Psi_a^* ns_a \Psi_a\right) + \frac{\partial}{\partial t}\left(\Psi_a^* nC_a \Psi_n\right) + \frac{\partial}{\partial t}\left(\Psi_a^* \rho_b \Psi_S\right) \\
& + \nabla\left(\Psi_a^* \underline{\mathbf{q}}^a \Psi_a\right) - \nabla\left(\Psi_a^* \widetilde{\mathbf{D}}_h^a \nabla \Psi_a\right) + \nabla\left(\Psi_a \widetilde{\mathbf{D}}_h^a \nabla \Psi_a^*\right) \\
& - \Psi_a^* \frac{\partial \hat{k}}{\partial C_a{}^0}\left(C_a^{eq} - C_a\right) + \Psi_n^* \frac{\partial \hat{k}}{\partial C_a{}^0}\left(C_a^{eq} - C_a\right) \\
& - \frac{\partial}{\partial t}\left(\Psi_n^* n\rho_n \Psi_n\right) \Bigg] dVdt
\end{aligned} \qquad \text{(B.11.33)}$$

Boundary conditions of the forward flow and transport equations are

$$-(\mathbf{K}\nabla h) \cdot \vec{n} = 0 \text{ on } \Gamma_1 \qquad \text{(B.11.34)}$$

$$-\left(\widetilde{\mathbf{D}}_h^a \nabla C_a\right) \cdot \vec{n} = 0 \text{ on } \Gamma_1 \qquad \text{(B.11.35)}$$

$$-\left(\widetilde{\mathbf{D}}_h^a \nabla C_a - \underline{\mathbf{q}}^a C_a\right) \cdot \vec{n} = g(\mathbf{x}, t) \text{ on } \Gamma_2 \qquad \text{(B.11.36)}$$

Differentiate the boundary equations with respect to $C_a{}^0$:

$$-\frac{\partial}{\partial C_a{}^0}\left(\widetilde{\mathbf{D}}_h^a \nabla C_a\right) \cdot \vec{n} = \left[-\widetilde{\mathbf{D}}_h^a \nabla \Psi_a\right] \cdot \vec{n} = 0 \qquad \text{(B.11.37)}$$

$$-\frac{\partial}{\partial C_a{}^0}\left(\widetilde{\mathbf{D}}_h^a \nabla C_a - \underline{\mathbf{q}}^a C_a\right) \cdot \vec{n} = -\left[\widetilde{\mathbf{D}}_h^a \nabla \Psi_a - \underline{\mathbf{q}}^a \Psi_a\right] \cdot \vec{n} = 0 \qquad \text{(B.11.38)}$$

Take an inner product of Ψ_a^* with (37) and integrate:

$$\iint_{V,t} -\nabla\left[\Psi_a^* \widetilde{\mathbf{D}}_h^a \nabla \Psi_a\right] dVdt = 0 \qquad \text{(B.11.39)}$$

Take an inner product of Ψ_a^* with (38) and integrate:

$$\iint_{V,t} -\nabla\left[\Psi_a^* \widetilde{\mathbf{D}}_h^a \nabla \Psi_a - \Psi_a^* \underline{\mathbf{q}}^a \Psi_a\right] dVdt = 0 \qquad \text{(B.11.40)}$$

The initial conditions of adjoint states are defined as:

$$\Psi_a^*(\tau = 0) = \Psi_n^*(\tau = 0) = \Psi_S^*(\tau = 0) = 0 \qquad \text{(B.11.41)}$$

Then:

$$\frac{\partial}{\partial t}(\Psi_a^* n C_a \Psi_n), \frac{\partial}{\partial t}(\Psi_a^* \rho_b \Psi_S), \frac{\partial}{\partial t}(\Psi_n^* n \rho_n \Psi_n) \text{ terms vanish}$$

$$\iint_{V,t} \left[\frac{\partial}{\partial t}(\Psi_a^* ns_a \Psi_a)\right] dV dt = \int_V \left[\Psi_a^* ns_a \Psi_a|_{t=t_f} - \Psi_a^* ns_a \frac{\partial C_a^0}{\partial C_a^0}\Big|_{t=0}\right] dV$$

$$= \int_V \left[-\Psi_a^*(t=0) ns_a(t=0)\right] dV \tag{B.11.42}$$

The boundary conditions of adjoint states are defined as:

$$-\left(\widetilde{\mathbf{D}}_h^a \nabla \Psi_a^* + \underline{\mathbf{q}}^a \Psi_a^*\right) \cdot \vec{n} = 0 \text{ on } \Gamma_1 \tag{B.11.43}$$

$$\left(\widetilde{\mathbf{D}}_h^a \nabla \Psi_a^*\right) \cdot \vec{n} = 0 \text{ on } \Gamma_2 \tag{B.11.44}$$

The final expression of marginal sensitivity becomes:

$$\frac{dP}{dC_a^0} = \int_V \left[-\Psi_a^*(t=0) ns_a(t=0)\right] dV \tag{B.11.45}$$

VII.B.12. Derivation of Adjoint States Control Equations and Marginal Sensitivity of Down-Gradient FAC with Respect to S^0

The control equations of forward flow and transport:

$$\nabla(\mathbf{K}\nabla h) = 0 \tag{B.12.1}$$

$$\frac{\partial}{\partial t}(ns_a C_a) + \rho_b \frac{\partial S}{\partial t} = -\nabla\left(\underline{\mathbf{q}}^a C_a\right) + \nabla\left(\widetilde{\mathbf{D}}_h^a \nabla C_a\right) + \hat{k}\left(C_a^{eq} - C_a\right) \tag{B.12.2}$$

$$\frac{\partial}{\partial t}(ns_n \rho_n) = -\hat{k}\left(C_a^{eq} - C_a\right) \tag{B.12.3}$$

$$S = K_d C_a \tag{B.12.4}$$

Differentiate the control equations with respect to S^0:

$$\nabla\left(\frac{\partial}{\partial S^0}(\mathbf{K}\nabla h)\right) = 0 \tag{B.12.5}$$

$$\frac{\partial}{\partial t}\left(\frac{\partial}{\partial S^0}(ns_a C_a)\right) + \rho_b \frac{\partial}{\partial S^0}\left(\frac{\partial S}{\partial t}\right)$$

$$= -\nabla\left(\frac{\partial}{\partial S^0}\left(\underline{\mathbf{q}}^a C_a\right)\right) + \nabla\left(\frac{\partial}{\partial S^0}\left(\widetilde{\mathbf{D}}_h^a \nabla C_a\right)\right) + \frac{\partial}{\partial S^0}\left(\hat{k}C_a^{eq} - \hat{k}C_a\right) \tag{B.12.6}$$

$$\frac{\partial}{\partial S^0}\left(\frac{\partial}{\partial t}(ns_n \rho_n)\right) = -\frac{\partial \hat{k}}{\partial S^0}\left(C_a^{eq} - C_a\right) \tag{B.12.7}$$

$$\frac{\partial S}{\partial S^0} = \frac{\partial}{\partial S^0}(K_d C_a) \tag{B.12.8}$$

Let:

$$\frac{\partial C_a}{\partial S^0} = \Psi_a \qquad \frac{\partial s_a}{\partial S^0} = \Psi_n \qquad \frac{\partial S}{\partial S^0} = \Psi_S \tag{B.12.9}$$

Thus:

$$\frac{\partial}{\partial t}(ns_a\Psi_a + nC_a\Psi_n) + \rho_b\frac{\partial \Psi_S}{\partial t}$$
$$= -\nabla\left(\underline{\mathbf{q}}^a\Psi_a + \frac{\partial \underline{\mathbf{q}}^a}{\partial S^0}C_a\right) + \nabla\left(\widetilde{\mathbf{D}}_h^a\nabla\Psi_a + \frac{\partial \widetilde{\mathbf{D}}_h^a}{\partial S^0}\nabla C_a\right) \tag{B.12.10}$$
$$+ \frac{\partial \widehat{k}}{\partial S^0}(C_a^{eq} - C_a) - \widehat{k}\Psi_a$$

$$\frac{\partial}{\partial t}(-n\rho_n\Psi_n) = -\frac{\partial \widehat{k}}{\partial S^0}(C_a^{eq} - C_a) + \widehat{k}\Psi_a \tag{B.12.11}$$

$$\Psi_S = K_d\Psi_a \tag{B.12.12}$$

Take an inner product of Ψ_a^* with (2) and integrate:

$$\iint_{V,t} \Psi_a^* \left[\frac{\partial}{\partial t}(ns_a\Psi_a + nC_a\Psi_n) + \rho_b\frac{\partial \Psi_S}{\partial t} + \nabla\left(\underline{\mathbf{q}}^a\Psi_a\right) - \nabla(\widetilde{\mathbf{D}}_h^a\nabla\Psi_a)\right.$$
$$\left. - \frac{\partial \widehat{k}}{\partial S^0}(C_a^{eq} - C_a) + \widehat{k}\Psi_a\right]dVdt = 0 \tag{B.12.13}$$

Take an inner product of Ψ_n^* with (3) and integrate:

$$\iint_{V,t} \Psi_n^* \left[-\frac{\partial}{\partial t}(n\rho_n\Psi_n) + \frac{\partial \widehat{k}}{\partial S^0}(C_a^{eq} - C_a) - \widehat{k}\Psi_a\right]dvdt = 0 \tag{B.12.14}$$

Take an inner produce of Ψ_s^* with (4) and integrate:

$$\iint_{V,t} \Psi_S^* [\Psi_S - K_d\Psi_a]dVdt = 0 \tag{B.12.15}$$

A performance measure that quantifies some state of the system is defined as:

$$P = \iint_{V,t} \varsigma(S^0, C_a, S, s_n)\, dVdt \tag{B.12.16}$$

where $\varsigma(S^0, C_a, S, s_n)$ is a functional of the state of the system.

The marginal sensitivity of this performance measure with respect to S^0 is obtained by differentiation equation:

$$\frac{dP}{dS^0} = \iint_{V,t} \left[\frac{\partial\, \varsigma(S^0, C_a, S, s_n)}{\partial S^0} + \frac{\partial\, \varsigma(S^0, C_a, S, s_n)}{\partial C_a}\Psi_a + \frac{\partial\, \varsigma(S^0, C_a, S, s_n)}{\partial s_a}\Psi_n\right.$$
$$\left. + \frac{\partial\, \varsigma(S^0, C_a, S, s_n)}{\partial S}\Psi_S\right]dVdt \tag{B.12.17}$$

Adding these three equations (13), (14), and (15) to the right side of equation (17):

$$\frac{dP}{dS^0} = \iint_{V,t} \left\{ \frac{\partial \varsigma(S^0, C_a, S, s_n)}{\partial S^0} + \frac{\partial \varsigma(S^0, C_a, S, s_n)}{\partial C_a} \Psi_a + \frac{\partial \varsigma(S^0, C_a, S, s_n)}{\partial s_a} \Psi_n \right.$$

$$+ \frac{\partial \varsigma(S^0, C_a, S, s_n)}{\partial S} \Psi_S$$

$$+ \Psi_a^* \left[\frac{\partial}{\partial t}(ns_a \Psi_a + nC_a \Psi_n) + \rho_b \frac{\partial \Psi_S}{\partial t} + \boldsymbol{\nabla}\left(\underline{\mathbf{q}}^a \Psi_a\right) - \boldsymbol{\nabla}(\widetilde{\mathbf{D}}_h^a \boldsymbol{\nabla} \Psi_a) \right.$$

$$\left. - \frac{\partial \widehat{k}}{\partial S^0}\left(C_a^{eq} - C_a\right) + \widehat{k} \Psi_a \right]$$

$$+ \Psi_n^* \left[-\frac{\partial}{\partial t}(n\rho_n \Psi_n) + \frac{\partial \widehat{k}}{\partial S^0}\left(C_a^{eq} - C_a\right) - \widehat{k} \Psi_a \right]$$

$$\left. + \Psi_S^* [\Psi_S - K_d \Psi_a] \right\} dVdt \tag{B.12.18}$$

Because:

$$\Psi_a^* \frac{\partial}{\partial t}(ns_a \Psi_a) = \frac{\partial}{\partial t}(\Psi_a^* ns_a \Psi_a) - ns_a \Psi_a \frac{\partial \Psi_a^*}{\partial t} \tag{B.12.19}$$

$$\Psi_a^* \frac{\partial}{\partial t}(nC_a \Psi_n) = \frac{\partial}{\partial t}(\Psi_a^* nC_a \Psi_n) - nC_a \Psi_n \frac{\partial \Psi_a^*}{\partial t} \tag{B.12.20}$$

$$\Psi_a^* \rho_b \frac{\partial \Psi_S}{\partial t} = \frac{\partial}{\partial t}(\Psi_a^* \rho_b \Psi_S) - \Psi_S \rho_b \frac{\partial \Psi_a^*}{\partial t} \tag{B.12.21}$$

$$\Psi_a^* \boldsymbol{\nabla} \cdot \left(\underline{\mathbf{q}}^a \Psi_a\right) = \boldsymbol{\nabla} \cdot \left(\Psi_a^* \underline{\mathbf{q}}^a \Psi_a\right) - \boldsymbol{\nabla} \Psi_a^* \cdot \left(\underline{\mathbf{q}}^a \Psi_a\right) \tag{B.12.22}$$

$$-\Psi_a^* \boldsymbol{\nabla} \cdot \left(\widetilde{\mathbf{D}}_h^a \boldsymbol{\nabla} \Psi_a\right) = -\boldsymbol{\nabla} \cdot \left(\Psi_a^* \widetilde{\mathbf{D}}_h^a \boldsymbol{\nabla} \Psi_a\right) + \boldsymbol{\nabla} \Psi_a^* \cdot \left(\widetilde{\mathbf{D}}_h^a \boldsymbol{\nabla} \Psi_a\right)$$
$$= -\boldsymbol{\nabla} \cdot \left(\Psi_a^* \widetilde{\mathbf{D}}_h^a \boldsymbol{\nabla} \Psi_a\right) + \boldsymbol{\nabla} \cdot \left(\Psi_a \widetilde{\mathbf{D}}_h^a \boldsymbol{\nabla} \Psi_a^*\right) - \Psi_a \boldsymbol{\nabla} \cdot \left(\widetilde{\mathbf{D}}_h^a \boldsymbol{\nabla} \Psi_a^*\right) \tag{B.12.23}$$

$$-\Psi_n^* \frac{\partial}{\partial t}(n\rho_n \Psi_n) = -\frac{\partial}{\partial t}(\Psi_n^* n\rho_n \Psi_n) + n\rho_n \Psi_n \frac{\partial \Psi_n^*}{\partial t} \tag{B.12.24}$$

Thus, the marginal sensitivity becomes:

$$\frac{dP}{dS^0} = \iint_{V,t} \left\{ \frac{\partial \varsigma(S^0, C_a, S, s_n)}{\partial S^0} + \frac{\partial \varsigma(S^0, C_a, S, s_n)}{\partial C_a} \Psi_a + \frac{\partial \varsigma(S^0, C_a, S, s_n)}{\partial s_a} \Psi_n \right.$$

$$+ \frac{\partial \varsigma(S^0, C_a, S, s_n)}{\partial S} \Psi_S + \frac{\partial}{\partial t}(\Psi_a^* ns_a \Psi_a) - ns_a \Psi_a \frac{\partial \Psi_a^*}{\partial t}$$

$$+ \frac{\partial}{\partial t}(\Psi_a^* nC_a \Psi_n) - nC_a \Psi_n \frac{\partial \Psi_a^*}{\partial t} + \frac{\partial}{\partial t}(\Psi_a^* \rho_b \Psi_S) - \Psi_S \rho_b \frac{\partial \Psi_a^*}{\partial t} + \boldsymbol{\nabla}$$

$$\cdot \left(\Psi_a^* \underline{\mathbf{q}}^a \Psi_a\right) - \boldsymbol{\nabla} \Psi_a^* \cdot \left(\underline{\mathbf{q}}^a \Psi_a\right) - \boldsymbol{\nabla} \cdot \left(\Psi_a^* \widetilde{\mathbf{D}}_h^a \boldsymbol{\nabla} \Psi_a\right) + \boldsymbol{\nabla} \cdot \left(\Psi_a \widetilde{\mathbf{D}}_h^a \boldsymbol{\nabla} \Psi_a^*\right) \tag{B.12.25}$$

$$- \Psi_a \boldsymbol{\nabla} \cdot \left(\widetilde{\mathbf{D}}_h^a \boldsymbol{\nabla} \Psi_a^*\right) - \Psi_a^* \frac{\partial \widehat{k}}{\partial S^0}\left(C_a^{eq} - C_a\right) + \Psi_a^* \widehat{k} \Psi_a - \frac{\partial}{\partial t}(\Psi_n^* n\rho_n \Psi_n)$$

$$+ n\rho_n \Psi_n \frac{\partial \Psi_n^*}{\partial t} + \Psi_n^* \frac{\partial \widehat{k}}{\partial S^0}\left(C_a^{eq} - C_a\right) - \Psi_n^* \widehat{k} \Psi_a + \Psi_S^* \Psi_S$$

$$\left. - \Psi_S^* K_d \Psi_a \right\} dVdt$$

$$\frac{dP}{dS^0} = \iint_{V,t} \left\{ \Psi_a \left[\frac{\partial \varsigma(S^0, C_a, S, s_n)}{\partial C_a} - ns_a \frac{\partial \Psi_a^*}{\partial t} - \underline{\mathbf{q}}^a \nabla \Psi_a^* - \nabla \left(\widetilde{\mathbf{D}}_h^a \nabla \Psi_a^* \right) + \hat{k} \Psi_a^* \right. \right.$$

$$\left. - \hat{k} \Psi_n^* - K_d \Psi_S^* \right] + \Psi_n \left[\frac{\partial \varsigma(S^0, C_a, S, s_n)}{\partial s_a} - nC_a \frac{\partial \Psi_a^*}{\partial t} + n\rho_n \frac{\partial \Psi_n^*}{\partial t} \right]$$

$$+ \Psi_S \left[\frac{\partial \varsigma(S^0, C_a, S, s_n)}{\partial S} - \rho_b \frac{\partial \Psi_a^*}{\partial t} + \Psi_S^* \right]$$

$$+ \left[\frac{\partial \varsigma(S^0, C_a, S, s_n)}{\partial S^0} + \frac{\partial}{\partial t} (\Psi_a^* ns_a \Psi_a) + \frac{\partial}{\partial t} (\Psi_a^* nC_a \Psi_n) \right. \quad \text{(B.12.26)}$$

$$+ \frac{\partial}{\partial t} (\Psi_a^* \rho_b \Psi_S) + \nabla \left(\Psi_a^* \underline{\mathbf{q}}^a \Psi_a \right) - \nabla \left(\Psi_a^* \widetilde{\mathbf{D}}_h^a \nabla \Psi_a \right) + \nabla \left(\Psi_a \widetilde{\mathbf{D}}_h^a \nabla \Psi_a^* \right)$$

$$- \Psi_a^* \frac{\partial \hat{k}}{\partial S^0} \left(C_a^{eq} - C_a \right) + \Psi_n^* \frac{\partial \hat{k}}{\partial S^0} \left(C_a^{eq} - C_a \right)$$

$$\left. \left. - \frac{\partial}{\partial t} (\Psi_n^* n\rho_n \Psi_n) \right] \right\} dVdt$$

The arbitrary functions Ψ_a^*, Ψ_n^*, and Ψ_S^* are now defined in order to eliminate the state sensitivities of Ψ_a, Ψ_n, and Ψ_S, yielding:

$$\frac{\partial \varsigma(S^0, C_a, S, s_n)}{\partial C_a} - ns_a \frac{\partial \Psi_a^*}{\partial t} - \underline{\mathbf{q}}^a \nabla \Psi_a^* - \nabla \left(\widetilde{\mathbf{D}}_h^a \nabla \Psi_a^* \right) + \hat{k} \Psi_a^* - \hat{k} \Psi_n^* - K_d \Psi_S^* = 0 \quad \text{(B.12.27)}$$

$$\frac{\partial \varsigma(S^0, C_a, S, s_n)}{\partial s_a} - nC_a \frac{\partial \Psi_a^*}{\partial t} + n\rho_n \frac{\partial \Psi_n^*}{\partial t} = 0 \quad \text{(B.12.28)}$$

$$\frac{\partial \varsigma(S^0, C_a, S, s_n)}{\partial S} - \rho_b \frac{\partial \Psi_a^*}{\partial t} + \Psi_S^* = 0 \quad \text{(B.12.29)}$$

Define $\tau = t_f - t$ as backward time, the governing equations of the adjoint states are:

$$\frac{\partial \varsigma(S^0, C_a, S, s_n)}{\partial C_a} + ns_a \frac{\partial \Psi_a^*}{\partial \tau} - \underline{\mathbf{q}}^a \nabla \Psi_a^* - \nabla \left(\widetilde{\mathbf{D}}_h^a \nabla \Psi_a^* \right) + \hat{k} \Psi_a^* - \hat{k} \Psi_n^* - K_d \Psi_S^* = 0 \quad \text{(B.12.30)}$$

$$\frac{\partial \varsigma(S^0, C_a, S, s_n)}{\partial s_a} + nC_a \frac{\partial \Psi_a^*}{\partial \tau} - n\rho_n \frac{\partial \Psi_n^*}{\partial \tau} = 0 \quad \text{(B.12.31)}$$

$$\frac{\partial \varsigma(S^0, C_a, S, s_n)}{\partial S} + \rho_b \frac{\partial \Psi_a^*}{\partial \tau} + \Psi_S^* = 0 \quad \text{(B.12.32)}$$

The marginal sensitivity turns out to be:

$$\frac{dP}{dS^0} = \iint_{V,t} \left[\frac{\partial \varsigma(S^0, C_a, S, s_n)}{\partial S^0} + \frac{\partial}{\partial t} (\Psi_a^* ns_a \Psi_a) + \frac{\partial}{\partial t} (\Psi_a^* nC_a \Psi_n) + \frac{\partial}{\partial t} (\Psi_a^* \rho_b \Psi_S) \right.$$

$$+ \nabla \left(\Psi_a^* \underline{\mathbf{q}}^a \Psi_a \right) - \nabla \left(\Psi_a^* \widetilde{\mathbf{D}}_h^a \nabla \Psi_a \right) + \nabla \left(\Psi_a \widetilde{\mathbf{D}}_h^a \nabla \Psi_a^* \right) \quad \text{(B.12.33)}$$

$$\left. - \Psi_a^* \frac{\partial \hat{k}}{\partial S^0} \left(C_a^{eq} - C_a \right) + \Psi_n^* \frac{\partial \hat{k}}{\partial S^0} \left(C_a^{eq} - C_a \right) - \frac{\partial}{\partial t} (\Psi_n^* n\rho_n \Psi_n) \right] dVdt$$

Boundary conditions of the forward flow and transport equations are

$$-(\mathbf{K\nabla}h) \cdot \vec{n} = 0 \text{ on } \Gamma_1 \tag{B.12.34}$$

$$-\left(\widetilde{\mathbf{D}}_h^a \mathbf{\nabla} C_a\right) \cdot \vec{n} = 0 \text{ on } \Gamma_1 \tag{B.12.35}$$

$$-\left(\widetilde{\mathbf{D}}_h^a \mathbf{\nabla} C_a - \underline{\mathbf{q}}^a C_a\right) \cdot \vec{n} = g(\mathbf{x}, t) \text{ on } \Gamma_2 \tag{B.12.36}$$

Differentiate the boundary equations with respect to S^0:

$$-\frac{\partial}{\partial S^0}\left(\widetilde{\mathbf{D}}_h^a \mathbf{\nabla} C_a\right) \cdot \vec{n} = \left[-\widetilde{\mathbf{D}}_h^a \mathbf{\nabla} \Psi_a\right] \cdot \vec{n} = 0 \tag{B.12.37}$$

$$-\frac{\partial}{\partial S^0}\left(\widetilde{\mathbf{D}}_h^a \mathbf{\nabla} C_a - \underline{\mathbf{q}}^a C_a\right) \cdot \vec{n} = -\left[\widetilde{\mathbf{D}}_h^a \mathbf{\nabla} \Psi_a - \underline{\mathbf{q}}^a \Psi_a\right] \cdot \vec{n} = 0 \tag{B.12.38}$$

Take an inner product of Ψ_a^* with (37) and integrate:

$$\iint_{V,t} -\mathbf{\nabla}\left[\Psi_a^* \widetilde{\mathbf{D}}_h^a \mathbf{\nabla} \Psi_a\right] dVdt = 0 \tag{B.12.39}$$

Take an inner product of Ψ_a^* with (38) and integrate:

$$\iint_{V,t} -\mathbf{\nabla}\left[\Psi_a^* \widetilde{\mathbf{D}}_h^a \mathbf{\nabla} \Psi_a - \Psi_a^* \underline{\mathbf{q}}^a \Psi_a\right] dVdt = 0 \tag{B.12.40}$$

The initial conditions of adjoint states are defined as:

$$\Psi_a^*(\tau = 0) = \Psi_n^*(\tau = 0) = \Psi_S^*(\tau = 0) = 0 \tag{B.12.41}$$

Then:

$$\frac{\partial}{\partial t}(\Psi_a^* n s_a \Psi_a), \frac{\partial}{\partial t}(\Psi_a^* n C_a \Psi_n), \frac{\partial}{\partial t}(\Psi_n^* n \rho_n \Psi_n) \text{ terms vanish}$$

$$\iint_{V,t}\left[\frac{\partial}{\partial t}(\Psi_a^* \rho_b \Psi_S)\right] dVdt = \int_V \left[\Psi_a^* \rho_b \Psi_S|_{t=t_f} - \Psi_a^* \rho_b \left.\frac{\partial S^0}{\partial S^0}\right|_{t=0}\right] dV$$
$$= \int_V [-\Psi_a^*(t = 0)\rho_b] dV \tag{B.12.42}$$

The boundary conditions of adjoint states are defined as:

$$-\left(\widetilde{\mathbf{D}}_h^a \mathbf{\nabla} \Psi_a^* + \underline{\mathbf{q}}^a \Psi_a^*\right) \cdot \vec{n} = 0 \text{ on } \Gamma_1 \tag{B.12.43}$$

$$\left(\widetilde{\mathbf{D}}_h^a \mathbf{\nabla} \Psi_a^*\right) \cdot \vec{n} = 0 \text{ on } \Gamma_2 \tag{B.12.44}$$

The final expression of marginal sensitivity becomes:

$$\frac{dP}{dS^0} = \int_V [-\Psi_a^*(t = 0)\rho_b] dV \tag{B.12.45}$$

VII.B.13. Derivation of Adjoint States Control Equations and Marginal Sensitivity of Down-gradient FAC with Respect to $s_n{}^0$

The control equations of forward flow and transport:

$$\mathbf{\nabla}(\mathbf{K\nabla}h) = 0 \tag{B.13.1}$$

$$\frac{\partial}{\partial t}(ns_a C_a) + \rho_b \frac{\partial S}{\partial t} = -\boldsymbol{\nabla}\left(\underline{\mathbf{q}}^a C_a\right) + \boldsymbol{\nabla}\left(\tilde{\mathbf{D}}_h^a \boldsymbol{\nabla} C_a\right) + \hat{k}(C_a^{eq} - C_a) \tag{B.13.2}$$

$$\frac{\partial}{\partial t}(ns_n \rho_n) = -\hat{k}(C_a^{eq} - C_a) \tag{B.13.3}$$

$$S = K_d C_a \tag{B.13.4}$$

Differentiate the control equations with respect to $s_n{}^0$:

$$\boldsymbol{\nabla}\left(\frac{\partial}{\partial s_n{}^0}(\mathbf{K}\boldsymbol{\nabla}h)\right) = 0 \tag{B.13.5}$$

$$\begin{aligned}
&\frac{\partial}{\partial t}\left(\frac{\partial}{\partial s_n{}^0}(ns_a C_a)\right) + \rho_b \frac{\partial}{\partial s_n{}^0}\left(\frac{\partial S}{\partial t}\right) \\
&= -\boldsymbol{\nabla}\left(\frac{\partial}{\partial s_n{}^0}\left(\underline{\mathbf{q}}^a C_a\right)\right) + \boldsymbol{\nabla}\left(\frac{\partial}{\partial s_n{}^0}(\tilde{\mathbf{D}}_h^a \boldsymbol{\nabla} C_a)\right) + \frac{\partial}{\partial s_n{}^0}\left(\hat{k}C_a^{eq} - \hat{k}C_a\right)
\end{aligned} \tag{B.13.6}$$

$$\frac{\partial}{\partial s_n{}^0}\left(\frac{\partial}{\partial t}(ns_n \rho_n)\right) = -\frac{\partial \hat{k}}{\partial s_n{}^0}(C_a^{eq} - C_a) \tag{B.13.7}$$

$$\frac{\partial S}{\partial s_n{}^0} = \frac{\partial}{\partial s_n{}^0}(K_d C_a) \tag{B.13.8}$$

Let:

$$\frac{\partial C_a}{\partial s_n{}^0} = \Psi_a \qquad \frac{\partial s_a}{\partial s_n{}^0} = \Psi_n \qquad \frac{\partial S}{\partial s_n{}^0} = \Psi_S \tag{B.13.9}$$

Thus:

$$\begin{aligned}
&\frac{\partial}{\partial t}(ns_a \Psi_a + nC_a \Psi_n) + \rho_b \frac{\partial \Psi_S}{\partial t} \\
&= -\boldsymbol{\nabla}\left(\underline{\mathbf{q}}^a \Psi_a + \frac{\partial \underline{\mathbf{q}}^a}{\partial s_n{}^0}C_a\right) + \boldsymbol{\nabla}\left(\tilde{\mathbf{D}}_h^a \boldsymbol{\nabla}\Psi_a + \frac{\partial \tilde{\mathbf{D}}_h^a}{\partial s_n{}^0}\boldsymbol{\nabla} C_a\right) \\
&\quad + \frac{\partial \hat{k}}{\partial s_n{}^0}(C_a^{eq} - C_a) - \hat{k}\Psi_a
\end{aligned} \tag{B.13.10}$$

$$\frac{\partial}{\partial t}(-n\rho_n \Psi_n) = -\frac{\partial \hat{k}}{\partial s_n{}^0}(C_a^{eq} - C_a) + \hat{k}\Psi_a \tag{B.13.11}$$

$$\Psi_S = K_d \Psi_a \tag{B.13.12}$$

Take an inner product of Ψ_a^* with (2) and integrate:

$$\begin{aligned}
\iint_{V,t} \Psi_a^* &\left[\frac{\partial}{\partial t}(ns_a \Psi_a + nC_a \Psi_n) + \rho_b \frac{\partial \Psi_S}{\partial t} + \boldsymbol{\nabla}\left(\underline{\mathbf{q}}^a \Psi_a\right) - \boldsymbol{\nabla}(\tilde{\mathbf{D}}_h^a \boldsymbol{\nabla}\Psi_a)\right. \\
&\left. - \frac{\partial \hat{k}}{\partial s_n{}^0}(C_a^{eq} - C_a) + \hat{k}\Psi_a\right]dVdt = 0
\end{aligned} \tag{B.13.13}$$

Take an inner product of Ψ_n^* with (3) and integrate:

$$\iint_{V,t} \Psi_n^* \left[-\frac{\partial}{\partial t}(n\rho_n \Psi_n) + \frac{\partial \hat{k}}{\partial s_n{}^0}\left(C_a^{eq} - C_a\right) - \hat{k}\Psi_a \right] dvdt = 0 \tag{B.13.14}$$

Take an inner produce of Ψ_S^* with (4) and integrate:

$$\iint_{V,t} \Psi_S^* [\Psi_S - K_d \Psi_a] dVdt = 0 \tag{B.13.15}$$

A performance measure that quantifies some state of the system is defined as:

$$P = \iint_{V,t} \varsigma(s_n{}^0, C_a, S, s_n) \, dVdt \tag{B.13.16}$$

where $\varsigma(s_n{}^0, C_a, S, s_n)$ is a functional of the state of the system.

The marginal sensitivity of this performance measure with respect to $s_n{}^0$ is obtained by differentiation equation:

$$\begin{aligned}
\frac{dP}{ds_n{}^0} = \iint_{V,t} \Bigg[& \frac{\partial \varsigma(s_n{}^0, C_a, S, s_n)}{\partial s_n{}^0} + \frac{\partial \varsigma(s_n{}^0, C_a, S, s_n)}{\partial C_a}\Psi_a + \frac{\partial \varsigma(s_n{}^0, C_a, S, s_n)}{\partial s_a}\Psi_n \\
& + \frac{\partial \varsigma(s_n{}^0, C_a, S, s_n)}{\partial S}\Psi_S \Bigg] dVdt
\end{aligned} \tag{B.13.17}$$

Adding these three equations (13), (14), and (15) to the right side of equation (17):

$$\begin{aligned}
\frac{dP}{ds_n{}^0} = \iint_{V,t} \Bigg\{ & \frac{\partial \varsigma(s_n{}^0, C_a, S, s_n)}{\partial s_n{}^0} + \frac{\partial \varsigma(s_n{}^0, C_a, S, s_n)}{\partial C_a}\Psi_a + \frac{\partial \varsigma(s_n{}^0, C_a, S, s_n)}{\partial s_a}\Psi_n \\
& + \frac{\partial \varsigma(s_n{}^0, C_a, S, s_n)}{\partial S}\Psi_S \\
& + \Psi_a^* \left[\frac{\partial}{\partial t}(ns_a \Psi_a + nC_a \Psi_n) + \rho_b \frac{\partial \Psi_S}{\partial t} + \nabla\left(\underline{q}^a \Psi_a\right) - \nabla(\tilde{D}_h^a \nabla \Psi_a) \right. \\
& \left. - \frac{\partial \hat{k}}{\partial s_n{}^0}\left(C_a^{eq} - C_a\right) + \hat{k}\Psi_a \right] \\
& + \Psi_n^* \left[-\frac{\partial}{\partial t}(n\rho_n \Psi_n) + \frac{\partial \hat{k}}{\partial s_n{}^0}\left(C_a^{eq} - C_a\right) - \hat{k}\Psi_a \right] \\
& + \Psi_S^* [\Psi_S - K_d \Psi_a] \Bigg\} dVdt
\end{aligned} \tag{B.13.18}$$

Because:

$$\Psi_a^* \frac{\partial}{\partial t}(ns_a \Psi_a) = \frac{\partial}{\partial t}(\Psi_a^* ns_a \Psi_a) - ns_a \Psi_a \frac{\partial \Psi_a^*}{\partial t} \tag{B.13.19}$$

$$\Psi_a^* \frac{\partial}{\partial t}(nC_a \Psi_n) = \frac{\partial}{\partial t}(\Psi_a^* nC_a \Psi_n) - nC_a \Psi_n \frac{\partial \Psi_a^*}{\partial t} \tag{B.13.20}$$

$$\Psi_a^* \rho_b \frac{\partial \Psi_S}{\partial t} = \frac{\partial}{\partial t}(\Psi_a^* \rho_b \Psi_S) - \Psi_S \rho_b \frac{\partial \Psi_a^*}{\partial t} \tag{B.13.21}$$

$$\Psi_a^* \boldsymbol{\nabla} \cdot \left(\underline{\mathbf{q}}^a \Psi_a \right) = \boldsymbol{\nabla} \cdot \left(\Psi_a^* \underline{\mathbf{q}}^a \Psi_a \right) - \boldsymbol{\nabla}\Psi_a^* \cdot \left(\underline{\mathbf{q}}^a \Psi_a \right) \tag{B.13.22}$$

$$\begin{aligned} -\Psi_a^* \boldsymbol{\nabla} \cdot \left(\widetilde{\mathbf{D}}_h^a \boldsymbol{\nabla}\Psi_a \right) &= -\boldsymbol{\nabla} \cdot \left(\Psi_a^* \widetilde{\mathbf{D}}_h^a \boldsymbol{\nabla}\Psi_a \right) + \boldsymbol{\nabla}\Psi_a^* \cdot \left(\widetilde{\mathbf{D}}_h^a \boldsymbol{\nabla}\Psi_a \right) \\ &= -\boldsymbol{\nabla} \cdot \left(\Psi_a^* \widetilde{\mathbf{D}}_h^a \boldsymbol{\nabla}\Psi_a \right) + \boldsymbol{\nabla} \cdot \left(\Psi_a \widetilde{\mathbf{D}}_h^a \boldsymbol{\nabla}\Psi_a^* \right) - \Psi_a \boldsymbol{\nabla} \cdot \left(\widetilde{\mathbf{D}}_h^a \boldsymbol{\nabla}\Psi_a^* \right) \end{aligned} \tag{B.13.23}$$

$$-\Psi_n^* \frac{\partial}{\partial t}(n\rho_n \Psi_n) = -\frac{\partial}{\partial t}(\Psi_n^* n\rho_n \Psi_n) + n\rho_n \Psi_n \frac{\partial \Psi_n^*}{\partial t} \tag{B.13.24}$$

Thus, the marginal sensitivity becomes:

$$\begin{aligned} \frac{dP}{ds_n{}^0} = \iint_{V,t} \Bigg\{ &\frac{\partial \varsigma(s_n{}^0, C_a, S, s_n)}{\partial s_n{}^0} + \frac{\partial \varsigma(s_n{}^0, C_a, S, s_n)}{\partial C_a}\Psi_a + \frac{\partial \varsigma(s_n{}^0, C_a, S, s_n)}{\partial s_a}\Psi_n \\ &+ \frac{\partial \varsigma(s_n{}^0, C_a, S, s_n)}{\partial S}\Psi_S + \frac{\partial}{\partial t}(\Psi_a^* n s_a \Psi_a) - n s_a \Psi_a \frac{\partial \Psi_a^*}{\partial t} \\ &+ \frac{\partial}{\partial t}(\Psi_a^* n C_a \Psi_n) - n C_a \Psi_n \frac{\partial \Psi_a^*}{\partial t} + \frac{\partial}{\partial t}(\Psi_a^* \rho_b \Psi_S) - \Psi_S \rho_b \frac{\partial \Psi_a^*}{\partial t} + \boldsymbol{\nabla} \\ &\cdot \left(\Psi_a^* \underline{\mathbf{q}}^a \Psi_a \right) - \boldsymbol{\nabla}\Psi_a^* \cdot \left(\underline{\mathbf{q}}^a \Psi_a \right) - \boldsymbol{\nabla} \cdot \left(\Psi_a^* \widetilde{\mathbf{D}}_h^a \boldsymbol{\nabla}\Psi_a \right) + \boldsymbol{\nabla} \cdot \left(\Psi_a \widetilde{\mathbf{D}}_h^a \boldsymbol{\nabla}\Psi_a^* \right) \\ &- \Psi_a \boldsymbol{\nabla} \cdot \left(\widetilde{\mathbf{D}}_h^a \boldsymbol{\nabla}\Psi_a^* \right) - \Psi_a^* \frac{\partial \widehat{k}}{\partial s_n{}^0}\left(C_a^{eq} - C_a \right) + \Psi_a^* \widehat{k}\Psi_a \\ &- \frac{\partial}{\partial t}(\Psi_n^* n\rho_n \Psi_n) + n\rho_n \Psi_n \frac{\partial \Psi_n^*}{\partial t} + \Psi_n^* \frac{\partial \widehat{k}}{\partial s_n{}^0}\left(C_a^{eq} - C_a \right) - \Psi_n^* \widehat{k}\Psi_a \\ &+ \Psi_S^* \Psi_S - \Psi_S^* K_d \Psi_a \Bigg\} dVdt \end{aligned} \tag{B.13.25}$$

$$\begin{aligned} \frac{dP}{ds_n{}^0} = \iint_{V,t} \Bigg\{ &\Psi_a \left[\frac{\partial \varsigma(s_n{}^0, C_a, S, s_n)}{\partial C_a} - n s_a \frac{\partial \Psi_a^*}{\partial t} - \underline{\mathbf{q}}^a \boldsymbol{\nabla}\Psi_a^* - \boldsymbol{\nabla}\left(\widetilde{\mathbf{D}}_h^a \boldsymbol{\nabla}\Psi_a^* \right) + \widehat{k}\Psi_a^* \right. \\ &\left. - \widehat{k}\Psi_n^* - K_d \Psi_S^* \right] + \Psi_n \left[\frac{\partial \varsigma(s_n{}^0, C_a, S, s_n)}{\partial s_a} - n C_a \frac{\partial \Psi_a^*}{\partial t} + n\rho_n \frac{\partial \Psi_n^*}{\partial t} \right] \\ &+ \Psi_S \left[\frac{\partial \varsigma(s_n{}^0, C_a, S, s_n)}{\partial S} - \rho_b \frac{\partial \Psi_a^*}{\partial t} + \Psi_S^* \right] \\ &+ \left[\frac{\partial \varsigma(s_n{}^0, C_a, S, s_n)}{\partial S^0} + \frac{\partial}{\partial t}(\Psi_a^* n s_a \Psi_a) + \frac{\partial}{\partial t}(\Psi_a^* n C_a \Psi_n) \right. \\ &+ \frac{\partial}{\partial t}(\Psi_a^* \rho_b \Psi_S) + \boldsymbol{\nabla}\left(\Psi_a^* \underline{\mathbf{q}}^a \Psi_a \right) - \boldsymbol{\nabla}\left(\Psi_a^* \widetilde{\mathbf{D}}_h^a \boldsymbol{\nabla}\Psi_a \right) + \boldsymbol{\nabla}\left(\Psi_a \widetilde{\mathbf{D}}_h^a \boldsymbol{\nabla}\Psi_a^* \right) \\ &- \Psi_a^* \frac{\partial \widehat{k}}{\partial s_n{}^0}\left(C_a^{eq} - C_a \right) + \Psi_n^* \frac{\partial \widehat{k}}{\partial s_n{}^0}\left(C_a^{eq} - C_a \right) \\ &\left.\left. - \frac{\partial}{\partial t}(\Psi_n^* n\rho_n \Psi_n) \right] \right\} dVdt \end{aligned} \tag{B.13.26}$$

The arbitrary functions Ψ_a^*, Ψ_n^*, and Ψ_S^* are now defined in order to eliminate the state sensitivities of Ψ_a, Ψ_n, and Ψ_S, yielding:

$$\frac{\partial \varsigma(s_n{}^0, C_a, S, s_n)}{\partial C_a} - n s_a \frac{\partial \Psi_a^*}{\partial t} - \underline{\mathbf{q}}^a \boldsymbol{\nabla}\Psi_a^* - \boldsymbol{\nabla}\left(\widetilde{\mathbf{D}}_h^a \boldsymbol{\nabla}\Psi_a^* \right) + \widehat{k}\Psi_a^* - \widehat{k}\Psi_n^* - K_d \Psi_S^* = 0 \tag{B.13.27}$$

$$\frac{\partial \varsigma(s_n{}^0, C_a, S, s_n)}{\partial s_a} - nC_a \frac{\partial \Psi_a^*}{\partial t} + n\rho_n \frac{\partial \Psi_n^*}{\partial t} = 0 \tag{B.13.28}$$

$$\frac{\partial \varsigma(s_n{}^0, C_a, S, s_n)}{\partial S} - \rho_b \frac{\partial \Psi_a^*}{\partial t} + \Psi_S^* = 0 \tag{B.13.29}$$

Define $\tau = t_f - t$ as backward time, the governing equations of the adjoint states are:

$$\frac{\partial \varsigma(s_n{}^0, C_a, S, s_n)}{\partial C_a} + ns_a \frac{\partial \Psi_a^*}{\partial \tau} - \underline{\mathbf{q}^a} \nabla \Psi_a^* - \nabla(\widetilde{\mathbf{D}}_h^a \nabla \Psi_a^*) + \hat{k}\Psi_a^* - \hat{k}\Psi_n^* - K_d \Psi_S^* = 0 \tag{B.13.30}$$

$$\frac{\partial \varsigma(s_n{}^0, C_a, S, s_n)}{\partial s_a} + nC_a \frac{\partial \Psi_a^*}{\partial \tau} - n\rho_n \frac{\partial \Psi_n^*}{\partial \tau} = 0 \tag{B.13.31}$$

$$\frac{\partial \varsigma(s_n{}^0, C_a, S, s_n)}{\partial S} + \rho_b \frac{\partial \Psi_a^*}{\partial \tau} + \Psi_S^* = 0 \tag{B.13.32}$$

The marginal sensitivity turns out to be:

$$\begin{aligned}
\frac{dP}{ds_n{}^0} = \iint_{V,t} & \left[\frac{\partial \varsigma(s_n{}^0, C_a, S, s_n)}{\partial s_n{}^0} + \frac{\partial}{\partial t}(\Psi_a^* ns_a \Psi_a) + \frac{\partial}{\partial t}(\Psi_a^* nC_a \Psi_n) + \frac{\partial}{\partial t}(\Psi_a^* \rho_b \Psi_S) \right. \\
& + \nabla\left(\Psi_a^* \underline{\mathbf{q}^a} \Psi_a\right) - \nabla(\Psi_a^* \widetilde{\mathbf{D}}_h^a \nabla \Psi_a) + \nabla(\Psi_a \widetilde{\mathbf{D}}_h^a \nabla \Psi_a^*) \\
& - \Psi_a^* \frac{\partial \hat{k}}{\partial s_n{}^0}(C_a^{eq} - C_a) + \Psi_n^* \frac{\partial \hat{k}}{\partial s_n{}^0}(C_a^{eq} - C_a) \\
& \left. - \frac{\partial}{\partial t}(\Psi_n^* n\rho_n \Psi_n) \right] dVdt
\end{aligned} \tag{B.13.33}$$

Boundary conditions of the forward flow and transport equations are

$$-(\mathbf{K}\nabla h) \cdot \vec{n} = 0 \text{ on } \Gamma_1 \tag{B.13.34}$$

$$-(\widetilde{\mathbf{D}}_h^a \nabla C_a) \cdot \vec{n} = 0 \text{ on } \Gamma_1 \tag{B.13.35}$$

$$-\left(\widetilde{\mathbf{D}}_h^a \nabla C_a - \underline{\mathbf{q}^a} C_a\right) \cdot \vec{n} = g(\mathbf{x}, t) \text{ on } \Gamma_2 \tag{B.13.36}$$

Differentiate the boundary equations with respect to $s_n{}^0$:

$$-\frac{\partial}{\partial s_n{}^0}(\widetilde{\mathbf{D}}_h^a \nabla C_a) \cdot \vec{n} = \left[-\widetilde{\mathbf{D}}_h^a \nabla \Psi_a\right] \cdot \vec{n} = 0 \tag{B.13.37}$$

$$-\frac{\partial}{\partial s_n{}^0}\left(\widetilde{\mathbf{D}}_h^a \nabla C_a - \underline{\mathbf{q}^a} C_a\right) \cdot \vec{n} = -\left[\widetilde{\mathbf{D}}_h^a \nabla \Psi_a - \underline{\mathbf{q}^a} \Psi_a\right] \cdot \vec{n} = 0 \tag{B.13.38}$$

Take an inner product of Ψ_a^* with (37) and integrate:

$$\iint_{V,t} -\nabla\left[\Psi_a^* \widetilde{\mathbf{D}}_h^a \nabla \Psi_a\right] dVdt = 0 \tag{B.13.39}$$

Take an inner product of Ψ_a^* with (38) and integrate:

$$\iint_{V,t} -\nabla \left[\Psi_a^* \widetilde{\mathbf{D}}_h^a \nabla \Psi_a - \Psi_a^* \underline{\mathbf{q}}^a \Psi_a\right] dVdt = 0 \tag{B.13.40}$$

The initial conditions of adjoint states are defined as:

$$\Psi_a^*(\tau = 0) = \Psi_n^*(\tau = 0) = \Psi_S^*(\tau = 0) = 0 \tag{B.13.41}$$

Then:

$$\frac{\partial}{\partial t}(\Psi_a^* n s_a \Psi_a), \frac{\partial}{\partial t}(\Psi_a^* \rho_b \Psi_S), \frac{\partial}{\partial t}(\Psi_n^* n \rho_n \Psi_n) \text{ terms vanish}$$

$$\iint_{V,t} \left[\frac{\partial}{\partial t}(\Psi_a^* n C_a \Psi_n)\right] dVdt = \int_V \left[\Psi_a^* n C_a \Psi_n|_{t=t_f} - \Psi_a^* n C_a \left.\frac{\partial s_n^0}{\partial s_n^0}\right|_{t=0}\right] dV$$

$$= \int_V [\Psi_a^*(t = 0) n C_a(t = 0)] dV \tag{B.13.42}$$

$$\iint_{V,t} \left[\frac{\partial}{\partial t}(\Psi_n^* n \rho_n \Psi_n)\right] dVdt = \int_V \left[\Psi_n^* n \rho_n \Psi_n|_{t=t_f} - \Psi_n^* n \rho_n \left.\frac{\partial s_n^0}{\partial s_n^0}\right|_{t=0}\right] dV$$

$$= \int_V [\Psi_n^*(t = 0) n \rho_n] dV \tag{B.13.43}$$

The boundary conditions of adjoint states are defined as:

$$-\left(\widetilde{\mathbf{D}}_h^a \nabla \Psi_a^* + \underline{\mathbf{q}}^a \Psi_a^*\right) \cdot \vec{n} = 0 \text{ on } \Gamma_1 \tag{B.13.44}$$

$$\left(\widetilde{\mathbf{D}}_h^a \nabla \Psi_a^*\right) \cdot \vec{n} = 0 \text{ on } \Gamma_2 \tag{B.13.45}$$

The final expression of marginal sensitivity becomes:

$$\frac{dP}{ds_n^0} = \int_V [\Psi_a^*(t = 0) n C_a(t = 0) - \Psi_n^*(t = 0) n \rho_n] dV$$

$$+ \iint_{V,t} \left[\frac{\partial \hat{k}}{\partial s_n^0}(C_a^{eq} - C_a) + \frac{\partial \hat{k}}{\partial s_n^0}(C_a^{eq} - C_a)(\Psi_n^* - \Psi_a^*)\right] dVdt \tag{B.13.46}$$

VIII.C. List of Scientific/Technical Publications

VIII.C.1. Articles in Peer-Reviewed Journals

Arshadi, M., De Paolis Kaluza, M. C., E. L. Miller, and L.M. Abriola. (2019). Subsurface Source Zone Characterization and Uncertainty Quantification Using Discriminative Random Fields. Submitted to *Water Resour. Res.*

Boroumand, A., and L. M. Abriola (2015). On the upscaling of mass transfer rate expressions for interpretation of source zone partitioning tracer tests, *Water Resour. Res.*, 51, 832–847, doi: 10.1002/2014WR015767.

Cápiro, N.L., F.E. Löffler and K.D. Pennell. (2015). "Spatial and Temporal Dynamics of Organohalide-Respiring Bacteria in a Heterogeneous PCE-DNAPL Source Zone." *Journal of Contaminant Hydrology.* 182, pp. 78-90. doi: 10.1016/j.jconhyd.2015.08.007

De Paolis Kaluza, M. C., E. L. Miller, and L.M. Abriola. (2015). Markov random field models for quantifying uncertainty in subsurface remediation, in IEEE International Geoscience and Remote Sensing Symposium, pp.4296-4299, 26-31 July 2015, doi: 10.1109/IGARSS.2015.7326776.

Elenius, M.T. and L.M. Abriola. (2019). Regressed models for multi-rate mass transfer in heterogeneous media. submitted.

Phelan, T. J., Abriola, L. M., Gibson, J. L., Smits, K. M., and Christ, J. A. (2015). "Development and application of a screening model for evaluating bioenhanced dissolution in DNAPL source zones." Journal of Contaminant Hydrology, 183, 1–15.

Yang, L., X. Wang, I. Mendoza-Sanchez, and L.M. Abriola. (2018). Modeling the influence of coupled mass transfer processes on chlorinated solvent plume persistence in heterogeneous source zones. *Journal of Contaminant Hydrology*, 211, pp. 1-14. doi:10.1016/j.jconhyd.2018.02.003.

Zhang, H., Mendoza-Sanchez, I., Miller, E. L., and Abriola, L. M. (2016). "Manifold Regression Framework for Characterizing Source Zone Architecture." *IEEE Transactions on Geoscience and Remote Sensing*, 54(1), 3–17.

VIII.C.2. Technical Reports

Yang, L. Exploring the Influence of Sorption and Back Diffusion on Dense Nonaqueous Phase Liquid (DNAPL) Source Zone Plume Persistence in Heterogeneous Formations. *Master's Thesis, Tufts University, Civil and Environmental Engineering.* 2015.

VIII.C.3. Conference or Symposium Abstracts

Abriola, L.M., Cápiro, N.L., Christ, J.A., Chu, L.L., Miller, E. and Pennell, K.D. Development of an integrated field test/modeling protocol for efficient in situ bioremediation design and performance uncertainty assessment. Poster presented at SERDP and ESTCP Workshop on the Long Term Management of Contaminated Groundwater Sites, August 13-14, 2013, Arlington, VA.

Arshadi, M., L.M. Abriola, E.L. Miller, C.D.P. Kaluza. Discriminative Random Field Models for Subsurface Source Zone Characterization and Uncertainty Quantification. Accepted for Presentation at Interpore 10th Annual Meeting, New Orleans, LA, May 14-17, 2018.

Arshadi, M., L.M. Abriola, E.L. Miller, and C.D.P. Kaluza. Discriminative Random Field Models for Subsurface Contamination Uncertainty Quantification. Poster presentation at *American Geophysical Union 2017 Fall Meeting*, New Orleans, LA, December 11-15, 2017.

Elenius, M.T, E.L. Miller and L.M. Abriola. Assessing the Impacts of Multi-Rate Mass Transfer and Sorption in Heterogeneous Media. Talk given at Society of Industrialized and Applied Mathematics (SIAM) 2015 Geosciences Meeting, Stanford, CA, July 1, 2015.

Elenius, M.T, E.L. Miller and L.M. Abriola. Source Zone Mass Depletion with Multi-Rate Mass Transfer in Heterogeneous Media. Invited talk given at Uni Research, Bergen, Norway, January 7, 2015.

Elenius, M.T, E.L. Miller and L.M. Abriola. Assessing Source Zone Mass Depletion in Heterogeneous Media: Application of a Multi-Rate Mass Transfer Approach Based on a Geostatistical Medium Description. Poster presented at American Geophysical Union 2014 Fall Meeting, San Francisco, CA, December 15-19, 2014.

Hnatko, J.P., L. Yang, L.M. Abriola, and N.L. Cápiro. Bioenhanced diffusion and dynamics of Dehalococcoides mccartyi strains in heterogeneous porous media. Presentation submittal to American Chemical Society National Meeting Division of Geochemistry, Boston, MA, August 19-23, 2018.

Hnatko, J.P., L. Yang, J.L. Elsey, L.M. Abriola, N.L. Cápiro, L. Chu, J.A. Christ, and K.D. Pennell. Comparison of Microbial Reductive Dechlorination Rates Observed at Laboratory and Field Scale. Poster presentation at SERDP and ESTCP Symposium, Washington, D.C, November 28, 2017.

Hnatko, J.P., L. Yang, J.L. Elsey, T. Tang, M. Arshadi, J.A. Christ, K.D. Pennell, N.L. Cápiro, and L.M. Abriola. Comparison of chlorinated solvent dichlorination rates across batch- laboratory- and pilot-scales. Poster presentation submittal to SERDP and ESTCP Symposium, Washington, D.C, November 27-29, 2018.

Hnatko, J.P., L. Yang, J.L. Elsey, T. Tang, M. Arshadi, K.D. Pennell, J.A. Christ, N.L. Cápiro, and L.M. Abriola. Comparison of Microbial Reductive Dechlorination Rates Observed at Laboratory and Field Scale. Poster presentation submittal to American Chemical Society National Meeting Division of Environmental Chemistry, Boston, MA, August 19-23, 2018.

Hnatko, J.P., L. Yang, K.D. Pennell, L.M. Abriola, and N.L. Cápiro. Bioenhanced Diffusion and Dynamics of Dehalococcoides mccartyi strains in Heterogeneous Porous Media. Poster presentation at Gordon Research Conference on Environmental Sciences: Water, Holderness, NH, June 24-29, 2018.

Phelan, T. J., L. M. Abriola, J. L. Gibson, K. M. Smits, and J. A. Christ. Laboratory Assessment of a Screening Model: Exploring the Coupling between Dissolution and Degradation Rates in Ganglia-Dominated Source Zones (Abstract H44C-05). Talk given at American Geophysical Union 2014 Fall Meeting, San Francisco, CA, December 18, 2014.

Tang, T., M. Arshadi, M.C.D.P. Kaluza, E.L. Miller, and L.M. Abriola. Source Zone Characterization Methods and Tools Development; First-Order Second-Moment Model for Source Zone Sampling Optimization. Poster presentation submittal to SERDP and ESTCP Symposium, Washington, D.C, November 27-29, 2018.

Tang, T., M. Arshadi, E.L. Miller, and L.M. Abriola. Hybrid machine learning/adjoint sensitivity model for source zone sampling optimization. Accepted for Presentation at Interpore 10th Annual Meeting, New Orleans, LA, May 14-17, 2018.

Tang, T., M. Arshadi, L. Yang, L.M. Abriola, N.L. Cápiro, J.A. Christ, E.L. Miller, and K.D. Pennell. Source Zone Characterization Methods and Tools Development; Sensitivity Analysis and

Uncertainty Quantification. Poster presentation at SERDP and ESTCP Symposium, Washington, D.C, November 28, 2017.

Tang, T., Boroumand, A., Abriola, L.M., and Miller, E.L. A coupled protocol for push-pull sensitivity analysis and inversion of source zone characterization. Poster presented at American Geophysical Union 2013 Fall Meeting, December 9-13, 2013, San Francisco, CA.

Tang, T., E.L. Miller and L.M. Abriola. Exploring mass flux response to local source zone properties using a coupled-process adjoint sensitivity method. Poster presentation at *American Geophysical Union 2016 Fall Meeting*, San Francisco, CA, December 12-16, 2016.

Yang, L. and L.M. Abriola. Modeling the influence of coupled mass transfer processes on chlorinated solvent plume persistence in heterogeneous source zones. Oral presentation at *American Geophysical Union 2016 Fall Meeting*, San Francisco, CA, December 12-16, 2016.

Yang, L. and Abriola, L.M. Modeling chlorinated solvent persistence due to back diffusion from low-permeability strata in heterogeneous aquifers. Poster presented at American Geophysical Union 2013 Fall Meeting, December 9-13, 2013, San Francisco, CA.

Zhang, H., I. Mendoza-Sanchez, J. Christ, L.M. Abriola, K. Pennell, and E.L. Miller. DNAPL Source Zone Characterization Using Machine Learning. *Battelle Ninth International Conference on Remediation of Chlorinated and Recalcitrant Compounds*. Monterey, CA, May 19-22, 2014.

Zhang, H., E.L. Miller and L.M. Abriola. Manifold Regression for Subsurface Contaminant Characterization based on Sparse Concentration Data. Talk given at *35th Annual IEEE Geoscience and Remote Sensing Society Symposium*, Québec, Canada, July 13-18, 2014.